IDENTIFICATION OF ACTIONABLE DRUG TARGETS IN TRIPLE-NEGATIVE BREAST CANCER

A DISSERTATION SUBMITTED TO

THE GRADUATE SCHOOL OF ENGINEERING AND SCIENCE

OF BILKENT UNIVERSITY

IN PARTIAL FULFILLMENT OF THE REQUIREMENTS FOR

THE DEGREE OF

DOCTOR OF PHILOSOPHY

IN

MOLECULAR BIOLOGY AND GENETICS

By

Ünal Metin Tokat

September 2022

IDENTIFICATION OF ACTIONABLE DRUG TARGETS IN TRIPLE-NEGATIVE BREAST CANCER

By Ünal Metin Tokat

September 2022

We certify that we have read this dissertation and that in our opinion it is fully adequate in scope and in quality, as a thesis for the degree of Doctor of Philosophy.

_____

Serkan İsmail Göktuna

(Advisor)

_____

Ayşe Elif Erson Bensan

_____

Onur Çizmecioğlu

_____

Tolga Can

_____

Urartu Özgür Şafak Şeker

Approved for Graduate School of Engineering and Science

_____

Orhan Arıkan

Director of the Graduate School of Engineering and Science

ABSTRACT

IDENTIFICATION OF ACTIONABLE DRUG TARGETS IN TRIPLE-NEGATIVE BREAST CANCER

Ünal Metin TOKAT

Ph.D. in Molecular Biology and Genetics

Advisor: Serkan İsmail Göktuna

September 2022

Triple-negative breast cancer (TNBC) is the most aggressive subtype of the breast cancer, representing 15-20% of all cases. Due to a lack of clinically available/approved targeted therapies, TNBC patients are still in desperate need of chemotherapy. Although TNBC patients initially have relatively high rates of response to chemotherapy, de novo and acquired resistance constitute a major problem, leading to worsened patient outcomes. Considering the initial high response rates and broad availability and affordability of the chemotherapy agents, it is of great utility to explore the molecular mechanisms driving or contributing to de novo and acquired chemoresistance. Therefore, I developed 9 acquired resistant cell lines and 3 acquired resistant xenografts and harnessed 4 de novo TNBC chemoresistance models to identify the resistance-driving factors for each chemotherapy class/agent. Following characterization of these models in comparison to their parental counterparts at protein level, I determined few candidate proteins involved in chemoresistance. By combining experimental and bioinformatic approaches, I showed translational potential of i) p38 and JNK MAPK, and PI3K/AKT inhibitors, and ER stress inducers in de novo and acquired resistance against antimetabolite

chemotherapy agents such as gemcitabine and fluorouracil; ii) dual EGFR/HER2, EGFR, SRC and CDK1 inhibitors against an antimicrotubule agent, paclitaxel; iii) FAK and dual PI3K/mTOR inhibitors against an alkylating chemotherapy agent, cisplatin, and iv) FAK, SRC and PI3K/AKT inhibitors against a topoisomerase II inhibitor, doxorubicin. I further observed that molecular underpinnings of de novo and acquired resistance were largely overlapping albeit not the same. We have also investigated cross chemotherapy resistance patterns in each acquired cell line model, which can guide second- or third-line treatment selection. As a result, I present a rational approach to exploit chemotherapy-small molecule inhibitor combinations for previously untreated or treated TNBC patients. In other words, using low-dose chemotherapy and targeted therapy combinations we provide promising preclinical in vitro data for future in vivo testing.

Keywords: triple-negative breast cancer, chemotherapy, de novo resistance, acquired resistance, cell line model, animal model, targeted therapy, chemotherapy-targeted therapy combination, chemotherapy-targeted therapy synergy, cross chemoresistance

ÖZET

ÜÇLÜ NEGATİF MEME KANSERİNDE HEDEFLENEBİLİR ADAYLARIN BELİRLENMESİ

Ünal Metin TOKAT

Moleküler Biyoloji ve Genetik, Doktora

Tez Danışmanı: Serkan İsmail Göktuna

Eylül 2022

Üçlü/triple negatif meme kanseri (TNMK) en agresif meme kanseri alt türü olup tüm vakaların %15-20'sini temsil etmektedir. Klinik kullanımı onaylanmış hedefli terapilerin azlığından dolayı, bu hastalar hala kemoterapi ile tedavi edilmektedir. TNMK hastaları başlangıçta, diğer meme kanseri alt türlerine kıyasla, kemoterapiye daha yüksek oranda yanıt verse de birincil ve kazanılmış kemoterapi direnci yüzünden tedavi başarısı azalmakta ve hastalar olumsuz olarak etkilenmektedir. Bu yüksek yanıt oranıyla birlikte kemoterapi ilaçlarının yaygın/ulaşılabilir ve görece uygun maliyetli oluşu göz önüne alındığında, birincil ve kazanılmış dirence yol açan ya da katkı sağlayan moleküler mekanizmaların ortaya konulması hala önem teşkil etmektedir. Bu bağlamda, dirence yol açan faktörleri belirlemek için, projemizde 9 kazanılmış direnç hücre ve 3 kazanılmış direnç ksenograft modeli geliştirip 4 de novo direnç hücre modeli kullandım. Modelleri köken aldıkları parental hücrelere kıyaslayarak protein seviyesinde karakterizasyonlarını gerçekleştirdim ve kemoterapi direncinden sorumlu bazı aday proteinleri saptadım. Deneysel ve biyoinformatik metotları harmanlayarak i) antimetabolitler gemsitabin ve 5-fluorourasil için ER stres

indükleyicileri ile p38 ve JNK MAPK ve PI3K/AKT; ii) anti-mikrotübül ajan paclitaksel için ikili EGFR/HER2, EGFR, SRC ve CDK1; iii) alkilleyici ajan sisplatin için FAK ve ikili PI3K/mTOR ve iv) topoizomeraz II inhibitörü doksorubisin için FAK, SRC ve PI3K/AKT inhibitörlerinin birincil ve kazanılmış direnç konusunda kliniğe uygulanabilirliğini gösterdim. Akabinde, birincil ve kazanılmış direncin temelinde yer alan moleküler faktörlerin büyük oranda örtüştüğünü ancak tamamıyla aynı olmadığını gözlemledim. Bunun yanı sıra, ikinci ve üçüncü sıra tedavi seçiminde yol gösterebileceği düşüncesi ile kazanılmış direnç hücre modellerinin diğer sınıflara ait kemoterapi ajanlarına yanıt ve direnç durumunu inceledim. Sonuç olarak, daha önce başka tedavi almış ya da almamış TNMK hastalarının tedavisi için kemoterapi-küçük molekül inhibitör kombinasyonlarından nasıl faydalanılabileceğini rasyonel bir yaklaşımla ortaya koydum. Diğer bir ifadeyle, düşük dozda kemoterapi ve hedefli terapi kombinasyonları kullanarak gelecekteki in vivo testler için umut vadeden klinik öncesi in vitro veriler sundum.

Anahtar Kelimeler: üçlü negatif meme kanseri, kemoterapi, birincil direnç, kazanılmış direnç, hücre hattı modeli, hayvan modeli, hedefli terapi, kemoterapi-hedefli terapi kombinasyonu, kemoterapi-hedefli terapi sinerjisi, çapraz kemoterapi direnci

To my brother

ACKNOWLEDGEMENTS

I would like to express my deepest gratitude to *Dr. Özgür Şahin* for providing me with the opportunity to fulfill my curiosity in science and supervising my doctoral studies until August 2018. I am truly grateful that his scientific mentality and encouraging remarks have tremendously helped shaping my scientific personality.

I am extremely grateful to *Dr. Serkan İsmail Göktuna*, my second and current Ph.D. advisor. His understanding and patient nature has immensely facilitated the progression of my project by providing a comfortable and peaceful working environment.

I would also like to extend my sincere thanks to all the members of the defense committee, *Dr. Ayşe Elif Erson Bensan*, *Dr. Onur Çizmecioğlu*, *Dr. Tolga Can* and *Dr. Urartu Özgür Şafak Şeker*. They have generously shared insightful comments, knowledge and expertise not only in my thesis defense but on many an occasion over the years.

This endeavor would not have been possible without the generous support from *The Scientific and Technological Research Council Of Turkey (TÜBİTAK)* through 2211/A General Domestic Doctorate Scholarship Program.

Words cannot express my appreciation to *Barış Küçükkaraduman*, who has been my teaching assistant, my friend and my brother all these years, and to *İrem Evcili*, who has always been by my side and kept me motivated by making me believe in myself.

I will always remember and cherish all the treasured memories we had, and you will forever be part of my heart and family.

I could not have undertaken this journey without my close friends, İbrahim Oğuzhan Tarman, Pelin Gülizar Ersan, Nevin Belder, Özge Akbulut, Erol Eyüpoğlu, Özge Saatci, Ege Dedeoğlu and Aybüke Işık. Their mental and emotional uplift has helped me survive tough times. I will always miss the joyous time we spent together in and outside of the lab.

I would also like to acknowledge all the former members of Özgür Şahin Lab: Umar Raza, Hilal Bal, Ridho Assidicky, Rasmi Mishra, Suhail Ansari, Özlem Şener Şahin, Merve Mutlu, Selvi Durmuş Erim, and Emre Yurdusev.

I am also thankful to *my professors*, Dr. İhsan Gürsel, Dr. Murat Alper Cevher and Dr. Ali Osmay Güre, and *my friends* at the MBG lab, Aslı Gülce Bartan, Tuğçe Bildik, Muzaffer Yıldırım, İrem Abraş, Yasemin Ceylan, Melike Dinççelik Aslan, Volkan Aslan, Seniye Targen, Erta Xhafa, Waqas Akbar, Havva Kılgöz, Naz Bozbeyoğlu, Yücehan Yazıcı and Berfu Saraydar. Thanks should also go to the former and current staff of the Department of Molecular Biology and Genetics as well as senior students and interns that contributed to multiple projects in our laboratory.

Lastly, I would be remiss in not mentioning my whole family. Their boundless and unconditional support is what has made all this possible. You have been amazing, and I would like to offer my biggest thanks and appreciation to you.

TABLE OF CONTENTS

ABSTRACT ii

ÖZET iv

ACKNOWLEDGEMENTS vii

TABLE OF CONTENTS ix

LIST OF FIGURES xiii

LIST OF TABLES xx

ABBREVIATIONS xxi

CHAPTER 1 1

INTRODUCTION 1

1.1 Cancer 1

1.2 Breast Cancer 3

1.2.1 HER2-Enriched Breast Cancer 5

1.2.2 Hormone Receptor (HR) Positive Breast Cancer 6

1.3 Triple-Negative Breast Cancer (TNBC) 7

1.3.1 Treatment Approaches and Therapy Resistance in TNBC 7

1.3.2 Triple-Negative Breast Cancer Heterogeneity and Subtypes 10

1.3.2.1 Immunohistochemistry-based Classifications 10

1.3.2.2 Transcriptome-based Classifications 12

1.3.2.3 Other Classification Strategies 18

1.4 Chemotherapy Agents Used in TNBC and Their Classification 20

1.4.1 Alkylating Agents 21

1.4.2 Antimetabolites 23

1.4.3 Anti-tumor Antibiotics 24
1.4.4 Plant Alkaloids (Mitotic Inhibitors) 25
1.4.5 Topoisomerase Inhibitors 26
1.5 Rationale and Aims of the Study 28
CHAPTER 2 29
MATERIALS AND METHODS 29
2.1 Materials 29
2.1.1 Buffers 29
2.1.2 Chemicals and Reagents 31
2.1.3 Media and Supplements 33
2.1.4 Kits 34
2.1.5 Equipment 35
2.1.6 Consumables 36
2.2 Methods 37
2.2.1 Cell Culture 37
2.2.1.1 Cell Line Maintenance 37
2.2.1.2 Development of Chemoresistant Cell Lines 38
2.2.1.3 Cryopreservation 39
2.2.2 Cell-based Assays 39
2.2.2.1 Drug Treatment and Cell Viability Assays 39
2.2.2.2 Annexin V/PI Staining and Flow Cytometry 41
2.2.3 Protein Biochemistry 42
2.2.3.1 Protein Isolation 42
2.2.3.2 Protein Quantification 43

2.2.3.3 Sodium Dodecyl Sulfate Polyacrylamide Gel Electrophoresis (SDS-PAGE) 44
2.2.3.4 Western Blotting 46
2.2.4 Animal Studies 50
2.2.4.1 Primary Xenografts 50
2.2.4.2 Development of Chemoresistant Xenografts 51
2.2.5 Bioinformatics 52
2.2.5.1 Gene Set Enrichment Analysis (GSEA) 52
2.2.5.2 Survival Analysis 52
2.2.6 Statistical Analysis 53
CHAPTER 3 54
RESULTS 54
3.1 Antimetabolite Resistance Models 54
3.2 Plant Alkaloid (Mitotic Inhibitor) Resistance Models 82
3.3 Alkylating Agent Resistance Models 107
3.4 Anti-tumor Antibiotic Resistance Models 119
3.5 HIF1-alpha/miR-326/ITGA5 axis in TNBC Doxorubicin Resistance 134
3.6 Overcoming Tamoxifen Resistance in ER-Positive Breast Cancer by PDE4D Inhibition 142
CHAPTER 4 145
DISCUSSION 145
4.1 TNBC Heterogeneity and Chemotherapy Resistance 145
4.2 Mechanisms of Resistance to Antimetabolites in TNBC 147
4.3 Mechanisms of Resistance to Plant Alkaloids in TNBC 151
4.4 Mechanisms of Resistance to Alkylating Agents in TNBC 154

4.5 Mechanisms of Resistance to Anti-tumor Antibiotics in TNBC 157
FUTURE PERSPECTIVES 160
BIBLIOGRAPHY 164
CHAPTER 5 181
APPENDIX 181
5.1 Copyright Permissions 181

LIST OF FIGURES

Figure 1.1. Estimated numbers of new cancer cases and deaths by sex in the USA in 2022 1

Figure 1.2. The most frequent causes of death as proportions of total deaths by country income level 2

Figure 1.3. TNBC and basal-like breast cancers are not identical though quite overlapping 8

Figure 1.4. Transcriptome-based TNBC classifications 16

Figure 1.5. Different approaches to TNBC classification by use of distinct data types 19

Figure 1.6. Some chemotherapy agent classes and their mechanism of action 27

Figure 3.1. Gemcitabine response of a panel of TNBC cell lines representing different subtypes 55

Figure 3.2. 5-FU response of a panel of TNBC cell lines representing different subtypes 56

Figure 3.3. The response of the selected TNBC cell line panel to gemcitabine after 72h drug treatment as determined by cell viability assays 57

Figure 3.4. The response of the selected TNBC cell line panel to fluorouracil after 72h drug treatment as determined by cell viability 58

Figure 3.5. Development of CAL-51 gemcitabine-resistant and CAL-51 fluorouracil-resistant cells 59

Figure 3.6. Changes in the PI3K/AKT/mTOR pathway components upon resistance development 61

Figure 3.7. Changes in the Integrin, MAPK and STAT3 pathway components upon resistance development 62

Figure 3.8. Changes in the ER stress markers and cell cycle-related proteins upon resistance development 63

Figure 3.9. p38 and JNK inhibitors could overcome antimetabolite resistance in TNBC, as shown by cell viability assay 64

Figure 3.10. p38 and JNK inhibitors could reverse gemcitabine resistance in TNBC, as shown by microscopy 65

Figure 3.11. p38 and JNK inhibitors could overcome fluorouracil resistance in TNBC, as shown by microscopy 66

Figure 3.12. p38 and JNK inhibitors could abrogate gemcitabine resistance in CAL-51 GemR model, as shown by Annexin V/PI staining 68

Figure 3.13. PI3K and AKT inhibitors could reverse antimetabolite resistance in TNBC, as shown by cell viability assay 69

Figure 3.14. PI3K and AKT inhibitors could overcome gemcitabine resistance in TNBC, as shown by microscopy 70

Figure 3.15. PI3K and AKT inhibitors could reverse fluorouracil resistance in TNBC, as shown by microscopy 71

Figure 3.16. PI3K and AKT inhibitors could overcome gemcitabine resistance in CAL-51 GemR model, as shown by Annexin V/PI staining 72

Figure 3.17. AKT and p38 inhibitors could induce mitotic arrest when combined with gemcitabine 73

Figure 3.18. Chloroquine, an ER stress inducer, could reverse antimetabolite resistance in TNBC, as shown by cell viability assay 74

Figure 3.19. Mitosis inhibitors could abrogate antimetabolite resistance in TNBC, as shown by cell viability assay 74

Figure 3.20. 5-gene expression predicts worse relapse-free survival in both adjuvant chemotherapy-treated TNBC and basal-like patients 75

Figure 3.21. p38 and JNK inhibitors could overcome de novo antimetabolite resistance in TNBC, as shown by cell viability assay 76

Figure 3.22. PI3K and AKT inhibitors could overcome de novo antimetabolite resistance in TNBC, as shown by cell viability assay 77

Figure 3.23. Thapsigargin could reverse de novo antimetabolite resistance in TNBC, as shown by cell viability assay 78

Figure 3.24. Normal breast epithelial cells have reduced response to antimetabolite chemotherapy 79

Figure 3.25. CAL-51 GemR and FUR show cross resistance to other antimetabolite chemotherapy agents 80

Figure 3.26. Response of CAL-51 GemR and CAL-51 FUR cells to other classes of chemotherapy 81

Figure 3.27. Paclitaxel response of the TNBC cell line panel 83

Figure 3.28. Paclitaxel response of the TNBC cell line panel, measured by cell viability assay 84

Figure 3.29. Development of CAL-51 and MDA-MB-157 paclitaxel-resistant cells 85

Figure 3.30. Differences in the PI3K/AKT/mTOR pathway components between the parental and paclitaxel-resistant cells 86

Figure 3.31. Differences in the Integrin and MAPK signaling components between the parental and paclitaxel-resistant cells 88

Figure 3.32. Extracellular matrix-related processes could contribute to paclitaxel resistance 88

Figure 3.33. Differences in the ER stress, autophagy, cell cycle and DNA damage markers between the parental and paclitaxel-resistant cells 89

Figure 3.34. Dual EGFR/HER2 or EGFR inhibitors could abolish paclitaxel resistance in TNBC, as shown by cell viability assay 89

Figure 3.35. SRC and FAK inhibitors could reverse paclitaxel resistance in TNBC, as shown by cell viability assay 91

Figure 3.36. SRC and EGFR inhibitors could overcome paclitaxel resistance in TNBC, as shown by microscopy 92

Figure 3.37. SRC and EGFR/HER2 inhibitors could abrogate paclitaxel resistance, as shown by Annexin V/PI staining 92

Figure 3.38. EGFR inhibitor could overcome paclitaxel resistance, as shown by Annexin V/PI staining 93

Figure 3.39. CDK1 inhibitor and general CDK inhibitor or TGF-beta could reverse paclitaxel resistance in TNBC, as shown by cell viability assay 94

Figure 3.40. CDK1 inhibitor and general CDK inhibitor could overcome paclitaxel resistance in TNBC, as shown by microscopy 95

Figure 3.41. CDK1 inhibitor or TGF-beta could reverse paclitaxel resistance in the MDA-MB-157 PtxR cells, as shown by Annexin V/PI staining 96

Figure 3.42. Synergism between the Paclitaxel and the Selected Inhibitors 97

Figure 3.43. The phenotype observed upon Saracatinib or Gefitinib treatment 98

Figure 3.44. 3-gene expression predicts worse relapse-free survival in both adjuvant chemotherapy-treated TNBC and basal-like patients 99

Figure 3.45. SRC, EGFR, and CDK1 inhibitors could reverse paclitaxel resistance in TNBC, as shown by cell viability assay 100

Figure 3.46. SRC and EGFR inhibitors could counteract paclitaxel resistance in TNBC, as shown by microscopy 101

Figure 3.47. SRC and EGFR inhibitors could abrogate paclitaxel resistance, as shown by Annexin V/PI staining 102

Figure 3.48. Development of in vivo paclitaxel-resistant xenografts with MDA-MB-231-luc2-GFP cells 103

Figure 3.49. Characterization of paclitaxel-resistant and -sensitive MDA-MB-231-luc2-GFP xenografts by Western Blot 104

Figure 3.50. Normal breast epithelial cells have reduced response to paclitaxel 104

Figure 3.51. CAL-51 PtxR cells are also resistant to docetaxel, another taxane 105

Figure 3.52. Cross chemotherapy response of the PtxR cell line models to antimetabolite chemo agents 106

Figure 3.53. Cross chemotherapy response of the PtxR cell line models to cisplatin and doxorubicin 107

Figure 3.54. Cisplatin response of the TNBC cell line panel 108

Figure 3.55. Cisplatin response of the TNBC cell line panel, measured by cell viability assay 109

Figure 3.56. Development of MDA-MB-436 and HCC1937 cisplatin-resistant cells 110

Figure 3.57. Differences in the PI3K/AKT/mTOR pathway components between the parental and cisplatin-resistant cells 111

Figure 3.58. Differences in the integrin, MAPK and STAT3 pathway components between the parental and cisplatin-resistant cells 112

Figure 3.59. Differences in the ER stress and autophagy markers and cell cycle proteins between the parental and cisplatin-resistant cells 113

Figure 3.60. PF-562271 and ATN-161 could not synergistically potentiate cisplatin response in TNBC, as shown by cell viability assay 114

Figure 3.61. The effect of p38, CDK1 or dual PI3K/mTOR inhibitors in cisplatin response in TNBC, as shown by cell viability assay 115

Figure 3.62. The selected inhibitors could not also abrogate de novo cisplatin resistance 116

Figure 3.63. Normal breast epithelial cells have reduced response to cisplatin relative to TNBC cell lines 116

Figure 3.64. The cisplatin-resistant cells are not cross resistant to oxaliplatin 117

Figure 3.65. Cross chemotherapy response of the CisR cell line models to gemcitabine and 5-FU 118

Figure 3.66. Cross chemotherapy response of the PtxR cell line models to paclitaxel and doxorubicin 119

Figure 3.67. Doxorubicin response of the TNBC cell line panel 120

Figure 3.68. Doxorubicin response of the TNBC cell line panel, measured by cell viability assay 121

Figure 3.69. Development of CAL-51 doxorubicin-resistant cells 122

Figure 3.70. Development of MDA-MB-231 doxorubicin-resistant cells 123

Figure 3.71. Differences in the PI3K/AKT/mTOR and integrin pathway components between the parental and doxorubicin-resistant cells 123

Figure 3.72. Differences in the MAPK signaling, ER stress, autophagy and cell cycle components between the parental and doxorubicin-resistant cells.....124

Figure 3.73. The effect of SRC and FAK inhibitors in doxorubicin response in TNBC, as shown by cell viability assay.....125

Figure 3.74. The effect of PI3K and AKT inhibitors in doxorubicin response in TNBC, as shown by cell viability assay.....126

Figure 3.75. The effect of SRC, FAK, PI3K and AKT inhibitors in de novo doxorubicin resistance in TNBC, as shown by cell viability assay.....127

Figure 3.76. FAK, SRC and AKT inhibitors could reverse de novo doxorubicin resistance in TNBC, as shown by microscopy 128

Figure 3.77. FAK, SRC and AKT inhibitors could counteract de novo doxorubicin resistance, as shown by Annexin V/PI staining.....128

Figure 3.78. Development of in vivo doxorubicin-resistant xenografts using MDA-MB-231LG cells 129

Figure 3.79. Development of in vivo doxorubicin-resistant xenografts using CAL-51 cells.....130

Figure 3.80. Characterization of in vivo doxorubicin-resistant CAL-51 xenografts at protein level 131

Figure 3.81. The response of normal breast epithelial cells to doxorubicin.....131

Figure 3.82. Cross chemotherapy response of the CAL-51 DoxoR model to Irinotecan 132

Figure 3.83. Cross chemotherapy response of the CAL-51 DoxoR model to other chemotherapy classes.....133

Figure 3.84. Project outline and analysis pipeline to find potential chemoresistance drivers in TNBC 135

Figure 3.85. Expression of miR-326 in TNBC patients and correlation of miR-326 or its target score with survival 136

Figure 3.86. miR-326 has a conserved target site in ITGA5 and could downregulate ITGA5 at protein level 137

Figure 3.87. miR-326 or shITGA5 could potentiate chemotherapy response in TNBC 138

Figure 3.88. Both miR-326 expression and ITGA5 knockdown could impair integrin signaling in vitro 139

Figure 3.89. Both miR-326 expression and ITGA5 knockdown could impair integrin signaling in vivo 139

Figure 3.90. HIF1A could downregulate miR-326 and thus contributes to chemoresistance 140

Figure 3.91. Doxorubicin resistance is driven by integrin signaling and hypoxia via blocking of the tumor suppressor miR-326 141

Figure 3.92. Project pipeline summarizing identification and validation of genes/processes driving tamoxifen resistance 142

Figure 3.93. Validation of PDE4D upregulation upon tamoxifen resistance at mRNA and protein levels 143

Figure 3.94. Tamoxifen resistance is driven by PDE4D through downregulation of cAMP and downstream ER stress-p38/JNK signaling 144

LIST OF TABLES

Table 1.1. Intrinsic and Clinical Subtypes of Breast Cancer 4

Table 1.2. IHC-based Classifications of Triple-Negative Breast Cancer 12

Table 2.1. RIPA Lysis and Extraction Buffer Composition 43

Table 2.2. Compositions of the Stacking (S) and Resolving (R) Gels 45

Table 2.3. 4X Protein Loading Dye Composition 45

Table 2.4. Primary and Secondary Antibodies Used in Western Blot 48

ABBREVIATIONS

5-FU	Fluorouracil
ADC	Antibody-drug conjugates
AI	Aromatase inhibitors
ANOVA	Analysis of variance
APS	Ammonium persulfate
AR	Androgen receptor
AV	Annexin V
BAPN	β-Aminopropionitrile
BCA	Bicinchoninic acid
BL	Basal-like
BLIA	Basal-like immune activated
BLIS	Basal-like and immune-suppressed
BRCA1	Breast cancer type 1 susceptibility protein
BSA	Bovine serum albumin
CIS	Cisplatin
CSC	Cancer stem cell
CTG	CellTiter-Glo
CTX	Cyclophosphamide
DCIS	Ductal carcinoma in situ
DMEM	Dulbecco’s Modified Eagle’s Medium
DMSO	Dimethyl sulfoxide
DOXO	Doxorubicin
DSS/DFS	Disease-specific survival/Disease-free survival

ECL	Enhanced chemiluminescence
EGF	Epidermal growth factor
ERα	Estrogen Receptor alpha
FACS	Fluorescence activating cell sorting
FBS	Fetal bovine serum
FDA	Food and Drug Administration
FITC	Fluorescein
GEM	Gemcitabine
GEO	Gene Expression Omnibus
GSEA	Gene Set Enrichment Analysis
HER2	Human Epidermal Growth Factor Receptor 2
HR	Hormone receptor
HRD	Homologous recombination deficiency
IAP	Inhibitors of apoptosis protein
ICI	Immune checkpoint inhibitors
IDC	Invasive/Infiltrating carcinoma
IHC	Immunohistochemistry
ILC	Invasive lobular carcinoma
IM	Immunomodulatory
kDa	Kilo-Dalton
LAR	Luminal androgen receptor
LCIS	Lobular carcinoma in situ
LCM	Laser capture microdissection
M	Mesenchymal
MES	Mesenchymal-like

MPS	Metabolic pathway-based subtype
MSL	Mesenchymal stem-like
NEAA	Non-essential amino acid
ORR	Objective response rate
OS	Overall survival
PBS	Phosphate buffered saline
pCR	Pathological complete response
PE	Phycoerythrin
PI	Propidium Iodide
PR	Progesterone Receptor
PTX	Paclitaxel
PVDF	Polyvinylidene difluoride
RFS	Relapse free survival
RIPA	Radio-immunoprecipitation assay
ROC	Receiver operating characteristic
SD	Standard deviation
SDS-PAGE	Sodium Dodecyl Sulfate Polyacrylamide Gel
Electrophoresis	
TBS	Tris buffer saline
TBST	Tris buffer saline Tween20
SEM	Standard error of the mean
SERD	Selective estrogen receptor degraders
SERM	Selective estrogen receptor modulators
SRB	Sulforhodamine B
TCA	Trichloroacetic acid

TEMED	Tetraacetylethylenediamine
TNBC	Triple-negative breast cancer
v/v	Volume/volume
w/v	Weight/volume

CHAPTER 1

INTRODUCTION

1.1 Cancer

Cancer is a global public health issue and an economic burden with ever increasing incidence and mortality numbers. In fact, one in 5 men or women is expected to develop cancer during their lifetime and one in 8 men and one in 11 women to die due to cancer (1). In the USA alone it is estimated that there will be approximately 2 million new cancer cases and more than 600,000 deaths in 2022 **(Figure 1.1)** (2). GLOBOCAN have recently reported more than 230,000 new cancer cases and 125,000 deaths in Turkey in 2020 (1). The trend is similar in many countries with only few exceptions.

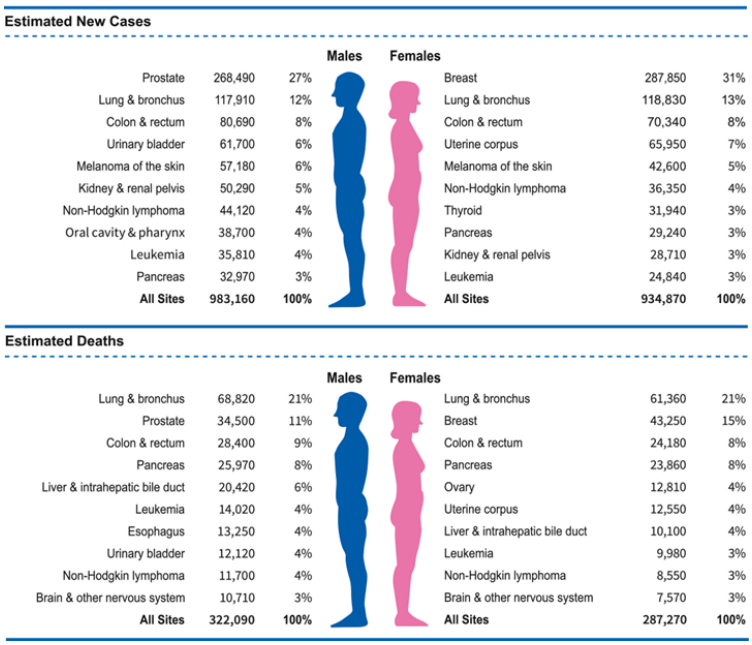


Figure 1.1. Estimated numbers of new cancer cases and deaths by sex in the USA in 2022 (2).

As a consequence, cancer is currently the second leading cause of death worldwide preceded only by cardiovascular diseases and even the top cause of death in some high- and mid-income countries including Turkey **(Figure 1.2)** (3). Moreover, World Health Organization forecasts that numbers of both new cancer cases and cancer-related deaths could be nearly doubled from 2012 to 2035 (4). On the economic side, it is predicted that global oncology spending excluding supportive care will exceed 300 billion dollars by 2026, quintupled from 2012 (5, 6). Considering that half of the cost stems from the increasing prices of targeted therapies (tripled in less than 20 years) (7), it is of vital importance to utilize the currently available drugs to their maximum and design better combination therapies while minimizing drug doses.

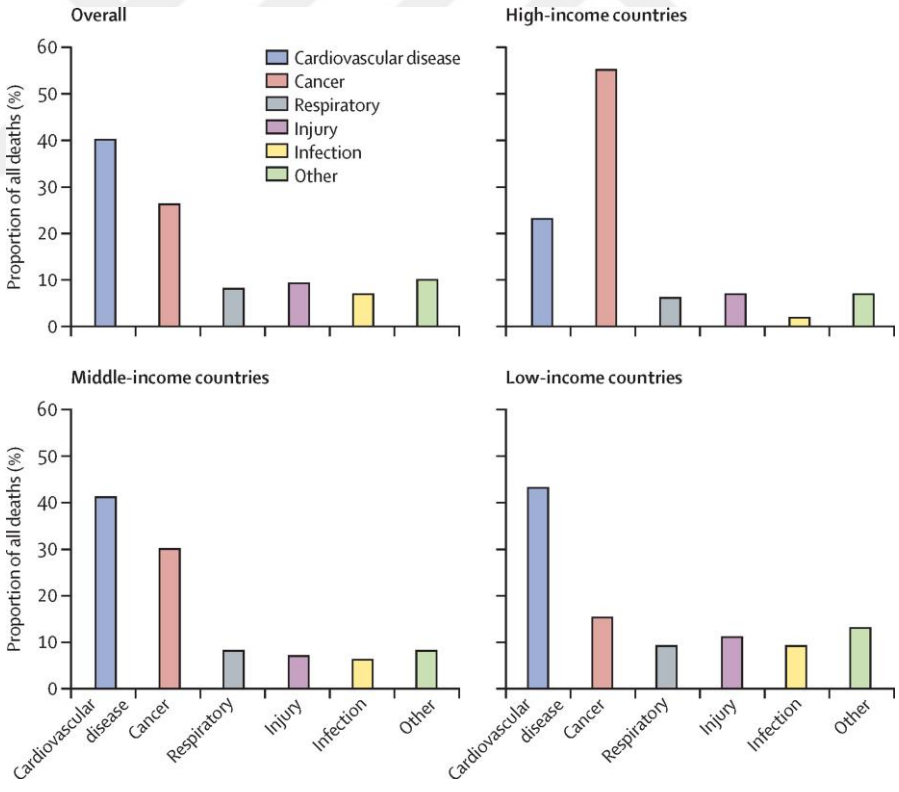


Figure 1.2. The most frequent causes of death as proportions of total deaths by country income level (3). Some upper MICs such as Turkey exhibited a pattern similar to the HICs.

Cancer is a highly heterogeneous disease tremendously varying within each tumor in an individual (intratumor heterogeneity) and between tumors of different individuals (intertumor heterogeneity). This is in part due to cancer being not a single entity but actually a collection of more than hundreds of diseases characterized by uncontrolled cell proliferation (8). Still, less than 15 cancer types account for roughly 80% of all cancer cases and mortalities (1). Among these, breast cancer has recently surpassed lung cancer to become the most commonly diagnosed cancer type worldwide, accounting for 12% of all diagnosed cases (1). Indeed, one in 8 women will be unfortunately diagnosed with breast cancer during her lifetime (9-11), necessitating an immediate and global effort for identification of innovative therapeutic strategies to combat it.

1.2 Breast Cancer

Breast organ is made up of multiple underlying tissues such lobules and ducts. The lobules are glands that produces milk and ducts are tubes carrying milk from the lobules. These two tissues are spread throughout the dense connective tissue and adipose tissue. This heterogenous nature virtually guarantees that tumor arising in breast will exhibit highly diverse characteristics. Accordingly, breast tumors can differ from each other in every possible aspect including, but not limited to, histology, gene expression, DNA architecture and mutations (12).

To make breast cancer more manageable and facilitate patient-oriented treatment, several classification schemes have been developed. As in many other cancers, breast cancer can be categorized by grade considering differentiation level of the tumor and by stage considering tumor size, lymph node status, and metastasis (13). At

histopathological level, there are 2 invasive subtypes, invasive/infiltrating ductal carcinoma (IDC or NST) and invasive lobular carcinoma (ILC), and 2 preinvasive subtypes, ductal carcinoma in situ (DICS) and lobular carcinoma in situ (LCIS) (14). IDC is the most frequent histology constituting more than 60% of all and approximately 75-80% of invasive cases (15, 16). More detailed and specific classifications made plausible with the advent of gene expression technologies, such as microarray and next-generation sequencing. For example, breast cancers were clustered into 5 intrinsic molecular subtypes by a 50-gene expression signature (PAM50), which are basal-like, human epidermal growth factor receptor 2 (HER2)-enriched, luminal A, luminal B and normal-like (17, 18). These subtypes quite overlap with the clinical classification **(Table 1.1)**, which is represented by 3 major subtypes: hormone receptor positive (HR+, mainly estrogen receptor then progesterone receptor), HER2-amplified, and triple-negative breast cancer (TNBC) (19).

Table 1.1. Intrinsic and Clinical Subtypes of Breast Cancer

Intrinsic Subtype	**Clinical Subtype**
Basal-like	Triple-negative
HER2-enriched	HER2-amplified
Luminal A	HR-positive
Luminal B	
Normal-like (resembling luminal A)	Predominantly triple-negative

1.2.1 HER2-Enriched Breast Cancer

Although the clinical definition of the HER2-enriched subtype is still debated (20), it is generally accepted to be characterized by HER2 overexpression/amplification and lacks the expression of hormone receptors, estrogen receptor alpha (ERα) and progesterone receptor (PR). It is the least prevalent subtype among the molecular subtypes, accounting nearly 5-10% depending on the patient cohort (21). HER2-positive breast cancer patients may be treated with a combination of surgery, chemotherapy, radiotherapy, and/or administration of a targeted therapy. Trastuzumab, a humanized monoclonal antibody, was the first HER2-directed therapy approved by the FDA in 1998 and remains standard choice of therapy for these patients alone or in combination with anthracycline, taxane or platinum chemotherapy (22). Similarly, the FDA granted approval to pertuzumab, another monoclonal antibody against HER2, in combination with trastuzumab and chemotherapy for the adjuvant treatment. Recently, they have been followed by antibody-drug conjugates (ADCs) such as trastuzumab emtansine (for HER2-positive early tumors) and trastuzumab deruxtecan (for unresectable or metastatic HER2-positive tumors) (23), and by tyrosine kinase inhibitors targeting not only HER2 but also other EGF family receptors such as lapatinib, tucatinib and neratinib (22). Although patient outcomes continuously improve thanks to the targeted therapies, most patients with high grade and late-stage cancer eventually die because of de novo or acquired resistance to therapy, and early stage patients with residual disease after systemic therapy experience a higher risk of distant recurrence and death (24).

1.2.2 Hormone Receptor (HR) Positive Breast Cancer

Hormone receptor positive clinical subtype is defined primarily by estrogen receptor status in conjunction with progesterone receptor status. It is the most frequent subtype of breast cancer corresponding to 70-80% of all breast cancer patients (25). It consists of luminal A and luminal B intrinsic subtypes, which are ER+, PR+/-, HER2- and ER+, PR+/-, HER2+/-, respectively (26). Therefore, these tumors are majorly driven by ER activity and have high levels of ER expression, and are frequently treated with ER-targeted or endocrine therapies. These therapies can be divided into 3 categories: selective estrogen receptor modulators (SERMs) such as tamoxifen and raloxifene; selective estrogen receptor degraders (SERDs) such as fulvestrant and elacestrant; and aromatase inhibitors (AIs) such exemestane and letrozole (27, 28).

Of the endocrine therapies, tamoxifen is the most extensively utilized thus the blockbuster drug for more than 4 decades in both pre- and postmenopausal women, especially in adjuvant setting. Recently, however, aromatase inhibitors alone or after tamoxifen first-line treatment have shown higher efficacy compared to tamoxifen alone, thereby alleviating the risk of local and distant recurrence (29). Therefore, AIs are now regarded as the standard adjuvant treatment of choice for postmenopausal women with HR+ breast cancer (30). As for the SERDs, fulvestrant was well-tolerated and displayed a similar efficacy to tamoxifen but efficacy end point differences between groups still favored tamoxifen (31). Considering wider adoption of tumor profiling in clinics, single-agent endocrine therapies are slowly substituted by combination therapies involving other targeted agents, such as PI3K/AKT/mTOR inhibitors, CDK4/6 inhibitors and tyrosine kinase inhibitors such as lapatinib (32). For example, everolimus in combination with exemestane (33) and Palbociclib in

combination with fulvestrant (34) were approved for HR+/HER2- patients. Most recently, fulvestrant has been approved in combination with Alpelisib for the treatment of *PIK3CA*-mutated, HR+/HER2- advanced or metastatic breast cancer (25, 35). Preoperative endocrine therapy, on the other hand, remains under-utilized in this patient group, particularly in locally advanced tumors, due to limited clinical guidelines on drug selection and optimal duration (36). However, clinical trials have demonstrated that AIs dramatically increase objective response rate (ORR) and mediate breast conserving surgery when compared to tamoxifen (37). Despite all these advances, 20% of HR+ tumors exhibit intrinsic resistance to endocrine treatment, and approximately 40% acquire resistance during the course of treatment, usually followed by primary relapse and metastasis and eventually death (38). Therefore, research on molecular mechanisms underlying resistance to single-agent endocrine therapies and their combination with other inhibitors should be prioritized to counter this unmet clinical issue.

1.3 Triple-Negative Breast Cancer (TNBC)

1.3.1 Treatment Approaches and Therapy Resistance in TNBC

Triple-negative breast cancer is the most aggressive clinical subtype of breast cancer with an incidence rate of 15%, particularly common among women of younger age and African-American race (39). It is frequently accompanied by early distant recurrence and poor prognosis independent of patient stage and grade (39). It largely (70-80%) coincides with the basal-like molecular subtype **(Figure 1.3)** and the terms are often used interchangeably albeit incorrect (40, 41). TNBC is portrayed by lack of expression of estrogen and progesterone receptors and lack of amplification or

expression of HER2, rendering triple-negative tumors unresponsive to endocrine and HER2-targeted therapies (42). As a result, TNBC patients still heavily rely on conventional therapeutic options such as chemotherapy, radiotherapy and surgery.

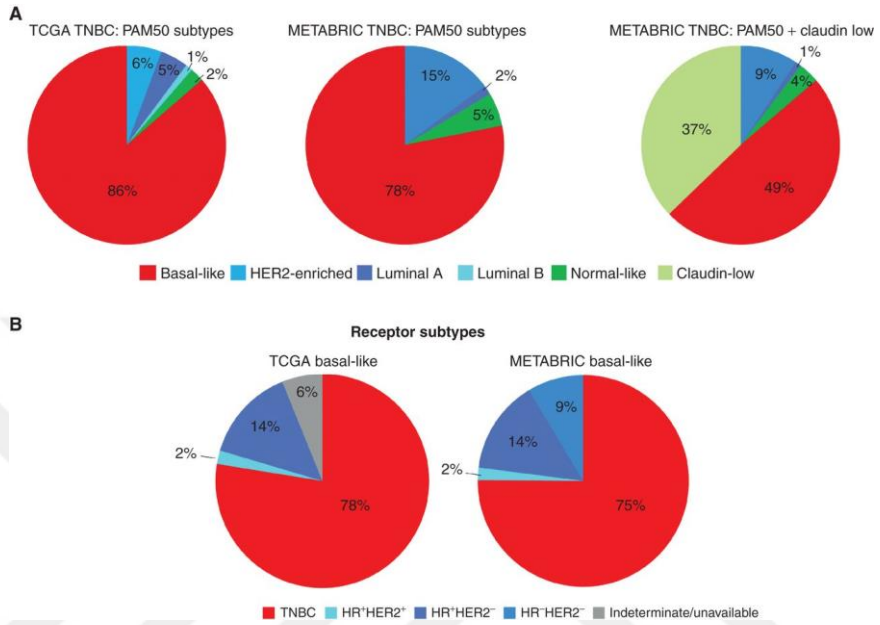


Figure 1.3. TNBC and basal-like breast cancers are not identical though quite overlapping (43).

Anthracycline- (e.g., doxorubicin) and taxane-based (e.g., paclitaxel) chemotherapy is currently the standard of care for these patients (44). Compared to other breast cancer patients, TNBC patients initially respond to the chemotherapy agents at a relatively higher rate (45). Unfortunately, more than half of the chemotherapy-treated TNBC patients undergo local and/or metastatic recurrence within 5 years following surgery (46, 47). Consequently, there is a desperate need to scrutinize novel mechanisms of chemotherapy resistance in TNBC, thereby maximizing pathological complete response (pCR) rates and minimizing disease-related discomfort among patients.

Some studies have recently presented alternative strategies to the clinical management of the TNBC patients by using immune checkpoint inhibitors (ICIs) (48, 49), PARP inhibitors (50-52) or other novel targeted therapies (53). Nonetheless, the clinical benefit of such therapies has been unsatisfactory at best and restrained by treatment-related adverse events as well as their premium price tag thus availability in low- and mid-income countries. For example, atezolizumab has received accelerated approval for the treatment of refractory TNBCs in 2019 but the improvement in progression-free survival (PFS) was limited to 3 months for only a fraction of patients and many experiencing drug-related adverse events (48, 54). For example, a recent retrospective study showed that 10.3% of patients receiving ICIs developed major adverse cardiac events (MACE) that is much higher than trastuzumab (2-7%) and even higher than high-dose/dose-dense doxorubicin treatment (9%) (55). More dramatically, this slightly longer PFS was accomplished through additional monthly and annual costs of nearly 20,000 and 120,000 dollars, respectively (56, 57). Similarly, sacituzumab govitecan-hziy (Trodelvy™), which is an antibody–drug conjugate of the cell surface glycoprotein TROP2 coupled to the active metabolite of irinotecan, has recently been approved as the first targeted therapy agent to be used in metastatic TNBC patients (53). However, only 28 out of 235 patients exhibited progression-free survival for more than 12 months, with 50% more incidences of treatment-related adverse events (≥ grade 3) and at the cost of more than 20,000 and 200,000 dollars per cycle and treatment, respectively (53, 58). Two recently approved PARP inhibitors, Olaparib and Talazoparib, for early-stage or metastatic TNBC harboring a germline *BRCA1* or *BRCA2* mutation share similar drawbacks with the aforementioned drugs although they have fewer or comparable proportions of adverse events compared to

chemotherapy arm (59, 60). The marginal success of these emerging therapies could be in part attributed to vast heterogeneity of the triple-negative breast tumors. Hence, a more in-depth exploration of TNBC subtypes and design of subtype-specific therapy regimens can improve drug response rates while lowering drug toxicities and increasing survival rates in TNBC.

Different chemotherapeutic approaches in TNBC will be discussed more comprehensively in **Section 1.4.**

1.3.2 Triple-Negative Breast Cancer Heterogeneity and Subtypes

Unlike hormone receptor positive or HER2-enriched breast cancer that are driven primarily by estrogen receptor alpha or HER2 activity, respectively, no single driver alteration predominates in case of TNBC. As a result, tumors may arise through collective actions of multiple activating and inactivating events in oncogenes and tumor suppressors, respectively (61). Therefore, TNBC should not be regarded as a uniform disease but involves multiple entities with striking histological, genomic, epigenomic, transcriptomic, proteomic and metabolic heterogeneity (62). Many patient stratification methodologies have been devised for the last 10 years to better identify molecularly guided treatment options and thus address clinical challenges posed by TNBC.

1.3.2.1 Immunohistochemistry-based Classifications

The initial methods for TNBC classification were built upon histological examination and immunohistochemistry (IHC). For example, Elsawaf et al. examined13 protein

markers by IHC and later utilized a hierarchical unsupervised cluster analysis to identify 4 distinct TNBC clusters: *basal A, basal B, basoluminal* and *luminal* **(Table 1.2)** (63). The *basal A* subtype was defined by cytoplasmic p16 expression and basal cytokeratins, such as KRT5, KRT6 and KRT14 coupled with a high proliferation index. The *basal B* subtype was portrayed by a pronounced p53 expression and often accompanied by medium-to-high levels of p16, BCL2, KIT, and WT1. The *basoluminal* histology accounted for majority of the cases and distinguished by high EGFR expression together with mixed basal and luminal cytokeratin expression. The *luminal* cluster had a low proliferation index and expressed high levels of luminal cytokeratins, such as KRT7 and KRT18 as well as little-to-none basal cytokeratins. While the basal subtypes were associated with better prognosis, luminal and basoluminal subtypes led to worse prognosis.

More recently, Zhao et al. have also reported another IHC-based classification using markers selected through differential mRNA expression and mRNA-protein correlation followed by receiver operating characteristic (ROC) analysis and stroma-tumor staining filtering (64). Accordingly, they assigned TNBC tumors into 5 groups **(Table 1.2)**. *IHC-Luminal androgen receptor (LAR)* group was positive for androgen receptor (AR) expression and more common between tumors of patients with older age. It is distinguished by lower proliferation index and noticeable HER2 pathway activation by complementary RNA-sequencing analysis. *IHC-Immunomodulatory (IM)* subtype was negative for AR but positive for cytotoxic T lymphocyte marker, CD8, resulting in high rates of stromal and intratumoral infiltrating lymphocytes and high expression of immune checkpoint molecules, such as CD274 and CTLA4. *IHC-Basal-like and immune-suppressed (BLIS)* subtype was negative for both AR and CD8

but positive for FOXC1. These tumors showed remarkable VEGF signature activity and homologous recombination deficiency (HRD). *IHC-Mesenchymal-like (MES)* was negative for AR, CD8, FOXC1 and positive for DCLK1 with distinct activation of JAK/STAT3 signaling. These patients had the worst relapse-free survival. Lastly, IHC-unclassifiable (IHC-UC) group was negative for all 4 markers.

Table 1.2. IHC-based Classifications of Triple-Negative Breast Cancer

Elsawaf et al. (2013)		**Zhao et al. (2020)**	
Group	**Characteristics**	**Group**	**Characteristics**
Basal A	EGFR < 10%, Ki-67 > 50%	IHC-BLIS	AR-, CD8-, FOXC1+
Basal B	EGFR < 10%, Ki-67 < 50%, High p53, 2 or more CK-	IHC-IM	AR-, CD8+
Basoluminal	EGFR > 10%	IHC-LAR	AR+
Luminal	EGFR < 10%, Ki-67 < 50%, 2 or more CK+	IHC-MES	AR-, CD8-, FOXC1-, DCLK1+
		IHC-UC	AR-, CD8-, FOXC1-, DCLK1-

1.3.2.2 Transcriptome-based Classifications

Several transcriptome-based classifications have also emerged owing to the accumulation of large microarray data and integration of sequencing technologies to clinical practice **(Figure 1.4)**. Consequently, Lehmann et al. published the first ever classification of TNBC (TNBCtype or TNBCtype-6) into multiple subtypes by

combining different breast cancer data sets and analyzing gene expression data of more than 500 TNBC patients (65). They discovered 6 subtypes, displaying not only unique gene expression patterns but also distinct gene ontology enrichment, by k-means-based consensus clustering. These consist of 2 *basal-like (BL1 and BL2)*, an *immunomodulatory (IM)*, a *luminal androgen receptor (LAR)*, a *mesenchymal (M)* and a *mesenchymal stem–like (MSL)* subtype. They also uncovered representative TNBC cell line models of each subtype.

In a second study, Lehmann and colleagues found out that transcripts in *MSL* and *IM* subtypes were originating from tumor-associated stromal cells and infiltrating lymphocytes, respectively, by histopathological quantification and laser-capture microdissection (LCM) (66). Therefore, they reported a refined classification system by re-assigning problematic subtypes to the second highest correlated cluster. Among these subtypes, *BL1* patients exhibited apparent sensitivity to neoadjuvant chemotherapy with more than 40-50% (depending on the regimen) achieving pathological complete response. These tumors belonged to higher grade but lower stage and were differentiated by elevated DNA damage response and cell cycle gene expression. In contrast to the *BL1*, the *basal-like 2* subtype displayed potential intrinsic resistance to chemotherapy and had the worst overall and relapse-free survival. Enriched growth factor signaling and increased levels of myoepithelial markers were differentiating features of this subtype. The *M* subtype was defined by mesenchymal differentiation, absence of infiltrating lymphocytes and a high frequency of metastasis to lungs. Finally, the *LAR* phenotype was found to be caused by the androgen receptor activity and exhibited a well-differentiated luminal histology. These tumors metastasized frequently to local lymph nodes and/or bone and

showed decreased response to neoadjuvant chemotherapy but paradoxically a better survival.

Before the refined classification by Lehmann et al., Burstein and colleagues had already reported a 4-subtype classification methodology by combining gene expression by microarray and copy number variation (67). These subtypes are basal-like *immune-activated (BLIA), basal-like immunosuppressed (BLIS), luminal androgen receptor* and *mesenchymal*. The *BLIA* subtype exhibited the best prognosis among all subtypes and was depicted by escalated lymphocyte infiltration via upregulation of genes mediating immune cell functions and of STAT genes. On the contrary, the *BLIS* subtype had the worst disease-free and disease-specific survival (DFS and DSS). These tumors showed diminished activity in innate and adaptive immune cell function/communication and immune cell differentiation due to downregulation of many cytokines and molecules facilitating immune cell crosstalk. Although the *LAR* tumors were hormone receptor negative by IHC, they manifested activation of multiple hormone-related pathways, such androgen receptor, estrogen receptor and prolactin signaling. The last subtype, *MES*, was characterized by deregulations in DNA damage and repair, cell cycle and hereditary breast cancer signaling pathways together with marked expression of some growth factors, such as IGF1 and initiation of adipocyte- or osteocyte-specific gene programs such as *PLIN1*.

An alternative approach was proposed by Shao Group at Fudan University Shanghai Cancer Center in 2 complementary studies (68, 69). Similar to the refined Lehmann and Burstein classifications, they classified tumors into 4 different clusters as follows: a *basal-like and immune-suppressed*, an *immunomodulatory*, a *luminal androgen*

receptor and a *mesenchymal-like* subtype. The *BLIS* subtype was the most frequent one with an incidence rate of approximately 40%. Unfortunately, these patients had worse recurrence-free survival, partly due to activated cell cycle and DNA repair genes (thus high chromosomal instability) as well as inactivated immunoresponse genes. The *mesenchymal-like* subtype was the least prevalent accounting for only 15% of the tumors but with a poor prognosis. They exhibited a gene expression profile similar to breast cancer stem cells (CSCs) and differentiated from other subtypes by JAK/STAT3 activation. The *LAR* subtype was represented by androgen receptor signaling, low chromosomal instability and significant association with *PIK3R1*, *PIK3CA*, *PTEN*, *ERBB2* and *HRAS* mutations. Lastly, the *IM* tumors were shown to boost immunological pathways such as interferon-gamma signaling and expression of multiple cytokines. This subtype had the best prognosis when adjusted for tumor size and lymph node status.

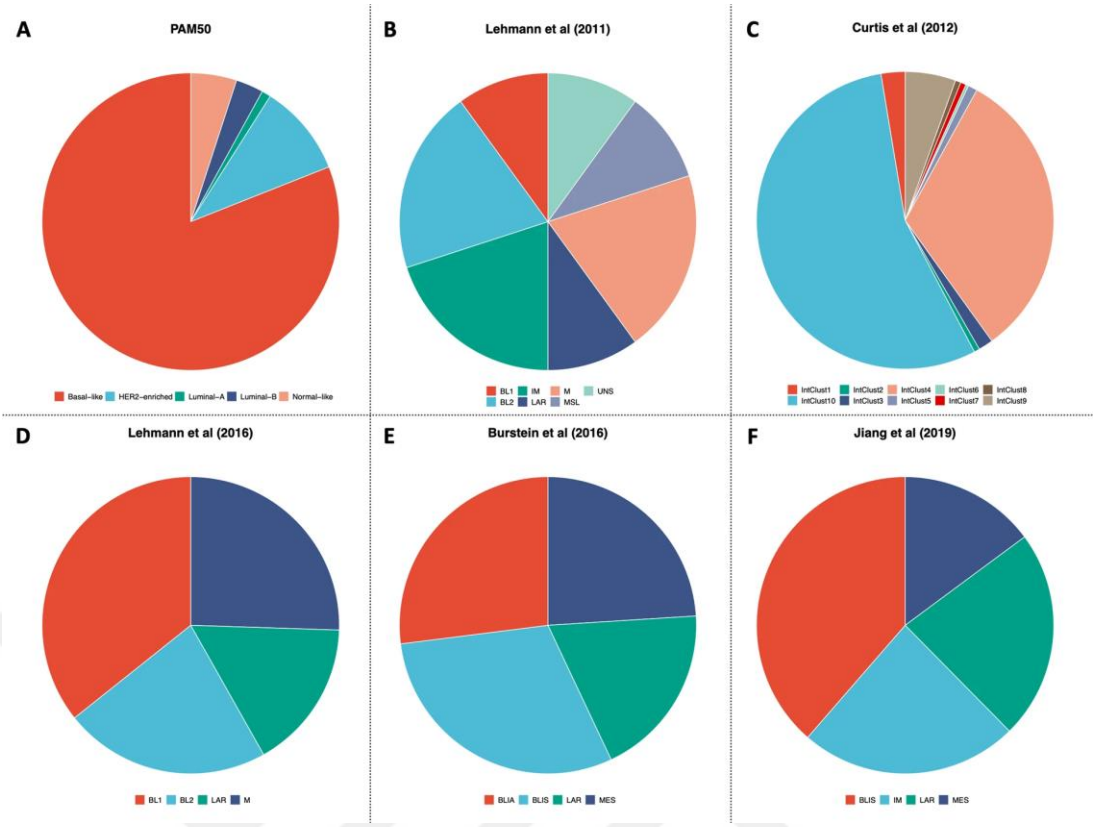


Figure 1.4. Transcriptome-based TNBC classifications (70).

As clearly seen, there is a good degree of concordance between subtypes identified by these studies. Thus, they collectively offer some insights into the putative therapy targets per TNBC subtype, of which some are purely theoretical but some validated by experimental data. Theoretically, several recommendations were made such as the use of immune checkpoint inhibitors in the *IM* subtype (66, 69), STAT3 or IGF inhibitors in the *MES* subtype (67, 69), CDK1 inhibitors in a subtype-agnostic manner but mostly for the *BLIA* subtype (67), and HER2-targeted therapies, CDK4/6 inhibitors and PI3K/mTOR inhibitors in the *LAR* subtype (39, 70, 71). As for recommendations supported by experiment in these studies, Lehmann et al. tested bicalutamide, an antiandrogen and 17-DMAG, an HSP90 inhibitor in a panel of TNBC cell lines belonging to the different TNBC subtypes (65). HSP90 was modulated as it

was needed for proper folding and stability of the androgen receptor. They found that the *LAR* cell lines showed relatively higher sensitivity to bicalutamide and much more potently to 17-DMAG with an average IC50 of 16 nM, which was also confirmed by in vivo xenograft models. They also evaluated the response of these cell lines to PARP inhibitors, Olaparib and Veliparib and cisplatin to exploit *BRCA1/2* mutations commonly observed in the *basal-like* subtypes. However, they obtained mixed results such that even though *basal-like* cells were significantly more sensitive to cisplatin while their response to either of the inhibitors varied dramatically. Other than this individual or small-scale investigations, there is only one study that systematically analyzes therapeutic vulnerabilities in triple-negative breast cancer subtypes through combination of 9 different data types (such as expression, mutation, phosphoproteomics, methylation, and chromosome accessibility) followed by genetic dependency, cell line and PDTX drug sensitivity analyses (72). Although promising, none of the findings in the article made its way into the clinics yet.

Apart from the preclinical examples, only Jiang et al. showcased utility of their classification in a *basal-like immunosuppressed* patient with a high HRD score (69). Upon treatment with a platinum-based chemotherapy and radiotherapy, the patient had a complete remission of both liver and brain metastases. Unfortunately, only one clinical trial (the FUTURE) has been designed and also published which integrates genomic testing and TNBC subtype data to guide therapy selection process (73). Although hindered by small sample size, it demonstrated the feasibility of subtype-based and biomarker-guided therapy in refractory metastatic TNBCs, at least for some treatment arms such as paclitaxel and anti-PD-1 combination for the *IM* patients.

1.3.2.3 Other Classification Strategies

TNBC subtyping is not confined to the histological and transcriptomic data **(Figure 1.5)**. Novel procedures utilizing new or emergent types of data such as epigenetics, metabolomics and proteomics have more recently been released. In one study, Gong et al. characterized TNBC heterogeneity on the basis of metabolome profiling and unveiled 3 distinct subtypes: *Metabolic-pathway-based subtype 1 (MPS1)*, *MPS2* and *MPS3* (74). *MPS1*, or lipogenic, subtype was largely overlapping with the *LAR* subtype and with PAM50 *non-basal* tumors to a lesser extent. This subtype was defined by elevated lipid metabolism and accelerated biosynthesis of fatty acids, steroids and cholesterol. The *MPS2*, or glycolytic, subtype was predominantly corresponded to the *basal-like* TNBCs and almost exclusively to PAM50 *basal* subtype. These tumors were marked by increased nucleotide or carbohydrate metabolism pathways such as pyrimidine metabolism and glycolysis. The *MPS3* subtype showed a more diffuse distribution to TNBC subtypes but was overwhelmingly of PAM50 *basal* phenotype (> 80%) and was depicted by partial but joint dysregulations in each major metabolic pathway. In another study, Masuda and colleagues categorized TNBC samples into 2 classes by reverse phase protein array: *inflammation and hormonal-related (I/H)* and *DNA damage (DD)-related* subtypes. The former was enriched for STAT phosphorylation, MAPK signaling proteins such as phospho-JNK and hormone receptors such as AR and ER. The latter was discriminated by elevated expression of cell cycle proteins such as cyclin B 1 and E1, mTOR downstream proteins such as 4EBP1 and S6, and DNA damage response proteins such as PCNA, BRCA1 and cleaved PARP. Finally, DiNome et al. reported an epigenetic strategy to TNBC classification and clustered TCGA TNBC patients via nonnegative matrix factorization by using DNA methylation data. They identified 4

epigenetic subtypes (epitypes) termed *Epi-CL-A*, *Epi-CL-B*, *Epi-CL-C* and *Epi-CL-D*, showing a significant but partial agreement with transcript-based classifications. The characteristic features of these subtypes include activation of mesenchymal differentiation and Wnt signaling in the *Epi-CL-A*, of cell cycle-related genes in the *B*, of cellular stress and hypoxia response in the *C*, and of immune-related processes such as IFN-γ signaling and antigen presentation in the *D* epitype. Considering less than 0.1% clinical approval rate compared to 13.4% of the investigational cancer drugs and suboptimal adoption of DNA methylation tests (75, 76), it would take remarkably more time for epigenetic-based approaches to be translated into the clinic.

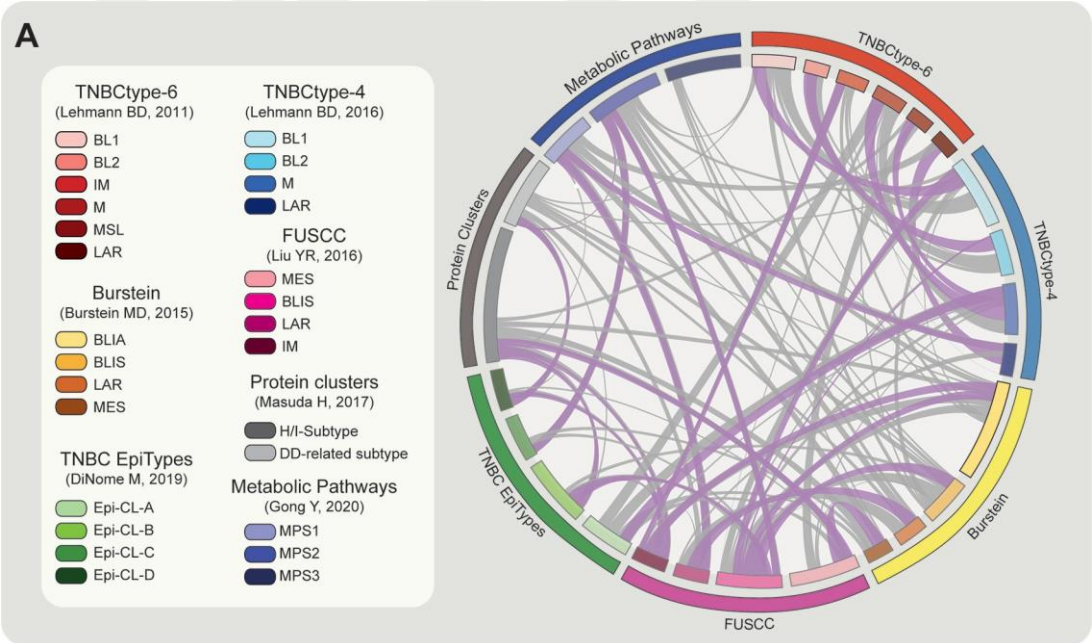


Figure 1.5. Different approaches to TNBC classification by use of distinct data types (62).

In summary, despite application of multi-omics technologies and sophisticated computational algorithms, TNBC classifications have largely remained theoretical and majority of the patients are still being treated with chemotherapy rather than

personalized approaches. Therefore, it is still essential to scrutinize and unveil unique molecular underpinnings of chemoresistance and design rational combination therapies with clinically approved and/or advanced phase targeted agents.

1.4 Chemotherapy Agents Used in TNBC and Their Classification

According to the 2022 National Comprehensive Cancer Network® (NCCN) Guidelines for Patients, only DCIS breast cancer patients are not treated with chemotherapy (77). For these patients, lumpectomy with total or accelerated partial breast radiotherapy or total mastectomy is the recommended treatment. On the other hand, dose-dense doxorubicin and cyclophosphamide followed by paclitaxel (AC-T) and docetaxel and cyclophosphamide (TC) are the most preferred options for invasive TNBC (44, 78). Other options include, but not limited to, docetaxel, antimetabolites (e.g., capecitabine and fluorouracil) and platinum agents, such as cisplatin and carboplatin as well as PARP inhibitor, Olaparib (50) and anti-PD-1, pembrolizumab (49). Similarly, metastatic TNBC is typically managed by anthracyclines (e.g., doxorubicin) or taxanes (e.g., paclitaxel), and to a lesser extent with anti-metabolites, microtubule inhibitors, and platinum compounds (79). Targeted therapies, such as sacituzumab govitecan-hziy, talazoparib, and pembrolizumab have recently been incorporated into the treatment regimens of these patients (49, 51, 52, 58). However, cancer treatment by targeted agents often does not rely on single agents, but routinely involves preceding, simultaneous or sequential use of chemotherapy drugs of different classes.

Chemotherapy can be broadly divided into 7 categories by how they work, their chemical structure, and their relationships to other drugs. These categories are

alkylating agents, antimetabolites, anti-tumor antibiotics, plant alkaloids (mitotic inhibitors), topoisomerase inhibitors, corticosteroids and other chemotherapeutics (80-83). Some chemotherapy agents can work in more than one way **(Figure 1.6)** and thus may belong to more than one group. Chemotherapy drugs from the first five categories are utilized for the treatment of triple-negative breast cancer and hence are explained in detail below.

1.4.1 Alkylating Agents

The highly reactive alkylating agents bind to DNA by intra and inter crosslinks to create DNA damage and then impair DNA replication and strand separation, resulting in inhibition of cell division (84). The subclasses of this group include alkylsulfonates, triazines, ethylenimines, nitrogen mustards, such as cyclophosphamide, platinum agents, such as cisplatin and nitrosoureas, such as carmustine, which are the only type of alkylating agents that can cross blood-brain barrier (81). These drugs can work in a cell cycle phase-agnostic manner and are used, often in combination with other anticancer drugs, to treat many different cancers including breast, lung and ovary (85-87).

As aforementioned in **Section 1.4**, standard care of therapy contains cyclophosphamide (CTX) when an anthracycline-based chemotherapy regimen is preferred. It is usually combined with doxorubicin and later followed by paclitaxel treatment. However, recent trials have evaluated the potential of new regimens, such as neoadjuvant dose-dense doxorubicin/cyclophosphamide concurrently with paclitaxel and an anti-PD-L1, durvalumab in early TNBC (88, 89), adjuvant cyclophosphamide combination with epirubicin following docetaxel and capecitabine

in early TNBC (90) and finally cyclophosphamide alone or in combination with veliparib, a PARP inhibitor in heavily pre-treated advanced TNBC (91). Only the last study allows us to evaluate the efficacy of CTX independent of other agents, and it concludes that CTX alone had similar response rates compared to the combination arm. Still, there are factors limiting the monotherapy of cyclophosphamide in cancer: i) high-dose cyclophosphamide monotherapy causes severe (up to 80%) adverse events such as cardiotoxicity, bladder damage, lymphopenia and hair loss (92), ii) initial response followed by acquired resistance (93), and iii) unsolved resistance mechanisms in case of breast cancer unlike proposed mechanisms for leukemia (94, 95), sarcoma (96) and prostate cancer (97).

Among the alkylating agents, platinum agents cisplatin and carboplatin are of great interest in TNBC patients with *BRCA1/2* mutations (BRCAness), which can be inherited or sporadic. The mutations are highly critical that while approximately 13% of women are expected to develop breast cancer during their lives (11), it is 55%–72% for women with inherited *BRCA1* mutation and 45%–69% for women with inherited *BRCA2* variant will develop breast cancer (98-100). Accordingly, these patients will exhibit homologous recombination deficiency thus impaired DNA repair and are usually more sensitive to DNA-damaging agents. Clinical trials report higher-than-average pathological complete response to platinum agents in TNBC, even up to 83% in some patient cohorts (101-103). These agents, especially carboplatin thanks to its more favorable toxicity profile, have also been incorporated into multi-chemotherapy regimens in recent years to treat invasive and metastatic TNBC in certain cases. Nonetheless, there are superior alternatives to platinum agents (104), and resistance to platinum agents can be found in some patients or eventually acquired (105, 106),

confining its clinical benefit. Reduced accumulation of cisplatin inside the cells due to elevated drug efflux, increased sequestration of cisplatin by scavenger molecules, inactivating mutations in *TP53*, elevated levels of FOXM1 followed by augmented DNA repair, metabolic rewiring together with enhanced anti-oxidative response, boosted Wnt/β-catenin signaling(107) and EGFR/HER2/ERK activation by ER-α36 expression are among the identified resistance mechanisms to platinum agents (106, 108-111).

1.4.2 Antimetabolites

These chemotherapeutics interfere with DNA replication in S phase of cell cycle by multiple mechanisms, such as substituting the original purine and pyrimidine nucleotides. They are further divided into multiple subclasses, such as antifolates (e.g., methotrexate), purine analogs (e.g., 6-mercaptourine), purine antagonists (e.g., fludarabine), pyrimidine antagonists [e.g., gemcitabine, capecitabine and fluorouracil (5-FU)] and ribonucleotide reductase inhibitors (e.g., hydroxyurea) (80). Of these, capecitabine and gemcitabine are utilized in the clinical management of both invasive and metastatic TNBC whereas 5-FU and methotrexate are used in combination with cyclophosphamide for invasive primary tumors, albeit less frequently. For example, CBCSG006 Phase 3 trial concluded that gemcitabine plus cisplatin could be considered an alternative or even the preferred first-line chemotherapy for metastatic TNBCs (112). However, more recent trials found out that paclitaxel plus carboplatin treatment achieved significantly higher progression-free survival in metastatic TNBC as compared to paclitaxel-gemcitabine or gemcitabine-carboplatin combination (113, 114). A more promising combination was eribulin plus gemcitabine for locally advanced or metastatic TNBC with an overall response rate of roughly 40% and

tolerable toxicity profile (115). Gemcitabine was also tested in combination with everolimus, an mTOR inhibitor and iniparib, a PARP inhibitor in 2 different trials but neither reported a significant survival advantage compared to the control arm (116, 117). The underlying mechanisms for tumor-intrinsic and/or therapy-driven resistance to gemcitabine may involve EGFR activation induced by exosomal Annexin A6, upregulation of inhibitors of apoptosis proteins (IAPs), high expression of drug efflux pumps, induction of Hedgehog signaling thus cancer stem cell markers, increase in phospho-Src levels, epithelial-mesenchymal transition and HIF-1α signaling pathway (118-122). Other antimetabolites, such as 5-FU and methotrexate can be used jointly with cyclophosphamide, as an alternative to docetaxel plus cyclophosphamide, to treat low-risk breast cancer patients (123). However, they did not establish an extensive presence in clinical administration of the breast cancer despite having well-tolerated toxicity profiles with minor symptoms (124, 125). Still, some resistance mechanisms were discovered in preclinical models such as *BAG3* overexpression and protective autophagy, epithelial-mesenchymal transition, and *RB1* knockdown (126-128).

1.4.3 Anti-tumor Antibiotics

The agents of this category work by hindering the activities of enzymes needed for DNA replication and independent of cell cycle phase. They can belong to anthracycline (e.g., doxorubicin and epirubicin) or nonanthracyclines (e.g., bleomycin and mitomycin C) subcategories (81). They have been incorporated into the chemotherapy treatment regimens of more types of cancer than any other class of chemotherapy, including breast, lung, ovary, melanoma, thyroid, kidney, bladder, pancreas, stomach and also cancer of soft tissues, blood and nerves (129). Doxorubicin, also known as Adriamycin, is the most frequently utilized anthracycline

chemotherapy owing to its early approval nearly 50 years ago and potent antitumor effects in tumors of different kind. It has been considered the gold standard once combined with cyclophosphamide and paclitaxel to treat TNBC patients at multiple stages, especially mid-to-high risk patients (130-132). However, the use of anthracycline-based chemotherapy displayed a declining trend in recent years, and more patients are increasingly directed to taxane-based chemotherapy options. The most questionable aspect of anthracyclines is the rare but potentially deadly cardiotoxicity, and thus should be avoided in those with high cardiac risk at all costs (123, 133, 134), which may in part explain this decline. In addition, several resistance mechanisms were also discovered for doxorubicin. Specific *TP53* mutations, hypoxia-induced extracellular matrix remodeling by LOX and downstream FAK/Src signaling, IL-8 secreted by mesenchymal stem cells, STAT5a activation, regulation of cell cycle factors by miR-449 and activation of MAPK/ERK pathways are a few examples leading to de novo and/or acquired resistance to doxorubicin in breast cancer (135-139).

1.4.4 Plant Alkaloids (Mitotic Inhibitors)

Plant alkaloids, also called mitotic inhibitors, are natural products mostly derived from plants and are composed of 2 major subcategories: taxanes (e.g., paclitaxel and docetaxel) and vinca alkaloid (e.g., vinorelbine and vincristine). They disrupt microtubule formation and depolymerization during cell division thus inhibits mitosis, leading to apoptosis (80). As aforementioned in **Section 1.4.3**, taxane-based chemotherapy regimens have become indispensable part of clinical management of early or advanced primary and metastatic TNBC patients. Both paclitaxel and docetaxel have wide spectrum of antitumor activity with reduced toxicity (140). This

has been made obvious through reported improved clinical outcomes by addition of a taxane to treatment (141-144) even though doxorubicin alone can offer better disease and symptom control than paclitaxel alone (145). As an inherent hallmark of all chemotherapy agents, primary and secondary resistance to taxanes constitutes a major issue towards its clinical utility, resulting in treatment failure and disease relapse/recurrence. Currently, known mechanisms driving taxane resistance in breast cancer include presence of *BCL2* 21 (C>T) variant, augmented JAK2 signaling, high SYTL4 expression by decreasing microtubule stability, FOXM1 stabilization by Aurora kinase A, TRA2A by creating a cancer-specific alternative splicing program and truncated *HDAC9* (146-150).

1.4.5 Topoisomerase Inhibitors

The last category of chemotherapy used in TNBC is the topoisomerase inhibitors. They are separated into 2 subclasses: topoisomerase I inhibitors and topoisomerase II inhibitors. The former, also called camptothecins, includes irinotecan and topotecan while the latter, also called epipodophyllotoxins, includes teniposide, etoposide, mitoxantrone, and many anthracyclines, which are more frequently categorized under anti-tumor antibiotic category. They serve their function by crippling winding and unwind of DNA strands, thereby halting DNA replication and generating DNA damage. These agents are currently not employed as single agents but can be integrated into some multi-chemo or targeted therapy regimens. The most noteworthy example is sacituzumab govitecan-hziy, an antibody-drug conjugate that is designed by coupling active metabolite of irinotecan, SN-38 (more potent than irinotecan) to a monoclonal antibody against TROP2. This antibody-drug conjugate emerged as one of the preferred options to treat heavily pretreated metastatic TNBC patients. Apart

from this, there are only small-scale clinical trials with some reporting encouraging results such as approximately 90% (7/8 patients, partial response) and superior response rate of irinotecan and veliparib combination compared to veliparib monotherapy (151).

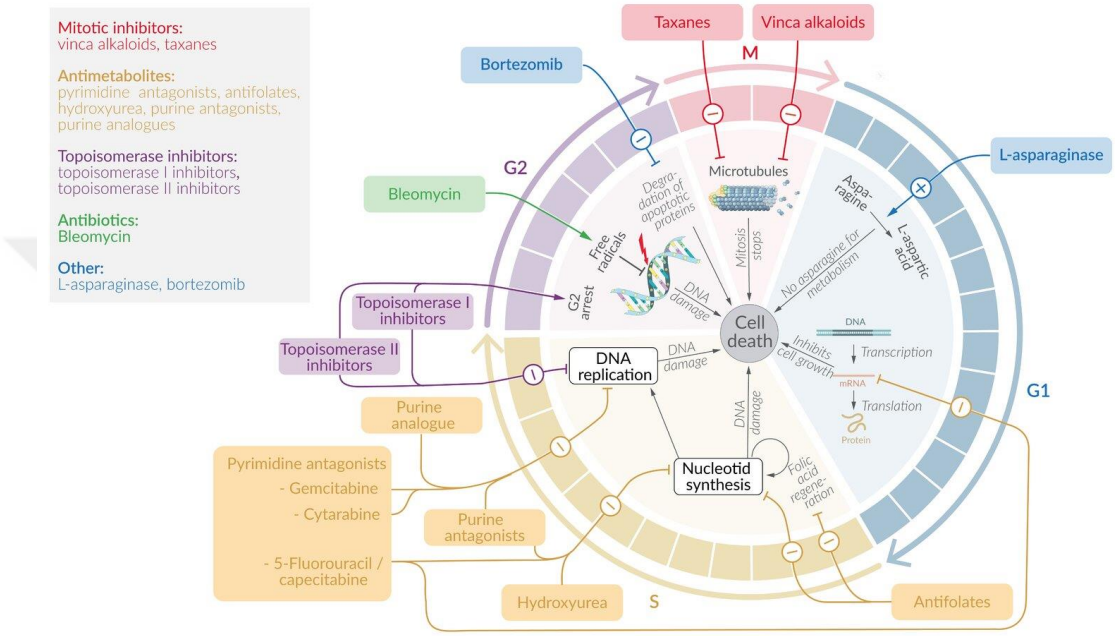


Figure 1.6. Some chemotherapy agent classes and their mechanism of action. Retrieved from "Mechanism of action: chemotherapeutic agents" ©AMBOSS, by following "Permitted Uses" guideline.

1.5 Rationale and Aims of the Study

Although the first targeted therapy for TNBC has been recently approved, patients of this most aggressive breast cancer subtype suffer from scarce therapeutic options and are still in need of chemotherapy. Worse yet, pathological complete response rates to chemotherapy in TNBC encountered an insurmountable barrier despite countless investigations of multi-chemo regimens, paradoxically high response rates to chemotherapy and relatively optimized toxicity profiles. Therefore, we have to come up with experimental and/or biocomputational approaches combining the best of both worlds, omnipresence of the chemotherapy agents and exceptional potential of the targeted agents, in the best interest of the patients.

In this thesis, by following an inclusive approach towards the patients of each TNBC subtype and striving to make a meaningful contribution to the field, I aimed:

- To develop acquired chemotherapy-resistant cell line and xenograft models of triple-negative breast cancer by accounting for TNBC heterogeneity and aggressiveness
- To delineate the similarities and differences between acquired and de novo chemoresistance models as well as between the cell line and xenograft models
- To examine cross resistance patterns of these models by chemotherapy classes
- To offer novel candidates that can overcome acquired and/or de novo resistance in TNBC

CHAPTER 2

MATERIALS AND METHODS

2.1 Materials

2.1.1 Buffers

1X Annexin V Binding Buffer	140 mM NaCl, 2.5 mM $CaCl_2$, 10 mM HEPES, diluted from 10X Annexin V Binding Buffer with dH_2O
1X Anode I Buffer	300 mM Tris base dissolved in ddH_2O, 20% (v/v) methanol
1X Anode II Buffer	25 mM Tris base dissolved in ddH_2O, 20% (v/v) methanol
1X Cathode Buffer	40 mM 6-aminocaproic acid dissolved in ddH_2O, 20% (v/v) methanol
1X PBS	137 mM NaCl, 2.7 mM KCl, 10 mM Na_2HPO_4, 1.8 mM KH_2PO_4, diluted from 10X PBS in ddH_2O (pH 7.4)
1X SDS-PAGE Running Buffer	25 mM Tris base, 192 mM glycine, 0.1% (w/v) SDS diluted from 10X SDS-PAGE Running Buffer
1X TBS	20 mM Tris base, 150 mM NaCl, diluted from 10X TBS with ddH2O

1X TBST	1X TBS supplemented with 0.1% (w/v) Tween 20 detergent
10X Annexin V Binding Buffer	1.4 M NaCl, 25 mM $CaCl_2$, 0.1 M HEPES (pH 7.4) dissolved in dH_2O
10X PBS	1.37 M NaCl, 27 mM KCl, 100 mM Na_2HPO_4, 18 mM KH_2PO_4 dissolved in ddH_2O (pH 6.8)
10X SDS-PAGE Running Buffer	250 mM Tris base, 1.92 M glycine, 1% (w/v) SDS dissolved in ddH_2O
10X TBS	200 mM Tris base, 1.5 M NaCl dissolved in ddH_2O (pH 7.6)
4X Protein loading dye	40% Glycerol, 240 mM Tris-HCl (pH: 6.8), 8% (w/v) SDS, 0.04 (w/v) bromophenol blue, 5% (v/v) beta-mercaptoethanol mixed in ddH_2O
Blocking Buffer for Western Blot	3% (w/v) BSA dissolved in 1x TBST
FACS Buffer	1% (w/v) BSA, 0.05% (w/v) NaN_3 dissolved in 1X PBS
Stripping Buffer for Western Blot	2.8 g/L Glycine, 10 g/L SDS dissolved in ddH_2O (pH 2.2)
RIPA Lysis and Extraction Buffer	150 mM NaCl, 1% (v/v) NP-40, 0.5% (v/v) sodium deoxycholate, 0.1% (v/v) SDS, 50 mM Tris-HCl (pH 8.0), 50 mM NAF, 1 mM Na_3VO_4, 4% (v/v) protease

	inhibitor, 4% (v/v) phosphatase inhibitor, mixed in ddH_2O

2.1.2 Chemicals and Reagents

3-Aminopropionitrile fumarate (BAPN)	Santa Cruz, Dallas, TX, USA
6-aminocaproic acid	Sigma Aldrich, St. Louis, MO, USA
Acetic acid	Sigma Aldrich, St. Louis, MO, USA
Acrylamide/Bisacrylamide	Applichem, Darmstadt, Germany
Alpelisib (BYL719)	Selleck Chemicals, Houston, TX, USA
Ammonium persulfate	Carlo Erba, Cornaredu, Italy
ATN-161	Sigma Aldrich, St. Louis, MO, USA
Beta-mercaptoethanol	Applichem, Darmstadt, Germany
BO-264	Synthesized in Erden Banoğlu's Lab
Bosutinib	Selleck Chemicals, Houston, TX, USA
Bovine serum albumin	PAN-Biotech, Aidenbach, Germany
Bromophenol blue	Amresco LLC, Solon, OH, USA
Buparlisib (BKM120)	Selleck Chemicals, Houston, TX, USA
Calcium chloride dihydrate	Sigma Aldrich, St. Louis, MO, USA
Cisplatin	Santa Cruz, Dallas, TX, USA
Chloroquine	Selleck Chemicals, Houston, TX, USA
cOmplete tablets protease inhibitor	Roche Diagnostics GmbH, Mannheim, Germany
Cremophor® EL	Sigma Aldrich, St. Louis, MO, USA
Cyclophosphamide (Endoxan)	Baxter Oncology, Halle, Germany
Dactolisib (BEZ235)	Selleck Chemicals, Houston, TX, USA

Doxorubicin (Adriamycin)	Saba İlaç, İstanbul, Turkey
ECL	Thermo Scientific, Rockford, IL, USA
	GE Healthcare, Buckinghamshire, UK
Ethanol	Sigma Aldrich, St. Louis, MO, USA
Etoposide (VP-16)	Selleck Chemicals, Houston, TX, USA
Everolimus (RAD001)	Selleck Chemicals, Houston, TX, USA
Fluorouracil (5-FU)	Santa Cruz, Dallas, TX, USA
Gefitinib	Selleck Chemicals, Houston, TX, USA
Gemcitabine	Selleck Chemicals, Houston, TX, USA
Glycerol	Isolab, Wertheim, Germany
Glycine	BioShop, Burlington, ON, Canada
HEPES	SERVA, Heidelberg, Germany
Isopropanol	Sigma Aldrich, St. Louis, MO, USA
Irinotecan	Selleck Chemicals, Houston, TX, USA
Lapatinib	Selleck Chemicals, Houston, TX, USA
Matrigel® Matrix	Corning, Bedford, MA, USA
Methanol	Sigma Aldrich, St. Louis, MO, USA
MK-2206	Selleck Chemicals, Houston, TX, USA
Nonidet P-40	Sigma Aldrich, St. Louis, MO, USA
Page Ruler protein ladder	Thermo Scientific, Rockford, IL, USA
PF-562271	Selleck Chemicals, Houston, TX, USA
PhosSTOP phosphatase inhibitor	Roche Diagnostics GmbH, Mannheim, Germany
Ponceau S	BioShop, Burlington, ON, Canada
Potassium chloride	Merck KGaA, Darmstadt, Germany

Potassium phosphate monobasic	Sigma Aldrich, St. Louis, MO, USA
Purvalanol A	Selleck Chemicals, Houston, TX, USA
RO-3306	Merck KGaA, Darmstadt, Germany
Saracatinib	Selleck Chemicals, Houston, TX, USA
SB203580	Selleck Chemicals, Houston, TX, USA
Selumetinib	Selleck Chemicals, Houston, TX, USA
Sodium azide	Sigma Aldrich, St. Louis, MO, USA
Sodium chloride	Isolab, Eschau, Germany
Sodium deoxycholate	Sigma Aldrich, St. Louis, MO, USA
Sodium dodecyl sulfate	Merck KGaA, Darmstadt, Germany
Sodium fluoride	Sigma Aldrich, St. Louis, MO, USA
Sodium orthovanadate	Sigma Aldrich, St. Louis, MO, USA
Sodium phosphate dibasic dihydrate	Sigma Aldrich, St. Louis, MO, USA
SP600125	Selleck Chemicals, Houston, TX, USA
Sulforhodamine B sodium salt	Sigma Aldrich, St. Louis, MO, USA
TEMED	SERVA, Heidelberg, Germany
Thapsigargin	Sigma Aldrich, St. Louis, MO, USA
Trichloroacetic acid	Sigma Aldrich, St. Louis, MO, USA
Tris base	Sigma Aldrich, St. Louis, MO, USA
Tween 20	SERVA, Heidelberg, Germany
Volasertib	Selleck Chemicals, Houston, TX, USA

2.1.3 Media and Supplements

Calf/Newborn calf serum	Capricorn Scientific, Ebsdorfergrund, Germany

DMEM (low glucose, w/ phenol red)	Capricorn Scientific, Ebsdorfergrund, Germany EcoTech Biotechnology, Erzurum, Turkey
DMEM/F-12 (1:1)	Lonza, Basel, Switzerland
RPMI-1640	Capricorn Scientific, Ebsdorfergrund, Germany EcoTech Biotechnology, Erzurum, Turkey
Epidermal growth factor (EGF)	Peprotech, London, UK
Fetal bovine serum	Biowest, Nuaille, France
Hydrocortisone	Sigma Aldrich, St. Louis, MO, USA
Insulin	Sigma Aldrich, St. Louis, MO, USA
L-glutamine solution (200 mM)	Sigma Aldrich, St. Louis, MO, USA
Non-essential amino acid solution	Sartorius, Göttingen, Germany
Penicillin-Streptomycin (100X)	Lonza, Basel, Switzerland
Trypsin (10X)	Biowest, Nuaille, France
Zinc chloride	Sigma Aldrich, St. Louis, MO, USA

2.1.4 Kits

Pierce™ BCA Protein Assay Kit	Thermo Scientific, Rockford, IL, USA
FITC Annexin V Apoptosis Detection Kit	BioLegend, San Diego, CA, USA
CellTiter-Glo Cell Viability Kit	Promega, Madison, WI, USA

2.1.5 Equipment

Amersham™ Imager 600	GE Healthcare, Chicago, IL, USA
Cell counting chamber (hemocytometer)	Marienfeld, Könighofen, Germany
Cell culture hood	Nüve, Ankara, Turkey
Cell culture incubator	Nüve, Ankara, Turkey
Centrifuges	Thermo Scientific, Rockford, IL, USA
	Beckman, Pasadena, CA, USA
EVOS® FL Auto	Thermo Scientific, Rockford, IL, USA
Freezer (-80 °C)	Hettich, Bäch, Switzerland
	Thermo Scientific, Rockford, IL, USA
Freezer (-20 °C)	Bosch, Stuttgart, Germany
	Arçelik, İstanbul, Turkey
Orbital shakers	Bellco, Vineland, NJ, USA
	FinePCR, Seoul, South Korea
Laminar flow hood	Nüve, Ankara, Turkey
Microbiological incubator	Binder GmbH, Tuttlingen, Germany
Mini-PROTEAN® gel casting module	Bio-Rad, Hercules, CA, USA
Mini-PROTEAN® Tetra Cell	Bio-Rad, Hercules, CA, USA
Multichannel pipette	Thermo Scientific, Rockford, IL, USA
Novocyte Flow Cytometer	Agilent, Santa Clara, CA, USA
Power supplies for SDS-PAGE	Bio-Rad, Hercules, CA, USA
Refrigerator (+4 and -20 °C)	Arçelik, İstanbul, Turkey
Synergy HT™ microplate reader	Biotek, Winooski, VT, USA
Trans-Blot® Turbo™ Transfer System	Bio-Rad, Hercules, CA, USA
Vortex	Isolab, Wertheim, Germany

Water bath	Nüve, Ankara, Turkey

2.1.6 Consumables

100/20 mm cell culture dishes	Greiner Bio-One, Frickenhausen, Germany
145/20 mm cell culture dishes	Greiner Bio-One, Frickenhausen, Germany
12-well cell culture plate	Greiner Bio-One, Frickenhausen, Germany
24-well cell culture plate	Greiner Bio-One, Frickenhausen, Germany
6-well cell culture plate	Sarstedt, Nümbrecht, Germany
96-well cell culture plate	Sarstedt, Nümbrecht, Germany
96-well plate, white opaque	Corning, Corning, NY, USA
Conical centrifuge tubes (15, 50 mL)	Greiner Bio-One, Frickenhausen, Germany
Cryovials	Nest Scientific, Woodbridge, NJ, USA
Filtered tips (20, 200, 1000 µL)	Greiner Bio-One, Frickenhausen, Germany
Glass storage bottles	Corning, Corning, NY, USA
Motorized pipette controller	Gilson, Middleton, WI, USA
Non-filtered tips (10, 200, 1000 µL)	Corning, Corning, NY, USA
Parafilm	Bemis, Neenah, WI, USA
Pipettes (2, 20, 200, 1000 µL)	Gilson, Middleton, WI, USA
Polypropylene pockets	Leitz, Oberkochen, Germany

PVDF membrane for blotting	Bio-Rad, Hercules, CA, USA
Reaction tubes (0.5, 1.5, 2 mL)	Greiner Bio-One, Frickenhausen, Germany
Reagent reservoirs	VWR, West Chester, PA, USA
Serological pipettes (5, 10 mL)	Greiner Bio-One, Frickenhausen, Germany
Syringe filters (0.2, 0.45 µm)	Sartorius, Göttingen, Germany
T25 tissue culture flask	Sarstedt, Nümbrecht, Germany
T75 tissue culture flask	Sarstedt, Nümbrecht, Germany
Whatman™ paper	GE Healthcare, Buckinghamshire, UK

2.2 Methods

2.2.1 Cell Culture

2.2.1.1 Cell Line Maintenance

Human triple-negative breast cancer and non-tumorigenic breast epithelial cell lines were purchased from ATCC (Manassas, VA, USA), except CAL-51 and HCC1143 which were kindly provided by Ali Osmay Güre (currently at Acıbadem University) and MDA-MB-231-luc2-GFP by Dihua Yu (MD Anderson Cancer Center, USA). BT-20, MDA-MB-157, MDA-MB-231, MDA-MB-231-luc2-GFP, MDA-MB-436 and MDA-MB-468 cells were cultured in Dulbecco's modified Eagle's medium (DMEM) supplemented with 8% FBS. 10 µg/mL insulin was also added to the MDA-MB-436 culture medium. CAL-51, HCC1143, HCC1937 and HCC70 cells were maintained in RPMI-1640 containing 6% calf or newborn calf serum. MCF10A and MCF-12A cells

were grown in DMEM/F12 (1:1) containing 8% FBS, 20 ng/mL EGF, 0.5 µg/mL hydrocortisone and 30 µM ZnCl2, an alternative to insulin. All the media were complemented with 1% NEAA, 1% L-glutamine, 1% Penicillin-Streptomycin and HEPES (10, 25, and 15 mM, respectively). The cells were kept in a humidified incubator at 37 °C, 5% CO_2 condition and checked daily under microscope to monitor their health and growth status. This was usually followed by either medium replenishment or passaging by trypsinization (at 80-90% confluency) every 2-3 days. The cells were not used for more than 40 passages except during the development of the chemoresistant cell line models when the parental cells were passaged in parallel to rule out the passage-related effects. None of these cell lines are included in the list version 11 of commonly misidentified cell lines published by ICLAC.

2.2.1.2 Development of Chemoresistant Cell Lines

Before starting to develop chemoresistant cell line models, the chemotherapy response data of each parental cell line was retrieved from Cancerrxgene and PharmacoDB in order to identify potentially chemosensitive cell lines for each drug, thereby facilitating the process and limiting excess drug use throughout. Each cell line was then tested by cell viability/cytotoxicity assay, either by Sulforhodamine B (SRB) or CellTiter-Glo (CTG) assay, to evaluate the concordance between the retrieved and my experimental data and thus enable reliable selection of the candidate cell lines. Thereafter, the chemoresistant cells were generated by chronic exposure to gradually increasing concentrations of each chemotherapy agent with the initial dose being selected as IC25. The cells were not maintained constantly in chemotherapy-containing medium, allowing them to recover in drug-free medium between drug

treatments. Whenever the cells showed no signs of obvious growth delay, treatment with the next dose was started. After every 3-dose increase, chemoresponse of the candidate resistant cells was evaluated in comparison to the parental ones to interpret their resistance status and guide the next dose selection if necessary.

2.2.1.3 Cryopreservation

To prepare stocks of the parental cell lines every few passages or the resistant cell lines after every 2-dose increase, the cells were cryopreserved according to the provider's instructions for each cell line. Briefly, once the cells reached 80-90% confluency, they were collected by trypsinization (2-15 minutes depending on cell line) in a tube containing 5-fold medium. The tubes were spun at 300 x *g* for 5 minutes at 4 °C while the cells were counted by using a hemocytometer. Then they were washed once with cold 1X PBS, and the centrifugation was repeated. Cell pellets were suspended in the appropriate complete culture medium. This medium was supplemented with 5-10% DMSO (for critical samples 25% FBS, 10% DMSO) to yield 0.5-2 x 10^6 cells/mL depending on the cell line. The suspension was aliquoted into multiple cryovials, which were kept at -20 °C for 1 h and then transferred to -80 °C for overnight storage. Subsequently, the vials were placed into liquid nitrogen tanks for long-term storage.

2.2.2 Cell-based Assays

2.2.2.1 Drug Treatment and Cell Viability Assays

Cells were seeded in 96-well plate in 80 µL medium at a low density to reach 30-40% confluency at the time of drug treatment. This density corresponds to 3 x 10^3 cells/well

for MDA-MB-157; 4 x 10^3 cells/well for CAL-51; 5 x 10^3 cells/well for BT-20 and MDA-MB-231; 6 x 10^3 cells/well for HCC1143, HCC1937, MCF10A, MCF-12A and MDA-MB-436; and 8 x 10^3 cells/well for HCC70 and MDA-MB-468. The numbers were determined based on the cellular size, growth patterns and doubling time. After overnight incubation, drug solutions were prepared/diluted using the appropriate cell culture medium, and then the cells were treated with varying doses of chemotherapy agents or inhibitors via 40 µL medium-drug mixture. After 72 h drug treatment, cell viability or growth inhibition was assessed by SRB or CTG assay.

For cell viability measurement by SRB, the 96-well plate was incubated at room temperature for 15 minutes for temperature equilibration. The cells were fixed by either 80 µL of 25% (w/v) cold TCA (directly added on top of the wells) or 80 µL of cold 10% (w/v) TCA (added after the removal of medium) for at least 1 h at 4 °C. The cells were then washed three times under tap water and stained with 50 µL of 0.4% (w/v) SRB dissolved in 1% acetic acid for 30 minutes at room temperature in the dark. Following incubation, the plates were washed three times using 1% acetic acid to remove unbound and excess dye. The plates were left to air dry for 10-15 minutes at room temperature after tapping the plate into a paper towel a few times. The retained dye in the wells were solubilized by 150 µL of 10 mM Tris base by shaking the plate for 15 minutes. Finally, absorbance was measured at 564 nm. The average absorbance value of the vehicle wells after subtraction of the average blank absorbance was assumed to show 100% viability. At least 3 biological replicates were used for each control and treatment condition.

For cell proliferation measurement by CTG, the 96-well plate and CTG reagent were incubated at room temperature for 30 minutes to equilibrate the temperature. 20 µL of the reagent was then directly added to the medium in each well and the plate was shaken on orbital shaker to induce cell lysis for 15 minutes. The content of the plate was transferred to a white opaque 96-well plate and luminescent signal was measured by microplate reader. The average luminescence signal of the vehicle wells after subtraction of the average blank luminescence was considered 100% viability. At least 3 biological replicates were used for each control and treatment condition.

2.2.2.2 Annexin V/PI Staining and Flow Cytometry

At the end of drug treatments, the medium in each well was collected to 1.5 mL tubes. Cells were trypsinized, collected to the same tubes and centrifuged at 2000 x *g* for 3 minutes at 4 °C. The samples were later suspended in 500 µL of FACS buffer and spun at 2000 x *g* for 3 minutes at 4 °C to wash the pellets once. They were then resuspended in 100 µL of 1X Annexin V binding buffer. The samples were gently vortexed after the addition of 1 µL of FITC Annexin V and 2 µL of propidium iodide (PI), and incubated in the dark for 15 minutes at room temperature. Following the incubation, 200 µL of 1X Annexin V binding buffer was added to each tube. Afterwards, unstained and single stained (Annexin V or PI alone) samples were analyzed by flow cytometer on FITC and PE-Texas Red channels to determine gating strategy. Later, the samples were analyzed to annotate double-negative (viable cells), double-positive (necrotic cells) and single-positive (AV+/PI- early apoptotic; AV-/PI+ late apoptotic) populations.

2.2.3 Protein Biochemistry

2.2.3.1 Protein Isolation

At the end of experiments, cell culture medium was collected to retain apoptotic cells/bodies and centrifuged at 2000 x *g* for 5 minutes at 4 °C. Simultaneously, the cells were washed once with 1X PBS and trypsinized for detachment. The medium supernatant from the initial centrifuge step was used to inactivate trypsin and collect the cells to the same tubes. The samples were then centrifuged at 300 x *g* for 5 minutes at 4 °C. The supernatant was removed, and 1X PBS was added to each tube without disturbing the pellet to wash the samples. The samples were again centrifuged at 300 x *g* for 5 minutes at 4 °C. After this step, the pellets were either stored at -80 °C (not more than 2 weeks) or directly used for protein isolation.

For protein isolation from the cells, RIPA lysis/extraction buffer was prepared according to the **Table 2.1**. The cell pellets were then lysed in 40-300 µL of RIPA buffer, depending on the pellet size, first by pipetting and then by vortexing every 5 minutes for a total of 15 minutes. After agitation, the lysates were centrifuged at 18,000 x *g* for 15 minutes at 4 °C and the supernatants were transferred to new tubes to store at -80 °C until the experiment. For protein isolation from the xenografts, a 50 mg sample was dissected and washed twice with 1X PBS at 18,000 x *g* for 1 minute. After adding 100-300 µL RIPA buffer, the minced samples were sonicated at 40% amplitude for 2 minutes (10 sec ON, 10 sec OFF) for 2 cycles. The lysates were vortexed for 10 seconds every 5 minutes for a total of 30 minutes and centrifuged at 18,000 x *g* for 15 minutes at 4 °C. The supernatants were transferred to the new tubes for long-term storage. The tubes were kept on ice for the entirety of the protocol.

Table 2.1. RIPA Lysis and Extraction Buffer Composition

Ingredient	Stock Concentration	Final Concentration	For 1 mL
NaCl	2 M	150 mM	75 µL
NP-40	10%	1%	100 µL
Sodium DOC	10%	0.5%	50 µL
SDS	10%	0.1%	10 µL
Tris-HCl (pH 8.0)	2 M	50 mM	25 µL
NAF	1 M	50 mM	50 µL
NA_3VO_4	100 mM	1 mM	10 µL
Protease inhibitor	25X	4%	40 µL
Phosphatase inhibitor	20X	4%	40 µL
ddH_2O	-	-	600 µL

2.2.3.2 Protein Quantification

Protein quantification was performed using Pierce™ BCA (Bicinchoninic Acid) Protein Assay Kit according to the manufacturer's instructions with some changes. Briefly, 24 µL of the BSA standard samples were loaded in duplicates to a clear 96-well plate. Similarly, 3 µL of the protein samples were loaded in duplicates, yielding a dilution factor of 8 between the standards and samples. 200 µL of the Solution A:Solution B (50:1 part) from the kit was pipetted to each well. The plate was mixed thoroughly for 1 minute on orbital shaker and later incubated for 32 minutes at a non-humidified 37 °C incubator. Without cooling the plate to room temperature, absorbance was immediately measured at 562 nm on the plate reader. The average

absorbance reading from the blank wells was subtracted from the standard and sample absorbance readings. Using the standard concentrations and absorbance values, a standard calibration curve was plotted and protein concentrations were determined from the line formula and multiplication by dilution factor.

2.2.3.3 Sodium Dodecyl Sulfate Polyacrylamide Gel Electrophoresis (SDS-PAGE)

Stacking (2 mL/gel) and resolving (5 mL/gel) polyacrylamide gel solutions were simultaneously prepared according to the **Table 2.2**, except TEMED that was added just before casting. The resolving gel percentage was determined by the set of proteins of interest at the current experiment. Following gel preparation, the resolving gels were casted via Pasteur pipettes between the spacer and short plates held together by Mini-PROTEAN gel casting module. Isopropanol was used to overlay the gel solution. After polymerization of the resolving gel for approximately 10-15 minutes, isopropanol was discarded. The plates were dried by paper towel and additionally left to air dry for 2 minutes. Subsequently, the stacking gels were poured and combs were placed into the gel solution straightaway. Meanwhile, 20-50 µg/µL of sample per lane was prepared by mixing the required amount of total protein sample, 4X protein loading dye **(Table 2.3)** and double-distilled water. One extra volume was prepared for every 10 loadings. The mixture was vortexed thoroughly and denatured at 95 °C for 3-4 min. 1.5 and 1 µL of protein ladder or 20 and 13 µL of samples were then loaded per lane for 10- and 15-well combs, respectively. The remaining lanes were filled with 1X protein loading dye. The electrophoresis was run first at 90 volts for 20

minutes to concentrate the protein samples within the stacking gel and later at 130 volts for 1 h to separate the proteins based primarily on their molecular weight.

Table 2.2. Compositions of the Stacking (S) and Resolving (R) Gels

Ingredient	**5% S Gel**	**8% R Gel**	**10% R Gel**	**12% R Gel**
ddH_2O	1.36 mL	2.3 mL	1.9 mL	1.6 mL
30% acrylamide mix	0.34 mL	1.3 mL	1.7 mL	2 mL
1M Tris	0.26 mL (pH 6.8)	1.3 mL (pH 8.8)		
10% SDS	20 µL	50 µL		
10% APS	20 µL	50 µL		
TEMED	2 µL	5 µL		
Total volume	**2 mL**	**5 mL**	**5 mL**	**5 mL**

Table 2.3. 4X Protein Loading Dye Composition

Ingredient	**Stock Concentration**	**Final Concentration**	**In 10 mL**
Glycerol	100%	40%	4 mL
Tris-HCl (pH 6.8)	1 M	240 mM	2.4 mL
SDS	-	8%	0.8 g
Bromophenol blue	-	0.04%	4 mg
Beta-mercaptoethanol	100%	5%	0.5 mL
ddH_2O	-	-	3.1 mL

2.2.3.4 Western Blotting

Proteins separated by SDS-PAGE were transferred to PVDF membrane (6.5 x 8.5 cm^2) via semi-dry transfer. Shortly, 3, 2 and 5 Whatman papers (7 x 9 cm^2) were soaked into Anode I, Anode II and Cathode buffers, respectively, for 2 minutes. First, the Whatman papers from the Anode I buffer was placed onto the transfer cassette and excess buffer/bubbles were removed by a roller. The same step was repeated for the Whatman papers from the Anode II buffer. The PVDF membrane, which was initially submerged in absolute methanol for activation for 2 minutes, was placed in Anode II buffer for 30 seconds and then placed onto the Whatman papers on the transfer cassette. Polyacrylamide gel was removed from the electrophoresis apparatus and wet inside 1X Running buffer to ease the separation of the short and spacer plates. Later, the stacking gel part was discarded, and the resolving gel part was put onto the PVDF membrane in the right direction. The gel was covered on top by the Whatman papers from the Cathode buffer, and the transfer cassette was closed/locked at once. Bio-Rad Trans-Blot® was run with the default protocols for 1 mini gel or 1 midi/2 mini gels.

After the transfer, the Whatman papers were discarded, and the PVDF membrane was shaken on orbital shaker for 2 minutes while dipped into Ponceau S solution for total protein staining. This served as both transfer and equal loading control and a guide for appropriate cutting of the membranes together with the protein ladder. The membranes were later serially washed in distilled water twice for 1 min each to remove excess dye and were cut according to the proteins of interest. Later, the cut membranes were washed in 1X TBS for 2 minutes to get rid of any remaining Ponceau S. They were later blocked in 3% BSA for 1 hour at room temperature to avoid non-specific binding of the antibodies. Subsequently, the blots were gently washed in 1X

TBS for 2 minutes to remove unbound BSA and placed in conical primary antibody tubes for overnight incubation at 4 °C on the orbital shaker. Following the primary antibody incubation, the membranes were rigorously washed three times in 1X TBST for 10 minutes each. They were then incubated with the appropriate secondary antibodies for 1 hour at room temperature or overnight at 4 °C on the orbital shaker followed by exactly the same washing step. The blots were maintained in 1X TBS until and during imaging. List of primary and secondary antibodies utilized in the Western blot is provided in **Table 2.4**.

The membranes were developed through chemiluminescence by using Amersham™ Imager 600. Briefly, the membranes first desiccated on a paper towel for 1-2 minutes. ECL mixture (1:1) was then applied starting from the first lane to the last while they were placed/covered in a punched pocket on the tray to avoid nonuniform ECL distribution. The blots were incubated for 1 minute to allow chemical reaction (luminol oxidation by horseradish peroxidase of the secondary antibody) to proceed and exposed at automatic capture mode.

Although not performed regularly, some blots were used to detect more than one protein after stripping. To strip off the primary and secondary antibodies, the membranes were agitated in acidic stripping buffer for 30 minutes and then washed in 1X PBS or 1X TBS twice for 10 minutes each. The membranes were later blocked in 3% BSA followed by reprobing with the primary and secondary antibodies.

Table 2.4. Primary and Secondary Antibodies Used in Western Blot

Antibody*	**Company**	**Catalog No**	**Host**	**Dilution**
4E-BP1	CST	9452	Rabbit	1:2,000
Akt	CST	9272	Rabbit	1:2,000
Alpha smooth muscle actin	Abcam	ab5694	Rabbit	1:2,000
Anti-mouse IgG, HRP-linked	CST	7076	Horse	1:20,000
Anti-rabbit IgG, HRP-linked	CST	7074	Goat	1:20,000
ATF-6α	Santa Cruz	sc-22799	Rabbit	1:2,000
ATM	CST	2873	Rabbit	1:2,000
Bax	CST	2774	Rabbit	1:1,000
Bcl-2	CST	15071	Mouse	1:1,000
Beclin-1	CST	3738	Rabbit	1:1,000
Bim	Santa Cruz	sc-11425	Rabbit	1:2,000
BRCA1	Abcam	ab191042	Rabbit	1:2,000
CA9	Novus	NB100-417	Rabbit	1:1,000
Calregulin	Santa Cruz	sc-166837	Mouse	1:2,000
Calreticulin	Abcam	ab2907	Rabbit	1:1,000
Caspase-8	Novus	NB100-56116	Rabbit	1:1,000
Cdk2	Sigma-Aldrich	C5223	Rabbit	1:2,000
Cdk4	Abcam	ab68266	Rabbit	1:2,000
Cdk6	Santa Cruz	sc-177	Rabbit	1:2,000
Cleaved Caspase-3 (N175)	CST	9664	Rabbit	1:1,000
Cleaved Caspase-7 (N198)	CST	8438	Rabbit	1:1,000
Cleaved Caspase-9 (N330)	CST	7237P	Rabbit	1:1,000
Cleaved PARP (N214)	CST	5625	Rabbit	1:1,000
CREB	CST	4820	Rabbit	1:2,000
Cyclin D1	CST	2922	Rabbit	1:1,000
E Cadherin	Abcam	ab1416	Mouse	1:500
EGF Receptor	CST	2646	Rabbit	1:1,000
eIF2α	Santa Cruz	sc-11386	Rabbit	1:2,000
FAK	CST	3285	Rabbit	1:2,000
FAK (p-Y397)	Abcam	ab39967	Rabbit	1:2,000
Fibronectin	Santa Cruz	sc-81767	Mouse	1:1,000
GAPDH	Santa Cruz	sc-47724	Mouse	1:10,000
HIF-1 alpha	Abcam	ab51608	Rabbit	1:2,000
Histone H2A.X	CST	2595	Rabbit	1:2,000

Integrin alpha 5	Abcam	ab150361	Rabbit	1:2,000
IRE1 (p-S724)	Abcam	ab124945	Rabbit	1:2,000
IRE1α	CST	3294	Rabbit	1:2,000
JNK1	CST	3708	Mouse	1:2,000
LC3A/B	CST	12741	Rabbit	1:2,000
Lyn	Santa Cruz	sc-7274	Mouse	1:2,000
MMP-1	Novus	NBP2-22123	Mouse	1:2,000
MMP2	Abcam	ab86607	Mouse	1:2,000
mTOR	CST	2972	Rabbit	1:2,000
N-cadherin	Santa Cruz	sc-7939	Rabbit	1:1,000
p16	BD	51-1325GR	Mouse	1:4,000
p21	BD	554288	Mouse	1:4,000
p27[Kip1]	BD	610241	Mouse	1:4,000
p38 MAPK	CST	9212	Rabbit	1:2,000
p44/42 MAPK (Erk1/2)	CST	4695	Rabbit	1:2,000
p-4E-BP1 (S65)	CST	9451	Rabbit	1:2,000
p-4E-BP1 (T37/46)	CST	2855	Rabbit	1:2,000
p53	CST	2527	Rabbit	1:2,000
p53 (p-S15)	Abcam	ab1431	Rabbit	1:2,000
p-Akt (S473)	CST	4058	Rabbit	1:2,000
p-Akt (T308)	CST	4056	Rabbit	1:2,000
p-AMPKα (T172)	CST	4188	Rabbit	1:2,000
Paxillin	Merck	05-417	Mouse	1:2,000
p-Bcl-xL (S62)	Invitrogen	44-428G	Rabbit	1:2,000
p-cdc2 (T14)	CST	2543	Rabbit	1:2,000
p-cdc25C (S216)	CST	4901	Rabbit	1:2,000
p-CREB (S133)	CST	9198	Rabbit	1:2,000
p-eIF2α (S51)	CST	3597	Rabbit	1:2,000
PERK	CST	5683	Rabbit	1:1,000
p-FOXO3 (S253)	MyBioSource	MBS128272	Rabbit	1:2,000
p-Histone H2A.X (S139)	CST	9718	Rabbit	1:1,000
p-Histone H3 (S10)	CST	9701	Rabbit	1:1,000
PLK1	Invitrogen	PA5-28023	Rabbit	1:2,000
p-mTOR (S2448)	CST	5536	Rabbit	1:2,000
p-p38 MAPK (T180/Y182)	CST	4511	Rabbit	1:2,000
p-p44/42 MAPK (Erk1/2) (T202/Y204)	CST	4376	Rabbit	1:2,000
p-PERK (T982)	Invitrogen	PA5-40294	Rabbit	1:2,000
p-PRAS40 (T246)	CST	2997	Rabbit	1:2,000

PRAS40	CST	2691	Rabbit	1:1,000
p-Rb (S807/811)	CST	8516	Rabbit	1:2,000
p-S6 Ribosomal Protein (S235/236)	CST	2211	Rabbit	1:4,000
p-S6 Ribosomal Protein (S240/244)	CST	5364	Rabbit	1:4,000
p-SAPK/JNK (T183/Y185)	CST	4668	Rabbit	1:1,000
p-Smad2 (S465/467)	CST	3108	Rabbit	1:1,000
p-Src Family (Y416)	CST	2101	Rabbit	1:2,000
p-Stat3 (S727)	CST	9134	Rabbit	1:1,000
p-Stat3 (Y705)	CST	9145	Rabbit	1:1,000
Rb	CST	9309	Mouse	1:2,000
S6 Ribosomal Protein	CST	2217	Rabbit	1:1,000
SLUG	Abcam	ab27568	Rabbit	1:1,000
Smad2/3	CST	8685	Rabbit	1:2,000
Snail (SNAI1)	CST	3879	Rabbit	1:1,000
SQSTM1/p62	CST	5114	Rabbit	1:2,000
Src	CST	2108	Rabbit	1:1,000
Stat3	CST	9139	Mouse	1:2,000
Superoxide Dismutase 1/SOD1	Santa Cruz	sc-17767	Mouse	1:2,000
Vimentin	CST	5741	Rabbit	1:1,000
ZEB1	Santa Cruz	sc-25388	Rabbit	1:1,000
ZO-1	CST	13663	Rabbit	1:1,000
β-Actin	Sigma-Aldrich	A5441	Mouse	1:10,000

*: Antibody names/symbols were written as in the antibody datasheet, except Phospho- was denoted by “p-” and single letter codes were used for amino acid abbreviations.

2.2.4 Animal Studies

2.2.4.1 Primary Xenografts

All animal experiment protocols were assessed and approved by Animal Ethics Committee at Bilkent University. To generate primary xenografts, the cells were detached by trypsinization and collected into conical tubes containing complete culture medium. After counting the cells by hemocytometer, the cells were pelleted at 300 x g for 5 minutes at 4 °C. They were washed once in ice-cold 1X PBS and

suspended in 1:1 Matrigel-PBS mixture (100 µL/mouse). 2 extra volumes were prepared for every 5 mice to compensate for the loss in syringe. 3 x 10^6 and 1 x 10^6 CAL-51 and MDA-MB-231-luc2-GFP cells, respectively, were subcutaneously injected into the 2nd mammary fat pad of 6-8-week-old female athymic nude mice. The cells were rigorously vortexed before each injection and kept on ice during the experimental procedure to minimize cell death and avoid Matrigel polymerization. After tumors became palpable, tumor dimensions were measured by caliper every 2-3 days, and tumor volume was calculated using the following formula, (length x width x width)/2.

2.2.4.2 Development of Chemoresistant Xenografts

To develop doxorubicin- or paclitaxel-resistant xenograft models, primary tumors were generated according to the protocol summarized in the previous section. Once tumors reached 80-100 mm^3 in volume, animals were randomly assigned into control and treatment groups. The animals in the control group for doxorubicin or paclitaxel were injected intravenously with 0.9% saline or intraperitoneally with DMSO:Cremophor EL:Saline (1:1:8) mixture, respectively, once a week. Accordingly, the treatment groups were weekly treated with 2 mg/kg (CAL-51) or 2.5 mg/kg (MDA-MB-231-luc2-GFP) doxorubicin or 10 mg/kg paclitaxel. The tumors that showed reduction or no/minimal increase in volume after 4 drug treatments were considered “sensitive” and were collected 3 days after the last treatment. Other tumors in the treatment arm were regarded as “resistant” and continued to receive chemotherapy. The vehicle and resistant group tumors were collected when their

volumes reached at least 1500 mm^3 or 3 days after they received 12-cycles of treatment.

2.2.5 Bioinformatics

2.2.5.1 Gene Set Enrichment Analysis (GSEA)

Gene set enrichment analysis (GSEA, Broad Institute) was performed to identify significantly altered pathways or processes between two biological conditions. To do this, normalized molecular profiling data (commonly microarray or RNA-seq) were retrieved from Gene Expression Omnibus (GEO, NCBI) and imported into the GSEA software after small modifications such as unifying sample names and labeling missing data as “na”. The samples were then divided into 2 phenotypes and phenotype labels were manually provided to the program. Gene sets of interest were downloaded directly through the application interface, and the analysis was run at default settings.

2.2.5.2 Survival Analysis

Patient survival data were downloaded from GEO or Kaplan-Meier Plotter. The patients were divided into 2 cohorts by median or through automatic best cut-off selection. The patients with missing data were not included in the analysis. The survival time and status for the remaining patients were provided to GraphPad Prism software to plot the graphs. Hazard ratio and significance comparison of survival curves were provided on each graph.

2.2.6 Statistical Analysis

All the experimental data were expressed as mean ± standard deviation (s.d.) or mean ± standard error of the mean (SEM). Normality and log-normality of the data distribution were assessed by D'Agostino & Pearson or Shapiro-Wilk test. To compare two-group experimental data, two-tailed *t* test (for normally distributed unpaired samples with equal variance or paired samples), two-tailed *t* test with Welch's correction (for normal unpaired samples with uneven variance) or Mann-Whitney test (for not normal unpaired samples) was used. To compare single agent groups to combination group and compare tumor volumes among all groups, ordinary one-way ANOVA followed by multiple comparison and two-way ANOVA were used, respectively. Statistical significance for survival curves was evaluated by log-rank test. Pearson correlation coefficients were calculated to evaluate mutual connection between different variables. Significance threshold was reported as follows: $*p < 0.05$; $**p < 0.01$; $***p < 0.001$; ns, not significant. All the analyses were performed using GraphPad Prism v9.4.

CHAPTER 3

RESULTS

Although many targeted therapies with immensely positive outcomes have improved the clinical management of cancer, some patient groups still rely on the use of systemic therapies. In **Part I and Part II Section 4.5** of my thesis, I will summarize our findings on the modeling of chemoresistance in triple-negative breast cancer in vitro/in vivo and how to overcome it by chemotherapy and targeted therapy/miRNA combinations. In **Part II Section 4.6**, I will briefly present an approach to overcome tamoxifen resistance, another systemic therapy, in ER-positive breast cancer through genetic and pharmacological inhibition of *PDE4D*.

PART I

3.1 Antimetabolite Resistance Models

Antimetabolites are a large class of chemotherapy commonly used in the treatment of multiple cancer types, such as breast, lung, pancreas and colon. Since they interfere with DNA/RNA synthesis, they effectively function during S phase of the cell cycle after extensively being metabolized from prodrug to active compound. Of these, pyrimidine analogues/antagonists are utilized to treat primary invasive and metastatic triple-negative breast cancer patients. Here I selected gemcitabine (GEM) and fluorouracil (5-FU) to model acquired antimetabolite resistance in TNBC. I first checked the response of a panel of TNBC cell lines to GEM and 5-FU from

CancerRxGene (152) and PharmacoDB (153), which gathers multiple drug response data sets such as GDSC and CTRP **(Figure 3.1 and Figure 3.2)**.

Cell Line	Drug	CancerRxGene (IC50 - µM)			PharmacoDB (IC50 - µM)			
		GDSC1_M	GDSC1_S	GDSC2	GDSC	CTRPv2	gCSI	FIMM
BT-20	GEM	0.181	0.136	18.7	0.085	ND	ND	NA
CAL-51	GEM	0.210	0.004	0.02	0.213	0.02	0.004	NA
HCC1143	GEM	NA	0.029	22.2	ND	NA	0.005	NA
HCC1937	GEM	20.2	0.061	225	ND	ND	ND	NA
HCC70	GEM	NA	0.047	35.6	ND	NA	NA	NA
MDA-MB-157	GEM	9.33	0.03	0.267	1.85	0.123	0.009	NA
MDA-MB-231	GEM	0.03	0.013	1.43	0.016	4.7	ND	NA
MDA-MB-436	GEM	0.764	0.011	1.76	ND	NA	0.017	NA
MDA-MB-468	GEM	0.016	0.022	0.165	0.015	0.013	0.008	NA

Figure 3.1. Gemcitabine response of a panel of TNBC cell lines representing different subtypes, retrieved from CancerRxGene and PharmacoDB. NA: not available, ND: not determined (not reached or cannot be calculated due to response curve). GDSC: Genomics of Drug Sensitivity in Cancer, M: Mass General Hospital, S: Sanger Institute, CTRP: Cancer Therapeutics Response Portal, gCSI: Genentech Cell Line Screening Initiative, FIMM: Institute for Molecular Medicine Finland.

Cell Line	Drug	CancerRxGene (IC50 - µM)			PharmacoDB (IC50 - µM)			
		GDSC1_M	GDSC1_S	GDSC2	GDSC	CTRPv2	gCSI	FIMM
BT-20	5-FU	180	NA	221	ND	200	NA	NA
CAL-51	5-FU	47.9	NA	28	78.7	21.8	NA	NA
HCC1143	5-FU	NA	NA	163	ND	2257	NA	NA

HCC1937	5-FU	160	NA	285	4.6e+10	29837	NA	NA
HCC70	5-FU	3.64	NA	283	3.39	NA	NA	NA
MDA-MB-157	5-FU	44.3	NA	32.7	ND	0.76	NA	NA
MDA-MB-231	5-FU	123	NA	79.4	5147	697	NA	NA
MDA-MB-436	5-FU	55.4	NA	153	ND	NA	NA	NA
MDA-MB-468	5-FU	20.1	NA	148	ND	187	NA	NA

Figure 3.2. 5-FU response of a panel of TNBC cell lines representing different subtypes, retrieved from CancerRxGene and PharmacoDB. NA: not available, ND: not determined (not reached or cannot be calculated due to response curve). GDSC: Genomics of Drug Sensitivity in Cancer, M: Mass General Hospital, S: Sanger Institute, CTRP: Cancer Therapeutics Response Portal, gCSI: Genentech Cell Line Screening Initiative, FIMM: Institute for Molecular Medicine Finland.

I also complemented these data by experimentally testing cell viability after 72 hours drug treatment **(Figure 3.3 and Figure 3.4)**, which overall shows a good concordance with the retrieved data in terms of relative sensitivity/insensitivity of the cell lines. By considering their overall sensitivity to drugs and to represent TNBC heterogeneity, I decided on CAL-51 and MDA-MB-468 to develop antimetabolite-resistant cell line models. CAL-51 is adenocarcinoma by histology, non-basal by PAM50, basal B by molecular, mesenchymal-like by FUSCC and metabolic-pathway based subtype 2 (MPS2) by metabolic classifications. MDA-MB-468 is ductal carcinoma, basal, basal A, basal-like immune suppressed and metabolic-pathway based subtype 3 by the respective classifications (74). BT-20 cell line (invasive ductal carcinoma, luminal androgen receptor subtype and MPS1) was considered de novo resistant to both drugs upon experimental testing, which implicates that there may be a common mechanism underlying resistance to GEM and 5-FU.

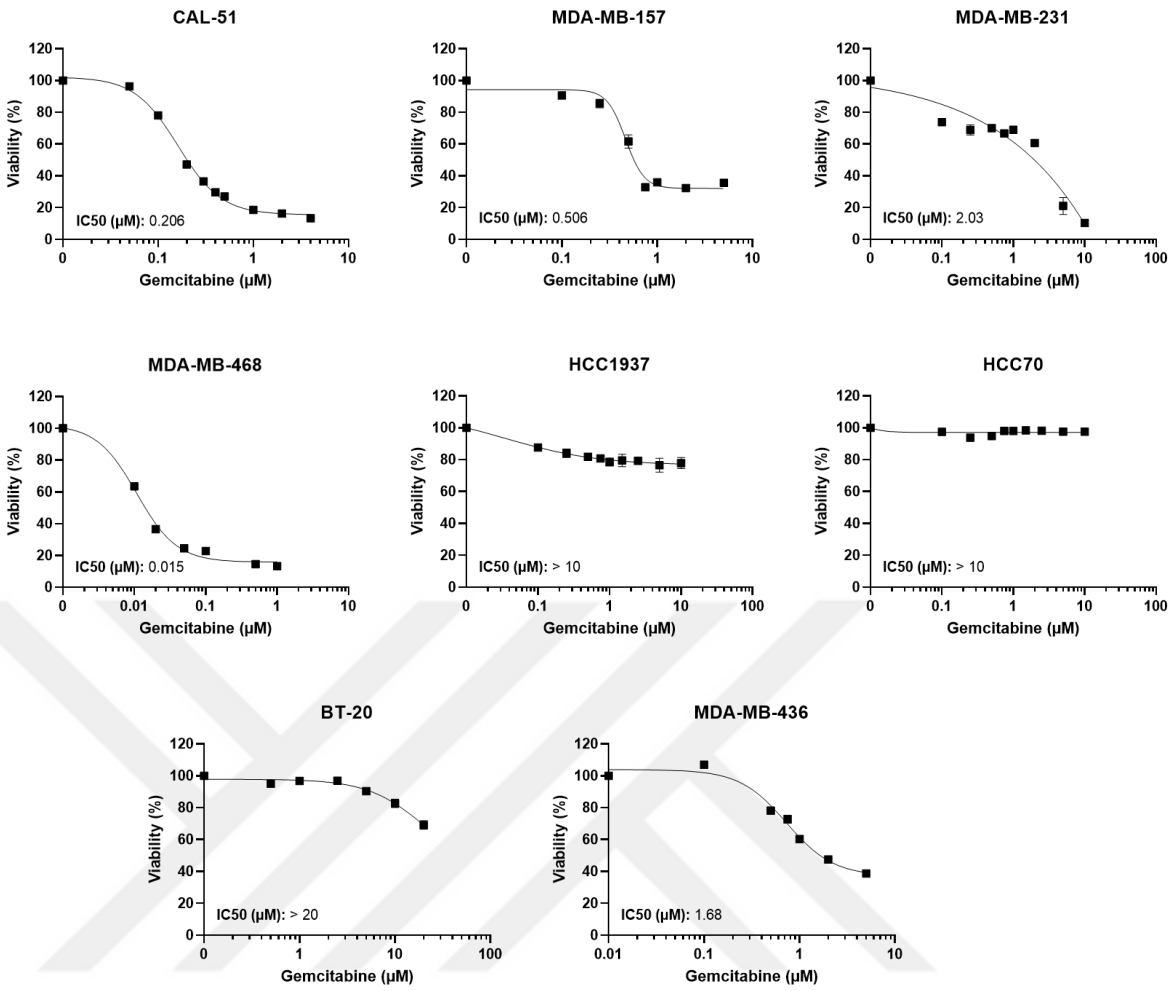
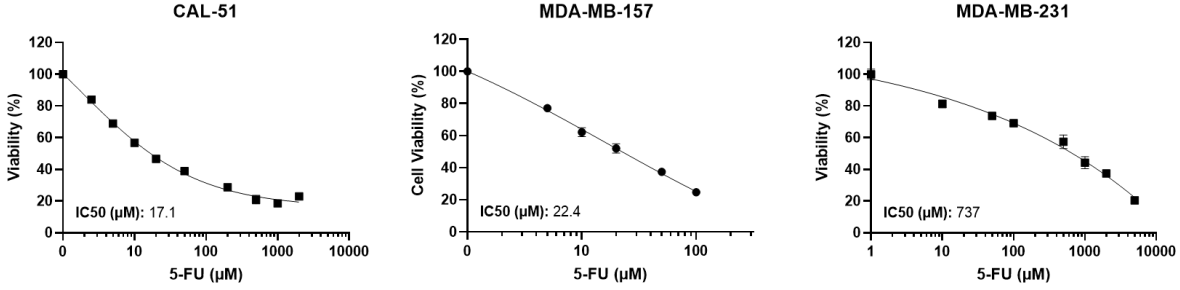


Figure 3.3. The response of the selected TNBC cell line panel to gemcitabine after 72h drug treatment as determined by cell viability assays.



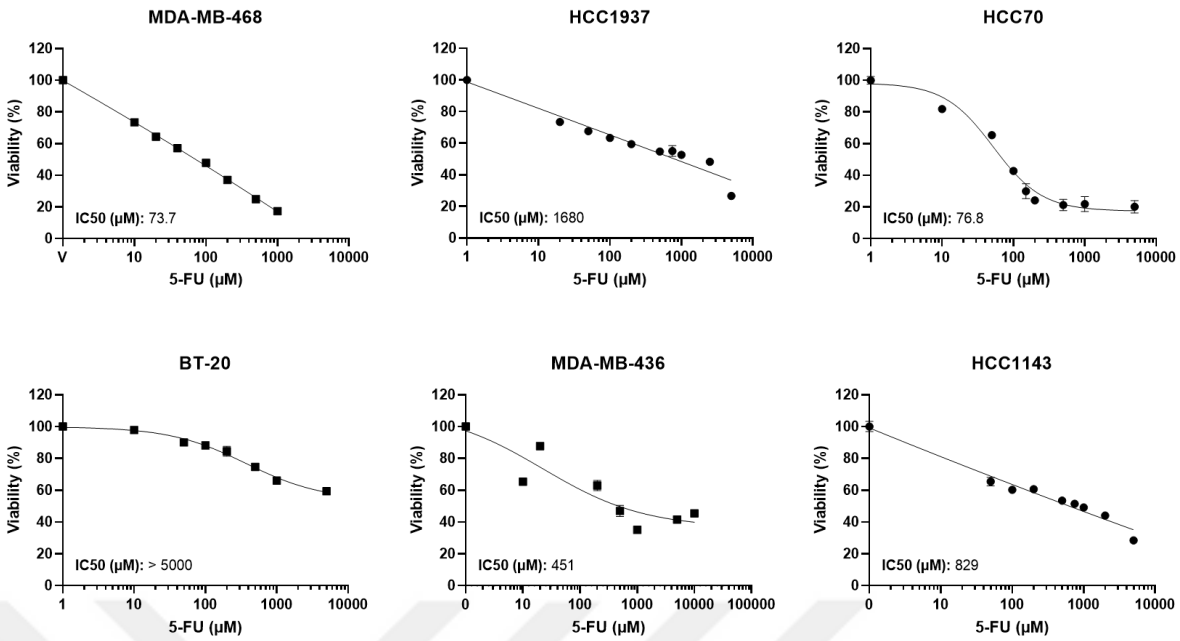
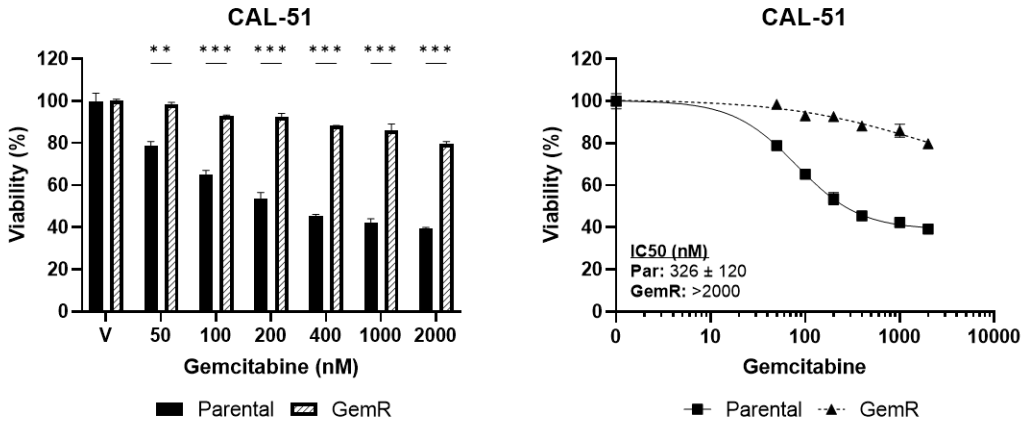


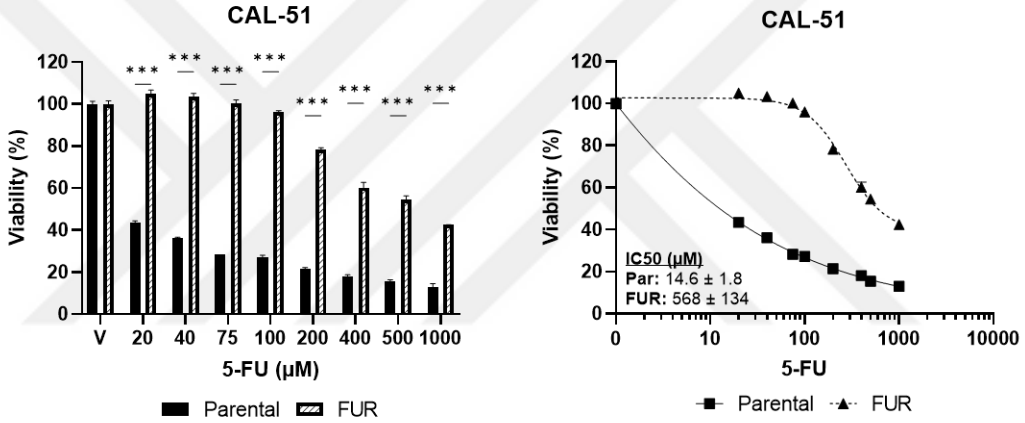
Figure 3.4. The response of the selected TNBC cell line panel to fluorouracil after 72h drug treatment as determined by cell viability.

I then started developing gemcitabine-resistant (CAL-51 GemR) and fluorouracil-resistant (CAL-51 FUR) counterparts of the CAL-51 parental cells by continuous exposure of the parental cells to increasing doses of the drugs. After 7-10 months, I tested the chemoresponse of the candidate resistant cells. I found that there are more than 5 and 30-fold difference between CAL-GemR **(Figure 3.5 A)** and CAL-51 FUR **(Figure 3.5 B)** IC50s, respectively, and marked reduction in apoptosis markers upon chemotherapy treatment in comparison to the parental cells **(Figure 3.5 C)**.

A



B



C

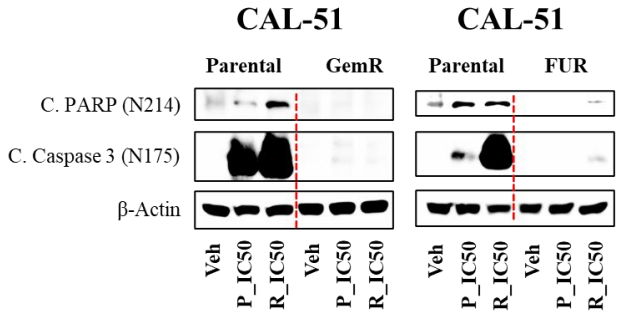


Figure 3.5. Development of CAL-51 gemcitabine-resistant and CAL-51 fluorouracil-resistant cells. A,B) The resistance relative to the parental cells was confirmed by cell viability assay C) Apoptosis markers upon vehicle (Veh), GEM or 5-FU treatment at IC50 of the parental cells (P_IC50) or IC50 of the resistant (R_IC50 or maximum dose tried) cells, respectively (*$p < 0.05$; **$p < 0.01$; ***$p < 0.001$; ns, not significant).

After validating the resistance in both drug models, I proceeded with the characterization of these models at protein level by extensive Western blotting. The scope of this characterization included the signaling pathways/processes or some key proteins, which were regularly implicated in breast cancer tumorigenesis, tumor progression, metastasis and drug resistance. These are PI3K/AKT/mTOR pathway (154), Integrin/FAK/SRC signaling (155), MAPK (p38, JNK, ERK1/2) pathways (156), STAT3 signaling (157), ER stress and autophagy (158), cell cycle proteins (159), DNA damage and repair proteins (160), and apoptosis (161), hypoxia (162)and EMT markers (163).

First, I investigated the differences between PI3K/AKT/mTOR pathway proteins upon resistance development in both models, relative to the parental cells **(Figure 3.6)**. AKT phosphorylation at threonine 308 and serine 473 residues was markedly increased in both models. However, this was not reflected to the downstream of AKT, such as mTORC1 and thus ribosomal protein S6 and 4EBP1 involved in protein synthesis, as their total and/or phosphoprotein levels showed either no significant change or dramatically reduced in the resistant cells. However, FOXO3 at serine 253 residue, the major inactivation target of the PI3K/AKT signaling, exhibited an enhanced phosphorylation. This phosphorylation (S253 or S252) by AKT or SGK in human, mouse and rat results in FOXO3 inhibition and prolonged pathway activity and survival (164). Consequently, PI3K/AKT could be driving gemcitabine and/or fluorouracil resistance independent of mTOR and its downstream targets.

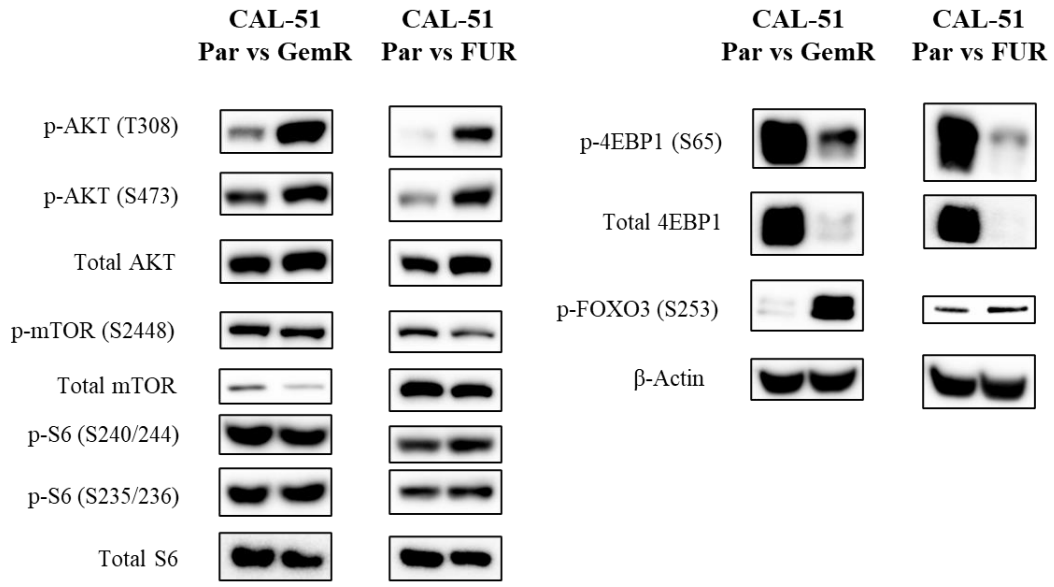


Figure 3.6. Changes in the PI3K/AKT/mTOR pathway components upon resistance development in CAL-51 GemR and FUR cells compared to the CAL-51 parental cells. Left lane: Parental, Right lane: Resistant.

I later compared the relative levels of integrin, MAPK and STAT3 signaling components between the parental and resistant cells **(Figure 3.7)**. Integrin signaling is initiated by FN1, recognized by ITGB1/ITGA5 heterodimeric receptor and later transmitted to downstream effector kinases such FAK and SRC (165). This mode of activation and signal transduction is more relevant in the context of 3D cell culture and in vivo but it can still be quite functional in 2D cell culture through less dispersed integrin clustering and focal adhesions (166). The activity of integrin signaling was hampered quite remarkably in the resistant cells. In contrast, MAP kinase signaling pathways (p38/SAPK – stress-activated protein kinase; JNK – Jun amino-terminal kinase; ERK – extracellular signal-regulated kinase) showed increased phosphorylation of the effector kinases except ERK1/2 phosphorylation in the GemR model. Similarly, STAT3 phosphorylation at two different residues (including canonical activation and dimerization site tyrosine 705) demonstrated obvious increase in the resistant cells. Although p38 and JNK are mostly known for their

proapoptotic functions, they can also mediate antiapoptotic and oncogenic activities in a cell type- and context-specific manner based on their isoforms (167, 168). STAT3, on the other hand, is a well-established oncogene in multiple oncogenic processes and cancer types. STAT3 could function in tandem with PI3K/AKT pathway to drive oncogenic transformation (169), limit the response to PI3K/AKT/mTOR inhibitor by activating compensatory survival processes (170), and also sequester p-FOXO1 and p-FOXO3a in the cytoplasm to prolong PI3K/AKT activity (171). These suggest a potential role for them during acquired resistance development.

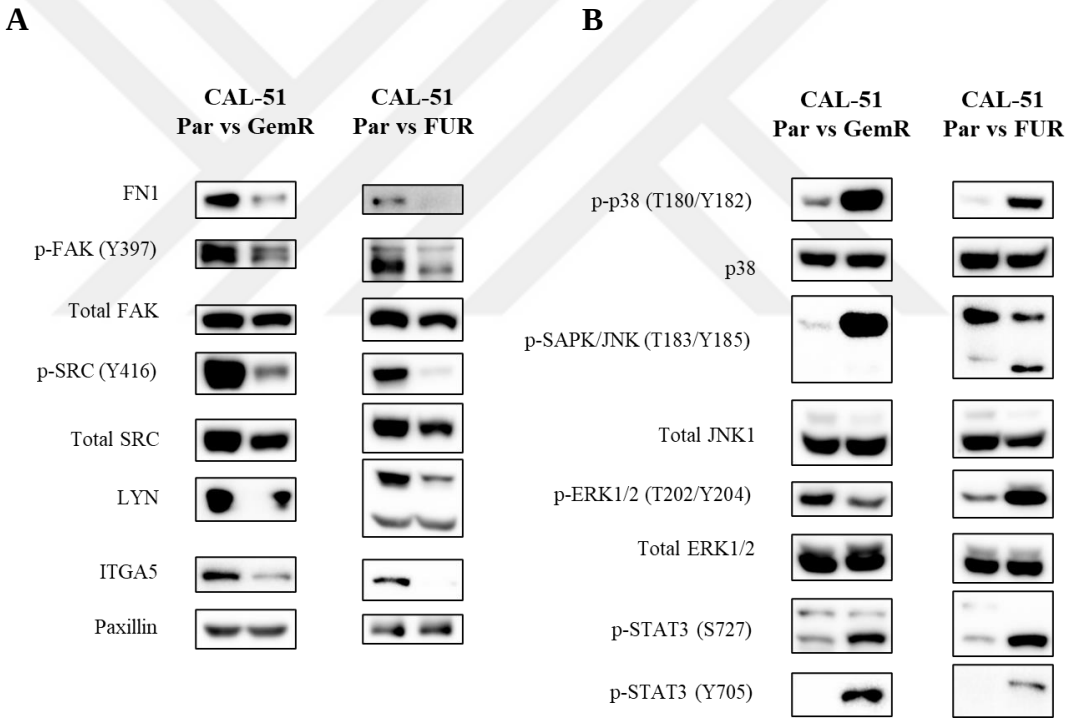


Figure 3.7. Changes in the Integrin, MAPK and STAT3 pathway components upon resistance development in CAL-51 GemR and FUR cells compared to the CAL-51 parental cells. Left lane: Parental, Right lane: Resistant.

Finally, I examined if or how ER stress markers **(Figure 3.8 A)** and cell cycle-related proteins **(Figure 3.8 B)** alter following acquisition of the resistance as they were implicated in chemoresistance to several agents (172, 173) While the GemR cells

shows a mixed phenotype, the FUR cells have predominantly reduced levels of ER stress markers. In terms of cell cycle, both models express decreased levels of G1 phase progression plus G1/S transition marker, CDK6 and increased levels of mitotic marker, phospho-Histone H3. However, G1 marker Cyclin D1 and G1/S transition markers such as CDK2 or senescence markers such as p21 and p27 (blocking G1/S transition and S phase progression) display a mixed phenotype between or within the models, respectively. Thus, it is not conclusively clear how cell cycle is regulated in the resistant models.

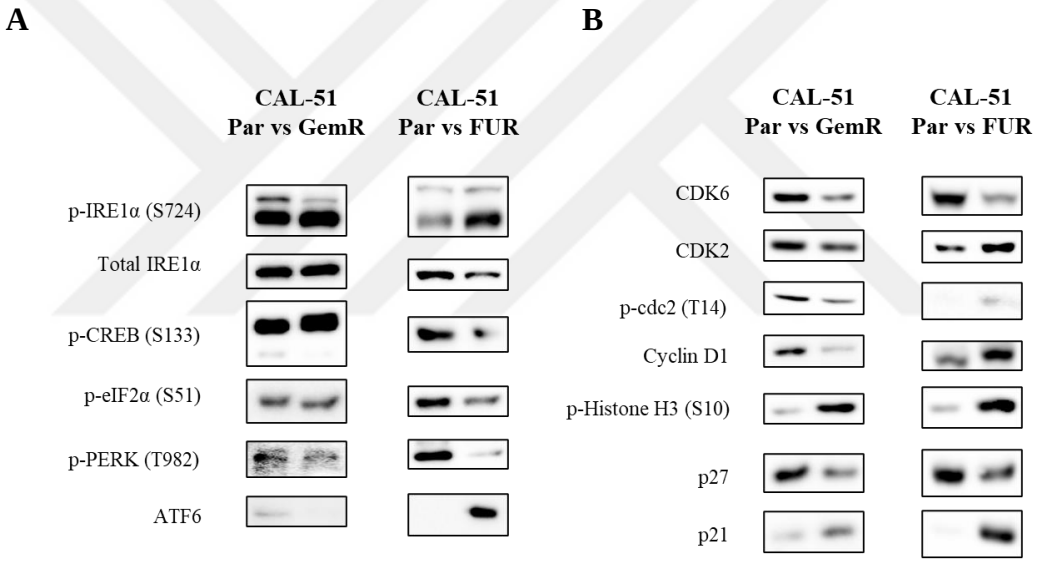


Figure 3.8. Changes in the ER stress markers and cell cycle-related proteins upon resistance development in CAL-51 GemR and FUR cells compared to the CAL-51 parental cells. Left lane: Parental, Right lane: Resistant.

Following the characterization of the resistance at protein level by Western blot, I decided to test if any of the activated pathway components could be substantially or partially promoting the acquisition of the resistance phenotype. Considering that MAP kinases exhibit almost uniform upregulation of their phosphoproteins in both models, I started by testing SB203580, a p38 MAPK inhibitor and SP600125, a JNK inhibitor

in combination with gemcitabine or fluorouracil in the GemR or FUR model, respectively. Chemotherapy and inhibitor combinations were capable of inducing significantly higher growth inhibition compared to the single agents in both chemoresistant models, except low gemcitabine (250 nM) combinations with SB203580, as shown by cell viability assay **(Figure 3.9)**, microscopy **(Figure 3.10 and Figure 3.11)** and Annexin V/PI staining by flow cytometry **(Figure 3.12,** done only for CAL-51 GemR**)**. Here I usually avoided not to exceed 40% growth inhibition in single agent groups, which is clinically relevant since drug combinations using the original single agent doses cause higher toxicity in patients compared to low-dose combinations.

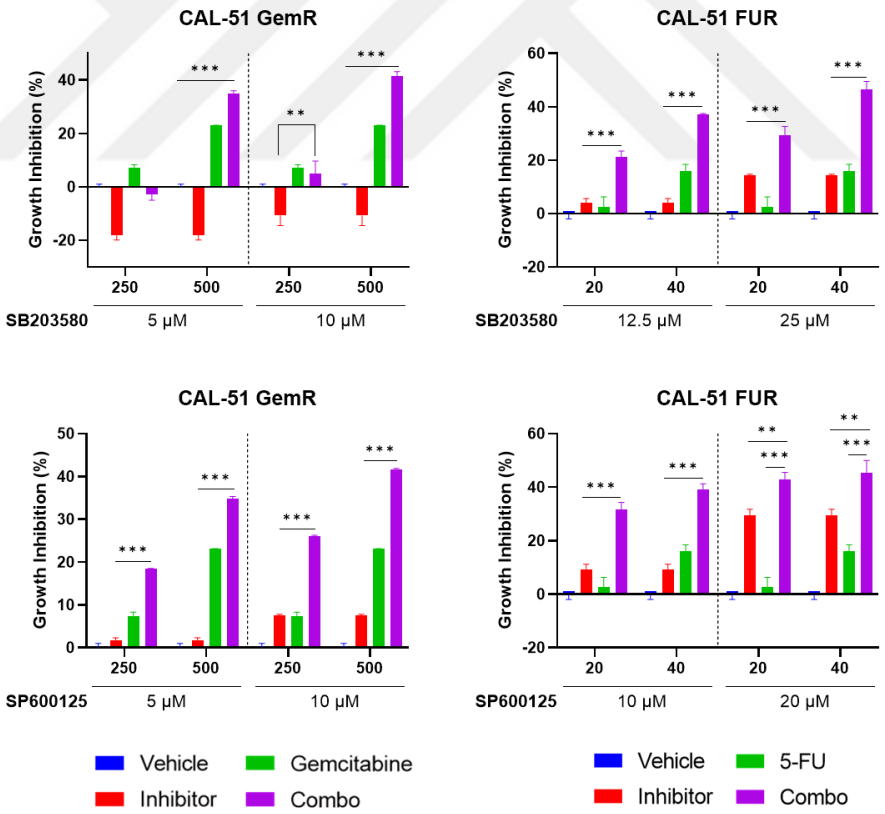
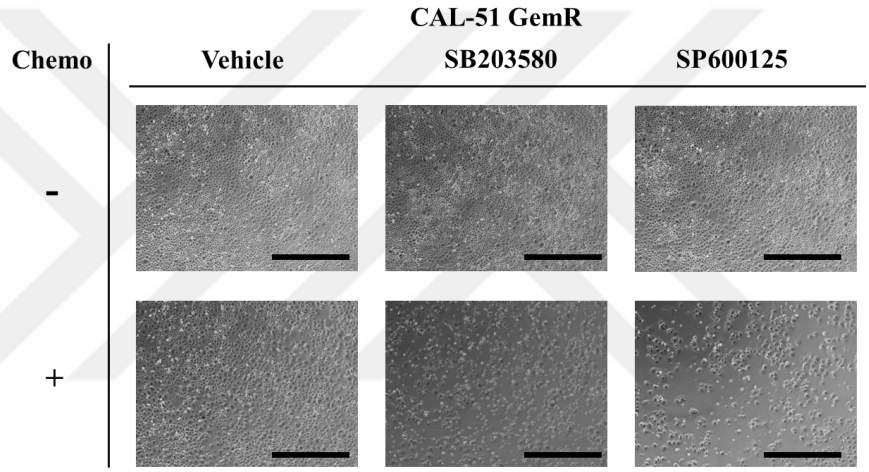


Figure 3.9. p38 and JNK inhibitors could overcome antimetabolite resistance in TNBC, as shown by cell viability assay. Chemotherapy doses (250/500 nM GEM and 20/40 μM 5-FU) were given on the X axis. Inhibitor doses were provided below

the figures, next to the inhibitor name (*$p < 0.05$; **$p < 0.01$; ***$p < 0.001$; ns, not significant). Blue: vehicle, red: inhibitor, green: chemotherapy, purple: combination.

Microscopic examination yielded an overall concordance with the cell viability results. While the effect of single agents to cell growth was minimal, combination treatment resulted in tremendous levels of growth inhibition, as evident by relative cell density at 4X images **(Figure 3.10 A and Figure 3.11 A)**.

A



B

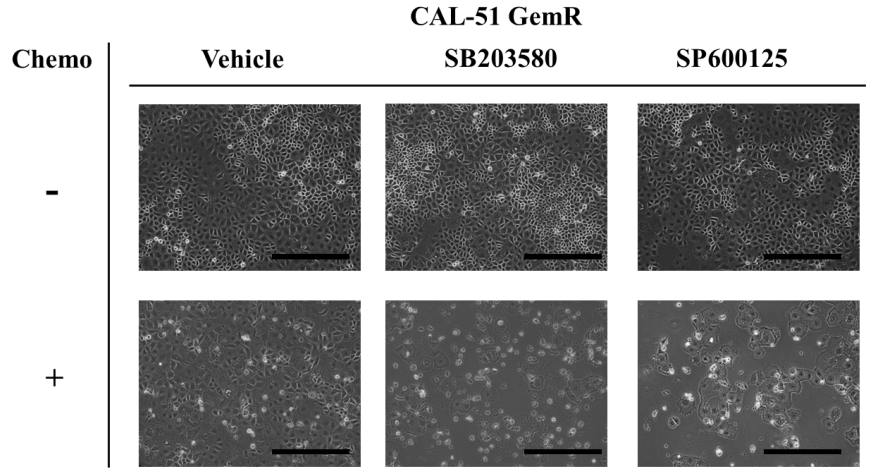
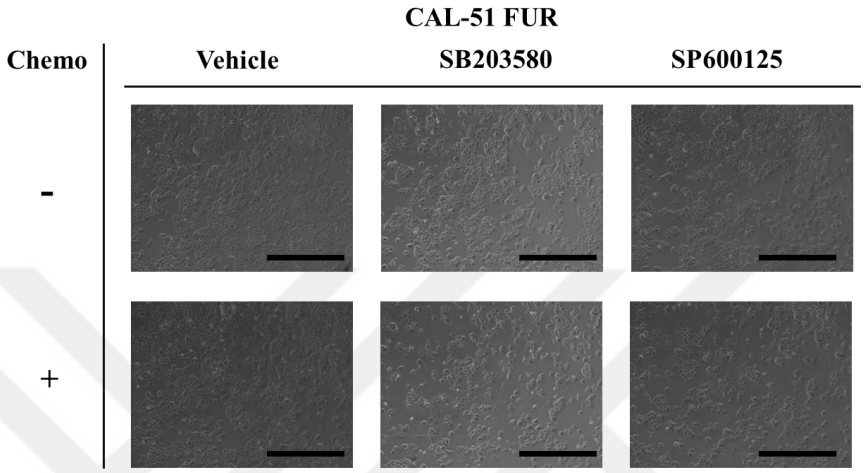


Figure 3.10. p38 and JNK inhibitors could reverse gemcitabine resistance in TNBC, as shown by microscopy. A) 4X images were given to show relative cell proliferation and viability (Scale bar: 1000 μm), and B) 10X images were given to

show overall morphology of the cells (Scale bar: 400 µm). Phase-contrast images were taken at Evos FL Auto. Chemotherapy status was provided on the left side whereas the inhibitors were present as single agent (top) or in combination with chemotherapy (bottom).

A



B

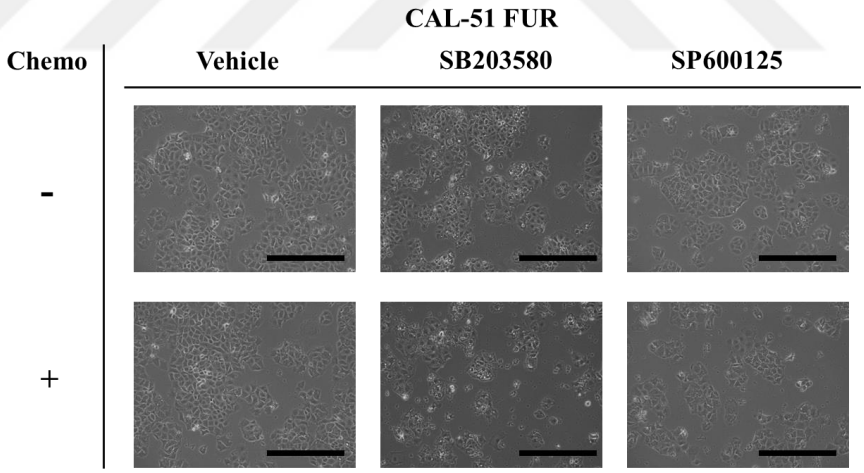


Figure 3.11. p38 and JNK inhibitors could overcome fluorouracil resistance in TNBC, as shown by microscopy. A) 4X images were provided to show relative cell proliferation and viability (Scale bar: 1000 µm), and B) 10X images were given to show overall morphology of the cells (Scale bar: 400 µm). Phase-contrast images were taken at Evos FL Auto. Chemotherapy status was provided on the left side whereas the inhibitors were present as single agent (top) or in combination with chemotherapy (bottom).

Similarly, when I assessed the effect of gemcitabine and inhibitor combinations in CAL-51 GemR cells by Annexin V/PI staining via flow cytometry, I observed roughly 50% or higher growth inhibition. Here, double-negative cells denote live cells, Annexin V+ cells denote early apoptotic cells, PI+ cells correspond to necrotic cells, and double-positive cells are considered late apoptotic. Although there were also increase in the late apoptotic cell population (AV+/PI+) in combination as compared to the single agents, growth inhibition mostly resulted in a striking increase in the early apoptotic cell population (AV+/PI-). In addition, when I counted the absolute number of cells in each group instead of counting a pre-specified number of events by flow cytometry, the difference was more pronounced that the combination groups frequently contained less than half the number of cells in the vehicle group (*data not shown*). These are actually in line with the literature, where it was reported that apoptotic effects of antimetabolites such gemcitabine was minimal and took place upon prolonged exposure while cell cycle arrest at S phase at low concentrations and cell cycle arrest at any phase at high concentrations were predominant mechanism of action against cell proliferation (174).

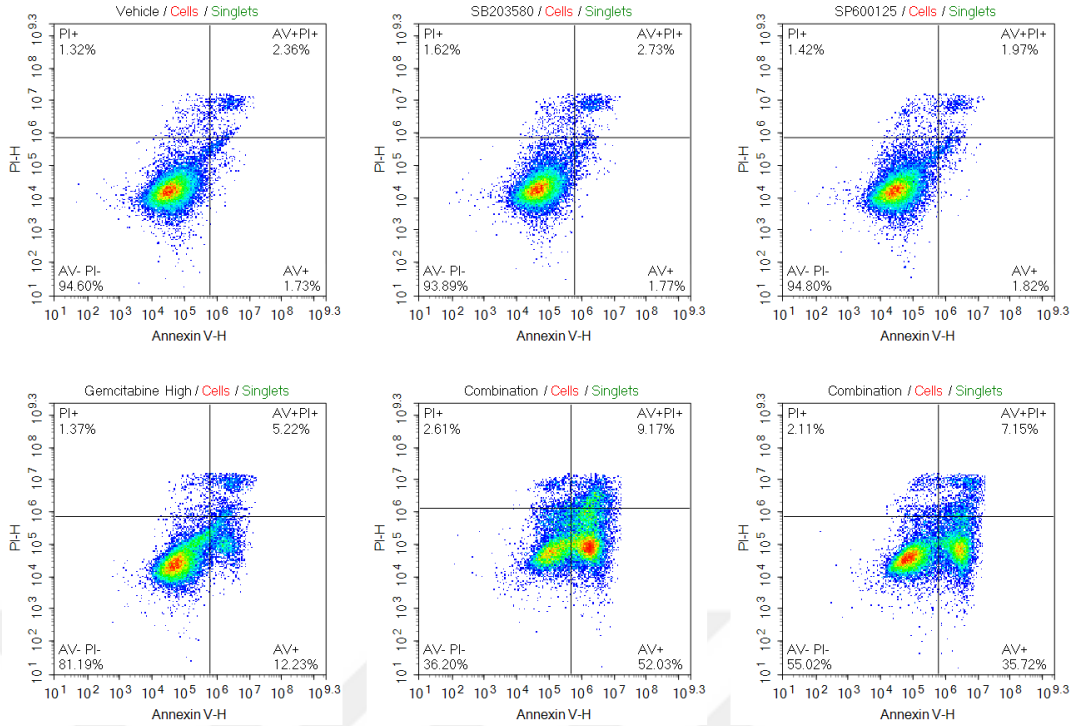


Figure 3.12. p38 and JNK inhibitors could abrogate gemcitabine resistance in CAL-51 GemR model, as shown by Annexin V/PI staining via flow cytometry. Vehicle (top left), Chemotherapy (gemcitabine, bottom left), SB203580 alone or in combination (top middle or bottom middle), SP600125 alone or in combination (top right or bottom right).

I later evaluated the contribution of activated PI3K/AKT signaling (inferred by commonly upregulated p-AKT and upregulated p-FOXO3 levels) to resistance development by using inhibitors such as BYL719 (Alpelisib, PI3Kα inhibitor), BKM120 (Buparlisib, pan-class I PI3K inhibitor) and MK-2206 (pan-AKT inhibitor). All 3 inhibitors exhibited a decent synergism with gemcitabine and 5-FU, except a few select cases, implying a potential role of this pathway **(Figure 3.13)**.

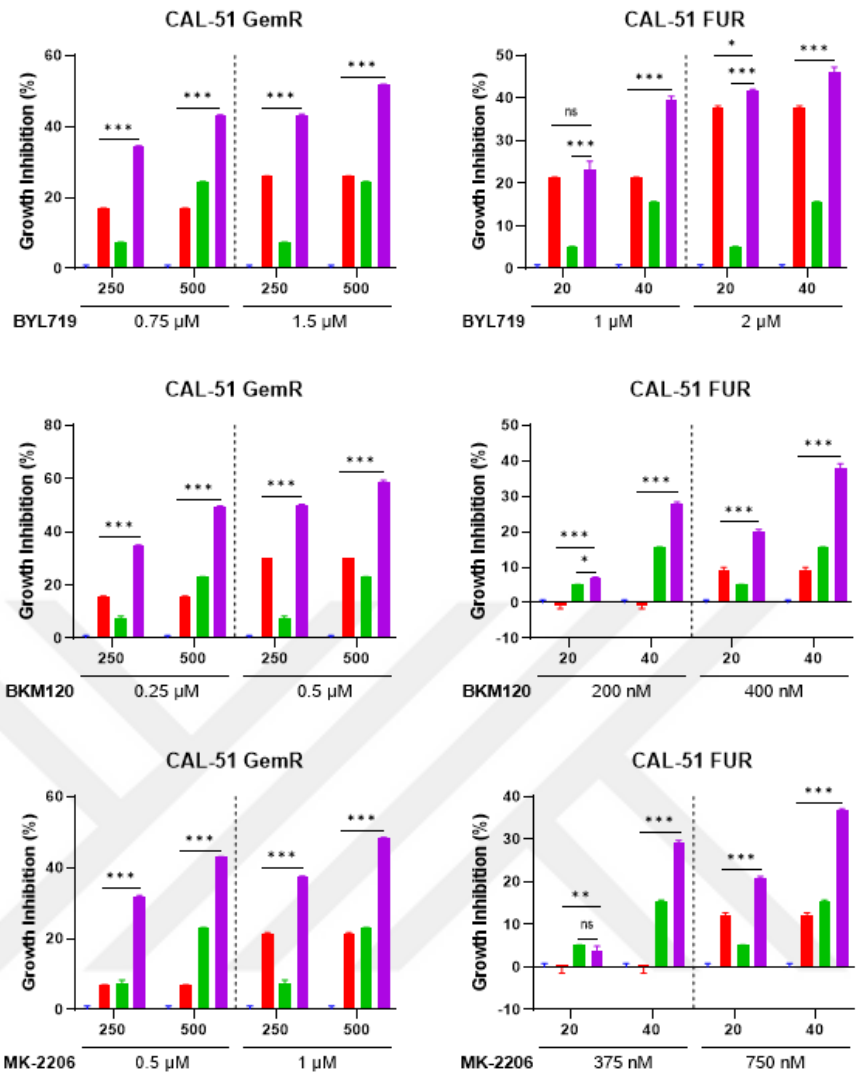


Figure 3.13. PI3K and AKT inhibitors could reverse antimetabolite resistance in TNBC, as shown by cell viability assay. Chemotherapy doses (250/500 nM GEM and 20/40 µM 5-FU) were given on the X axis. Inhibitor doses were provided below the figures, next to the inhibitor name (*$p < 0.05$; **$p < 0.01$; ***$p < 0.001$; ns, not significant). Blue: vehicle, red: inhibitor, green: chemotherapy, purple: combination.

A similar observation was made by microscopy when I combined the selected single doses of the inhibitors with the single doses of chemotherapy agents. Although cell morphology by condition did not change dramatically, the cell density showed quite a remarkable difference, probably due to cell cycle arrest induced by the antimetebolite chemotherapies **(Figure 3.14 and Figure 3.15)**.

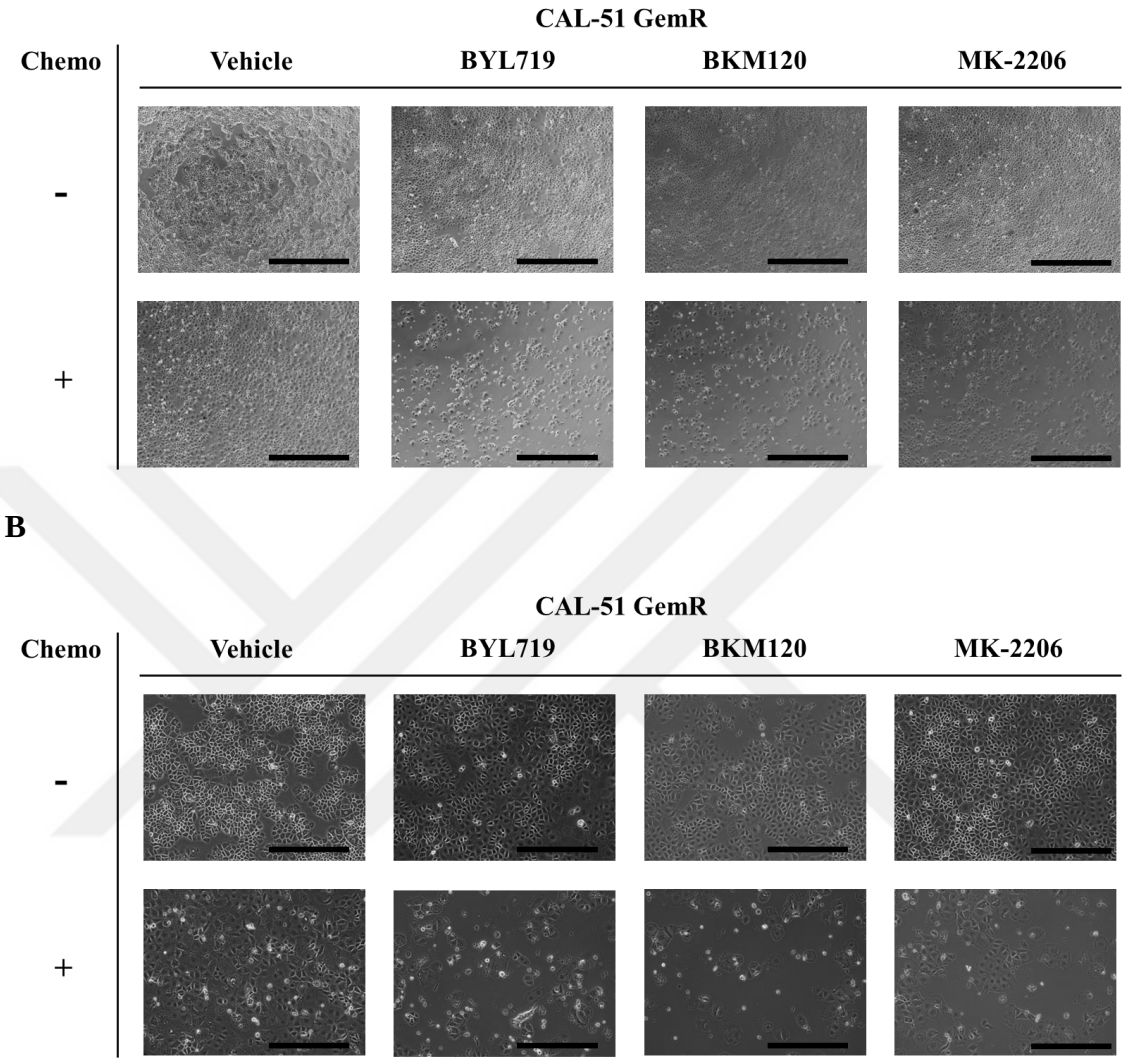
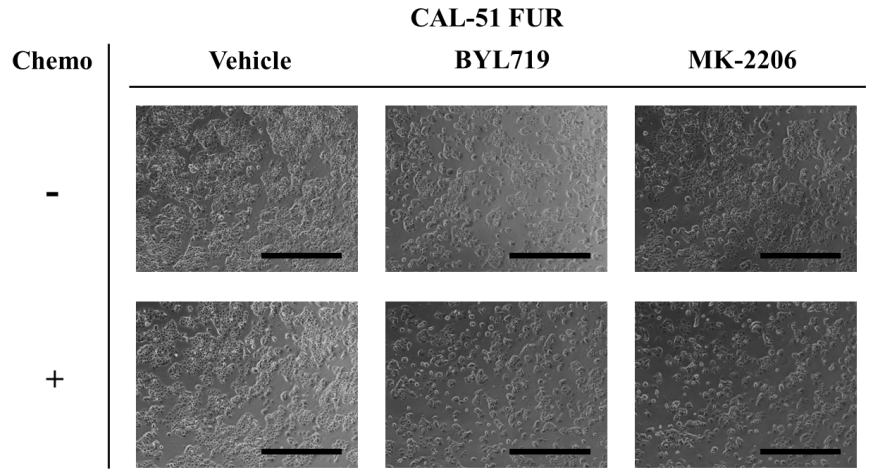


Figure 3.14. PI3K and AKT inhibitors could overcome gemcitabine resistance in TNBC, as shown by microscopy. A) 4X images were provided to show relative cell proliferation and viability (Scale bar: 1000 µm), and B) 10X images were given to show overall morphology of the cells (Scale bar: 400 µm). Phase-contrast images were taken at Evos FL Auto. Chemotherapy status was provided on the left side whereas the inhibitors were present as single agent (top) or in combination with chemotherapy (bottom).

A



B

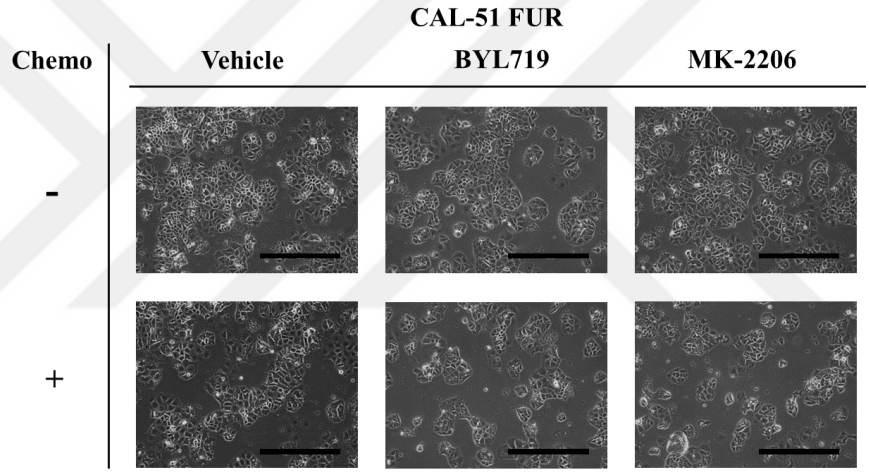


Figure 3.15. PI3K and AKT inhibitors could reverse fluorouracil resistance in TNBC, as shown by microscopy. A) 4X images were provided to show relative cell proliferation and viability (Scale bar: 1000 µm), and B) 10X images were given to show overall morphology of the cells (Scale bar: 400 µm). Phase-contrast images were taken at Evos FL Auto. Chemotherapy status was provided on the left side whereas the inhibitors were present as single agent (top) or in combination with chemotherapy (bottom).

Consequently, when examined by flow cytometry, early apoptosis in the combination group was much higher than the single-agent treatments **(Figure 3.16)**. Again, this was accompanied by much lower cell counts observed in the combination groups in comparison to the vehicle.

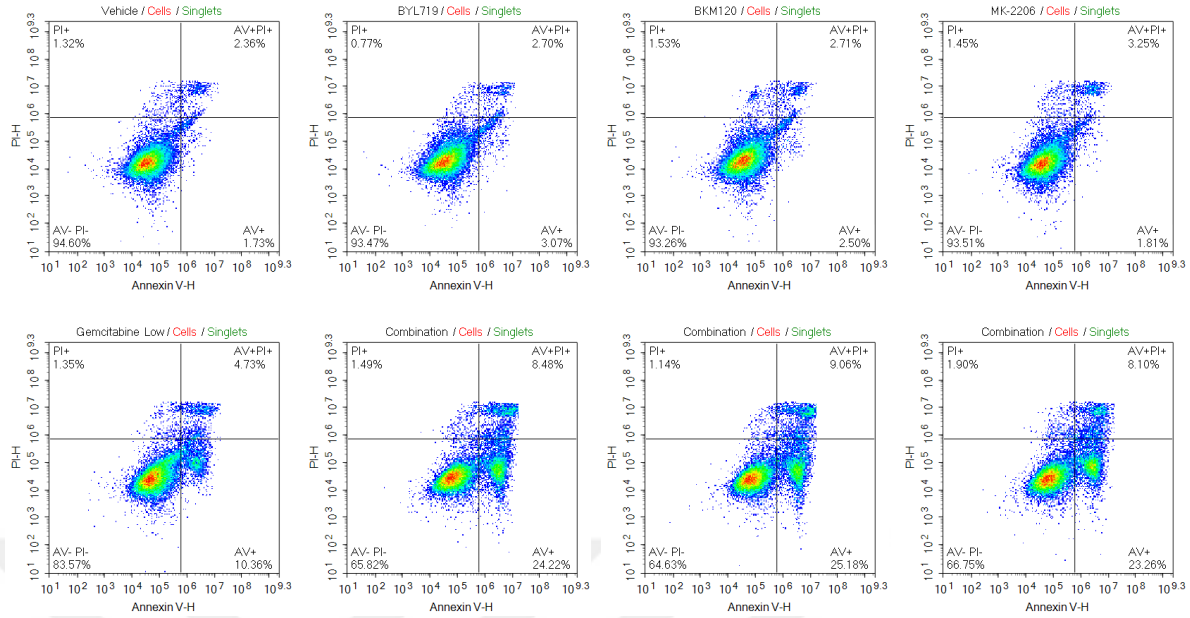


Figure 3.16. PI3K and AKT inhibitors could overcome gemcitabine resistance in CAL-51 GemR model, as shown by Annexin V/PI staining via flow cytometry. Vehicle (top left), Chemotherapy (gemcitabine, bottom left), SB203580 alone or in combination (top middle or bottom middle), SP600125 alone or in combination (top right or bottom right).

I then investigated the phenotypic effects of MK-2206 and SB203580 alone or in combination with gemcitabine. There was an apparent decrease in p-AKT levels upon combination treatment with a concurrent increase in mitotic arrest marker **(Figure 3.17)**. However, this was not the case for the apoptotic markers. As previously explained, this could be due to the fact that antimetabolite chemotherapy agents induce cell cycle arrest early time points, and apoptosis induction was observed in the longer time frames.

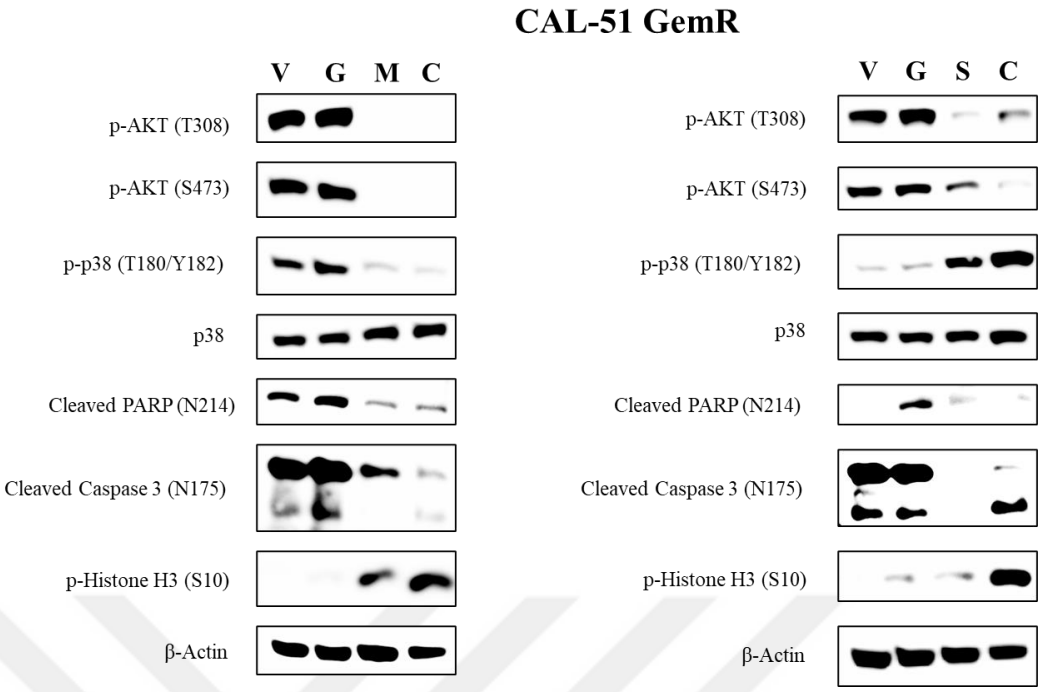


Figure 3.17. AKT and p38 inhibitors could induce mitotic arrest when combined with gemcitabine. V: vehicle, G: gemcitabine, M: MK-2206, S: SB203580, C: combination.

Following the PI3K/AKT inhibitors, I proceeded with an ER stress inducer and multiple inhibitors against proteins involved in the cell cycle to see if they could potentiate chemotherapy response in these models. The CAL-51 FUR model had largely reduced phosphorylation of ER stress markers although the GemR model manifested an ambiguous pattern. Nevertheless, chloroquine was highly effective not only in the former but also in the latter model **(Figure 3.18)**.

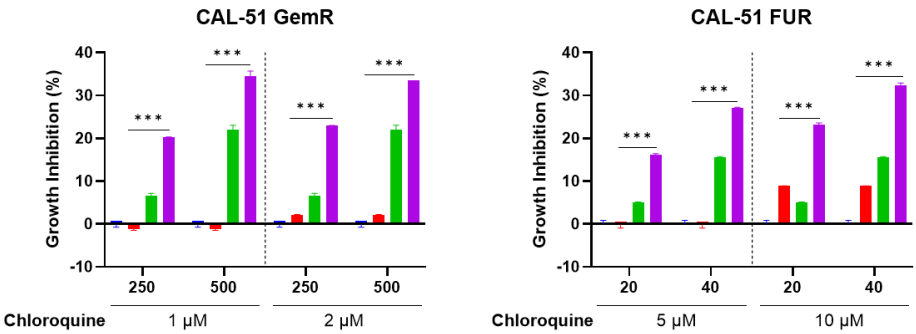


Figure 3.18. Chloroquine, an ER stress inducer, could reverse antimetabolite resistance in TNBC, as shown by cell viability assay. Chemotherapy doses (250/500 nM GEM and 20/40 µM 5-FU) were given on the X axis. Inhibitor doses were provided below the figures, next to the inducer name (*p < 0.05; **p < 0.01; ***p < 0.001; ns, not significant). Blue: vehicle, red: inhibitor, green: chemotherapy, purple: combination.

Alternatively, in the GemR cells, I have tested volasertib, a polo-like kinase 1 (PLK1) inhibitor and BO-264, a TACC3 inhibitor. Both PLK1 and TACC3 function as critical regulators during mitosis. Volasertib inhibits its target in both cancer and normal cells; however, this is irreversible and causes cell death in cancer cells due to G2/M arrest while a reversible and temporary G1 and G2 arrest is the common observation in the healthy cells (175). Both inhibitors were able to re-sensitize the cells, especially at low-dose inhibitor combinations, by potentially inducing mitotic arrest **(Figure 3.19)**. Considering the inhibitors tested until now, I checked prognostic potential of these 5 target genes in the TNBC or basal-like patients, which were adjuvant chemotherapy treated **(Figure 3.20)**. Although high *AKT or TACC3* expression alone could predict worse relapse-free survival, high mean expression of these genes could much significantly separate patients into good or bad prognosis groups.

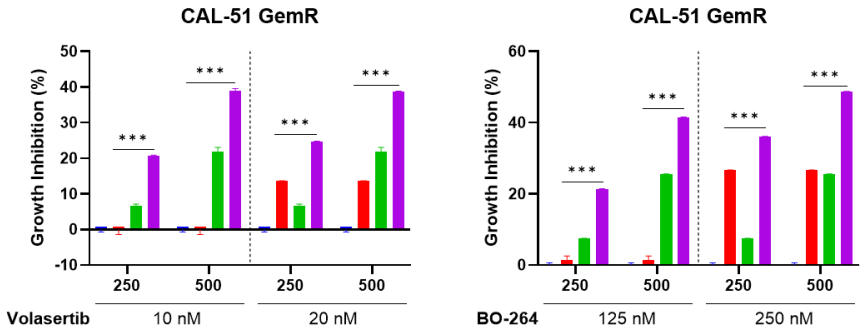
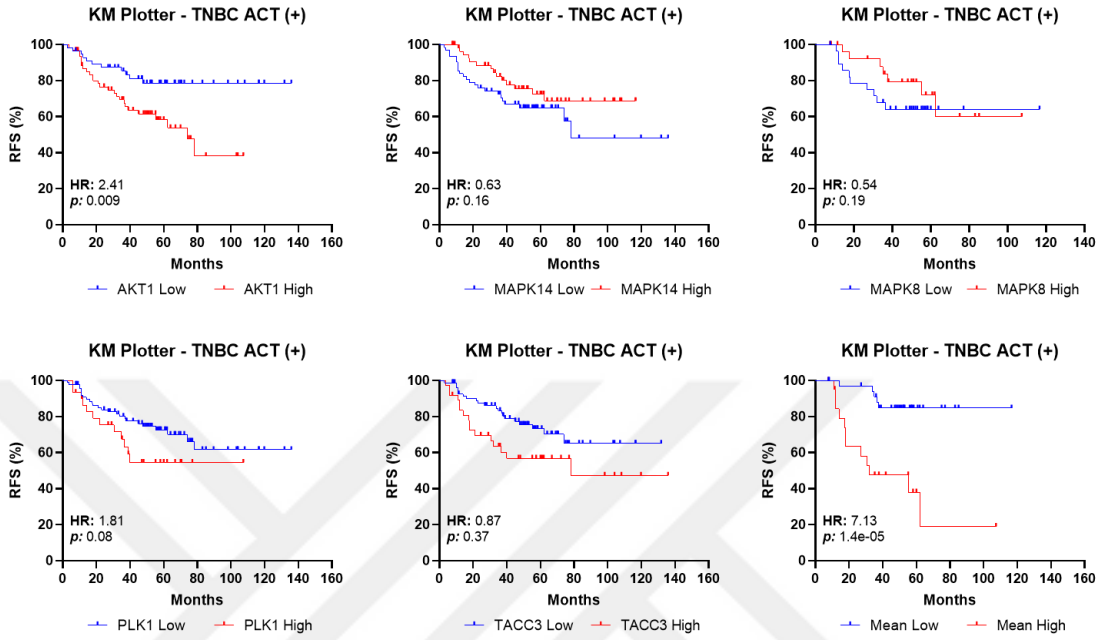


Figure 3.19. Mitosis inhibitors could abrogate antimetabolite resistance in TNBC, as shown by cell viability assay. Chemotherapy doses (250/500 nM GEM and 20/40 µM 5-FU) were given on the X axis. Inhibitor doses were provided below

the figures, next to the inhibitor name (*p < 0.05; **p < 0.01; ***p < 0.001; ns, not significant). Blue: vehicle, red: inhibitor, green: chemotherapy, purple: combination.

A



B

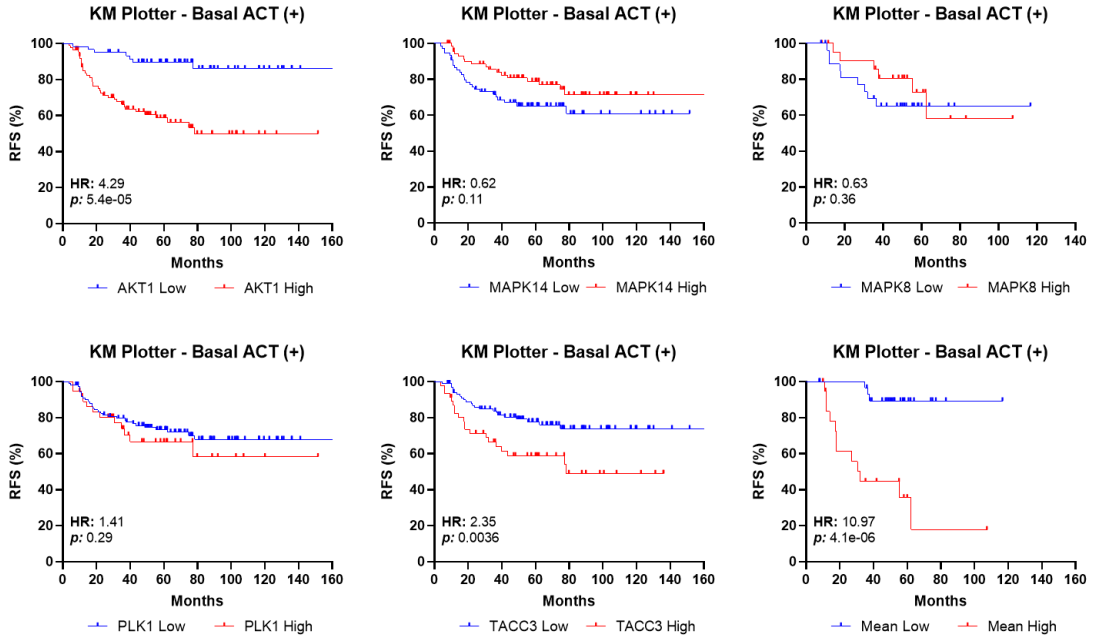


Figure 3.20. 5-gene expression predicts worse relapse-free survival in both adjuvant chemotherapy-treated TNBC and basal-like patients .

As previously shown in the **Figure 3.3** and **Figure 3.4**, BT-20 cell line was presumably a de novo model for both gemcitabine and fluorouracil. De novo (primary) and acquired (secondary) resistance chemotherapy could have common driver events but this is not necessarily the case for each agent or in each cancer type. Still, considering our findings in the acquired resistant models, I explored whether de novo resistance could be driven or overcome by activation or inhibition of the studied pathways, respectively. p38 and JNK inhibitors synergistically inhibited cell growth of de novo gemcitabine and fluorouracil resistant BT-20 cells upon chemotherapy combination **(Figure 3.21)**, emphasizing the importance of MAPK signaling in de novo resistance.

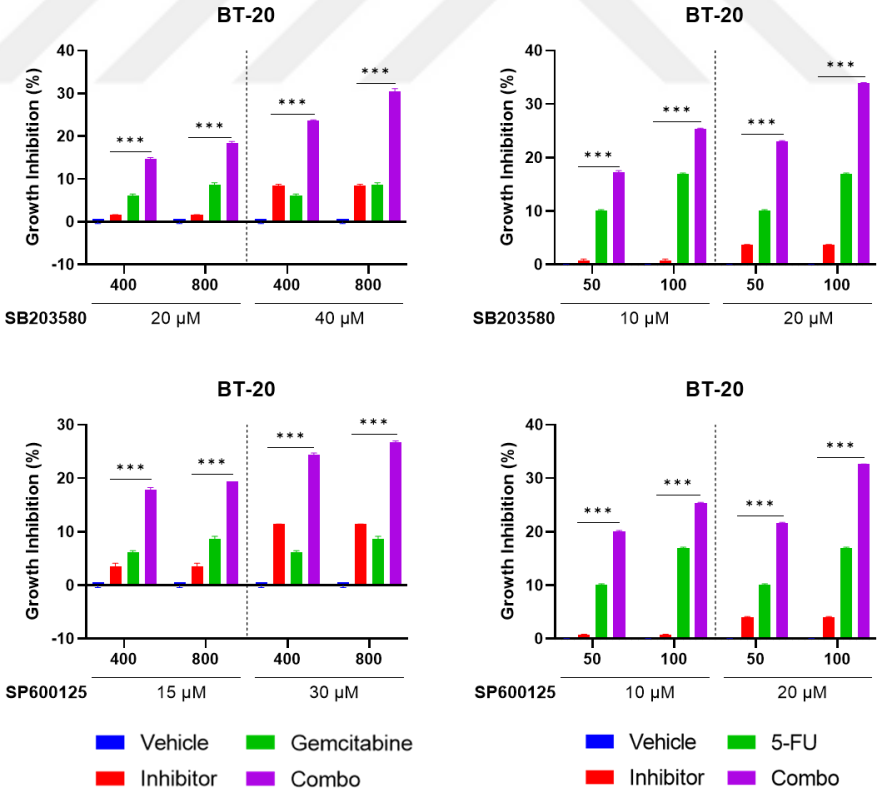


Figure 3.21. p38 and JNK inhibitors could overcome de novo antimetabolite resistance in TNBC, as shown by cell viability assay. Chemotherapy doses (400/800

nM GEM and 50/100 µM 5-FU) were given on the X axis. Inhibitor doses were provided below the figures, next to the inhibitor name (*$p < 0.05$; **$p < 0.01$; ***$p < 0.001$; ns, not significant). Blue: vehicle, red: inhibitor, green: chemotherapy, purple: combination.

Similarly, I investigated if PI3K or AKT inhibitor could alleviate de novo gemcitabine and 5-FU resistance in the BT-20 cells. Both PI3Kα and pan-AKT inhibitor acted as an antimetabolite chemotherapy sensitizer **(Figure 3.22)**, which strengthens that a common mechanism could be in place in the CAL-51 models and BT-20.

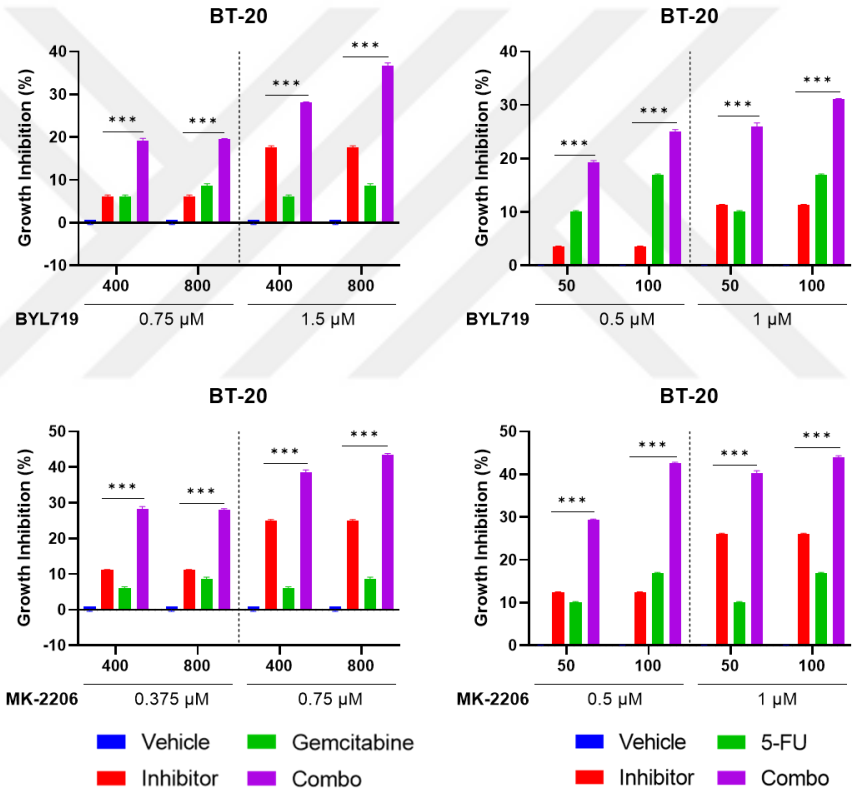


Figure 3.22. PI3K and AKT inhibitors could overcome de novo antimetabolite resistance in TNBC, as shown by cell viability assay. Chemotherapy doses (400/800 nM GEM and 50/100 µM 5-FU) were given on the X axis. Inhibitor doses were provided below the figures, next to the inhibitor name (*$p < 0.05$; **$p < 0.01$; ***$p < 0.001$; ns, not significant). Blue: vehicle, red: inhibitor, green: chemotherapy, purple: combination.

Finally, I analyzed thapsigargin, another ER stress inducer to reveal if ER stress and cell cycle regulation could mediate secondary resistance. Even though thapsigargin could counteract both de novo gemcitabine and fluorouracil resistance, it was more effective at doing so in case of gemcitabine in a synergistic manner **(Figure 3.23)**. This was in accordance with our expectations and represent a great example whereby an almost entirely overlapping set of pathways and their components could instigate chemoresistance before and during treatment.

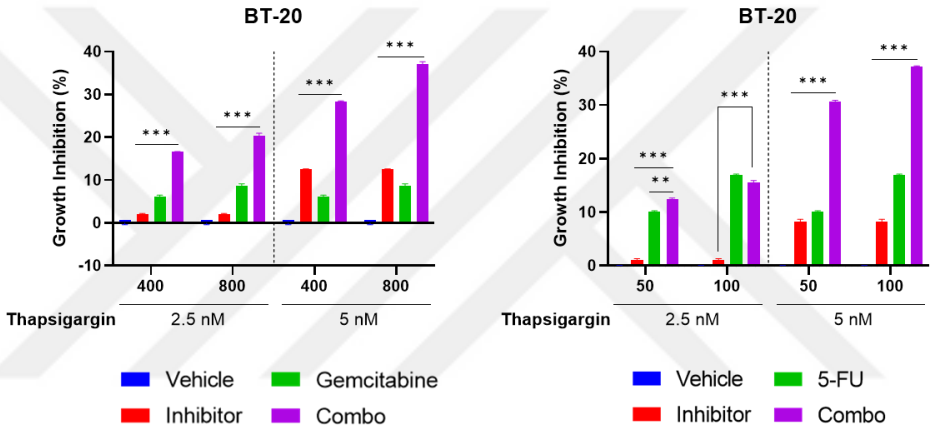


Figure 3.23. Thapsigargin could reverse de novo antimetabolite resistance in TNBC, as shown by cell viability assay. Chemotherapy doses (400/800 nM GEM and 50/100 µM 5-FU) were given on the X axis. Inhibitor doses were provided below the figures, next to the inhibitor name (*$p < 0.05$; **$p < 0.01$; ***$p < 0.001$; ns, not significant). Blue: vehicle, red: inhibitor, green: chemotherapy, purple: combination.

A general problem with the chemotherapy agents is that they not only target cancer cells but also healthy, normal cells of the body. Here, I tested the response of 2 non-tumorigenic epithelial normal breast cell lines to gemcitabine and fluorouracil. They showed negligible response to gemcitabine while they exhibited relatively low response rate to 5-FU as compared to the most TNBC cell lines studied **(Figure 3.24)**.

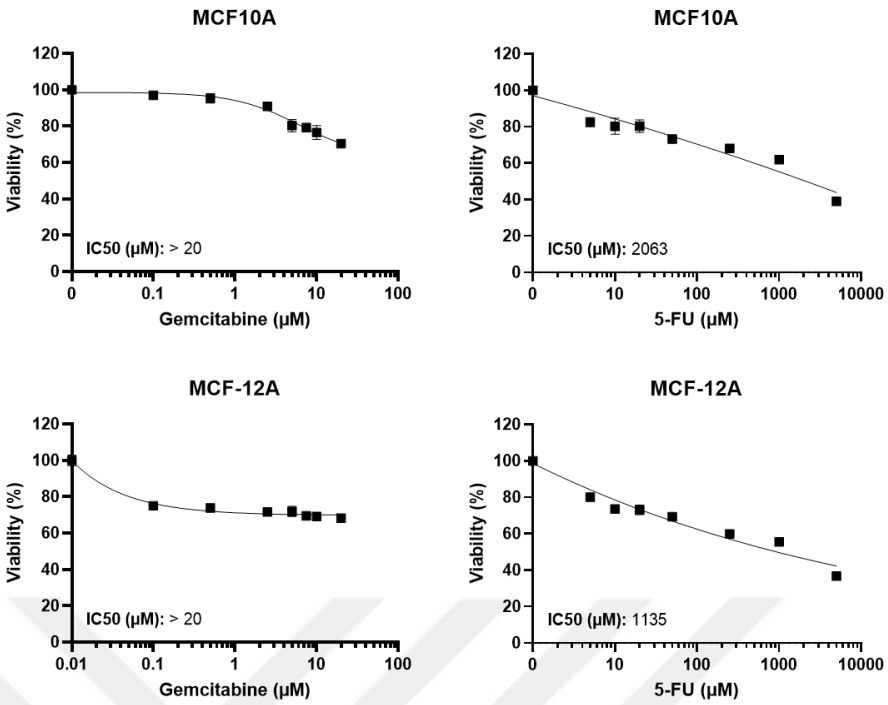


Figure 3.24. Normal breast epithelial cells have reduced response to antimetabolite chemotherapy.

I finally assessed if the acquired gemcitabine and fluorouracil models of the CAL51 could exhibit cross resistance to the other antimetabolite or to other classes of chemotherapy. While CAL-51 FUR cells showed cross resistance only to gemcitabine **(Figure 3.25, right)**, CAL-51 displayed a broader partial or complete cross resistance pattern not only to 5-FU **(Figure 3.25, left)** but also paclitaxel, cisplatin and doxorubicin **(Figure 3.26)**.

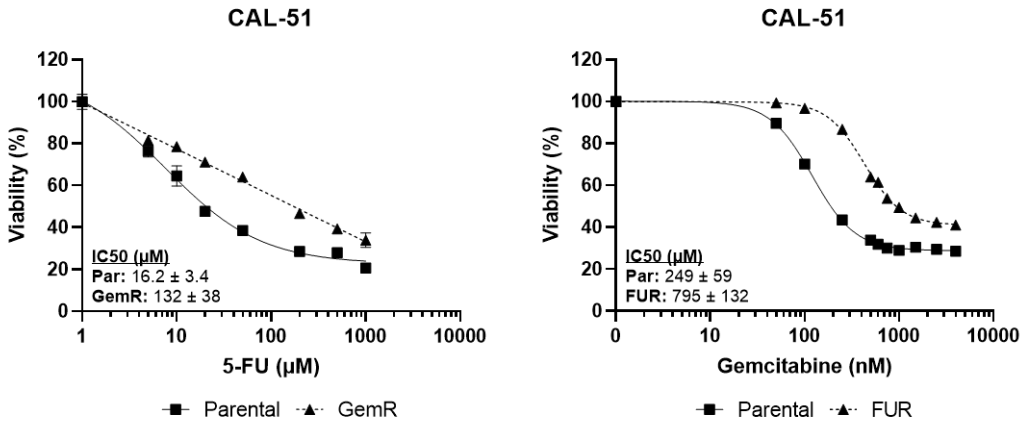


Figure 3.25. CAL-51 GemR and FUR show cross resistance to other antimetabolite chemotherapy agents.

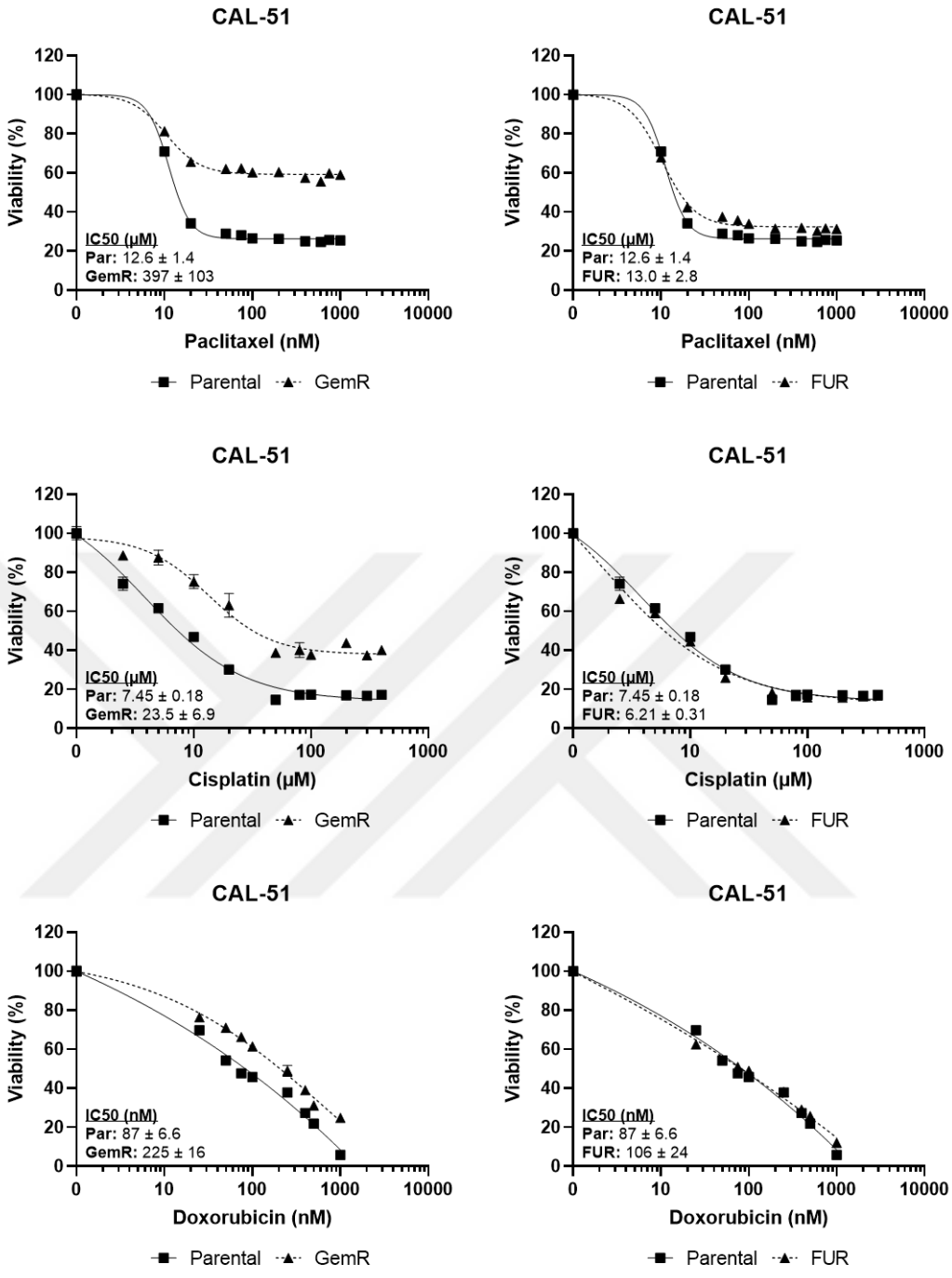


Figure 3.26. Response of CAL-51 GemR and CAL-51 FUR cells to other classes of chemotherapy.

3.2 Plant Alkaloid (Mitotic Inhibitor) Resistance Models

Mitotic inhibitors, especially taxanes such as paclitaxel and docetaxel, are among the most commonly utilized chemotherapy agents in the clinics. This is in part by their broad anticancer spectrum and high cytotoxic activity with a lower cardiotoxicity profile. Although solvent-based paclitaxel was inferior to docetaxel in breast cancer trials, albumin-bound form (nab-paclitaxel) had the most favorable safety profile and the highest therapeutic and cost-effectiveness index compared to paclitaxel and docetaxel (176). Therefore, this form has been incorporated into the treatment scheme of multiple cancer types including primary and metastatic TNBC. Inevitably, however, many patients either do not respond to paclitaxel from the beginning or acquire resistance after a few cycles of treatment.

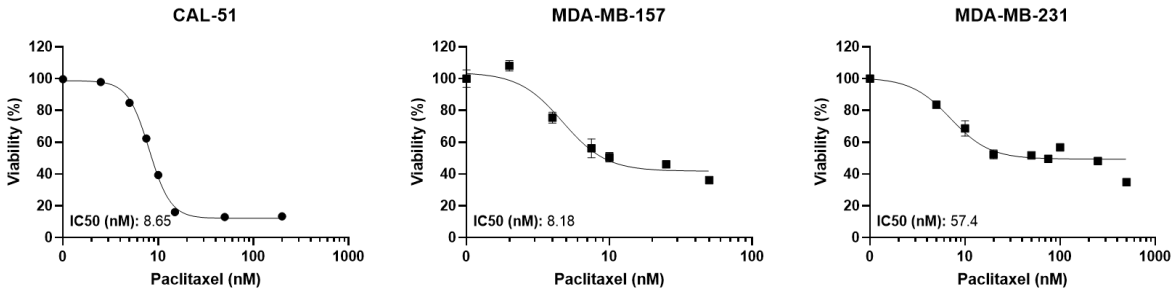
To imitate paclitaxel resistance in vitro, I have followed exactly the same approach as in **Section 3.1**. Accordingly, I first retrieved paclitaxel response of the TNBC cell line panel from 2 different databases **(Figure 3.27)**. MDA-MB-468 was overall the most sensitive cell line, followed by BT-20, MDA-MB-436 and CAL-51.

Cell Line	Drug	CancerRxGene (IC50 - nM)			PharmacoDB (IC50 - nM)			
		GDSC1_M	GDSC1_S	GDSC2	GDSC	CTRPv2	gCSI	FIMM
BT-20	PTX	NA	NA	24.9	NA	0.49	21.6	NA
CAL-51	PTX	NA	NA	244	NA	6.21	12.1	16
HCC1143	PTX	NA	NA	69.4	NA	ND	23.3	11.3
HCC1937	PTX	NA	NA	469	NA	ND	ND	5.72
HCC70	PTX	NA	NA	81.8	NA	NA	NA	NA

MDA-MB-157	PTX	NA	NA	129	NA	8.5	33.8	NA
MDA-MB-231	PTX	NA	NA	88.8	NA	ND	37.1	4.28
MDA-MB-436	PTX	NA	NA	121	NA	NA	26.3	11.5
MDA-MB-468	PTX	NA	NA	17	NA	0.006	6.28	15.3

Figure 3.27. Paclitaxel response of the TNBC cell line panel, retrieved from CancerRxGene and PharmacoDB. NA: not available, ND: not determined (not reached or cannot be calculated due to response curve). GDSC: Genomics of Drug Sensitivity in Cancer, M: Mass General Hospital, S: Sanger Institute, CTRP: Cancer Therapeutics Response Portal, gCSI: Genentech Cell Line Screening Initiative, FIMM: Institute for Molecular Medicine Finland.

However, cell viability assay results unveiled a slightly different relative response for MDA-MB-468, MDA-MB-436 and CAL-51 while BT-20 cells exhibited a dramatically lower response to paclitaxel **(Figure 3.28)**. Considering TNBC classifications and the fact that MDA-MB-157 paclitaxel-resistant models was developed before the start of this project (of which the parental cells show great sensitivity to paclitaxel), I have selected CAL-51 cell line as the second model. These cell lines differ from each other at multiple levels including histology, PAM50, refined Lehmann and Burstein classifications. BT-20 cells were again utilized as the de novo resistance model.



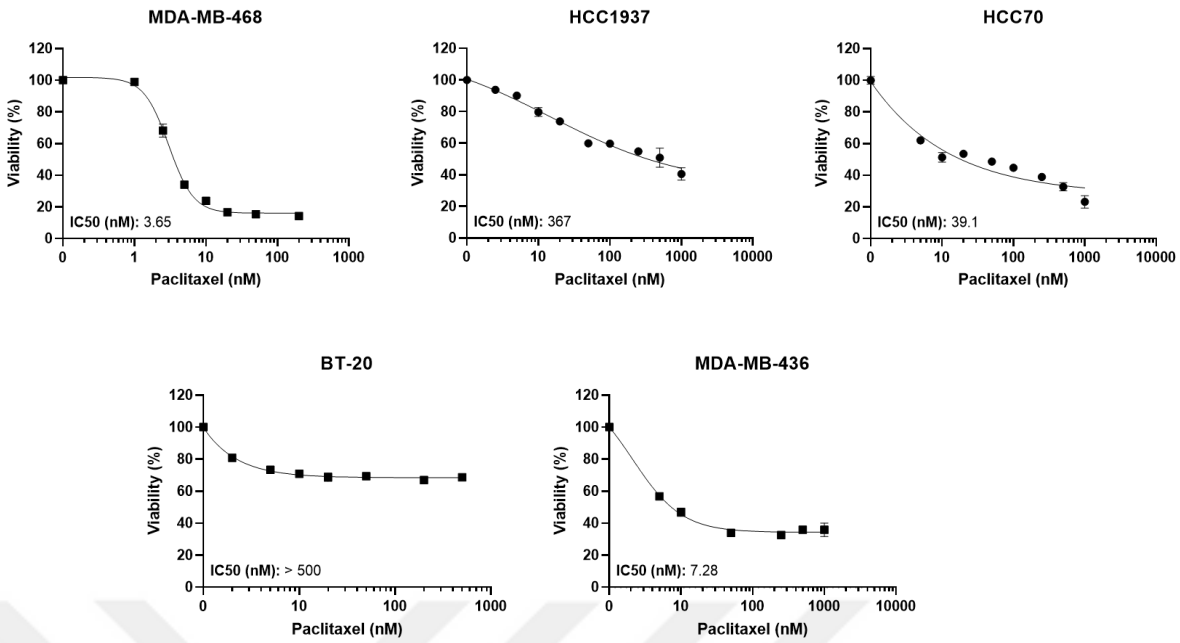
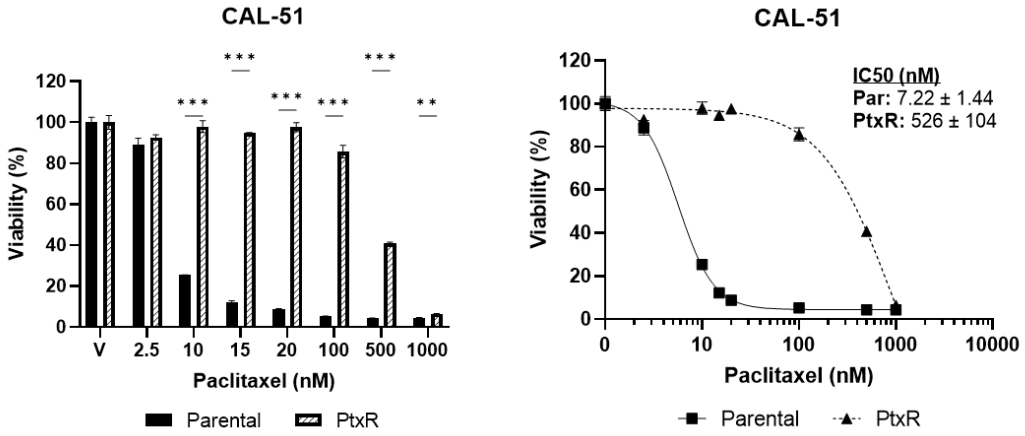


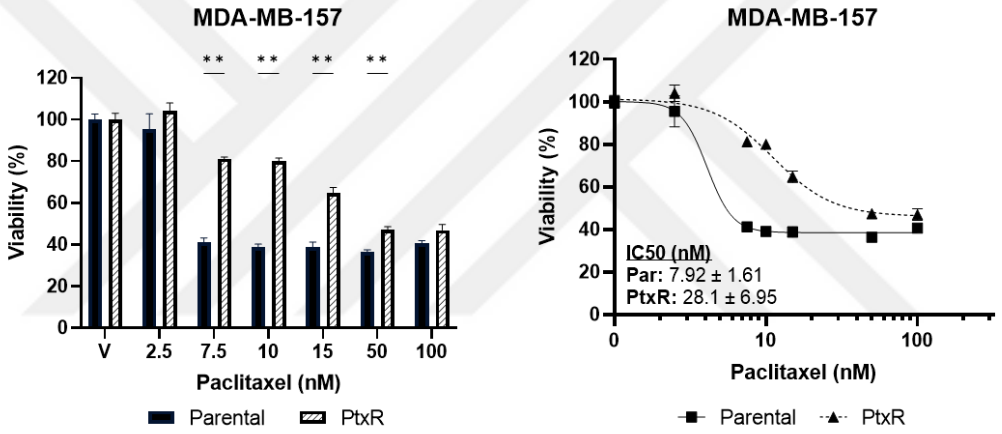
Figure 3.28. Paclitaxel response of the TNBC cell line panel, measured by cell viability assay following 72h drug treatment.

Similar to the gemcitabine- and fluorouracil-resistant cells, after calculating IC25 dose of paclitaxel, I started drug treatment and gradually but continually increased drug dose to the next each time the cells showed no signs of delayed growth or abnormal morphology. After 4-6 months of drug treatment, the cells had a significant separation in terms of their response with IC50s 70- to 4-fold of their parental counterparts, as well as apoptotic marker phenotype **(Figure 3.29)**.

A



B



C

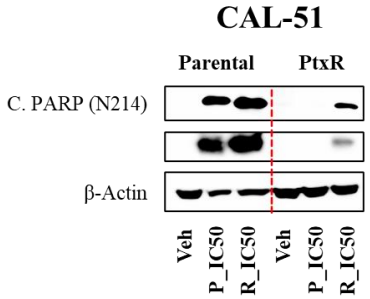


Figure 3.29. Development of CAL-51 and MDA-MB-157 paclitaxel-resistant cells. A, B) The resistance relative to the parental cells was confirmed by cell viability assay. C) Apoptosis markers upon vehicle (Veh) or PTX treatment at IC50 of the parental cells (P_IC50) or IC50 of the resistant (R_IC50) cells (*$p < 0.05$; **$p < 0.01$; ***$p < 0.001$; ns, not significant).

After confirming that both cells were resistant to paclitaxel, I started to characterize these cells by Western blot relative to their parental cells. The same set of pathways with the addition of autophagy and DNA damage markers were included at this step but the set of proteins may not be exactly the same. Except for AKT phosphorylation at threonine 308, CAL-51 PtxR cells almost exclusively showed prominent upregulation of both total and phosphoprotein levels of the PI3K/AKT/mTOR pathway components **(Figure 3.30)**. MDA-MB-157 PtxR cells, on the other hand, had a mixed phenotype with a tendency toward pathway inactivation. The commonly deregulated proteins included EGFR, p-AKT (T308), and p-S6 (S235/236) albeit at opposite directions **(Figure 3.30)** as EGFR could directly and indirectly activate PI3K, which can then drive downstream activations of AKT, mTOR and other pathway components, such as S6 (177).

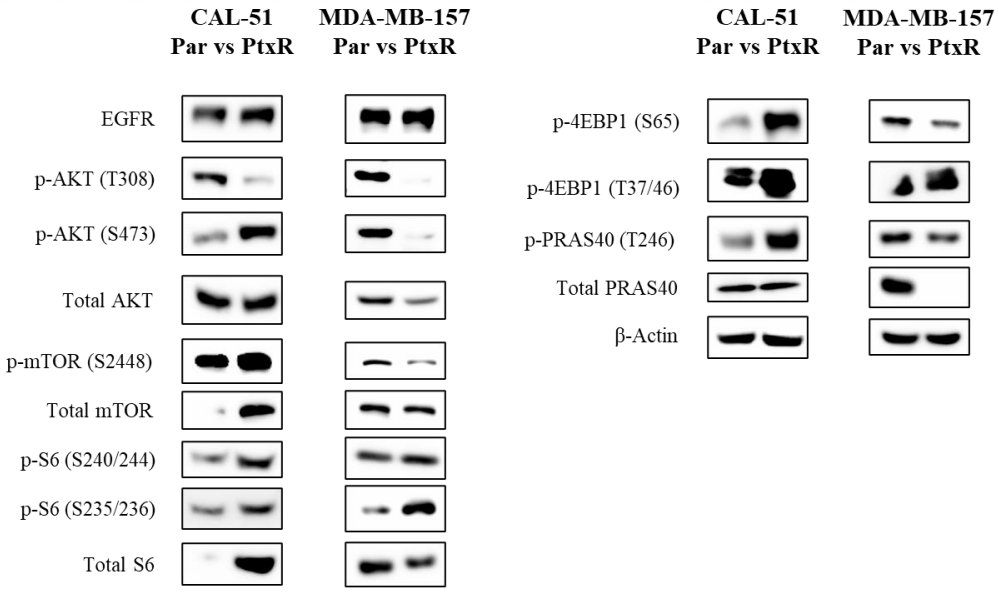


Figure 3.30. Differences in the PI3K/AKT/mTOR pathway components between the parental and paclitaxel-resistant cells. Left lane: Parental, Right lane: Resistant.

I have then proceeded to integrin and MAPK signaling pathway proteins. The situation was the same for these pathways as well, meaning that the PtxR models were more different than similar **(Figure 3.31)**. Interestingly, downregulation of ITGA5 was not followed by decrease in p-FAK or p-SRC levels. This potentially implies that they could be activated by some other upstream signaling protein, not through integrin alpha 5 signaling. In the literature, it was reported that chemotherapy-induced cell motility and metastasis could be driven by collagen IV through activation of FAK and SRC kinases (178). Similarly, Devarajan et al. showed that collagen XVIII could promote breast cancer through EGFR/ErbB signaling (179). In line with these, inhibition of SRC was found to block EGFR transactivation and collagen synthesis (180). As a result, collagens could be one of the potential non-integrin regulators of the paclitaxel resistance **(Figure 3.32)**. They also showed a consistently higher phosphorylation of the major MAP kinases, which might be actionable to abrogate the resistance. As aforementioned, the similarities were scarce between the models and limited to ITGA5, α-SMA, paxillin, and STAT3 phosphorylation at serine 727.

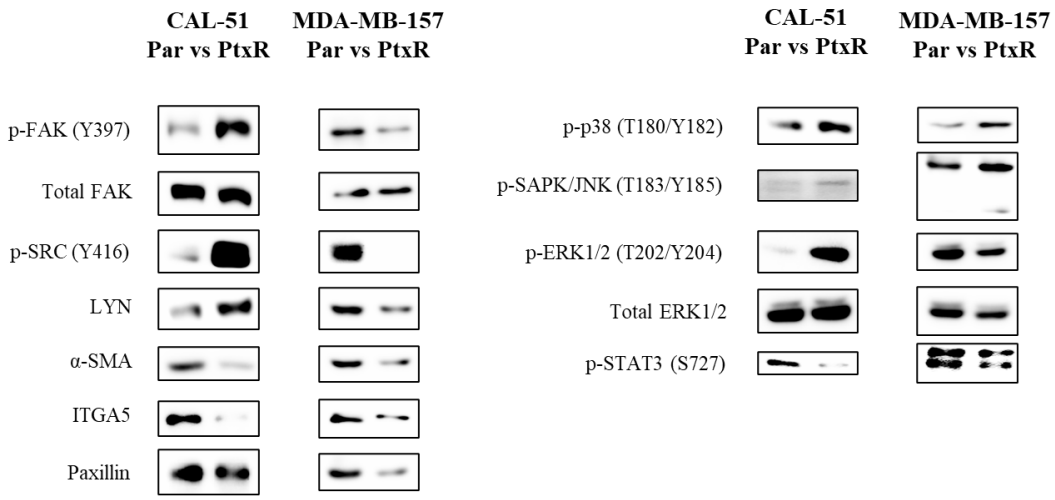


Figure 3.31. Differences in the Integrin and MAPK signaling components between the parental and paclitaxel-resistant cells. Left lane: Parental, Right lane: Resistant.

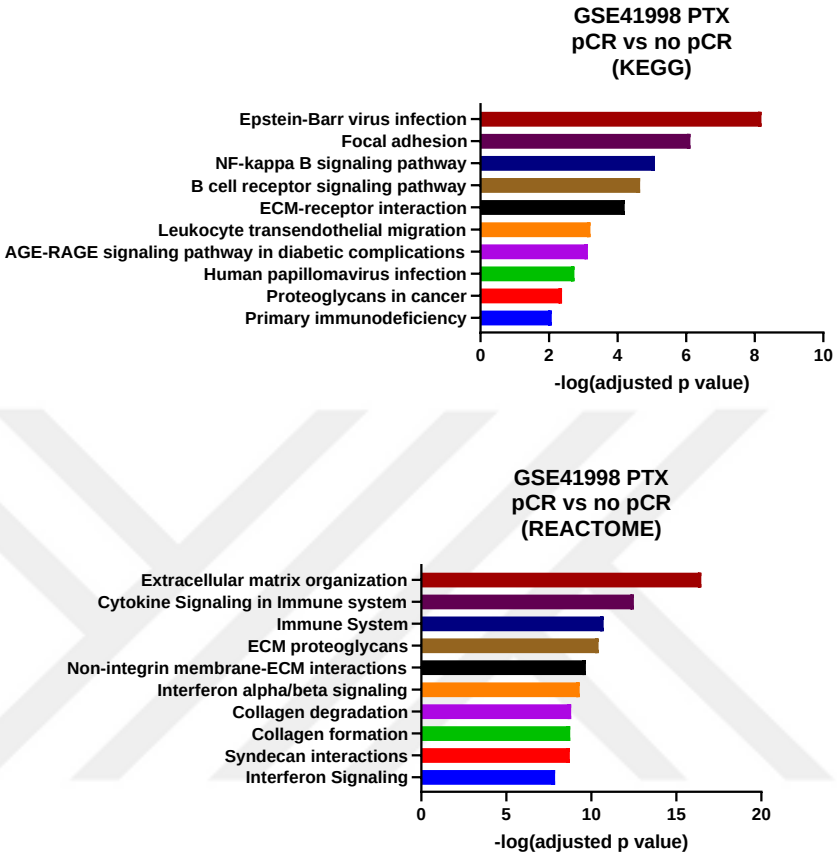


Figure 3.32. Extracellular matrix-related processes could contribute to paclitaxel resistance, independent of ITGA5-mediated signaling.

Finally, I compared the relative activity or level ER stress and autophagy markers as well as cell cycle and DNA damage markers **(Figure 3.33)**. CAL-51 PtxR cells showed a tendency toward ER stress activation while MDA-MB-157 PtxR cells displayed a mixed phenotype for ER stress and reduced autophagy markers. Both models had reduced levels of DNA damage marker, phosphor-Histone H2A.X but no clear phenotype could be estimated by the levels of cell cycle proteins.

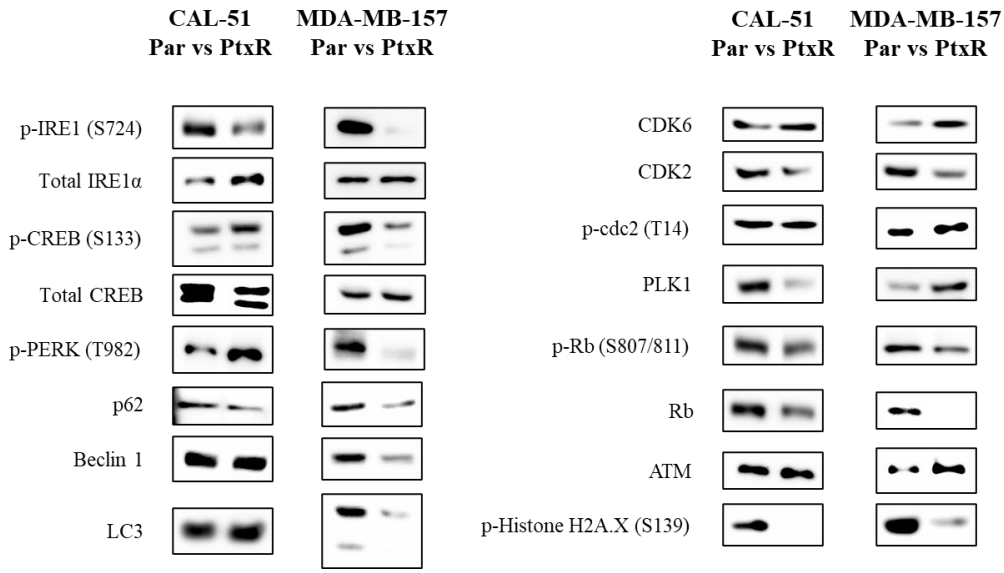


Figure 3.33. Differences in the ER stress, autophagy, cell cycle and DNA damage markers between the parental and paclitaxel-resistant cells. Left lane: Parental, Right lane: Resistant.

According to the Western blot results, I decided on potential actionable targets from each pathway. First, I tested lapatinib (dual EGFR/HER2 inhibitor) and gefitinib (EGFR inhibitor) against EGFR, one of the few upregulated common proteins in both models. Combining even really low doses of both paclitaxel and inhibitors led to an exceptional synergistic response **(Figure 3.34)**, implying the potential dependence of the resistant cells to EGFR and probably its downstream activities.

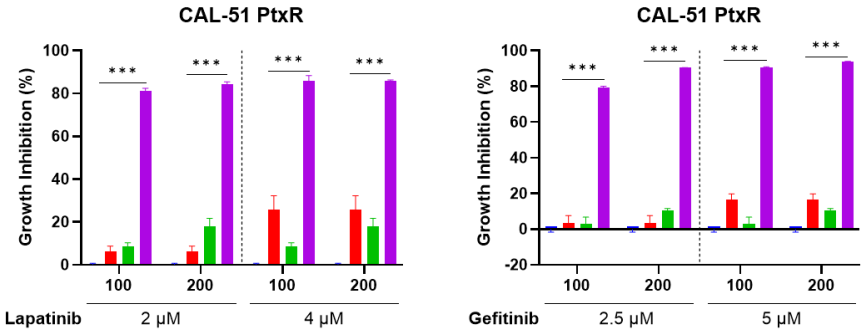


Figure 3.34. Dual EGFR/HER2 or EGFR inhibitors could abolish paclitaxel resistance in TNBC, as shown by cell viability assay. Chemotherapy doses (100/200

nM PTX) were given on the X axis. Inhibitor doses were provided below the figures, next to the inhibitor name (*$p < 0.05$; **$p < 0.01$; ***$p < 0.001$; ns, not significant). Blue: vehicle, red: inhibitor, green: chemotherapy, purple: combination.

As I have previously mentioned, p-FAK and p-SRC levels were markedly increased in the CAL-51 PtxR even though ITGA5 was downregulated. Considering that EGFR could activate FAK/SRC and in turn SRC could trigger EGFR activity, I hypothesized that they can function as the downstream effectors of the EGFR signaling in this context. Accordingly, I tested the response of the CAL-51 PtxR cells to SRC and FAK inhibitors (Saracatinib and PF-562271, respectively). Quite remarkably, both inhibitors could abrogate the resistance in all conditions tested **(Figure 3.35)**. Furthermore, ITGA5 inhibitor ATN-161 could not reverse the paclitaxel resistance. This actually consolidates our hypothesis of FAK/SRC not functioning through integrin here.

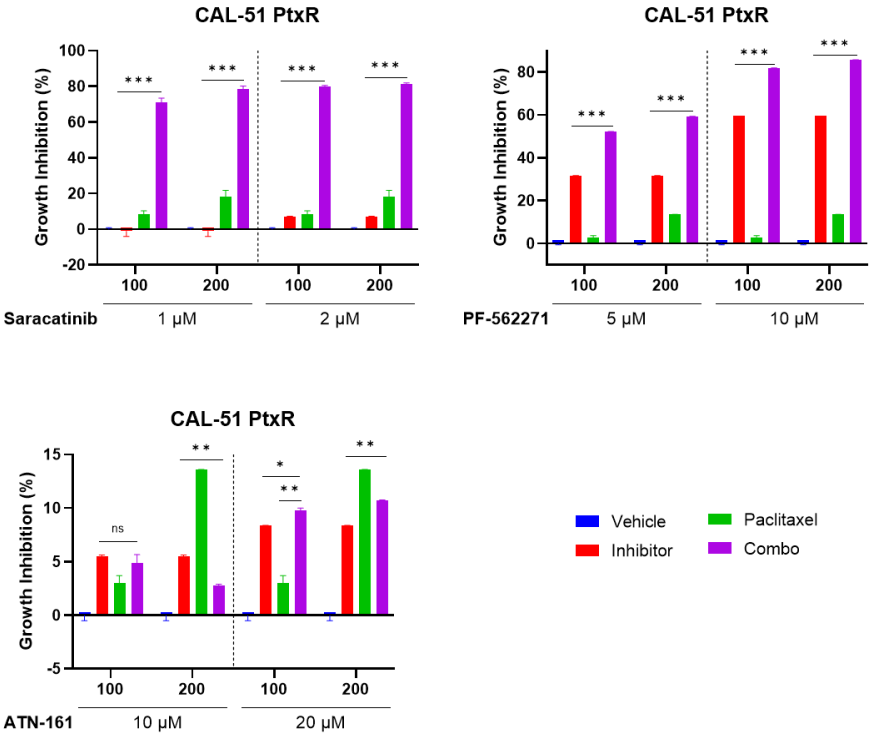


Figure 3.35. SRC and FAK inhibitors could reverse paclitaxel resistance in TNBC, **as shown by cell viability assay.** unlike ITGA5 inhibitor. Chemotherapy doses (100/200 nM PTX) were given on the X axis. Inhibitor doses were provided below the figures, next to the inhibitor name (*$p < 0.05$; **$p < 0.01$; ***$p < 0.001$; ns, not significant). Blue: vehicle, red: inhibitor, green: chemotherapy, purple: combination.

The cell viability outcomes could be perfectly reproduced and supported by microscopical examination for SRC and EGFR inhibitors **(Figure 3.36)**, as evident by both cell density and morphology.

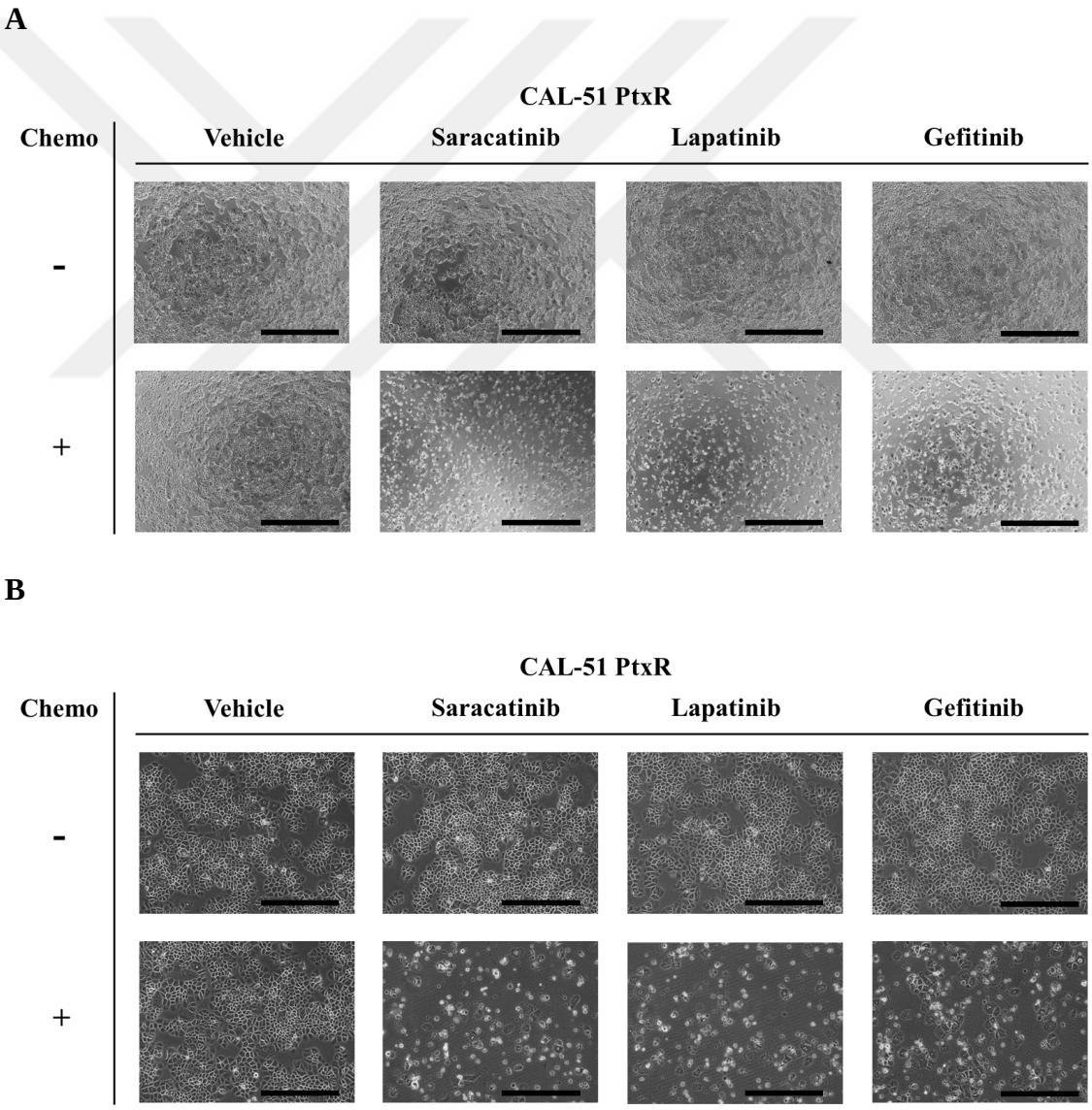


Figure 3.36. SRC and EGFR inhibitors could overcome paclitaxel resistance in TNBC, as shown by microscopy. A) 4X images were provided to show relative cell proliferation and viability (Scale bar: 1000 µm), and B) 10X images were given to show overall morphology of the cells (Scale bar: 400 µm). Phase-contrast images were taken at Evos FL Auto. Chemotherapy status was provided on the left side whereas the inhibitors were present as single agent (top) or in combination with chemotherapy (bottom).

I was also able to replicate these findings by Annexin V/PI staining via flow cytometry. Unlike gemcitabine, however, paclitaxel and inhibitor combinations could induce both early and late apoptosis **(Figure 3.37 and Figure 3.38).**

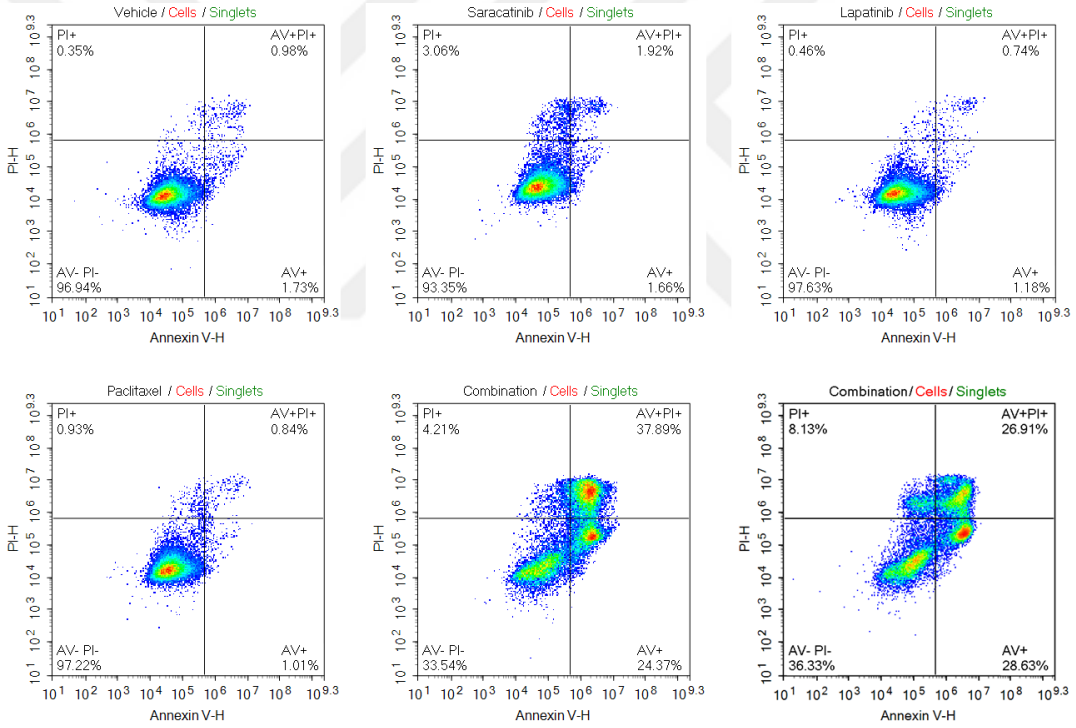


Figure 3.37. SRC and EGFR/HER2 inhibitors could abrogate paclitaxel resistance, as shown by Annexin V/PI staining via flow cytometry. Vehicle (top left), Chemotherapy (paclitaxel, bottom left), Saracatinib alone or in combination (top middle or bottom middle), Lapatinib alone or in combination (top right or bottom right).

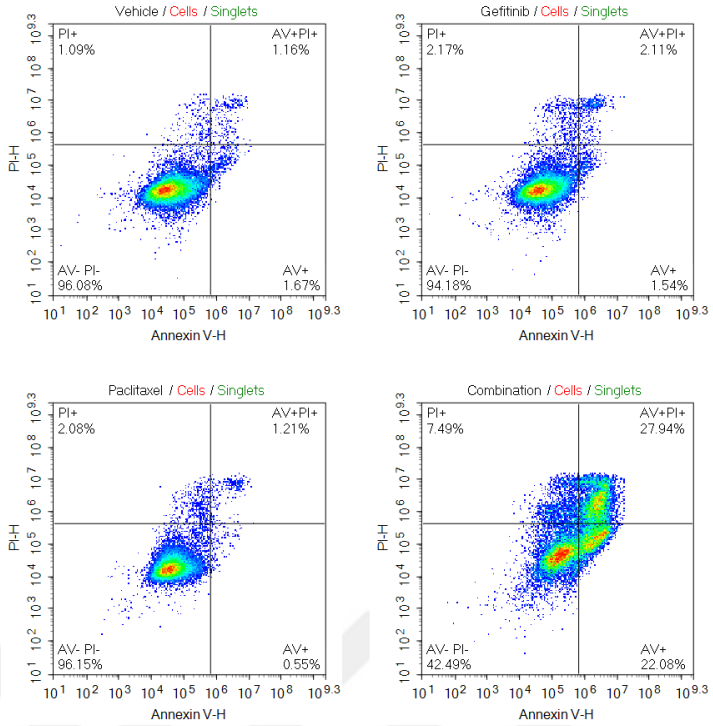


Figure 3.38. EGFR inhibitor could overcome paclitaxel resistance, as shown by Annexin V/PI staining via flow cytometry. Vehicle (top left), Chemotherapy (paclitaxel, bottom left), Saracatinib alone or in combination (top middle or bottom middle), Lapatinib alone or in combination (top right or bottom right).

It is known that CDK1 is an essential gene for almost all TNBC cell lines. Besides, phospho-cdc2 (=phospho-CDK1) was upregulated in the MDA-MB-157 PtxR cells **(Figure 3.33)**. Therefore, I examined if it could reverse paclitaxel resistance in both models. I found that it could significantly impair the resistance at all combinations tested for the CAL-51 PtxR and in the low-dose combinations for MDA-MB-157 PtxR cells **(Figure 3.39)**. In line with this, purvalanol A could also synergistically abolish the resistance phenotype. It is important to note that purvalanol A is not a specific but a general CDK inhibitor, interfering with CDK1-Cyclin B, CDK2-Cyclin A, CDK2-Cyclin E, and CDK4-Cyclin D1 interactions. Interestingly, MDA-MB-157 PtxR cells had diminished levels of multiple mesenchymal markers such as vimentin and SLUG. Hence, I combined TGF-beta inducing EMT with paclitaxel to find out that they could

staggeringly hamper cellular growth together. Previously, it was shown that TGF-β treatment caused pancreatic cancer cells to undergo lethal EMT, which was mediated by changing function of Smad4 from pro-tumor to pro-apoptotic and was prevented by Smad4 loss (181). Assumingly, a similar process could have been activated in the MDA-MB-157 PtxR cells.

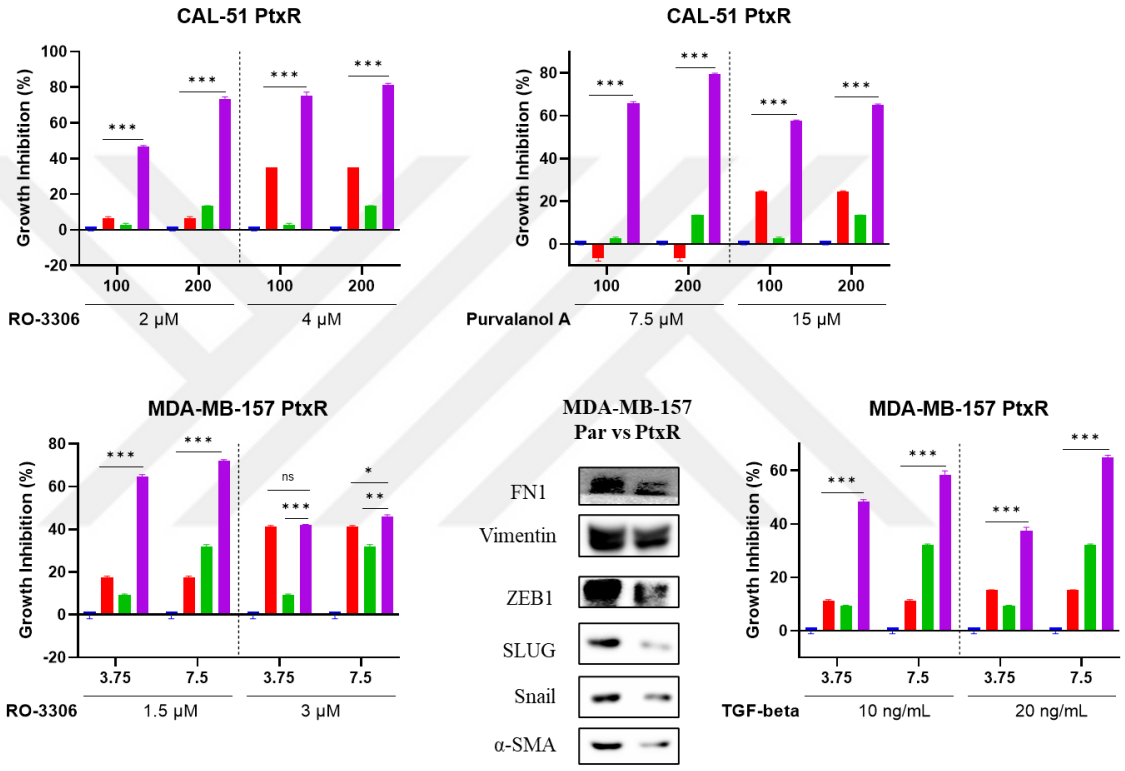
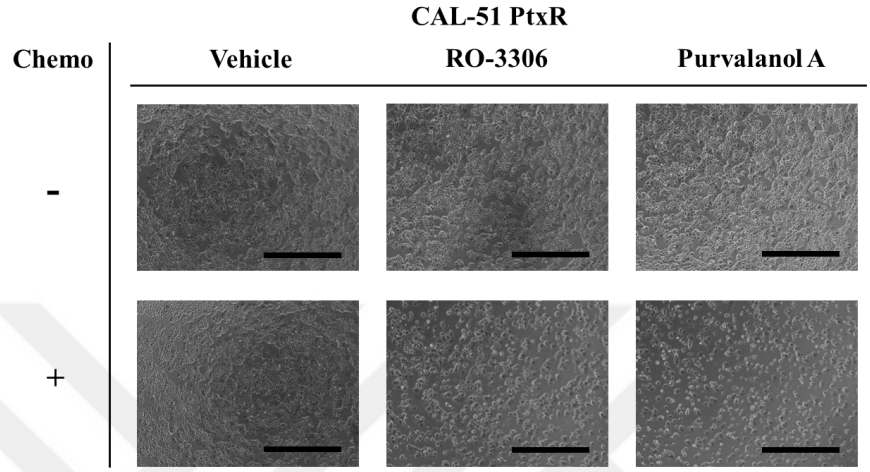


Figure 3.39. CDK1 inhibitor and general CDK inhibitor or TGF-beta could reverse paclitaxel resistance in TNBC, as shown by cell viability assay. Chemotherapy doses (100/200 nM PTX and 3.75/7.5 nM PTX) were given on the X axis. Inhibitor/inducer doses were provided below the figures, next to the inhibitor name (*$p < 0.05$; **$p < 0.01$; ***$p < 0.001$; ns, not significant). Viability - Blue: vehicle, red: inhibitor, green: chemotherapy, purple: combination. Western blot - Left lane: Parental, Right lane: Resistant.

The synergistic combination of the RO-3306 and purvalanol A with chemotherapy was also evident under microscope with one difference to SRC or EGFR inhibitors.

Although the cell density was noticeably lower in the combination groups, their morphology was healthier in this case **(Figure 3.40)**.

A



B

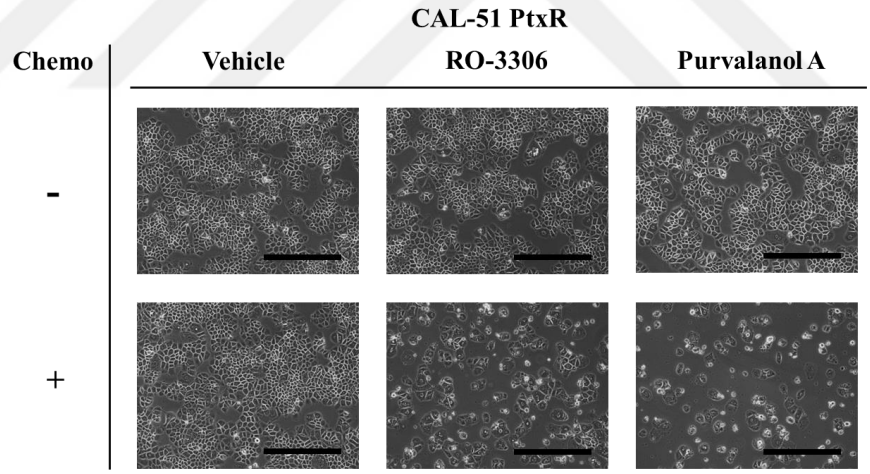


Figure 3.40. CDK1 inhibitor and general CDK inhibitor could overcome paclitaxel resistance in TNBC, as shown by microscopy. A) 4X images were provided to show relative cell proliferation and viability (Scale bar: 1000 µm), and B) 10X images were given to show overall morphology of the cells (Scale bar: 400 µm). Phase-contrast images were taken at Evos FL Auto. Chemotherapy status was provided on the left side whereas the inhibitors were present as single agent (top) or in combination with chemotherapy (bottom).

On the other hand, I have tested RO-3306 and TGF-beta combinations with paclitaxel by Annexin V/PI staining. The dead cell population was not dominated by late apoptotic cells but by early apoptotic cells **(Figure 3.41)**, unlike what I observed for other inhibitors in the CAL-51 PtxR cells.

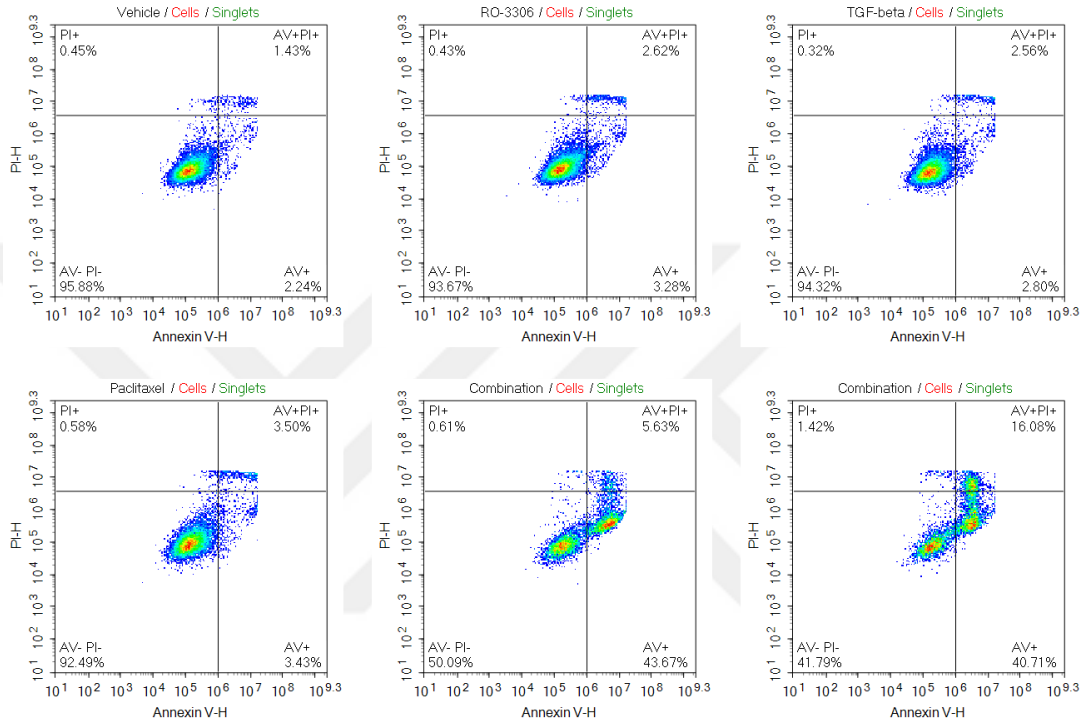


Figure 3.41. CDK1 inhibitor or TGF-beta could reverse paclitaxel resistance in the MDA-MB-157 PtxR cells, as shown by Annexin V/PI staining via flow cytometry. Vehicle (top left), Chemotherapy (paclitaxel, bottom left), RO-3306 alone or in combination (top middle or bottom middle), TGF-beta alone or in combination (top right or bottom right).

Due to having 6 inhibitors with promising results, it was not manageable to test their multiple dose combinations with paclitaxel. Instead, I tested a single dose of each inhibitor in combination with multiple doses of chemotherapy in the CAL-51 PtxR cells to unveil where a potentially synergistic response was first observed and where a synergistic range lies in each case. Some inhibitors such as Saracatinib and Lapatinib

were able to induce a synergistic combination response starting from the second lowest PTX dose, 12.5 nM **(Figure 3.42)**.

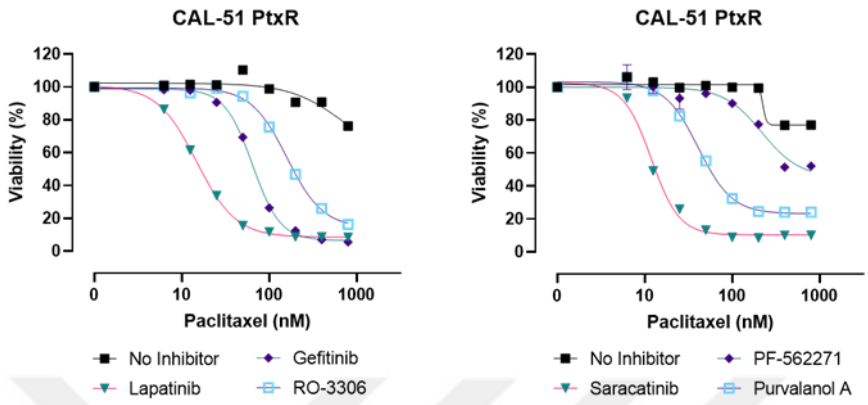


Figure 3.42. Synergism between the Paclitaxel and the Selected Inhibitors.

I then selected Saracatinib and Gefitinib to examine their phenotypic effect alone or in combination with paclitaxel. There was a clear reduction in EGFR, p-SRC and p-CDK1 (=p-cdc2) levels in the combination, accompanied by marked increase in apoptotic or mitotic arrest markers, in both cases **(Figure 3.43)**. Accordingly, I checked prognostic potential of these 3 genes in the TNBC or basal-like patients, which were adjuvant chemotherapy treated. Although high *SRC* expression alone could predict worse relapse-free survival, high mean expression of these genes could much dramatically differentiate between patients with good or bad prognosis **(Figure 3.44)**. EGFR or CDK1 expression alone, on the other hand, was associated with better patient survival.

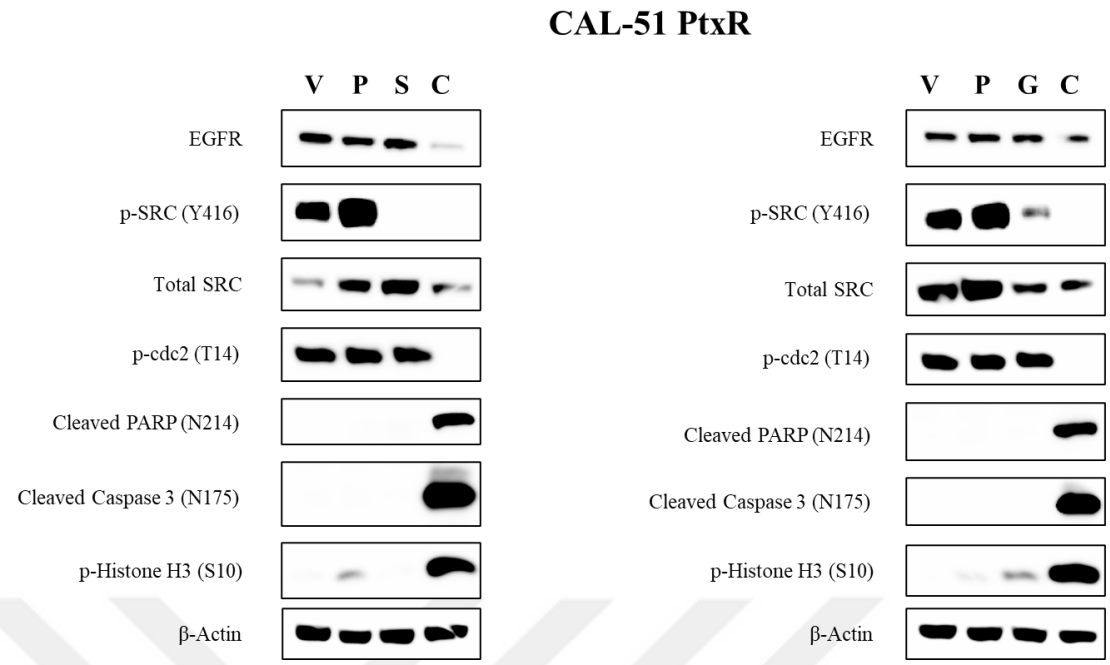
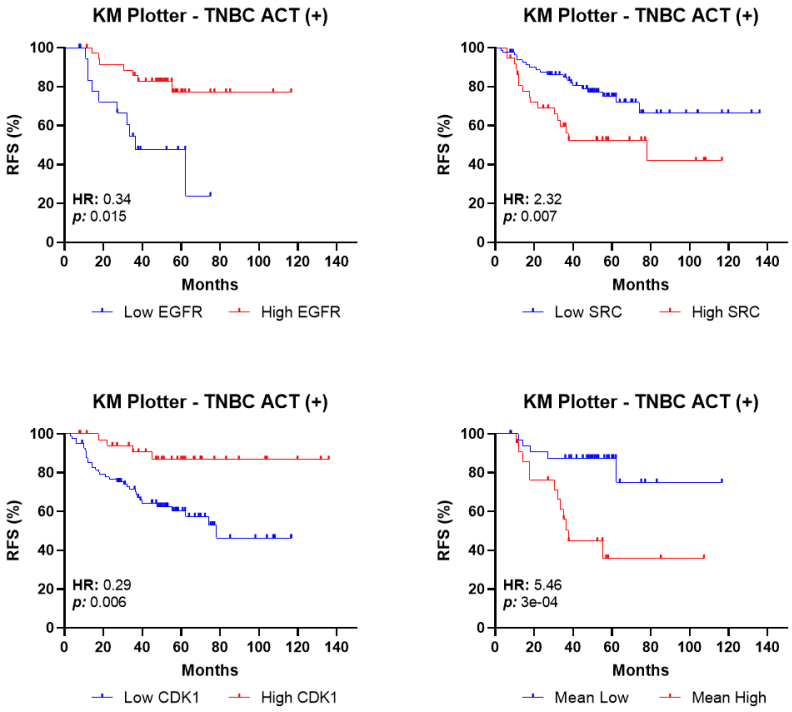


Figure 3.43. The phenotype observed upon Saracatinib or Gefitinib treatment alone or in combination with Paclitaxel. V: vehicle, P: paclitaxel, S: Saracatinib, G: Gefitinib, and C: Combination.

A



B

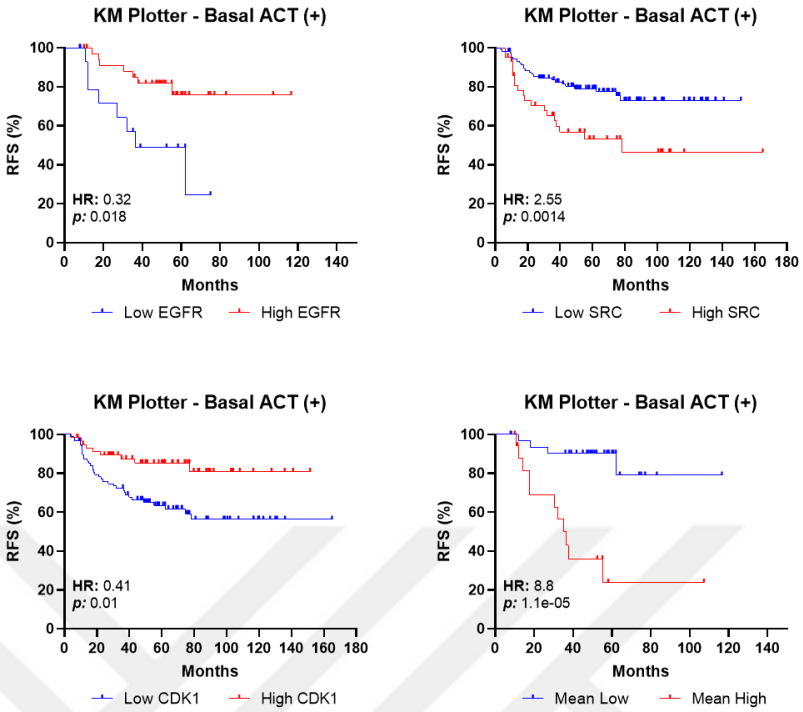


Figure 3.44. 3-gene expression predicts worse relapse-free survival in both adjuvant chemotherapy-treated TNBC and basal-like patients .

I again asked the same question: if the primary (de novo) and secondary (acquired) resistant models have a similar and shared mechanism. Except PF-562271, FAK inhibitor, all the inhibitors could abrogate de novo resistance as well **(Figure 3.45)**. Not surprisingly, FAK inhibitor was also less effective in the cell viability. These could be caused by suboptimal dose selection.

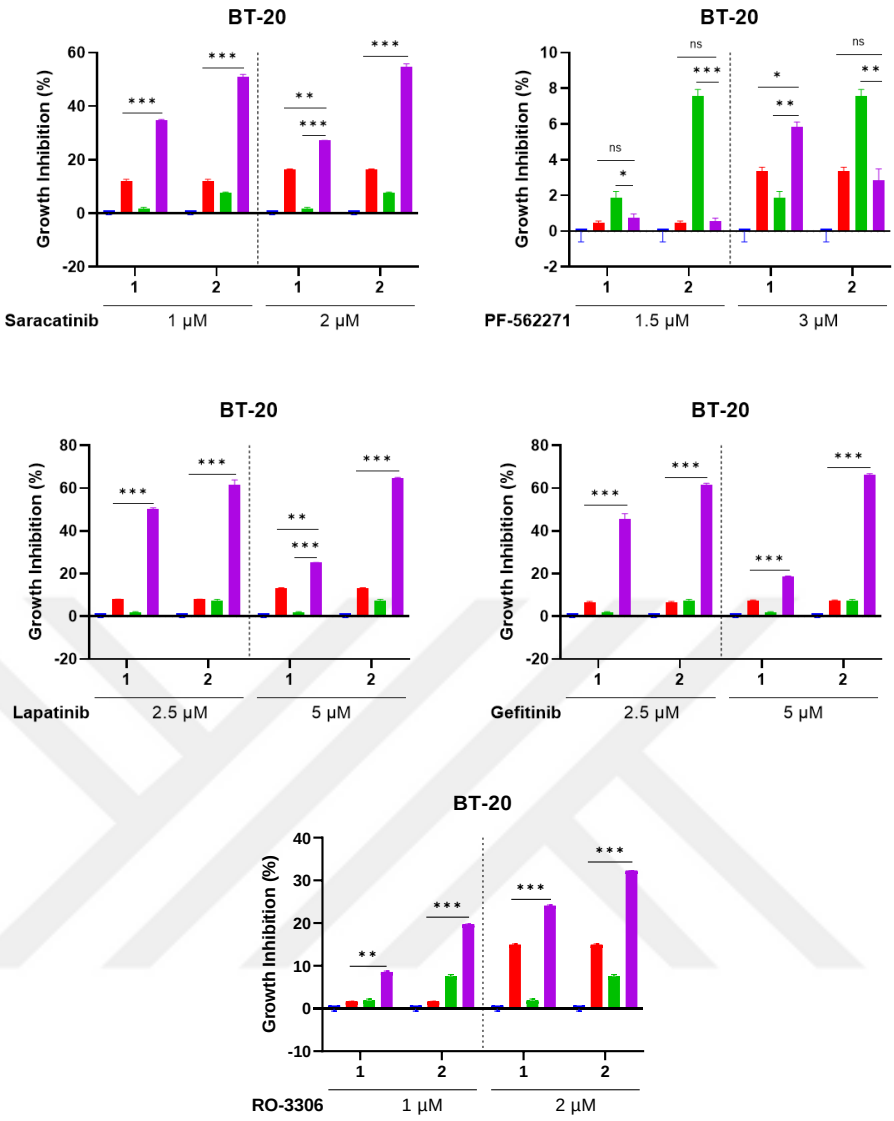


Figure 3.45. SRC, EGFR, and CDK1 inhibitors could reverse paclitaxel resistance in TNBC, as shown by cell viability assay. Chemotherapy doses (1/2 nM PTX) were given on the X axis. Inhibitor doses were provided below the figures, next to the inhibitor name (*$p < 0.05$; **$p < 0.01$; ***$p < 0.001$; ns, not significant). Blue: vehicle, red: inhibitor, green: chemotherapy, purple: combination.

When examined the cell morphology under microscopy, I observed that SRC and EGFR inhibitors could potentiate the chemoresponse of the de novo PTX-resistant BT-20 cells **(Figure 3.46)**.

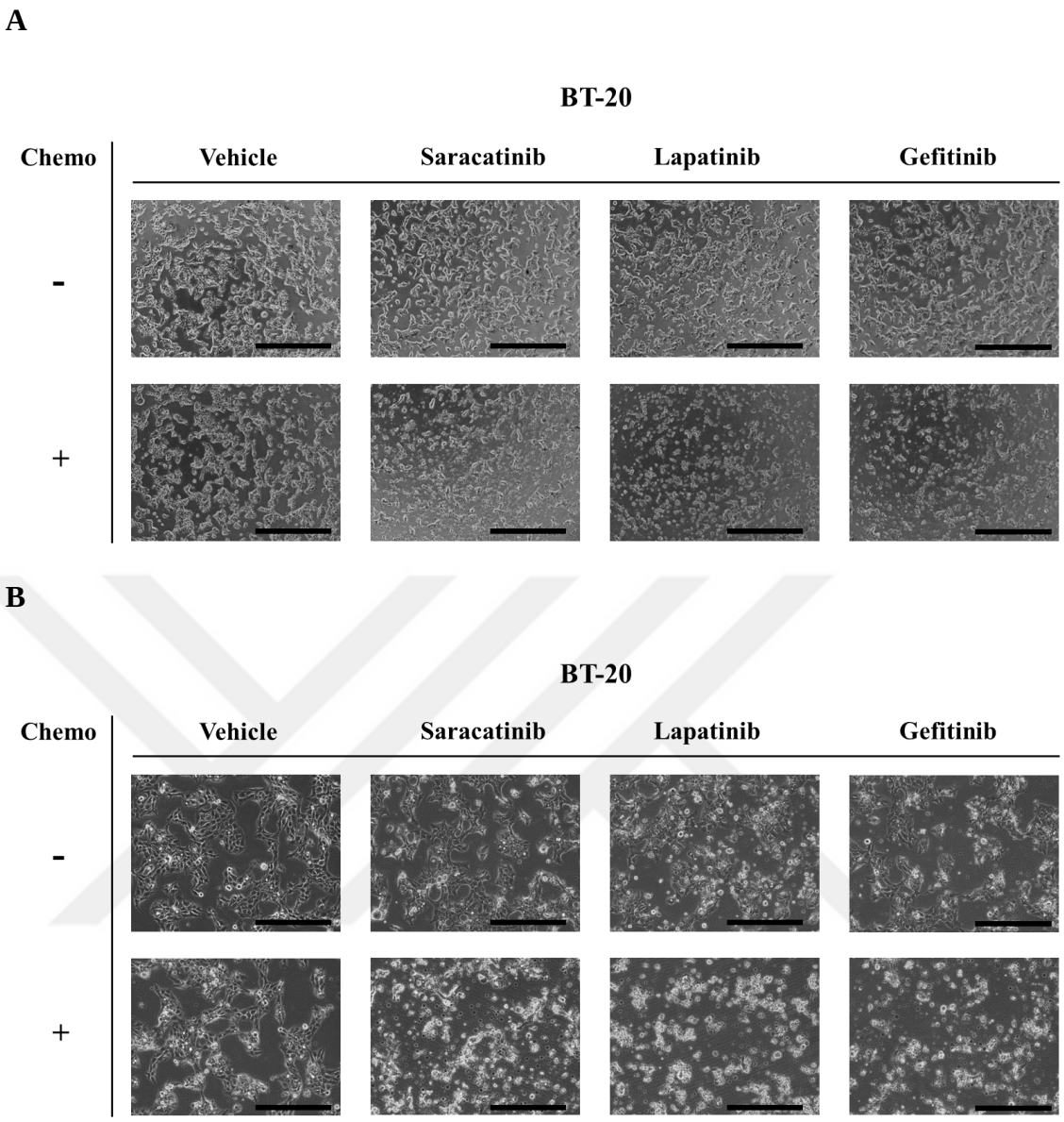


Figure 3.46. SRC and EGFR inhibitors could counteract paclitaxel resistance in TNBC, as shown by microscopy. A) 4X images were provided to show relative cell proliferation and viability (Scale bar: 1000 µm), and B) 10X images were given to show overall morphology of the cells (Scale bar: 400 µm). Phase-contrast images were taken at Evos FL Auto. Chemotherapy status was provided on the left side whereas the inhibitors were present as single agent (top) or in combination with chemotherapy (bottom).

Similarly, Annexin V/PI staining revealed that combining paclitaxel with any of these inhibitors results in marked increase in the early apoptotic cell population and to some extent at double-positive, late apoptotic cell population **(Figure 3.47).**

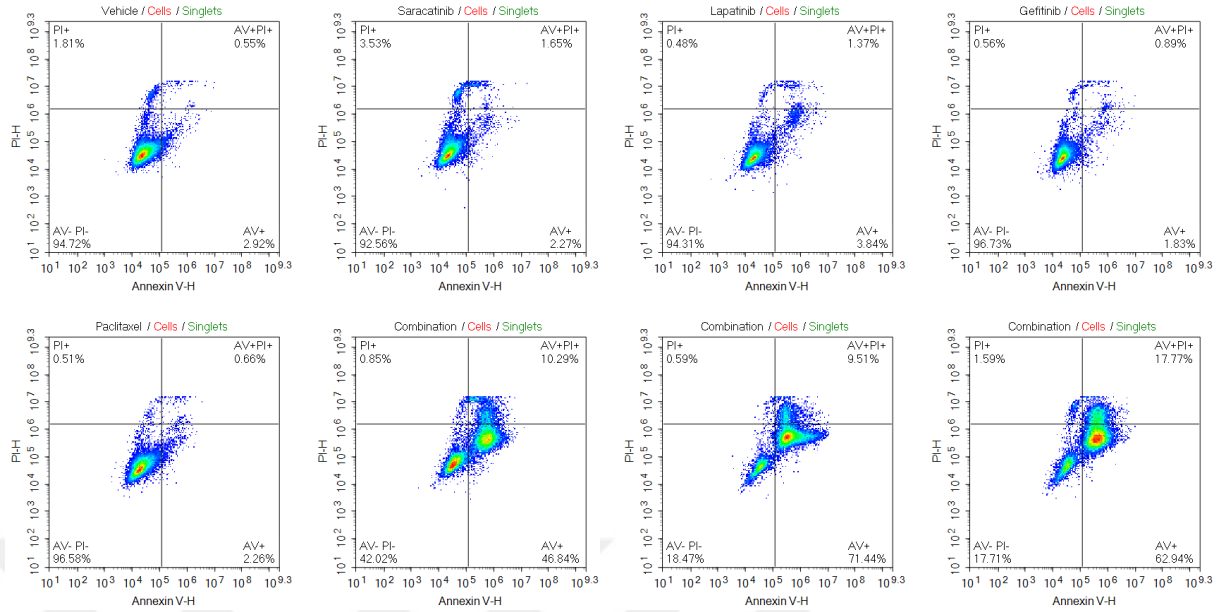


Figure 3.47. SRC and EGFR inhibitors could abrogate paclitaxel resistance, as shown by Annexin V/PI staining via flow cytometry. Vehicle (top left), Chemotherapy (paclitaxel, bottom left), Saracatinib alone or in combination (top or bottom), Lapatinib alone or in combination (top or bottom), and Gefitinib (top or bottom).

To complement the cell line models, I also generated an in vivo paclitaxel resistance model **(Figure 3.48)**. I have used MDA-MB-231-luc2-GFP cells for this purpose, partly due to time limitations (much faster growth pattern in vivo compared to CAL-51) and partly due to increase our coverage of the TNBC heterogeneity. Those tumors who did not grow in size or exhibited minimal growth after 4 cycles of paclitaxel treatment were considered sensitive. The remaining tumors in the treatment arm continued to receive weekly paclitaxel until they completed 12 cycles of treatment or reached 1500 mm^3.

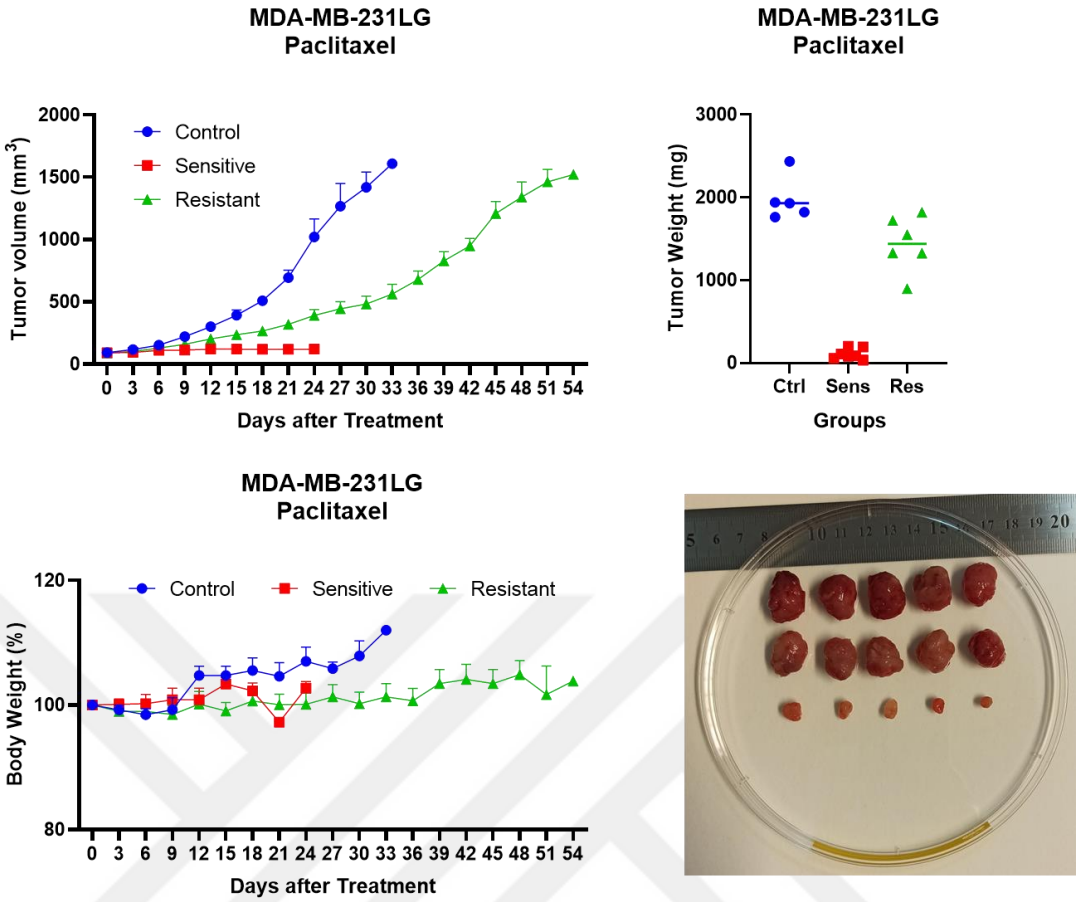


Figure 3.48. Development of in vivo paclitaxel-resistant xenografts with MDA-MB-231-luc2-GFP cells.

The resistant xenografts compared to the sensitive ones had a phenotype in between CAL-51 and MDA-MB-157 PtxR, but were mostly similar to the CAL-51 model such as elevated levels of PI3K/mTOR and FAK/SRC signaling proteins, upregulated p-p38 and p-ERK1/2, and increased ER stress markers (p-CREB) **(Figure 3.49)**. This presents a hopeful scenario where the inhibitors reversing paclitaxel resistance in vitro could be tested and offer alternative approaches for patients non-responsive to paclitaxel.

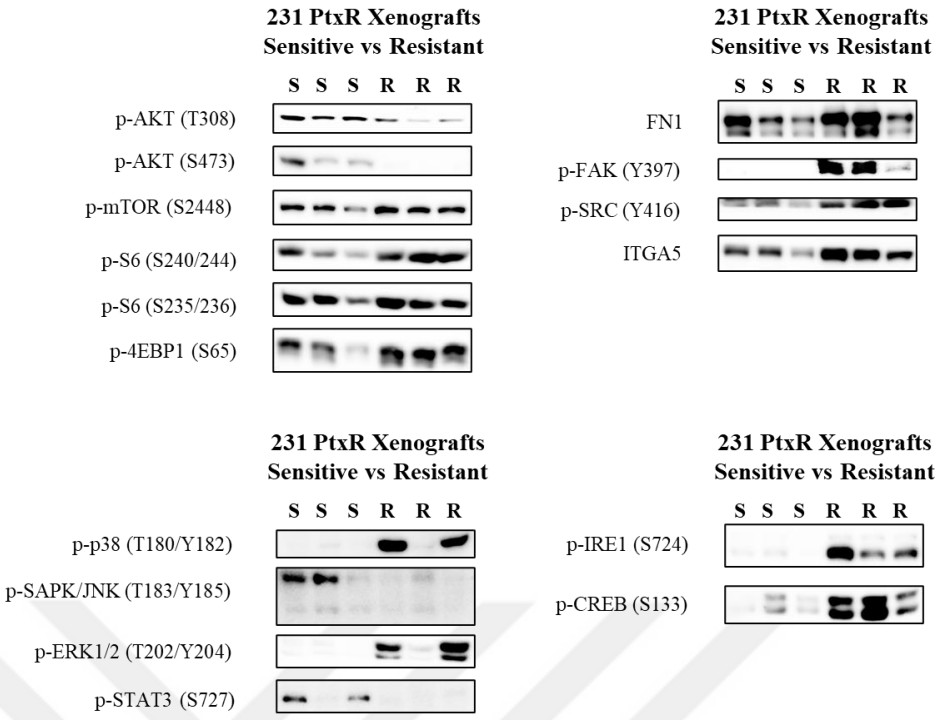


Figure 3.49. Characterization of paclitaxel-resistant and -sensitive MDA-MB-231-luc2-GFP xenografts by Western Blot.

MCF10A and MCF-12A normal breast cell lines had relatively high IC50 values, potentially rendering them partially resistant to paclitaxel treatment **(Figure 3.50)**.

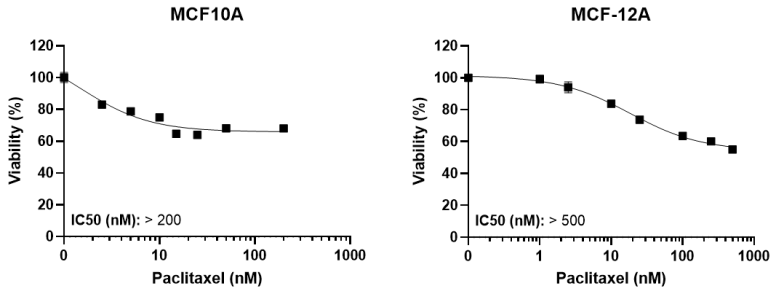


Figure 3.50. Normal breast epithelial cells have reduced response to paclitaxel.

Before testing cross resistance with agents from other chemo classes, I compared the response of the CAL-51 Parental and PtxR cells to docetaxel, another taxane. This

yielded a cell viability curve quite similar to that of paclitaxel and demonstrated that CAL-51 PtxR is also cross resistant to docetaxel **(Figure 3.51)**.

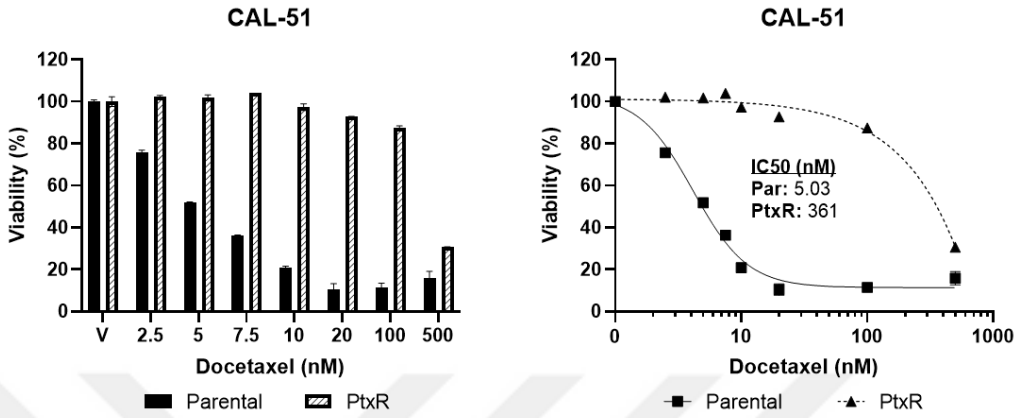


Figure 3.51. CAL-51 PtxR cells are also resistant to docetaxel, another taxane.

The response of both models to other chemotherapy classes also differed from each other. While 157 PtxR model showed partial or complete resistance to cisplatin or 5-FU and doxorubicin, respectively, CAL-51 PtxR cells were resistant to gemcitabine and doxorubicin but more sensitive towards cisplatin **(Figure 3.52 and Figure 3.53)**.

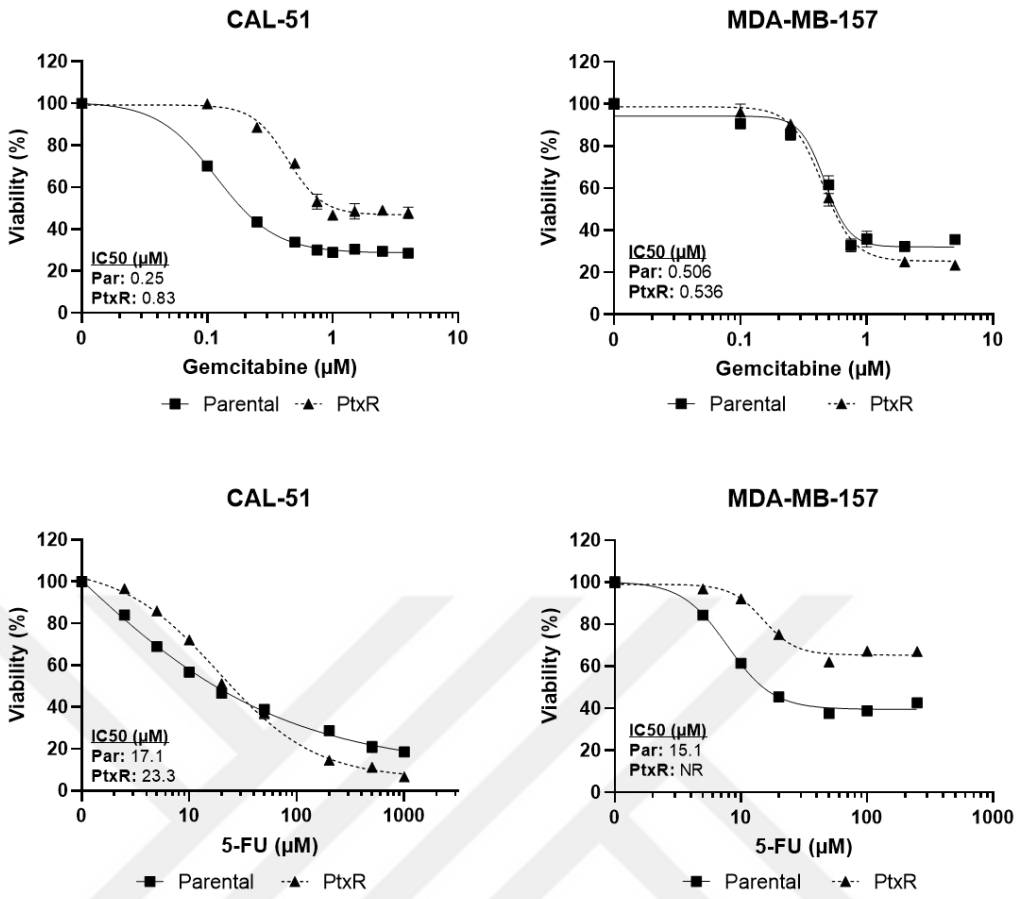


Figure 3.52. Cross chemotherapy response of the PtxR cell line models to antimetabolite chemo agents.

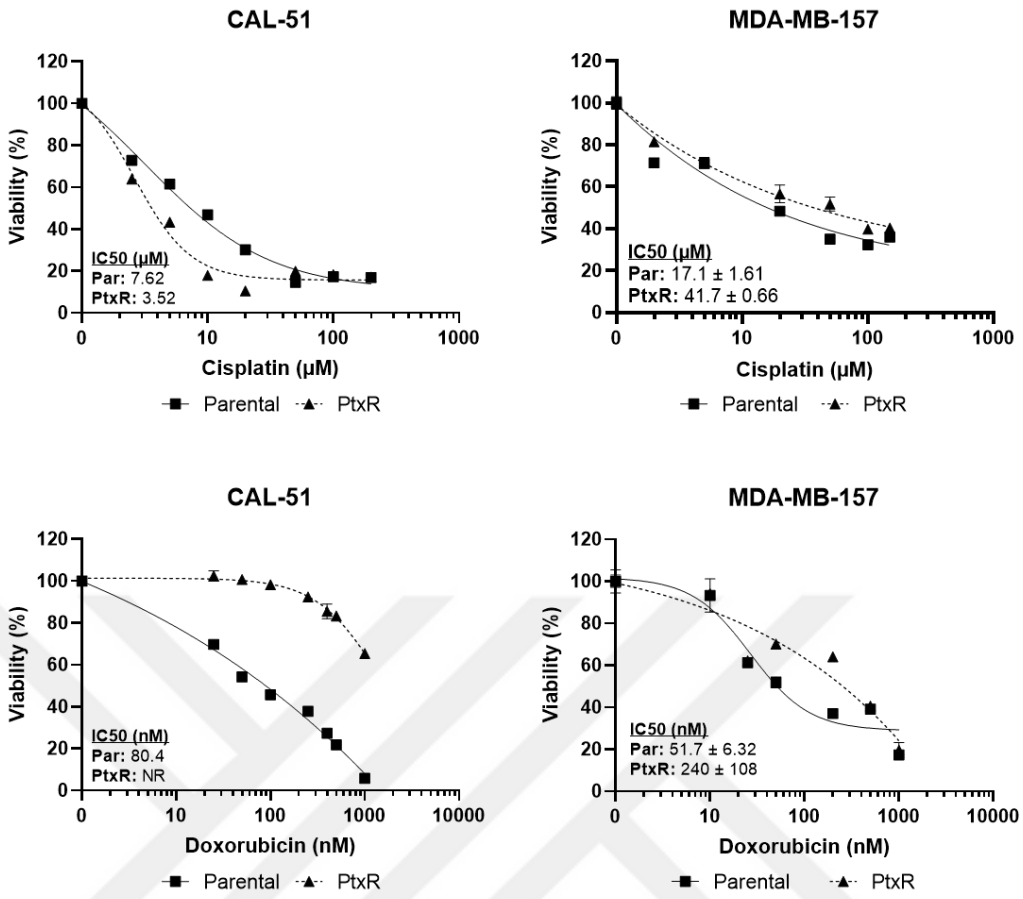


Figure 3.53. Cross chemotherapy response of the PtxR cell line models to cisplatin and doxorubicin.

3.3 Alkylating Agent Resistance Models

Another important class of chemotherapy is alkylating agents and are routinely used in the treatment of TNBC patients. Of these, platinum agents are especially utilized to treat *BRCA1*-mutated TNBC patients. Here, similar to the previous 2 sections, I first retrieved the cell line responses to cisplatin from 2 different databases **(Figure 3.54)**.

Cell Line	Drug	CancerRxGene (IC50 - µM)			PharmacoDB (IC50 - µM)			
		GDSC1_M	GDSC1_S	GDSC2	GDSC	CTRPv2	gCSI	FIMM
BT-20	CIS	NA	26.7	36.8	10	NA	NA	NA
CAL-51	CIS	NA	9.02	6.66	6.1	NA	NA	NA
HCC1143	CIS	NA	33.7	317	34.7	NA	NA	NA
HCC1937	CIS	NA	32.9	134	ND	NA	NA	NA
HCC70	CIS	NA	8.09	12.6	27	NA	NA	NA
MDA-MB-157	CIS	NA	41.8	216	NA	NA	NA	NA
MDA-MB-231	CIS	NA	19.1	43.2	38.9	NA	NA	NA
MDA-MB-436	CIS	NA	4.79	51.8	4.14	NA	NA	NA
MDA-MB-468	CIS	NA	6.09	3.78	6.43	NA	NA	NA

Figure 3.54. Cisplatin response of the TNBC cell line panel, retrieved from CancerRxGene and PharmacoDB. NA: not available, ND: not determined (not reached or cannot be calculated due to response curve). GDSC: Genomics of Drug Sensitivity in Cancer, M: Mass General Hospital, S: Sanger Institute, CTRP: Cancer Therapeutics Response Portal, gCSI: Genentech Cell Line Screening Initiative, FIMM: Institute for Molecular Medicine Finland.

I also experimentally tested cisplatin response of these cell lines after 72 hours drug treatment. In line with the databases, MDA-MB-468, CAL-51 and MDA-MB-436 cells were overall the most sensitive cell lines **(Figure 3.55)**. However, both MDA-MB-468 and CAL-51 cells are not *BRCA1*-mutated thus BRCA proficient. Unlike these, MDA-MB-436 harbors a *BRCA1* mutation and BRCA deficient. Therefore, I selected MDA-MB-436 and also another *BRCA1*-mutation carrier cell line, HCC1937 to develop cisplatin-resistant TNBC models.

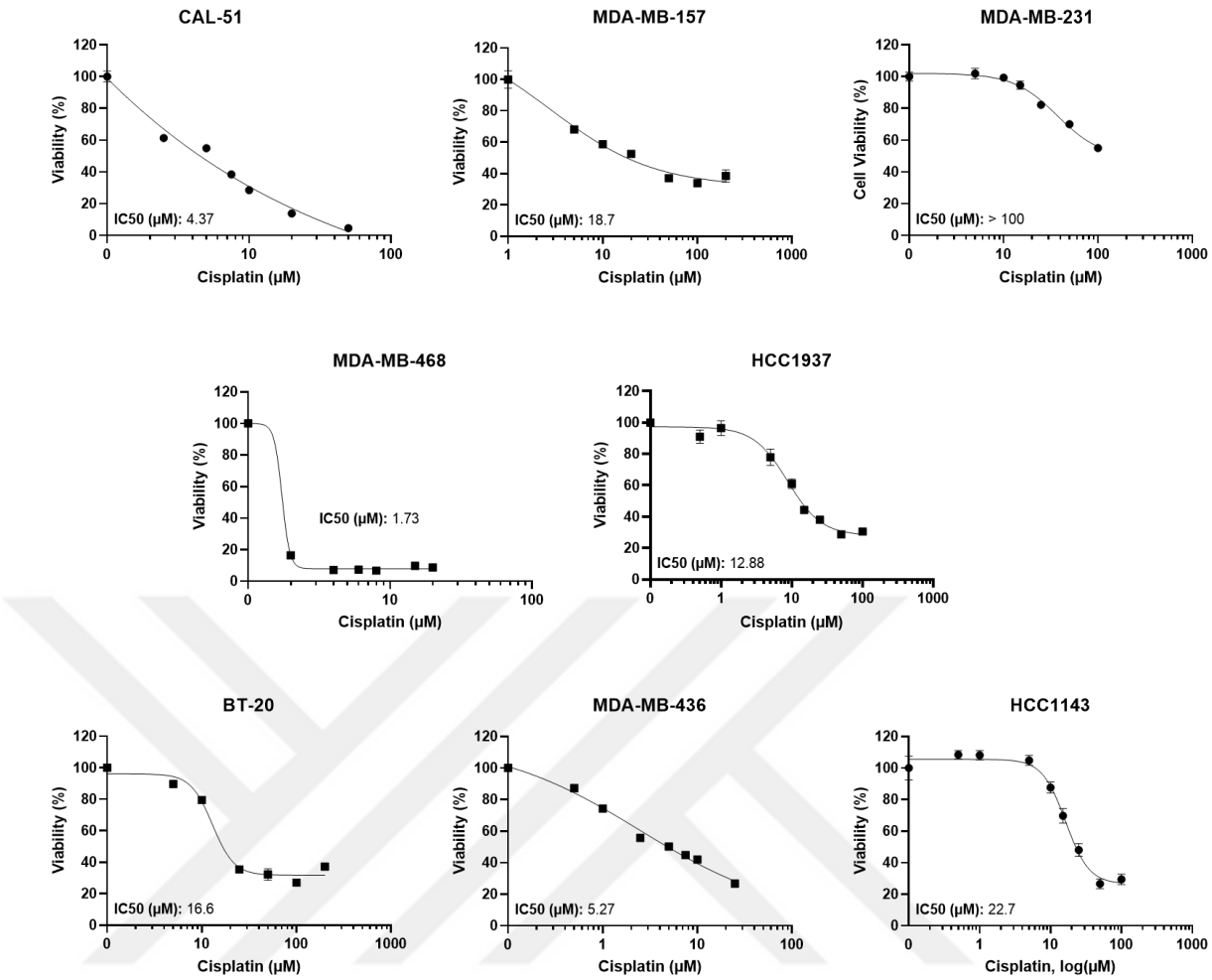
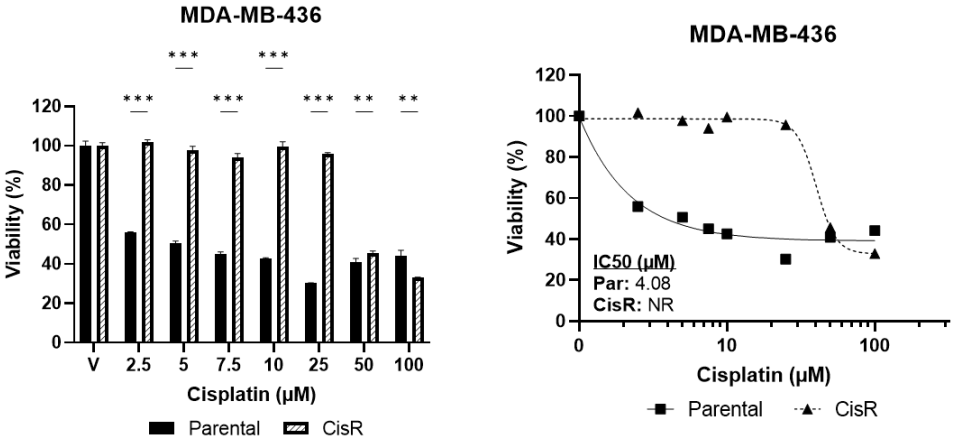


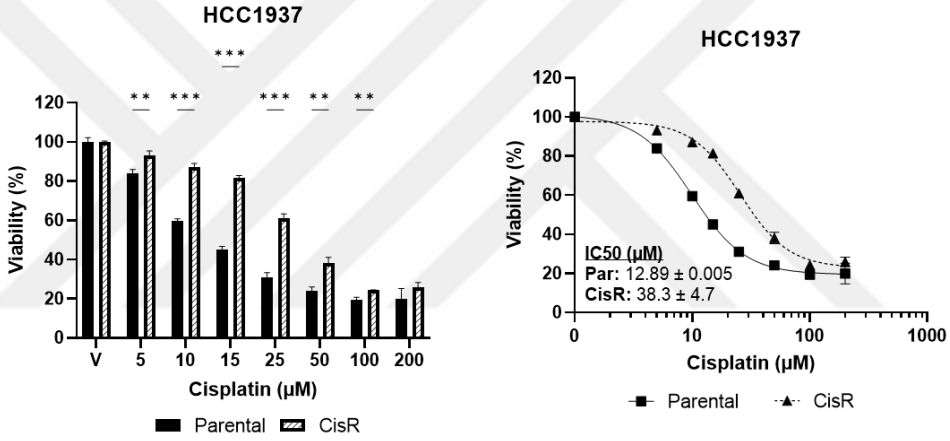
Figure 3.55. Cisplatin response of the TNBC cell line panel, measured by cell viability assay following 72h drug treatment.

Accordingly, our group have developed these cells by following the same approach presented in the previous sections. The resistance was validated by cell viability assays in comparison to the parental cell lines **(Figure 3.56)**. There were approximately 25- and 3-fold increase in the IC50s of the MDA-MB-436 CisR and HCC1937 CisR cells, respectively.

A



B



C

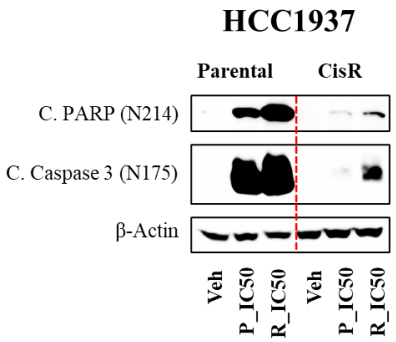


Figure 3.56. Development of MDA-MB-436 and HCC1937 cisplatin-resistant cells. A, B) The resistance relative to the parental cells was confirmed by cell viability assay. C) Apoptosis markers upon vehicle (Veh) or CIS treatment at IC50 of the parental (P_IC50) or IC50 of the resistant (R_IC50) cells (*$p < 0.05$; **$p < 0.01$; ***$p < 0.001$; ns, not significant).

Upon verifying the resistance in both cell lines, I started their characterization by Western blot for multiple pathways and processes. In terms of PI3K/AKT/mTOR signaling proteins, the similarities between the models were minimal and includes decreased levels of p-AKT (S473) and p-PRAS and elevated p-AKT (T308) **(Figure 3.57)**, limiting the use of PI3K/AKT/mTOR inhibitors as general cisplatin sensitizers.

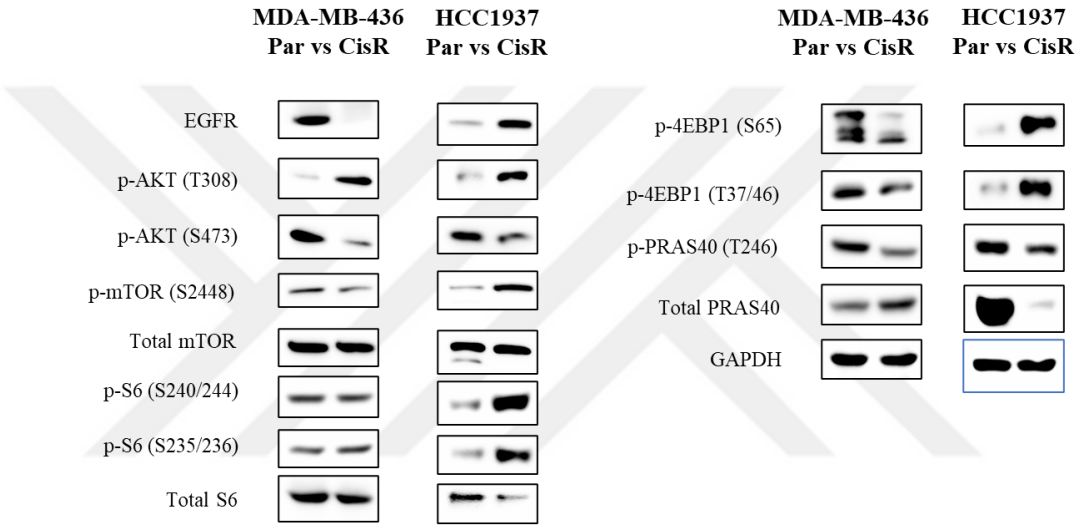


Figure 3.57. Differences in the PI3K/AKT/mTOR pathway components between the parental and cisplatin-resistant cells. Left lane: Parental, Right lane: Resistant.

When we examined integrin and MAPK signaling pathways, there were much better concordance between the models with an activated integrin signaling and increase in phospho-levels of MAP kinases **(Figure 3.58)**. This potentially implicates that both pathways could be common denominators underlying cisplatin resistance.

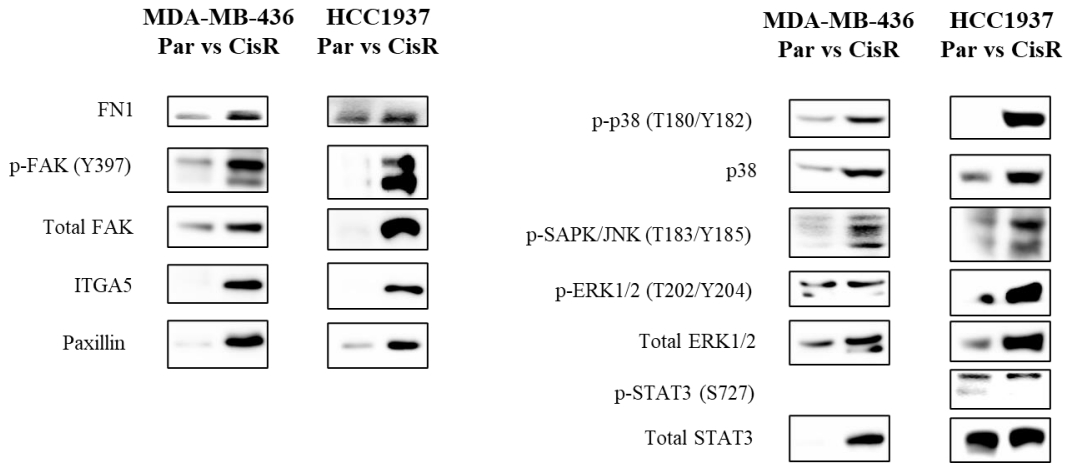


Figure 3.58. Differences in the integrin, MAPK and STAT3 pathway components between the parental and cisplatin-resistant cells. Left lane: Parental, Right lane: Resistant.

I observed a similar trend for ER stress markers, which were consistently and exclusively activated in the CisR cells while autophagy markers had a mixed pattern **(Figure 3.59, left)**. However, I could not test if ER stress modulation render cells resistant to cisplatin since I did not have any ER stress inhibitor. Other common alterations between the cells include upregulation of BRCA1 and elevated p-cdc25C **(Figure 3.59, right)**.

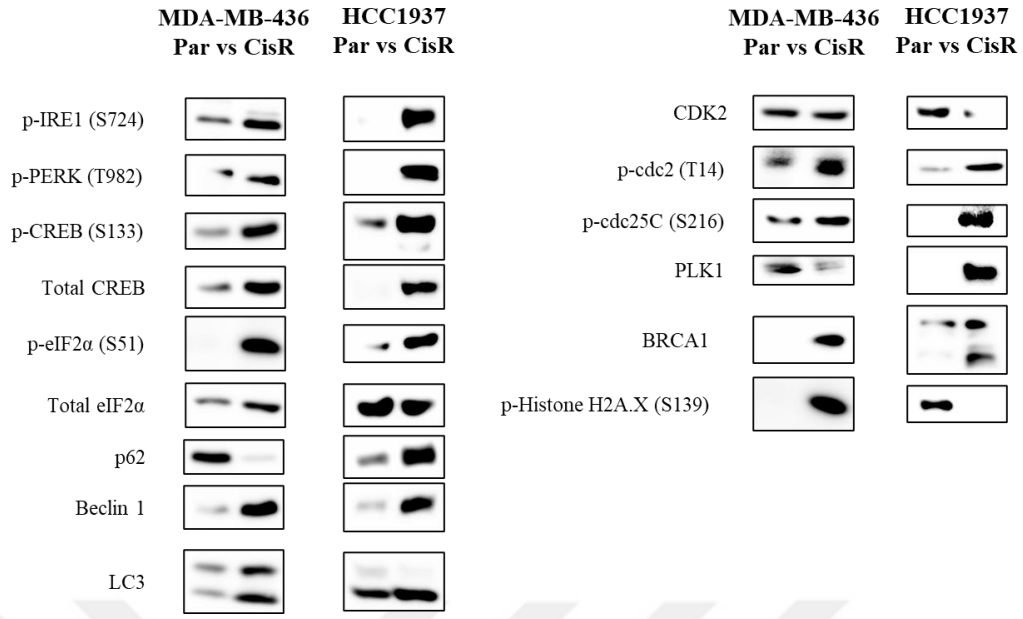


Figure 3.59. Differences in the ER stress and autophagy markers and cell cycle proteins between the parental and cisplatin-resistant cells. Left lane: Parental, Right lane: Resistant.

Considering the overall pathway activation/inhibition patterns, I have decided to exploit common alterations thus initially used FAK and ITGA5 inhibitors **(Figure 3.60)**. While FAK inhibitor produced an additive chemotherapy response in both models, this was only the case in the HCC1937 CisR for ATN-161 and did not give any meaningful data in the MDA-MB-436 CisR cells. However, these could be caused by suboptimal dose selections. Lower doses of PF-562271 in the 436 CisR and higher doses in the 1937 CisR as well as higher doses of ATN-161 in both cells could yield a better outcome.

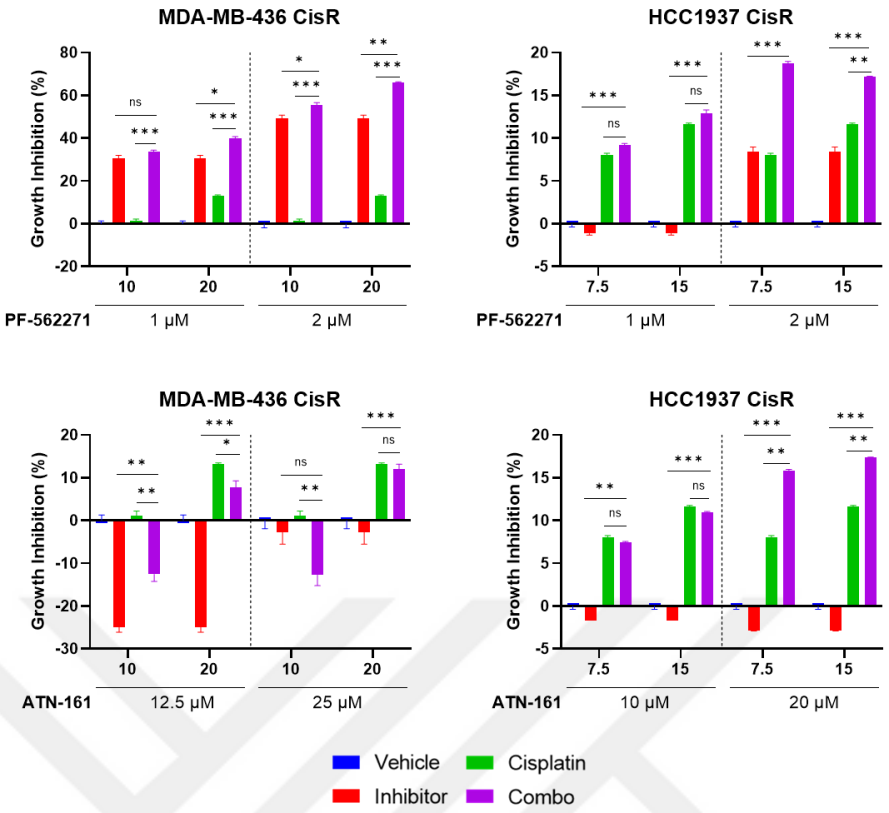


Figure 3.60. PF-562271 and ATN-161 could not synergistically potentiate cisplatin response in TNBC, as shown by cell viability assay. Chemotherapy doses (10/20 μM CIS for MDA-MB-436 CisR and 7.5/15 μM for HCC1937 CisR) were given on the X axis. Inhibitor doses were provided below the figures, next to the inhibitor name (*$p < 0.05$; **$p < 0.01$; ***$p < 0.001$; ns, not significant). Blue: vehicle, red: inhibitor, green: chemotherapy, purple: combination.

Unlike FAK and ITGA5 inhibitors, p38 inhibitor SB203580 could impose a synergistic response at select conditions such as high-dose combinations with cisplatin in the 436 CisR but low-dose combinations in the 1937 CisR **(Figure 3.61, top)**. Similarly, CDK1 inhibitor RO-3306 shows a dose-dependent synergism while dual PI3K/mTOR inhibitor BEZ235 exerted its effect remarkably well at all 4 combinations **(Figure 3.61, bottom)**.

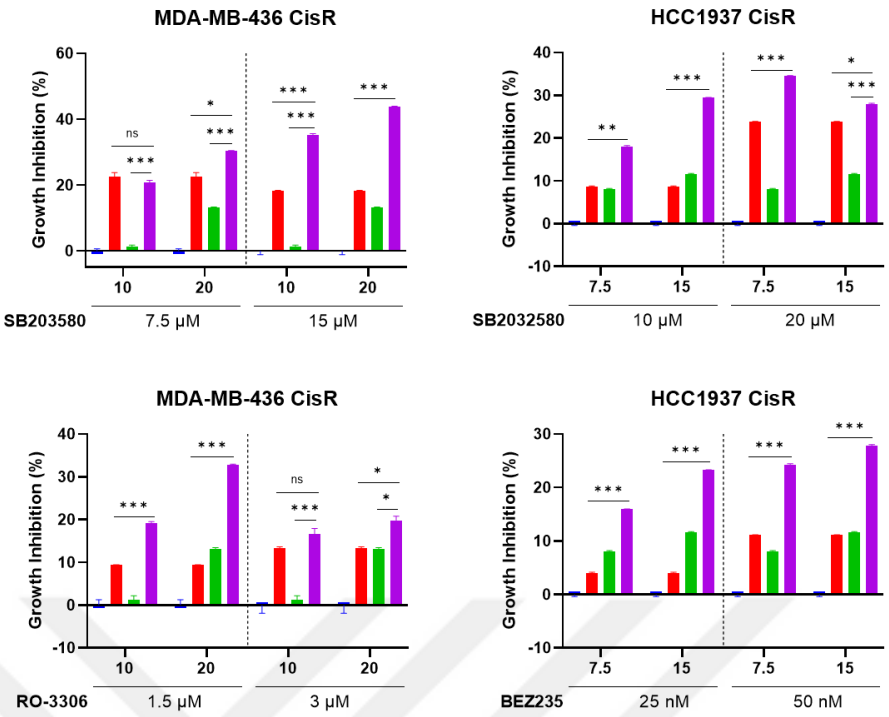


Figure 3.61. The effect of p38, CDK1 or dual PI3K/mTOR inhibitors in cisplatin response in TNBC, as shown by cell viability assay. Chemotherapy doses (10/20 µM CIS for MDA-MB-436 CisR and 7.5/15 µM for HCC1937 CisR) were given on the X axis. Inhibitor doses were provided below the figures, next to the inhibitor name (*$p < 0.05$; **$p < 0.01$; ***$p < 0.001$; ns, not significant). Blue: vehicle, red: inhibitor, green: chemotherapy, purple: combination.

I have also tested these inhibitors except ATN-161 in the case of de novo resistance. MDA-MB-231 is highly nonresponsive to cisplatin up to 100 µM and therefore was selected as the de novo model. In line with the acquired resistance models, the inhibitor-cisplatin combinations did not lead to synergistic response except one or two conditions **(Figure 3.62)**. This potentially means that cisplatin resistance could be driven by small contributions of multiple driver events instead of a major or predominant mechanism.

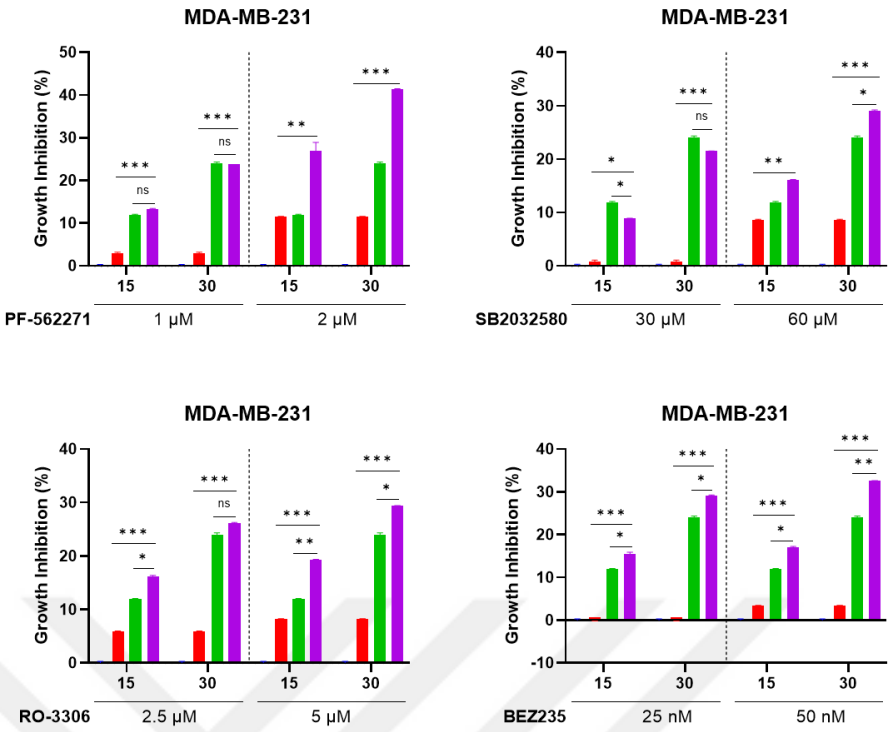


Figure 3.62. The selected inhibitors could not also abrogate de novo cisplatin resistance. Chemotherapy doses (15/30 μM CIS) were given on the X axis. Inhibitor doses were provided below the figures, next to the inhibitor name (*$p < 0.05$; **$p < 0.01$; ***$p < 0.001$; ns, not significant). Blue: vehicle, red: inhibitor, green: chemotherapy, purple: combination.

Similar to previously tested chemotherapies, the normal breast epithelial cell lines had relatively higher IC50s and thus reduced response to cisplatin when compared to the TNBC cell lines **(Figure 3.63)**.

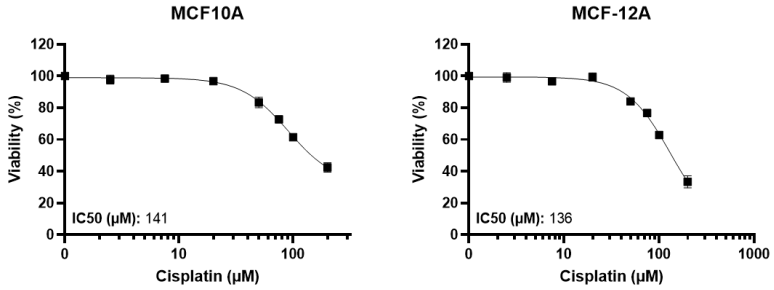


Figure 3.63. Normal breast epithelial cells have reduced response to cisplatin relative to TNBC cell lines.

Before characterizing cross resistance patterns of the CisR models to other classes of chemotherapy, I tested the response of HCC1937 CisR cells to another platinum analogue, oxaliplatin. It is actually distinctive from both cisplatin and carboplatin and is utilized in the treatment of other types of cancers such as gastric and pancreatic cancer, not in the breast. Accordingly, the 1937 CisR cells did not show cross resistance to oxaliplatin **(Figure 3.64)**.

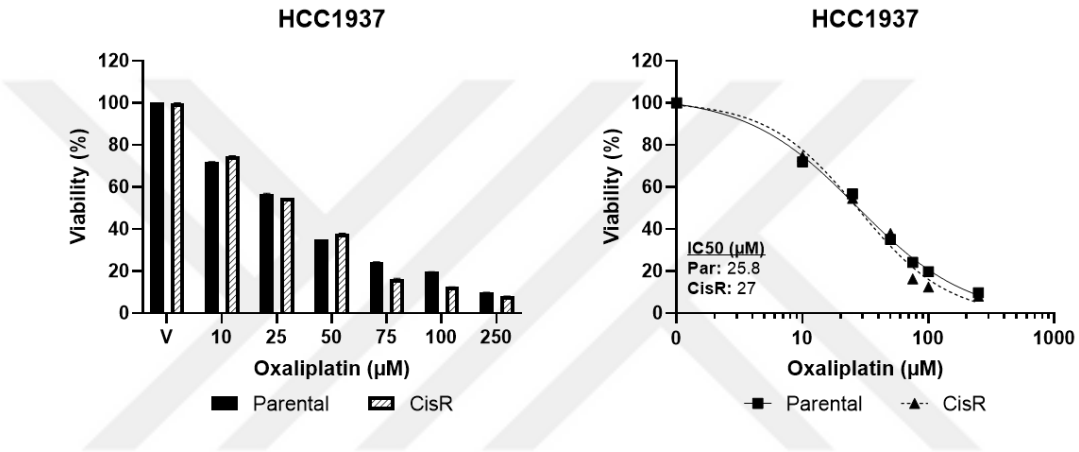


Figure 3.64. The cisplatin-resistant cells are not cross resistant to oxaliplatin another platinum agent.

Later I characterized the cross-resistance patterns in both cell lines to antimetabolite, anti-tumor antibiotics and mitotic inhibitors. HCC1937 CisR cells did not exhibit cross-resistance to other chemotherapeutics while the 436 CisR cells were partially or highly cross resistant to gemcitabine, paclitaxel and doxorubicin **(Figure 3.65 and Figure 3.66)**.

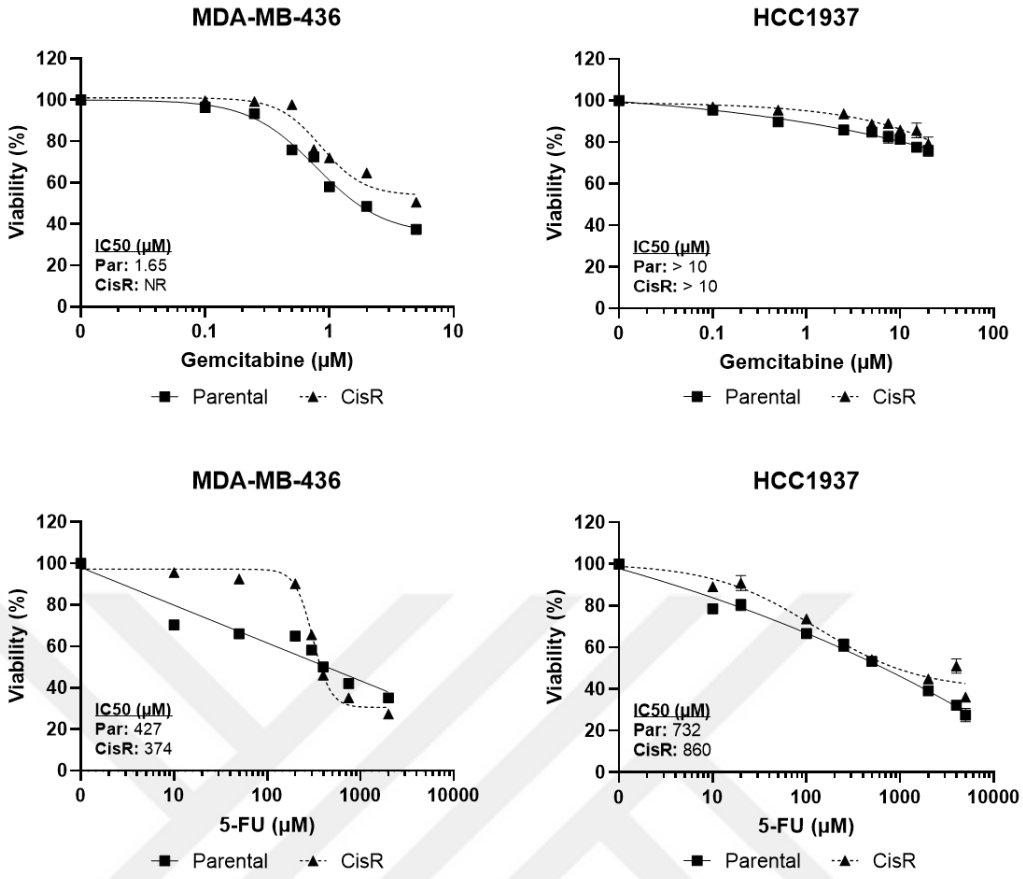


Figure 3.65. Cross chemotherapy response of the CisR cell line models to gemcitabine and 5-FU.

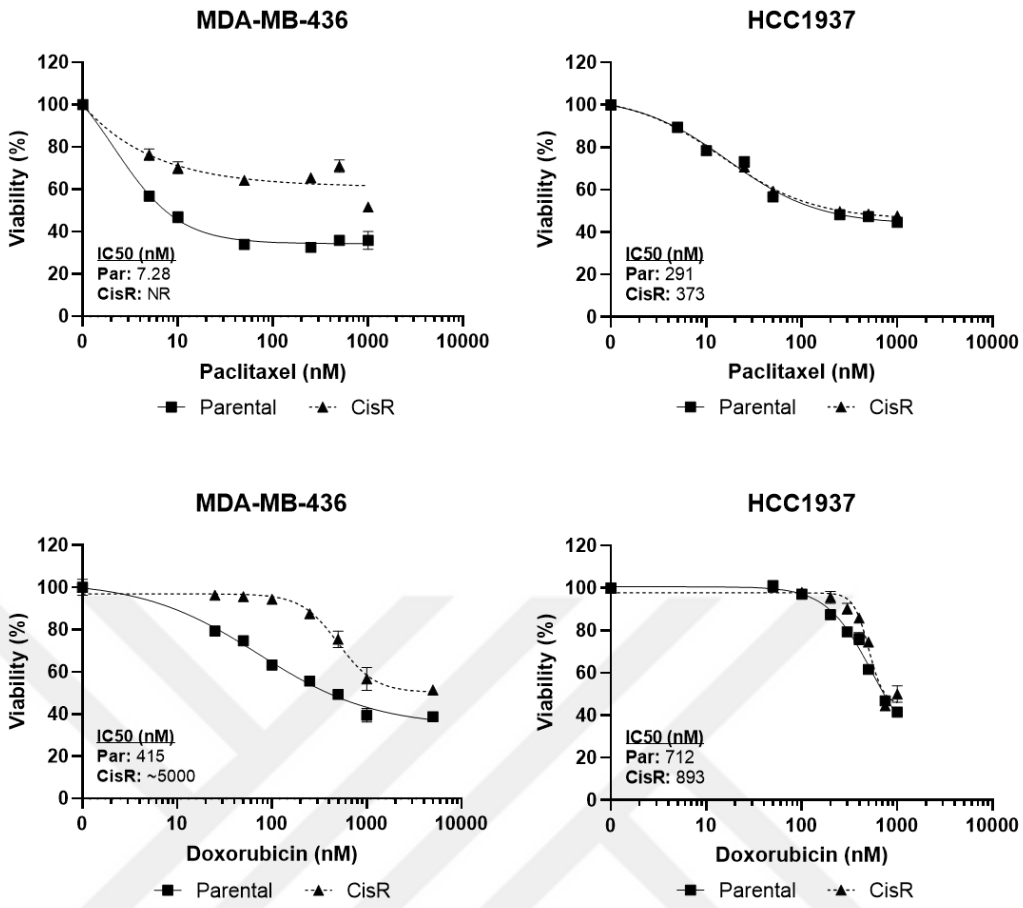


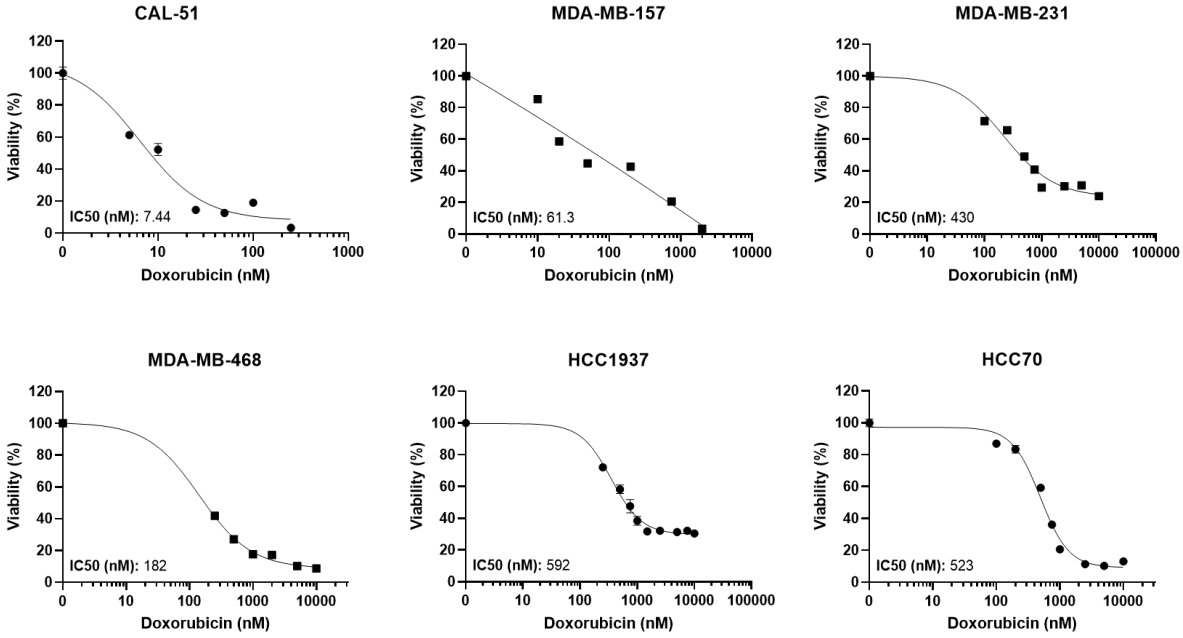
Figure 3.66. Cross chemotherapy response of the PtxR cell line models to paclitaxel and doxorubicin.

3.4 Anti-tumor Antibiotic Resistance Models

In the last section of Part I, I have developed in vitro and in vivo models of doxorubicin resistance in TNBC. Again CAL-51 cells were highly sensitive to doxorubicin as shown by the data obtained from the databases **(Figure 3.67)** and my experimental findings **(Figure 3.68)**.

Cell Line	Drug	CancerRxGene (IC50 - nM)			PharmacoDB (IC50 - nM)			
		GDSC1_M	GDSC1_S	GDSC2	GDSC	CTRPv2	gCSI	FIMM
BT-20	DOXO	1030	186	NA	645	1254	559	NA
CAL-51	DOXO	21.1	25.4	NA	20.6	86	77.1	151
HCC1143	DOXO	NA	215	NA	1314	784	890	218
HCC1937	DOXO	137	289	NA	114	994	1689	70.2
HCC70	DOXO	610	291	NA	587	NA	NA	NA
MDA-MB-157	DOXO	570	344	NA	428	78.7	264	NA
MDA-MB-231	DOXO	1262	108	NA	1405	1509	496	183
MDA-MB-436	DOXO	1672	126	NA	1812	NA	322	189
MDA-MB-468	DOXO	78.3	72.6	NA	74.7	172	283	150

Figure 3.67. Doxorubicin response of the TNBC cell line panel, retrieved from CancerRxGene and PharmacoDB. NA: not available, ND: not determined (not reached or cannot be calculated due to response curve). GDSC: Genomics of Drug Sensitivity in Cancer, M: Mass General Hospital, S: Sanger Institute, CTRP: Cancer Therapeutics Response Portal, gCSI: Genentech Cell Line Screening Initiative, FIMM: Institute for Molecular Medicine Finland.



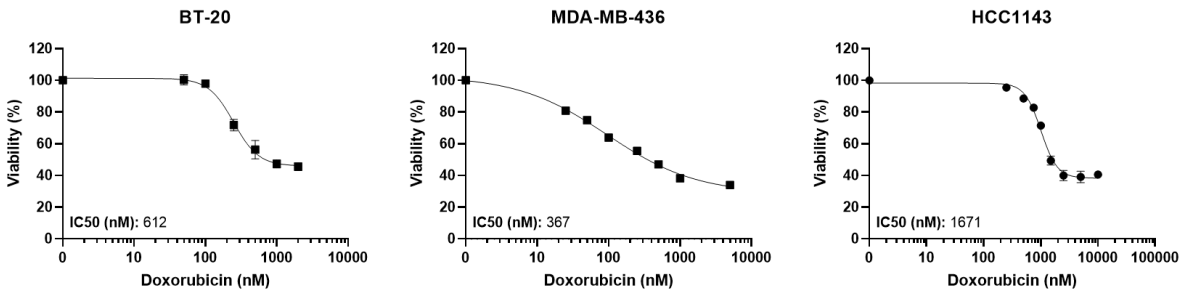
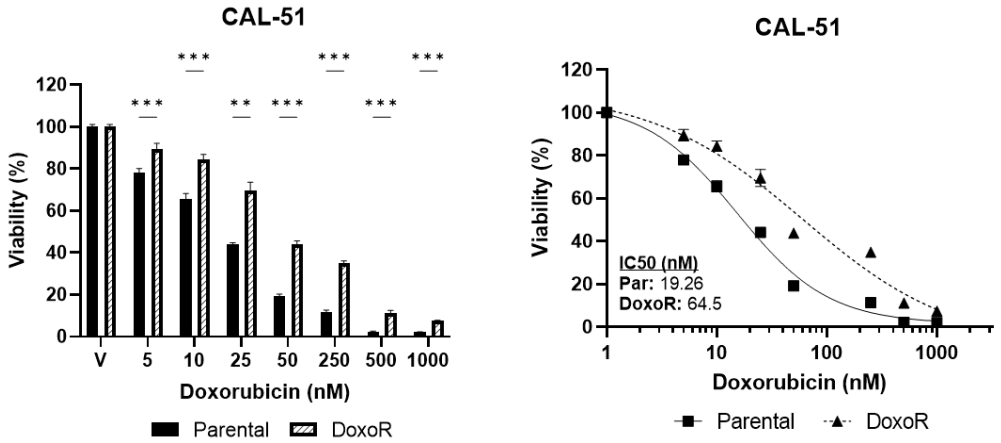


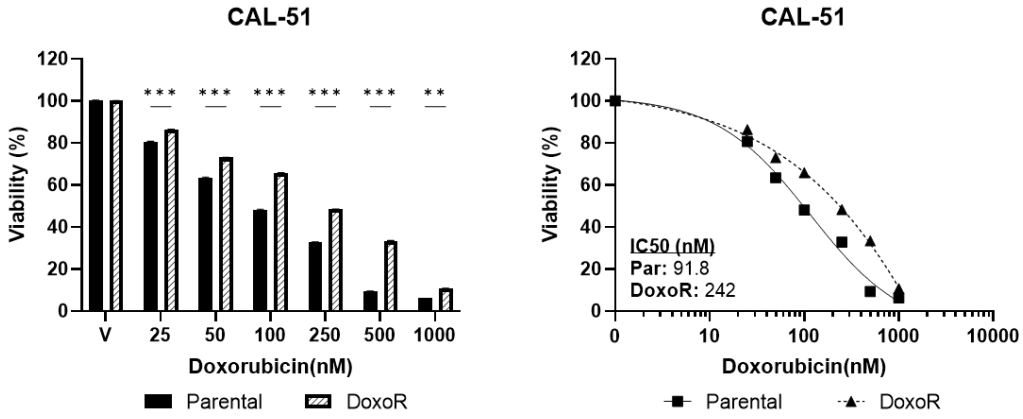
Figure 3.68. Doxorubicin response of the TNBC cell line panel, measured by cell viability assay following 72h drug treatment.

In addition to the CAL-51 cells, I have utilized MDA-MB-231 cells considering their high tumorigenic potential and to have a cell pair representing TNBC heterogeneity. I have evaluated the doxorubicin response of potential resistant cells by cell viability after approximately 8-9 months. Both models had roughly 3-fold the IC50 value in comparison to their parental counterparts **(Figure 3.69 and Figure 3.70)**.

A



B



C

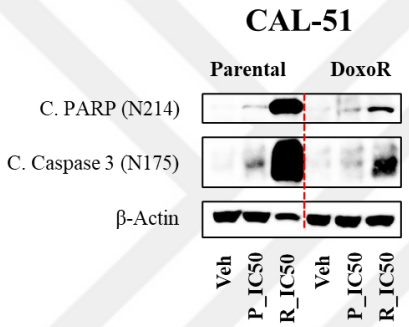


Figure 3.69. Development of CAL-51 doxorubicin-resistant cells. The resistance relative to the parental cells was confirmed by cell viability assays, A) by CellTiter-Glo and B) SRB C) Apoptosis markers upon vehicle (Veh) or DOXO treatment at IC50 of the parental (P_IC50) or IC50 of the resistant (R_IC50) cells (*$p < 0.05$; **$p < 0.01$; ***$p < 0.001$; ns, not significant).

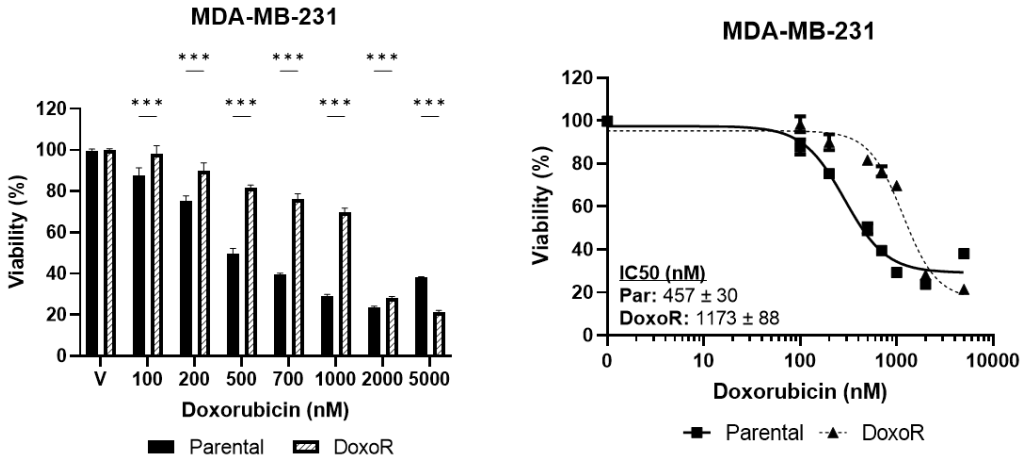


Figure 3.70. Development of MDA-MB-231 doxorubicin-resistant cells. The resistance relative to the parental cells was confirmed by cell viability assay (*$p < 0.05$; **$p < 0.01$; ***$p < 0.001$; ns, not significant).

Following the validation of resistance profile, I characterized doxorubicin resistance in the CAL-51 DoxoR cells by multiple pathways via Western blot. The cells had an overall activation of PI3K/mTOR and overall inactivation of integrin signaling **(Figure 3.71)**. However, they exhibited a mixed phenotype for MAPK, STAT3 and ER stress pathways as well as cell cycle proteins **(Figure 3.72)**.

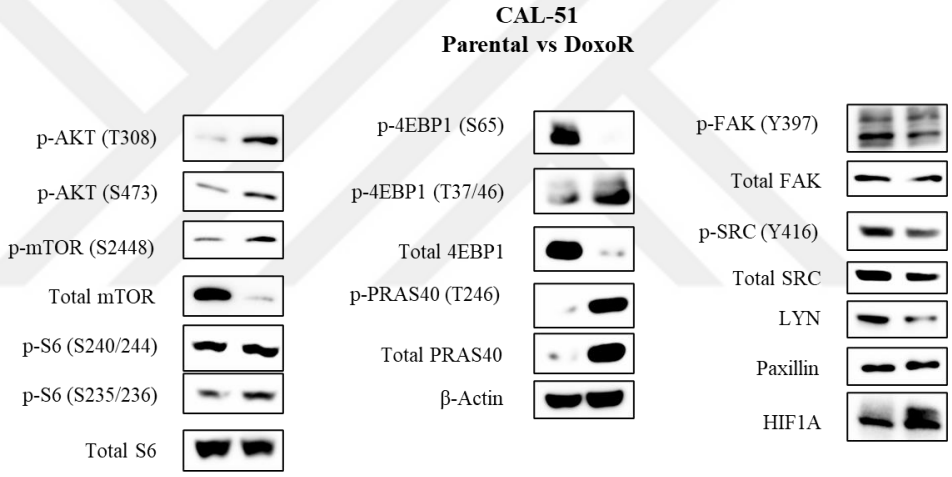


Figure 3.71. Differences in the PI3K/AKT/mTOR and integrin pathway components between the parental and doxorubicin-resistant cells. Left lane: Parental, Right lane: Resistant.

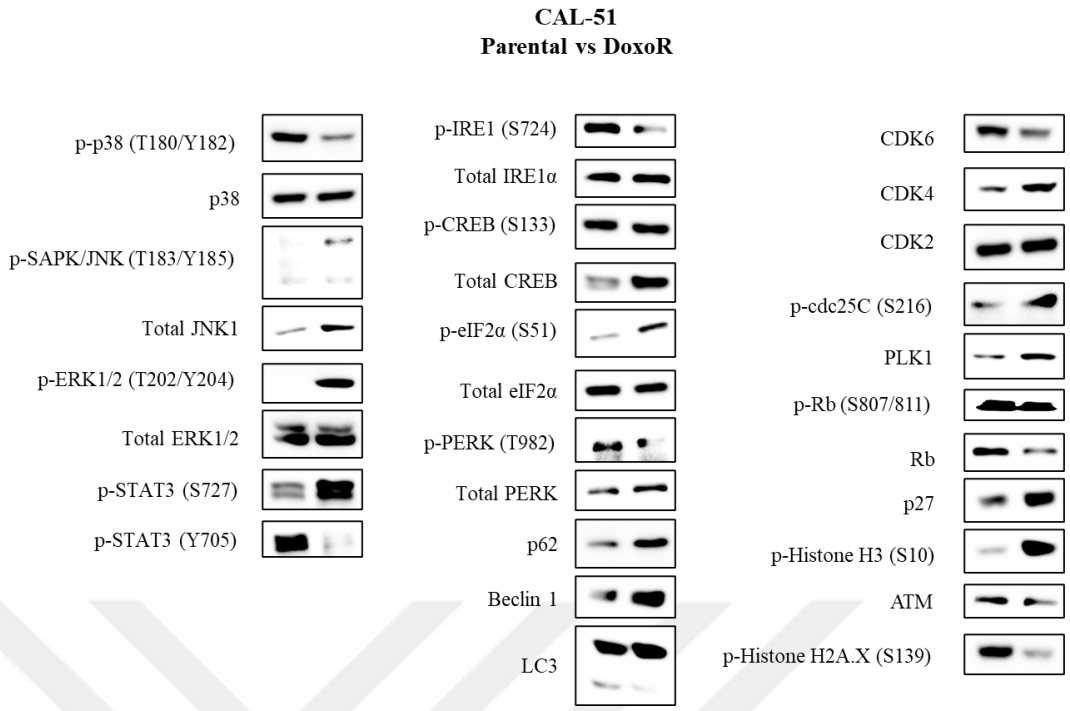


Figure 3.72. Differences in the MAPK signaling, ER stress, autophagy and cell cycle components between the parental and doxorubicin-resistant cells. Left lane: Parental, Right lane: Resistant.

Considering the resistance profile of CAL-51 DoxoR cells as well as our previous publication reporting the role of integrin/FAK/SRC signaling in the doxorubicin resistance, I have tested the combinatorial effects of PI3K/AKT inhibitors or FAK and SRC inhibitors in both models **(Figure 3.73)**. As expected, SRC and FAK inhibitors resulted in the reversal of acquired resistance in the 231 DoxoR cells while they were ineffective at doing so in the CAL-51 DoxoR cells. This was reasonable as both total and phosphoprotein levels of SRC and FAK diminished in the CAL-51 DoxoR cells.

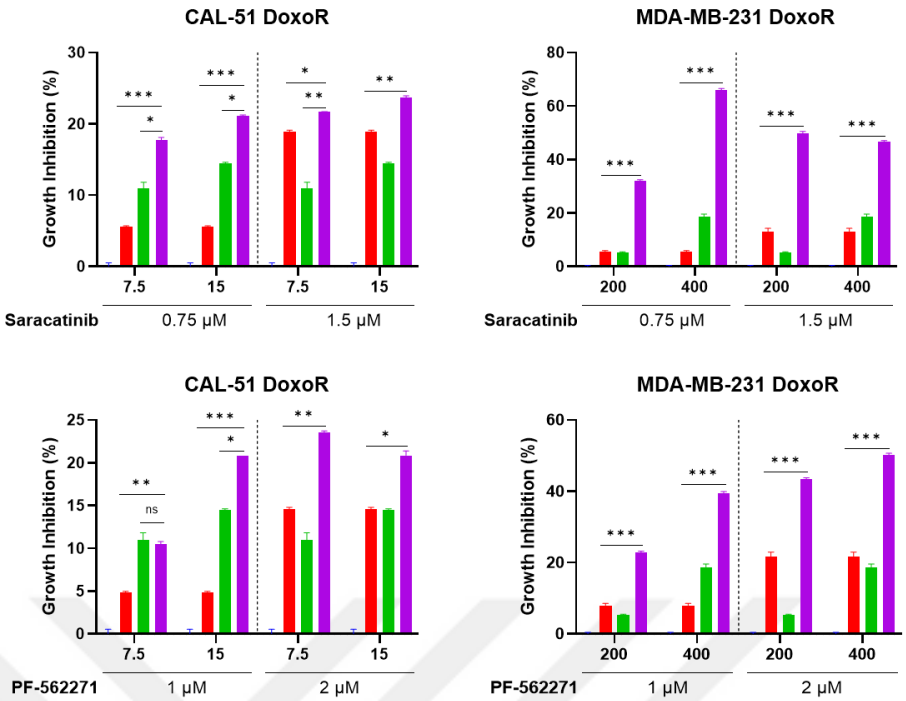


Figure 3.73. The effect of SRC and FAK inhibitors in doxorubicin response in TNBC, as shown by cell viability assay. Chemotherapy doses (7.5/15 nM Doxorubicin for CAL-51 DoxoR and 200/400 nM for MDA-MB-231 DoxoR) were given on the X axis. Inhibitor doses were provided below the figures, next to the inhibitor name (*$p < 0.05$; **$p < 0.01$; ***$p < 0.001$; ns, not significant). Blue: vehicle, red: inhibitor, green: chemotherapy, purple: combination.

I have later tested BYL719 and MK-2206 in combination with doxorubicin, which was guided by increased p-AKT proteins **(Figure 3.74)**. While both inhibitors worked in a synergistic manner in the 231 DoxoR cells at all combinations, only MK-2206 yielded a synergistic response for some combinations in the CAL-51 DoxoR cells and the response was either additive or even antagonistic for BYL719.

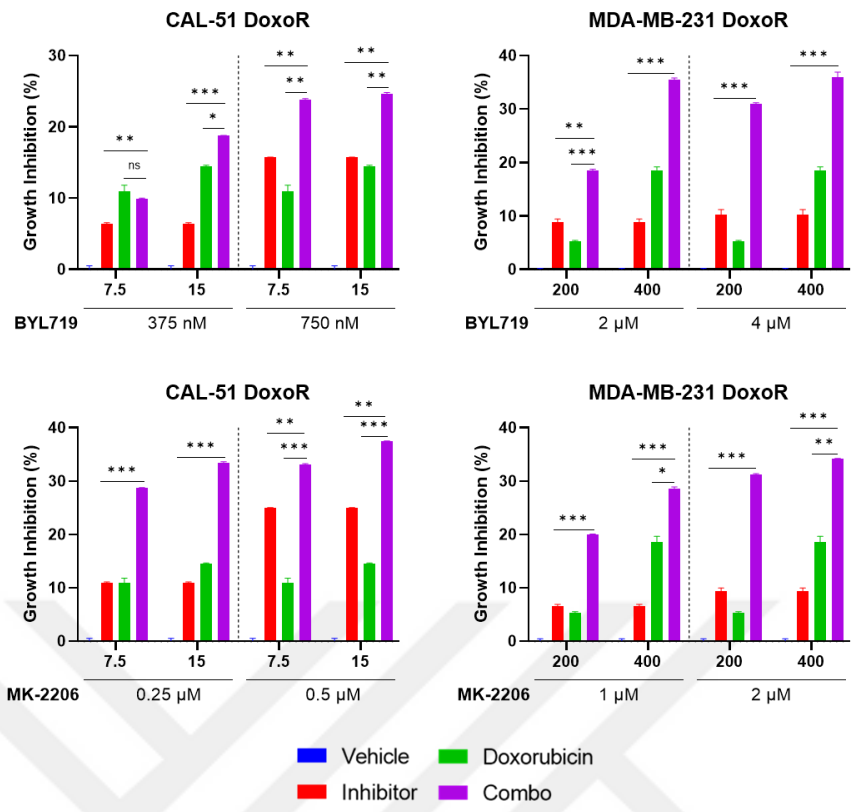


Figure 3.74. The effect of PI3K and AKT inhibitors in doxorubicin response in TNBC, as shown by cell viability assay. Chemotherapy doses (7.5/15 nM Doxorubicin for CAL-51 DoxoR and 200/400 nM for MDA-MB-231 DoxoR) were given on the X axis. Inhibitor doses were provided below the figures, next to the inhibitor name (*$p < 0.05$; **$p < 0.01$; ***$p < 0.001$; ns, not significant). Blue: vehicle, red: inhibitor, green: chemotherapy, purple: combination.

I examined the potential of all 4 inhibitors in overcoming de novo doxorubicin resistance in HCC143 cells. The de novo resistance model was more similar to the 231 DoxoR models in terms of drug response and had an overall synergistic response pattern. The results were reproducible by multiple experiments such as cell viability assay **(Figure 3.75)**, microscopy **(Figure 3.76)** and Annexin V/PI staining **(Figure 3.77)**.

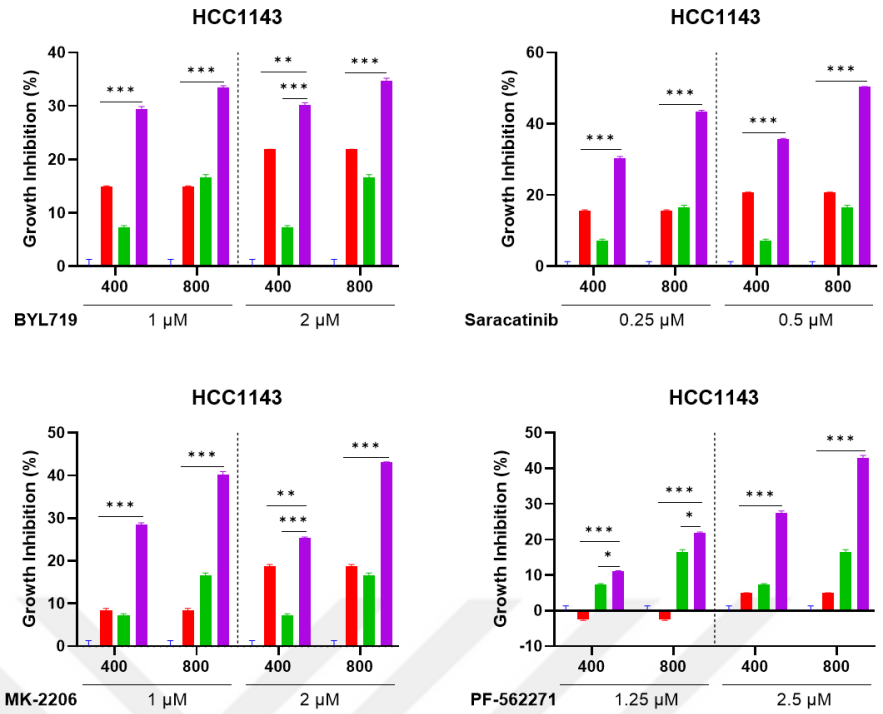
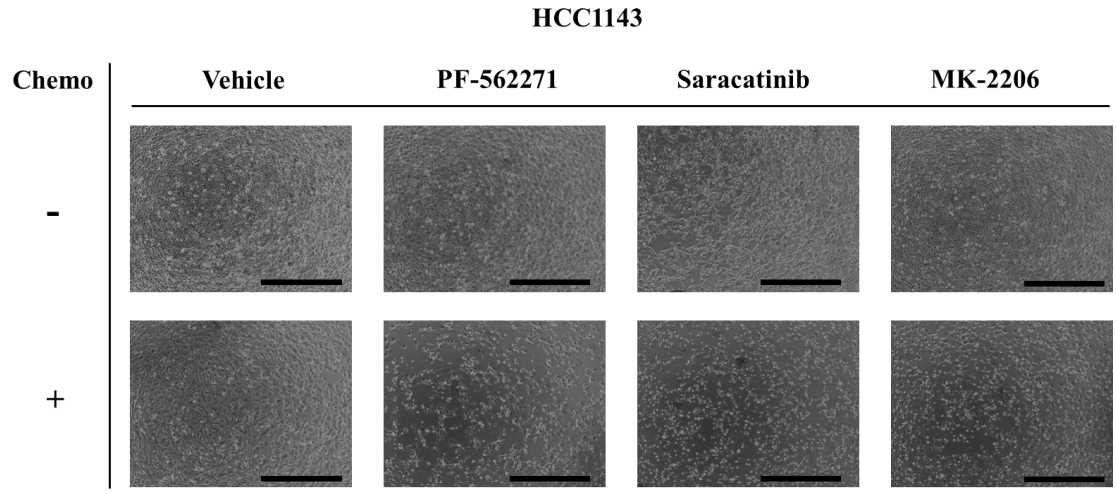


Figure 3.75. The effect of SRC, FAK, PI3K and AKT inhibitors in de novo doxorubicin resistance in TNBC, as shown by cell viability assay. Chemotherapy doses (400/800 nM) were given on the X axis. Inhibitor doses were provided below the figures, next to the inhibitor name (*$p < 0.05$; **$p < 0.01$; ***$p < 0.001$; ns, not significant). Blue: vehicle, red: inhibitor, green: chemotherapy, purple: combination.

A



B

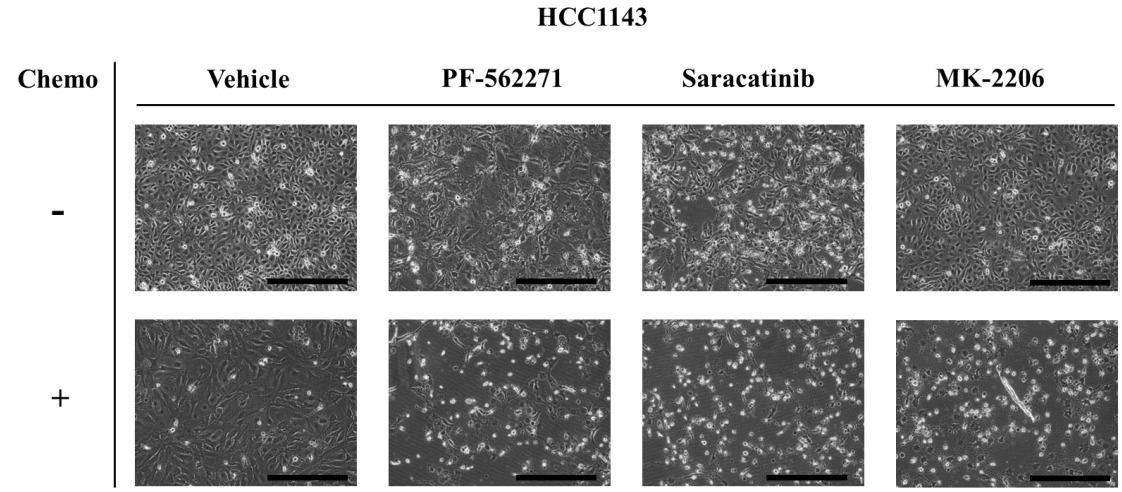


Figure 3.76. FAK, SRC and AKT inhibitors could reverse de novo doxorubicin resistance in TNBC, as shown by microscopy. A) 4X images were provided to show relative cell proliferation and viability (Scale bar: 1000 µm), and B) 10X images were given to show overall morphology of the cells (Scale bar: 400 µm). Phase-contrast images were taken at Evos FL Auto. Chemotherapy status was provided on the left side whereas the inhibitors were present as single agent (top) or in combination with chemotherapy (bottom).

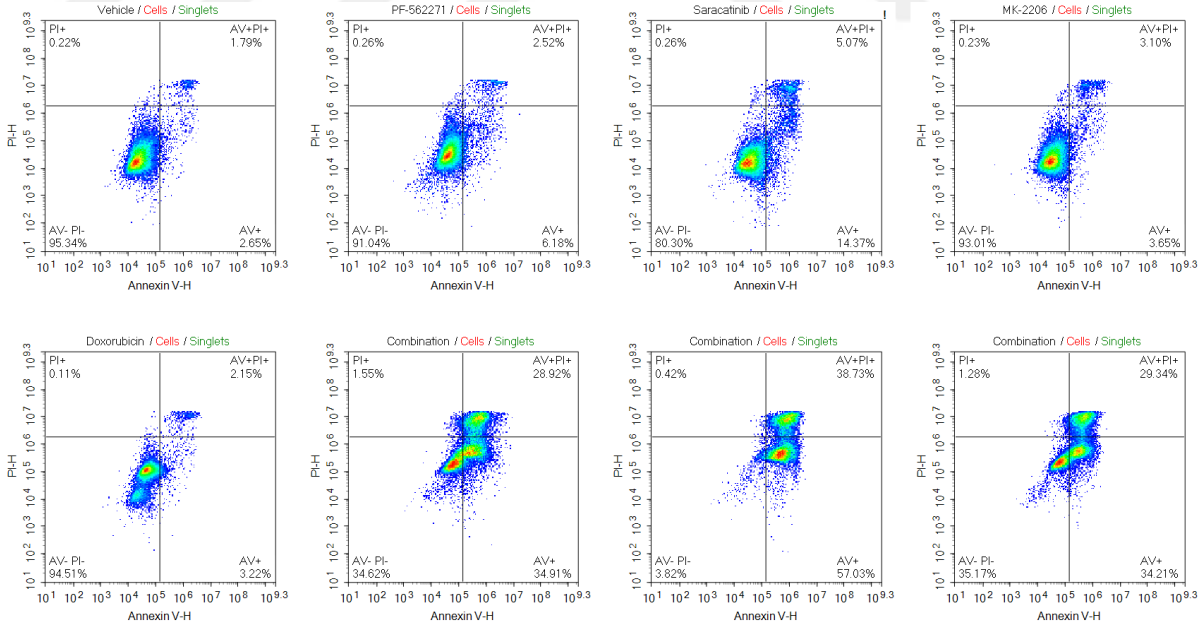


Figure 3.77. FAK, SRC and AKT inhibitors could counteract de novo doxorubicin resistance, as shown by Annexin V/PI staining via flow cytometry. Vehicle (top left), Chemotherapy (doxorubicin, bottom left), PF-562271 alone or in combination (top or bottom), Saracatinib alone or in combination (top or bottom), and MK-2206 (top or bottom).

Following the characterization of acquired and de novo resistance in the cell line models, I tried to establish in vivo models of acquired resistance using 2 different cell lines. In our previous publication (136), we reported the development of these models in MDA-MB-231LG cells using a weekly 5 mg/kg doxorubicin i.v. injection., In this case, I used 2.5 mg/kg doxorubicin dose but here it remained suboptimal to ensure that tumors initially respond and then develop insensitivity to the drug **(Figure 3.78)**. In terms of development pattern, CAL-51 model was more representative model and I therefore used only this model for further analysis **(Figure 3.79)**.

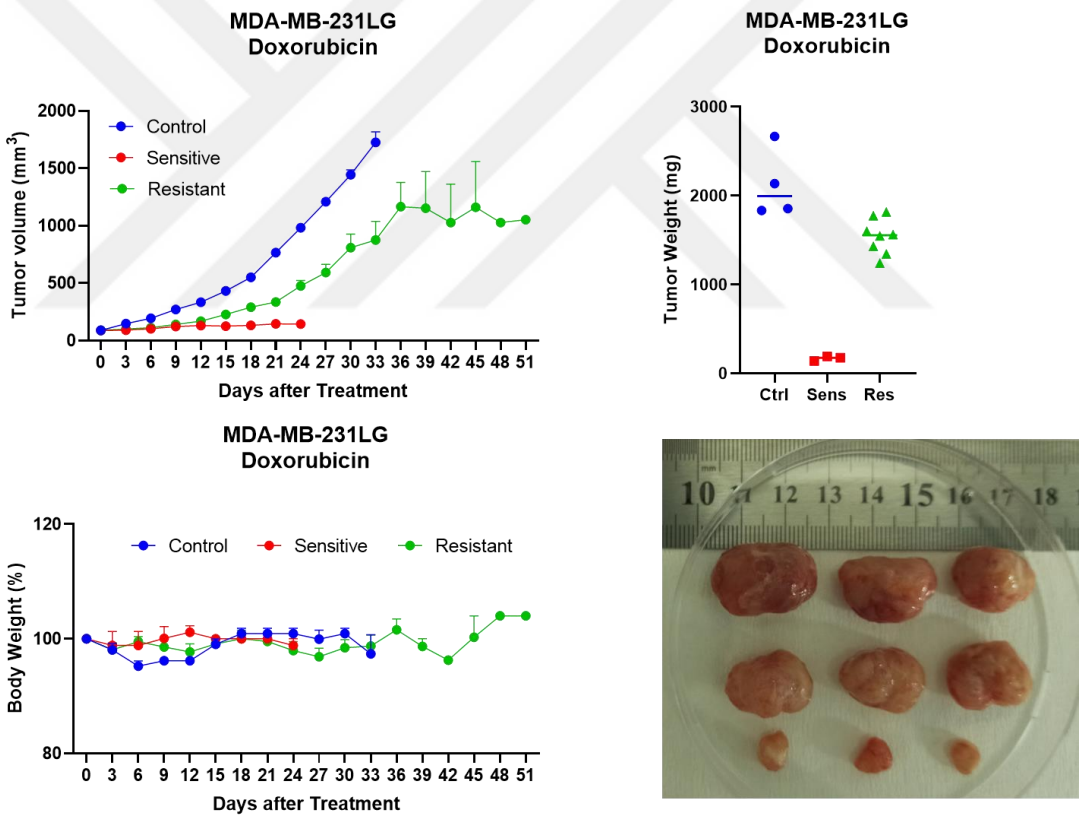


Figure 3.78. Development of in vivo doxorubicin-resistant xenografts using MDA-MB-231LG cells.

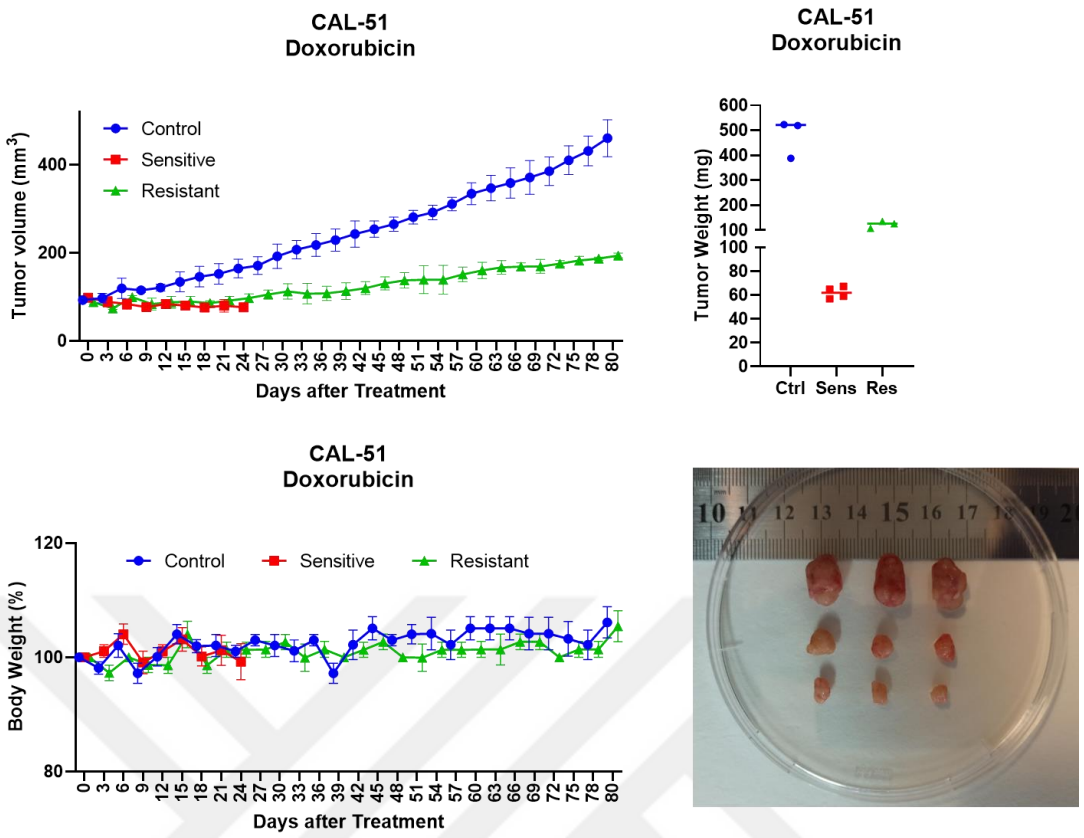


Figure 3.79. Development of in vivo doxorubicin-resistant xenografts using CAL-51 cells.

Compared to its cell line model, CAL-51 DoxoR xenografts showed half opposing half overlapping phenotype for all the pathways tested **(Figure 3.71, Figure 3.72 and Figure 3.80)**.

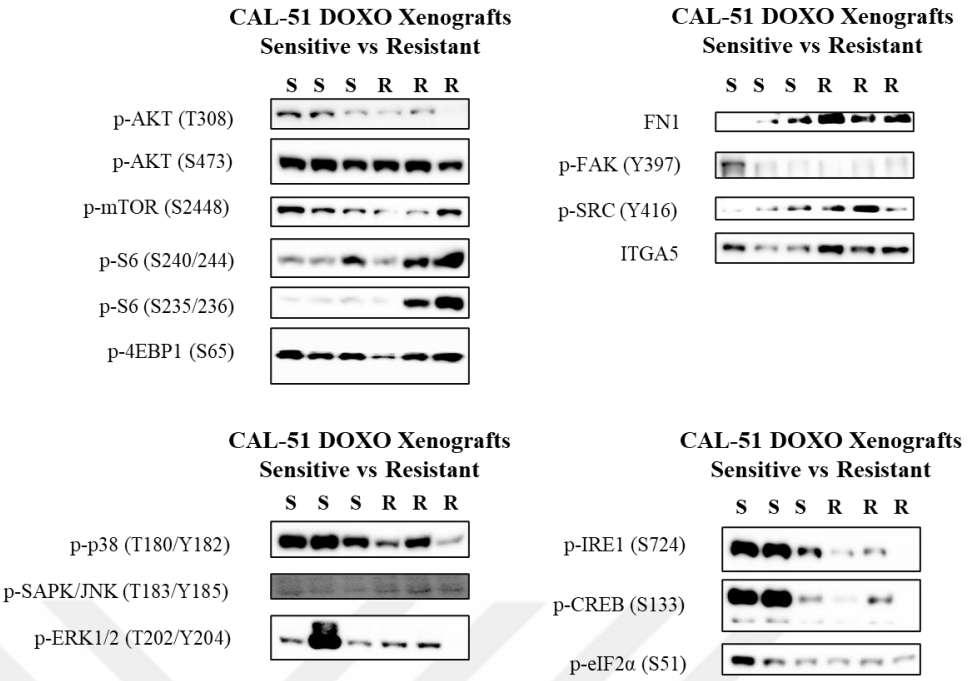


Figure 3.80. Characterization of in vivo doxorubicin-resistant CAL-51 xenografts at protein level.

Unlike the previous chemotherapy agents, the normal breast epithelial cells were highly responsive to doxorubicin treatment, especially MCF10A **(Figure 3.81)**.

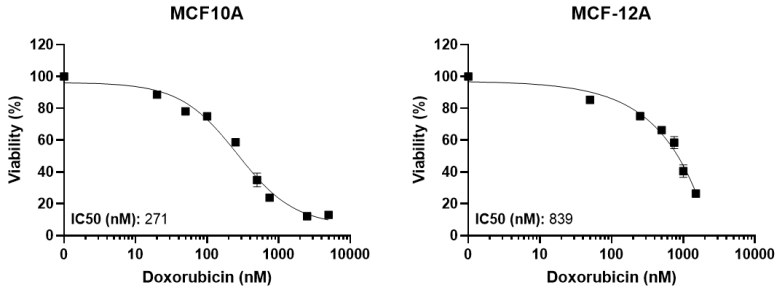


Figure 3.81. The response of normal breast epithelial cells to doxorubicin.

Finally, I have evaluated the cross resistance of CAL-51 DoxoR model to another topoisomerase inhibitor, Irinotecan and to other classes of chemotherapy drugs. Although it would be more ideal to test etoposide (topoisomerase II inhibitor) instead

of irinotecan but I did not have any etoposide left at the time these cells were ready. Still, they showed a tendency towards irinotecan and also partial or high degree of cross-resistance to other agents **(Figure 3.82 and Figure 3.83)**.

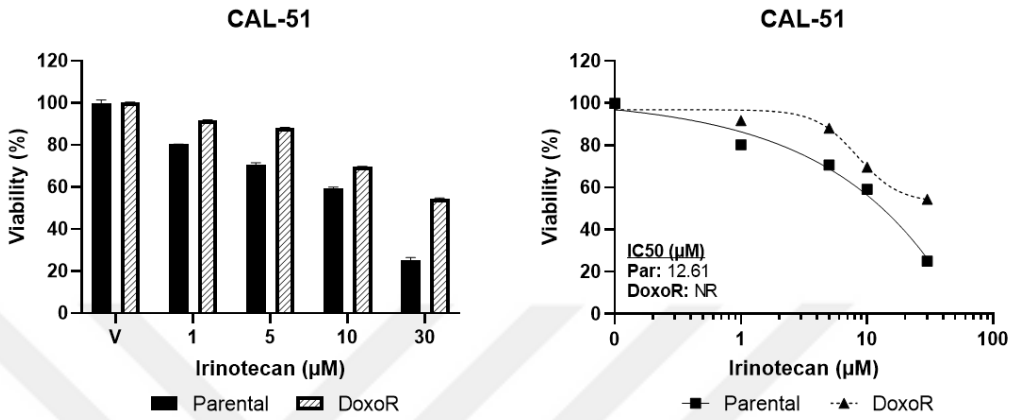


Figure 3.82. Cross chemotherapy response of the CAL-51 DoxoR model to Irinotecan.

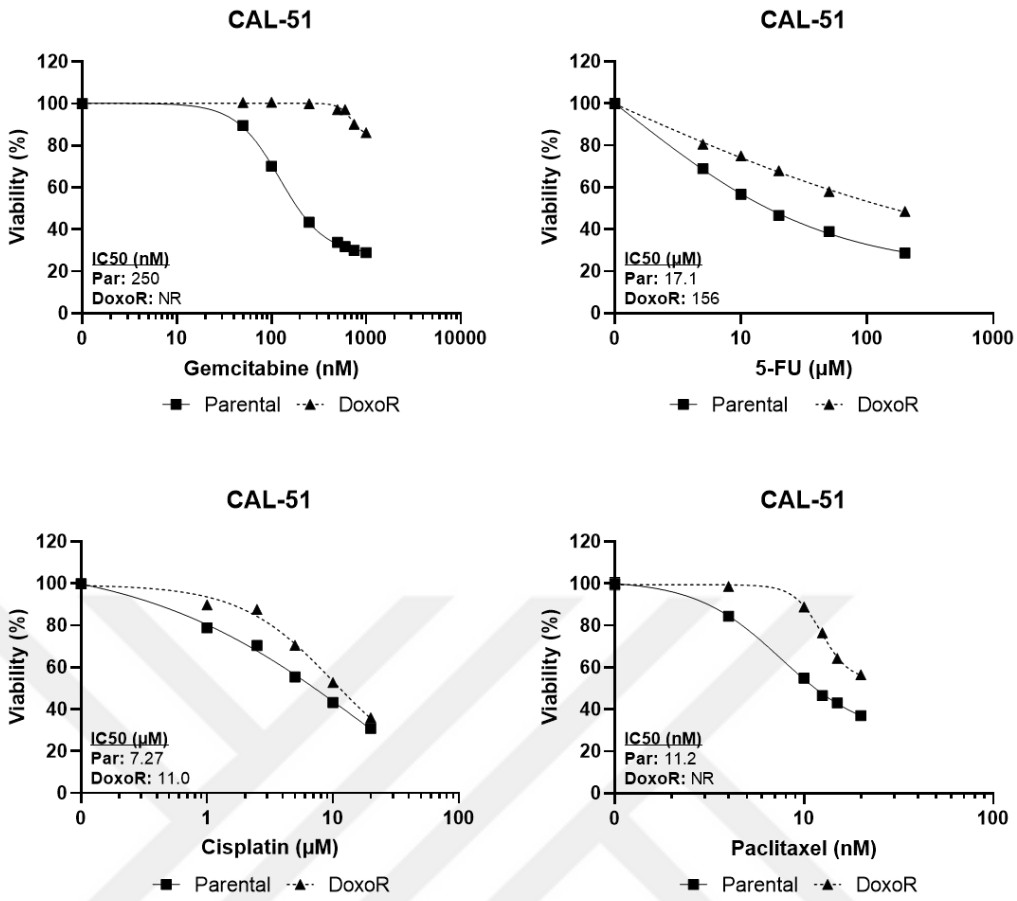


Figure 3.83. Cross chemotherapy response of the CAL-51 DoxoR model to other chemotherapy classes.

PART II

3.5 HIF1-alpha/miR-326/ITGA5 axis in TNBC Doxorubicin Resistance

In this project, we aim to identify the drivers of chemotherapy resistance by generating in vivo doxorubicin resistance model and by RNA/small RNA-sequencing of the resistant and sensitive tumors. Mice were treated intravenously by 5 mg/kg doxorubicin once a week and their volumes were monitored regularly by caliper measurement. After 2-3 months of treatment, the tumors in the treatment arm were divided into 2 separate groups. The sensitive tumors were collected but the ones in the resistant arm continue to receive weekly doxorubicin. After 4-5 months, they were also collected once they lost their chemoresponse and grow despite the treatment. Later total RNA was isolated from the tumors and sequencing was performed to deduce an mRNA and miRNA network governing chemoresistance, of which some components were later functionally tested and validated by multiple approaches, as summarized in **Figure 3.84.** Project outline and analysis pipeline to find potential chemoresistance drivers in TNBC.

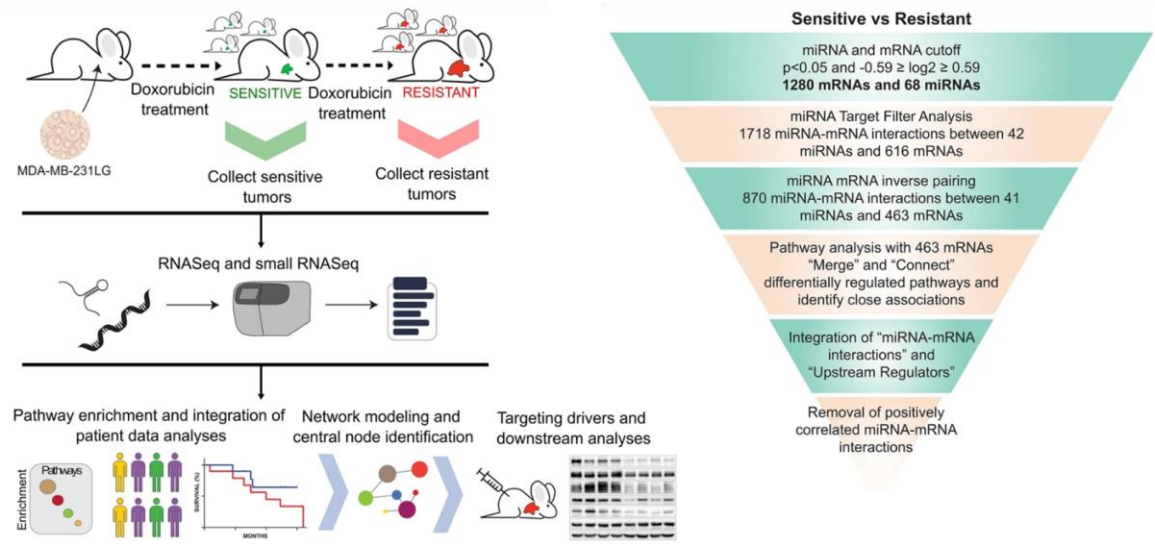
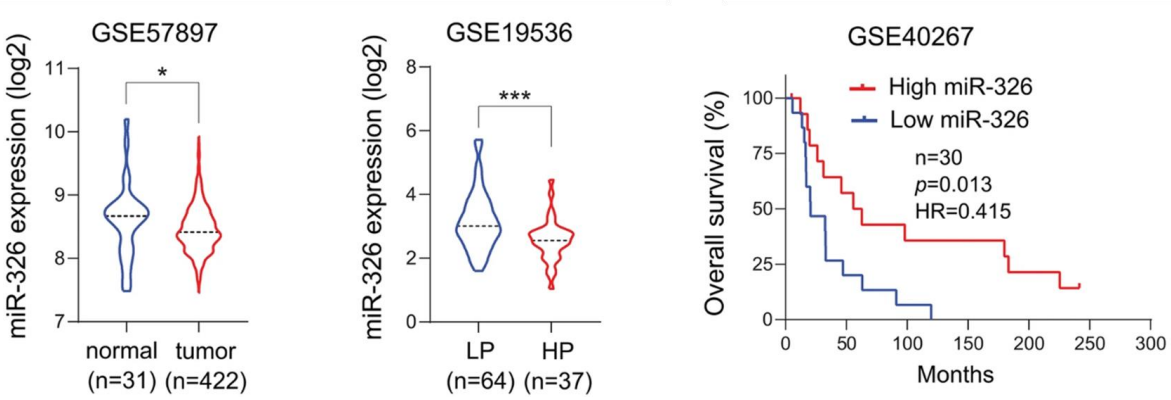


Figure 3.84. Project outline and analysis pipeline to find potential chemoresistance drivers in TNBC.

Upon a stringent bioinformatic pipeline, whereby we integrate differential expression, inverse pairing of mRNA-miRNA pairs, upstream regulators and patient survival data, we selected ITGA5-miR-326 as the most promising pair. I later tested the clinical relevance of miR-326 expression in breast cancer patients as it was downregulated in our chemoresistant xenografts, potentially implying a tumor suppressor role. In line with this, miR-326 had a lower expression in tumors compared to the normal tissue as well as lower expression in tumors with high proliferation rate **(Figure 3.85, top left and middle)**. Low miR-326 alone or high miR-326 target score was able to predict worse overall survival in the TNBC patients **(Figure 3.85, top right and bottom panel)**.

A



B

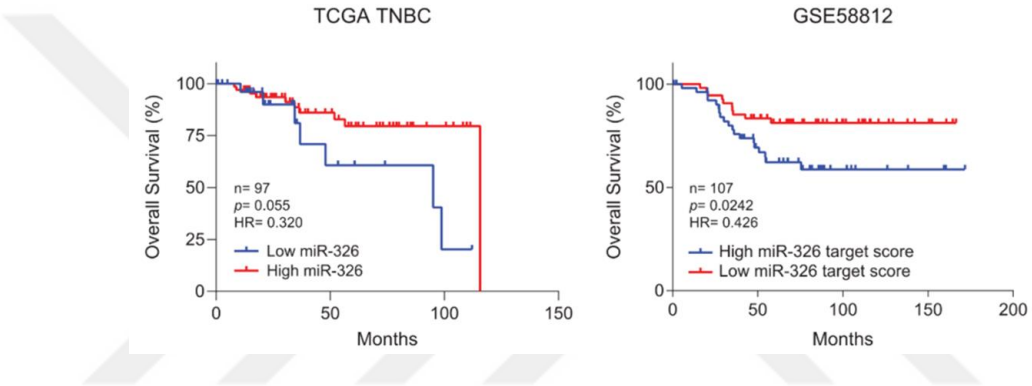


Figure 3.85. Expression of miR-326 in TNBC patients and correlation of miR-326 or its target score with survival.

I later confirmed that miR-326 targets *ITGA5*, which is conserved in multiple species, by utilizing multiple miRNA target prediction tools **(Figure 3.86, top panel)**. Subsequently, I experimentally verified in 2 different TNBC cell lines that miR-326 could potently reduce protein levels of ITGA5 **(Figure 3.86, bottom left)**. We also generated MDA-MB-231.shITGA5 cells that inducibly express shITGA5 and decrease ITGA5 at protein level **(Figure 3.86, bottom right)**.

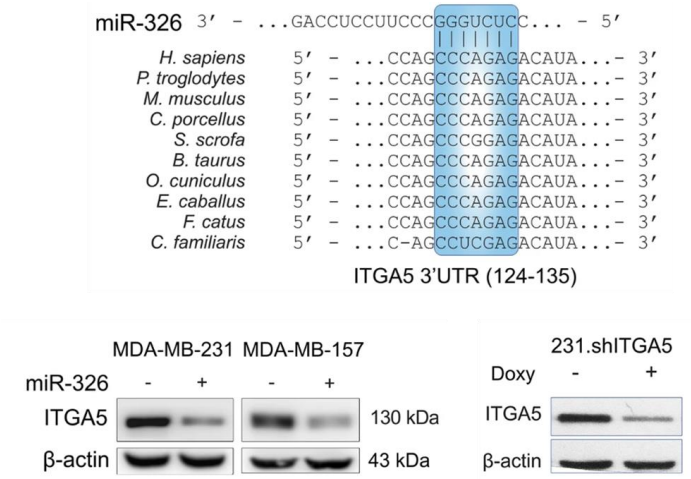
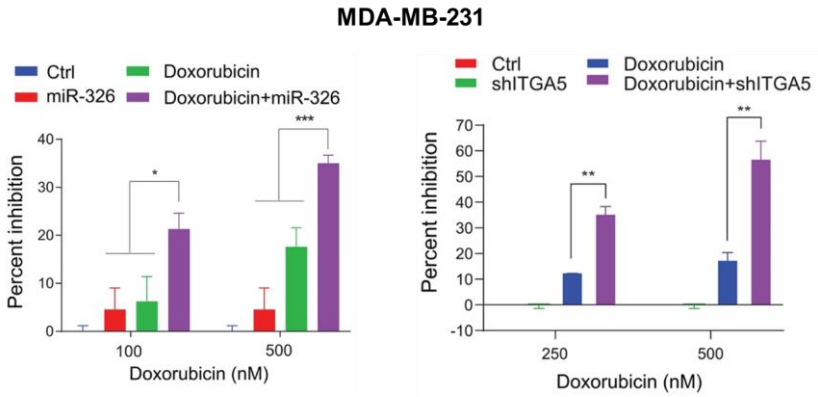


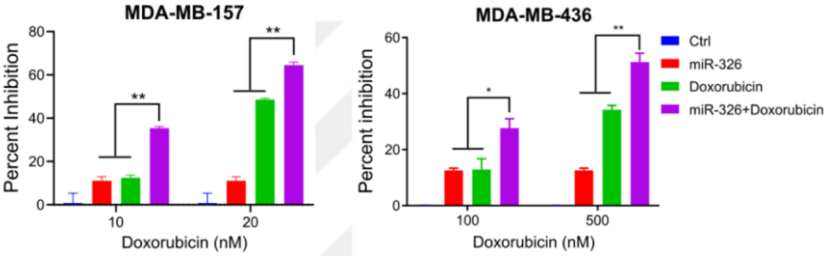
Figure 3.86. miR-326 has a conserved target site in ITGA5 and could downregulate ITGA5 at protein level.

I then tested if miR-326 mimic transfection or induction of shITGA5 when combined with different chemotherapy agents could potentiate chemoresponse of different TNBC cell lines. Starting with doxorubicin, we showed that miR-326 overexpression and I showed that ITGA5 knockdown by shITGA5 enhances the response in a synergistic manner in MDA-MB-231 cells **(Figure 3.87 A)**. I also confirmed it in MDA-MB-157 and MDA-MB-436 cells when miR-326 and doxorubicin was combined **(Figure 3.87 B)**. This observation was not limited to doxorubicin as I revealed that miR-326 could also augment paclitaxel response to a great extent in multiple TNBC cell lines **(Figure 3.87 C)**.

A



B



C

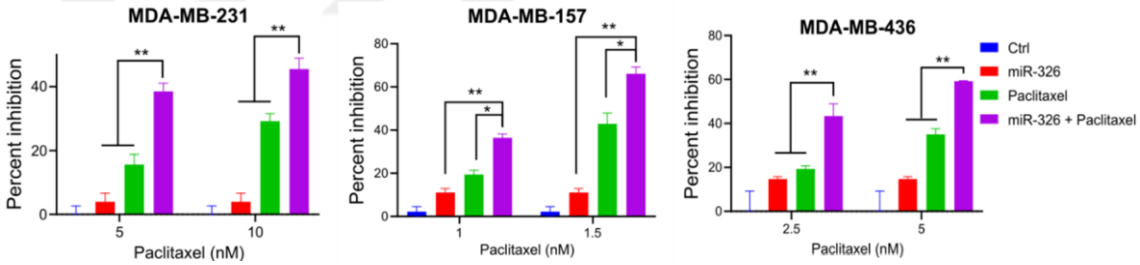


Figure 3.87. miR-326 or shITGA5 could potentiate chemotherapy response in TNBC.

Afterwards, I examined the effect of miR-326 overexpression or *ITGA5* knockdown on the integrin signaling and its downstream components. Both resulted in a highly correlated phenotype showing reduced integrin signaling activity **(Figure 3.88)**.

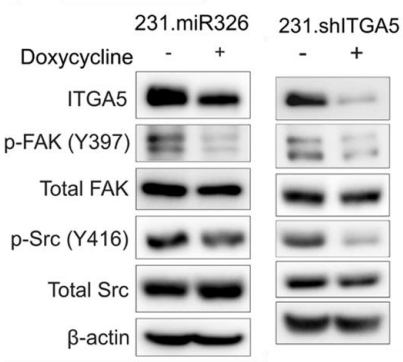


Figure 3.88. Both miR-326 expression and ITGA5 knockdown could impair integrin signaling in vitro.

We used these inducible cell line models to evaluate chemotherapy response in vivo as well. Compared to the single-agent arms, combination group exhibited a dramatically reduced tumor growth rate and volume *(data not shown)*. When I characterized these xenografts at protein level by Western blot, I made a similar observation to in vitro and found that integrin signaling was hindered by miR-326 overexpression or *ITGA5* knockdown **(Figure 3.89)**.

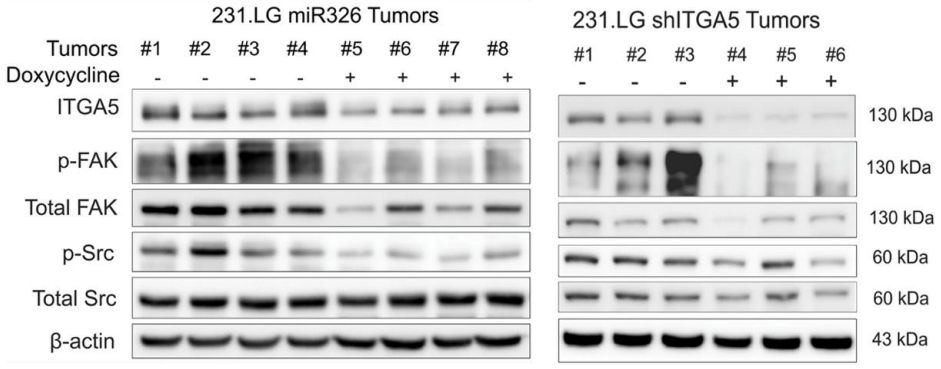


Figure 3.89. Both miR-326 expression and ITGA5 knockdown could impair integrin signaling in vivo.

In our network, *HIF1A* was shown to negatively regulates miR-326. As we have previously reported that HIF1A was important for chemoresistance in TNBC through actions of LOX and integrin signaling, we tested if it was functionally related to miR-326 in this context. In accordance with the network, there was a negative correlation between miR-326 vs *HIF1A* expression or hypoxia score in the TNBC patients, as my analyses have shown. We later validated by ChIP that HIF1A displays an enriched binding to hypoxia response elements at promoter of the host gene, *ARRB1*, of miR-326 **(Figure 3.90)**, where I annotated the HRE/HAS motifs and designed the ChIP primers.

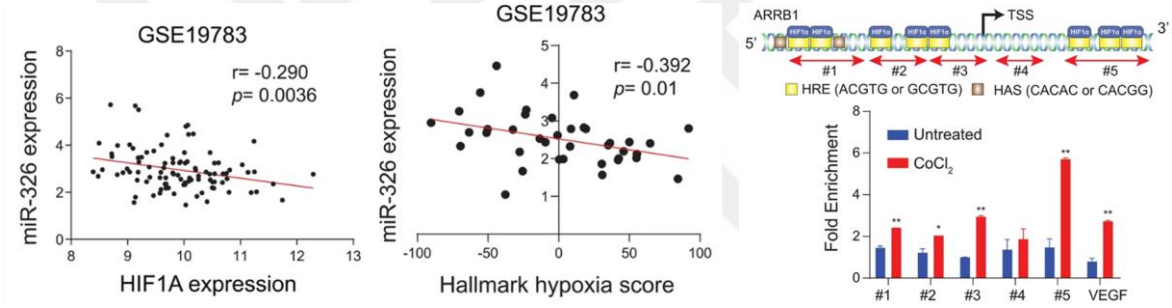


Figure 3.90. HIF1A could downregulate miR-326 and thus contributes to chemoresistance.

Our findings were summarized below in our graphical abstract, showing how each component functionally contributes to the development of doxorubicin resistance **(Figure 3.91)**.

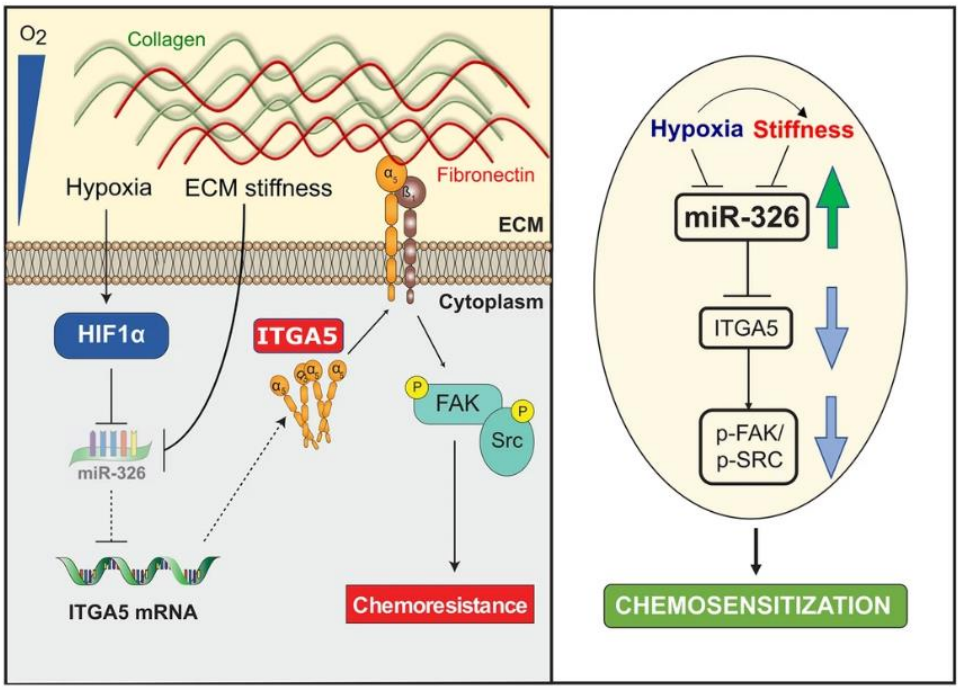


Figure 3.91. Doxorubicin resistance is driven by integrin signaling and hypoxia via blocking of the tumor suppressor miR-326.

3.6 Overcoming Tamoxifen Resistance in ER-Positive Breast Cancer by PDE4D Inhibition

In another project, I contributed to the identification of candidate genes mediating tamoxifen resistance in a cell line model of ER+ breast cancer. We started with the development of the resistant cells by chronic exposure to tamoxifen over a long period of time. Subsequently, total RNA from the parental and resistant cells were quantified in triplicates via RNA-sequencing. By integrating differential expression, pathway enrichment and patient survival data, we identified *PDE4D* as the candidate gene controlling endocrine resistance through cAMP signaling **(Figure 3.92)**.

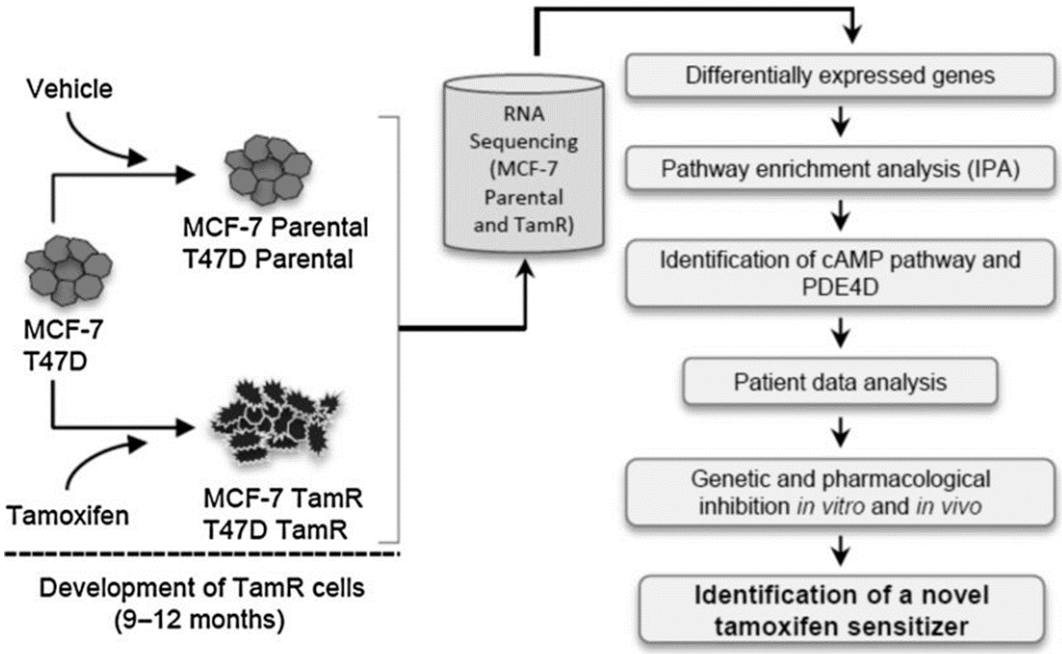


Figure 3.92. Project pipeline summarizing identification and validation of genes/processes driving tamoxifen resistance.

Although we identified PDE4D as the candidate gene, it has multiple mRNA and protein isoforms, making it hard to precisely assess the role of PDE4D. To alleviate this issue, I performed isoform-aware RNA-seq analysis to determine major mRNA

isoforms thus their protein products and later helped isoform-specific design of experimental materials such as primers. Accordingly, we could verify the upregulation of PDE4D at both mRNA and protein levels in 2 different tamoxifen-resistant cell line models **(Figure 3.93)**.

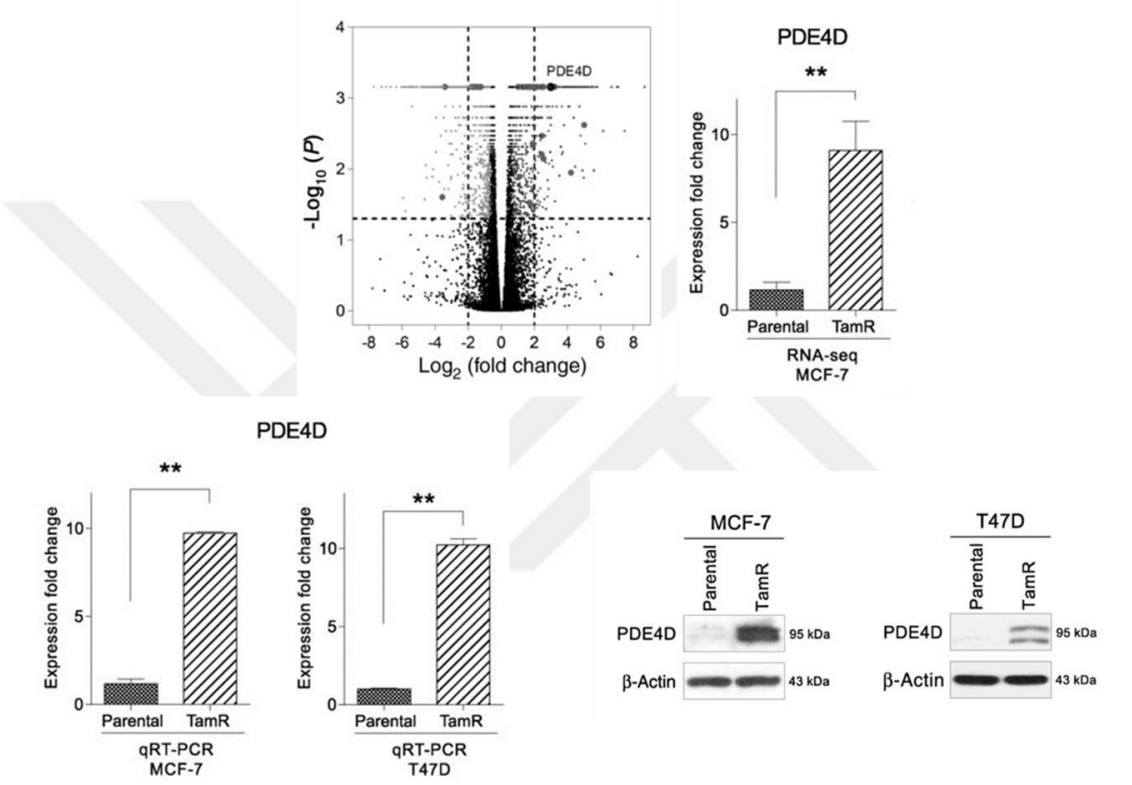


Figure 3.93. Validation of PDE4D upregulation upon tamoxifen resistance at mRNA and protein levels.

We summarized our findings in the graphical abstract below **(Figure 3.94)**. Briefly, genetic and pharmacological inhibition of PDE4D reverses resistance phenotype and this takes place via cAMP-mediated induction of ER stress followed by activation of p38/JNK and then apoptosis.

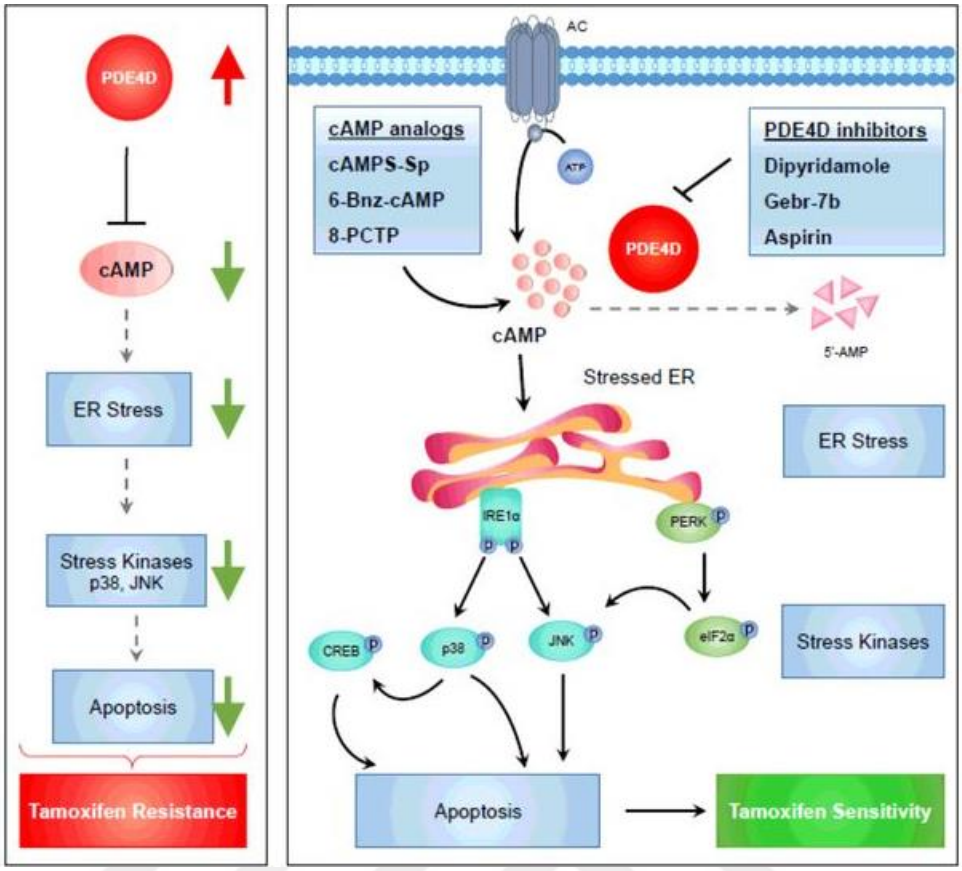


Figure 3.94. Tamoxifen resistance is driven by PDE4D through downregulation of cAMP and downstream ER stress-p38/JNK signaling.

CHAPTER 4

DISCUSSION

4.1 TNBC Heterogeneity and Chemotherapy Resistance

Chemotherapy agents are ubiquitously used medications to treat a great variety of neoplastic disease. Although targeted therapies and more recently immunotherapies have offered alternative approaches to clinical practice, their utility was mostly restrained by their cost, their eligibility to small groups of patients or diseases, higher rates of adverse events and inevitable presence or development of drug resistance. Therefore, chemotherapeutics is here to stay at least to avoid disease progression owing to their relatively lower cost and higher accessibility (182) even when long-pledged personalized treatment becomes reality.

Chemotherapy is a kind of systemic therapy with little-to-none cell specificity but patients show substantial differences in their response to different classes of chemotherapy agents. There could be various underlying cancer-, patient- and/or tumor-specific reasons for this as each tumor is a collection of unique entities represented by a wide spectrum of oncogenic and/or tumor suppressor alterations. Remarkably, the average number of driver events per tumor changes (from 1 to 24) by cancer type, cancer stage and with age (183). For example, while the number of driver mutation events per tumor is 3.52 ± 0.6 in one group of melanoma, the other can be driven only by 0.75 ± 0.45 driver (184). In TNBC, the most common alteration is by far the mutations in *TP53* gene followed by *PIK3CA*, *USH2A*, *MYO3A*, *PTEN* and *RB* when mutations in each gene were analyzed independent of each other and

their functional consequences (185). Similarly, the enriched pathways underline the importance of p53-related pathways together with PIK3, ERBB, and WNT/cadherin signaling, integrin signaling and focal adhesion, chromatin remodeling, and ATM/RB-related pathways. When mutations and copy number alterations were evaluated by integrating their association with extreme expression changes, a common set of genes is clearly distinguished. Nonetheless, the identified driver alterations show a heterogeneous distribution even in TNBC subtype of the breast cancer. It is, therefore, required to categorize the patients further into subtypes to guide better selection of the treatment options. In line with this, multiple approaches have been proposed for TNBC classification. Although it started with histological classifications that offer little insight into the treatment of choice, transcriptomic and mutational profiling of the patient samples could spark the next revolution in the clinical cancer management. However, the aim should not only be delineating the potential drivers but also assessing their actionability in clinical practice as many proteins are still deemed undruggable. Although many biotechnological advances such as CRISPR, PROTACs and molecular glues improved our arsenal against cancer, their practical applications are still at infancy. Briefly, combinations of low-dose chemotherapy and small molecule inhibitors or antibodies (targeted therapy) are currently our best bet in fight against the cancer. Therefore, I focused on combining available inhibitors with chemotherapy to overcome chemoresistance in de novo and acquired chemotherapy resistant models.

4.2 Mechanisms of Resistance to Antimetabolites in TNBC

One approach to model and study chemoresistance is to utilize cell line panels and develop in vitro acquired cell line models, thereby reflecting patient and response heterogeneity (186-190). Gemcitabine and fluorouracil, although included in different regimens, are under-studied in TNBC. Therefore, the first models in this study were designed to mimic gemcitabine and fluorouracil resistance **(Figure 3.5)**. Both agents belong to antimetabolite class of chemotherapy drugs. In line with this, the GemR model was also resistant to 5-FU and the FUR model to gemcitabine as well **(Figure 3.25)**. More importantly, characterization at protein level by extensive Western blotting demonstrated that there is a high concordance between gemcitabine and 5-FU resistance profiles **(Figure 3.6, Figure 3.7 and Figure 3.8)**, implicating potentially converging driver events leading to resistance.

Inhibitors against PI3K or AKT, MAP kinases p38 and JNK, and ER stress inducers have shown promise to counteract both de novo and acquired resistance to both chemotherapy agents. Previously, it has been reported in MDA-MB-231 gemcitabine-resistant breast cancer models that LY294002, a PI3K inhibitor and rapamycin, an mTOR inhibitor could potentiate gemcitabine response. Compared to my CAL-51 GemR model, only p-AKT changes shows consistent upregulation but not p-mTOR, p-p38 and p-ERK1/2. Additionally in the CAL-51 resistance models, the negative regulator of the PI3K/AKT pathway, FOXO3 had higher levels of phosphorylation, resulting in its inactivation **(Figure 3.6)**. In line with these, there are several studies reporting the potential involvement of these proteins in gemcitabine or fluorouracil resistance in various types of cancer. For example, elevated p-AKT levels was shown to trigger gemcitabine resistance in pancreas cancer models (191). In

cholangiocarcinoma, LINC01714 was shown to enhance gemcitabine sensitivity by modulating FOXO3 phosphorylation (192). In neuroblastoma, *FOXO3* expression was decreased in aggressive late-stage tumors compared to low-stage tumors and normal neuroblasts (193). Expectedly, apoptosis induced by PI3K/mTOR, PI-103 or AKT inhibitor, MK-2206 was potentiated by FOXO3a overexpression. Accordingly, phosphorylated FOXO3a level was also correlated closely with apoptotic sensitivity to MK-2206. CAL-51 is a *PIK3CA*-mutant cell line but BYL719 response upon chemotherapy combination was less promising than MK-2206 and BKM120. Although it may be due to the fact that selected doses may be out of the synergistic range and could be optimized on a per cell line basis, there could be other factors rendering PI3Kα inhibitors less potent. In 2 different studies, it was found that mTORC1 inhibition is required for sensitivity to PI3K p110α inhibitors in *PIK3CA*-mutant breast cancer and *PIK3CA* mutations enable targeting of breast cancer growth through mTOR-mediated mechanisms (194, 195). Therefore, adding an mTOR inhibitor could augment BYL719-antimetabolite chemotherapy combination response although major components of mTOR pathway remained unchanged or even downregulated in CAL-51 GemR and FUR models. The mechanisms through which PI3K/AKT and mTOR inhibitor reverse antimetabolite resistance involve the upregulation of drug efflux transporters (196), inhibition of aerobic glycolysis by modulation of multiple metabolites (197), HIF-1α-induced metabolic reprogramming (198), and enhanced ribonucleotide reductase activity for efficient DNA replication (199).

In contrary to my TNBC models showing dose-dependent synergism of gemcitabine and MAP kinase inhibitors **(Figure 3.9)**, gemcitabine-induced apoptosis is mediated

by p38 and p38 inhibitor, SB203580 but not JNK inhibitor, SP600125 impairs apoptosis in pancreas cancer (200). In urothelial carcinoma, the gemcitabine resistant clones exhibited lower p38 and ERK MAPK activities, and p38 inhibitor, SB203580 specifically promoted the survival of the cells in the presence of gemcitabine (201). In another study, however, it was reported that JNK inhibition effectively sensitizes otherwise chemoresistant pancreatic cancer stem cells to 5-FU and GEM (202). Similarly, it was found that activated JNK/ABCG2 pathway induces chemoresistance to fluorouracil in colorectal cancer cells (203). Therefore, there could be an alternate mechanism explaining the potential role switch of MAP kinases in my case. It has been shown that MAP kinases can have dichotomous function in a context-dependent manner. They could function as a tumor suppressor in normal cells and during the initial phase of oncogenic transformation by controlling cell cycle, senescence, apoptosis and differentiation (204-206). Nevertheless, from the early stage to late-stage evolution of the tumors, they could exert tumor-promoting processes such as migration and invasion, angiogenesis, resistance to anti-cancer drugs and diminished immune activity. Furthermore, p38 can regulate AKT at both transcriptional and protein level (207). Similarly, JNK and STAT3 signaling cascade could also converge on AKT (208-210), which have been linked to chemotherapy and inhibitor resistance (170, 202, 211). Considering that MAP kinases have also play extensive roles in ER stress, they could be connecting nexus between PI3K/AKT signaling and ER stress (212, 213). Mechanistically, the resistance to gemcitabine and fluorouracil could be also driven by oncogene- or -treatment-induced senescence, in which interplay between MAPK and PI3K/AKT/mTOR pathways play a major role (214, 215). In addition, this could be supported by the consistent increase of p21, one of the most well-known marker of senescence together with p16, in my models **(Figure 3.8)**. In

short, it is evident that gemcitabine resistance profile differs dramatically by cancer type. As a result, the common mechanism ostensibly mediated by PI3K/AKT but not mTOR could be exploited to abrogate resistance in different contexts including breast cancer (216, 217).

In terms of their cross-chemotherapy resistance patterns, the cell line and/or tumor models exhibit a heterogeneous pattern as expected. For example, MDA-MB-231 FUR cells was characterized by resistance to not only 5-FU, but also gemcitabine, vinorelbine, and paclitaxel (218). Similarly, Chen et al. showed that gemcitabine-resistant pancreas cancer cells exhibit a multidrug resistance phenotype against paclitaxel (219). In another study, 6 gemcitabine-resistant and 4 highly resistant subclones of pancreatic cancer cell lines did not develop a specific pattern of cross-resistance to cisplatin, irinotecan and docetaxel except that all highly resistant clones showed cross-resistance with 5-FU (220). Similarly, my CAL-51 GemR and FUR models were resistant to the other antimetabolite as well.

CAL-51 GemR cells also showed cross resistance to a broad range of chemotherapy agents including paclitaxel unlike the CAL-51 FUR cells with cross resistance to only gemcitabine **(Figure 3.25 and Figure 3.26)**. In an ovarian cancer cell line model, however, the gemcitabine-resistant cells were found to be significantly more resistant to vincristine, paclitaxel, docetaxel, etoposide and irinotecan but not to 5-FU, doxorubicin and cisplatin (221). In contrast, a large-scale study done in primary cultures of solid or hematologic tumors revealed that gemcitabine was mainly effective in hematologic tumors and in a subset of solid tumors, and these tumors showed cross-resistance to primarily doxorubicin but not to cisplatin and etoposide

(222). Briefly, it is much more complex to estimate cross-resistance than anticipated given the opposing results obtained in different cell line or xenograft models.

4.3 Mechanisms of Resistance to Plant Alkaloids in TNBC

Paclitaxel is one of the essential chemotherapy agents for the treatment of TNBC patients, where it can be utilized alone or in combination with diverse chemotherapy agents such as doxorubicin and carboplatin. Although relatively higher efficacy of docetaxel compared to paclitaxel in some clinical trials overshadowed its enormous success, nanoparticle albumin-bound paclitaxel (nab-paclitaxel) is currently and widely considered the best-in-class. In this study, I developed 2 cell line and 1 in vivo models of acquired paclitaxel resistance in TNBC **(Figure 3.29 and Figure 3.48)**. These 3 models represent all the categorical differences between TNBC cell lines, such as PAM50 basal vs non-basal, transcriptomic classifications by refined Lehmann and Burstein as well as metabolic pathway-based subtyping. In these models, I have discovered potential actionable targets such as SRC, EGFR and CDK1. Recently, Song et al. (GSE199779) reported a synthetic lethality between afatinib (irreversible ErbB family inhibitor) and paclitaxel in MDA-MB-231 cells. Here, in a different model, we showed that both EGFR (gefitinib) or dual EGFR/HER2 (lapatinib) as well as SRC inhibitor (Saracatinib) exhibited an enormous synergistic response upon paclitaxel combination **(Figure 3.34 and Figure 3.35)**. The effect was so pronounced that inhibitor or chemotherapy doses inhibiting less than 5-15% cell growth caused up to 90% inhibition. Therefore, I speculate that neither of the single agents would probably create intolerable toxicity at the clinically equivalent doses. In another study, Canonici et al. utilized afatinib-resistant, HCC1937 and afatinib-sensitive, HDQP1

TNBC cell lines to test afatinib and dasatinib (SRC/ABL inhibitor) combination response (223). While the individual agents blocked cell growth by approximately 30 and 55%, respectively, the combination resulted in 70% inhibition in the afatinib-resistant model. The inhibition rates were 50% and 80% for the single agents whereas it was more than 90% in the combination treatment in the sensitive cells. However, when afatinib with paclitaxel were investigated in neoadjuvant setting, the combination produced a modest effect and the nonresponsive patients had augmented PI3K and JAK2 pathways in addition to mutations in homologous recombination genes (224). Hence, alternative approaches utilizing different EGFR inhibitors with taxanes or other inhibitors should be tested to evaluate if the clinical efficacy could be improved. For example, co-targeting EGFR and mTOR with gefitinib and everolimus in TNBC induced synergistic growth inhibition in the *PI3K* and *PTEN*-mutant CAL-51 cell line, but not in the *PTEN*-null HCC-1937 cell line (225). Since CAL-51 PtxR cells have uniform upregulation of total and phospho-levels of mTOR pathway proteins (mTOR, S6, 4EBP1), a triple combination including paclitaxel and inhibitors of EGFR and mTOR even at lower doses could trigger a potent response in my model and maybe in a subgroup of patients with the same mutation profile.

In the paclitaxel-resistant CAL-51 and MDA-MB-157 models, I also found that CDK1 inhibition could dramatically abrogate paclitaxel resistance **(Figure 3.39)**. Importantly, Liu et al. have recently identified CDC25 in a drug screen as a common therapeutic target for TNBC, which activates CDK1 by removing inhibitory phospho-residues. In the same screen, the other 3 most promising candidates included an FAK inhibitor. In line with this, SRC is a substrate for phosphorylation and activated by both epidermal growth factor receptors (may be indirectly through PKC) and CDK1

(226, 227), which in turn can regulate EGFR transactivation (228). CDK1 even functions as the link between cell cycle machinery and the regulation of cell adhesion to the ECM via integrin–receptor adhesion complexes (229). In the same manner, EGFR/SRC-dependent β4 integrin/FAK complex was shown to exacerbate malignancy of breast cancer (230). As a result, this extensive connection and crosstalk from EGFR to SRC and to CDK1 (and vice versa) suggests that EGFR/SRC/CDK1 axis could hold a promising potential to treat taxane-resistant breast cancer patients. For example, combined SRC and EGFR signaling drives resistance to a mitotic inhibitor in glioblastoma (231). In line, reduced activation of SRC/EGFR signaling activation results in cycle arrest and apoptosis in MDA-MB-231 cells (232). However, it should be noted that if not a dual but a triple combination of paclitaxel, EGFR inhibitor and SRC inhibitor is to be utilized, *EGFR* and *RAS* mutational status should be determined since SRC inhibitors act through different mechanisms depending on their mutational status (233).

When assessing the cross-resistance patterns of these models, I found that paclitaxel-resistant CAL-51 cells were also resistant to docetaxel, another taxane chemotherapy **(Figure 3.51)**. However, CAL-51 PtxR and MDA-MB-157 PtxR cells exhibited distinct cross-resistance patterns. While CAL-51 PtxR cells exhibited cross-resistance to gemcitabine and doxorubicin and were more sensitive to cisplatin, 157 PtxR cells were fully resistant to fluorouracil and partially to cisplatin and doxorubicin **(Figure 3.52 and Figure 3.53)**. In the paclitaxel subclones of MDA-MB-231 cells, all except one clone exhibited partial or full cross-resistance to doxorubicin, but not to 5-FU (234). There was a mixed profile for cisplatin with high paclitaxel resistance accompanied by increased cisplatin sensitivity and moderate paclitaxel resistance by

no change or reduced cisplatin response. However, Kenicer et al. found that MDA-MB-231 PtxR cells were not cross-resistant to either anthracyclines or carboplatin, while ER-positive, ZR-75-1 PtxR and DtxR (docetaxel-resistant) cells exhibited cross resistance to anthracyclines (epirubicin and doxorubicin) but not to carboplatin (235). Again, in an ER-positive cell line, MCF-7 PtxR there was an obvious collateral sensitivity to platinum agents, cisplatin and carboplatin (236). Similarly, in small-cell lung cancer models, Jensen et al. reported that taxane-resistant models were highly cross-resistant to topoisomerase II inhibitors but showed collateral sensitivity to cisplatin (53). These are more in line with my findings in the CAL-51 PtxR model. In another study, however, paclitaxel-resistant prostate cancer models were reported to be significantly less responsive to docetaxel, cisplatin and fluorouracil (237). In this case, it is more representative of my findings in the MDA-MB-157 cells. The distinct cross-resistance patterns between the models would be attributed to their differences in TNBC subtyping according to Burstein and refined Lehmann classifications.

4.4 Mechanisms of Resistance to Alkylating Agents in TNBC

Cisplatin is intensely harnessed for neoadjuvant and/or adjuvant treatment of many solid tumors whilst not that frequently in breast cancer (238). Similarly, cisplatin is the most commonly used drug to generate chemoresistant cell line models encompassing multiple cancer origins such as osteosarcoma, hepatocellular carcinoma, colorectal adenocarcinoma, oral carcinoma, and breast, ovarian, lung and gastric cancers (190). While platinum agents have proven effective against these tumors, significant relapse/recurrence and progression rates as well as decreased overall survival are still observed in the clinics. Here we generated 2 acquired cisplatin

resistance models in addition to utilizing 1 intrinsic cisplatin resistance models to explore the potential of multiple inhibitors in reverting the resistance **(Figure 3.56 and Figure 3.55)**. Of these models, while both are *BRCA1*-mutant, MDA-MB-436 belongs to Basal A molecular and immunomodulatory (IM) TNBC subtype, HCC1937 falls under Basal B molecular and basal-like immune suppressed (BLIS) TNBC subtype. Perhaps illustrating their categorical differences, I observed a clear increase in multiple components of the PI3K/AKT/mTOR pathway such as p-AKT (T308), p-mTOR, p-S6 and p-4EBP1 in our HCC1937 CisR model but not in the other one **(Figure 3.57)**. This collective and consistent increase implies the functional importance of the pathway in cisplatin response in a subtype-specific manner. Previously, it has been reported in lung (239) and bladder cancers (240), osteosarcoma (241) and hypopharyngeal squamous cell carcinoma (242) that cisplatin combination with dual PI3K/mTOR inhibitor, BEZ235 could synergistically enhance chemosensitivity in vitro and in vivo models. Consequently, I found that BEZ235 could counteract cisplatin resistance in TNBC as well **(Figure 3.61)**. However, dose selection could be optimized or more inhibitor-chemo dose combinations could be tested for both HCC1937 CisR and MDA-MB-231 de novo model to identify ideal range of synergistic response.

The 436 CisR and 1937 CisR models were more similar in terms of MAPK pathway activity **(Figure 3.58)**. Inhibition of p38 MAPK has been demonstrated to potentiate cisplatin-induced apoptosis in kidney epithelial cells (243), colon cancer and ER-positive breast cancer, in which case it is mediated by JNK and reactive oxygen species (244). My findings also support that it could be a common target in *BRCA1*-mutated TNBC cells to improve chemoresponse rates. However, the most striking

similarity between the models was almost uniform activation of the integrin/FAK signaling components **(Figure 3.58)**. In contrary to the literature that FAK could mediate de novo and acquired cisplatin resistance and that FAK inhibition could partially or fully reverse it (245, 246), FAK inhibitor combined with cisplatin produced at most additive response in my hands although integrin alpha 5 inhibitor has shown promise in high-dose inhibitor combinations in the HCC1937 CisR model **(Figure 3.60)**. This could be explained by suboptimal dose combination selections and/or potentially nominal effect of the integrin pathway components in TNBC cisplatin response.

As for cross chemoresistance, the models again exhibited distinct patterns such that while the HCC1937 CisR cells did not show any apparent cross chemoresistance, the MDA-MB-436 cells were cross resistant to gemcitabine, paclitaxel and doxorubicin to different degrees **(Figure 3.65 and Figure 3.66)**. Similarly, there are reports supporting heterogeneous nature of the cell line or animal models in terms of cross resistance. For example, Hamaguchi et al. reported that a panel of cisplatin-resistant ovarian cancer cell lines displayed cross resistance to carboplatin, etoposide, doxorubicin, paclitaxel and mitoxantrone but not to irradiation (247). Later, Stordal and colleagues have shown that cisplatin-resistant IGROV cells were also resistant to paclitaxel (248). More recently, however, cisplatin-resistant cell line W1 were reported not to exhibit any cross resistance to paclitaxel, doxorubicin, methotrexate, vincristine, and topotecan (249). Therefore, it would be more reasonable to assess cross chemoresistance on a per cell line or possibly per patient basis.

4.5 Mechanisms of Resistance to Anti-tumor Antibiotics in TNBC

Doxorubicin is one of the most widely utilized chemotherapy agents to date, since its FDA approval nearly 50 years ago, despite its cardiotoxic effects at high doses. However, single-agent doxorubicin is so potent, even more potent than single-agent paclitaxel at lower doses (145), that it is included in multiple treatment regimens either alone or as part of a combination. It is also the second most commonly used chemotherapy to generate chemoresistant cancer models after cisplatin (190). We have previously developed in vivo model of acquired doxorubicin resistance in TNBC, culminating in 2 different publications, one of which was summarized in **Results Part II, Section 3.5**. Similarly, in this project, I have created 3 new models (CAL-51 DoxoR cell line and xenograft, and MDA-MB-231 DoxoR cell line) that were not used before **(Figure 3.69, Figure 3.70 and Figure 3.79)**. Of these, CAL-51 is mesenchymal by Burstein and MPS2 by metabolic TNBC classifications while MDA-MB-231 is basal-like immune activated and MPS3, respectively. Unlike the previously published MDA-MB-231-luc2-GFP in vivo doxorubicin resistant model, CAL-51 DoxoR cell line did not show elevated integrin/FAK signaling but even decreased activity while CAL-51 xenograft model had elevated FN1 and p-SRC but decreased p-FAK levels. This could potentially be due to differences in the in vivo vs. in vitro resistance mechanisms. Consequently, FAK and SRC inhibitors could not overcome doxorubicin resistance in the CAL-51 DoxoR cell line model **(Figure 3.73)**. I did not characterize MDA-MB-231 DoxoR cell line model at protein level but it exhibited a synergistic response pattern upon FAK or SRC inhibitor combination with doxorubicin similar to its in vivo counterpart **(Figure 3.73)** (136). De novo doxorubicin resistance model, HCC1143 yielded a similar result **(Figure 3.75)**. In line with this, integrin signaling components were implicated in de novo and acquired

doxorubicin resistance of diverse cancer types such as leukemia (250, 251), bladder cancer (252), laryngeal carcinoma (253), hepatocellular carcinoma (254), and NSCLC (255). The CAL-51 DoxoR cells exhibited a mixed overall phenotype in terms of PI3K/AKT/mTOR activity but a consistent increase in phospho-AKT levels at both residues **(Figure 3.71)**. Of these, increase in nuclear p-AKT (S473) was shown to predict synergy of PI3K inhibition and doxorubicin in ovarian and breast cancers (256). Accordingly, I have tested pan-AKT inhibitor, MK-2206 and PI3Kα-specific inhibitor, BYL719 in combination with doxorubicin in CAL-51, MDA-MB-231 and HCC1143 models. While MK-2206 resulted in promising response rates in all models tested, BYL719 could produce a desired effect only in MDA-MB-231 and HCC1143 **(Figure 3.74 and Figure 3.75)**. MK-2206 has shown to enhance chemosensitivity in multiple cancers such as leukemia (257), and gastric (258), lung and ovarian cancers (259). On the other hand, BYL719 and doxorubicin combination was not studied to the same extent. However, one study reports that their combination causes weight loss, heart atrophy and thus death in female murine models (260). Consequently, this combination could be avoided in TNBC or lower doses could be preferred to alleviate toxicity-related issues. Although I have not tested in my models, there was an increase also in CDK4 levels in the CAL-51 DoxoR cells, and BYL719 and CDK4/6 inhibitor combination demonstrated to trigger synergistic response in TNBC (261).

When I examined the cross-resistance patterns in the CAL-51 DoxoR cells, it was clear that they displayed partial or high degree of resistance to all other 4 chemotherapy agents, most notably to gemcitabine and paclitaxel **(Figure 3.83)**. A study compared multiple doxorubicin-resistant subclones of MDA-MB-231 cells and demonstrated that all subclones were at least 3 or more-fold less responsive to

paclitaxel as well, which was not the case for cisplatin or 5-FU (234). In a clinical trial, it was documented that patients receiving first-line doxorubicin were 4-fold less responsive to paclitaxel in the second-line treatment (145). The same outcome has been obtained in a doxorubicin-resistant leukemia cell line model (262) and in a large panel of multidrug resistant cell lines (263). Subsequently, doxorubicin-paclitaxel cross-resistance is more or less evident in many models; however, cross-resistance to other agents should be explored in detail in further studies.

Conclusions

Overall, to model chemoresistance and identify actionable targets to overcome de novo and acquired resistance in TNBC, I have utilized 9 TNBC cell lines and 2 normal breast epithelial cell lines, 8 chemotherapy agents of different classes and more than 20 small molecule inhibitors in this project. I have generated 9 acquired cell line and 3 acquired xenograft models and utilized 4 de novo resistance models. I identified some actionable targets such as AKT, SRC, EGFR and CDK1, and successfully demonstrated their translational potential through tremendously high synergistic responses to different chemotherapy agents commonly used in TNBC treatment.

FUTURE PERSPECTIVES

In Vitro Approaches

In this study, I aimed to elucidate molecular mechanisms prompting or cultivating de novo and/or acquired resistance in TNBC by combining cell line and in vivo models. During this process, I have considered the heterogeneity of the TNBC to capture subtype-level differences and similarities. Following the development of chemoresistant models, I performed characterization of some acquired models at protein level by extensive Western blotting. My set of proteins, although included proteins that were frequently implicated in chemotherapy resistance in diverse types of cancer, was noninclusive or incomplete. Therefore, I could be missing the links or cross talks between distinct cellular processes. To compensate for this to some extent, I have utilized publicly available data sets generated with the same/similar cell line or animal models or patient tumors. However, resistance acquisition upon chronic drug exposure could follow different trajectories, creating diverse cell subgroups thus diverse phenotypes that are all resistant but distinct. Therefore, the best way to complement my findings in these models could be their analysis by more comprehensive techniques such as RPPA and/or by more types of data such as transcriptome and mutation profiling. Similarly, I had a finite library of inhibitors not covering all the potential targets or pathways characterized. Therefore, in vitro CRISPR and RNAi screens could be performed in both parental and resistant cells to identify novel vulnerabilities specific to the resistance models. Later, this could be complemented by a small- or large-library drug screen (consisting especially of the FDA approved or advanced phase drugs) to expose a much better picture for our understanding of tiny details causing resistance, instead of individual testing of a

handful inhibitors. For example, the difference between isoform-specific and isoform-agnostic PI3K inhibitors or even the difference between 2 inhibitors targeting the same isoform could be delineated by a library screen followed by total protein or kinome profiling. Total protein profiling could be much more informative; still, kinome profiling could also highlight potential hubs governing the resistance. In addition, I observed changes in some proteins that currently considered "undruggable" or do not have any potent inhibitor available. These could be targeted by genomic approaches such as shRNA or CRISPR, or by newer pharmacological tools such as PROTACs and molecular glues, which could be even better owing to potentially increased specificity/selectivity and efficacy against some target proteins (264). Another important aspect that was not evaluated within the scope of this study is the time- and dose-dependent effects of the chemotherapy agents in both parental and resistant cells. This would be highly valuable due to multiple reasons. First, it could reveal the mechanism of action of the drug in both conditions and thus how it drives apoptosis and/or cell cycle arrest. Second, it could be deduced whether the resistant cells divert the original function of the drug thereby become resistant or the drug exhibits a similar effect to a lower extent but the cells activated/inhibited pathways to neutralize or outweigh it. Third, it could guide time and dose optimization for chemotherapy combination with each inhibitor unlike simultaneous application of both agents as we did.

In Vivo Approaches

To characterize these models further, multiple in vivo approaches could be followed. First, I could investigate the growth patterns and metastatic potential of the parental and resistant cells without any treatment to check if in vitro resistant phenotype

provides any survival advantage and/or dissemination capacity. Similarly, the response of the parental and resistant cells could be evaluated upon single-agent chemotherapy treatment to see if the resistance could be sustained in vivo and if it does, to delineate not only tumor-intrinsic resistance mechanisms but also extrinsic mechanisms contributed by the cells in the microenvironment. All 3 acquired xenograft models developed in this project were propagated in athymic nude mice, which is immunocompromised due to having mostly intact innate immunity but impaired adaptive immune activity. Therefore, therapy resistance in human could not be fully recapitulated in nude mice while omitting the immune cells that are integral to every tumor microenvironment. To account for this, I could use a syngeneic model and examine the contribution of the tumor-fighting and tumor-promoting immune cells or processes. Second, I have identified potential targets that could abrogate chemotherapy resistance but our testing remained primarily in vitro. Although one could expect a similar outcome upon inhibitor treatment in vitro and in vivo, this may not often be the case or even an opposite effect could be exerted by single-agent or combination treatment. To better delineate novel targets and innovative therapeutic interventions, in vivo CRISPR and drug library screens could be harnessed although they could be costly (265). Later, it would be ideal to test at least 1 combination treatment for each chemotherapy class in vivo setting and provide an additional proof towards its translational potential. Third, although I explored cross chemoresistance patterns in the cell line models, we did not test chemotherapy combinations whereas this is usually the way they are utilized in the clinics. I could better recapitulate the chemotherapy regimens and/or combinations both in vitro and in vivo setting, thereby not discover single-chemo resistance but multi-chemo resistance mechanisms. Similarly, multi-inhibitor combinations could be evaluated, but in low-dose

conditions, in both de novo and acquired chemoresistant models. A more clinically-relevant approach could be the use of patient-derived xenografts as they maintain histological and genetic features of origin and thus have higher predictive value. There are several established models of each breast cancer subtype, especially TNBC (266-272), which are both commercially available or could be established in-house. PDX models make it possible to simultaneously study multiple aspects of tumor progression and evolution, from tumor growth rate/aggressiveness and chemotherapy resistance to testing of novel therapeutic approaches, characterization of cancer stem cells and determination of metastatic potential and tropism. Each of these are highly interconnected and are predictive markers of single-agent and/or combination therapy responses.

In conclusion, this study could be improved in multiple aspects but especially by scaling up the experimental setup, by characterizing the models through incorporation of more data types, by utilizing genomic or other pharmacological approaches, by elucidating the similarities and discrepancies in drugs' mechanism of action in the parental and resistant models, by validating in vitro findings in vivo via xenotransplantation and syngeneic transplantation, by testing combinatorial or sequential chemotherapy regimens, and finally by examining low-dose multi-inhibitor combinations in both primary and secondary resistance models.

BIBLIOGRAPHY

1. Sung H, Ferlay J, Siegel RL, Laversanne M, Soerjomataram I, Jemal A, et al. Global Cancer Statistics 2020: GLOBOCAN Estimates of Incidence and Mortality Worldwide for 36 Cancers in 185 Countries. CA Cancer J Clin. 2021;71(3):209-49.
2. Siegel RL, Miller KD, Fuchs HE, Jemal A. Cancer statistics, 2022. CA Cancer J Clin. 2022;72(1):7-33.
3. Dagenais GR, Leong DP, Rangarajan S, Lanas F, Lopez-Jaramillo P, Gupta R, et al. Variations in common diseases, hospital admissions, and deaths in middle-aged adults in 21 countries from five continents (PURE): a prospective cohort study. Lancet. 2020;395(10226):785-94.
4. Fidler MM, Bray F. Global Cancer Inequalities. Front Oncol. 2018;8:293.
5. Ward ZJ, Scott AM, Hricak H, Atun R. Global costs, health benefits, and economic benefits of scaling up treatment and imaging modalities for survival of 11 cancers: a simulation-based analysis. Lancet Oncol. 2021;22(3):341-50.
6. Mikulic M. Projected spending and growth in the global oncology market between 2022 and 2026. 20221209 ed. Statista: IQVIA; 2022.
7. Sussell J, Vanderpuye-Orgle J, Vania D, Goertz H-P, Lakdawalla D. Understanding price growth in the market for targeted oncology therapies. The American Journal of Managed Care. 2019;25(6): 273–7.
8. Benz EJ, Jr. The Jeremiah Metzger Lecture Cancer in the Twenty-First Century: An Inside View from an Outsider. Trans Am Clin Climatol Assoc. 2017;128:275-97.
9. Soare GR, Soare CA. Immunotherapy for Breast Cancer: First FDA Approved Regimen. Discoveries (Craiova). 2019;7(1):e91.
10. Jarman R, Ribeiro-Milograna S, Kalle W. Potential of the Microbiome as a Biomarker for Early Diagnosis and Prognosis of Breast Cancer. J Breast Cancer. 2020;23(6):579-87.
11. DeSantis CE, Ma J, Gaudet MM, Newman LA, Miller KD, Goding Sauer A, et al. Breast cancer statistics, 2019. CA Cancer J Clin. 2019;69(6):438-51.
12. Bertos NR, Park M. Breast cancer - one term, many entities? J Clin Invest. 2011;121(10):3789-96.
13. Rakha EA, Reis-Filho JS, Baehner F, Dabbs DJ, Decker T, Eusebi V, et al. Breast cancer prognostic classification in the molecular era: the role of histological grade. Breast Cancer Res. 2010;12(4):207.
14. Eheman CR, Shaw KM, Ryerson AB, Miller JW, Ajani UA, White MC. The changing incidence of in situ and invasive ductal and lobular breast carcinomas: United States, 1999-2004. Cancer Epidemiol Biomarkers Prev. 2009;18(6):1763-9.
15. Li CI, Moe RE, Daling JR. Risk of mortality by histologic type of breast cancer among women aged 50 to 79 years. Arch Intern Med. 2003;163(18):2149-53.
16. Liu GF, Yang Q, Haffty BG, Moran MS. Clinical-pathologic features and long-term outcomes of tubular carcinoma of the breast compared with invasive ductal carcinoma treated with breast conservation therapy. Int J Radiat Oncol Biol Phys. 2009;75(5):1304-8.
17. Perou CM, Sorlie T, Eisen MB, van de Rijn M, Jeffrey SS, Rees CA, et al. Molecular portraits of human breast tumours. Nature. 2000;406(6797):747-52.

18. Sorlie T, Perou CM, Tibshirani R, Aas T, Geisler S, Johnsen H, et al. Gene expression patterns of breast carcinomas distinguish tumor subclasses with clinical implications. Proc Natl Acad Sci U S A. 2001;98(19):10869-74.
19. de Ronde J, Wessels L, Wesseling J. Molecular subtyping of breast cancer: ready to use? Lancet Oncol. 2010;11(4):306-7.
20. Russnes HG, Lingjaerde OC, Borresen-Dale AL, Caldas C. Breast Cancer Molecular Stratification: From Intrinsic Subtypes to Integrative Clusters. Am J Pathol. 2017;187(10):2152-62.
21. American Cancer Society. Breast Cancer Facts & Figures 2019-2020. Atlanta: American Cancer Society, Inc.; 2019.
22. Schlam I, Swain SM. HER2-positive breast cancer and tyrosine kinase inhibitors: the time is now. NPJ Breast Cancer. 2021;7(1):56.
23. Cortes J, Kim SB, Chung WP, Im SA, Park YH, Hegg R, et al. Trastuzumab Deruxtecan versus Trastuzumab Emtansine for Breast Cancer. N Engl J Med. 2022;386(12):1143-54.
24. Choong GM, Cullen GD, O'Sullivan CC. Evolving standards of care and new challenges in the management of HER2-positive breast cancer. CA Cancer J Clin. 2020;70(5):355-74.
25. Andre F, Ciruelos E, Rubovszky G, Campone M, Loibl S, Rugo HS, et al. Alpelisib for PIK3CA-Mutated, Hormone Receptor-Positive Advanced Breast Cancer. N Engl J Med. 2019;380(20):1929-40.
26. He L, Lv Y, Song Y, Zhang B. The prognosis comparison of different molecular subtypes of breast tumors after radiotherapy and the intrinsic reasons for their distinct radiosensitivity. Cancer Manag Res. 2019;11:5765-75.
27. Patel HK, Bihani T. Selective estrogen receptor modulators (SERMs) and selective estrogen receptor degraders (SERDs) in cancer treatment. Pharmacol Ther. 2018;186:1-24.
28. Lin X, Xiang H, Luo G. Targeting estrogen receptor alpha for degradation with PROTACs: A promising approach to overcome endocrine resistance. Eur J Med Chem. 2020;206:112689.
29. Early Breast Cancer Trialists' Collaborative G. Aromatase inhibitors versus tamoxifen in early breast cancer: patient-level meta-analysis of the randomised trials. Lancet. 2015;386(10001):1341-52.
30. Li JJ, Shao ZM. Endocrine therapy as adjuvant or neoadjuvant therapy for breast cancer: selecting the best agents, the timing and duration of treatment. Chin Clin Oncol. 2016;5(3):40.
31. Howell A, Robertson JF, Abram P, Lichinitser MR, Elledge R, Bajetta E, et al. Comparison of fulvestrant versus tamoxifen for the treatment of advanced breast cancer in postmenopausal women previously untreated with endocrine therapy: a multinational, double-blind, randomized trial. J Clin Oncol. 2004;22(9):1605-13.
32. Lau KH, Tan AM, Shi Y. New and Emerging Targeted Therapies for Advanced Breast Cancer. Int J Mol Sci. 2022;23(4).
33. Baselga J, Campone M, Piccart M, Burris HA, 3rd, Rugo HS, Sahmoud T, et al. Everolimus in postmenopausal hormone-receptor-positive advanced breast cancer. N Engl J Med. 2012;366(6):520-9.
34. Turner NC, Slamon DJ, Ro J, Bondarenko I, Im SA, Masuda N, et al. Overall Survival with Palbociclib and Fulvestrant in Advanced Breast Cancer. N Engl J Med. 2018;379(20):1926-36.

35. Andre F, Ciruelos EM, Juric D, Loibl S, Campone M, Mayer IA, et al. Alpelisib plus fulvestrant for PIK3CA-mutated, hormone receptor-positive, human epidermal growth factor receptor-2-negative advanced breast cancer: final overall survival results from SOLAR-1. Ann Oncol. 2021;32(2):208-17.
36. Madigan LI, Dinh P, Graham JD. Neoadjuvant endocrine therapy in locally advanced estrogen or progesterone receptor-positive breast cancer: determining the optimal endocrine agent and treatment duration in postmenopausal women-a literature review and proposed guidelines. Breast Cancer Res. 2020;22(1):77.
37. Eiermann W, Paepke S, Appfelstaedt J, Llombart-Cussac A, Eremin J, Vinholes J, et al. Preoperative treatment of postmenopausal breast cancer patients with letrozole: A randomized double-blind multicenter study. Ann Oncol. 2001;12(11):1527-32.
38. Anurag M, Ellis MJ, Haricharan S. DNA damage repair defects as a new class of endocrine treatment resistance driver. Oncotarget. 2018;9(91):36252-3.
39. Hwang SY, Park S, Kwon Y. Recent therapeutic trends and promising targets in triple negative breast cancer. Pharmacol Ther. 2019;199:30-57.
40. Bertucci F, Finetti P, Cervera N, Esterni B, Hermitte F, Viens P, et al. How basal are triple-negative breast cancers? Int J Cancer. 2008;123(1):236-40.
41. Prat A, Adamo B, Cheang MC, Anders CK, Carey LA, Perou CM. Molecular characterization of basal-like and non-basal-like triple-negative breast cancer. Oncologist. 2013;18(2):123-33.
42. Sousa B, Cardoso F. Neoadjuvant treatment for HER-2-positive and triple-negative breast cancers. Ann Oncol. 2012;23 Suppl 10:x237-42.
43. Garrido-Castro AC, Lin NU, Polyak K. Insights into Molecular Classifications of Triple-Negative Breast Cancer: Improving Patient Selection for Treatment. Cancer Discov. 2019;9(2):176-98.
44. Kim MJ, Kim EK, Park S, Moon HJ, Kim SI, Park BW. Evaluation with 3.0-T MR imaging: predicting the pathological response of triple-negative breast cancer treated with anthracycline and taxane neoadjuvant chemotherapy. Acta Radiol. 2015;56(9):1069-77.
45. Santonja A, Sanchez-Munoz A, Lluch A, Chica-Parrado MR, Albanell J, Chacon JI, et al. Triple negative breast cancer subtypes and pathologic complete response rate to neoadjuvant chemotherapy. Oncotarget. 2018;9(41):26406-16.
46. Bianchini G, Balko JM, Mayer IA, Sanders ME, Gianni L. Triple-negative breast cancer: challenges and opportunities of a heterogeneous disease. Nat Rev Clin Oncol. 2016;13(11):674-90.
47. Liedtke C, Mazouni C, Hess KR, Andre F, Tordai A, Mejia JA, et al. Response to neoadjuvant therapy and long-term survival in patients with triple-negative breast cancer. J Clin Oncol. 2008;26(8):1275-81.
48. Schmid P, Adams S, Rugo HS, Schneeweiss A, Barrios CH, Iwata H, et al. Atezolizumab and Nab-Paclitaxel in Advanced Triple-Negative Breast Cancer. N Engl J Med. 2018;379(22):2108-21.
49. Schmid P, Cortes J, Pusztai L, McArthur H, Kummel S, Bergh J, et al. Pembrolizumab for Early Triple-Negative Breast Cancer. N Engl J Med. 2020;382(9):810-21.
50. Robson ME, Tung N, Conte P, Im SA, Senkus E, Xu B, et al. OlympiAD final overall survival and tolerability results: Olaparib versus chemotherapy treatment of physician's choice in patients with a germline BRCA mutation and HER2-negative metastatic breast cancer. Ann Oncol. 2019;30(4):558-66.

51. Robson M, Im SA, Senkus E, Xu B, Domchek SM, Masuda N, et al. Olaparib for Metastatic Breast Cancer in Patients with a Germline BRCA Mutation. N Engl J Med. 2017;377(6):523-33.
52. Litton JK, Rugo HS, Ettl J, Hurvitz SA, Goncalves A, Lee KH, et al. Talazoparib in Patients with Advanced Breast Cancer and a Germline BRCA Mutation. N Engl J Med. 2018;379(8):753-63.
53. Bardia A, Mayer IA, Vahdat LT, Tolaney SM, Isakoff SJ, Diamond JR, et al. Sacituzumab Govitecan-hziy in Refractory Metastatic Triple-Negative Breast Cancer. N Engl J Med. 2019;380(8):741-51.
54. Keenan TE, Tolaney SM. Role of Immunotherapy in Triple-Negative Breast Cancer. J Natl Compr Canc Netw. 2020;18(4):479-89.
55. Checkpoint Inhibitors Can Up Heart Harm. Cancer Discov. 2022:OF1.
56. Phua LC, Lee SC, Ng K, Abdul Aziz MI. Cost-effectiveness analysis of atezolizumab in advanced triple-negative breast cancer. BMC Health Serv Res. 2020;20(1):581.
57. Giuliani J, Mantoan B, Bonetti A. The cost-effectiveness of atezolizumab in first-line for metastatic triple negative breast cancer is heavily linked to PD-L1 level. J Oncol Pharm Pract. 2021;27(5):1245-7.
58. Seligson JM, Patron AM, Berger MJ, Harvey RD, Seligson ND. Sacituzumab Govitecan-hziy: An Antibody-Drug Conjugate for the Treatment of Refractory, Metastatic, Triple-Negative Breast Cancer. Ann Pharmacother. 2021;55(7):921-31.
59. Barchiesi G, Roberto M, Verrico M, Vici P, Tomao S, Tomao F. Emerging Role of PARP Inhibitors in Metastatic Triple Negative Breast Cancer. Current Scenario and Future Perspectives. Front Oncol. 2021;11:769280.
60. Saito S, Nakazawa K, Nagahashi M, Ishikawa T, Akazawa K. Cost-effectiveness of BRCA1/2 mutation profiling to target olaparib use in patients with metastatic breast cancer. Per Med. 2019;16(6):439-48.
61. Vagia E, Mahalingam D, Cristofanilli M. The Landscape of Targeted Therapies in TNBC. Cancers (Basel). 2020;12(4).
62. Ensenyat-Mendez M, Llinas-Arias P, Orozco JIJ, Iniguez-Munoz S, Salomon MP, Sese B, et al. Current Triple-Negative Breast Cancer Subtypes: Dissecting the Most Aggressive Form of Breast Cancer. Front Oncol. 2021;11:681476.
63. Elsawaf Z, Sinn HP, Rom J, Bermejo JL, Schneeweiss A, Aulmann S. Biological subtypes of triple-negative breast cancer are associated with distinct morphological changes and clinical behaviour. Breast. 2013;22(5):986-92.
64. Zhao S, Ma D, Xiao Y, Li XM, Ma JL, Zhang H, et al. Molecular Subtyping of Triple-Negative Breast Cancers by Immunohistochemistry: Molecular Basis and Clinical Relevance. Oncologist. 2020;25(10):e1481-e91.
65. Lehmann BD, Bauer JA, Chen X, Sanders ME, Chakravarthy AB, Shyr Y, et al. Identification of human triple-negative breast cancer subtypes and preclinical models for selection of targeted therapies. J Clin Invest. 2011;121(7):2750-67.
66. Lehmann BD, Jovanovic B, Chen X, Estrada MV, Johnson KN, Shyr Y, et al. Refinement of Triple-Negative Breast Cancer Molecular Subtypes: Implications for Neoadjuvant Chemotherapy Selection. PLoS One. 2016;11(6):e0157368.
67. Burstein MD, Tsimelzon A, Poage GM, Covington KR, Contreras A, Fuqua SA, et al. Comprehensive genomic analysis identifies novel subtypes and targets of triple-negative breast cancer. Clin Cancer Res. 2015;21(7):1688-98.

68. Liu YR, Jiang YZ, Xu XE, Yu KD, Jin X, Hu X, et al. Comprehensive transcriptome analysis identifies novel molecular subtypes and subtype-specific RNAs of triple-negative breast cancer. Breast Cancer Res. 2016;18(1):33.
69. Jiang YZ, Ma D, Suo C, Shi J, Xue M, Hu X, et al. Genomic and Transcriptomic Landscape of Triple-Negative Breast Cancers: Subtypes and Treatment Strategies. Cancer Cell. 2019;35(3):428-40 e5.
70. Marra A, Trapani D, Viale G, Criscitiello C, Curigliano G. Practical classification of triple-negative breast cancer: intratumoral heterogeneity, mechanisms of drug resistance, and novel therapies. NPJ Breast Cancer. 2020;6:54.
71. Bareche Y, Venet D, Ignatiadis M, Aftimos P, Piccart M, Rothe F, et al. Unravelling triple-negative breast cancer molecular heterogeneity using an integrative multiomic analysis. Ann Oncol. 2018;29(4):895-902.
72. Lehmann BD, Colaprico A, Silva TC, Chen J, An H, Ban Y, et al. Multi-omics analysis identifies therapeutic vulnerabilities in triple-negative breast cancer subtypes. Nat Commun. 2021;12(1):6276.
73. Jiang YZ, Liu Y, Xiao Y, Hu X, Jiang L, Zuo WJ, et al. Molecular subtyping and genomic profiling expand precision medicine in refractory metastatic triple-negative breast cancer: the FUTURE trial. Cell Res. 2021;31(2):178-86.
74. Gong Y, Ji P, Yang YS, Xie S, Yu TJ, Xiao Y, et al. Metabolic-Pathway-Based Subtyping of Triple-Negative Breast Cancer Reveals Potential Therapeutic Targets. Cell Metab. 2021;33(1):51-64 e9.
75. Koch A, Joosten SC, Feng Z, de Ruijter TC, Draht MX, Melotte V, et al. Analysis of DNA methylation in cancer: location revisited. Nat Rev Clin Oncol. 2018;15(7):459-66.
76. DiMasi JA, Reichert JM, Feldman L, Malins A. Clinical approval success rates for investigational cancer drugs. Clin Pharmacol Ther. 2013;94(3):329-35.
77. National Comprehensive Cancer Network. NCCN Guidelines for Patients: Ductal Carcinoma in Situ Breast Cancer. National Comprehensive Cancer Network; 2022.
78. National Comprehensive Cancer Network. NCCN Guidelines for Patients: Invasive Breast Cancer. National Comprehensive Cancer Network; 2022.
79. National Comprehensive Cancer Network. NCCN Guidelines for Patients: Metastatic Breast Cancer. National Comprehensive Cancer Network; 2022.
80. Bukowski K, Kciuk M, Kontek R. Mechanisms of Multidrug Resistance in Cancer Chemotherapy. Int J Mol Sci. 2020;21(9).
81. Sharma A, Houshyar R, Bhosale P, Choi JI, Gulati R, Lall C. Chemotherapy induced liver abnormalities: an imaging perspective. Clin Mol Hepatol. 2014;20(3):317-26.
82. Olsen MM, LeFebvre KB, Brassil KJ, Oncology Nursing Society. Chemotherapy and immunotherapy guidelines and recommendations for practice. Pittsburgh, Pennsylvania: Oncology Nursing Society; 2019. xiii, 644 pages p.
83. DeVita VT, Hellman S, Rosenberg SA. Cancer, principles & practice of oncology. 7th ed. Philadelphia, PA: Lippincott Williams & Wilkins; 2005. lxxv, 2898 p. p.
84. More GS, Thomas AB, Chitlange SS, Nanda RK, Gajbhiye RL. Nitrogen Mustards as Alkylating Agents: A Review on Chemistry, Mechanism of Action and Current USFDA Status of Drugs. Anticancer Agents Med Chem. 2019;19(9):1080-102.

85. Pujol JL, Carestia L, Daures JP. Is there a case for cisplatin in the treatment of small-cell lung cancer? A meta-analysis of randomized trials of a cisplatin-containing regimen versus a regimen without this alkylating agent. Br J Cancer. 2000;83(1):8-15.
86. Kaplan HG, Calip GS, Malmgren JA. Maximizing Breast Cancer Therapy with Awareness of Potential Treatment-Related Blood Disorders. Oncologist. 2020;25(5):391-7.
87. Conteduca V, Scarpi E, Farolfi A, Brighi N, Rossi L, Gurioli G, et al. Melphalan as a Promising Treatment for BRCA-Related Ovarian Carcinoma. Front Oncol. 2021;11:716467.
88. Blenman KRM, Marczyk M, Karn T, Qing T, Li X, Gunasekharan V, et al. Predictive Markers of Response to Neoadjuvant Durvalumab with Nab-Paclitaxel and Dose-Dense Doxorubicin/Cyclophosphamide in Basal-Like Triple-Negative Breast Cancer. Clin Cancer Res. 2022;28(12):2587-97.
89. Foldi J, Silber A, Reisenbichler E, Singh K, Fischbach N, Persico J, et al. Neoadjuvant durvalumab plus weekly nab-paclitaxel and dose-dense doxorubicin/cyclophosphamide in triple-negative breast cancer. NPJ Breast Cancer. 2021;7(1):9.
90. Li J, Yu K, Pang D, Wang C, Jiang J, Yang S, et al. Adjuvant Capecitabine With Docetaxel and Cyclophosphamide Plus Epirubicin for Triple-Negative Breast Cancer (CBCSG010): An Open-Label, Randomized, Multicenter, Phase III Trial. J Clin Oncol. 2020;38(16):1774-84.
91. Kummar S, Wade JL, Oza AM, Sullivan D, Chen AP, Gandara DR, et al. Randomized phase II trial of cyclophosphamide and the oral poly (ADP-ribose) polymerase inhibitor veliparib in patients with recurrent, advanced triple-negative breast cancer. Invest New Drugs. 2016;34(3):355-63.
92. Fraiser LH, Kanekal S, Kehrer JP. Cyclophosphamide toxicity. Characterising and avoiding the problem. Drugs. 1991;42(5):781-95.
93. Laux DC, Lausch RN. Evaluation of factors contributing to tumor resistance to cyclophosphamide. J Natl Cancer Inst. 1974;52(3):863-8.
94. Magni M, Shammah S, Schiro R, Mellado W, Dalla-Favera R, Gianni AM. Induction of cyclophosphamide-resistance by aldehyde-dehydrogenase gene transfer. Blood. 1996;87(3):1097-103.
95. He X, Deng Y, Yue W. Investigating critical genes and gene interaction networks that mediate cyclophosphamide sensitivity in chronic myelogenous leukemia. Mol Med Rep. 2017;16(1):523-32.
96. McGown AT, Fox BW. A proposed mechanism of resistance to cyclophosphamide and phosphoramide mustard in a Yoshida cell line in vitro. Cancer Chemother Pharmacol. 1986;17(3):223-6.
97. Emmenegger U, Francia G, Chow A, Shaked Y, Kouri A, Man S, et al. Tumors that acquire resistance to low-dose metronomic cyclophosphamide retain sensitivity to maximum tolerated dose cyclophosphamide. Neoplasia. 2011;13(1):40-8.
98. Kuchenbaecker KB, Hopper JL, Barnes DR, Phillips KA, Mooij TM, Roos-Blom MJ, et al. Risks of Breast, Ovarian, and Contralateral Breast Cancer for BRCA1 and BRCA2 Mutation Carriers. JAMA. 2017;317(23):2402-16.
99. Antoniou A, Pharoah PD, Narod S, Risch HA, Eyfjord JE, Hopper JL, et al. Average risks of breast and ovarian cancer associated with BRCA1 or BRCA2 mutations detected in case Series unselected for family history: a combined analysis of 22 studies. Am J Hum Genet. 2003;72(5):1117-30.

100. Chen S, Parmigiani G. Meta-analysis of BRCA1 and BRCA2 penetrance. J Clin Oncol. 2007;25(11):1329-33.
101. De Iuliis F, Salerno G, Corvino R, D'Aniello D, Cefali K, Taglieri L, et al. Anthracycline-Free Neoadjuvant Chemotherapy Ensures Higher Rates of Pathologic Complete Response in Breast Cancer. Clin Breast Cancer. 2017;17(1):34-40.
102. Hahnen E, Lederer B, Hauke J, Loibl S, Krober S, Schneeweiss A, et al. Germline Mutation Status, Pathological Complete Response, and Disease-Free Survival in Triple-Negative Breast Cancer: Secondary Analysis of the GeparSixto Randomized Clinical Trial. JAMA Oncol. 2017;3(10):1378-85.
103. Shinde AM, Zhai J, Yu KW, Frankel P, Yim JH, Luu T, et al. Pathologic complete response rates in triple-negative, HER2-positive, and hormone receptor-positive breast cancers after anthracycline-free neoadjuvant chemotherapy with carboplatin and paclitaxel with or without trastuzumab. Breast. 2015;24(1):18-23.
104. Isakoff SJ. Triple-negative breast cancer: role of specific chemotherapy agents. Cancer J. 2010;16(1):53-61.
105. Shen DW, Pouliot LM, Hall MD, Gottesman MM. Cisplatin resistance: a cellular self-defense mechanism resulting from multiple epigenetic and genetic changes. Pharmacol Rev. 2012;64(3):706-21.
106. Li J, Xu X, Peng X. NDC80 Enhances Cisplatin-resistance in Triple-negative Breast Cancer. Arch Med Res. 2022;53(4):378-87.
107. Abreu de Oliveira WA, Moens S, El Laithy Y, van der Veer BK, Athanasouli P, Cortesi EE, et al. Wnt/beta-Catenin Inhibition Disrupts Carboplatin Resistance in Isogenic Models of Triple-Negative Breast Cancer. Front Oncol. 2021;11:705384.
108. Galluzzi L, Senovilla L, Vitale I, Michels J, Martins I, Kepp O, et al. Molecular mechanisms of cisplatin resistance. Oncogene. 2012;31(15):1869-83.
109. Hill DP, Harper A, Malcolm J, McAndrews MS, Mockus SM, Patterson SE, et al. Cisplatin-resistant triple-negative breast cancer subtypes: multiple mechanisms of resistance. BMC Cancer. 2019;19(1):1039.
110. Kwok JM, Peck B, Monteiro LJ, Schwenen HD, Millour J, Coombes RC, et al. FOXM1 confers acquired cisplatin resistance in breast cancer cells. Mol Cancer Res. 2010;8(1):24-34.
111. Zhu L, Zou J, Zhao Y, Jiang X, Wang Y, Wang X, et al. ER-alpha36 mediates cisplatin resistance in breast cancer cells through EGFR/HER-2/ERK signaling pathway. J Exp Clin Cancer Res. 2018;37(1):123.
112. Hu XC, Zhang J, Xu BH, Cai L, Ragaz J, Wang ZH, et al. Cisplatin plus gemcitabine versus paclitaxel plus gemcitabine as first-line therapy for metastatic triple-negative breast cancer (CBCSG006): a randomised, open-label, multicentre, phase 3 trial. Lancet Oncol. 2015;16(4):436-46.
113. Yardley DA, Coleman R, Conte P, Cortes J, Brufsky A, Shtivelband M, et al. nab-Paclitaxel plus carboplatin or gemcitabine versus gemcitabine plus carboplatin as first-line treatment of patients with triple-negative metastatic breast cancer: results from the tnAcity trial. Ann Oncol. 2018;29(8):1763-70.
114. Gluz O, Nitz U, Liedtke C, Christgen M, Grischke EM, Forstbauer H, et al. Comparison of Neoadjuvant Nab-Paclitaxel+Carboplatin vs Nab-Paclitaxel+Gemcitabine in Triple-Negative Breast Cancer: Randomized WSG-ADAPT-TN Trial Results. J Natl Cancer Inst. 2018;110(6):628-37.
115. Pellegrino B, Cavanna L, Boggiani D, Zamagni C, Frassoldati A, Schirone A, et al. Phase II study of eribulin in combination with gemcitabine for the treatment of patients with locally advanced or metastatic triple negative breast cancer (ERIGE

trial). Clinical and pharmacogenetic results on behalf of the Gruppo Oncologico Italiano di Ricerca Clinica (GOIRC). ESMO Open. 2021;6(1):100019.
116. Park IH, Kong SY, Kwon Y, Kim MK, Sim SH, Joo J, et al. Phase I/II clinical trial of everolimus combined with gemcitabine/cisplatin for metastatic triple-negative breast cancer. J Cancer. 2018;9(7):1145-51.
117. Dieras V, Bonnefoi H, Alba E, Awada A, Coudert B, Pivot X, et al. Iniparib administered weekly or twice-weekly in combination with gemcitabine/carboplatin in patients with metastatic triple-negative breast cancer: a phase II randomized open-label study with pharmacokinetics. Breast Cancer Res Treat. 2019;177(2):383-93.
118. Li T, Tao Z, Zhu Y, Liu X, Wang L, Du Y, et al. Exosomal annexin A6 induces gemcitabine resistance by inhibiting ubiquitination and degradation of EGFR in triple-negative breast cancer. Cell Death Dis. 2021;12(7):684.
119. Xie X, Lee J, Liu H, Pearson T, Lu AY, Tripathy D, et al. Birinapant Enhances Gemcitabine's Antitumor Efficacy in Triple-Negative Breast Cancer by Inducing Intrinsic Pathway-Dependent Apoptosis. Mol Cancer Ther. 2021;20(2):296-306.
120. Wang R, Cheng L, Xia J, Wang Z, Wu Q, Wang Z. Gemcitabine resistance is associated with epithelial-mesenchymal transition and induction of HIF-1alpha in pancreatic cancer cells. Curr Cancer Drug Targets. 2014;14(4):407-17.
121. Wu ZH, Lin C, Liu MM, Zhang J, Tao ZH, Hu XC. Src Inhibition Can Synergize with Gemcitabine and Reverse Resistance in Triple Negative Breast Cancer Cells via the AKT/c-Jun Pathway. PLoS One. 2016;11(12):e0169230.
122. Tanaka H, Nakamura M, Kameda C, Kubo M, Sato N, Kuroki S, et al. The Hedgehog signaling pathway plays an essential role in maintaining the CD44+CD24-/low subpopulation and the side population of breast cancer cells. Anticancer Res. 2009;29(6):2147-57.
123. Jasra S, Anampa J. Anthracycline Use for Early Stage Breast Cancer in the Modern Era: a Review. Curr Treat Options Oncol. 2018;19(6):30.
124. Yap HY, Blumenschein GR, Yap BS, Hortobagyi GN, Tashima CK, Wang AY, et al. High-dose methotrexate for advanced breast cancer. Cancer Treat Rep. 1979;63(5):757-61.
125. Paul DM, Garrett AM, Meshad M, DeVore RD, Porter LL, Johnson DH. Paclitaxel and 5-fluorouracil in metastatic breast cancer: the US experience. Semin Oncol. 1996;23(1 Suppl 1):48-52.
126. Das CK, Linder B, Bonn F, Rothweiler F, Dikic I, Michaelis M, et al. BAG3 Overexpression and Cytoprotective Autophagy Mediate Apoptosis Resistance in Chemoresistant Breast Cancer Cells. Neoplasia. 2018;20(3):263-79.
127. Soung YH, Chung H, Yan C, Ju J, Chung J. Arrestin Domain Containing 3 Reverses Epithelial to Mesenchymal Transition and Chemo-Resistance of TNBC Cells by Up-Regulating Expression of miR-200b. Cells. 2019;8(7).
128. Marangoni E, Laurent C, Coussy F, El-Botty R, Chateau-Joubert S, Servely JL, et al. Capecitabine Efficacy Is Correlated with TYMP and RB1 Expression in PDX Established from Triple-Negative Breast Cancers. Clin Cancer Res. 2018;24(11):2605-15.
129. Hortobagyi GN. Anthracyclines in the treatment of cancer. An overview. Drugs. 1997;54 Suppl 4:1-7.
130. Kaklamani VG, Gradishar WJ. Epirubicin versus doxorubicin: which is the anthracycline of choice for the treatment of breast cancer? Clin Breast Cancer. 2003;4 Suppl 1:S26-33.

131. Paluch-Shimon S, Friedman E, Berger R, Papa M, Dadiani M, Friedman N, et al. Neo-adjuvant doxorubicin and cyclophosphamide followed by paclitaxel in triple-negative breast cancer among BRCA1 mutation carriers and non-carriers. Breast Cancer Res Treat. 2016;157(1):157-65.
132. Carey LA, Dees EC, Sawyer L, Gatti L, Moore DT, Collichio F, et al. The triple negative paradox: primary tumor chemosensitivity of breast cancer subtypes. Clin Cancer Res. 2007;13(8):2329-34.
133. Shi Y, Moon M, Dawood S, McManus B, Liu PP. Mechanisms and management of doxorubicin cardiotoxicity. Herz. 2011;36(4):296-305.
134. Chan S, Friedrichs K, Noel D, Pinter T, Van Belle S, Vorobiof D, et al. Prospective randomized trial of docetaxel versus doxorubicin in patients with metastatic breast cancer. J Clin Oncol. 1999;17(8):2341-54.
135. Aas T, Borresen AL, Geisler S, Smith-Sorensen B, Johnsen H, Varhaug JE, et al. Specific P53 mutations are associated with de novo resistance to doxorubicin in breast cancer patients. Nat Med. 1996;2(7):811-4.
136. Saatci O, Kaymak A, Raza U, Ersan PG, Akbulut O, Banister CE, et al. Targeting lysyl oxidase (LOX) overcomes chemotherapy resistance in triple negative breast cancer. Nat Commun. 2020;11(1):2416.
137. Chen DR, Lu DY, Lin HY, Yeh WL. Mesenchymal stem cell-induced doxorubicin resistance in triple negative breast cancer. Biomed Res Int. 2014;2014:532161.
138. Li Z, Chen C, Chen L, Hu D, Yang X, Zhuo W, et al. STAT5a Confers Doxorubicin Resistance to Breast Cancer by Regulating ABCB1. Front Oncol. 2021;11:697950.
139. Christowitz C, Davis T, Isaacs A, van Niekerk G, Hattingh S, Engelbrecht AM. Mechanisms of doxorubicin-induced drug resistance and drug resistant tumour growth in a murine breast tumour model. BMC Cancer. 2019;19(1):757.
140. Shulman LN, Berry DA, Cirrincione CT, Becker HP, Perez EA, O'Regan R, et al. Comparison of doxorubicin and cyclophosphamide versus single-agent paclitaxel as adjuvant therapy for breast cancer in women with 0 to 3 positive axillary nodes: CALGB 40101 (Alliance). J Clin Oncol. 2014;32(22):2311-7.
141. Du F, Wang W, Wang Y, Li M, Zhu A, Wang J, et al. Carboplatin plus taxanes are non-inferior to epirubicin plus cyclophosphamide followed by taxanes as adjuvant chemotherapy for early triple-negative breast cancer. Breast Cancer Res Treat. 2020;182(1):67-77.
142. Henderson IC, Berry DA, Demetri GD, Cirrincione CT, Goldstein LJ, Martino S, et al. Improved outcomes from adding sequential Paclitaxel but not from escalating Doxorubicin dose in an adjuvant chemotherapy regimen for patients with node-positive primary breast cancer. J Clin Oncol. 2003;21(6):976-83.
143. Gianni L, Baselga J, Eiermann W, Porta VG, Semiglazov V, Lluch A, et al. Phase III trial evaluating the addition of paclitaxel to doxorubicin followed by cyclophosphamide, methotrexate, and fluorouracil, as adjuvant or primary systemic therapy: European Cooperative Trial in Operable Breast Cancer. J Clin Oncol. 2009;27(15):2474-81.
144. Jacquin JP, Jones S, Magne N, Chapelle C, Ellis P, Janni W, et al. Docetaxel-containing adjuvant chemotherapy in patients with early stage breast cancer. Consistency of effect independent of nodal and biomarker status: a meta-analysis of 14 randomized clinical trials. Breast Cancer Res Treat. 2012;134(3):903-13.

145. Paridaens R, Biganzoli L, Bruning P, Klijn JG, Gamucci T, Houston S, et al. Paclitaxel versus doxorubicin as first-line single-agent chemotherapy for metastatic breast cancer: a European Organization for Research and Treatment of Cancer Randomized Study with cross-over. J Clin Oncol. 2000;18(4):724-33.
146. Ben-Hamo R, Zilberberg A, Cohen H, Bahar-Shany K, Wachtel C, Korach J, et al. Resistance to paclitaxel is associated with a variant of the gene BCL2 in multiple tumor types. NPJ Precis Oncol. 2019;3:12.
147. Han J, Yun J, Quan M, Kang W, Jung JG, Heo W, et al. JAK2 regulates paclitaxel resistance in triple negative breast cancers. J Mol Med (Berl). 2021;99(12):1783-95.
148. Liu XY, Jiang W, Ma D, Ge LP, Yang YS, Gou ZC, et al. SYTL4 downregulates microtubule stability and confers paclitaxel resistance in triple-negative breast cancer. Theranostics. 2020;10(24):10940-56.
149. Yang N, Wang C, Wang J, Wang Z, Huang D, Yan M, et al. Aurora kinase A stabilizes FOXM1 to enhance paclitaxel resistance in triple-negative breast cancer. J Cell Mol Med. 2019;23(9):6442-53.
150. Liu T, Sun H, Zhu D, Dong X, Liu F, Liang X, et al. TRA2A Promoted Paclitaxel Resistance and Tumor Progression in Triple-Negative Breast Cancers via Regulating Alternative Splicing. Mol Cancer Ther. 2017;16(7):1377-88.
151. LoRusso PM, Tolaney SM, Wong S, Parchment RE, Kinders RJ, Wang L, et al. Combination of the PARP inhibitor veliparib (ABT888) with irinotecan in patients with triple negative breast cancer: Preliminary activity and signature of response. 2015.
152. Yang W, Soares J, Greninger P, Edelman EJ, Lightfoot H, Forbes S, et al. Genomics of Drug Sensitivity in Cancer (GDSC): a resource for therapeutic biomarker discovery in cancer cells. Nucleic Acids Res. 2013;41(Database issue):D955-61.
153. Feizi N, Nair SK, Smirnov P, Beri G, Eeles C, Esfahani PN, et al. PharmacoDB 2.0: improving scalability and transparency of in vitro pharmacogenomics analysis. Nucleic Acids Res. 2022;50(D1):D1348-D57.
154. Paplomata E, O'Regan R. The PI3K/AKT/mTOR pathway in breast cancer: targets, trials and biomarkers. Ther Adv Med Oncol. 2014;6(4):154-66.
155. Cooper J, Giancotti FG. Integrin Signaling in Cancer: Mechanotransduction, Stemness, Epithelial Plasticity, and Therapeutic Resistance. Cancer Cell. 2019;35(3):347-67.
156. Santen RJ, Song RX, McPherson R, Kumar R, Adam L, Jeng MH, et al. The role of mitogen-activated protein (MAP) kinase in breast cancer. J Steroid Biochem Mol Biol. 2002;80(2):239-56.
157. To SQ, Dmello RS, Richards AK, Ernst M, Chand AL. STAT3 Signaling in Breast Cancer: Multicellular Actions and Therapeutic Potential. Cancers (Basel). 2022;14(2).
158. Sisinni L, Pietrafesa M, Lepore S, Maddalena F, Condelli V, Esposito F, et al. Endoplasmic Reticulum Stress and Unfolded Protein Response in Breast Cancer: The Balance between Apoptosis and Autophagy and Its Role in Drug Resistance. Int J Mol Sci. 2019;20(4).
159. Thu KL, Soria-Bretones I, Mak TW, Cescon DW. Targeting the cell cycle in breast cancer: towards the next phase. Cell Cycle. 2018;17(15):1871-85.
160. Ali R, Rakha EA, Madhusudan S, Bryant HE. DNA damage repair in breast cancer and its therapeutic implications. Pathology. 2017;49(2):156-65.

161. Mohammad RM, Muqbil I, Lowe L, Yedjou C, Hsu HY, Lin LT, et al. Broad targeting of resistance to apoptosis in cancer. Semin Cancer Biol. 2015;35 Suppl:S78-S103.
162. McAleese CE, Choudhury C, Butcher NJ, Minchin RF. Hypoxia-mediated drug resistance in breast cancers. Cancer Lett. 2021;502:189-99.
163. Huang J, Li H, Ren G. Epithelial-mesenchymal transition and drug resistance in breast cancer (Review). Int J Oncol. 2015;47(3):840-8.
164. Wang X, Hu S, Liu L. Phosphorylation and acetylation modifications of FOXO3a: Independently or synergistically? Oncol Lett. 2017;13(5):2867-72.
165. Assidicky R, Tokat UM, Tarman IO, Saatci O, Ersan PG, Raza U, et al. Targeting HIF1-alpha/miR-326/ITGA5 axis potentiates chemotherapy response in triple-negative breast cancer. Breast Cancer Res Treat. 2022;193(2):331-48.
166. Howe GA, Addison CL. beta1 integrin: an emerging player in the modulation of tumorigenesis and response to therapy. Cell Adh Migr. 2012;6(2):71-7.
167. Yue J, Lopez JM. Understanding MAPK Signaling Pathways in Apoptosis. Int J Mol Sci. 2020;21(7).
168. Tian X, Traub B, Xie X, Zhou S, Henne-Bruns D, Knippschild U, et al. Opposing Oncogenic Functions of p38 Mitogen-activated Protein Kinase Alpha and Beta in Human Pancreatic Cancer Cells. Anticancer Res. 2020;40(10):5545-56.
169. Hart JR, Liao L, Yates JR, 3rd, Vogt PK. Essential role of Stat3 in PI3K-induced oncogenic transformation. Proc Natl Acad Sci U S A. 2011;108(32):13247-52.
170. Wang J, Lv X, Guo X, Dong Y, Peng P, Huang F, et al. Feedback activation of STAT3 limits the response to PI3K/AKT/mTOR inhibitors in PTEN-deficient cancer cells. Oncogenesis. 2021;10(1):8.
171. Oh HM, Yu CR, Dambuza I, Marrero B, Egwuagu CE. STAT3 protein interacts with Class O Forkhead transcription factors in the cytoplasm and regulates nuclear/cytoplasmic localization of FoxO1 and FoxO3a proteins in CD4(+) T cells. J Biol Chem. 2012;287(36):30436-43.
172. Bahar E, Kim JY, Yoon H. Chemotherapy Resistance Explained through Endoplasmic Reticulum Stress-Dependent Signaling. Cancers (Basel). 2019;11(3).
173. Shah MA, Schwartz GK. Cell cycle-mediated drug resistance: an emerging concept in cancer therapy. Clin Cancer Res. 2001;7(8):2168-81.
174. Hamed SS, Straubinger RM, Jusko WJ. Pharmacodynamic modeling of cell cycle and apoptotic effects of gemcitabine on pancreatic adenocarcinoma cells. Cancer Chemother Pharmacol. 2013;72(3):553-63.
175. Rudolph D, Steegmaier M, Hoffmann M, Grauert M, Baum A, Quant J, et al. BI 6727, a Polo-like kinase inhibitor with improved pharmacokinetic profile and broad antitumor activity. Clin Cancer Res. 2009;15(9):3094-102.
176. Dranitsaris G, Yu B, King J, Kaura S, Zhang A. Nab-paclitaxel, docetaxel, or solvent-based paclitaxel in metastatic breast cancer: a cost-utility analysis from a Chinese health care perspective. Clinicoecon Outcomes Res. 2015;7:249-56.
177. Freudlsperger C, Burnett JR, Friedman JA, Kannabiran VR, Chen Z, Van Waes C. EGFR-PI3K-AKT-mTOR signaling in head and neck squamous cell carcinomas: attractive targets for molecular-oriented therapy. Expert Opin Ther Targets. 2011;15(1):63-74.
178. Fatherree JP, Guarin JR, McGinn RA, Naber SP, Oudin MJ. Chemotherapy-Induced Collagen IV Drives Cancer Cell Motility through Activation of Src and Focal Adhesion Kinase. Cancer Res. 2022;82(10):2031-44.

179. Devarajan R, Peltoketo H, Izzi V, Ruotsalainen H, Kauppila S, Väisänen MR, et al. Collagen XVIII promotes breast cancer through EGFR/ErbB signaling and its ablation improves the efficacy of ErbB-targeting inhibitors. BioRxiv. 2022.
180. Taniguchi K, Xia L, Goldberg HJ, Lee KW, Shah A, Stavar L, et al. Inhibition of Src kinase blocks high glucose-induced EGFR transactivation and collagen synthesis in mesangial cells and prevents diabetic nephropathy in mice. Diabetes. 2013;62(11):3874-86.
181. David CJ, Huang YH, Chen M, Su J, Zou Y, Bardeesy N, et al. TGF-beta Tumor Suppression through a Lethal EMT. Cell. 2016;164(5):1015-30.
182. Fundytus A, Sengar M, Lombe D, Hopman W, Jalink M, Gyawali B, et al. Access to cancer medicines deemed essential by oncologists in 82 countries: an international, cross-sectional survey. Lancet Oncol. 2021;22(10):1367-77.
183. Vyatkin AD, Otnyukov DV, Leonov SV, Belikov AV. Comprehensive patient-level classification and quantification of driver events in TCGA PanCanAtlas cohorts. PLoS Genet. 2022;18(1):e1009996.
184. Iranzo J, Martincorena I, Koonin EV. Cancer-mutation network and the number and specificity of driver mutations. Proc Natl Acad Sci U S A. 2018;115(26):E6010-E9.
185. Shah SP, Roth A, Goya R, Oloumi A, Ha G, Zhao Y, et al. The clonal and mutational evolution spectrum of primary triple-negative breast cancers. Nature. 2012;486(7403):395-9.
186. Hoare JI, Hockings H, Saxena J, Silva VL, Haughey MJ, Wood GE, et al. A novel cell line panel reveals non-genetic mediators of platinum resistance and phenotypic diversity in high grade serous ovarian cancer. Gynecol Oncol. 2022.
187. Gillet JP, Varma S, Gottesman MM. The clinical relevance of cancer cell lines. J Natl Cancer Inst. 2013;105(7):452-8.
188. Niu N, Wang L. In vitro human cell line models to predict clinical response to anticancer drugs. Pharmacogenomics. 2015;16(3):273-85.
189. Michaelis M, Wass MN, Cinatl J. Drug-adapted cancer cell lines as preclinical models of acquired resistance. Cancer Drug Resist. 2019;2(3):447-56.
190. Amaral MVS, AJ DESP, EL DAS, L DEOS, JH DASM, MEA DEM, et al. Establishment of Drug-resistant Cell Lines as a Model in Experimental Oncology: A Review. Anticancer Res. 2019;39(12):6443-55.
191. Kagawa S, Takano S, Yoshitomi H, Kimura F, Satoh M, Shimizu H, et al. Akt/mTOR signaling pathway is crucial for gemcitabine resistance induced by Annexin II in pancreatic cancer cells. J Surg Res. 2012;178(2):758-67.
192. Shen S, Wang J, Zheng B, Tao Y, Li M, Wang Y, et al. LINC01714 Enhances Gemcitabine Sensitivity by Modulating FOXO3 Phosphorylation in Cholangiocarcinoma. Mol Ther Nucleic Acids. 2020;19:446-57.
193. Santo EE, Stroeken P, Sluis PV, Koster J, Versteeg R, Westerhout EM. FOXO3a is a major target of inactivation by PI3K/AKT signaling in aggressive neuroblastoma. Cancer Res. 2013;73(7):2189-98.
194. Elkabets M, Vora S, Juric D, Morse N, Mino-Kenudson M, Muranen T, et al. mTORC1 inhibition is required for sensitivity to PI3K p110alpha inhibitors in PIK3CA-mutant breast cancer. Sci Transl Med. 2013;5(196):196ra99.
195. Anderson GR, Wardell SE, Cakir M, Crawford L, Leeds JC, Nussbaum DP, et al. PIK3CA mutations enable targeting of a breast tumor dependency through mTOR-mediated MCL-1 translation. Sci Transl Med. 2016;8(369):369ra175.

196. Gu J, Huang W, Wang X, Zhang J, Tao T, Zheng Y, et al. Hsa-miR-3178/RhoB/PI3K/Akt, a novel signaling pathway regulates ABC transporters to reverse gemcitabine resistance in pancreatic cancer. Mol Cancer. 2022;21(1):112.
197. Cui J, Guo Y, Wu H, Xiong J, Peng T. Everolimus regulates the activity of gemcitabine-resistant pancreatic cancer cells by targeting the Warburg effect via PI3K/AKT/mTOR signaling. Mol Med. 2021;27(1):38.
198. Dong S, Liang S, Cheng Z, Zhang X, Luo L, Li L, et al. ROS/PI3K/Akt and Wnt/beta-catenin signalings activate HIF-1alpha-induced metabolic reprogramming to impart 5-fluorouracil resistance in colorectal cancer. J Exp Clin Cancer Res. 2022;41(1):15.
199. Tian L, Chen C, Guo Y, Zhang F, Mi J, Feng Q, et al. mTORC2 regulates ribonucleotide reductase to promote DNA replication and gemcitabine resistance in non-small cell lung cancer. Neoplasia. 2021;23(7):643-52.
200. Habiro A, Tanno S, Koizumi K, Izawa T, Nakano Y, Osanai M, et al. Involvement of p38 mitogen-activated protein kinase in gemcitabine-induced apoptosis in human pancreatic cancer cells. Biochem Biophys Res Commun. 2004;316(1):71-7.
201. Kao YT, Hsu WC, Hu HT, Hsu SH, Lin CS, Chiu CC, et al. Involvement of p38 mitogen-activated protein kinase in acquired gemcitabine-resistant human urothelial carcinoma sublines. Kaohsiung J Med Sci. 2014;30(7):323-30.
202. Suzuki S, Okada M, Shibuya K, Seino M, Sato A, Takeda H, et al. JNK suppression of chemotherapeutic agents-induced ROS confers chemoresistance on pancreatic cancer stem cells. Oncotarget. 2015;6(1):458-70.
203. Hu L, Liang Y, Wu K, Wang C, Zhang T, Peng R, et al. Repressing PDCD4 activates JNK/ABCG2 pathway to induce chemoresistance to fluorouracil in colorectal cancer cells. Ann Transl Med. 2021;9(2):114.
204. Martinez-Limon A, Joaquin M, Caballero M, Posas F, de Nadal E. The p38 Pathway: From Biology to Cancer Therapy. Int J Mol Sci. 2020;21(6).
205. Tournier C. The 2 Faces of JNK Signaling in Cancer. Genes Cancer. 2013;4(9-10):397-400.
206. Zhi Y, Zhou X, Yu J, Yuan L, Zhang H, Ng DCH, et al. Pathophysiological Significance of WDR62 and JNK Signaling in Human Diseases. Front Cell Dev Biol. 2021;9:640753.
207. Cabane C, Coldefy AS, Yeow K, Derijard B. The p38 pathway regulates Akt both at the protein and transcriptional activation levels during myogenesis. Cell Signal. 2004;16(12):1405-15.
208. Chen B, Liu J, Chang Q, Beezhold K, Lu Y, Chen F. JNK and STAT3 signaling pathways converge on Akt-mediated phosphorylation of EZH2 in bronchial epithelial cells induced by arsenic. Cell Cycle. 2013;12(1):112-21.
209. Shao Z, Bhattacharya K, Hsich E, Park L, Walters B, Germann U, et al. c-Jun N-terminal kinases mediate reactivation of Akt and cardiomyocyte survival after hypoxic injury in vitro and in vivo. Circ Res. 2006;98(1):111-8.
210. Xu W, Chen GS, Shao Y, Li XL, Xu HC, Zhang H, et al. Gastrin acting on the cholecystokinin2 receptor induces cyclooxygenase-2 expression through JAK2/STAT3/PI3K/Akt pathway in human gastric cancer cells. Cancer Lett. 2013;332(1):11-8.
211. Lee HJ, Zhuang G, Cao Y, Du P, Kim HJ, Settleman J. Drug resistance via feedback activation of Stat3 in oncogene-addicted cancer cells. Cancer Cell. 2014;26(2):207-21.

212. Heberle AM, Razquin Navas P, Langelaar-Makkinje M, Kasack K, Sadik A, Faessler E, et al. The PI3K and MAPK/p38 pathways control stress granule assembly in a hierarchical manner. Life Sci Alliance. 2019;2(2).
213. Rasool RU, Nayak D, Chakraborty S, Faheem MM, Rah B, Mahajan P, et al. AKT is indispensable for coordinating Par-4/JNK cross talk in p21 downmodulation during ER stress. Oncogenesis. 2017;6(5):e341.
214. Chakrabarty A, Chakraborty S, Bhattacharya R, Chowdhury G. Senescence-Induced Chemoresistance in Triple Negative Breast Cancer and Evolution-Based Treatment Strategies. Front Oncol. 2021;11:674354.
215. Xu Y, Li N, Xiang R, Sun P. Emerging roles of the p38 MAPK and PI3K/AKT/mTOR pathways in oncogene-induced senescence. Trends Biochem Sci. 2014;39(6):268-76.
216. Yang XL, Lin FJ, Guo YJ, Shao ZM, Ou ZL. Gemcitabine resistance in breast cancer cells regulated by PI3K/AKT-mediated cellular proliferation exerts negative feedback via the MEK/MAPK and mTOR pathways. Onco Targets Ther. 2014;7:1033-42.
217. Su P, Ahmad B, Zou K, Zou L. beta-Elemene Enhances the Chemotherapeutic Effect of 5-Fluorouracil in Triple-Negative Breast Cancer via PI3K/AKT, RAF-MEK-ErK, and NF-kappaB Signaling Pathways. Onco Targets Ther. 2020;13:5207-22.
218. Takahashi K, Tanaka M, Inagaki A, Wanibuchi H, Izumi Y, Miura K, et al. Establishment of a 5-fluorouracil-resistant triple-negative breast cancer cell line. Int J Oncol. 2013;43(6):1985-91.
219. Chen C, Zhao S, Zhao X, Cao L, Karnad A, Kumar AP, et al. Gemcitabine resistance of pancreatic cancer cells is mediated by IGF1R dependent upregulation of CD44 expression and isoform switching. Cell Death Dis. 2022;13(8):682.
220. Yoneyama H, Takizawa-Hashimoto A, Takeuchi O, Watanabe Y, Atsuda K, Asanuma F, et al. Acquired resistance to gemcitabine and cross-resistance in human pancreatic cancer clones. Anticancer Drugs. 2015;26(1):90-100.
221. Bergman AM, Giaccone G, van Moorsel CJ, Mauritz R, Noordhuis P, Pinedo HM, et al. Cross-resistance in the 2',2'-difluorodeoxycytidine (gemcitabine)-resistant human ovarian cancer cell line AG6000 to standard and investigational drugs. Eur J Cancer. 2000;36(15):1974-83.
222. Csoka K, Liliemark J, Larsson R, Nygren P. Evaluation of the cytotoxic activity of gemcitabine in primary cultures of tumor cells from patients with hematologic or solid tumors. Semin Oncol. 1995;22(4 Suppl 11):47-53.
223. Canonici A, Browne AL, Ibrahim MFK, Fanning KP, Roche S, Conlon NT, et al. Combined targeting EGFR and SRC as a potential novel therapeutic approach for the treatment of triple negative breast cancer. Ther Adv Med Oncol. 2020;12:1758835919897546.
224. Lin PH, Tseng LM, Lee YH, Chen ST, Yeh DC, Dai MS, et al. Neoadjuvant afatinib with paclitaxel for triple-negative breast cancer and the molecular characteristics in responders and non-responders. J Formos Med Assoc. 2022.
225. El Guerrab A, Bamdad M, Bignon YJ, Penault-Llorca F, Aubel C. Co-targeting EGFR and mTOR with gefitinib and everolimus in triple-negative breast cancer cells. Sci Rep. 2020;10(1):6367.
226. Roskoski R, Jr. Src kinase regulation by phosphorylation and dephosphorylation. Biochem Biophys Res Commun. 2005;331(1):1-14.

227. Sutton P, Borgia JA, Bonomi P, Plate JM. Lyn, a Src family kinase, regulates activation of epidermal growth factor receptors in lung adenocarcinoma cells. Mol Cancer. 2013;12:76.
228. Watson LJ, Alexander KM, Mohan ML, Bowman AL, Mangmool S, Xiao K, et al. Phosphorylation of Src by phosphoinositide 3-kinase regulates beta-adrenergic receptor-mediated EGFR transactivation. Cell Signal. 2016;28(10):1580-92.
229. Jones MC, Askari JA, Humphries JD, Humphries MJ. Cell adhesion is regulated by CDK1 during the cell cycle. J Cell Biol. 2018;217(9):3203-18.
230. Tai YL, Chu PY, Lai IR, Wang MY, Tseng HY, Guan JL, et al. An EGFR/Src-dependent beta4 integrin/FAK complex contributes to malignancy of breast cancer. Sci Rep. 2015;5:16408.
231. Kenchappa RS, Dovas A, Argenziano MG, Meyer CT, Stopfer LE, Banu MA, et al. Activation of STAT3 through combined SRC and EGFR signaling drives resistance to a mitotic kinesin inhibitor in glioblastoma. Cell Rep. 2022;39(12):110991.
232. Moiseeva EP, Heukers R, Manson MM. EGFR and Src are involved in indole-3-carbinol-induced death and cell cycle arrest of human breast cancer cells. Carcinogenesis. 2007;28(2):435-45.
233. Formisano L, D'Amato V, Servetto A, Brillante S, Raimondo L, Di Mauro C, et al. Src inhibitors act through different mechanisms in Non-Small Cell Lung Cancer models depending on EGFR and RAS mutational status. Oncotarget. 2015;6(28):26090-103.
234. Tegze B, Szallasi Z, Haltrich I, Penzvalto Z, Toth Z, Liko I, et al. Parallel evolution under chemotherapy pressure in 29 breast cancer cell lines results in dissimilar mechanisms of resistance. PLoS One. 2012;7(2):e30804.
235. Kenicer J, Spears M, Lyttle N, Taylor KJ, Liao L, Cunningham CA, et al. Molecular characterisation of isogenic taxane resistant cell lines identify novel drivers of drug resistance. BMC Cancer. 2014;14:762.
236. Ajabnoor GM, Crook T, Coley HM. Paclitaxel resistance is associated with switch from apoptotic to autophagic cell death in MCF-7 breast cancer cells. Cell Death Dis. 2012;3:e260.
237. Aldonza MB, Hong JY, Alinsug MV, Song J, Lee SK. Multiplicity of acquired cross-resistance in paclitaxel-resistant cancer cells is associated with feedback control of TUBB3 via FOXO3a-mediated ABCB1 regulation. Oncotarget. 2016;7(23):34395-419.
238. Ferreira JA, Peixoto A, Neves M, Gaiteiro C, Reis CA, Assaraf YG, et al. Mechanisms of cisplatin resistance and targeting of cancer stem cells: Adding glycosylation to the equation. Drug Resist Updat. 2016;24:34-54.
239. Xia A, Li H, Li R, Lu L, Wu X. Co-treatment with BEZ235 enhances chemosensitivity of A549/DDP cells to cisplatin via inhibition of PI3K/Akt/mTOR signaling and downregulation of ERCC1 expression. Oncol Rep. 2018;40(4):2353-62.
240. Moon du G, Lee SE, Oh MM, Lee SC, Jeong SJ, Hong SK, et al. NVP-BEZ235, a dual PI3K/mTOR inhibitor synergistically potentiates the antitumor effects of cisplatin in bladder cancer cells. Int J Oncol. 2014;45(3):1027-35.
241. Huang JC, Cui ZF, Chen SM, Yang LJ, Lian HK, Liu B, et al. NVP-BEZ235 synergizes cisplatin sensitivity in osteosarcoma. Oncotarget. 2018;9(12):10483-96.
242. Hsu CM, Lin PM, Tsai YT, Tsai MS, Tseng CH, Lin SF, et al. NVP-BEZ235, a dual PI3K-mTOR inhibitor, suppresses the growth of FaDu hypopharyngeal

squamous cell carcinoma and has a synergistic effect with Cisplatin. Cell Death Discov. 2018;4:57.
243. Rodriguez-Garcia ME, Quiroga AG, Castro J, Ortiz A, Aller P, Mata F. Inhibition of p38-MAPK potentiates cisplatin-induced apoptosis via GSH depletion and increases intracellular drug accumulation in growth-arrested kidney tubular epithelial cells. Toxicol Sci. 2009;111(2):413-23.
244. Pereira L, Igea A, Canovas B, Dolado I, Nebreda AR. Inhibition of p38 MAPK sensitizes tumour cells to cisplatin-induced apoptosis mediated by reactive oxygen species and JNK. EMBO Mol Med. 2013;5(11):1759-74.
245. Diaz Osterman CJ, Ozmadenci D, Kleinschmidt EG, Taylor KN, Barrie AM, Jiang S, et al. FAK activity sustains intrinsic and acquired ovarian cancer resistance to platinum chemotherapy. Elife. 2019;8.
246. Zhang S, Ma H, Zhang D, Xie S, Wang W, Li Q, et al. LncRNA KCNQ1OT1 regulates proliferation and cisplatin resistance in tongue cancer via miR-211-5p mediated Ezrin/Fak/Src signaling. Cell Death Dis. 2018;9(7):742.
247. Hamaguchi K, Godwin AK, Yakushiji M, O'Dwyer PJ, Ozols RF, Hamilton TC. Cross-resistance to diverse drugs is associated with primary cisplatin resistance in ovarian cancer cell lines. Cancer Res. 1993;53(21):5225-32.
248. Stordal B, Hamon M, McEneaney V, Roche S, Gillet JP, O'Leary JJ, et al. Resistance to paclitaxel in a cisplatin-resistant ovarian cancer cell line is mediated by P-glycoprotein. PLoS One. 2012;7(7):e40717.
249. Januchowski R, Wojtowicz K, Sujka-Kordowska P, Andrzejewska M, Zabel M. MDR gene expression analysis of six drug-resistant ovarian cancer cell lines. Biomed Res Int. 2013;2013:241763.
250. Berrazouane S, Boisvert M, Salti S, Mourad W, Al-Daccak R, Barabe F, et al. Beta1 integrin blockade overcomes doxorubicin resistance in human T-cell acute lymphoblastic leukemia. Cell Death Dis. 2019;10(5):357.
251. Naci D, El Azreq MA, Chetoui N, Lauden L, Sigaux F, Charron D, et al. alpha2beta1 integrin promotes chemoresistance against doxorubicin in cancer cells through extracellular signal-regulated kinase (ERK). J Biol Chem. 2012;287(21):17065-76.
252. Deng L, Jin K, Zhou X, Zhang Z, Ge L, Xiong X, et al. Blockade of integrin signaling reduces chemotherapy-induced premature senescence in collagen cultured bladder cancer cells. Precis Clin Med. 2022;5(2):pbac007.
253. Brozovic A, Majhen D, Roje V, Mikac N, Jakopec S, Fritz G, et al. alpha(v)beta(3) Integrin-mediated drug resistance in human laryngeal carcinoma cells is caused by glutathione-dependent elimination of drug-induced reactive oxidative species. Mol Pharmacol. 2008;74(1):298-306.
254. Yu M, Zou Q, Wu X, Han G, Tong X. Connexin 32 affects doxorubicin resistance in hepatocellular carcinoma cells mediated by Src/FAK signaling pathway. Biomed Pharmacother. 2017;95:1844-52.
255. Dragoj M, Milosevic Z, Bankovic J, Tanic N, Pesic M, Stankovic T. Targeting CXCR4 and FAK reverses doxorubicin resistance and suppresses invasion in non-small cell lung carcinoma. Cell Oncol (Dordr). 2017;40(1):47-62.
256. Wallin JJ, Guan J, Prior WW, Edgar KA, Kassees R, Sampath D, et al. Nuclear phospho-Akt increase predicts synergy of PI3K inhibition and doxorubicin in breast and ovarian cancer. Sci Transl Med. 2010;2(48):48ra66.

257. Simioni C, Neri LM, Tabellini G, Ricci F, Bressanin D, Chiarini F, et al. Cytotoxic activity of the novel Akt inhibitor, MK-2206, in T-cell acute lymphoblastic leukemia. Leukemia. 2012;26(11):2336-42.
258. Jin P, Wong CC, Mei S, He X, Qian Y, Sun L. MK-2206 co-treatment with 5-fluorouracil or doxorubicin enhances chemosensitivity and apoptosis in gastric cancer by attenuation of Akt phosphorylation. Onco Targets Ther. 2016;9:4387-96.
259. Hirai H, Sootome H, Nakatsuru Y, Miyama K, Taguchi S, Tsujioka K, et al. MK-2206, an allosteric Akt inhibitor, enhances antitumor efficacy by standard chemotherapeutic agents or molecular targeted drugs in vitro and in vivo. Mol Cancer Ther. 2010;9(7):1956-67.
260. McLean BA, Patel VB, Zhabyeyev P, Chen X, Basu R, Wang F, et al. PI3Kalpha Pathway Inhibition With Doxorubicin Treatment Results in Distinct Biventricular Atrophy and Remodeling With Right Ventricular Dysfunction. J Am Heart Assoc. 2019;8(9):e010961.
261. Yuan Y, Wen W, Yost SE, Xing Q, Yan J, Han ES, et al. Combination therapy with BYL719 and LEE011 is synergistic and causes a greater suppression of p-S6 in triple negative breast cancer. Sci Rep. 2019;9(1):7509.
262. Johnson RK, Chitnis MP, Embrey WM, Gregory EB. In vivo characteristics of resistance and cross-resistance of an adriamycin-resistant subline of P388 leukemia. Cancer Treat Rep. 1978;62(10):1535-47.
263. Duan Z, Choy E, Jimeno JM, Cuevas Cdel M, Mankin HJ, Hornicek FJ. Diverse cross-resistance phenotype to ET-743 and PM00104 in multi-drug resistant cell lines. Cancer Chemother Pharmacol. 2009;63(6):1121-9.
264. Rana S, Mallareddy JR, Singh S, Boghean L, Natarajan A. Inhibitors, PROTACs and Molecular Glues as Diverse Therapeutic Modalities to Target Cyclin-Dependent Kinase. Cancers (Basel). 2021;13(21).
265. Chow RD, Chen S. Cancer CRISPR Screens In Vivo. Trends Cancer. 2018;4(5):349-58.
266. Mendez-Pertuz M, Martinez P, Blanco-Aparicio C, Gomez-Casero E, Belen Garcia A, Martinez-Torrecuadrada J, et al. Modulation of telomere protection by the PI3K/AKT pathway. Nat Commun. 2017;8(1):1278.
267. Wang D, Xu J, Liu B, He X, Zhou L, Hu X, et al. IL6 blockade potentiates the anti-tumor effects of gamma-secretase inhibitors in Notch3-expressing breast cancer. Cell Death Differ. 2018;25(2):330-9.
268. Ruiz de Garibay G, Mateo F, Stradella A, Valdes-Mas R, Palomero L, Serra-Musach J, et al. Tumor xenograft modeling identifies an association between TCF4 loss and breast cancer chemoresistance. Dis Model Mech. 2018;11(5).
269. Kanaya N, Somlo G, Wu J, Frankel P, Kai M, Liu X, et al. Characterization of patient-derived tumor xenografts (PDXs) as models for estrogen receptor positive (ER+HER2- and ER+HER2+) breast cancers. J Steroid Biochem Mol Biol. 2017;170:65-74.
270. Contreras-Zarate MJ, Ormond DR, Gillen AE, Hanna C, Day NL, Serkova NJ, et al. Development of Novel Patient-Derived Xenografts from Breast Cancer Brain Metastases. Front Oncol. 2017;7:252.
271. Hu Y, Yague E, Zhao J, Wang L, Bai J, Yang Q, et al. Sabutoclax, pan-active BCL-2 protein family antagonist, overcomes drug resistance and eliminates cancer stem cells in breast cancer. Cancer Lett. 2018;423:47-59.
272. Murayama T, Gotoh N. Patient-Derived Xenograft Models of Breast Cancer and Their Application. Cells. 2019;8(6).

CHAPTER 5

APPENDIX

5.1 Copyright Permissions

For Figure 1.1

JOHN WILEY AND SONS LICENSE
TERMS AND CONDITIONS

Sep 10, 2022

This Agreement between Mr. Ünal Tokat ("You") and John Wiley and Sons ("John Wiley and Sons") consists of your license details and the terms and conditions provided by John Wiley and Sons and Copyright Clearance Center.

License Number	5385390569315
License date	Sep 10, 2022
Licensed Content Publisher	John Wiley and Sons
Licensed Content Publication	CA: A Cancer Journal for Clinicians
Licensed Content Title	Cancer statistics, 2022
Licensed Content Author	Ahmedin Jemal, Hannah E. Fuchs, Kimberly D. Miller, et al
Licensed Content Date	Jan 12, 2022
Licensed Content Volume	72
Licensed Content Issue	1
Licensed Content Pages	27
Type of Use	Dissertation/Thesis
Requestor type	University/Academic
Format	Print and electronic
Portion	Figure/table
Number of figures/tables	1
Will you be translating?	No
Title	Identification Of Actionable Drug Targets In Triple-Negative Breast Cancer
Institution name	Bilkent University
Expected presentation date	Sep 2022
Portions	Figure 1
Requestor Location	Mr. Ünal Tokat Bilkent University Main Campus Faculty of Science - Department of Molecular Biology and Genetics Room SB-252 Ankara, other Turkey Attn: Mr. Ünal Tokat
Publisher Tax ID	EU826007151
Total	**0.00 USD**
Terms and Conditions	

TERMS AND CONDITIONS

This copyrighted material is owned by or exclusively licensed to John Wiley & Sons, Inc. or one of its group companies (each a"Wiley Company") or handled on behalf of a society with which a Wiley Company has exclusive publishing rights in relation to a particular work (collectively "WILEY"). By clicking "accept" in connection with completing this licensing transaction, you agree that the following terms and conditions apply to this transaction (along with the billing and payment terms and conditions established by the Copyright Clearance Center Inc., ("CCC's Billing and Payment terms and conditions"), at the time that you opened your RightsLink account (these are available at any time at http://myaccount.copyright.com).

Terms and Conditions

- The materials you have requested permission to reproduce or reuse (the "Wiley Materials") are protected by copyright.
- You are hereby granted a personal, non-exclusive, non-sub licensable (on a stand-alone basis), non-transferable, worldwide, limited license to reproduce the Wiley Materials for the purpose specified in the licensing process. This license, **and any CONTENT (PDF or image file) purchased as part of your order**, is for a one-time use only and limited to any maximum distribution number specified in the license. The first instance of republication or reuse granted by this license must be completed within two years of the date of the grant of this license (although copies prepared before the end date may be distributed thereafter). The Wiley Materials shall not be used in any other manner or for any other purpose, beyond what is granted in the license. Permission is granted subject to an appropriate acknowledgement given to the author, title of the material/book/journal and the publisher. You shall also duplicate the copyright notice that appears in the Wiley publication in your use of the Wiley Material. Permission is also granted on the understanding that nowhere in the text is a previously published source acknowledged for all or part of this Wiley Material. Any third party content is expressly excluded from this permission.
- With respect to the Wiley Materials, all rights are reserved. Except as expressly granted by the terms of the license, no part of the Wiley Materials may be copied, modified, adapted (except for minor reformatting required by the new Publication), translated, reproduced, transferred or distributed, in any form or by any means, and no derivative works may be made based on the Wiley Materials without the prior permission of the respective copyright owner.**For STM Signatory Publishers clearing permission under the terms of the STM Permissions Guidelines only, the terms of the license are extended to include subsequent editions and for editions in other languages, provided such editions are for the work as a whole in situ and does not involve the separate exploitation of the permitted figures or extracts,** You may not alter, remove or suppress in any manner any copyright, trademark or other notices displayed by the Wiley Materials. You may not license, rent, sell, loan, lease, pledge, offer as security, transfer or assign the Wiley Materials on a stand-alone basis, or any of

the rights granted to you hereunder to any other person.

- The Wiley Materials and all of the intellectual property rights therein shall at all times remain the exclusive property of John Wiley & Sons Inc, the Wiley Companies, or their respective licensors, and your interest therein is only that of having possession of and the right to reproduce the Wiley Materials pursuant to Section 2 herein during the continuance of this Agreement. You agree that you own no right, title or interest in or to the Wiley Materials or any of the intellectual property rights therein. You shall have no rights hereunder other than the license as provided for above in Section 2. No right, license or interest to any trademark, trade name, service mark or other branding ("Marks") of WILEY or its licensors is granted hereunder, and you agree that you shall not assert any such right, license or interest with respect thereto
- NEITHER WILEY NOR ITS LICENSORS MAKES ANY WARRANTY OR REPRESENTATION OF ANY KIND TO YOU OR ANY THIRD PARTY, EXPRESS, IMPLIED OR STATUTORY, WITH RESPECT TO THE MATERIALS OR THE ACCURACY OF ANY INFORMATION CONTAINED IN THE MATERIALS, INCLUDING, WITHOUT LIMITATION, ANY IMPLIED WARRANTY OF MERCHANTABILITY, ACCURACY, SATISFACTORY QUALITY, FITNESS FOR A PARTICULAR PURPOSE, USABILITY, INTEGRATION OR NON-INFRINGEMENT AND ALL SUCH WARRANTIES ARE HEREBY EXCLUDED BY WILEY AND ITS LICENSORS AND WAIVED BY YOU.
- WILEY shall have the right to terminate this Agreement immediately upon breach of this Agreement by you.
- You shall indemnify, defend and hold harmless WILEY, its Licensors and their respective directors, officers, agents and employees, from and against any actual or threatened claims, demands, causes of action or proceedings arising from any breach of this Agreement by you.
- IN NO EVENT SHALL WILEY OR ITS LICENSORS BE LIABLE TO YOU OR ANY OTHER PARTY OR ANY OTHER PERSON OR ENTITY FOR ANY SPECIAL, CONSEQUENTIAL, INCIDENTAL, INDIRECT, EXEMPLARY OR PUNITIVE DAMAGES, HOWEVER CAUSED, ARISING OUT OF OR IN CONNECTION WITH THE DOWNLOADING, PROVISIONING, VIEWING OR USE OF THE MATERIALS REGARDLESS OF THE FORM OF ACTION, WHETHER FOR BREACH OF CONTRACT, BREACH OF WARRANTY, TORT, NEGLIGENCE, INFRINGEMENT OR OTHERWISE (INCLUDING, WITHOUT LIMITATION, DAMAGES BASED ON LOSS OF PROFITS, DATA, FILES, USE, BUSINESS OPPORTUNITY OR CLAIMS OF THIRD PARTIES), AND WHETHER OR NOT THE PARTY HAS BEEN ADVISED OF THE POSSIBILITY OF SUCH DAMAGES. THIS LIMITATION SHALL APPLY NOTWITHSTANDING ANY FAILURE OF ESSENTIAL PURPOSE OF ANY LIMITED REMEDY PROVIDED HEREIN.
- Should any provision of this Agreement be held by a court of competent jurisdiction to be illegal, invalid, or unenforceable, that provision shall be deemed amended to achieve as nearly as possible the same economic effect as the original provision, and the legality, validity and enforceability of the remaining provisions of this Agreement shall not be affected or impaired thereby.
- The failure of either party to enforce any term or condition of this Agreement shall not constitute a waiver of either party's right to enforce each and every term and condition of this Agreement. No breach under this agreement shall be deemed waived or excused by either party unless such waiver or consent is in writing signed by the party granting such waiver or consent. The waiver by or consent of a party to a breach of any provision of this Agreement shall not operate or be construed as a waiver of or consent to any other or subsequent breach by such other party.
- This Agreement may not be assigned (including by operation of law or otherwise) by you without WILEY's prior written consent.
- Any fee required for this permission shall be non-refundable after thirty (30) days from receipt by the CCC.
- These terms and conditions together with CCC's Billing and Payment terms and conditions (which are incorporated herein) form the entire agreement between you and WILEY concerning this licensing transaction and (in the absence of fraud) supersedes all prior agreements and representations of the parties, oral or written. This Agreement may not be amended except in writing signed by both parties. This Agreement shall be binding upon and inure to the benefit of the parties' successors, legal representatives, and authorized assigns.
- In the event of any conflict between your obligations established by these terms and conditions and those established by CCC's Billing and Payment terms and conditions, these terms and conditions shall prevail.
- WILEY expressly reserves all rights not specifically granted in the combination of (i) the license details provided by you and accepted in the course of this licensing transaction, (ii) these terms and conditions and (iii) CCC's Billing and Payment terms and conditions.
- This Agreement will be void if the Type of Use, Format, Circulation, or Requestor Type was misrepresented during the licensing process.
- This Agreement shall be governed by and construed in accordance with the laws of the State of New York, USA, without regards to such state's conflict of law rules. Any legal action, suit or proceeding arising out of or relating to these Terms and Conditions or the breach thereof shall be instituted in a court of competent jurisdiction in New York County in the State of New York in the United States of America and each party hereby consents and submits to the personal jurisdiction of such court, waives any objection to venue in such court and consents to service of process by registered or certified mail, return receipt requested, at the last known address of such party.

WILEY OPEN ACCESS TERMS AND CONDITIONS

Wiley Publishes Open Access Articles in fully Open Access Journals and in Subscription journals offering Online Open. Although most of the fully Open Access journals publish open access articles under the terms of the Creative Commons Attribution (CC BY) License only, the subscription journals and a few of the Open Access Journals offer a choice of Creative Commons Licenses. The license type is clearly identified on the article.

The Creative Commons Attribution License

The Creative Commons Attribution License (CC-BY) allows users to copy, distribute and transmit an article, adapt the article and make commercial use of the article. The CC-BY license permits commercial and non-

Creative Commons Attribution Non-Commercial License

The Creative Commons Attribution Non-Commercial (CC-BY-NC)License permits use, distribution and reproduction in any medium, provided the original work is properly cited and is not used for commercial purposes.(see below)

Creative Commons Attribution-Non-Commercial-NoDerivs License

The Creative Commons Attribution Non-Commercial-NoDerivs License (CC-BY-NC-ND) permits use, distribution and reproduction in any medium, provided the original work is properly cited, is not used for commercial purposes and no modifications or adaptations are made. (see below)

Use by commercial "for-profit" organizations

Use of Wiley Open Access articles for commercial, promotional, or marketing purposes requires further explicit permission from Wiley and will be subject to a fee. Further details can be found on Wiley Online Library http://olabout.wiley.com/WileyCDA/Section/id-410895.html

Other Terms and Conditions:

v1.10 Last updated September 2015

Questions? customercare@copyright.com or +1-855-239-3415 (toll free in the US) or +1-978-646-2777.

For Figure 1.2

ELSEVIER LICENSE
TERMS AND CONDITIONS

Sep 10, 2022

This Agreement between Mr. Ünal Tokat ("You") and Elsevier ("Elsevier") consists of your license details and the terms and conditions provided by Elsevier and Copyright Clearance Center.

License Number	5385390743725
License date	Sep 10, 2022
Licensed Content Publisher	Elsevier
Licensed Content Publication	The Lancet
Licensed Content Title	Variations in common diseases, hospital admissions, and deaths in middle-aged adults in 21 countries from five continents (PURE): a prospective cohort study
Licensed Content Author	Gilles R Dagenais,Darryl P Leong,Sumathy Rangarajan,Fernando Lanas,Patricio Lopez-Jaramillo,Rajeev Gupta,Rafael Diaz,Alvaro Avezum,Gustavo B F Oliveira,Andreas Wielgosz,Shameena R Parambath,Prem Mony,Khalid F Alhabib,Ahmet Temizhan et al.
Licensed Content Date	7–13 March 2020
Licensed Content Volume	395
Licensed Content Issue	10226
Licensed Content Pages	10
Start Page	785
End Page	794
Type of Use	reuse in a thesis/dissertation
Portion	figures/tables/illustrations
Number of figures/tables/illustrations	1
Format	both print and electronic
Are you the author of this Elsevier article?	No
Will you be translating?	No
Title	Identification Of Actionable Drug Targets in Triple-Negative Breast Cancer
Institution name	Bilkent University
Expected presentation date	Sep 2022
Portions	Figure 3
Requestor Location	Mr. Ünal Tokat Bilkent University Main Campus Faculty of Science - Department of Molecular Biology and Genetics Room SB-252 Ankara, other Turkey Attn: Mr. Ünal Tokat
Publisher Tax ID	GB 494 6272 12
Total	**0.00 USD**
Terms and Conditions	

INTRODUCTION

1. The publisher for this copyrighted material is Elsevier. By clicking "accept" in connection with completing this licensing transaction, you agree that the following terms and conditions apply to this transaction (along with the Billing and Payment terms and conditions established by Copyright Clearance Center, Inc. ("CCC"), at the time that you opened your Rightslink account and that are available at any time at http://myaccount.copyright.com).

GENERAL TERMS

2. Elsevier hereby grants you permission to reproduce the aforementioned material subject to the terms and conditions indicated.
3. Acknowledgement: If any part of the material to be used (for example, figures) has appeared in our publication with credit or acknowledgement to another source, permission must also be sought from that source. If such permission is not obtained then that material may not be included in your publication/copies. Suitable acknowledgement to the source must be made, either as a footnote or in a reference list at the end of your publication, as follows:
"Reprinted from Publication title, Vol /edition number, Author(s), Title of article / title of chapter, Pages No., Copyright (Year), with permission from Elsevier [OR APPLICABLE SOCIETY COPYRIGHT OWNER]." Also Lancet special credit - "Reprinted from The Lancet, Vol. number, Author(s), Title of article, Pages No., Copyright (Year), with permission from Elsevier."
4. Reproduction of this material is confined to the purpose and/or media for which permission is hereby given.
5. Altering/Modifying Material: Not Permitted. However figures and illustrations may be altered/adapted minimally to serve your work. Any other abbreviations, additions, deletions and/or any other alterations shall be made only with prior written authorization of Elsevier Ltd. (Please contact Elsevier's permissions helpdesk here). No modifications can be made to any Lancet figures/tables and they must be reproduced in full.
6. If the permission fee for the requested use of our material is waived in this instance, please be advised that your future requests for Elsevier materials may attract a fee.
7. Reservation of Rights: Publisher reserves all rights not specifically granted in the combination of (i) the license details provided by you and accepted in the course of this licensing transaction, (ii) these terms and conditions and (iii) CCC's Billing and Payment terms and conditions.

8. License Contingent Upon Payment: While you may exercise the rights licensed immediately upon issuance of the license at the end of the licensing process for the transaction, provided that you have disclosed complete and accurate details of your proposed use, no license is finally effective unless and until full payment is received from you (either by publisher or by CCC) as provided in CCC's Billing and Payment terms and conditions. If full payment is not received on a timely basis, then any license preliminarily granted shall be deemed automatically revoked and shall be void as if never granted. Further, in the event that you breach any of these terms and conditions or any of CCC's Billing and Payment terms and conditions, the license is automatically revoked and shall be void as if never granted. Use of materials as described in a revoked license, as well as any use of the materials beyond the scope of an unrevoked license, may constitute copyright infringement and publisher reserves the right to take any and all action to protect its copyright in the materials.
9. Warranties: Publisher makes no representations or warranties with respect to the licensed material.
10. Indemnity: You hereby indemnify and agree to hold harmless publisher and CCC, and their respective officers, directors, employees and agents, from and against any and all claims arising out of your use of the licensed material other than as specifically authorized pursuant to this license.
11. No Transfer of License: This license is personal to you and may not be sublicensed, assigned, or transferred by you to any other person without publisher's written permission.
12. No Amendment Except in Writing: This license may not be amended except in a writing signed by both parties (or, in the case of publisher, by CCC on publisher's behalf).
13. Objection to Contrary Terms: Publisher hereby objects to any terms contained in any purchase order, acknowledgment, check endorsement or other writing prepared by you, which terms are inconsistent with these terms and conditions or CCC's Billing and Payment terms and conditions. These terms and conditions, together with CCC's Billing and Payment terms and conditions (which are incorporated herein), comprise the entire agreement between you and publisher (and CCC) concerning this licensing transaction. In the event of any conflict between your obligations established by these terms and conditions and those established by CCC's Billing and Payment terms and conditions, these terms and conditions shall control.
14. Revocation: Elsevier or Copyright Clearance Center may deny the permissions described in this License at their sole discretion, for any reason or no reason, with a full refund payable to you. Notice of such denial will be made using the contact information provided by you. Failure to receive such notice will not alter or invalidate the denial. In no event will Elsevier or Copyright Clearance Center be responsible or liable for any costs, expenses or damage incurred by you as a result of a denial of your permission request, other than a refund of the amount(s) paid by you to Elsevier and/or Copyright Clearance Center for denied permissions.

LIMITED LICENSE

The following terms and conditions apply only to specific license types:
15. **Translation**: This permission is granted for non-exclusive world **English** rights only unless your license was granted for translation rights. If you licensed translation rights you may only translate this content into the languages you requested. A professional translator must perform all translations and reproduce the content word for word preserving the integrity of the article.
16. **Posting licensed content on any Website**: The following terms and conditions apply as follows: Licensing material from an Elsevier journal: All content posted to the web site must maintain the copyright information line on the bottom of each image; A hyper-text must be included to the Homepage of the journal from which you are licensing at http://www.sciencedirect.com/science/journal/xxxxx or the Elsevier homepage for books at http://www.elsevier.com; Central Storage: This license does not include permission for a scanned version of the material to be stored in a central repository such as that provided by Heron/XanEdu.
Licensing material from an Elsevier book: A hyper-text link must be included to the Elsevier homepage at http://www.elsevier.com . All content posted to the web site must maintain the copyright information line on the bottom of each image.

Posting licensed content on Electronic reserve: In addition to the above the following clauses are applicable: The web site must be password-protected and made available only to bona fide students registered on a relevant course. This permission is granted for 1 year only. You may obtain a new license for future website posting.
17. **For journal authors**: the following clauses are applicable in addition to the above:
Preprints:
A preprint is an author's own write-up of research results and analysis, it has not been peer-reviewed, nor has it had any other value added to it by a publisher (such as formatting, copyright, technical enhancement etc.).
Authors can share their preprints anywhere at any time. Preprints should not be added to or enhanced in any way in order to appear more like, or to substitute for, the final versions of articles however authors can update their preprints on arXiv or RePEc with their Accepted Author Manuscript (see below).
If accepted for publication, we encourage authors to link from the preprint to their formal publication via its DOI. Millions of researchers have access to the formal publications on ScienceDirect, and so links will help users to find, access, cite and use the best available version. Please note that Cell Press, The Lancet and some society-owned have different preprint policies. Information on these policies is available on the journal homepage.
Accepted Author Manuscripts: An accepted author manuscript is the manuscript of an article that has been accepted for publication and which typically includes author-incorporated changes suggested during submission, peer review and editor-author communications.
Authors can share their accepted author manuscript:

- immediately
  - via their non-commercial person homepage or blog
  - by updating a preprint in arXiv or RePEc with the accepted manuscript
  - via their research institute or institutional repository for internal institutional uses or as part of an invitation-only research collaboration work-group
  - directly by providing copies to their students or to research collaborators for their personal use
  - for private scholarly sharing as part of an invitation-only work group on commercial sites with which Elsevier has an agreement
- After the embargo period
  - via non-commercial hosting platforms such as their institutional repository
  - via commercial sites with which Elsevier has an agreement

In all cases accepted manuscripts should:

- link to the formal publication via its DOI
- bear a CC-BY-NC-ND license - this is easy to do
- if aggregated with other manuscripts, for example in a repository or other site, be shared in alignment with our hosting policy not be added to or enhanced in any way to appear more like, or to substitute for, the published journal article.

Published journal article (JPA): A published journal article (PJA) is the definitive final record of published research that appears or will appear in the journal and embodies all value-adding publishing activities including peer review co-ordination, copy-editing, formatting, (if relevant) pagination and online enrichment.
Policies for sharing publishing journal articles differ for subscription and gold open access articles:
Subscription Articles: If you are an author, please share a link to your article rather than the full-text. Millions of researchers have access to the formal publications on ScienceDirect, and so links will help your users to find, access, cite, and use the best available version.
Theses and dissertations which contain embedded PJAs as part of the formal submission can be posted publicly by the awarding institution with DOI links back to the formal publications on ScienceDirect.
If you are affiliated with a library that subscribes to ScienceDirect you have additional private sharing rights for others' research accessed under that agreement. This includes use for classroom teaching and internal training at the institution (including use in course packs and courseware programs), and inclusion of the article for grant funding purposes.

Gold Open Access Articles: May be shared according to the author-selected end-user license and should contain a CrossMark logo, the end user license, and a DOI link to the formal publication on ScienceDirect.
Please refer to Elsevier's posting policy for further information.
18. **For book authors** the following clauses are applicable in addition to the above: Authors are permitted to place a brief summary of their work online only. You are not allowed to download and post the published electronic version of your chapter, nor may you scan the printed edition to create an electronic version. **Posting to a repository:** Authors are permitted to post a summary of their chapter only in their institution's repository.
19. **Thesis/Dissertation:** If your license is for use in a thesis/dissertation your thesis may be submitted to your institution in either print or electronic form. Should your thesis be published commercially, please reapply for permission. These requirements include permission for the Library and Archives of Canada to supply single copies, on demand, of the complete thesis and include permission for Proquest/UMI to supply single copies, on demand, of the complete thesis. Should your thesis be published commercially, please reapply for permission. Theses and dissertations which contain embedded PJAs as part of the formal submission can be posted publicly by the awarding institution with DOI links back to the formal publications on ScienceDirect.

Elsevier Open Access Terms and Conditions
You can publish open access with Elsevier in hundreds of open access journals or in nearly 2000 established subscription journals that support open access publishing. Permitted third party re-use of these open access articles is defined by the author's choice of Creative Commons user license. See our open access license policy for more information.
Terms & Conditions applicable to all Open Access articles published with Elsevier:
Any reuse of the article must not represent the author as endorsing the adaptation of the article nor should the article be modified in such a way as to damage the author's honour or reputation. If any changes have been made, such changes must be clearly indicated.
The author(s) must be appropriately credited and we ask that you include the end user license and a DOI link to the formal publication on ScienceDirect.
If any part of the material to be used (for example, figures) has appeared in our publication with credit or acknowledgement to another source it is the responsibility of the user to ensure their reuse complies with the terms and conditions determined by the rights holder.
Additional Terms & Conditions applicable to each Creative Commons user license:
CC BY: The CC-BY license allows users to copy, to create extracts, abstracts and new works from the Article, to alter and revise the Article and to make commercial use of the Article (including reuse and/or resale of the Article by commercial entities), provided the user gives appropriate credit (with a link to the formal publication through the relevant DOI), provides a link to the license, indicates if changes were made and the licensor is not represented as endorsing the use made of the work. The full details of the license are available at http://creativecommons.org/licenses/by/4.0.
CC BY NC SA: The CC BY-NC-SA license allows users to copy, to create extracts, abstracts and new works from the Article, to alter and revise the Article, provided this is not done for commercial purposes, and that the user gives appropriate credit (with a link to the formal publication through the relevant DOI), provides a link to the license, indicates if changes were made and the licensor is not represented as endorsing the use made of the work. Further, any new works must be made available on the same conditions. The full details of the license are available at http://creativecommons.org/licenses/by-nc-sa/4.0.
CC BY NC ND: The CC BY-NC-ND license allows users to copy and distribute the Article, provided this is not done for commercial purposes and further does not permit distribution of the Article if it is changed or edited in any way, and provided the user gives appropriate credit (with a link to the formal publication through the relevant DOI), provides a link to the license, and that the licensor is not represented as endorsing the use made of the work. The full details of the license are available at http://creativecommons.org/licenses/by-nc-nd/4.0. Any commercial reuse of Open Access articles published with a CC BY NC SA or CC BY NC ND license requires permission from Elsevier and will be subject to a fee.
Commercial reuse includes:

- Associating advertising with the full text of the Article
- Charging fees for document delivery or access
- Article aggregation
- Systematic distribution via e-mail lists or share buttons

Posting or linking by commercial companies for use by customers of those companies.

20. **Other Conditions:**

v1.10

Questions? customercare@copyright.com or +1-855-239-3415 (toll free in the US) or +1-978-646-2777.

For Figure 1.3

AMERICAN ASSOCIATION FOR CANCER RESEARCH LICENSE TERMS AND CONDITIONS

Sep 10, 2022

This Agreement between Mr. Ünal Tokat ("You") and American Association for Cancer Research ("American Association for Cancer Research") consists of your license details and the terms and conditions provided by American Association for Cancer Research and Copyright Clearance Center.

License Number	5385390948568
License date	Sep 10, 2022
Licensed Content Publisher	American Association for Cancer Research
Licensed Content Publication	Cancer Discovery
Licensed Content Title	Insights into Molecular Classifications of Triple-Negative Breast Cancer: Improving Patient Selection for Treatment
Licensed Content Author	Garrido-Castro, Ana C.; Lin, Nancy U.
Licensed Content Date	Feb 8, 2019
Licensed Content Volume	9
Licensed Content Issue	2
Type of Use	Thesis/Dissertation
Requestor type	academic/educational
Format	print and electronic
Portion	figures/tables/illustrations
Number of figures/tables/illustrations	1
Will you be translating?	no
Circulation	5
Territory of distribution	Worldwide
Title	Identification Of Actionable Drug Targets In Triple-Negative Breast Cancer
Institution name	Bilkent University
Expected presentation date	Sep 2022
Portions	Figure 2
Requestor Location	Mr. Ünal Tokat Bilkent University Main Campus Faculty of Science - Department of Molecular Biology and Genetics Room SB-252 Ankara, other Turkey Attn: Mr. Ünal Tokat
Total	**0.00 USD**
Terms and Conditions	

American Association for Cancer Research (AACR) Terms and Conditions

INTRODUCTION
The Publisher for this copyright material is the American Association for Cancer Research (AACR). By clicking "accept" in connection with completing this licensing transaction, you agree to the following terms and conditions applying to this transaction. You also agree to the Billing and Payment terms and conditions established by Copyright Clearance Center (CCC) at the time you opened your Rightslink account.

LIMITED LICENSE
The AACR grants exclusively to you, the User, for onetime, non-exclusive use of this material for the purpose stated in your request and used only with a maximum distribution equal to the number you identified in the permission process. Any form of republication must be completed within one year although copies made before then may be distributed thereafter and any electronic posting is limited to a period of one year. Reproduction of this material is confined to the purpose and/or media for which permission is granted. Altering or modifying this material is not permitted. However, figures and illustrations may be minimally altered or modified to serve the new work.

GEOGRAPHIC SCOPE
Licenses may be exercised as noted in the permission process

RESERVATION OF RIGHTS
The AACR reserves all rights not specifically granted in the combination of 1) the license details provided by you and accepted in the course of this licensing transaction, 2) these terms and conditions , and 3) CCC's Billing and Payment terms and conditions.

DISCLAIMER
You may obtain permission via Rightslink to use material owned by AACR. When you are requesting permission to reuse a portion for an AACR publication, it is your responsibility to examine each portion of content as published to determine whether a credit to, or copyright notice of a third party owner is published next to the item. You must obtain permission from the third party to use any material which has been reprinted with permission from the said third party. If you have not obtained permission from the third party, AACR disclaims any responsibility for the use you make of items owned by them.

LICENSE CONTINGENT ON PAYMENT
While you may exercise the rights licensed immediately upon issuance of the license at the end of the licensing process for the transaction, provided that you have disclosed complete and accurate details of your proposed use, no license is finally effective unless and until full payment is received from you, either by the publisher or by the CCC, as provided in CCC's Billing and Payment terms and conditions. If full payment is not received on a timely basis, then any license preliminarily granted shall be deemed automatically revoked and shall be void as if never granted. Further, in the event that you breach any of these terms and conditions, or any of the

CCC's Billing and Payment terms and conditions, the license is automatically revoked and shall be void as if never granted. Use of materials as described in a revoked license, as well as any use of the materials beyond the scope of an unrevoked license, may constitute copyright infringement and the publisher reserves the right to take any and all action to protect its copyright in the materials.

COPYRIGHT NOTICE

You must include the following credit line in connection with your reproduction of the licensed material: "Reprinted (or adapted) from Publication Title, Copyright Year, Volume/Issue, Page Range, Author, Title of Article, with permission from AACR".

TRANSLATION

This permission is granted for non-exclusive world English rights only.

WARRANTIES

Publisher makes no representations or warranties with respect to the licensed material.

INDEMNIFICATION

You hereby indemnify and agree to hold harmless the publisher and CCC, and their respective officers, directors, employees and agents, from and against any and all claims arising out of your use of the licensed material other than as specifically authorized pursuant to this license.

REVOCATION

The AACR reserves the right to revoke a license for any reason, including but not limited to advertising and promotional uses of AACR content, third party usage and incorrect figure source attribution.

NO TRANSFER OF LICENSE

This license is personal to you and may not be sublicensed, assigned, or transferred by you to any other person without publisher's written permission.

NO AMENDMENT EXCEPT IN WRITING

This license may not be amended except in a writing signed by both parties (or, in the case of publisher, by CCC on publisher's behalf).

OBJECTION TO CONTRARY TERMS

Publishers hereby objects to any terms contained in any purchase order, acknowledgement, check endorsement or other writing prepared by you, which terms are inconsistent with these terms and conditions or CCC's Billing and Payment terms and conditions. These terms and conditions together with CCC's Billing and Payment terms and conditions (which are incorporated herein) comprise the entire agreement between you and publisher (and CCC) concerning this licensing transaction. In the event of any conflict between your obligations established by these terms and conditions, and those established by CCC's Billing and Payment terms and conditions, these terms and conditions shall control.

THESIS/DISSERTATION TERMS

If your request is to reuse an article authored by you and published by the AACR in your dissertation/thesis, your thesis may be submitted to your institution in either in print or electronic form. Should your thesis be published commercially, please reapply.

ELECTRONIC RESERVE

If this license is made in connection with a course, and the Licensed Material or any portion thereof is to be posted to a website, the website is to be password protected and made available only to the students registered for the relevant course. The permission is granted for the duration of the course. All content posted to the website must maintain the copyright information notice.

JURISDICTION

This license transaction shall be governed by and construed in accordance with the laws of Pennsylvania. You hereby agree to submit to the jurisdiction of the federal and state courts located in Pennsylvania for purposes of resolving any disputes that may arise in connection with this licensing transaction.

Other Terms and Conditions:

v1.0

Questions? customercare@copyright.com or +1-855-239-3415 (toll free in the US) or +1-978-646-2777.

For Figure 1.4

SPRINGER NATURE

Practical classification of triple-negative breast cancer: intratumoral heterogeneity, mechanisms of drug resistance, and novel therapies

Author: Antonio Marra et al

Publication: npj Breast Cancer

Publisher: Springer Nature

Date: Oct 16, 2020

Copyright © 2020, The Author(s)

Creative Commons

This is an open access article distributed under the terms of the Creative Commons CC BY license, which permits unrestricted use, distribution, and reproduction in any medium, provided the original work is properly cited.

You are not required to obtain permission to reuse this article.

To request permission for a type of use not listed, please contact Springer Nature

For Figure 1.5

Current Triple-Negative Breast Cancer Subtypes: Dissecting the Most Aggressive Form of Breast Cancer

OPEN ACCESS

Miquel Ensenyat-Mendez[1†], Pere Llinàs-Arias[1†], Javier I. J. Orozco[2], Sandra Íñiguez-Muñoz[1], Matthew P. Salomon[3], Borja Sesé[1], Maggie L. DiNome[4] and Diego M. Marzese[1*]*

Copyright © 2021 Ensenyat-Mendez, Llinàs-Arias, Orozco, Íñiguez-Muñoz, Salomon, Sesé, DiNome and Marzese. This is an open-access article distributed under the terms of the Creative Commons Attribution License (CC BY). The use, distribution or reproduction in other forums is permitted, provided the original author(s) and the copyright owner(s) are credited and that the original publication in this journal is cited, in accordance with accepted academic practice. No use, distribution or reproduction is permitted which does not comply with these terms.

***Correspondence:** Maggie L. DiNome, mdinome@mednet.ucla.edu; Diego M. Marzese, diego.marzese@ssib.es

For Figure 1.6

The use of the figure in a thesis is covered by Permitted Uses according to ©AMBOSS Website Terms, Policies, And Conditions. This has been also verified by AMBOSS Customer Support.

Permitted uses: Some of the Licensed Materials are configured in a manner that permits you to print them for your personal use ("Printable Content"). You may print out the Printable Content from the most current version of the Website solely for your personal educational use. No other copies may be made and/or transmitted. All print-outs of Printable Content must include the AMBOSS copyright notice, which appears on the Printable Content. AMBOSS reserves the right to withdraw permission to print content at any time in its sole and absolute discretion. Except as provided in these Terms, you may not print any of the content appearing on the Website.

If you wish to make any use of material on the Website other than that set out in this section, please address your request to: info@amboss.com

Ünal Metin Tokat

E-mail: umtokat@gmail.com § Phone: +90-554-3619746

Bilkent University, Faculty of Science SB Building, Department of Molecular Biology and Genetics, 06800 Cankaya/Ankara, TURKEY

EDUCATION & DEGREES

Bilkent University **Sep 2015 – Sep 2022**

Department of Molecular Biology and Genetics

Ph.D.

"Identification Of Actionable Drug Targets in Triple-Negative Breast Cancer"

Bilkent University **Sep 2010 – Jun 2015**

Department of Molecular Biology and Genetics

BSc – CGPA: 3.65 / 4.00, Rank: 4

Haci Omer Tarman Anatolian High School **Sep 2006 – Jun 2010**

Field of Sciences

CPGA: 92.18 / 100, Rank: 2

EXPERIENCE & TRAINING

Bilkent University **Sep 2021 – Jan 2022**

MBG210 Genetics

Lab assistant- Conducted and supervised wet lab experiments

Bilkent University **Sep 2015 – Jan 2021**

MBG311 Biochemistry I

Lab assistant - Conducted and supervised wet lab experiments

Bilkent University **Jun 2018 – Aug 2020**

Lab manager

Organized lab orders, project budgets, and material shipments

IBENS **Jan 2017**

Functional Genomics Section

Visiting researcher at Prof. Denis Thieffry's Lab

Bilkent University **Jun 2016 – Jul 2017**

Youth Academy

Workshop Instructor

Bilkent University **Sep 2014 – Jun 2015**

Department of Molecular Biology and Genetics

Research trainee at Assoc. Prof. Ozgur Sahin's Lab

"Therapy & drug resistance in breast cancer and re-sensitization mechanisms"

Erciyes University **Jul 2014 – Sep 2014**

Genome and Stem Cell Center

Intern at Genome and Stem Cell Units

"Analyzing DNA polymorphisms associated with the selected diseases & Investigation of anti-oxidant effect of cherry laurel in DNA damage and repair mechanisms"

Bilkent University **Sep 2011 – Jun 2014**

Department of Molecular Biology and Genetics

Undergraduate research trainee

ACADEMIC HONORS & AWARDS

TÜBİTAK **Mar 2016 – Sep 2022**

The Scientific and Technological Research Council of Turkey

BİDEB 2211/A (National Scholarship Programme for PhD Students) Scholarship

(given to only around 100 students per year)

Bilkent University **Jun 2012 – Jun 2015**

Department of Molecular Biology and Genetics

High Honor student (x6)

Bilkent University **Jan 2012 & Jun 2014**

Department of Molecular Biology and Genetics

Honor student (x2)

Bilkent University **Sep 2010 – Jun 2015**

Department of Molecular Biology and Genetics

Full (comprehensive) scholarship

University Entrance Examination (YGS/LYS) **Jun 2010**

7 Degrees (varying between 1250th and 4800th)

Among more than 1,350,000 students

Haci Omer Tarman Anatolian High School **Sep 2006 – Jun 2010**

Field of Sciences

The second best (runner-up) Student at Graduation

ACADEMIC CONFERENCES & MEETINGS

European Molecular Biology Laboratory (EMBL) **Jan 2019**

EMBO YIP PhD Course 2019

Workshop & Poster Presentation

"In Vivo Bioluminescence and Fluorescence Imaging on the IVIS Platform"

"Identification and targeting of the molecular determinants of breast cancer lung metastasis in triple-negative breast cancer"

Bahcesehir University **Dec 2018**

6th International BAU Drug Design Congress

Poster Presentation

"Identification and targeting of the molecular determinants of breast cancer lung metastasis in triple-negative breast cancer"

Weizmann Institute of Science & Bar Ilan University **Dec 2017**

Israel – Turkey (WIS – UNAM) Workshop

Poster Presentation

"Competing Endogenous RNA (ceRNAs) Interaction Network Regulating Lung Metastasis in Triple Negative Breast Cancer"

Bogazici University **Sep 2017**

5th International Congress of the Molecular Biology Association of Turkey

Poster Presentation

"Targeting the interactome controlling metastatic colonization of triple negative breast cancer"

Middle East Technical University (METU) **Nov 2015**

4th International Congress of the Molecular Biology Association of Turkey

Participant

Bilkent Genetics Society (BilGenT) **Apr 2013**

Horizons in Molecular Biology and Genetics V

Participant

Bilkent University **Apr 2012**

The Ihsan Dogramaci Memorial Lecture

Participant

QUALIFICATIONS

Certificate

Certificate in Laboratory Animal Use, June 2016

Bilkent University

Computer

Microsoft Office Suite (Word, Excel, PowerPoint, OneNote), RNA-sequencing Data Analysis Tools on Linux, Intermediate R Programming - RStudio, Basic MATLAB and Java, Intermediate Image Editing and Illustration Tools

Language

Turkish (native) – English (fluent), Spanish (basic), German (basic)

Laboratory

General skills (micropipetting, centrifuge, light microscopy, preparation of lab solutions etc.), Cell and tissue culture, Handling of model organisms (mouse, fruit fly, zebra fish), Animal experimentation (Primary Breast and Prostate, Metastatic Breast Cancer Models), *In vivo* bioluminescence and fluorescence imaging, Molecular biology techniques (PCR, qRT-PCR, RFLP, Western blotting, DNA-RNA-protein isolation), Cell-based functional assays (cytotoxicity/viability, migration, invasion and extravasation)

LIST OF PUBLICATIONS

1) R. Assidicky, **U. M. Tokat**, I. O. Tarman, O. Saatci, P. G. Ersan, U. Raza, H. Ogul, Y. Riazalhosseini, T. Can, O. Sahin. Targeting HIF1-alpha/miR-326/ITGA5 axis potentiates chemotherapy response in triple negative breast cancer. *Breast Cancer Res Treat*, (2022).
2) Y. Kartal, **U. M. Tokat**, P. Kelicen Ugur, S. Karahan,M. T. Budak, Evaluation of the Relationship Between Aromatase/Sirtuin1 Interaction and miRNA Expression in Human Neuroblastoma Cells. *Current Molecular Pharmacology*, (2022).
3) M. Biondini, A. Kiepas, L. El-Houjeiri, M. G. Annis, B. E. Hsu, A. M. Fortier, G. Morin, J. A. Martina, I. Sirois, A. Aguilar-Mahecha, T. Gruosso, S. McGuirk, A. A. N. Rose, **U. M. Tokat**, R. M. Johnson, O. Sahin, E. Bareke, J. St-Pierre, M. Park, M. Basik, J. Majewski, R. Puertollano, A. Pause, S. Huang, T. Keler, P. M. Siegel, HSP90 inhibitors induce GPNMB cell-surface expression by modulating lysosomal positioning and sensitize breast cancer cells to glembatumumab vedotin. *Oncogene*, (2022).
4) M. Yildirim, T. C. Yildirim, N. Turay, T. Bildik, B. Ibibik, I. Evcili, P. G. Ersan, **U. M. Tokat**, O. Sahin, I. Gursel. TLR ligand loaded exosome mediated immunotherapy of established mammary Tumor in mice. *Immunol Lett* **239**, 32-41 (2021).
5) O. Saatci, A. Kaymak, U. Raza, P. G. Ersan, O. Akbulut, C. E. Banister, V. Sikirzhytski, **U. M. Tokat**, G. Aykut, S. A. Ansari, H. T. Dogan, M. Dogan, P. Jandaghi, A. Isik, F. Gundogdu, K. Kosemehmetoglu, O. Dizdar, S. Aksoy, A. Akyol, A. Uner, P. J. Buckhaults, Y. Riazalhosseini, O. Sahin. Targeting lysyl oxidase (LOX) overcomes chemotherapy resistance in triple negative breast cancer. *Nat Commun* **11**, 2416 (2020).
6) R. R. Mishra, N. Belder, S. A. Ansari, M. Kayhan, H. Bal, U. Raza, P. G. Ersan, **U. M. Tokat**, E. Eyupoglu, O. Saatci, P. Jandaghi, S. Wiemann, A. Uner, C. Cekic, Y. Riazalhosseini, O. Sahin, Reactivation of cAMP Pathway by PDE4D Inhibition Represents a Novel Druggable Axis for Overcoming Tamoxifen Resistance in ER-positive Breast Cancer. Clin Cancer Res 24, 1987-2001 (2018).

SCIENTIFIC INTERESTS

- Cancer biology and genetics
- Drug resistance and metastasis in cancer

PERSONAL INTERESTS

- Trying new softwares and gadgets
- Reading humor/tech magazines and sports biographies
- Watching documentaries about nature, science and tech
- Visiting archeological sites, ruins and museums
- Playing basketball

Breast Cancer Research and Treatment (2022) 193:331–348
https://doi.org/10.1007/s10549-022-06569-5

PRECLINICAL STUDY

Targeting HIF1-alpha/miR-326/ITGA5 axis potentiates chemotherapy response in triple-negative breast cancer

Ridho Assidicky[1] · Unal Metin Tokat[1] · Ibrahim Oguzhan Tarman[1] · Ozge Saatci[2] · Pelin Gulizar Ersan[1] · Umar Raza[1] · Hasan Ogul[3] · Yasser Riazalhosseini[4,5] · Tolga Can[6] · Ozgur Sahin[2]

Received: 6 December 2021 / Accepted: 13 March 2022 / Published online: 25 March 2022
© The Author(s), under exclusive licence to Springer Science+Business Media, LLC, part of Springer Nature 2022

Abstract

Purpose Triple-negative breast cancer (TNBC) is the most aggressive subtype of breast cancer that is frequently treated with chemotherapy. However, many patients exhibit either de novo chemoresistance or ultimately develop resistance to chemotherapy, leading to significantly high mortality rates. Therefore, increasing the efficacy of chemotherapy has potential to improve patient outcomes.

Methods Here, we performed whole transcriptome sequencing (both RNA and small RNA-sequencing), coupled with network simulations and patient survival data analyses to build a novel miRNA-mRNA interaction network governing chemoresistance in TNBC. We performed cell proliferation assay, Western blotting, RNAi/miRNA mimic experiments, FN coating, 3D cultures, and ChIP assays to validate the interactions in the network, and their functional roles in chemoresistance. We developed xenograft models to test the therapeutic potential of the identified key miRNA/proteins in potentiating chemoresponse in vivo. We also analyzed several patient datasets to evaluate the clinical relevance of our findings.

Results We identified fibronectin (FN1) as a central chemoresistance driver gene. Overexpressing miR-326 reversed FN1-driven chemoresistance by targeting FN1 receptor, ITGA5. miR-326 was downregulated by increased hypoxia/HIF1A and ECM stiffness in chemoresistant tumors, leading to upregulation of ITGA5 and activation of the downstream FAK/Src signaling pathways. Overexpression of miR-326 or inhibition of ITGA5 overcame FN1-driven chemotherapy resistance in vitro by inhibiting FAK/Src pathway and potentiated the efficacy of chemotherapy in vivo. Importantly, lower expression of miR-326 or higher levels of predicted miR-326 target genes was significantly associated with worse overall survival in chemotherapy-treated TNBC patients.

Conclusion FN1 is central in chemoresistance. In chemoresistant tumors, hypoxia and resulting ECM stiffness repress the expression of the tumor suppressor miRNA, miR-326. Hence, re-expression of miR-326 or inhibition of its target ITGA5 reverses FN1-driven chemoresistance making them attractive therapeutic approaches to enhance chemotherapy response in TNBCs.

Keywords TNBC · miRNA-mRNA network · Chemoresistance · miR-326 · Fibronectin · Integrin · Hypoxia · ECM stiffness

✉ Ozgur Sahin
sahinozgur@gmail.com; sahin@cop.sc.edu

[1] Department of Molecular Biology and Genetics, Faculty of Science, Bilkent University, 06800 Ankara, Turkey

[2] Department of Drug Discovery and Biomedical Sciences, University of South Carolina, Columbia, SC 29208, USA

[3] Faculty of Computer Sciences, Østfold University College, NO-1757 Halden, Norway

[4] McGill University Genome Centre, Montreal, QC H3A 0G1, Canada

[5] Department of Human Genetics, McGill University, Montreal, QC H3A 1B1, Canada

[6] Department of Computer Engineering, Middle East Technical University, 06800 Ankara, Turkey

Introduction

Breast cancer is the leading cause of cancer deaths among women worldwide [1]. Triple-negative breast cancer (TNBC) represents 15–20% of all breast cancers and is a heterogeneous disease that is molecularly characterized by lack of estrogen receptor (ER), progesterone receptor (PR), and human epidermal growth factor receptor 2 (HER2) expression [2]. TNBC is the most aggressive breast cancer subtype that is frequently observed in women at younger ages, is diagnosed at an advanced stage and has poor prognosis [3]. Due to lack of targetable receptors, TNBC patients heavily rely on chemotherapy, particularly anthracycline- (e.g., doxorubicin) and taxane-based (e.g., paclitaxel) agents [4, 5]. Even though TNBC patients initially respond to chemotherapy at relatively higher rates compared to non-TNBCs [5–8], more than half of the chemotherapy-treated TNBC patients experience disease relapse [4, 9]. The improvement in progression-free survival with the immune checkpoint inhibitor (ICI), atezolizumab which has been approved for the treatment of refractory TNBCs in 2019 [10], is limited to 3 months with only a small portion of the patients benefiting this therapy and many experiencing treatment-related adverse events [11]. Therefore, there is an urgent need to unravel novel mechanisms of chemotherapy resistance in TNBCs and to achieve pathological complete response (pCR) among patients that are not responsive to chemotherapy. The first targeted therapy agent, sacituzumab govitecan-hziy (Trodelvy), which is an antibody–drug conjugate of the human trophoblast cell-surface antigen 2 (Trop-2) coupled to SN-38 (topoisomerase I inhibitor), has recently been approved by the Food and Drug Administration (FDA) to be used in metastatic TNBC patients that have progressed on at least two prior therapies; however, only 16.7% of the patients exhibit response for 12 or more months [12]. Therefore, there is still a dire need to identify novel therapy options that can improve survival rates in TNBCs.

Tumor cells are surrounded by a complex network of stromal cells and factors that collectively form the tumor microenvironment (TME). The extracellular matrix (ECM) is an important part of the TME that consists of proteoglycans and various fibrous proteins, such as collagen, fibronectin (FN1), and laminin of which expression and secretion are frequently induced in low oxygen, i.e., hypoxic environments [13]. The increase in tumor stiffness by increased abundance and crosslinking of different ECM components correlates with reduced drug delivery, cancer cell invasion, and metastasis and associates with worse clinical outcome [14]. For instance, we have shown that upregulation of lysyl oxidase (LOX) in TNBC tumors mediates chemoresistance via enhancing collagen crosslinking and fibronectin assembly in ECM, thereby reducing chemotherapy penetration, and activating pro-survival signaling [15]. The cues originating from tumor ECM are transduced into the cell via integrin family of proteins which are composed of 24 heterodimeric receptors that mediate adhesion to various ECM components. Binding of integrins to ECM has been shown to trigger intracellular signaling cascades that induce cell survival, proliferation, migration, and promote resistance to chemotherapy [16–18]. For instance, Integrin Subunit Alpha 5 (ITGA5) which is a subunit of the heterodimeric receptor (ITGA5/ITGB1) recognizing FN1 is found to be a prognostic biomarker in different cancers [19, 20] and also strongly correlates with LOX expression in TNBC patients [15]. Owing to these multifaceted roles of tumor ECM in promoting tumor aggressiveness, therapeutic strategies that modulate tumor stiffness or disrupt the signal transduction from ECM to cancer cells have great potential in overcoming resistance to given therapy in cancers accommodating stiff tumors [21, 22].

The systems biology approaches, involving analyses of multiple types of discrete and continuous data, such as omics data (transcriptomics, genomics, etc.), clinical data (subtyping, survival, etc.), and mathematical data (network simulation, etc.) have undergone tremendous improvements over the last few decades, offering new approaches for candidate prioritization, target modulation, and cancer treatment [23]. Integration of these approaches with multilayered analyses of miRNAs and their potential mRNA targets can enable the identification of the most prominent interactions present in a given cellular state, providing a unique opportunity to robustly determine the key drivers of disease progression. Modulation of these drivers can, therefore, provide efficient blockage of the complex network of interactions present in refractory tumors and has great potential to promote tumor regression in the presence of a given therapy [24].

Here, we built the first miRNA-mRNA interaction network of chemoresistance in TNBC to discover novel molecular players. We showed that chemoresistance in TNBCs is, in part, driven by the miR-326/ITGA5-FN1 axis that is regulated by hypoxia and ECM stiffness. Increasing miR-326 expression or inhibiting its downstream target, ITGA5 overcomes ECM-mediated chemoresistance. Our results provide pre-clinical rationale for modulating miR-326 or its target to enhance chemoresponse in TNBCs.

Results

miRNA-mRNA interaction network of TNBC chemoresistance identifies FN1 as a central node

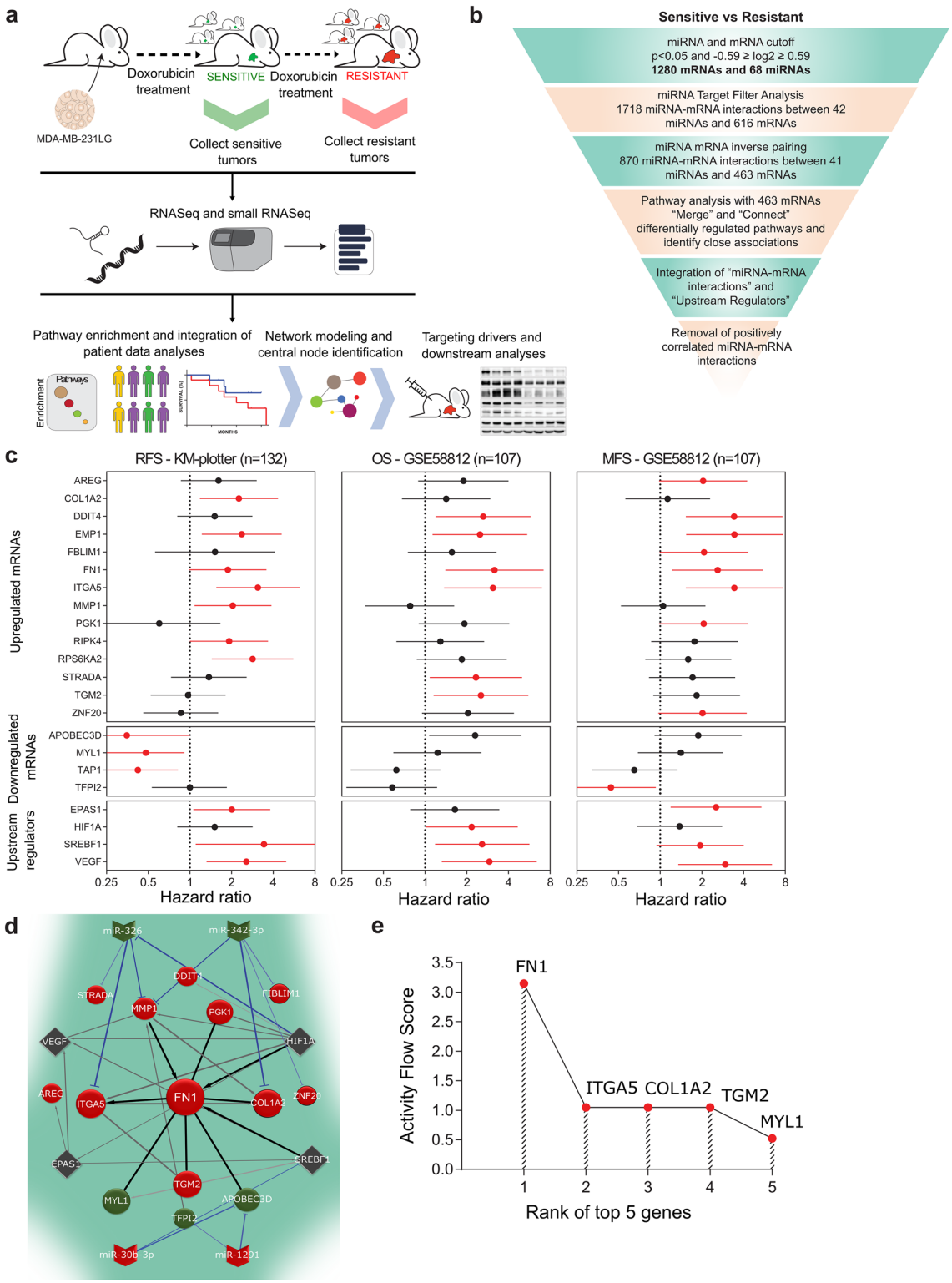
To identify the miRNA-mRNA interaction network regulating chemoresistance in TNBCs, we developed an in vivo doxorubicin-resistance model by continuous doxorubicin treatment of the xenografts of a highly aggressive TNBC cell line, MDA-MB-231 (Fig. 1a) [15]. We collected tumors from several mice when they were responsive to therapy as assessed by the reduction in tumor size, and we classified them as sensitive. The rest of the mice were kept under doxorubicin treatment until the tumors exhibited re-growth at rates comparable to vehicle-treated tumors, and the tumors were classified as resistant [15]. We performed mRNA and miRNA profiling of the doxorubicin-sensitive and resistant tumors and analyzed the differentially expressed mRNAs and miRNAs ($-0.59 \geq \log2FC \geq 0.59$, $P < 0.05$) using the Ingenuity Pathway Analysis (IPA) (Fig. 1a, b). Upon a multi-step analysis pipeline that is based on directional pairing of miRNAs and their predicted mRNA targets and grouping into relevant pathways by integrating the upstream regulators (Fig. 1b), we obtained a network composed of 72 mRNAs, 20 miRNAs and 13 upstream regulators (Fig. S1). To further narrow down the list of miRNAs and mRNAs in the doxorubicin-resistance network, we integrated TNBC patient survival data into our pipeline. Using Kaplan–Meier Plotter [25] and GSE58812 [26] dataset, we identified the down or upregulated prognostic transcription factors (TFs) and mRNAs that either positively or negatively associate with chemo-treated TNBC patient survival, respectively (Fig. 1c). Accordingly, we shortlisted the genes that have hazard ratio (HR) > 1 in chemo-treated TNBC patients and at the same time, are upregulated in resistant xenografts and predicted to be the targets of downregulated miRNAs in the network, and vice versa. As a result, we obtained a core doxorubicin-resistance (DoxoR) network including 14 mRNAs, 4 miRNAs targeting those mRNAs and 4 TFs regulating their expression (Fig. 1d). In this network, we performed a random walk-based activity flow analysis to measure and rank each network component according to their centrality. Importantly, FN1 has the highest activity flow score showing its central role, followed by its receptor, ITGA5 and its functional partner, type I collagen, COL1A2 (Fig. 1e). These results show that our unbiased approach identified FN1 as a central node in the TNBC miRNA-mRNA chemoresistance network.

Fibronectin confers chemoresistance that is reversed by miR-326 overexpression

Deregulation of ECM composition, deposition, and crosslinking have previously been associated with chemotherapy response [14]. We have recently demonstrated the roles of the collagen crosslinking enzyme, LOX in driving doxorubicin resistance in TNBC, supporting the notion that ECM modulation is a critical regulator of chemotherapy response in TNBC. Here, we identified another key component of tumor-associated ECM, FN1 (protein: fibronectin) as the center of our doxorubicin-resistance network (Fig. 1). To experimentally demonstrate the involvement of FN1 in driving doxorubicin resistance, we examined the proliferation of MDA-MB-231 cells in uncoated vs. fibronectin-coated wells upon treatment with increasing doses of doxorubicin. We observed that cells grown on top of fibronectin exhibited higher proliferative capacity compared to those grown in the absence of fibronectin upon doxorubicin treatment, implying that FN1 could render TNBC cells resistant to doxorubicin in vitro (Fig. 2a). Furthermore, we observed a dose-dependent increase in the level of the apoptotic marker, cleaved PARP in doxorubicin-treated cells grown in the absence of fibronectin, while the degree of apoptotic cell death was considerably less in the presence of fibronectin (Fig. 2b).

Of the 4 miRNAs in the DoxoR network, two of them (miR-326 and miR-342-3p) were downregulated in doxorubicin-resistant xenografts (Figs. 2c and S2a). We examined if re-expression of these miRNAs (with miRNA mimic transfection or inducible miRNA expression) could overcome FN1-driven doxorubicin resistance in vitro. miR-326 overexpression, but not miR-342-3p, led to a higher growth inhibition mediated by doxorubicin in MDA-MB-231 cells cultured on fibronectin at different doses of doxorubicin (Figs. 2d and S2b). The role of miR-326 in chemosensitization was further validated in MDA-MB-157 and MDA-MB-436 cells cultured in fibronectin-coated wells (Fig. S3a, b). Furthermore, miR-326 overexpression increased the response to not only doxorubicin but also to paclitaxel (Fig. S3c–e), supporting the notion that miR-326 could be a general chemosensitizer in TNBC. We have also observed a marked increase in apoptosis upon combination treatment compared to miR-326 overexpression or doxorubicin alone (Fig. 2e).

To uncover the clinical relevance of miR-326, we first examined the expression of miR-326 in noncancerous breast vs. breast cancer tissues (GSE57897 [27]) and in tumors with low proliferative vs. high proliferative capacity (GSE19536 [28]). We demonstrated that miR-326 expression is lower in cancer tissues or tumors with high proliferative capacity, supporting its tumor suppressor role (Fig. 2f). Similarly, we observed that low miR-326 expression in TNBC patients with adjuvant therapy associated with poorer overall



survival compared to patients with high miR-326 expression (GSE40267 [29]) (Fig. 2g). Survival analysis using TCGA TNBC patients yielded a similar result with a trend ($p = 0.055$) towards worse survival in case of low expression of miR-326 (Fig. S4a). Importantly, higher expression of the predicted targets of miR-326 also predicts worse overall survival, similar to patients with low miR-326 expression (Fig. S4b). Overall, we conclude that miR-326 may function as a tumor suppressor in TNBC and can overcome FN1-mediated doxorubicin resistance.

◂**Fig. 1** Constructing miRNA-mRNA interaction network of TNBC chemoresistance. **a** Schematic representation of the study plan and methodology. **b** Workflow describing the step-by-step selection process of the candidate miRNAs and mRNAs via IPA to generate doxorubicin-resistance miRNA-mRNA interaction network. **c** Forest plot showing survival analyses of the genes significantly stratifying patients in KM-Plotter (RFS (relapse-free survival), $n = 132$) or GSE58812 (OS (overall survival) and MFS (metastasis-free survival), $n = 107$) in chemotherapy-treated TNBC patients. Genes with no significant effect are not shown and excluded from further analysis. Circles indicate the hazard ratio, and the horizontal bars show the 95% confidence interval. Red color indicates significant ($P < 0.05$) hazard ratio (HR). **d** FN1-centered network comprising mRNAs, miRNAs, and upstream regulators involved in the doxorubicin resistance. Red and green nodes represent up- and downregulated mRNAs (circles) or miRNAs (fletching), respectively, where dark gray rhombus nodes represent the upstream regulators. **e** Random walk-based activity flow analysis to rank each network component according to their centrality. Five genes with the highest activity flow score are shown. Outliers in any data were identified via ROUT method. Statistical significance was evaluated by the Log-rank (Mantel-Cox) test in patient survival analysis

miR-326 potentiates doxorubicin response in vivo

We next tested if miR-326 could potentiate doxorubicin response in vivo. To this end, we used derivatives of the luciferase expressing MDA-MB-231-Luc2-GFP cells ("231.Luc2.GFP") that stably express doxycycline-inducible miR-326 ("231.miR-326"). Next, we orthotopically injected the control and inducible miR-326 expressing cells into mammary fat pads (MFPs) of nude mice. Induction of miR-326 expression in combination with a low dose of doxorubicin after tumors became palpable led to a prominent decrease in tumor growth as compared to single-agent treatments (Fig. 3a). Accordingly, in vivo imaging revealed a marked reduction (> 3-fold) of luminescence signal coming from the combination-treated tumors (Fig. 3b and c). Moreover, tumors obtained from the combination group were considerably smaller than those of the miR-326, doxorubicin, and control groups (Fig. 3d and e). Finally, we confirmed the upregulation of miR-326 in doxycycline-treated tumors collected at the end of the experiment (Fig. 3f). These data suggest that miR-326 overexpression potentiates the efficacy of doxorubicin in vivo.

miR-326 targets the FN1 receptor, ITGA5 and blocks the downstream FAK/Src signaling

To elucidate the molecular mechanisms of doxorubicin sensitization upon miR-326 overexpression, we re-examined our DoxoR miRNA-mRNA network. ITGA5, which is a subunit of the major FN1-recognizing heterodimeric receptor (ITGA5/ITGB1), was among the predicted targets of miR-326. Furthermore, we have previously showed that inhibition of the ECM remodeler, LOX downregulated ITGA5 and FN1 and led to de-activation of downstream FAK/Src signaling and chemosensitization, suggesting that ITGA5-FN1 axis is a critical effector in modulating chemotherapy response [15]. Based on these, we hypothesize that miR-326 might function as a chemotherapy sensitizer via targeting ITGA5. Using TargetScan [30], we identified a conserved miR-326 binding site in the 3'-UTR of the *ITGA5* mRNA (Fig. 4a). Overexpressing miR-326 in three different TNBC cell lines, MDA-MB-231, MDA-MB-157, and MDA-MB-436 was able to suppress *ITGA5* at mRNA and protein levels (Figs. 4b, c, S3f). We further validated the direct binding of miR-326 to *ITGA5* 3'-UTR by dual-luciferase assay (Fig. 4d).

To experimentally test the effect of miR-326 on the pathways downstream of FN1/ITGA5, we performed Western blot analysis of the relevant downstream targets. We demonstrated that p-FAK Y397 and p-Src Y416 were strongly diminished, which were accompanied by a concomitant decrease in ITGA5 protein levels following miR-326 overexpression upon doxycycline induction (Fig. 4e). We observed similar results when we compared ITGA5 expression and the signaling activity in miR-326 overexpressing tumors to the control tumors (Fig. 4f–g). Overall, we showed that miR-326 directly targets ITGA5, a subunit of the FN1 receptor, thus, inhibiting the activity of the downstream FAK/Src pathway.

Inhibiting ITGA5 overcomes FN1-driven chemoresistance in vitro and potentiates chemoresponse in vivo

We next tested if ITGA5 is involved in fibronectin-driven chemoresistance downstream of miR-326. We first engineered MDA-MB-231-Luc2-GFP cells to stably express shITGA5 upon induction with doxycycline ("231.shITGA5"). After validating ITGA5 knockdown with doxycycline induction at mRNA and protein levels (Fig. 5a, b), we examined the combinatorial effect of ITGA5 knockdown and doxorubicin on the viability of cells seeded onto fibronectin-coated wells. We observed that cells became more sensitive to doxorubicin treatment upon induction of shITGA5 (Fig. 5c), indicating that ITGA5 downregulation potentiates doxorubicin response. Moreover, there was a noticeable increase in the level of the apoptotic marker, cleaved PARP, upon shITGA5 induction combined with doxorubicin compared to their individual effects (Fig. 5d). Importantly, we observed a reduction in p-FAK Y397 and p-Src Y416 following ITGA5 silencing (Fig. 5e). These results suggest that ITGA5, whose expression is controlled by miR-326, is a central gene that conveys signals from fibronectin-rich ECM to intracellular space, leading to activation of survival pathways, inhibition of drug-induced apoptosis, and induction of chemoresistance.

Next, we tested the effects of ITGA5 silencing on potentiating doxorubicin response in vivo. We developed primary tumor xenografts of the 231.shITGA5 cells and treated

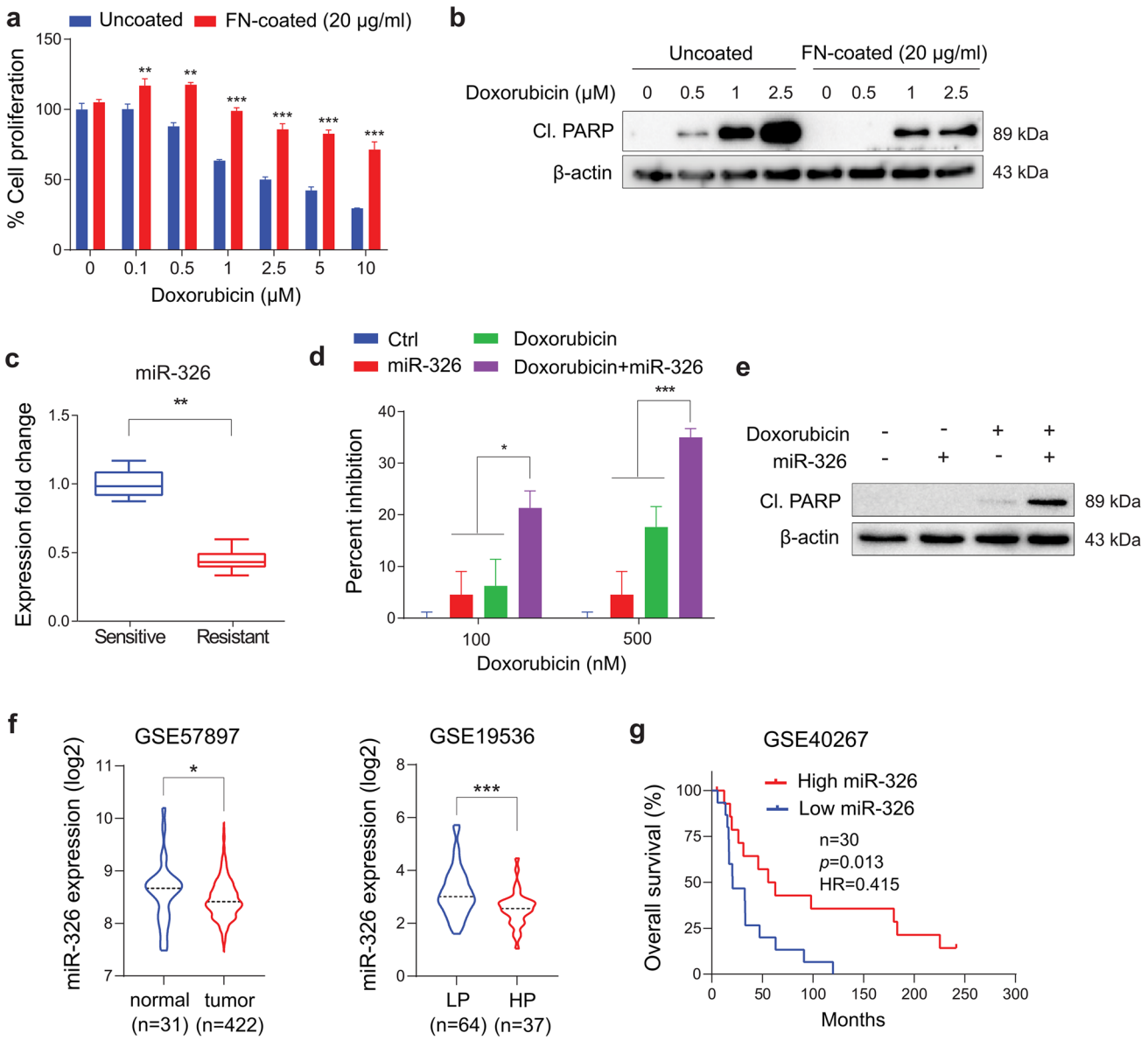


Fig. 2 Fibronectin confers chemoresistance that is reversed by miR-326 overexpression. **a** Percent cell proliferation of MDA-MB-231 cells grown on uncoated or 20 µg/mL Fibronectin-coated wells upon doxorubicin treatment. **b** Western blot analysis showing changes in apoptosis marker cleaved PARP (Cl. PARP) upon doxorubicin treatment for 48 h on uncoated or 20 µg/mL Fibronectin-coated wells in MDA-MB-231 cells. β-actin was used as a loading control. **c** Expression of miR-326 in doxorubicin-sensitive vs. resistant tumor xenografts. **d** Percent growth inhibition of MDA-MB-231 cells seeded in 20 µg/ml fibronectin upon combination of miR-326 mimic or doxycycline induction of 231.miR-326 cells with doxorubicin. **e** Western blot analysis showing changes in the apoptosis marker, cleaved PARP upon combination of miR-326 mimic and doxorubicin in MDA-MB-231 cells seeded on 20 µg/mL FN. β-actin was used as a loading control. **f** Expression of miR-326 (in $\log_2$ scale) in normal vs. tumor tissues (left) and in low vs. highly proliferative tissues (right) from GSE57897 and GSE19536, respectively. **g** Kaplan–Meier survival curve showing overall survival percentage in TNBC patients (n = 30) separated based on low vs. high miR-326 expression (Q1 vs Q4). * $P < 0.05$; ** $P < 0.01$; *** $P < 0.001$. Normality/Lognormality was assessed by D'Agostino-Pearson or Shapiro–Wilk test. Statistical significance was evaluated by unpaired t test or Mann–Whitney test for all figures except by the Log-rank (Mantel-Cox) test in g

them with a low dose of doxorubicin along with doxycycline to induce shITGA5 expression (Fig. 5f). We showed that combination treatment induced a significant delay in tumor growth compared to single-agent treatments, as clearly shown by bioluminescent imaging and tumor weight measurements (Fig. 5g–j). We also compared the signaling activity in shITGA5 expressing tumors to the control tumors and observed an overall reduction in p-FAK Y397 and p-Src Y416 levels in addition to a clear decrease in ITGA5 (Fig. 5k). Altogether, these results corroborate our

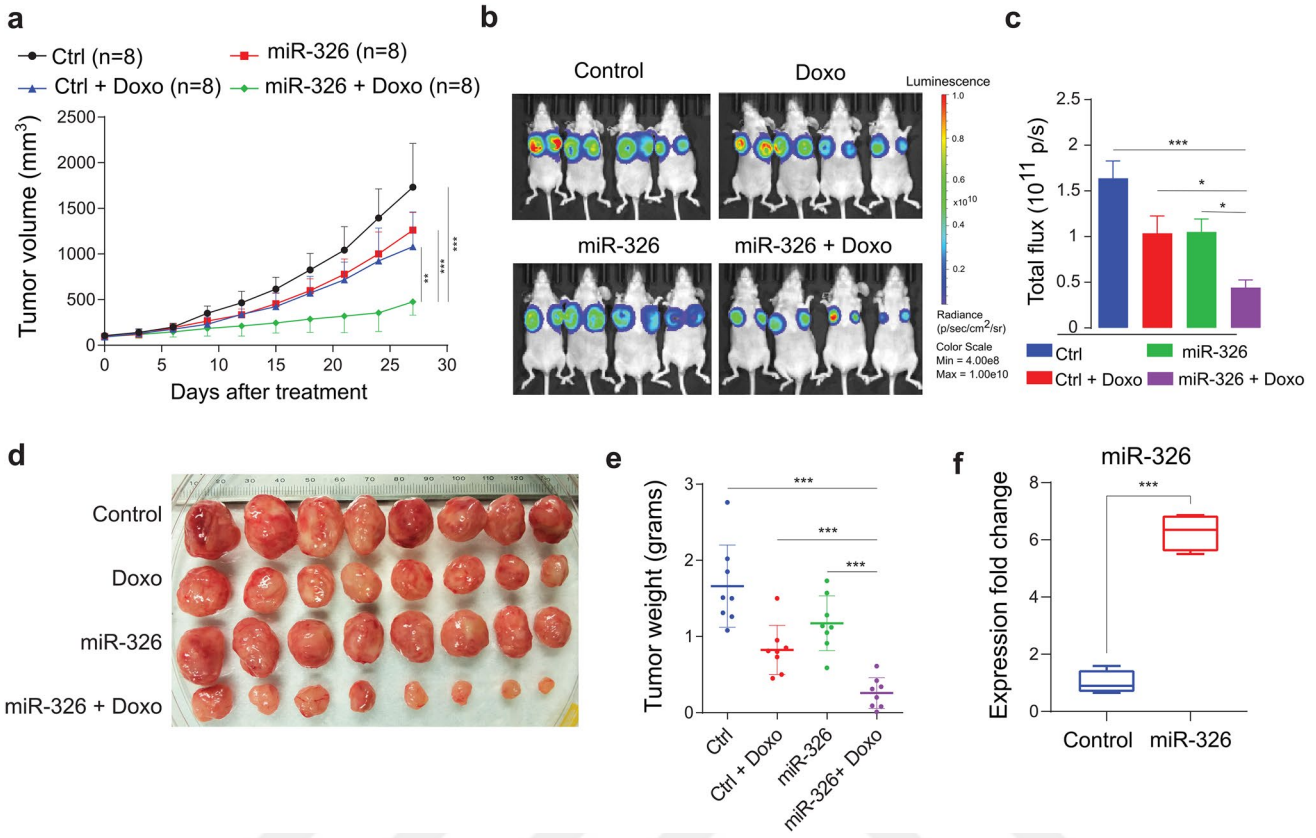


Fig. 3 miR-326 potentiates doxorubicin response in vivo. **a** Changes in tumor volume in MDA-MB-231 xenografts upon vehicle treatment or miR-326 induction in the presence or absence of doxorubicin treatment ($n=8$). Treatments and miR-326 induction were started once tumors reached to 100 mm^3. n indicates tumor number. **b** IVIS images of mice ($n=4$) from A, taken on the last day of the experiment. **c** Quantifications of luciferase intensity in tumors from b. **d** Images showing isolated tumors from a. **e** Dot plots comparing the weights of tumors from each group shown in a. **f** Expression of miR-326 in control vs miR-326 group xenografts. Normality/Lognormality was assessed by D'Agostino-Pearson or Shapiro–Wilk test. Statistical significance was evaluated by unpaired t test

hypothesis that ITGA5 is the principal component of the DoxoR miRNA-mRNA network that is activated by FN1 and suppressed by miR-326 to reduce doxorubicin response.

HIF1α and ECM stiffness regulate miR-326 expression

Having showed miR-326 as a key determinant of doxorubicin response, we next sought to identify its upstream regulators. Increased tumor stiffness was shown to modulate the expression of genes including *HIF1A* and *VEGFA* [31]. Furthermore, we previously demonstrated that TNBC tumors become stiff as they acquire chemoresistance via LOX-mediated collagen crosslinking and fibronectin assembly [15]. These data suggest that expression of miR-326 which we identified to be downregulated in chemoresistant TNBC tumors could be controlled by tumor stiffness. To test this hypothesis, we first examined the association of miR-326 expression with ECM stiffness in TNBC patient tumors and observed a significant enrichment of genes related to ECM organization (including genes modulating ECM stiffness) in TNBC tumors expressing low miR-326 in two different datasets (Figs. 6a, S5a). To experimentally test the role of ECM stiffness in regulating miR-326 expression, we modeled increased stiffness in vitro, using 3D culture of MDA-MB-231 cells. To this end, collagen type I and matrigel were mixed at different concentrations as previously reported. It was shown that increasing collagen concentration [32], or addition of matrigel to collagen matrices increases ECM stiffness [33]. In line with this, we observed a gradual decrease in miR-326 expression with increasing ECM stiffness (Fig. 6b), supporting the critical role it has in ECM-driven chemoresistance.

In the DoxoR miRNA-mRNA network, it was predicted that the hypoxia-regulated transcription factor, HIF1α inhibits miR-326 expression (Fig. 1d). Furthermore, we had previously shown that doxorubicin-resistant tumors are hypoxic, and hypoxia can increase ECM stiffness via HIF1α-mediated transcription of genes involved in ECM modulation, including LOX [15]. Here, we demonstrated

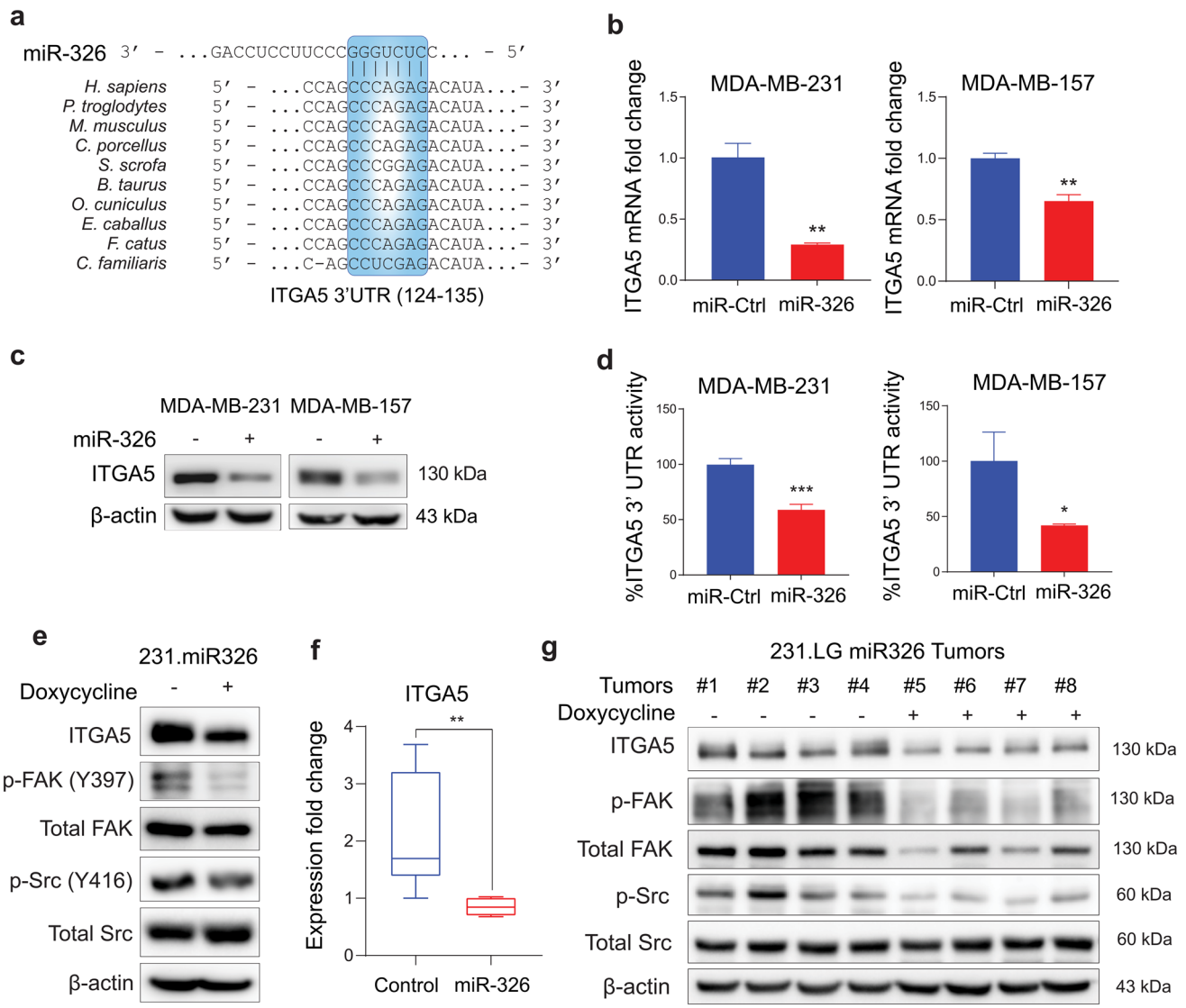


Fig. 4 miR-326 targets FN1 receptor, ITGA5 and blocks its downstream FAK/Src signaling. **a** Graphical representation of conserved miR-326-binding site within the 3′-UTRs of *ITGA5* from different species. **b, c** qRT-PCR (**b**) and Western blot (**c**) analyses showing changes at ITGA5 levels upon miR-326 transfection in MDA-MB-231 (left) and MDA-MB-157 (right) cells for 48 h. **d** Luciferase activity of the reporter construct fused with 3′-UTR of *ITGA5* in MDA-MB-231 (left) and MDA-MB-157 (right) cells transfected with miR-Ctrl or miR-326. **e** Western blot analysis showing changes in ITGA5, p-FAK, total FAK, p-Src, and total Src levels in 231. miR-326 cells either not induced or induced with doxycycline to express miR-326. **f** Expression of ITGA5 mRNA in control vs. miR-326 expression-induced tumors. **g** Western blot analysis showing changes in FN1, ITGA5, p-FAK, total FAK, p-Src, and total Src levels in 231. miR-326 xenografts either not induced or induced with doxycycline to express miR-326. Statistical significance was evaluated by unpaired *t* test

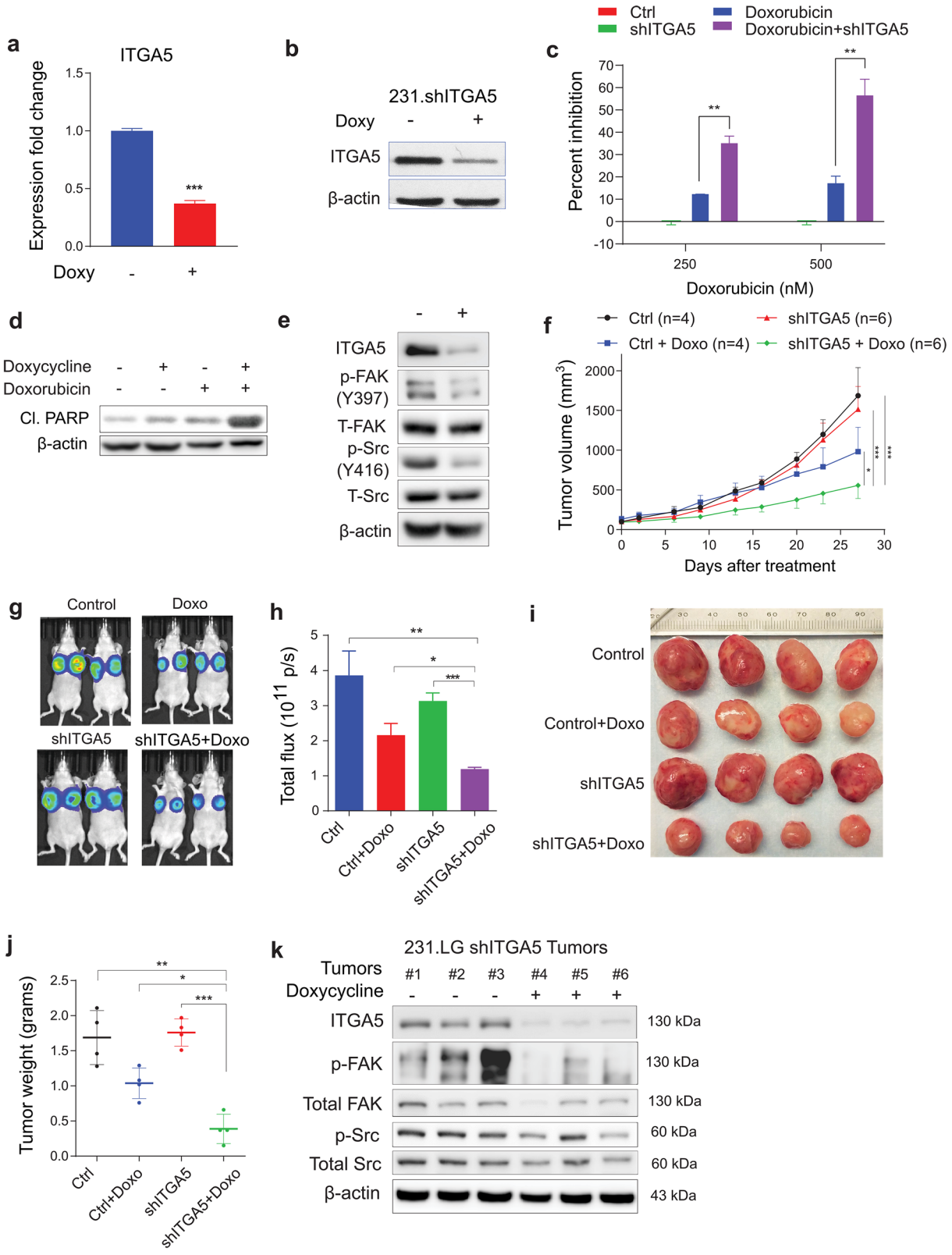
that expression of HIF1α and hallmark hypoxia score are negatively correlated with the expression of miR-326 in multiple breast cancer patient datasets (Figs. 6c and S5b), suggesting that HIF1α may be negatively regulating miR-326 expression. Furthermore, genes upregulated in response to hypoxia are enriched in tumors of patients with low miR-326 expression (Fig. 6d). Experimentally, we demonstrated that culturing MDA-MB-231 cells under hypoxic conditions for 12 and 24 h resulted in a significant decrease in miR-326 levels by qRT-PCR (Fig. 6e). To test whether the down-regulation of miR-326 was mediated directly by HIF1α, we inhibited HIF1α in MDA-MB-231 cells and observed a significant increase in miR-326 levels (Fig. 6f). Our in-silico analysis revealed multiple hypoxia response elements (HRE) and hypoxia ancillary sequences (HAS) in the genomic locus in which miR-326 resides (Fig. 6g). HREs are functionally activated when the region contains an adjacent HAS within 7 to 15 nt downstream [34, 35]. Accordingly, we designed

4 different sets of primers that collectively target all HREs, including those adjacent to HAS, and 1 primer set that does not target any HRE, as a negative control (region #4). We used a primer set amplifying the promoter region of VEGF as the positive control. We then carried out a ChIP experiment and pulled down HIF1α under hypoxic conditions induced by $CoCl_2$ treatment. This showed that HIF1α directly binds to HREs within the miR-326 locus at elevated levels, leading to its transcriptional repression.

Discussion

Although TNBC patients respond to chemotherapy at relatively higher rates—as high as 60% for some chemotherapy regimens—compared to non-TNBC patients, many patients either have de novo resistance or ultimately develop resistance to chemotherapy, limiting their long-term use and dramatically exacerbating the mortality rates [5, 7–9]. Despite the recent approval of the immune checkpoint inhibitors, e.g., atezolizumab [10], and the antibody–drug conjugate, Sacituzumab govitecan-hziy [12] in refractory, metastatic TNBCs, the improvement in progression-free survival is limited, which necessitates the identification of novel therapy options that can improve survival rates in TNBCs. Here, we developed, to the best of our knowledge, the first miRNA-mRNA network of chemoresistance in TNBCs by integrating mRNA- and miRNA-sequencing, network simulations, and patient data analyses (Fig. 1a). This identified FN1 as the hub of the chemoresistance network (Fig. 1d, e). We further demonstrated the functional importance of FN1 in the acquisition of resistance via activation of its cell-surface receptor ITGA5, and the downstream pro-survival signaling, leading to the blockage of drug-induced apoptosis in TNBC (Fig. 2a, b). The activity of integrin signaling was controlled by hypoxia-regulated miR-326, whose overexpression transcriptionally suppressed ITGA5 and deactivated the downstream FAK/Src signaling pathway, leading to increased response to chemotherapy in vitro and in vivo. These results were recapitulated by ITGA5 knockdown in vitro and in vivo, supporting the role of miR-326 on chemoresponse via modulation of integrin signaling in TNBCs.

Fibronectin (gene: *FN1*) is a fibrillary protein that constitutes one of the crucial ECM components and acts as a mechanical support for cells owing to its elastic characteristics [36]. In addition, the interaction of fibronectin with the integrin α5β1 receptor facilitates bidirectional signaling processes between ECM and the intracellular compartments [37]. The role of the heterodimeric integrin α5β1 receptor in tumorigenesis and as a potential therapeutic target has previously been studied in detail [38, 39]. ITGB1 is the well-studied component of the heterodimeric receptor that has been demonstrated to provide de novo doxorubicin resistance in both hormone receptor positive and negative models in vitro, as well as to facilitate acquired doxorubicin resistance in multiple cancer types including TNBC [16, 18, 40]. However, ITGA5 has not been studied to the same extent although it confers high specificity for the binding of the complex to fibronectin [39, 41]. Our study identified FN1 and ITGA5 as crucial players in determining response to different chemotherapy agents, including doxorubicin and paclitaxel which are among the commonly used chemotherapies in TNBC, through integrin signaling activation (Figs. 2a, b, 5, S3). We validated our results using three different TNBC cell lines, namely, MDA-MB-231, MDA-MB-157 and MDA-MB-436. Among those, MDA-MB-231 is the well-established and commonly used tumorigenic cell line [42, 43]. Hence, we generated xenografts of MDA-MB-231 cells expressing miR-326/shITGA5 to test the role of miR-326/ITGA5 axis in chemotherapy response in vivo. Future studies are needed to further support the roles of miR-326/ITGA5-FN1 axis in regulating in vivo response of cell line models belonging to different TNBC subtypes to different classes of chemotherapies, such as the platinum-based agents. We have previously demonstrated that expressions of both of these genes were regulated by the ECM remodeler, LOX, and were significantly associated with clinical outcome in chemotherapy-treated TNBC patients [15]. LOX crosslinks and stabilizes collagen and elastin fibers together with the induction of fibronectin assembly, thereby controlling tissue stiffness [44], which further leads to reduced drug uptake [15]. In addition to regulating drug penetration, tissue stiffness may also modulate the expression of genes that are important for growth and invasiveness, such as HIF1A and VEGFA [31]. Along these lines, we showed that miR-326 expression is strongly reduced upon culturing TNBC cells in the presence of ECM with increasing stiffness. Given the functional roles of LOX in increasing tumor stiffness in chemoresistant TNBC tumors, it would be interesting to test a potential regulation of the miR-326/ITGA5-FN1 axis by LOX and a potential contribution of the axis to drug penetration. Moreover, a type I collagen (COL1A2) was also found in our miRNA–mRNA network of doxorubicin resistance that further corroborates the importance of ECM modulation, at the level of transcription, post-transcription, and assembly in chemoresistant TNBCs. Given the well-known association of ECM regulation and integrin signaling with metastasis, a potential role of miR-326 in breast cancer metastasis can also be investigated in the future. There are indeed a few studies showing a potential involvement of miR-326 in inhibiting cell invasion in vitro in different cancers including breast cancer [45, 46]. Nevertheless, a more extensive investigation including in vivo testing is warranted.



MicroRNAs post-transcriptionally regulate more than 60% of human protein-coding genes, ultimately linking them to a plethora of cellular and physiological processes. They are indispensable for animal development, differentiation, and homeostasis and are also involved in cancer initiation, progression, and drug resistance as tumor suppressors or

◂**Fig. 5** Inhibiting ITGA5 overcomes FN1-driven chemoresistance in vitro and potentiates chemoresponse in vivo. **a, b** qRT-PCR (**a**) and Western blot (**b**) analysis validating ITGA5 knockdown in 231.shITGA5 cells after 48 h of induction. **c** Percent growth inhibition of 231.shITGA5 cells seeded onto 20 µg/mL fibronectin upon combination of doxycycline induction and doxorubicin. **d** Western blot analysis showing changes in the apoptosis marker, cleaved PARP, upon combination of shITGA5 induction and doxorubicin in MDA-MB-231.shITGA5 cells seeded onto 20 µg/mL FN. **e** Western blot analysis showing changes in ITGA5, p-FAK, total FAK, p-Src, and total Src levels in 231.shITGA5 cells either not induced or induced with doxycycline to express shITGA5. **f** Changes in tumor volume in MDA-MB-231 xenografts upon vehicle treatment or shITGA5 induction in the presence or absence of doxorubicin treatment ($n=4$ for control and Doxo groups, and $n=6$ for shITGA5 and combination groups). Treatments and shITGA5 induction were started once tumors reached to 100 mm^3. n indicates tumor number. **g** IVIS images of mice from F, taken on the last day of the experiment. **h** Quantifications of luciferase intensity in tumors from g. **i** Images showing isolated tumors from f. **j** Dot plots comparing the weights of tumors from each group shown in f. **k** Western blot analysis showing changes in FN1, ITGA5, p-FAK, total FAK, p-Src, and total Src levels in 231.shITGA5 xenografts either not induced or induced with doxycycline to express shITGA5. Statistical significance was evaluated by unpaired *t* test

oncogenes [47, 48]. Accordingly, miR-326 has been reported to function as a tumor suppressor in different cancer types including breast cancer [45], cervical cancer [49], lung cancer [50], and glioblastoma [51]. Furthermore, miR-326 was shown to regulate multidrug resistance-associated protein (MDR) and confer sensitivity to VP-16 and doxorubicin in ER-positive breast cancer cells [52]. Here, we demonstrated the tumor suppressor role of miR-326 as a stiffness- and hypoxia-regulated chemosensitizer in TNBC that post-transcriptionally regulate several key components of the ECM, including FN1 and its receptor ITGA5 (Figs. 2c–e, 3a–e, and 4e–g). These findings together with our previously published data on the role of ECM crosslinking in the acquisition of chemoresistance suggest a multilayered modulation of the ECM at transcriptional, post-transcriptional, and protein assembly levels that controls not only drug penetration but also the expression of resistance-regulating miRNAs (here: miR-326) and thereby modulating downstream survival signaling pathways (here: integrin signaling). In this line, we anticipate a strong translational potential of targeting the ECM re-modelers or integrins or restoring the expression of ECM-regulating miRNAs to augment clinical outcome in chemoresistant TNBCs.

Hypoxia is a hallmark of high-stage tumors which is generally observed within the core of solid tumors that is characterized by oxygen deprivation due to incomplete vascularization [53]. Hypoxia drives certain intracellular and extracellular changes that ultimately provides better adaptation to the microenvironment and to evade apoptosis under drug treatment. Hypoxia-driven changes frequently occur via activation of the hypoxia-inducible factors (HIFs) [54]. *HIF1A* encodes HIF-1α protein which constitutes the oxygen-sensitive subunit of the heterodimeric HIF transcription factor [55]. It has previously been reported by us and others as a modulator of several ECM components, including FN1 and ITGA5 to advance the tumorigenic process and also as a mediator of doxorubicin resistance in multiple cancer types [15, 38, 56, 57]. In this study, we identified a novel miRNA target of HIF-1α (Figs. 1d, 6), miR-326, upstream of integrin signaling that triggers chemoresistance in TNBCs. We identified several HREs in miR-326 promoter and showed direct binding of HIF-1α, leading to suppression of miR-326 expression under hypoxic conditions (Fig. 6e–g).

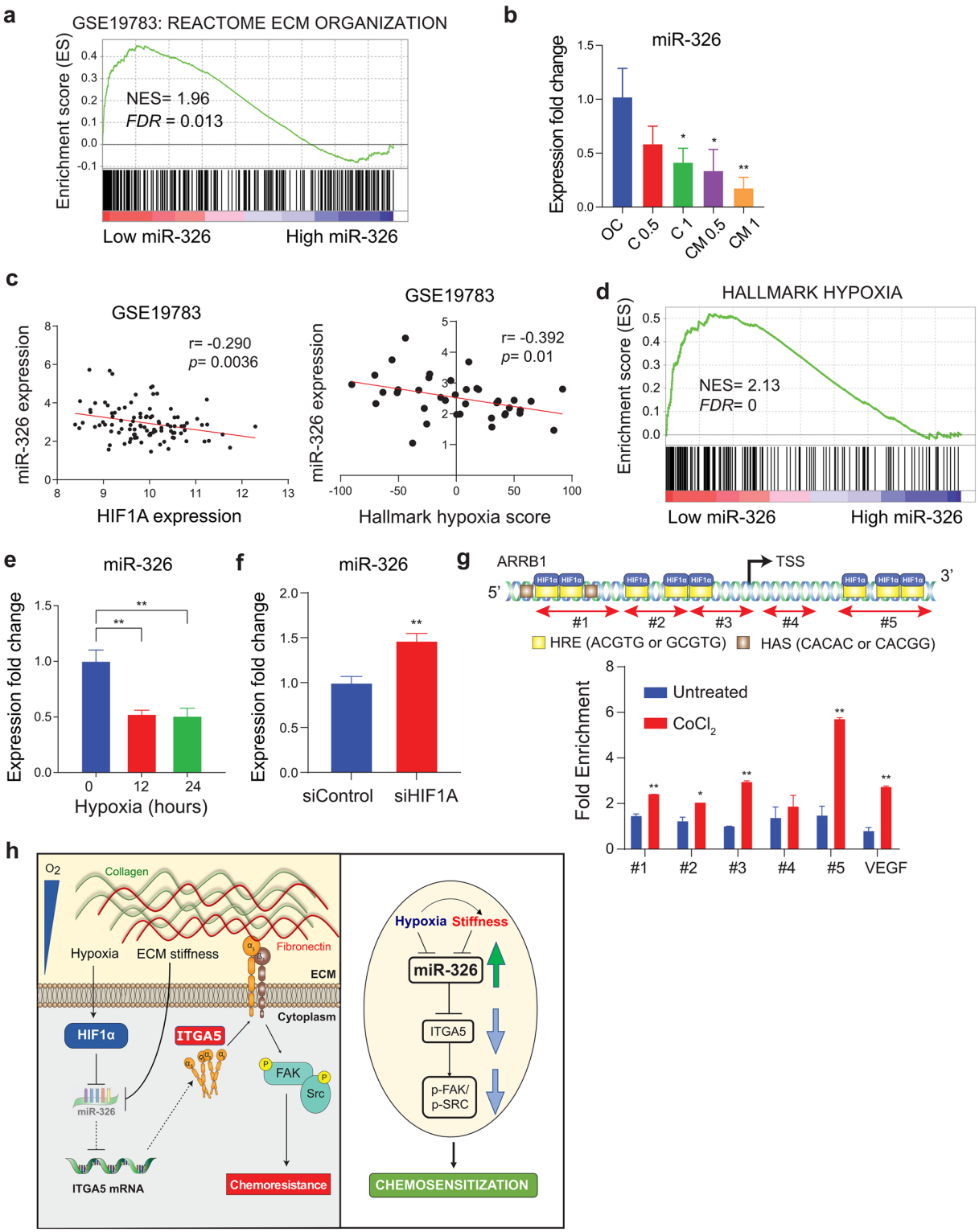
Conclusion

In brief, we deciphered a novel molecular mechanism of chemotherapy resistance in TNBC that involves the stiffness/hypoxia-regulated HIF1A/miR-326/ITGA5-FN1 axis by utilizing a network-based approach that integrates profiling of miRNA and mRNAs, network simulations, and patient data analyses. Downregulation of miR-326 in cancer cells in contact with a stiff ECM under hypoxia, and the subsequent activation of integrin/FAK signaling pathway upon increased ITGA5 lead to chemotherapy resistance (Fig. 6h). Therefore, we propose that ectopic expression of miR-326 decreases ITGA5 expression and impairs downstream signaling, thus, resulting in chemotherapy sensitization and tumor growth inhibition (Fig. 6h). These findings provide a pre-clinical support for the potential use of miR-326 or inhibitors against miR-326 targets, namely ITGA5, to overcome chemotherapy resistance in TNBC.

Materials and methods

In vivo experiments

All animal experiments were approved by the Animal Ethics Committee of Bilkent University. The studies were carried out in compliance with the ARRIVE guidelines. All methods were carried out in accordance with relevant guidelines and regulations. 6–8-week-old female athymic nu/nu mice were subcutaneously injected with 2×10^6 231.Luc2.GFP cells prepared in 100 µL PBS:Matrigel (1:1) solution into the left and right mammary fat pads (MFPs). After tumors became palpable, their growth was measured regularly twice a week using a caliper, and tumor volume was calculated as (length × $width^2$)/2. Development of doxorubicin-sensitive/resistance xenografts has previously been described [15]. To test the effects of miR-326 overexpression or shITGA5 on doxorubicin response, mice with palpable tumors were treated



with doxorubicin (2.5 mg/kg) after induction of miR-326 or shITGA5 expressions with doxycycline (100 µg/mL). To perform the tumor bioluminescence imaging, mice were anesthetized with isoflurane, 150 mg/kg D-luciferin (Sigma Aldrich, St Louis, MO, USA) was injected into intraperitoneal (i.p.) cavity, and the images were acquired using Lumina III In vivo Imaging System (Perkin Elmer, Waltham, MA, USA). All mice were sacrificed when the tumors of control group reached 1500 mm^3, and the tumors were collected and weighed.

◂**Fig. 6** HIF-1α and tumor stiffness regulate miR-326 expression. **a** Genes associated with extracellular matrix organization are enriched in tumors of patients with low miR-326 expression in GSE19783 dataset. **b** qRT-PCR analysis of miR-326 expression in MDA-MB-231 cells embedded in ECM with increasing stiffness generated by 0.5 or 1 mg/mL collagen type I (C) with or without Matrigel (M) in comparison with only cells (OC). **c** Pearson correlation analysis of miR-326 expression with HIF1A expression or hallmark hypoxia score in GSE19783 dataset. **d** Genes associated with hypoxia are enriched in tumors of patients with low miR-326 expression in GSE19783 dataset. **e** qRT-PCR analysis showing miR-326 expression in MDA-MB-231 cells under hypoxic conditions at 0, 12, and 24 h time points. **f** qRT-PCR analysis showing miR-326 expression upon HIF1A siRNA transfection in MDA-MB-231 cells for 48 h. **g** HRE and HAS motifs on miR-326-host gene, *ARRB1,* promoter region, and ChIP analysis showing increased *ARRB1* promoter occupancy by HIF-1α upon $CoCl_2$ treatment. **h** Schematic representation of the mechanistic summary. Statistical significance was evaluated by unpaired *t* test

Whole transcriptome sequencing (RNA-Seq and small RNA-Seq) and data analyses

After total RNA was isolated from doxorubicin-sensitive and doxorubicin-resistance tumors, RNA-Seq and small RNA-Seq were performed with 4 tumors from each group using Illumina HiSeq 2500 platform at McGill University Genome Centre. The procedure on how RNA-Seq was done and analyzed is described previously [15], and the raw data are uploaded with an accession number of PRJNA607780. Data analysis for miRNA-Seq was done by aligning raw sequence data with UCSC *Homo sapiens* reference genome (hg19, GRCh37) using Bowtie v1.1.2 according to default parameters. Identification of the differentially expressed miRNA was performed using three different differential expression algorithms (edgeR, DESeq, and NOISEQ) to increase robustness. Consensus miRNAs from these three programs were taken for further analyses.

Network activity flow

Activity flow analysis was used to measure and simulate the effects of regulatory interactions between miRNAs, upstream regulators, and proteins in the given network based on random walks on graphs. Briefly, initial activity level of upstream regulators and upregulated proteins and miRNAs were designated as "1" while the rest was valued as "0." Induction edges and inhibition edges exerted positive and negative effects, respectively, over the interacted nodes (proteins, miRNAs, and upstream regulators). Activity flow score of each node is modeled as a discrete-time continuous-state Markov processes and the steady-state activity levels are found by simulation via our in-house code written in Java. Later, each node was ranked according to its activity flow score that also reflected the centrality of that node in the given network.

Cell culture and reagents

Human breast cancer cell lines MDA-MB-231, MDA-MB-157, and MDA-MB-436 were obtained from ATCC (Manassas, VA, USA) whereas MDA-MB-231.Luc2.GFP (shortly 231.Luc2.GFP), a modified and labeled version of MDA-MB-231, was a kind gift from Dr. Dihua Yu (MD Anderson Cancer Center, Houston, TX, USA). All cell lines were cultured in Dulbecco Modified Eagle Medium (DMEM) supplemented with 50 U/ml penicillin/streptomycin, 1% non-essential amino acids, and 10% fetal bovine serum (FBS). Mycoplasma contamination test was performed regularly using MycoAlert mycoplasma detection kit (Lonza, Basel, Switzerland).

Cell seeding on fibronectin-coated wells

The concentration of fibronectin (Sigma Aldrich, St Louis, MO, USA) was adjusted to 20 µg/mL in PBS, and as much as 40 µL or 900 µL was added to 96 or 6-well plates, respectively. Plates were incubated at 4 °C overnight and then washed once with PBS. Then, 8000 cells/well or 200,000 cells/well were seeded on top of fibronectin-coated wells in 2% FBS containing DMEM for 96-well or 6-well plates, respectively.

Cell embedding to ECM with increasing stiffness

Mixtures of collagen type I and matrigel were prepared at a ratio of 1:1 with different collagen concentrations. Collagen mixtures were prepared as described before [15] at a final concentration of 0.5 or 1 mg/mL with or without an equal volume of matrigel. MDA-MB-231 cells were suspended in these mixtures and seeded on 12 well plates and cultured for 4 days.

Transient transfection with miRNA mimics and reporter constructs

Transfections were performed as previously described [58–60]. miR-326 mimic and siHIF1A were transfected at 20 nM concentrations, then RNA or protein was isolated 48-h post-transfection. Reporter construct carrying the 3'-UTR of human *ITGA5* (NM_002205) was transfected at a dose of 50 ng per well in 96-well experiment setup for the luciferase reporter assay experiments.

Cell viability assays

Fibronectin coating and cell seeding were performed as described above. Doxorubicin and paclitaxel treatments were carried out 12 h after miRNA mimics or siRNA transfection. In case of experiments without transfection, drug was given 24 h after cell seeding. Cell viability assay was performed with Cell Titer-Glo Luminescent Cell Viability (Promega, Madison, WI, USA) 48 h post-drug treatment.

Quantitative RT-PCR analysis

Total RNA was obtained from cultured cells or mice xenograft tumors using TRIsure (Bioline, Luckenwalde, Germany). For isolating RNA from ECM-embedded cells, collagen was degraded using 2 mg/mL collagenase at 37 °C for 10 min, followed by 3 washes with cold PBS. For isolation of RNA from xenograft tumors, tumors were sliced into small pieces, a part of which was homogenized for complete lysis. Then, cDNA synthesis was performed using RevertAid RT Reverse Transcription Kit (Life Technologies) following manufacturer's protocol. Quantitative real-time PCR assay was carried out using Light Cycler 480 SYBR Green I Master kit (Roche) in triplicates. *GAPDH* and *HPRT* were used as housekeeping genes. The sequences of the qRT-PCR primers are provided in Supplementary Table 1a. For qRT-PCR data analysis, $\Delta\Delta C_T$ method was utilized. For miRNA qRT-PCR experiments, *RNU44* and *RNU48* were used as housekeeping genes, and qRT-PCR was performed by TaqMan Real-Time PCR Assays (Thermo Fisher Scientific).

Chromatin immunoprecipitation (ChIP) assay

ChIP experiment was done using the EZ-Magna ChIP™ A/G Chromatin Immunoprecipitation Kit from Sigma-Aldrich (17–10,086), following manufacturer's instructions. Briefly, 10×10^6 MDA-MB-231 cells were fixed with 1% formaldehyde for 10 min followed by quenching with 125 mM glycine for 5 min. Cells were lysed in 500 uL lysis buffer, and nuclear lysates were extracted. Sonication was done for 20 s intervals for a total of 15 rounds. 150 uL chromatin was incubated with the beads together with the HIF-1α (39,665, Active Motif) or IgG antibodies at + 4 °C, overnight with slow agitation. Samples were washed with low and high salt wash buffers, and Proteinase K treatment was done for 2 h at 62 C with shaking. Samples were incubated at 95 °C for 10 min and separated from the beads using a magnetic separator. DNA was isolated, and RT-PCR was performed using primers targeting miR-326 or VEGF promoters. The results are normalized to IgG and input controls.

Western blotting

Protein isolation and Western blotting were performed as previously described [59, 60]. Briefly, proteins were extracted using RIPA lysis buffer with the addition of protease and phosphatase inhibitor cocktails, and protein concentrations were measured using the BCA Protein Assay Reagent Kit (Thermo Scientific, Rockford, IL). Equal amounts of protein were separated using 8–10% SDS-PAGE gel. Separated proteins were transferred onto PVDF membranes (Bio-Rad, USA) using Trans-Blot turbo transfer system (Bio-Rad) and incubated with primary antibodies (Supplementary Table 1b). Horseradish peroxidase-conjugated anti-mouse or anti-rabbit antibodies (Cell signaling Technology, USA) were used as secondary antibodies, and signals were detected by enhanced chemiluminescence reagent (Amersham Pharmacia Biotech, Amersham, UK) using a CCD imager (GE Healthcare, Chicago, Illinois, USA).

Hypoxia assay

MDA-MB-231 cells were seeded into 6-well plate and incubated at 37 °C in normoxic conditions. 24-h post-cell seeding, plates were transferred in Hypoxia Incubator Chamber (StemCell Technologies, Vancouver, Canada) with 1% oxygen, 5% CO_2, and 94% nitrogen at 37 °C. At certain time points, cells were harvested by trypsinization and preserved for RNA isolation.

Construction of 3′-UTR plasmids

The construction of plasmids was carried out as previously described [61]. The 3′-UTR of *ITGA5* containing binding sites for miR-326 was amplified using primers listed in Supplementary Table 1c. Amplicons of 3′-UTR of *ITGA5* were ligated into psiCHECK2 vector backbone.

Dual-luciferase reporter assay

Dual-luciferase reporter assay was performed as previously described [61]. Luciferase activity was measured in Synergy HT microplate reader (BioTek, Vermont, USA) 24 h post-transfection, and the values were normalized to *firefly* luciferase activity.

Stable transfections using lentiviral vectors

shMIMIC-inducible mCMV-turboRFP human lentiviral hsa-miR-326, TRIPZ-inducible lentiviral non-silencing shRNA Control, and TRIPZ-inducible Lentiviral human ITGA5 shRNA (shortly shITGA5) were purchased from Dharmacon (Lafayette, CO, USA). Transduction using miR-326 viral particles into 231.Luc2.GFP cells was performed in 6-well

plates. 20-h post-transduction, the medium containing virus was changed with fresh medium, allowing cells to grow further. Selection was done by incubating cells in the medium containing 2 µg/mL puromycin for 72 h. To generate viral particles used for shRNA vectors, 6 µg of vectors along with 4.3 µL of trans-lentiviral packaging mix was co-transfected into HEK293FT cells in 6-well plate using $CaCl_2$ reagent as suggested in the manufacturer's protocol (Dharmacon). After 48 h incubation, the viral particles were collected and transduced into 231.Luc2.GFP cells. Further selection was done by treating cells with the medium containing 2 µg/mL puromycin for 72 h.

miRNA–mRNA interaction network construction

The threshold of differentially expressed miRNAs and mRNAs between sensitive and resistant xenografts was set as $\log2FC \leq -0.59$ and $\log2FC \geq +0.59$, P value < 0.05, yielding 1280 mRNAs and 68 miRNAs. List of these mRNAs and miRNAs was then uploaded to web-based software application for omics analysis, namely Ingenuity Pathway Analysis (IPA) (QIAGEN Inc., https://qiagenbioinformatics.com/). In IPA, the miRNAs were initially paired with their predicted mRNA targets using "microRNA target filter" analysis. This resulted in 616 mRNAs being regulated by 42 miRNAs in 1718 interactions. As miRNA-mRNA expressions are expected to be inversely correlated, inverse pairing analysis was performed using "expression pairing" filter. This reduced the numbers into 463 mRNAs, 41 miRNAs, and 870 interactions. List of 463 mRNAs was again uploaded to the IPA core analysis to check the associated pathways. Genes from identified pathways were recollected and constructed in network used IPA "connect" function. In addition, "grow within own data" function provided in IPA was also used to find the closely related genes from the initial uploaded genes. Then, upstream regulators were added to the network followed by miRNA integration. The network was finalized by removing positively correlated miRNA-mRNA interactions. Open-source platform-based program, namely Cytoscape (https://cytoscape.org/), was also utilized to re-visualize the network obtained from IPA.

Pathway analysis, patient data, and statistical analyses

Patient data were retrieved from the NCBI GEO database and from online survival analysis tool, KM plotter [62]. Survival curves were generated based on median separation using Kaplan–Meier method, and significance between groups was calculated by Log-rank test. Chemotherapy-treated patient subgroup from the KM Plotter database (release version 2017) was created by selecting the adjuvant chemotherapy-treated patients and excluding the endocrine-treated ones.

miRWalk2.0 [63] was used as target prediction algorithm to predict miRNA gene targets in the network. This online available tool is a comprehensive program for miRNA target prediction that can combine other 11 miRNA target prediction databases including TargetScan, PITA, and miRDB in the analysis. To get more robust data, a stringent threshold was applied by taking common genes identified from at least 8 of those 12 databases.

We generated miR-326 target signature using the list of predicted miR-326 targets and Hallmark hypoxia signature directly from the Molecular Signatures Database and calculated a score for both signatures for each patient in GSE19783 [28] dataset using the following approach: We extracted the expression values of genes found in either of the signatures and converted them into z-scores. We then added up the z-scores to assign a signature score for each patient.

Pearson correlation co-efficient was used for correlation analysis. 2-tailed Student's t test was performed to compare two experimental groups. Box plots show median number, and the 25th to 75th quartiles. Upper and lower whiskers denote the minimum and maximum values in the corresponding group. Graphs and curves were drawn using GraphPad software (GraphPad software Inc., La Jolla, CA, USA). Significance threshold was described as $*P < 0.05$; $**P < 0.01$; $***P < 0.001$; ns, not significant.

Supplementary Information The online version contains supplementary material available at https://doi.org/10.1007/s10549-022-06569-5.

Acknowledgements We are thankful to the members of the Ozgur Sahin laboratory for invaluable discussion and advice. We thank Jitao David Zhang for his help with RNA-sequencing data.

Authors contributions OS supervised the study. OS and UR conceptualized the study. RA, UMT, IOT, OzgeS, PG, and UR designed and performed the experiments, data acquisition, and data analysis. RA, UMT, IOT, OzgeS, and OS contributed to writing, review, and/or revision of the manuscript. HO and TC helped building the miRNA–mRNA network. YR oversaw RNA-seq and small RNA-seq experiments. All authors read and approved the final manuscript.

Funding This work was supported by European Commission FP7 Marie Curie Career Integration Grant PCIG14-GA-2013-631149 (OS), the American Cancer Society Institutional Research Grant IRG-17-179-04 (OS), NIH Research Project Grants R01-CA267101 (OS) and 2P20GM109091-06 (OS), the scholarship from Higher Education Commission of Pakistan (UR), the scholarship from 2211/A TÜBİTAK Domestic PhD Scholarship Program (UMT), and Susan G. Komen Interdisciplinary Graduate Training to Eliminate Cancer Disparities (IGniTE-CD) GTDR17500160 (OzgeS). YR is a research scholar of Fonds de recherche du Québec—Santé (FRQS).

Data availability Raw RNA-seq data analyzed in the current study have been made available on NCBI Sequence Read Archive with accession PRJNA607780. The small RNA-Seq data have also been deposited to the SRA with the submission ID: PRJNA806717.

Declarations

Conflict of interest O.S. is the co-founder and manager of OncoCube Therapeutics LLC and founder and president of LoxiGen, Inc. The other authors declare no potential conflict of interest.

References

1. Bray F, Ferlay J, Soerjomataram I, Siegel RL, Torre LA, Jemal A (2018) Global cancer statistics 2018: GLOBOCAN estimates of incidence and mortality worldwide for 36 cancers in 185 countries. CA Cancer J Clin 68:394–424. https://doi.org/10.3322/caac.21492
2. Hwang SY, Park S, Kwon Y (2019) Recent therapeutic trends and promising targets in triple negative breast cancer. Pharmacol Ther 199:30–57. https://doi.org/10.1016/j.pharmthera.2019.02.006
3. Boyle P (2012) Triple-negative breast cancer: epidemiological considerations and recommendations. Ann Oncol 23(6):7–12. https://doi.org/10.1093/annonc/mds187
4. Bianchini G, Balko JM, Mayer IA, Sanders ME, Gianni L (2016) Triple-negative breast cancer: challenges and opportunities of a heterogeneous disease. Nat Rev Clin Oncol 13:674–690. https://doi.org/10.1038/nrclinonc.2016.66
5. Santonja A, Sanchez-Munoz A, Lluch A, Chica-Parrado MR, Albanell J, Chacon JI et al (2018) Triple negative breast cancer subtypes and pathologic complete response rate to neoadjuvant chemotherapy. Oncotarget 9:26406–26416. https://doi.org/10.18632/oncotarget.25413
6. Carey LA, Dees EC, Sawyer L, Gatti L, Moore DT, Collichio F et al (2007) The triple negative paradox: primary tumor chemosensitivity of breast cancer subtypes. Clin Cancer Res 13:2329–2334. https://doi.org/10.1158/1078-0432.CCR-06-1109
7. Gass P, Lux MP, Rauh C, Hein A, Bani MR, Fiessler C et al (2018) Prediction of pathological complete response and prognosis in patients with neoadjuvant treatment for triple-negative breast cancer. BMC Cancer 18:1051. https://doi.org/10.1186/s12885-018-4925-1
8. Lebert JM, Lester R, Powell E, Seal M, McCarthy J (2018) Advances in the systemic treatment of triple-negative breast cancer. Curr Oncol 25:S142–S150. https://doi.org/10.3747/co.25.3954
9. Liedtke C, Mazouni C, Hess KR, Andre F, Tordai A, Mejia JA et al (2008) Response to neoadjuvant therapy and long-term survival in patients with triple-negative breast cancer. J Clin Oncol 26:1275–1281. https://doi.org/10.1200/JCO.2007.14.4147
10. Schmid P, Adams S, Rugo HS, Schneeweiss A, Barrios CH, Iwata H et al (2018) Atezolizumab and nab-paclitaxel in advanced triple-negative breast cancer. N Engl J Med 379:2108–2121. https://doi.org/10.1056/NEJMoa1809615
11. Keenan TE, Tolaney SM (2020) Role of immunotherapy in triple-negative breast cancer. J Natl Compr Canc Netw 18:479–489. https://doi.org/10.6004/jnccn.2020.7554
12. Bardia A, Mayer IA, Vahdat LT, Tolaney SM, Isakoff SJ, Diamond JR et al (2019) Sacituzumab govitecan-hziy in refractory metastatic triple-negative breast cancer. N Engl J Med 380:741–751. https://doi.org/10.1056/NEJMoa1814213
13. Egeblad M, Nakasone ES, Werb Z (2010) Tumors as organs: complex tissues that interface with the entire organism. Dev Cell 18:884–901. https://doi.org/10.1016/j.devcel.2010.05.012
14. Henke E, Nandigama R, Ergun S (2019) Extracellular matrix in the tumor microenvironment and its impact on cancer therapy. Front Mol Biosci 6:160. https://doi.org/10.3389/fmolb.2019.00160
15. Saatci O, Kaymak A, Raza U, Ersan PG, Akbulut O, Banister CE et al (2020) Targeting lysyl oxidase (LOX) overcomes chemotherapy resistance in triple negative breast cancer. Nat Commun 11:2416. https://doi.org/10.1038/s41467-020-16199-4
16. Berrazouane S, Boisvert M, Salti S, Mourad W, Al-Daccak R, Barabe F et al (2019) Beta1 integrin blockade overcomes doxorubicin resistance in human T-cell acute lymphoblastic leukemia. Cell Death Dis 10:357. https://doi.org/10.1038/s41419-019-1593-2
17. Cooper J, Giancotti FG (2019) Integrin signaling in cancer: mechanotransduction, stemness, epithelial plasticity, and therapeutic resistance. Cancer Cell 35:347–367. https://doi.org/10.1016/j.ccell.2019.01.007
18. Lovitt CJ, Shelper TB, Avery VM (2018) Doxorubicin resistance in breast cancer cells is mediated by extracellular matrix proteins. BMC Cancer 18:41. https://doi.org/10.1186/s12885-017-3953-6
19. Zhu H, Wang G, Zhu H, Xu A (2021) ITGA5 is a prognostic biomarker and correlated with immune infiltration in gastrointestinal tumors. BMC Cancer 21:269. https://doi.org/10.1186/s12885-021-07996-1
20. Zhou C, Shen Y, Wei Z, Shen Z, Tang M, Shen Y et al (2022) ITGA5 is an independent prognostic biomarker and potential therapeutic target for laryngeal squamous cell carcinoma. J Clin Lab Anal. https://doi.org/10.1002/jcla.24228
21. Gilbert LA, Hemann MT (2011) Chemotherapeutic resistance: surviving stressful situations. Cancer Res 71:5062–5066. https://doi.org/10.1158/0008-5472.CAN-11-0277
22. Senthebane DA, Rowe A, Thomford NE, Shipanga H, Munro D, Mazeedi M et al (2017) The role of tumor microenvironment in chemoresistance: to survive, keep your enemies closer. Int J Mol Sci. https://doi.org/10.3390/ijms18071586
23. Hwang D, Rust AG, Ramsey S, Smith JJ, Leslie DM, Weston AD et al (2005) A data integration methodology for systems biology. Proc Natl Acad Sci U S A 102:17296–17301. https://doi.org/10.1073/pnas.0508647102
24. Archer TC, Fertig EJ, Gosline SJ, Hafner M, Hughes SK, Joughin BA et al (2016) Systems approaches to cancer biology. Cancer Res 76:6774–6777. https://doi.org/10.1158/0008-5472.CAN-16-1580
25. Nagy A, Lanczky A, Menyhart O, Gyorffy B (2018) Validation of miRNA prognostic power in hepatocellular carcinoma using expression data of independent datasets. Sci Rep 8:9227. https://doi.org/10.1038/s41598-018-27521-y
26. Jezequel P, Loussouarn D, Guerin-Charbonnel C, Campion L, Vanier A, Gouraud W et al (2015) Gene-expression molecular subtyping of triple-negative breast cancer tumours: importance of immune response. Breast Cancer Res 17:43. https://doi.org/10.1186/s13058-015-0550-y
27. Zhao XG, Hu JY, Tang J, Yi W, Zhang MY, Deng R et al (2019) miR-665 expression predicts poor survival and promotes tumor metastasis by targeting NR4A3 in breast cancer. Cell Death Dis 10:479. https://doi.org/10.1038/s41419-019-1705-z
28. Enerly E, Steinfeld I, Kleivi K, Leivonen SK, Aure MR, Russnes HG et al (2011) miRNA-mRNA integrated analysis reveals roles for miRNAs in primary breast tumors. PLoS ONE 6:e16915. https://doi.org/10.1371/journal.pone.0016915
29. de Rinaldis E, Gazinska P, Mera A, Modrusan Z, Fedorowicz GM, Burford B et al (2013) Integrated genomic analysis of triple-negative breast cancers reveals novel microRNAs associated with clinical and molecular phenotypes and sheds light on the pathways

they control. BMC Genomics 14:643. https://doi.org/10.1186/1471-2164-14-643
30. Agarwal V, Bell GW, Nam JW, Bartel DP (2015) Predicting effective microRNA target sites in mammalian mRNAs. Elife. https://doi.org/10.7554/eLife.05005
31. Szot CS, Buchanan CF, Freeman JW, Rylander MN (2011) 3D in vitro bioengineered tumors based on collagen I hydrogels. Biomaterials 32:7905–7912. https://doi.org/10.1016/j.biomaterials.2011.07.001
32. Motte S, Kaufman LJ (2013) Strain stiffening in collagen I networks. Biopolymers 99:35–46. https://doi.org/10.1002/bip.22133
33. Anguiano M, Castilla C, Maska M, Ederra C, Pelaez R, Morales X et al (2017) Characterization of three-dimensional cancer cell migration in mixed collagen-Matrigel scaffolds using microfluidics and image analysis. PLoS ONE 12:e0171417. https://doi.org/10.1371/journal.pone.0171417
34. Kimura H, Weisz A, Ogura T, Hitomi Y, Kurashima Y, Hashimoto K et al (2001) Identification of hypoxia-inducible factor 1 ancillary sequence and its function in vascular endothelial growth factor gene induction by hypoxia and nitric oxide. J Biol Chem 276:2292–2298. https://doi.org/10.1074/jbc.M008398200
35. Rashid I, Pathak AK, Kumar R, Srivastava P, Singh M, Murali S et al (2019) Genome-wide comparative analysis of HIF binding sites in cyprinus carpio for in silico identification of functional hypoxia response elements. Front Genet 10:659. https://doi.org/10.3389/fgene.2019.00659
36. Singh P, Carraher C, Schwarzbauer JE (2010) Assembly of fibronectin extracellular matrix. Annu Rev Cell Dev Biol 26:397–419. https://doi.org/10.1146/annurev-cellbio-100109-104020
37. Hamidi H, Pietila M, Ivaska J (2016) The complexity of integrins in cancer and new scopes for therapeutic targeting. Br J Cancer 115:1017–1023. https://doi.org/10.1038/bjc.2016.312
38. Ju JA, Godet I, Ye IC, Byun J, Jayatilaka H, Lee SJ et al (2017) Hypoxia selectively enhances integrin alpha5beta1 receptor expression in breast cancer to promote metastasis. Mol Cancer Res 15:723–734. https://doi.org/10.1158/1541-7786.MCR-16-0338
39. Schaffner F, Ray AM, Dontenwill M (2013) Integrin alpha5beta1, the fibronectin receptor, as a pertinent therapeutic target in solid tumors. Cancers 5:27–47. https://doi.org/10.3390/cancers5010027
40. Morozevich GE, Kozlova NI, Susova OY, Lupatov AY, Berman AE (2017) Hyperexpression of Integrin alpha5beta1 Promotes Resistance of MCF-7 Human Breast Carcinoma Cells to Doxorubicin via ERK Protein Kinase Down-regulation. Biochemistry (Mosc) 82:1017–1024. https://doi.org/10.1134/S000629791709004 8
41. Aota S, Nomizu M, Yamada KM (1994) The short amino acid sequence Pro-His-Ser-Arg-Asn in human fibronectin enhances cell-adhesive function. J Biol Chem 269:24756–24761
42. Chavez KJ, Garimella SV, Lipkowitz S (2010) Triple negative breast cancer cell lines: one tool in the search for better treatment of triple negative breast cancer. Breast Dis 32:35–48. https://doi.org/10.3233/BD-2010-0307
43. Holliday DL, Speirs V (2011) Choosing the right cell line for breast cancer research. Breast Cancer Res 13:215. https://doi.org/10.1186/bcr2889
44. Lucero HA, Kagan HM (2006) Lysyl oxidase: an oxidative enzyme and effector of cell function. Cell Mol Life Sci 63:2304–2316. https://doi.org/10.1007/s00018-006-6149-9
45. Ghaemi Z, Soltani BM, Mowla SJ (2019) MicroRNA-326 functions as a tumor suppressor in breast cancer by targeting ErbB/PI3K signaling pathway. Front Oncol 9:653. https://doi.org/10.3389/fonc.2019.00653
46. Hu S, Ran Y, Chen W, Zhang Y, Xu Y (2017) MicroRNA-326 inhibits cell proliferation and invasion, activating apoptosis in hepatocellular carcinoma by directly targeting LIM and SH3 protein 1. Oncol Rep 38:1569–1578. https://doi.org/10.3892/or.2017.5810
47. Hong BS, Ryu HS, Kim N, Kim J, Lee E, Moon H et al (2019) Tumor suppressor miRNA-204-5p regulates growth, metastasis, and immune microenvironment remodeling in breast cancer. Cancer Res 79:1520–1534. https://doi.org/10.1158/0008-5472.CAN-18-0891
48. Rupaimoole R, Calin GA, Lopez-Berestein G, Sood AK (2016) miRNA deregulation in cancer cells and the tumor microenvironment. Cancer Discov 6:235–246. https://doi.org/10.1158/2159-8290.CD-15-0893
49. Zhang P, Kong F, Deng X, Yu Y, Hou C, Liang T et al (2017) MicroRNA-326 suppresses the proliferation, migration and invasion of cervical cancer cells by targeting ELK1. Oncol Lett 13:2949–2956. https://doi.org/10.3892/ol.2017.5852
50. Sun C, Huang C, Li S, Yang C, Xi Y, Wang L et al (2016) Hsa-miR-326 targets CCND1 and inhibits non-small cell lung cancer development. Oncotarget 7:8341–8359. https://doi.org/10.18632/oncotarget.7071
51. Nawaz Z, Patil V, Paul Y, Hegde AS, Arivazhagan A, Santosh V et al (2016) PI3 kinase pathway regulated miRNome in glioblastoma: identification of miR-326 as a tumour suppressor miRNA. Mol Cancer 15:74. https://doi.org/10.1186/s12943-016-0557-8
52. Liang Z, Wu H, Xia J, Li Y, Zhang Y, Huang K et al (2010) Involvement of miR-326 in chemotherapy resistance of breast cancer through modulating expression of multidrug resistance-associated protein 1. Biochem Pharmacol 79:817–824. https://doi.org/10.1016/j.bcp.2009.10.017
53. Hockel M, Vaupel P (2001) Tumor hypoxia: definitions and current clinical, biologic, and molecular aspects. J Natl Cancer Inst 93:266–276. https://doi.org/10.1093/jnci/93.4.266
54. Rohwer N, Cramer T (2011) Hypoxia-mediated drug resistance: novel insights on the functional interaction of HIFs and cell death pathways. Drug Resist Updat 14:191–201. https://doi.org/10.1016/j.drup.2011.03.001
55. Bertout JA, Patel SA, Simon MC (2008) The impact of O2 availability on human cancer. Nat Rev Cancer 8:967–975. https://doi.org/10.1038/nrc2540
56. Krishnamachary B, Berg-Dixon S, Kelly B, Agani F, Feldser D, Ferreira G et al (2003) Regulation of colon carcinoma cell invasion by hypoxia-inducible factor 1. Cancer Res 63:1138–1143
57. Song X, Liu X, Chi W, Liu Y, Wei L, Wang X et al (2006) Hypoxia-induced resistance to cisplatin and doxorubicin in non-small cell lung cancer is inhibited by silencing of HIF-1alpha gene. Cancer Chemother Pharmacol 58:776–784. https://doi.org/10.1007/s00280-006-0224-7
58. Botla SK, Gholami AM, Malekpour M, Moskalev EA, Fallah M, Jandaghi P et al (2012) Diagnostic values of GHSR DNA methylation pattern in breast cancer. Breast Cancer Res Treat 135:705–713. https://doi.org/10.1007/s10549-012-2197-z
59. Mishra RR, Belder N, Ansari SA, Kayhan M, Bal H, Raza U et al (2018) Reactivation of cAMP pathway by PDE4D inhibition represents a novel druggable axis for overcoming tamoxifen resistance in ER-positive breast cancer. Clin Cancer Res 24:1987–2001. https://doi.org/10.1158/1078-0432.CCR-17-2776
60. Saatci O, Borgoni S, Akbulut O, Durmus S, Raza U, Eyupoglu E et al (2018) Targeting PLK1 overcomes T-DM1 resistance via CDK1-dependent phosphorylation and inactivation of Bcl-2/xL in HER2-positive breast cancer. Oncogene 37:2251–2269. https://doi.org/10.1038/s41388-017-0108-9
61. Raza U, Saatci O, Uhlmann S, Ansari SA, Eyupoglu E, Yurdusev E et al (2016) The miR-644a/CTBP1/p53 axis suppresses drug resistance by simultaneous inhibition of cell survival and epithelial-mesenchymal transition in breast cancer. Oncotarget 7:49859–49877. https://doi.org/10.18632/oncotarget.10489

62. Gyorffy B, Lanczky A, Eklund AC, Denkert C, Budczies J, Li Q et al (2010) An online survival analysis tool to rapidly assess the effect of 22,277 genes on breast cancer prognosis using microarray data of 1,809 patients. Breast Cancer Res Treat 123:725–731. https://doi.org/10.1007/s10549-009-0674-9
63. Dweep H, Gretz N (2015) miRWalk20: a comprehensive atlas of microRNA-target interactions. Nat Methods 12:697. https://doi.org/10.1038/nmeth.3485

Publisher's Note Springer Nature remains neutral with regard to jurisdictional claims in published maps and institutional affiliations.

Supplementary Information

Targeting HIF1-alpha/miR-326/ITGA5 axis potentiates chemotherapy response in triple negative breast cancer

Ridho Assidicky[1], Unal Metin Tokat[1], Ibrahim Oguzhan Tarman[1], Ozge Saatci[2], Pelin Gulizar Ersan[1], Umar Raza[1], Hasan Ogul[3], Yasser Riazalhosseini[4,5], Tolga Can[6], Ozgur Sahin[2]*

[1]Department of Molecular Biology and Genetics, Faculty of Science, Bilkent University, 06800 Ankara, Turkey; [2]Department of Drug Discovery and Biomedical Sciences, University of South Carolina, Columbia, SC, 29208, USA; [3]Faculty of Computer Sciences, Østfold University College, NO-1757, Halden, Norway; [4]McGill University Genome Centre, Montreal, QC, H3A 0G1, Canada; [5]Department of Human Genetics, McGill University, Montreal, QC, H3A 1B1, Canada; [6]Department of Computer Engineering, Middle East Technical University, 06800, Ankara, Turkey

*** Corresponding author**

Ozgur Sahin, PhD

Associate Professor

University of South Carolina

Department of Drug Discovery and Biomedical Sciences

715 Sumter Street, CLS 609D

Columbia, SC, 29208, USA

Phone: +1 803 7771891

Email: sahinozgur@gmail.com or sahin@cop.sc.edu

Supplementary Figures

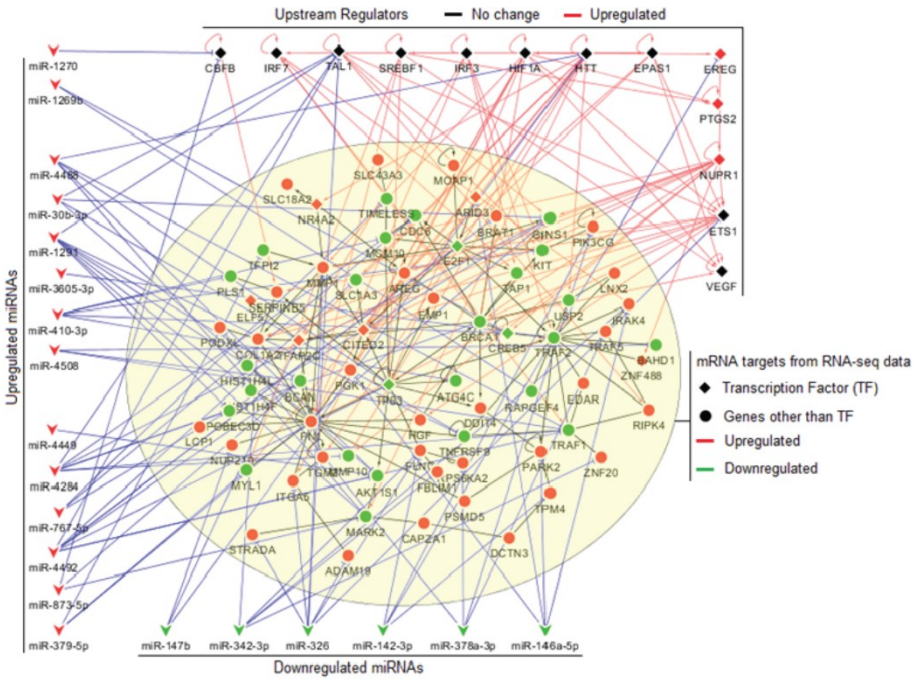


Figure S1. Construction of a miRNA-mRNA interaction network of TNBC chemoresistance. The interactions between mRNA, miRNA, and upstream regulators were generated with literature-based IPA analysis. Red and green nodes represent upregulated and down regulated mRNAs or miRNAs, respectively, while black nodes represent upstream regulators (including transcription factors). Red and blue edges represent induction and inhibition interactions, respectively.

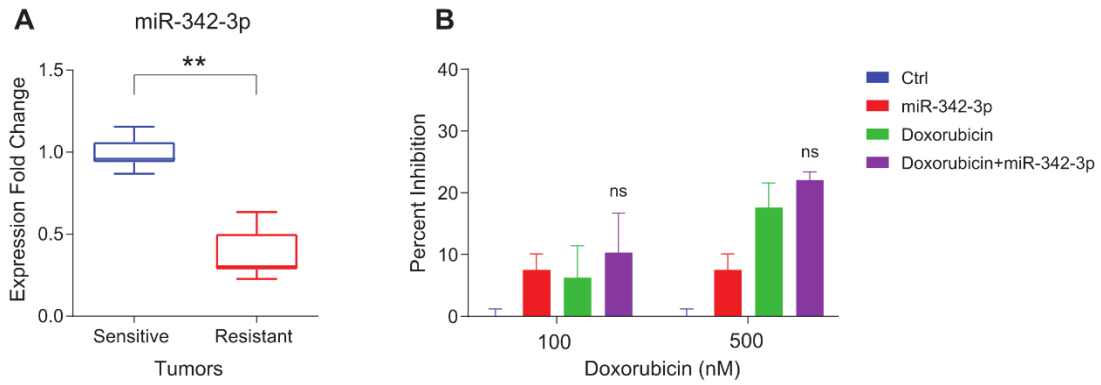


Figure S2. Testing the potential role of miR-324-3p in doxorubicin resistance. (**a**) Expression of miR-342-3p in doxorubicin sensitive vs. resistant tumor xenografts. (**b**) Percent growth inhibition of MDA-MB-231 cells seeded on 20 µg/ml fibronectin upon combination of miR-342-3p mimic with doxorubicin. $^{**}P < 0.01$; ns: not significant.

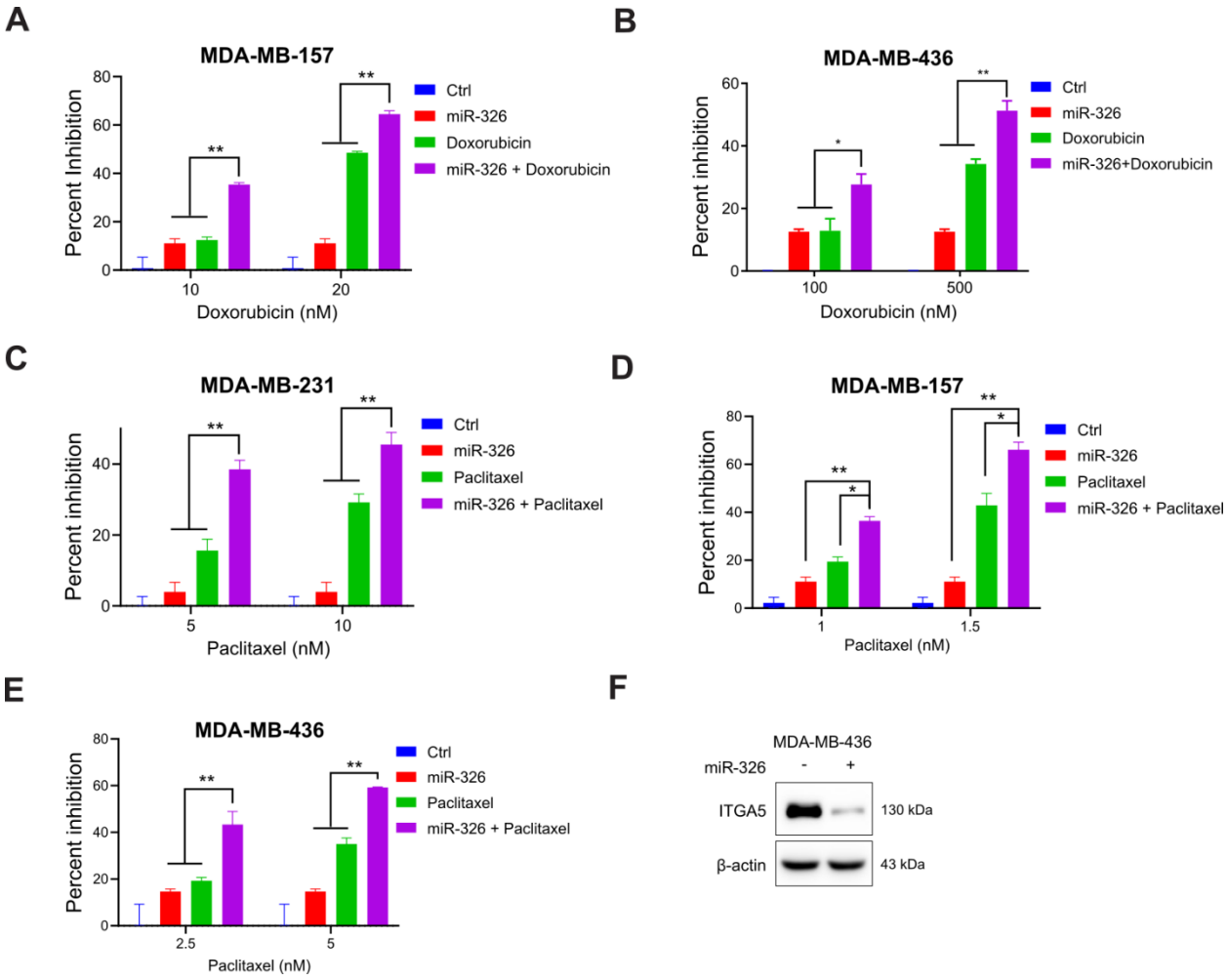


Figure S3. Testing the potential role of miR-326 in FN1-mediated doxorubicin and paclitaxel resistance in TNBC cell lines. (**a, b**) Percent growth inhibition of MDA-MB-157 and MDA-MB-436 cells seeded on 20 µg/ml fibronectin upon combination of miR-326 mimic with doxorubicin. (**c-e**) Percent growth inhibition of MDA-MB-231 (c), MDA-MB-157 (d) and MDA-MB-436 (e) cells seeded on 20 µg/ml fibronectin upon combination of miR-326 mimic with and paclitaxel. (**f**) Western blot analyses showing changes at ITGA5 levels upon miR-326 transfection in MDA-MB-436 cells for 48 hours. $*P < 0.05$; $**P < 0.01$.

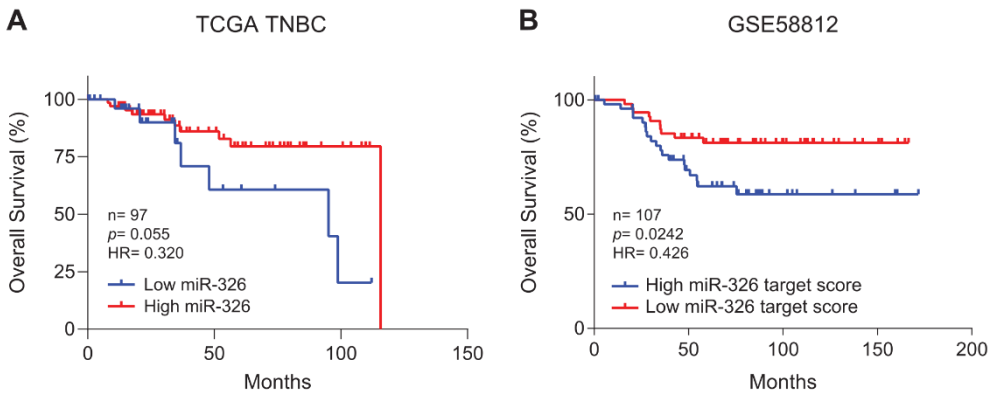


Figure S4. Association of the expression of miR-326 or its targets with survival of TNBC patients. (**a**) Kaplan-Meier survival curve showing overall survival percentage in TNBC patients from TCGA (n=97) separated based on low vs. high miR-326 expression. (**b**) Kaplan-Meier survival curve showing overall survival percentage in TNBC patients from GSE58812 (n=107) separated based on low vs. high miR-326 target score. HR: hazard ratio.

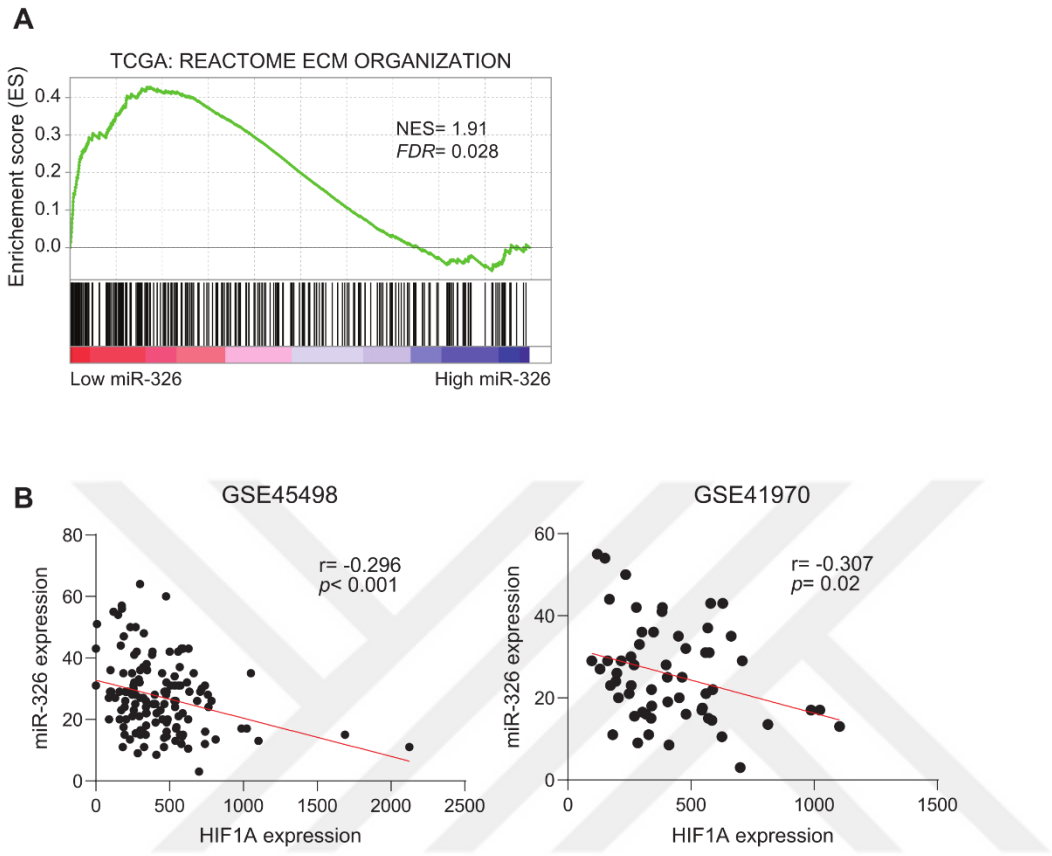


Figure S5. Association of miR-326 expression with ECM organization and HIF1A expression. (**a**) Genes associated with extracellular matrix organization are enriched in tumors of patients with low miR-326 expression in TCGA dataset. (**b**) Pearson correlation analysis of miR-326 expression with HIF1A expression in GSE45498 and GSE41970 datasets.

Supplementary Tables

Supplementary Table 1a. Sequences of forward and reverse primers used for qRT-PCR.

Gene Symbol	Gene ID	Forward Primer	Reverse Primer
ACTB	60	5'ccaaccgcgagaagatga-3'	5'ccagaggcgtacagggatag-3'
HPRT	3251	5'-tgaccttgatttattttgcatacc-3'	5'-cgagcaagacgttcagtcct-3'
ITGA5	3678	5'-gtcgggggcttcaacttagac-3'	5'-cctggctggctggtattagc-3'

Supplementary Table 1b. List of primary antibodies used for Western blot.

Name	Manufacturer	Catalog Number	Dilution
Cleaved PARP	CST	5625S	1:1000
ITGA5	Sigma Aldrich	HPA002642	1:1000
phospho-FAK (Y397)	Abcam	39967	1:1000
phospho-Src (Y416)	Abcam	2685	1:1000
Total FAK	CST	3285S	1:1000
Total Src	CST	2108S	1:1000
β-actin	MP Biomedicals	691001	1:10000

Supplementary Table 1c. Primer sequences for 3'-UTR cloning.

Gene Symbol	Gene ID	Direction	Primer
ITGA5	3678	Forward	5'-ccgctcgagcccaatttcagactcccattcctg-3'
		Reverse	5'-atttgcggccgcgttctggtcagtgggggcac-3'

ARTICLE

HSP90 inhibitors induce GPNMB cell-surface expression by modulating lysosomal positioning and sensitize breast cancer cells to glembatumumab vedotin

Marco Biondini[1,2], Alex Kiepas[1,3], Leeanna El-Houjeiri[1,4], Matthew G. Annis[1,2], Brian E. Hsu[1,2], Anne-Marie Fortier[1,4], Geneviève Morin[1,4], José A. Martina[5], Isabelle Sirois[6], Adriana Aguilar-Mahecha[6], Tina Gruosso[1,4], Shawn McGuirk[1,3], April A. N. Rose[7], Unal M. Tokat[8], Radia M. Johnson[9], Ozgur Sahin[10], Eric Bareke[11,12], Julie St-Pierre[13], Morag Park[1,2,4], Mark Basik[6,7], Jacek Majewski[11,12], Rosa Puertollano[5], Arnim Pause[1,2], Sidong Huang[1,4], Tibor Keler[14] and Peter M. Siegel[1,2,4]✉

© The Author(s), under exclusive licence to Springer Nature Limited 2022

Transmembrane glycoprotein NMB (GPNMB) is a prognostic marker of poor outcome in patients with triple-negative breast cancer (TNBC). Glembatumumab Vedotin, an antibody drug conjugate targeting GPNMB, exhibits variable efficacy against GPNMB-positive metastatic TNBC as a single agent. We show that GPNMB levels increase in response to standard-of-care and experimental therapies for multiple breast cancer subtypes. While these therapeutic stressors induce GPNMB expression through differential engagement of the MiTF family of transcription factors, not all are capable of increasing GPNMB cell-surface localization required for Glembatumumab Vedotin inhibition. Using a FACS-based genetic screen, we discovered that suppression of heat shock protein 90 (HSP90) concomitantly increases GPNMB expression and cell-surface localization. Mechanistically, HSP90 inhibition resulted in lysosomal dispersion towards the cell periphery and fusion with the plasma membrane, which delivers GPNMB to the cell surface. Finally, treatment with HSP90 inhibitors sensitizes breast cancers to Glembatumumab Vedotin in vivo, suggesting that combination of HSP90 inhibitors and Glembatumumab Vedotin may be a viable treatment strategy for patients with metastatic TNBC.

Oncogene (2022) 41:1701–1717; https://doi.org/10.1038/s41388-022-02206-z

INTRODUCTION

Triple-negative breast cancer (TNBC) is an aggressive disease, affecting 10–20% of all breast cancer patients. A combination of surgery, radiation and chemotherapy remains the standard of care for TNBC. Unfortunately, most patients develop chemo-resistance [1]. TNBC is a collection of highly heterogenous breast tumors [2], which requires a shift away from the use of chemotherapy as a "one size fits all" approach to disease management. Molecular profiling of TNBC has led to the identification of new biomarkers and the development of novel targeted therapies that are currently under clinical investigation [3].

Our previous work revealed that 40% of TNBC patients exhibit elevated glycoprotein NMB (GPNMB) levels in their tumor epithelium, which is prognostic of poor outcome [4, 5]. GPNMB induces pro-tumorigenic signaling in breast cancer cells, leading to enhanced plasticity/stem cell characteristics, increased migration/invasion and metastasis [6, 7]. As a cell-surface protein, GPNMB represents an attractive candidate for molecular targeted therapy. In this regard, an antibody drug conjugate (ADC) that links a GPNMB-targeting antibody (CR011) to a potent cytotoxin, monomethyl auristatin E (MMAE), has been developed (Glembatumumab Vedotin) [7, 8]. Glembatumumab Vedotin induced cytotoxic responses in preclinical models, leading to regression of GPNMB-expressing breast tumors [4]. Following promising phase I/II and II trials [5, 9], a phase IIb clinical trial, termed the METastatic TRIple-Negative Breast Cancer (METRIC) trial was completed. The METRIC trial included 327 patients with metastatic TNBC and demonstrated that Glembatumumab Vedotin exhibited comparable clinical activity as a single agent against GPNMB-positive tumors (overall response rate (ORR): 16%) relative to Capecitabine (ORR: 15%). However, the use of glembatumumab vedotin was not associated with improved progression-free (2.9 vs. 2.8 months) or median overall survival (8.9 vs. 8.7 months) [10]. Modest efficacy of Glembatumumab Vedotin as a monotherapy was also observed in a phase II study that evaluated the anti-GPNMB therapy in patients with advanced melanoma [11]. We and others have shown that MEK/BRAF inhibition enhances cell-surface GPNMB expression in melanoma cells [12, 13] and

[1]Goodman Cancer Research Institute, McGill University, Montreal, QC, Canada. [2]Department of Medicine, McGill University, Montreal, QC, Canada. [3]Department of Physiology, McGill University, Montreal, QC, Canada. [4]Department of Biochemistry, McGill University, Montreal, QC, Canada. [5]Cell and Developmental Biology Center, National Heart, Lung, and Blood Institute, NIH, Bethesda, MD, USA. [6]Segal Cancer Center, Lady Davis Institute for Medical Research, Sir Mortimer B. Davis Jewish General Hospital, Montreal, QC, Canada. [7]Department of Oncology and Surgery, McGill University, Montreal, QC, Canada. [8]Department of Molecular Biology and Genetics, Bilkent University, Ankara, Turkey. [9]1 DNA Way South, Genentech, San Francisco, CA, USA. [10]Department of Drug Discovery and Biomedical Sciences, University of South Carolina, Columbia, SC, USA. [11]Genome Québec Innovation Center, McGill University, Montreal, QC, Canada. [12]Department of Human Genetics, McGill University, Montreal, QC, Canada. [13]Department of Biochemistry, Microbiology and Immunology and Ottawa Institute of Systems Biology, University of Ottawa, Ottawa, ON, Canada. [14]Celldex Therapeutics, Hampton, NJ, USA.
✉email: peter.siegel@mcgill.ca

Received: 11 August 2021 Revised: 29 December 2021 Accepted: 20 January 2022
Published online: 2 February 2022

Glembatumumab Vedotin is highly effective when used in combination with these inhibitors. Indeed, the combination of MEK inhibition and lembatumumab Vedotin reduced tumor growth and delayed resistance to MEK inhibitors [13]. These data suggest that agents promoting cell-surface GPNMB expression may be used to enhance the clinical utility of Glembatumumab Vedotin.

In the present study, we investigated whether standard-of-care or experimental drugs used to treat intrinsic breast cancer subtypes can enhance GPNMB expression and sensitize breast cancer cells to Glembatumumab Vedotin. We demonstrate that standard-of-care therapies and small molecule inhibitors (trametinib, torin-1, HSP90 inhibitors) upregulate GPNMB expression predominantly via engagement of the TFE3 transcription factor. Intriguingly, only HSP90 inhibitors simultaneously upregulate and localize GPNMB to the cell surface via increased anterograde lysosome trafficking to the plasma membrane. These data have clinical relevance as HSP90 inhibitors augment the anti-tumoricidal activity of Glembatumumab Vedotin in TNBCs.

RESULTS

Acute treatment with standard-of-care therapies for breast cancer subtypes enhances GPNMB expression

To assess combination strategies targeting GPNMB in breast cancer, we tested whether standard-of-care drugs routinely used to treat patients with distinct molecular subtypes could induce GPNMB expression. MDA-MB-436 cells, a TNBC model [14], were incubated for 48 h with chemotherapy drugs commonly administered to patients diagnosed with TNBC [15]. Immunoblot analyses revealed that doxorubicin (Dox), paclitaxel (Pac) or cisplatin (Cis) treatment increased GPNMB levels in these cells compared to untreated controls (Fig. 1A). Similarly, RT-qPCR analysis showed an approximate threefold significant increase in *GPNMB* mRNA levels following drug treatment, suggesting that *GPNMB* is actively transcribed in response to therapeutic stress (Fig. 1B). We further demonstrate that these observations can be extended to estrogen receptor positive (ER+) breast tumors. Indeed, fulvestrant (selective ER degrader) or tamoxifen (selective ER modulator) similarly induced GPNMB levels in MCF7 and T47D cells, at both the protein and mRNA levels (Fig. 1C–F). These data indicate that acute therapy-induced stress increases GPNMB expression in a variety of breast cancer subtypes, suggesting an adaptive response that may mediate drug resistance.

Therapy-resistant breast cancer cells exhibit high GPNMB levels

Consistently, we observed that chemo-resistant breast cancer cells expressed elevated GPNMB protein levels relative to their parental controls (Fig. S1A, B). Analysis of publicly available gene expression data from biopsies of seven TNBC patients taken pre- and post-chemotherapy revealed that 1 of 7 patients exhibited a 2.5-fold increase in *GPNMB* mRNA expression following chemotherapy (Fig. S1C). Further analysis conducted on pre- and post-chemotherapy biopsies from another 13 TNBC patients confirmed heterogeneity in GPNMB expression following treatment. In this cohort, 62% (8/13) of patients presented moderate to high (2.5-fold change) levels of chemotherapy-induced *GPNMB* expression (Fig. S1D). Immunohistochemical (IHC) analysis of breast tumor samples with low, intermediate or high GPNMB levels revealed that only the samples with the highest *GPNMB* mRNA levels could be validated by IHC (Fig. S1E).

Elevated GPNMB expression was also observed in tamoxifen resistant T47D and MCF7 breast cancer cells (Fig. S1F, G). Analysis of expression data from serial biopsies obtained from patients prior to initiation of hormone therapy (fulvestrant or letrozole) and during treatment (on-treatment) revealed a significant increase in *GPNMB* mRNA expression levels (Fig. S1H, I). These data indicate that elevated GPNMB expression is selected for in therapy-resistant luminal and TNBC cells.

MEK inhibitors enhance GPNMB expression in TNBC

Inhibition of MEK signaling enhances GPNMB expression in melanoma [12, 13]. Several clinical trials are currently evaluating the efficacy of MEK inhibitors (MEKi) in breast cancer [16]. We compared the activity of the MEK/ERK pathway in breast tumors relative to 31 other cancers types present in the cancer genome atlas (TCGA) by stratifying cancers based on a 52-gene signature indicative of the transcriptional output of the MEK/ERK pathway [17]. On the continuum of MEK/ERK activity, breast cancers (all subtypes) showed low MEK/ERK activity (Fig. 1G). We refined our analysis by investigating MEK/ERK activity in different breast cancer subtypes based on the prediction analysis of microarray 50 (PAM50) [18] gene expression signature within the TCGA dataset. Basal breast tumors harbored higher MEK/ERK activity when compared to other subtypes (Fig. 1H). This result agrees with the observation that 90% of TNBC harbor at least one genetic aberration in genes encoding components that regulate MAP kinase signaling (*KRAS*, *BRAF*, *RAF1*, *PI3K*) and various receptor tyrosine kinases (RTK) [19]. Moreover, TNBC cells display increased sensitivity to MEKi when compared to luminal cells [20]. MEK inhibitors (trametinib or cobimetinib) induced an increase in GPNMB mRNA and protein levels in MDA-MB-436 and Hs578T cells (Fig. 1I–L). Elevated GPNMB levels following MEKi administration were also observed in breast cancer cells representative of the ER+ and Her2+ subtypes (Fig. S1J) Finally, we analyzed RNA-seq data from serial biopsies of TNBC patients obtained prior to initiation of MEKi therapy and following 7 days of daily treatment. One patient out of six, whose tumor was classified as claudin-low, showed a strong increase in GPNMB expression upon trametinib treatment (Fig. S1K). Taken together our data demonstrate that MEK inhibition can enhance GPNMB levels in breast cancer cells and suggest that a subset of TNBC patients might benefit from MEKi/Glembatumumab Vedotin combination.

Cancer cells upregulate GPNMB in response to cellular stress

The observation that multiple drug classes enhance GPNMB levels supports the existence of a common mechanism triggering GPNMB expression that is independent from drug-specific mechanisms of action. We hypothesized that GPNMB is expressed as part of a global cell stress response, which we assessed by exposing breast cancer cells to a variety of stressors. MDA-MB-436 and HS578T TNBC cells cultured for 16 h without serum exhibited higher GPNMB levels relative to those cultured in full serum (Fig. S2A). Similar results were obtained with a variety of inhibitors including torin-1, a dual mammalian target of rapamycin complex (mTORC1/2) inhibitor and hydroxy chloroquine (HCQ), which induces lysosomal stress (Fig. S2A). Moreover, amino acid deprivation induced GPNMB expression in MDA-MB-436 but not Hs578T cells (Fig. S2A). In parallel, RT-qPCR analyses confirmed high *GPNMB* mRNAs levels in MDA-MB-436 cells incubated with the indicated stressors; however, *GPNMB* mRNA levels in Hs578T cells were significantly increased only in response to serum starvation (Fig. S2B). In line with these results, these stressors also induced GPNMB mRNA and protein levels in both MCF7 and T47D ER+ breast cancer cells (Fig. S2C, D).

TFE3 transcriptionally regulates stress-induced GPNMB expression

The MiTF/TFE family of transcription factors is comprised of four family members that include MITF, TFEB, TFE3 and TFEC [21]. TFEB and TFE3 are key mediators of adaptive cellular stress responses [22]. Under basal conditions, TFEB and TFE3 localize to the cytosol where they are phosphorylated by mTORC1 on S211 in TFEB and S321 in TFE3 [23, 24]. When phosphorylated, TFEB and TFE3 are retained on the lysosomal surface through interactions with Rag

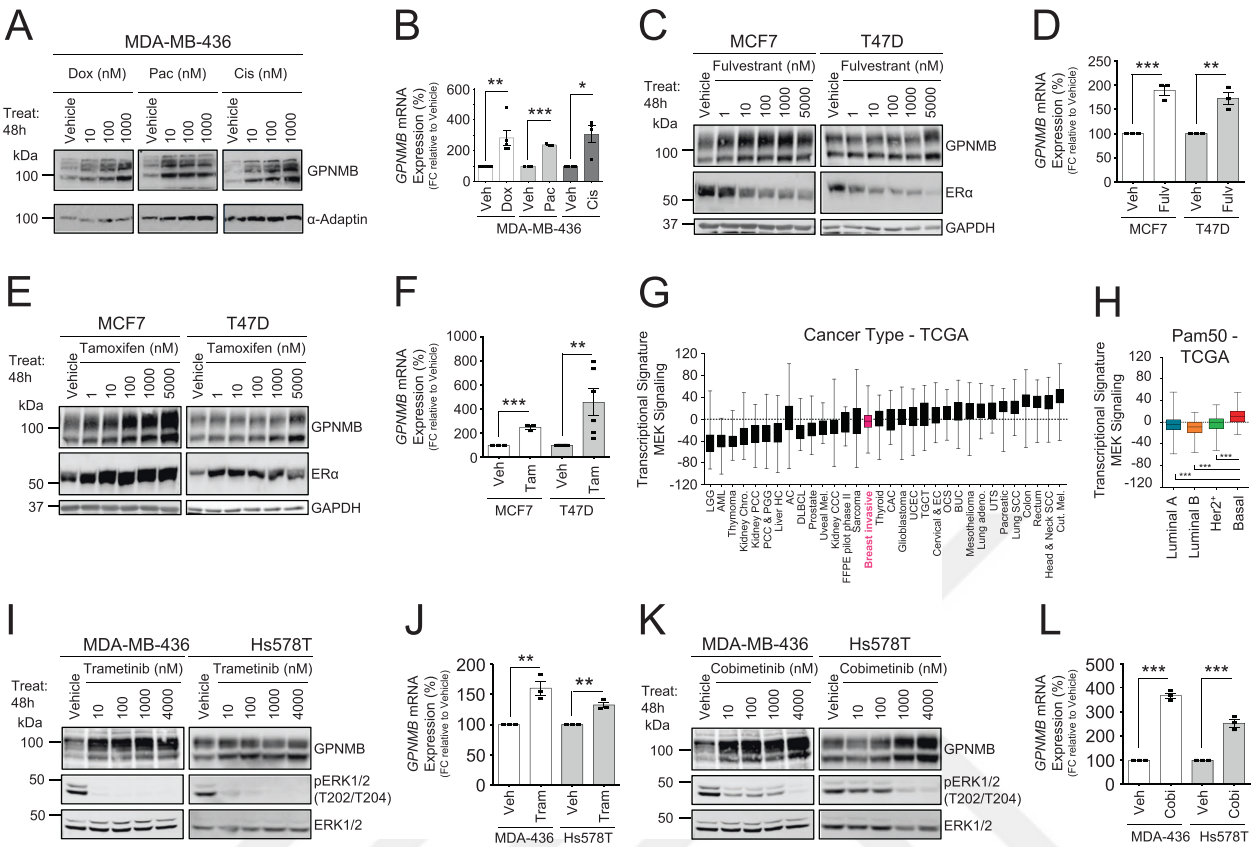


Fig. 1 Standard-of-care and experimental treatments induce GPNMB expression in breast cancer cells. A Immunoblot analysis of GPNMB expression in MDA-MB-436 cells treated for 48 h with increasing doses of doxorubicin (Dox), paclitaxel (Pac) and cisplatin (Cis). α-Adaptin served a loading control. **B** RT-qPCR analysis of *GPNMB* mRNA levels in MDA-MB-436 cells treated for 48 h with 1000 nM doxorubicin, paclitaxel or cisplatin. Data represent the mean values derived from at least three independent experiments. Error bars indicate the SEM. *$P \leq 0.05$ and **$P \leq 0.01$; ***$P \leq 0.0001$, by unpaired Student's *t* test. **C** Immunoblot analysis of GPNMB expression in MCF7 and T47D cells treated for 48 h with increasing doses of fulvestrant. Fulvestrant mediated receptor degradation was confirmed by immunoblotting for ERα. GAPDH served as a loading control. **D** RT-qPCR analysis of *GPNMB* mRNA levels in MCF7 and T47D cells treated for 48 h with 5000 nM fulvestrant. Data represent the mean values derived from three independent experiments. Error bars indicate the SEM. **$P \leq 0.01$; ***$P \leq 0.0001$, by unpaired Student's *t* test. **E** Immunoblot analysis of GPNMB expression in MCF7 and T47D cells treated for 48 h with increasing doses of tamoxifen. ERα levels remained largely unchanged in response to Tamoxifen treatment. GAPDH served as a loading control. **F** RT-qPCR analysis of *GPNMB* mRNA levels in MCF7 and T47D cells treated for 48 h with 5000 nM tamoxifen. Data represent the mean values derived from at least three independent experiments. Error bars indicate the SEM. **$P \leq 0.005$; ***$P \leq 0.0001$, by unpaired Student's *t* test. **G** All cancer types in TCGA were stratified based on a 53-gene signature indicative of the transcriptional output from the MEK/ERK pathway. AML Acute Myeloid Leukemia, AC Adrenocortical Cancer, LGG Low Grade Glioma, HCC Hepatocellular carcinoma, PCC Pheochromocytoma, PGG Paraganglioma, CAC Cholangiocarcinoma, GBM Glioblastoma, UCEC Uterine Corpus Endometrial Carcinoma, UCS Uterine Carcinosarcoma, OSC Ovarian Serous Cystadenocarcinoma, BUC Bladder Urethral Carcinoma, Testicular Germ Cell Tumor, Kidney CCC Kidney Clear Cell Carcinoma, Lung Adeno. Lung Adenocarcinoma, Cervical and EC Cervical and Endocervical Cancer, Kidney PCC Kidney Papillary Cell Carcinoma, DLBCL Diffuse Large B Cell Lymphoma, Kidney Chro. Kidney Chromophobe, H&N SCC Head and Neck Squamous Cell Carcinoma, Uveal Mel. Uveal melanoma, Cut. Mel. Cutaneous Melanoma. **H** MEK/ERK activity in the different molecular subtypes of breast cancer from the TCGA dataset (53-gene signature used in **G**), as defined by prediction analysis of microarray 50 (PAM50) gene signature. ***$P \leq 0.0001$, by unpaired Student's *t* test. **I** Immunoblot analysis of GPNMB expression in MDA-MB-436 and Hs578T cells stimulated for 48 h with increasing concentrations of trametinib. Phosphorylation of ERK1/2 on T202/204 was assessed to determine the efficacy of MEK inhibition. Total ERK1/2 served as a loading control. **J** RT-qPCR analysis of *GPNMB* mRNA levels in TNBC cells treated for 48 h with 1000 nM trametinib. Data represent the mean values derived from three independent experiments. Error bars indicate the SEM. **$P \leq 0.01$, by unpaired Student's *t* test. **K** Immunoblot analysis of GPNMB expression in MDA-MB-436 and Hs578T cells stimulated for 48 h with increasing concentrations of cobimetinib. Phosphorylation of ERK1/2 on T202/204 was assessed as a measure of MEK inhibition. Total ERK1/2 served as a loading control. **L** RT-qPCR analysis of *GPNMB* mRNA levels in TNBC cells treated for 48 h with 1000 nM cobimetinib. Data represent the mean values derived from three independent experiments. Error bars indicate the SEM. ***$P \leq 0.0001$, by unpaired Student's *t* test.

GTPases and 14-3-3 proteins [24–26]. Nutrient deprivation or cellular stress inactivates mTORC1, allowing nuclear translocation of TFEB and TFE3 where they mediate a transcriptional program that enables cellular adaptation to stress by promoting autophagy, lysosomal biogenesis, mitochondria homeostasis and metabolism [24, 27]. Analysis of the *GPNMB* promoter revealed a highly conserved E box sequence (TCACATG), which is recognized by the MiTF/TFE family of transcription factors [28].

To test whether TFEB or TFE3 can induce GPNMB expression, we expressed constitutively nuclear mutants of TFEB (TFEB-S211A) or TFE3 (TFE3-S321A) in T47D and MDA-MB-436 breast cancer cells. TFEB-S211A or TFE3-S321A induced GPNMB expression; however, TFEB-S211A induced higher GPNMB levels in T47D cells when compared to TFE3-S321A (Fig. S2E). Conversely, TFE3-S321A induced higher GPNMB levels in MDA-MB-436 cells when compared to TFEB-S211A (Fig. S2E).

To determine the MiTF/TFE family members responsible for stress-induced GPNMB expression, we transiently depleted MITF, TFEB, or TFE3 in MDA-MB-436 breast cancer cells. RT-qPCR analysis revealed that *GPNMB* mRNA expression induced by amino acid deprivation is largely mediated by TFE3 (Fig. S2F). MiTF/TFE transcription factors can bind the promoters of target genes both as homo- or heterodimers [29, 30]. Combined MiTF and TFE family member depletion confirmed that TFE3 plays a predominant role in promoting *GPNMB* expression in response to cellular stress (Fig. S2F). Furthermore, we extended this siRNA approach to demonstrate that TFE3-dependent *GPNMB* expression is primarily restricted to TNBC cells (data not shown).

TFE3 enhances GPNMB expression in response to diverse therapeutic stresses

We next asked whether TFE3 regulated GPNMB expression in response to therapeutic agents. Trametinib- or doxorubicin-induced GPNMB expression in MDA-MB-436 cells required TFE3, with a minor contribution from MITF (Fig. 2A, B). Indeed, these treatments lead to a significant increase in the percentage of cells

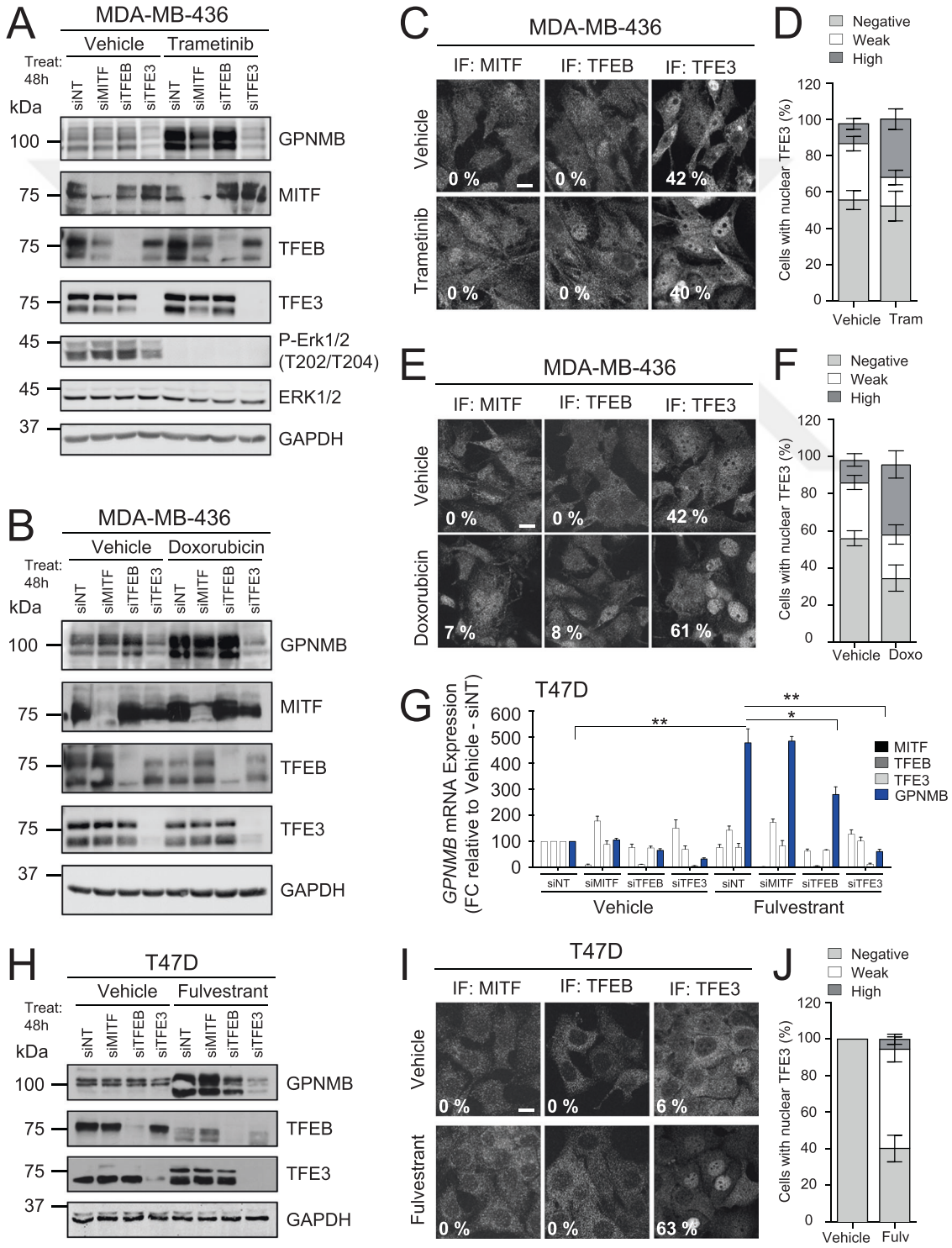


Fig. 2 TFE3 regulates GPNMB expression in response to therapy-induced cell stress. A Immunoblot analysis of GPNMB and ERK1/2 phosphorylation (T202/204) levels in MDA-MB-436 cells transiently depleted of MITF, TFEB or TFE3 and stimulated for 48 h with trametinib (1 μM). MITF, TFEB and TFE3 levels were assessed by immunoblotting to confirm efficacy of each knockdown. GAPDH served as a loading control. **B** Immunoblot analysis of GPNMB expression in MDA-MB-436 cells transiently depleted of MITF, TFEB, or TFE3 and stimulated for 48 h with doxorubicin (1 μM). MITF, TFEB, and TFE3 levels were assessed by immunoblotting to confirm efficacy of each knockdown. GAPDH served as a loading control. **C** MITF, TFEB, and TFE3 localization was assessed by indirect immunofluorescence in MDA-MB-436 cells treated for 48 h with trametinib as described in (**A**). The percentage of cells positive for MITF, TFEB, or TFE3 is reported in the images. Scale bar: 20 μm, applies to all images. **D** The percentage of cells in (**C**) that scored negative for TFE3 nuclear localization or express low or high levels of TFE3 in the nucleus based on fluorescence intensity. Error bars indicate the SEM. **E** MITF, TFEB, and TFE3 localization was assessed by indirect immunofluorescence in MDA-MB-436 cells treated for 48 h with doxorubicin as described in B. The percentage of cells positive for MITF, TFEB, or TFE3 is reported in images. Scale bar: 20 μm, applies to all images. **F** The percentage of cells in E that scored negative for TFE3 nuclear localization or express low or high levels of TFE3 in the nucleus based on fluorescence intensity. Error bars indicate the SEM. **G** T47D cells were incubated for 48 h with fulvestrant (5 μM) and *GPNMB* mRNA levels were assessed by RT-qPCR. The efficiency of each MiTF/TFE family member knockdown was assessed by RT-qPCR analyses of *MITF*, *TFEB* and *TFE3* levels. The graph depicts the mean ± SEM of the RNA fold change for the indicated mRNAs normalized to β2M mRNA from three or more independent experiments. $^{*}P \leq 0.05$ and $^{**}P \leq 0.01$, by unpaired Student's *t* test. **H** Immunoblot analysis of GPNMB expression in T47D cells transiently depleted of MITF, TFEB, TFE3, and treated for 48 h with fulvestrant (5 μM). TFEB and TFE3 levels were assessed by immunoblotting to confirm efficacy of each knockdown. GAPDH served as a loading control. **I** MITF, TFEB, and TFE3 localization was assessed by indirect immunofluorescence in T47D cells treated for 48 h with fulvestrant as described in (**G**). The percentage of cells positive for MITF, TFEB, or TFE3 is indicated in each image. Scale bar: 20 μm, applies to all images. **J** The percentage of cells in (**I**) that scored negative for TFE3 nuclear localization or express low or high levels of TFE3 in the nucleus based on fluorescence intensity. Error bars indicate the SEM.

with high nuclear TFE3 staining (Fig. 2C–F). Similarly, GPNMB expression was induced by fulvestrant, which largely relied on TFE3 activity, with a minor contribution from TFEB (Fig. 2G, H). Furthermore, treatment with fulvestrant induced nuclear localization of TFE3 in ~63% of T47D cells, with a small percentage of cells displaying high TFE3 staining intensity in the nucleus (Fig. 2I, J). Although immunoblot analysis revealed an electrophoretic mobility shift for TFEB following fulvestrant treatment, which is consistent with TFEB hypo-phosphorylation and a bona fide indicator of TFEB nuclear translocation, we could not detect TFEB in the nucleus by immunofluorescence (Fig. 2I). Our data highlight TFE3 as the master regulator of GPNMB expression in response to a multitude of therapy-induced stressors.

mTOR inactivation promotes stress-induced GPNMB expression via TFE3

Our data suggest that TFE3 is a key transcriptional regulator of GPNMB under basal and cell stress conditions. Inactivation of mTOR by torin-1 leads to increased GPNMB expression in breast cancer cells (Fig. S2A–D). Using siRNAs to target individual MiTF/TFE family members, we demonstrate that torin-1 induced GPNMB protein and mRNA expression in MDA-MB-436 breast cancer cells relies on the activity of TFE3 but not on TFEB or MITF (Fig. S3A, B).

Immunofluorescence experiments revealed that ~18% of MDA-MB-436 breast cancer cells are negative for nuclear TFE3, ~40% exhibit weak nuclear TFE3 staining and ~42% possess high nuclear TFE3 staining in cells treated with vehicle for 2 h (Fig. S3C, D). Torin-1 treatment induced the rapid nuclear translocation of TFE3, which was sustained over 48 h (Fig. S3C, D). Time course analyses indicated that *GPNMB* mRNA levels are highly expressed after 16 h of torin-1 treatment (Fig. S3E). TFE3 also mediated torin-1 induced GPNMB protein and mRNA expression in T47D breast cancer cells, with a minor contribution from TFEB and MITF (Fig. S3A, B). Immunofluorescence experiments revealed that very little TFE3 is localized in the nucleus of T47D cells under basal conditions; however, torin-1 treatment rapidly induced TFE3 nuclear translocation in these cells (Fig. S3F). Indeed, the majority of T47D breast cancer cells displayed high nuclear TFE3 staining as early as 2 h post torin-1 treatment (Fig. S3G). In keeping with the rapid nuclear TFE3 translocation, *GPNMB* mRNA levels started to increase in a time-dependent manner with a clear induction observed 6 h after torin-1 addition and maximal levels reached at 48 h (Fig. S3H).

We next tested whether additional mTOR inhibitors (mTORi) developed for the treatment of solid cancers can regulate GPNMB expression in a similar manner as torin-1. As expected, torin-1 treatment increased GPNMB protein expression in MDA-MB-436 breast cells (Fig. 3A). Rapamycin, a specific inhibitor of mTORC1, induced maximal GPNMB expression at the lowest dose tested (Fig. 3A). Higher concentrations of INK-128 and AZD2014, both of which are ATP-competitive kinase inhibitors of mTORC1 and 2, were required to induce GPNMB expression (Fig. 3A). In T47D cells, all mTORi, except rapamycin, were able to induce GPNMB expression (Fig. 3B). Moreover, all pharmacological mTOR inhibitors tested induced TFE3 nuclear localization in MDA-MB-436 cells (Fig. 3C). In T47D cells, rapamycin failed to localize TFE3 to the nucleus, while torin-1, INK-128 and AZD2014 each induced TFE3 nuclear localization (Fig. 3D). Treatment with everolimus, a mTORC1 inhibitor analog to rapamycin, also failed to induce TFE3 nuclear localization in T47D cells (Fig. 3D). Together, our data demonstrate that many pharmacological inhibitors of mTOR enhance GPNMB expression by mobilizing TFE3.

Combination of glembatumumab vedotin with MEKi or mTORi reduces tumor growth of triple-negative breast cancer cells

To test whether pharmacological inhibitors that induce GPNMB expression can sensitize breast cancer cells to Glembatumumab Vedotin, we performed preclinical studies in a TNBC patient-derived xenograft (PDX) model (HCI-010) [31]. Mice bearing mammary tumors were divided into four cohorts: (1) vehicle, (2) continuous treatment with trametinib alone, (3) Glembatumumab Vedotin alone (once/week), and (4) a combination of both therapeutic agents. Immunohistochemical analysis following 7 days of trametinib treatment revealed an increase in GPNMB expression in the tumor epithelium (Fig. 4A, B). Trametinib-treated tumors grew slower than their vehicle-treated counterparts; however, 5 weeks after treatment was initiated, tumors resumed growing albeit with slower kinetics relative to tumors in vehicle-treated mice (Fig. 4C). Glembatumumab Vedotin administered as single agent resulted in a more significant impairment of tumor growth when compared to trametinib; similar to trametinib-treated group, tumor growth resumed after ~42 days of treatment (Fig. 4C). In contrast, the combination of trametinib plus Glembatumumab Vedotin resulted in the greatest impairment in PDX growth leading to tumor regression without a secondary growth rebound (Fig. 4C, D).

We also tested the ability of AZD2014, an mTOR inhibitor, to increase the sensitivity of HCI-010 breast cancer cells to glembatumumab vedotin. Mice bearing HCI-010 breast tumors in the mammary fat pad were divided into four cohorts: (1) vehicle, (2) daily administration of AZD2014 alone, (3) Glembatumumab Vedotin alone (once/week), and (4) a combination of both therapeutic agents. In contrast to trametinib-treated tumors, AZD2014 only modestly induced GPNMB expression in the tumor epithelium (Fig. 4E, F). Mammary tumors in the vehicle and

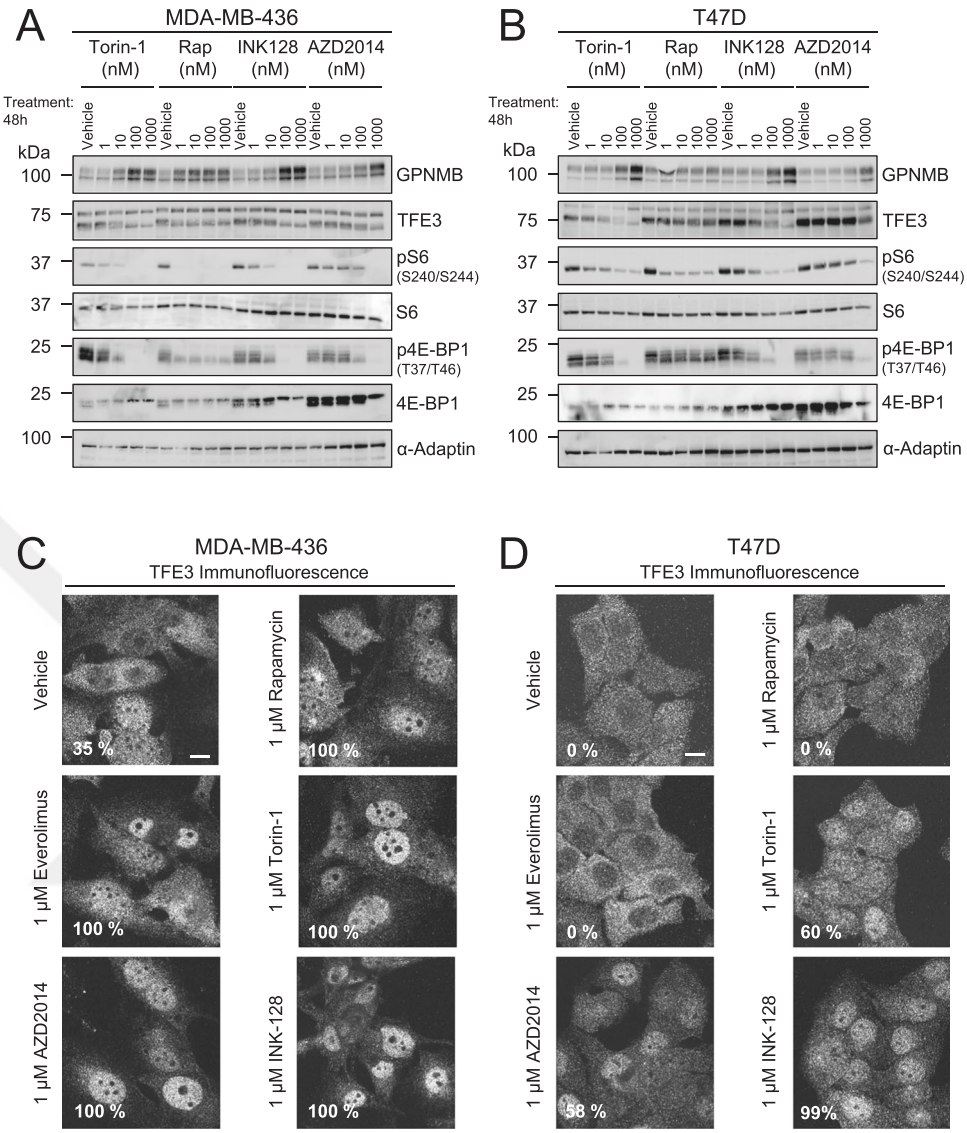
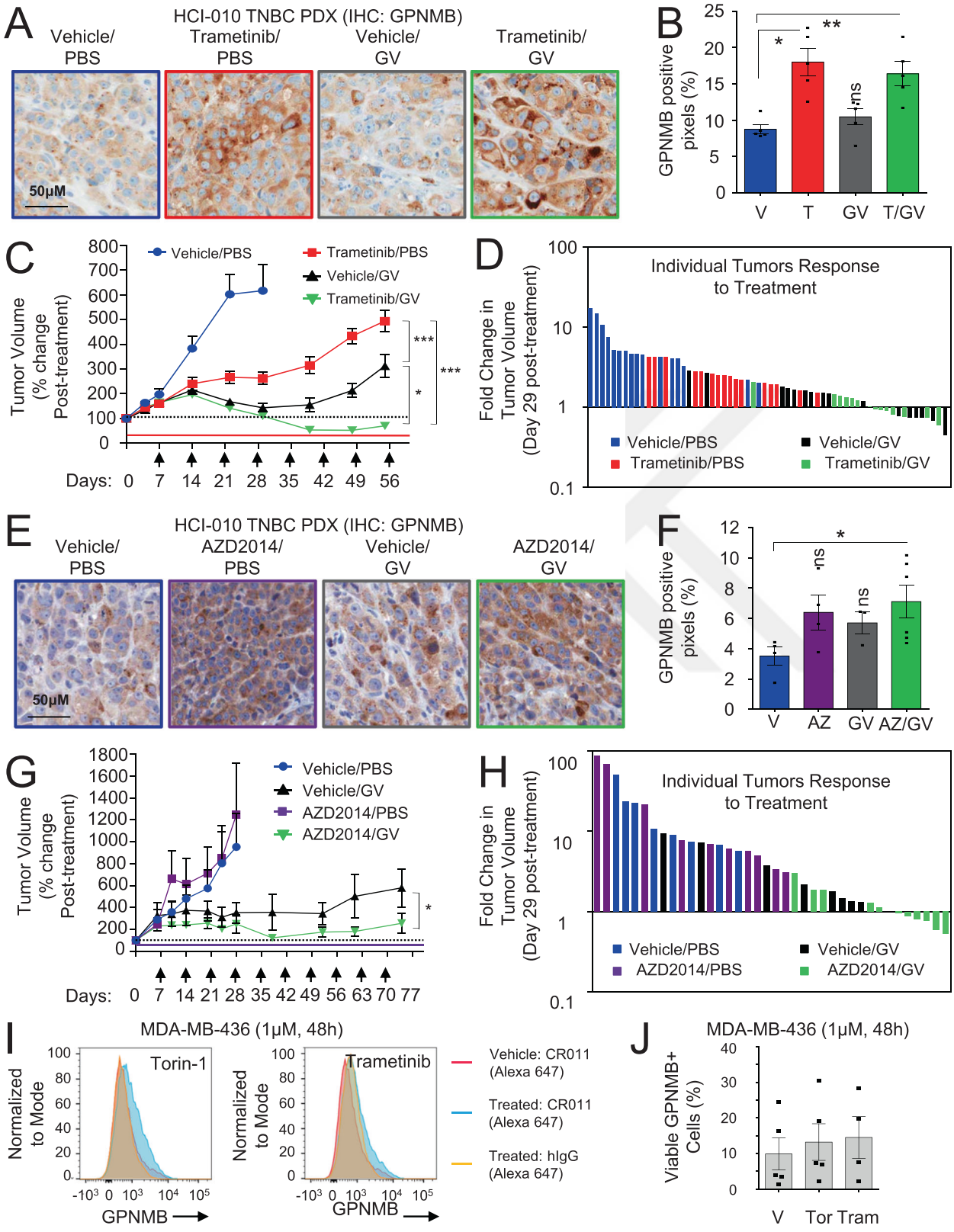


Fig. 3 Pharmacological inhibition of mTOR enhances GPNMB expression. A Immunoblot analysis of GPNMB expression in MDA-MB-436 cells treated for 48 h with different concentrations of the indicated mTORi. pS6/S6 and p4E-BP1/4E-BP1 levels revealed the efficacy of mTOR inhibition with each of the indicated inhibitors. α-Adaptin served as a loading control. **B** Immunoblot analysis of GPNMB expression in T47D cells treated for 48 h with different concentrations of the indicated mTORi. pS6/S6 and p4E-BP1/4E-BP1 levels revealed the efficacy of mTOR inhibition with each of the indicated inhibitors. α-Adaptin served as a loading control. **C** Representative images of TFE3 localization in MDA-MB-436 cells treated for 48 h with the indicated inhibitors. The percentage of cells with TFE3 nuclear localization is indicated in each image. Scale bar: 10 μm, applies to all images. **D** Representative images of TFE3 localization in T47D cells treated for 48 h with the indicated inhibitors. The percentage of cells with TFE3 nucellar localization is indicated in each image. Scale bar: 10 μm, applies to all images.

AZD2014 treated cohorts grew rapidly and at the same rate (Fig. 4G). Growth of mammary tumors in the cohort treated with Glembatumumab Vedotin alone plateaued after 1 week of treatment; however, they began to grow again after 7 weeks posttreatment tumors resumed. The smallest tumor volumes and an extended period of stable disease was observed only in the cohort of mice treated with the combination of Glembatumumab Vedotin and AZD2014 (Fig. 4G, H). Taken together these data demonstrate that MEKi or mTORi sensitizes TNBCs to Glembatumumab Vedotin.

Loss of FLCN increases GPNNMB expression and cell-surface localization sensitizing tumors cells to glembatumumab vedotin

Although combination of MEKi and mTORi with Glembatumumab Vedotin significantly impaired tumor growth in vivo, none of the mice experienced a complete response (CR), contrary to what we previously observed when MEKi were combined with Glembatumumab Vedotin to treat melanoma tumors [13]. To better understand these observations, we analyzed GPNMB localization to the cell surface in cells treated with MEKi and mTORi. Flow cytometry analysis revealed that torin-1 or trametinib treatment induced GPNMB localization at the cell surface only in a small fraction of the MDA-MB-436 cell population (Fig. 4I, J). These results argued that, while therapeutic stressors increase GPNMB levels, they do not greatly increase cell-surface GPNMB localization. We reasoned that agents capable of increasing cell-surface GPNMB levels might induce a more drastic synergy when employed with Glembatumumab Vedotin. GPNMB localizes to endosomal/lysosomal compartments via a cytoplasmic dileucine-based sorting motif present in GPNMB cytosolic domain [32]. Disruption of the adaptor protein complex-3 (AP-3), a clathrin-



associated complex that mediates intracellular membrane trafficking along endocytic and secretory transport pathways, resulted in altered trafficking of quail neuroretina clone 71 gene (QNR-71), the quail ortholog of GPNMB, and lysosomal-associated membrane protein 1 (LAMP1), to the cell surface [32] suggesting that GPNMB and lysosomes could traffic together to the cell surface. Previous work showed that inactivation of the tumor suppressor gene folliculin (FLCN) induces high GPNMB mRNA and protein expression by regulating TFE3 nuclear localization in renal cancer cells [28]. Interestingly, FLCN also regulates lysosomal positioning

Fig. 4 Combination of Glembatumumab Vedotin with either MEK or mTOR inhibitors reduces TNBC growth. A Immunohistochemistry (IHC) analysis of GPNMB expression in samples from HCI-010 TNBC PDX tumors treated with vehicle (blue), 2 mg/kg trametinib alone (red), 5 mg/kg Glembatumumab Vedotin alone (black) and trametinib administered in combination with Glembatumumab Vedotin (green). **B** Quantification of GPNMB IHC expression in (**A**). Error bars indicate the SEM. $*P \leq 0.05$ and $**P \leq 0.01$, by unpaired Student's *t* test. **C** Growth curves of HCI-010 tumors upon treatment with vehicle (blue line), 2 mg/kg trametinib alone (red line), 5 mg/kg Glembatumumab Vedotin alone (black line) and trametinib administered in combination with Glembatumumab Vedotin (green line). All treatments were initiated when tumors reached 300 mm^3 and were administered as follows: glembatumumab vedotin (black arrows below *x*-axis) was administered as a single agent once every week and trametinib was administered daily (continuous red line above *x*-axis). Black dashed line above the *x*-axis represents normalized tumor volumes relative to tumor volumes at the beginning of treatment. Error bars indicate the SEM. $*P \leq 0.05$ and $***P \leq 0.001$ by unpaired Student's *t* test. **D** Waterfall plot demonstrating the response of individual HCI-010 tumors to the indicated treatments. Mice were treated as indicated in (**A**). **E** IHC analysis of GPNMB expression in samples from HCI-010 TNBC PDX tumors treated with vehicle (blue), 15 mg/kg AZD2014 alone (purple), 5 mg/kg Glembatumumab Vedotin alone (black) and AZD2014 administered in combination with Glembatumumab Vedotin (green). **F** Quantification of GPNMB IHC expression in (**E**). Error bars indicate the SEM. $*P \leq 0.05$ by unpaired Student's *t* test. **G** Growth curves of HCI-010 tumors upon treatment with vehicle (blue line), 15 mg/kg AZD2014 alone (purple line), 5 mg/kg glembatumumab vedotin alone (black line) or AZD2014 administered in combination with Glembatumumab Vedotin (green line). Glembatumumab Vedotin was administered as a single agent once every week (black arrows below *x*-axis) and AZD2014 was administered daily (continuous purple line above *x*-axis). Error bars indicate the SEM. $*P \leq 0.05$ by unpaired Student's *t* test. **H** Waterfall plot demonstrating responses of individual HCI-010 tumors to the indicated treatments. Mice were treated as indicated in (**E**). **I** FACS-based analysis of cell-surface GPNMB localization in MDA-MB-436 cells treated for 48 h with 1 μM of torin-1, trametinib. FACS plots reveal a modest shift in GPNMB cell-surface expression following staining with the CR011 antibody, in cells treated with the indicated inhibitors (in blue) relative to cells treated with vehicle (in red). Yellow traces indicate cells treated with the indicated inhibitors and stained with hIgG antibody (isotype control). **J** FACS-based analysis of cell-surface GPNMB localization in MDA-MB-436 cells treated for 48 h with the indicated drugs. Data represents the percentage of live cells positive for cell-surface GPNMB expression in breast cancer cells treated with the indicated inhibitors. Error bars indicate the SEM.

in response to nutrient deprivation [33]. We investigated whether modulation of FLCN levels results in cell-surface localization of GPNMB. We first investigated whether FLCN loss increased GPNMB expression in breast cancer cells using FLCN-null MCF7 cells. Immunoblot analyses revealed high levels of GPNMB protein expression in MCF7 $FLCN^{KO}$ cells (Fig. S4A). We found that *FLCN* knockout dramatically increased the percentage of MCF7 cells positive for cell-surface GPNMB from ~0.4 to ~60% (Fig. S4B, C). We next assessed if MCF7 $FLCN^{KO}$ tumor cells are more responsive to glembatumumab vedotin when compared to parental MCF7 breast cancer cells. IHC analysis showed that GPNMB is highly and uniformly expressed in MCF7 $FLCN^{KO}$ at 2 weeks postinjection and at experimental endpoint (Fig. S4D, *bottom panels*). In contrast, tumors derived from MCF7 parental cells displayed a small fraction of GPNMB+ cells that was detectable only at 2 weeks postinjection, but not at endpoint (Fig. S4D, *upper panels*). Glembatumumab Vedotin treatment of mice injected with MCF7 $FLCN^{KO}$ cells resulted in almost complete tumor regression as compared to the static tumor growth response observed in mice injected with parental MCF7 cells (Fig. S4E, F), reinforcing the idea that increasing GPNMB cell-surface localization is a key element to improving cancer cell sensitivity to glembatumumab vedotin. We observed that lysosomes were more scattered/localized to the cellular periphery in *FLCN* knockout cells when compared to MCF7 parental cells (Fig. S4G), confirming a role for FLCN in lysosomal positioning. Furthermore, flow cytometry analysis revealed increased LAMP1 cell-surface localization suggesting lysosomal fusion with the plasma membrane in MCF7 $FLCN^{KO}$ cells (Fig. S4H). The high levels of GPNMB localized to the cell-surface observed in MCF7 $FLCN^{KO}$ cells (Fig. S4C, D) suggest a potential link between lysosomal positioning at the cell periphery and the localization of GPNMB.

FACS-based shRNA screen identifies HSP90 as a novel regulator of GPNMB expression and cell-surface localization

FLCN inactivation increases both GPNMB protein levels and GPNMB cell-surface localization, thus representing a proof-of-concept candidate to target in combination with Glembatumumab Vedotin. *FLCN* is as a tumor suppressor gene whose germline inactivation is responsible for Birt-Hogg-Dubé syndrome in humans, a pathology associated with increased risk for developing kidney tumors [34]. For this reason, FLCN is not an ideal candidate to target in cancer. We therefore performed a pooled shRNA screen to identify new druggable targets whose suppression causes an increase in cell-surface localized GPNMB. We combined two previously published shRNA libraries targeting the human kinome [35] and known targets of clinically approved drugs (both agonists and antagonists) [36] to create a total of 10,224 shRNAs against 1688 genes. This focused library was chosen because pharmacological inhibitors targeting candidates identified from our screens, if available, would have the highest chance of clinical implementation. In addition, incomplete gene suppression by RNAi could provide a more realistic mimic of drug inhibition.

MCF7 breast cancer cells, which have low endogenous levels of GPNMB, were infected with the lentiviral shRNA library and subjected to rapid drug selection for stable library integration. These MCF7 cells were subsequently subjected to FACS to isolate the subpopulation of cells with high GPNMB cell-surface localization (Fig. 5A). Upon screen deconvolution by bar-code sequencing of the shRNA inserts, we employed MAGeCK statistical analysis software [37] to identify genes whose silencing led to elevated GPNMB cell-surface localization when compared with the full library-expressing population, which was collected immediately before FACS sorting (Fig. 5B). An independent, hand-curated analysis (see Methods) confirmed the principal top candidates predicted by MAGeCK (Fig. 5C and Table S1). We next validated candidates that were common to both approaches (Table S1) and against which pharmacological inhibitors were commercially available, by comparing their ability to induce total GPNMB expression relative to torin-1. Only inhibition of heat shock protein 90 (HSP90AA) enhanced GPNMB expression to a level comparable to torin-1 treatment (Fig. 5D).

HSP90 inhibition increases GPNMB localization at the cell surface

Heat shock proteins are a large family of molecular chaperones well-known for their roles in protein maturation, re-folding and degradation in response to stress [38]. To further confirm that HSP90 can regulate GPNMB expression, we treated MDA-MB-436 and MCF7 cells with different doses of four independent HSP90 inhibitors (HSP90i), including NMS-E973, onalespib, luminespib and 17-DMAG. Immunoblot analyses revealed that GPNMB protein levels increased upon treatment with all four inhibitors (Fig. 5E). HSP90 inhibition suppresses the PI3K/AKT/mTOR signaling pathway [39] and both MDA-MB-436 and MCF7 breast cancer cells treated with the indicated HSP90i exhibited reduced phosphorylation of

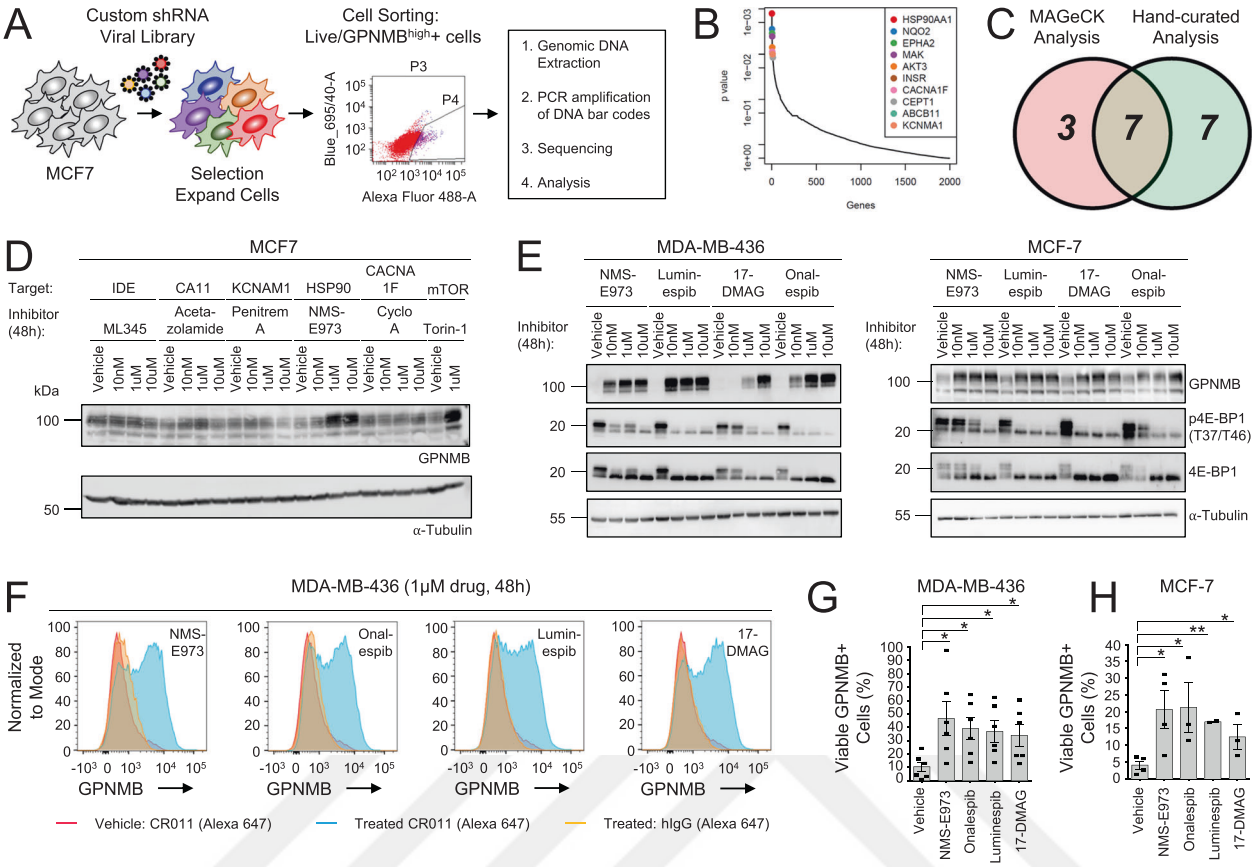


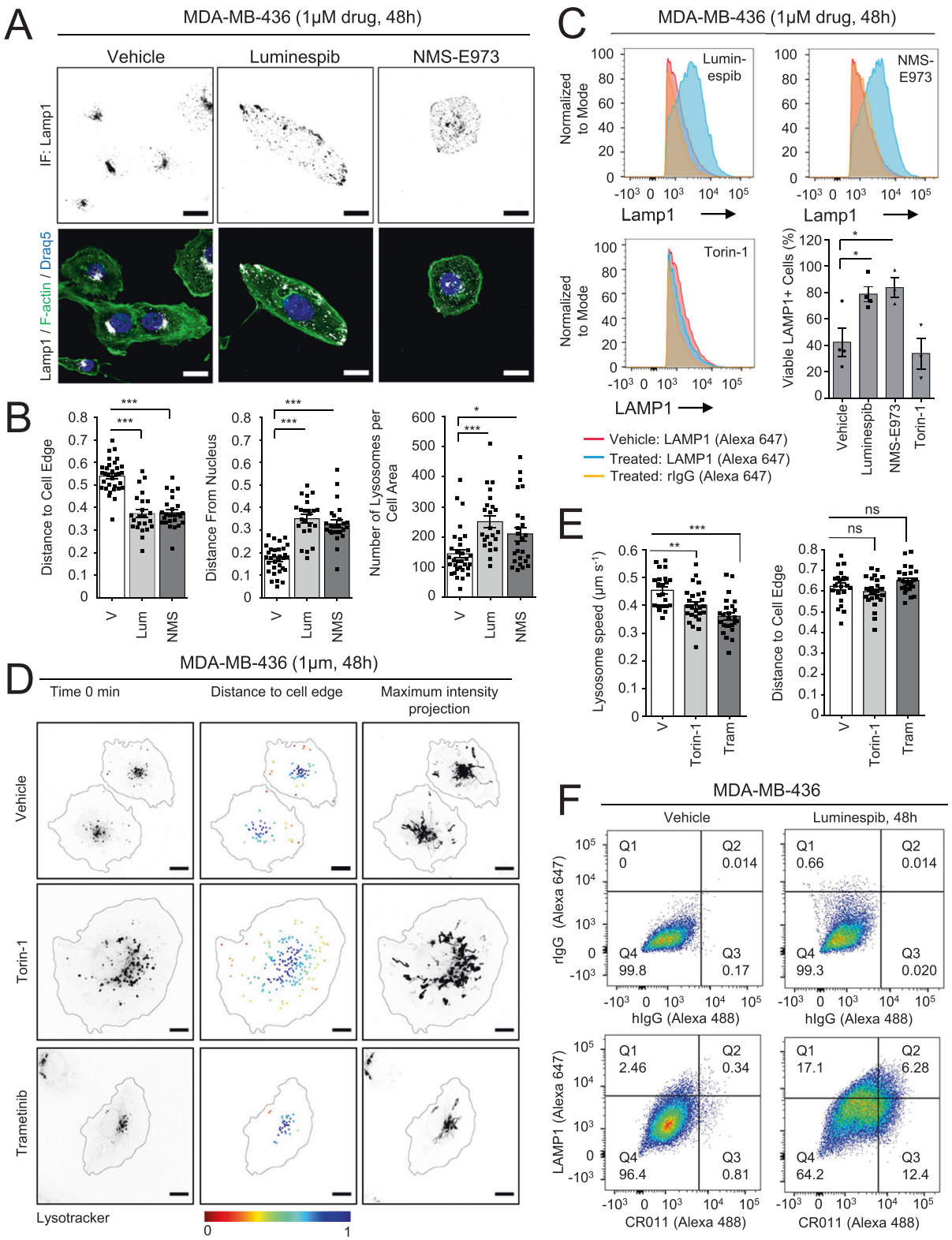
Fig. 5 shRNA screen to identify novel modulators of cell-surface GPNMB expression. A Schematic of FACS-based shRNA screen to identify negative regulators of GPNMB cell-surface localization in MCF7 breast cancer cells. **B** FACS-based shRNA screen identified HSP90AA1 as the "top hit" for a novel negative regulator of GPNMB cell-surface localization in MCF7 cells. Hits were ranked according to robust rank aggregation score. **C** MAGeCK computational analysis and further hand-curated analysis of the data revealed a similar list of top candidates, of which seven were common to both analyses. **D** Immunoblot analysis of GPNMB levels in MCF7 in response to inhibitors targeting several top hit genes identified by the screen in (**B**). The ability of the inhibitors to induce GPNMB expression was compared to torin-1. α-Tubulin served as a loading control. **E** Immunoblot analysis of GPNMB expression in MDA-MB-436 and MCF7 cells treated for 48 h with different concentrations of the indicated HSP90i. The efficacy of HSP90 inhibition was assessed by immunoblot analysis of p4E-BP1/4E-BP1 levels. α-Tubulin served as a loading control. **F** FACS-based analysis of cell-surface GPNMB expression in MDA-MB-436 cells treated for 48 h with 1 μM the indicated HSP90i (NMS-E973, onalespib, luminespib, and 17-DMAG). FACS plots reveal the shift in GPNMB cell-surface localization following staining with the CR011 antibody, in cells treated with the indicated inhibitors (in blue) relative to cells treated with vehicle (in red). Yellow traces indicate cells treated with the indicated inhibitors and stained with hIgG antibody (isotype control). **G**, **H** FACS-based analysis of cell-surface GPNMB localization in MDA-MB-436 in (**G**) and MCF7 in (**H**) cells treated for 48 h with 1 μM the indicated HSP90i (NMS-E973, onalespib, luminespib, and 17-DMAG). Data represents the percentage of live cells positive for cell-surface GPNMB. Error bars indicate the SEM. $^{*}P \leq 0.05$ and $^{**}P \leq 0.01$, by unpaired Student's *t* test.

4E-BP1 (T37/46), confirming mTOR pathway inhibition (Fig. 5E). Importantly, all four HSP90i significantly increased GPNMB cell-surface localization in MDA-MB-436 (Fig. 5F, G) and MCF7 (Fig. 5H) breast cancer cells. Inhibition of HSP90 increased the percentage of GPNMB+ cells in MDA-MB-436 cells from ~10 to ~46% (Fig. 5G). The degree of GPNMB upregulation was considerably greater in HSP90i treated MDA-MB-436 cells when compared to torin-1 and trametinib-treated cells (Fig. 4I, J). In MCF7 cells, which have low basal levels of GPNMB, treatment with the HSP90i increased the percentage of GPNMB^{+} cells in the MCF7 cell population from ~4 to ~20% (Fig. 5H). Using siRNAs individually targeting the MiTF/TFE family members, we demonstrated that HSP90i upregulate GPNMB expression, in part, through the activity of TFE3 (Fig. S5A, B). As previously observed for therapeutic stressors like trametinib and doxorubicin (Fig. 2A, B), GPNMB protein upregulation following HSP90 inhibition also partially relied on MITF (Fig. S5A). Consistent with our previous results, TFEB was dispensable for HSP90i mediated GPNMB protein upregulation (Fig. S5A). We noticed that inhibition of HSP90 upregulated *MITF* and *TFEB* mRNA levels but downregulated *TFE3* mRNA levels (Fig. S5B); however, total protein levels for TFEB and TFE3 were unaffected (Fig. S5A). Taken together these data reveal that HSP90i increase GPNMB expression and cell-surface localization, raising the possibility that HSP90 inhibition may sensitize breast cancer cells to glembatumumab vedotin.

HSP90 inhibition induces lysosomal scattering and fusion with the plasma membrane

We next investigated how HSP90 inhibition induces GPNMB localization to the cell surface. Previous observations have shown that HSP90 localizes to the lysosomal membrane, where it complexes with heat shock cognate 70 (HSC70) to regulate chaperone-mediated autophagy in response to cellular stress [40, 41]. Our results in MCF7 FLCN^{KO} cells raised the possibility that GPNMB localization to the cell surface might depend on lysosomal repositioning to the periphery. We reasoned that HSP90i might induce GPNMB cell-surface localization by affecting lysosomal scattering.

To further investigate this hypothesis, we assessed endosome/lysosome distribution in cells treated with HSP90i. Immunofluorescence analyses of endogenous LAMP1 in MDA-MB-436 cells



displayed an increase in the number of lysosomes per cell following HSP90 inhibition and confirmed lysosomal scattering towards the cell periphery (Fig. 6A, B). Treatment with luminespib and NMS-E973 increased the percentage of cells with LAMP1 localization at the cell surface in the MDA-MB-436 cell population from 40% to 80%, suggesting active lysosomal fusion with the plasma membrane upon HSP90 inhibition-induced scattering (Fig. 6C). In contrast, torin-1 treatment failed to increase LAMP1 cell-surface localization. Accordingly, live imaging analysis showed that both torin-1 and trametinib failed to induce dispersion of endosomes/lysosomes to the cell edges (Fig. 6D, E). Notably, both torin-1 and trametinib also failed to increase GPNMB localization at the cell surface (Fig. 4I, J), supporting a link between lysosomal scattering and GPNMB cell-surface localization. Indeed, flow

Fig. 6 HSP90 inhibitors induce lysosomal scattering and fusion with the plasma membrane in MDA-MD-436 cells. A Representative images of LAMP1 localization in parental and MDA-MB-436 cells treated with vehicle, luminespib or NMS-E973 for 48 h. LAMP1 images are shown with an inverted lookup table to enhance visualization. Nucleus is in blue and F-actin in green. Scale bar: 20 μm. **B** Quantification of the images in (**A**). Black squares indicate the average for each cell analyzed ($n = 32$ for vehicle, $n = 23$ for luminespib, $n = 25$ for NMS-E973). Error bars indicate the SEM. *$P < 0.05$ and ***$P < 0.001$, by Mann–Whitney U test. **C** FACS-based analysis of cell-surface LAMP1 localization in MDA-MB-436 cells incubated with vehicle, luminespib, NMS-E973, or torin-1 for 48 h. FACS plots reveal the shift in LAMP1 cell-surface expression in cells treated with the inhibitors (in blue) relative to vehicle-treated cells (in red). Yellow traces indicate cells treated with the indicated inhibitors and stained with rIgG antibody (isotype control). **D** Representative images of MDA-MB-436 cells treated with vehicle, torin-1 or trametinib for 48 h and stained with 200 nM LysoTracker to visualize endosome/lysosome positioning in live cells. Images were continuously acquired for ~32.6 s. LysoTracker images are shown with an inverted lookup table to enhance visualization. Lysosome positions were plotted and pseudocolored to visualize distance (red lysosomes are close to the cell edge while blue lysosomes are far away). Scale bar: 10 μm. **E** Quantification of the videos in (**D**). Black squares indicate the average for each cell analyzed ($n = 22$ for vehicle, $n = 26$ for torin-1, $n = 25$ for trametinib). Error bars indicate the SEM. **$P < 0.01$ and ***$P < 0.001$, by Mann–Whitney U test. **F** FACS-based analysis of cell-surface GPNMB and LAMP1 localization in MDA-MB-436 cells incubated with vehicle or 1 μM luminespib for 48 h. FACS plots in the upper panel do not reveal a shift in GPNMB and LAMP1 cell-surface expression following luminespib treatment of cells stained with rIgG antibody and hIgG (isotype control). FACS plots in the lower panel reveal a shift in the percentage of cells positive both for GPNMB and LAMP1 at the cell surface following treatment with luminespib (population Q2).

cytometry analysis showed that cells positive for surface GPNMB were also positive for surface LAMP1 (Fig. 6F) following luminespib treatment. The impact of HSP90 inhibition on lysosomal scattering was also observed in MCF7 cells. In vehicle-treated MCF7 cells, LAMP1 positive structures were diffuse throughout the cell body when compared to MDA-MB-436 cells. In contrast, HSP90 inhibition markedly induced lysosomal scattering and accumulation to the cell periphery (Fig. S6A, B). Flow cytometry analysis confirmed an increase in LAMP1 staining at the cell surface of MCF7 cells treated with HSP90i, which was not observed in cells treated with torin-1 (Fig. S6C). Collectively, our data suggest that HSP90 inhibition may increase GPNMB expression at the cell surface by inducing lysosomal scattering and plasma membrane fusion.

To gain insight into lysosomal dynamics following HSP90 inhibition in live MDA-MB-436 cells we used LysoTracker, which selectively accumulates in acidic vesicular compartments such as late endosomes and lysosomes. In vehicle-treated cells, LysoTracker-positive structures localized predominantly to the perinuclear region, which is consistent with lysosomal localization in non-polarized cells [42]. In contrast, treatment with luminespib and NMS-E973 induced a marked repositioning of endosomes/lysosomes to the cell periphery (Fig. 7A). LysoTracker-labeled structures moved with higher speed and localized closer to the cell edge following HSP90 treatment (Fig. 7B). We confirmed that LysoTracker-positive structures were lysosomes by LAMP1 staining.

GPNMB traffics with lysosomes to the cell surface following HSP90 inhibition

To determine if GPNMB reached the cell surface via lysosome-mediated transport in cells treated with HSP90i, we expressed RFP-GPNMB in MDA-MB-436 cells and visualized lysosomal distribution by LysoTracker. In vehicle-treated cells, RFP-GPNMB localized to the perinuclear region, largely co-staining with LysoTracker-positive structures. Upon treatment with luminespib or NMS-E973, we observed scattering of structures positive for RFP-GPNMB that localized closer to the cellular edge (Fig. 7C). The number of RFP-GPNMB-positive structures increased in response to HSP90 inhibition, suggesting that more RFP-GPNMB fusion proteins were sorted into lysosomes in response to HSP90i (Fig. 7D). In response to HSP90 inhibition, we confirmed scattering of Lysotracker-positive structures as previously observed. Co-localization analysis showed that Lysotracker-positive structures extensively co-localize with RFP-GPNMB (Fig. 7D). We previously observed that luminespib and NMS-E973 increase the number of lysosomes found per cell area (Fig. 6B). These results suggest that more RFP-GPNMB was sorted into lysosomes in response to HSP90i. In addition, the percentage co-localization between RFP-GPNMB and Lysotracker decreased following luminespib and NMS-E973 treatment, suggesting that GPNMB may be deposited on the plasma membrane as a result of lysosomal exocytosis (Fig. 7D). These data suggest that, under normal conditions, GPNMB is situated within the perinuclear region where it co-localizes with late endosome/lysosomes. Following treatment with HSP90i, GPNMB-containing lysosomes are scattered to the cell periphery and fuse with the plasma membrane. We next investigated the mechanism responsible for lysosomal scattering following HSP90 inhibition. A recent work identified FLCN as a client protein of HSP90 and showed that treatment with the HSP90i, ganetespib, induced FLCN degradation [43]. As we demonstrated in Fig. S4G, *FLCN* knockout resulted in lysosomal accumulation to the cellular periphery in MCF7 cells. Therefore, we reasoned that HSP90i induce lysosomal scattering by inducing FLCN degradation. We analyzed FLCN levels in MDA-MB-436 and MCF7 cells treated with luminespib. Our data show that FLCN levels were not significantly changed upon HSP90 inhibition (Fig. S6D), suggesting the existence of alternative mechanisms responsible for lysosomal repositioning to the cell periphery in cells treated with HSP90i.

Combining HSP90 inhibition with Glembatumumab Vedotin impairs the growth of TNBC cells in vivo

Among the different therapeutic agents tested, HSP90i were the only class capable of effectively increasing both total GPNMB expression and GPNMB localization at the cell surface. Increased expression of HSP90 has been associated with poor prognosis in breast cancer patients, including women with TNBC [44]. Several HSP90i have been tested in clinical trials. We investigated whether administration of HSP90i to mice bearing TNBC-derived mammary tumors could enhance the efficacy of Glembatumumab Vedotin. Secondarily, we determined whether the combination of HSP90/Glembatumumab Vedotin was able to prevent the onset of HSP90 inhibitor resistance. Mice harboring HCI-010 TNBC PDX tumors were divided into four cohorts and received: (1) vehicle, (2) luminespib alone (3 times/week), Glembatumumab Vedotin alone (once/week), or (4) a combination of both therapeutic agents. Luminespib, as a single agent, slowed tumor growth compared to vehicle, which then resumed after 35 days posttreatment (Fig. 8A). Tumors treated with Glembatumumab Vedotin as a single agent displayed a more significant growth impairment relative to luminespib alone; however, tumor growth resumed after ~28 days of treatment (Fig. 8A). The combination of luminespib and Glembatumumab Vedotin further impaired tumor growth (Fig. 8A). Importantly, tumors rapidly responded to combination treatment, displaying significantly impaired growth by 14 days relative to cohorts treated with luminespib or Glembatumumab Vedotin alone (Fig. 8B). Administration of these therapeutic agents did not negatively impact the overall health of the mice under treatment, as revealed by the mouse body weights measured in

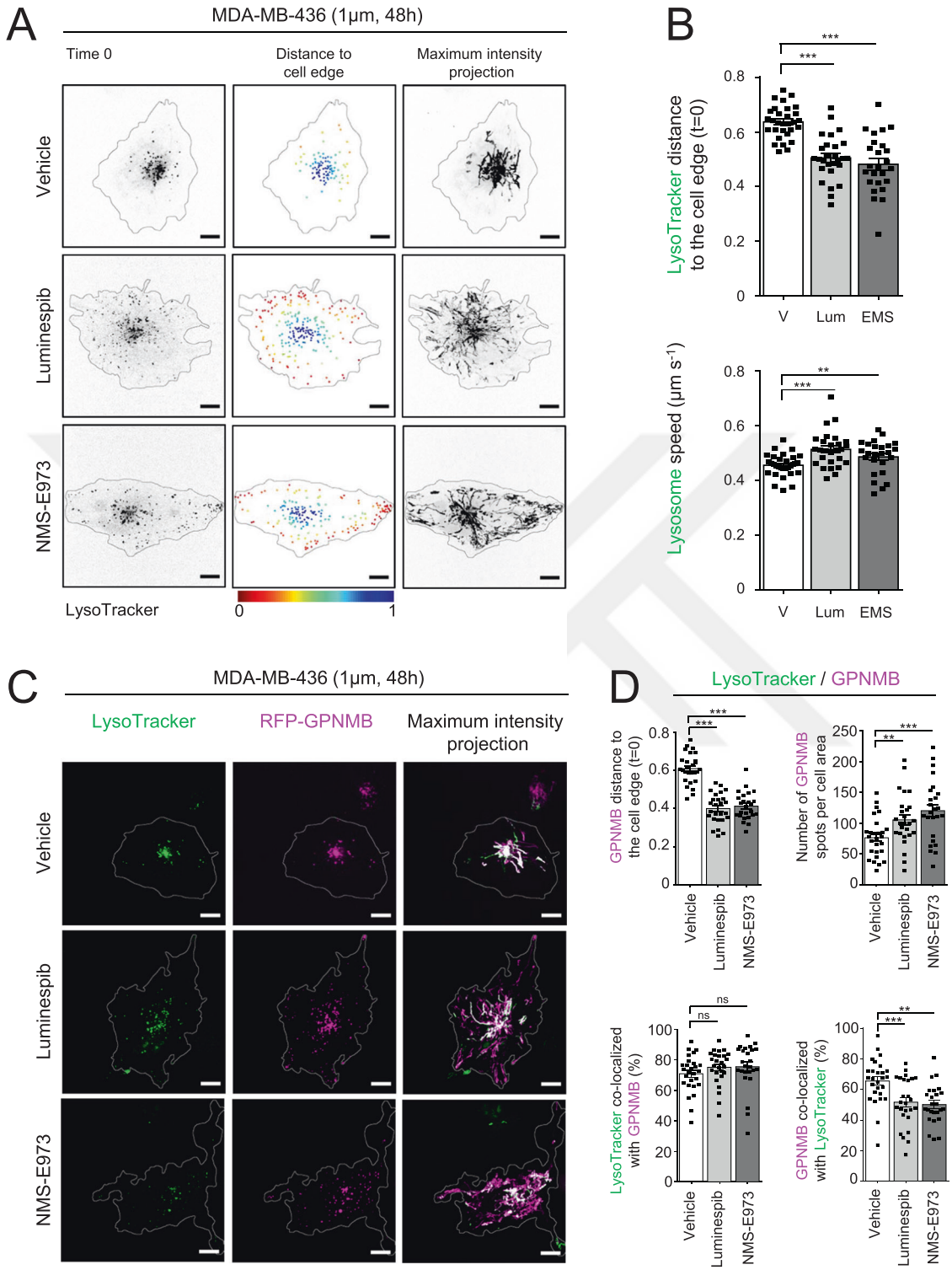


Fig. 7 HSP90 inhibitors increase lysosome proximity to the cell periphery and deliver GPNMB to the cell surface. A Representative images of MDA-MB-436 cells treated with vehicle, luminespib or NMS-E973 for 48 h and stained with 200 nM LysoTracker to visualize endosome/lysosome positioning in live cells. Images were continuously acquired for ~32.6 s. LysoTracker images are shown with an inverted lookup table to enhance visualization. Lysosome positions were plotted and pseudo- colored to visualize distance (red lysosomes are close to the cell edge while blue lysosomes are far away). Scale bar: 10 μm. **B** Quantification of the videos in (**A**). Black squares indicate the average for each cell analyzed ($n = 31$ for vehicle, $n = 27$ for luminespib, $n = 25$ for NMS-E973). Error bars indicate the SEM. $^{**}P < 0.01$; $^{***}P < 0.001$, by Mann–Whitney *U* test. **C** Representative images of MDA-MB-436 cells transfected with RFP-GPNMB, treated with vehicle, luminespib or NMS-E973, and stained with LysoTracker, as described in (**A**). Scale bar: 10 μm. **D** Quantification of the videos from (**C**). Black squares indicate the average for each cell analyzed ($n = 27$ for vehicle, $n = 26$ for luminespib, $n = 25$ for NMS-E973). Error bars indicate the SEM. $^{**}P < 0.01$; $^{***}P < 0.001$, by Mann–Whitney *U* .test.

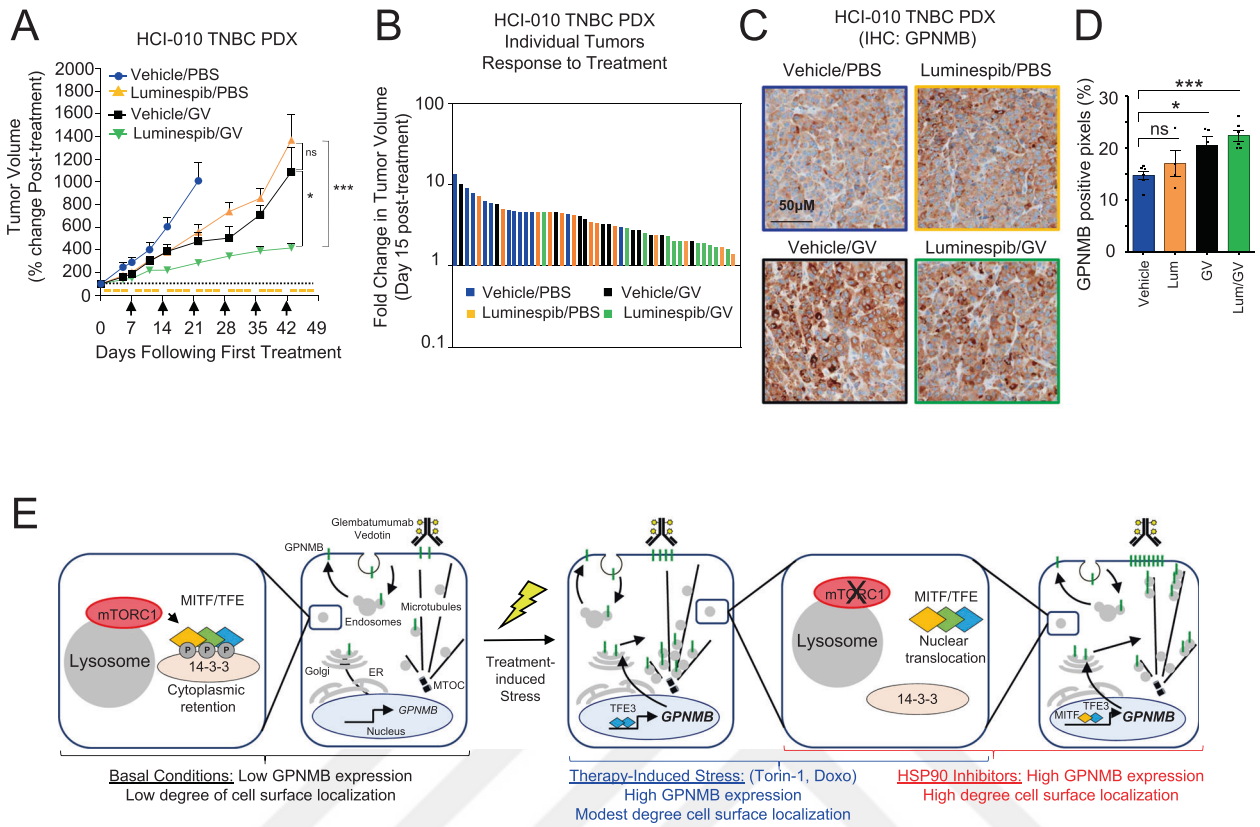


Fig. 8 A combination of HSP90 inhibition and Glembatumumab dramatically impairs the growth of TNBC cells in vivo. A Growth curves of HCI-010 tumors upon treatment with vehicle (blue line), 25 mg/kg luminespib alone (orange line), 5 mg/kg Glembatumumab Vedotin alone (black line) and trametinib administered in combination with glembatumumab vedotin (green line). Glembatumumab Vedotin was administered as a single agent once every week (black arrows below *x*-axis) and Luminespib was administered three times per week (orange dashes above *x*-axis). Error bars indicate the SEM. $^{*}P \leq 0.01$; $^{***}P \leq 0.0001$, by unpaired Student's *t* test. **B** Waterfall plot demonstrating responses of individual HCI-010 tumors to the indicated treatments. Mice were treated as indicated in (**A**). **C** Immunohistochemistry (IHC) analysis of GPNMB expression in samples from HCI-010 TNBC PDX tumors treated with vehicle (blue), 25 mg/kg luminespib alone (orange line), 5 mg/kg Glembatumumab Vedotin alone and luminespib administered in combination with Glembatumumab Vedotin (green). Glembatumumab Vedotin was administered as a single agent once every week (black arrows below *x*-axis) and luminespib was administered three times per week (orange dashes above *x*-axis). **D** Quantification of GPNMB IHC expression in (**C**). Error bars indicate the SEM. $^{*}P \leq 0.05$ and $^{***}P \leq 0.0001$, by unpaired Student's *t* test. **E** Model of therapy-induced GPNMB expression and subsequent sensitization to Glembatumumab Vedotin. Under basal conditions, in the absence of physiological or therapy-induced stresses, the MITF family members are phosphorylated by mTOR at the lysosomal surface. Active mTOR phosphorylates MITF, TFEB, or TFE3 and results in their cytoplasmic sequestration by 14-3-3 proteins. Nuclear exclusion of MiTF family members results in low GPNMB expression and cell-surface localization. Under therapy-induced stress (torin, doxorubicin), mTOR activity at the lysosomal surface is reduced. This leads to reduced phosphorylation of MITF family members and their subsequent nuclear accumulation. TFE3 is required for the elevated expression of GPNMB in response to cellular stresses. A TFE/TFEB cell stress program is also engaged, which results in the trafficking of lysosomes from the periphery to the cell center (see text in discussion). While much of the increased GPNMB that is expressed in the treated cancer cells, some GPNMB makes it to the cell surface, which increases the sensitivity of these cancer cells to Glembatumumab Vedotin. HSP90 inhibition leads to a reduction in PI3K/Akt/mTOR signaling, which results in diminished phosphorylation of MiTF family members, enabling their nuclear translocation. MITF and TFE are required for GPNMB upregulation in response to HSP90 inhibition. Interestingly, the HSP90 chaperone has been shown to regulate endosomal/lysosomal fusion with the plasma membrane. Thus, treatment with HSP90 inhibitors not only results in an induction in GPNMB expression but favors lysosomal fusion and delivery of GPNMB to the cells surface. Thus, HSP90 inhibitor treated cells are highly sensitized to glembatumumab vedotin.

each cohort throughout the duration of the experiment (data not shown). Immunohistochemistry analysis of HCI-010 tumors harvested at experimental endpoint showed increased GPNMB expression in the tumor epithelium of luminespib-treated mice and glembatumumab vedotin combination treated mice (Fig. 8D, E). Similar results were obtained with 17-DMAG, an independent inhibitor specifically targeting HSP90 (Fig. S7A–D).

DISCUSSION

Glembatumumab Vedotin is an ADC specifically targeting GPNMB [8] that has been tested in a Phase II clinical trial (NCT#01997333) as a stand-alone therapy for women with metastatic GPNMB-overexpressing TNBC. When compared to capecitabine, Glembatumumab Vedotin alone did not provide superior advantage in progression-free survival, overall response rate, duration of response and overall survival. While GPNMB remains a viable target in oncology, combination strategies to increase the efficacy of Glembatumumab Vedotin are clearly required. Indeed, there is a growing appreciation in the field for the need to design rationale drug combination therapies based on detailed mechanistic insights [45].

Our results reveal that GPNMB expression is regulated via a variety of cellular stressors, including nutrient deprivation, oxidative stressors and therapy-induced stress. Lysosomal storage diseases/lysosomal stress [46] and endoplasmic reticulum stress [47] also induce GPNMB expression, which argues that GPNMB is part of a transcriptional stress response. The *GPNMB* promoter

contains a conserved E box sequence (TCACATG) that is recognized by MiTF/TFE family members [28], which plays a well-established role in orchestrating adaptive responses to stress by promoting lysosomal biogenesis, autophagy, mitochondrial biogenesis and cellular metabolism [48]. Indeed, *GPNMB* is a transcriptional target of TFE3 or MITF depending on cellular context [13, 28, 49]. In TNBC cells, the expression of GPNMB in response to a variety of cellular and therapeutic stress predominantly relies on TFE3 activity. Our findings are consistent with previous data showing that hydrophobic weak base chemotherapeutics like doxorubicin can induce nuclear translocation of MiTF/TFE family of transcription factors [50]. We showed that GPNMB expression is also elevated in TNBC cells resistant to doxorubicin and epirubicin and in ER+ resistant to tamoxifen rising the intriguing possibility that high GPNMB expression is a selected trait and might be required for drug resistance. In this regard, GPNMB is required for the fusion between phagosomes and lysosomes to create autophagolysosomes during autophagy [51], a pro-survival program exploited by cancer cells to survive metabolic and therapeutic stresses [52].

MAPK and mTOR signaling control TFEB and TFE3 function by regulating nuclear/cytoplasmic shuttling of these transcription factors. ERK2 can phosphorylate TFEB on serine residue 142 and enhance cytoplasmic retention of TFEB [53]. Similarly, mTOR phosphorylates TFEB on serine residues 121, 142, and 211 [25–27, 53, 54]. The net result of these phosphorylation events is to enhance interactions between TFEB/TFE3 and 14-3-3 proteins, which leads to cytoplasmic retention and reduced expression of TFEB/TFE3 transcriptional targets [25, 26]. It is believed that key phosphorylation sites and regulatory events are conserved among all MiTF/TFE family members [55–57]. Thus, the use of MEK or mTOR inhibitors in this study leads to enhanced TFE3 nuclear localization and increased GPNMB expression. Our in vivo results show that combining Glembatumumab Vedotin with either a MAPK or mTOR pathway inhibitors results in a significant impairment of tumor growth compared to individual treatment arms. Although both combination strategies significantly reduced tumor growth, residual tumors were still detectable in mice treated with MEKi/Glembatumumab Vedotin or mTORi/Glembatumumab Vedotin. These results may be explained by the observation that MEKi or mTORi failed to substantially increase GPNMB cell-surface localization. The ability of MEKi or mTORi to enhance the efficacy of Glembatumumab Vedotin may also be due to the impact of these inhibitors on ADC internalization/intracellular processing or through mechanisms that impair the onset of ADC resistance.

Many factors influence the efficacy of ADCs: expression and accessibility of the target, ADC internalization rate, ADC trafficking route upon internalization, the chemistry/cleavage of the linker, and the efficacy of the conjugated drug [58]. We and others have shown that GPNMB localization at the cell surface of cancer cells can predict a response to glembatumumab vedotin in vitro [4, 12]. The identification of HSP90 as a regulator of GPNMB cell-surface localization is interesting for several reasons. Several classes of HSP90i are available and some have been explored for their efficacy in clinical trials for diverse solid cancers, including breast cancer [59].Our observation that independent Hsp90 inhibitors induce GPNMB mRNA and protein levels are in agreement with recent studies demonstrating that targeting HSP90 suppresses signaling through the PI3K/AKT/mTOR pathway in Burkitt's lymphoma, prostate cancer and sarcoma [39, 60, 61]. Importantly, inhibition of HSP90 also resulted in an increase in GPNMB cell-surface localization. Although the Hsp90i were initially successful at controlling tumor growth, tumors resumed growing after 5 weeks of treatment. In contrast, treatment with luminespib and 17-DMAG in combination with Glembatumumab Vedotin blunted the rebound in tumor growth. Currently, the utility of HSP90i as monotherapies has been limited due to toxicity or lack of clinical efficacy [62]. The majority of HSP90i developed and tested in the clinic target the N-terminal region of HSP90. The lack of clinical efficacy of HSP90-N inhibitors has been ascribed to their ability to induce a pro-survival mechanism in cancer cells known as a heat shock response [63]. Alternative molecules are currently being investigated that inhibit HSP90 without inducing a heat shock response, such as HSP90-C inhibitors [64]. Our data show that HSP90i increase GPNMB expression and cell-surface localization, providing the rationale for combining Glembatumumab Vedotin and HSP90i in order to avoid the onset of tumor resistance.

Our findings raise the intriguing possibility that, following HSP90i treatment, GPNMB reaches the cell surface via lysosomal trafficking. GPNMB contains a dileucine motif (EKDLL) in its cytoplasmic tail, which is required for its targeting to the lysosomal/endosomal compartment [32]. The concept of lysosomal positioning/exocytosis has gained interest in the context of cancer [65], with anterograde trafficking of late endosomes/lysosomes and their redistribution to the cell periphery recognized as a common feature of cancer cells [66]. Recently, it was shown that FLCN controls dynamic lysosome positioning by promoting the interaction between Rab34 and RILP [33]. This is of great interest given that we observe increased GPNMB cell-surface localization in luminal breast cancer cells that have lost FLCN. Moreover, FLCN loss also increases the nuclear accumulation of TFEB and TFE3 [28, 67, 68] and leads to elevated GPNMB expression [28]. In our work, loss of FLCN resulted in accumulation of the lysosomes at the cell periphery. Similarly, treatment with HSP90i greatly increased GPNMB at the cell surface and resulted in lysosomal dispersion to the cell edge.

Although HSP70 and HSP90 can lead to the degradation of FLCN [43], our data, suggests that HSP90 inhibition leads to lysosomal repositioning through an alternative mechanism. It has been reported that HSP90 possesses a membrane deformation function that enhances the fusion of multivesicular bodies (MVBs) with the plasma membrane, releasing intraluminal vesicles as exosomes [69]. HSP90i that target the C-terminus (e.g., SM122, SM253) bind to HSP90 dimers in a "closed" state, which blocks both the chaperone activity and the membrane deformation functions of HSP90 and results in diminished MVB fusion with the plasma membrane. In contrast, HSP90i that target the N-terminus (e.g., 17-AAG) bind HSP90 dimers in an "open" confirmation and blunt the chaperone activity of HSP90 without impairing its membrane deformation function, which is required MVB fusion. The HSP90i employed in our study (NMS-E973, luminespib, 17-DMAG and onalespib) bind the ATP-binding site at the N-terminus, in a manner similar to 17-AAG [70]. It would be interesting to further investigate whether the membrane deformation functions of HSP90 play a role in delivering of GPNMB to the cell surface. It is tempting to speculate that HSP90i suppress HSP90 chaperone functions, which diminish PI3K-AKT/mTOR signaling and ultimately engage TFE3 nuclear accumulation and GPNMB upregulation. Simultaneously, HSP90 dimers that are not acting as chaperones are now free to enhance membrane fusion of MVBs with the plasma membrane (unaffected by the class of HSP90i used in this study), which may result in increased GPNMB localization to the plasma membrane. In this way, HSP90i can fulfill the two criteria required to sensitize breast cancer cells to Glembatumumab Vedotin, namely an increase in GPNMB expression that is localized to the cell surface (Fig. 8).

We describe several strategies, along with underlying molecular mechanisms, which sensitize breast cancer cells to the activity of Glembatumumab Vedotin. Such strategies have the potential to be effective in multiple solid cancers in which GPNMB is highly expressed [7]. Indeed, Glembatumumab Vedotin has been used in the context of Osteosarcoma with some degree of ant-tumor activity [71]. Recently, GPNMB was shown to be the most upregulated gene in osteosarcoma cells following HSP70 knockdown [72]. Thus, combining broad specificity HSP inhibitors with

Glembatumumab Vedotin may prove effective in many solid cancer indications.

MATERIAL AND METHODS

Mice

Female NSG mice (6–8 weeks old) were purchased from Charles River. Animals were housed in facilities managed by the McGill University Animal Resources Center and all animal experiments were conducted under a McGill University-approved Animal Use Protocol (AUP#2001-4830). Animal experiments involving live animals were subjected to peer review for scientific merit, in accordance with guidelines established by the Canadian Council on Animal Care.

Cell lines

MDA-MB-436, Hs578T, MDA-468, MCF7, T47D, SkBr3, BT474, and breast cancer cells were obtained from the American Type Culture Collection (ATCC). MCF7 and MCF7 FLCN^{KO} were a gift from AP [73]. MCF7 DoxR and EpiR cells were a gift from JSP [74]. MDA-MB-436 DoxR cells were a gift from MB and their culture conditions were described before [75]. Detailed culture conditions are described in Supplementary Methods.

Treatments

Details regarding the drugs and treatments employed in this study can be found in Supplementary Methods.

siRNA and DNA transfections

For gene-silencing experiments, breast cancer cells were transfected with 10 nM siRNA duplexes using Lipofectamine RNAiMax (Thermo Fisher, Cat. #: 13778030) according to manufacturer's instructions. Cellular phenotypes were assessed 72 h post-transfection. The siRNAs used in this study are listed in Supplementary Methods. For DNA transfection, breast cancer cells were transfected using Lipofectamine 3000 (Thermo Fisher, Cat. #: L3000015) according to manufacturer's instructions. Culture media was changed 2 h post-transfection and cellular phenotypes were assessed 24 h post-transfection. p-mRFP1.3-N1 rat GPNMB DNA plasmid was a gift of Dr. Jeremy S. Duffield.

Immunoblotting

Sub-confluent cells were lysed in TNE lysis buffer (50 mM Tris-HCL pH8, 150 mM NaCl, 2 mM EDTA pH8, 10% NP40) freshly supplemented with 2 mM Na3VO4, 10 mM NaF, 10 mM β-glycerophosphate, 10 µg/ml Leupeptin, and 10 µg/ml Aprotinin. Protein concentrations were determined by BCA assay, proteins were diluted in Laemmli sample buffer and resolved by SDS-PAGE. The antibodies used in this study are listed in Supplementary Methods.

Immunofluorescence

Detailed methodology relative to immunofluorescence can be found in Supplementary Methods.

Immunohistochemistry

Mammary tumors were fixed overnight in formalin embedded in paraffin and sectioned by the Goodman Cancer Research Center (GCRC) histology core facility. Sections were stained using routine immunohistochemical protocols provided by the GCRC Histology Core using Ventana BenchMark ULTRA system (Roche). Tissue sections were dehydrated in ethanol series, washed with xylene and mounted with Acrytol mounting media (Cat. #: 3801705, Leica). The antibody used for GPNMB staining is anti-GPNMB (1:1000 dilution) (Cell Signaling, Cat. #: 38313).

Adenovirus

Adenovirus expressing TFEB-S211A-Flag and TFE3-S321A-Myc were purchased from Welgen: Ad-Control virus (Welgen, Cat. #: V1000); Ad-TFEB-S211A (Welgen, Cat. #: S3000); Ad-TFEB-S321A (Welgen, Cat. #: S3000). Infections were performed as previously described [24].

Real-time PCR

RNA extraction was performed from sub-confluent cell cultures using a RNeasy Mini Kit and total RNA was reverse transcribed with a High-Capacity cDNA Reverse Transcription Kit. cDNAs were analyzed in duplicate using FastStart Universal SYBR Green Master (Rox). Relative mRNA concentrations were determined using Bio-Rad CFX Maestro Software. Primers used in this study are described in Supplementary Materials.

Mammary fat pad injections and therapy treatments

For in vivo studies, a TNBC PDX (HCI-010) (gift from Dr. Alana Welm) [31] mammary tumor was first dissociated using a tumor dissociation kit (Miltenyi, Cat. #130-095-929) and 1×10^6 breast cancer cells were resuspended in a 50/50 mixture of 1 × PBS:matrigel (Corning, Cat. #: 35623) and injected bilaterally into the fourth mammary fat pads of NSG female mice (NOD.Cg-Prkdcscid Il2rgtm1Wjl/SzJ). Upon reaching a preestablished tumor volume (300–400 mm^3), mice were randomized into experimental cohorts. Trametinib (in oral suspending vehicle; ORA PLUS) was administered daily by oral gavage at 2 mg/kg, AZD2014 administered daily by oral gavage at 15 mg/kg in ORA PLUS vehicle. Luminespib and 17-DMAG were resuspended in 5% DMSO + 40% PEG300 (Sigma, Cat # 202371) + 5% Tween-80 (BDH Chemicals, VWR Cat # BDH7781-2) + 45% Saline and administered by IP injection at 25 mg/kg. Glembatumumab Vedotin was administered once per week by tail vein injection at 5 mg/kg. PBS was used as vehicle for Glembatumumab Vedotin.

Flow cytometry

Detailed methods relative to flow cytometry are provided in Supplementary Methods.

FACS-based shRNA screen and data analysis

The shRNA libraries used in this study were from SH and were previously described (PMID: 31722999) (PMID: 30718512). MCF7 cells were infected with virus pools of the shRNA library (MOI ~0.3) and quickly selected in puromycin for stably transduced cells. Cells with stable shRNA integration were stained for cell-surface GPNMB using the anti-GPNMB CR011 antibody (gift from Celldex Therapeutics) and submitted for fluorescence-activated cell sorting (FACS). The top 4.1% of live cells with high cell-surface GPNMB expression (GPNMB^{high}), when compared to pre-sort cells, were collected and expanded. Genomic DNA was extracted and shRNA inserts were recovered by PCR amplification, as previously reported [76]. The relative abundance of shRNAs in the pre-sort population and in GPNMB^{high} cells was determined by next-generation sequencing and the resulting data analyzed using MAGeCK software (version 0.5.9.2) [37]. Briefly, total count normalization was used instead of median normalization due to many 0-counts in the sorted population. The top 10 candidates identified by the screen are listed in Table S1 (section 1). In parallel, we performed a hand-curated analysis of the entire list of candidates produced using the MAGeCK tool. We selected only those targets against which 3 or more shRNAs induced a 2-fold increase of GPNMB cell-surface localization, resulting in 14 potential candidates (Table S1, section 2). Comparing these two approaches revealed 7 genes that were common to both analyses (Table S1, section 3).

Immunofluorescence for lysosome positioning

Methods relative to the immunofluorescence analysis of lysosome positioning are described in Supplementary Methods.

Lysosomal and GPNMB live dynamics

Methods relative to the analysis of lysosomal and GPNMB dynamics can be found in Supplementary Methods.

REFERENCES

1. Liedtke C, Mazouni C, Hess KR, André F, Tordai A, Mejia JA, et al. Response to neoadjuvant therapy and long-term survival in patients with triple-negative breast cancer. J Clin Oncol. 2008;26:1275–81.
2. Shah SP, Roth A, Goya R, Oloumi A, Ha G, Zhao Y, et al. The clonal and mutational evolution spectrum of primary triple-negative breast cancers. Nature. 2012;486:395–9.
3. Damaskos C, Garmpi A, Nikolettos K, Vavourakis M, Diamantis E, Patsouras A, et al. Triple-negative breast cancer: the progress of targeted therapies and future tendencies. Anticancer Res. 2019;39:5285–96.
4. Rose AA, Grosset AA, Dong Z, Russo C, Macdonald PA, Bertos NR, et al. Glycoprotein nonmetastatic B is an independent prognostic indicator of recurrence and a novel therapeutic target in breast cancer. Clin Cancer Res. 2010;16:2147–56.

5. Yardley DA, Weaver R, Melisko ME, Saleh MN, Arena FP, Forero A, et al. EMERGE: a randomized phase II study of the antibody-drug conjugate glembatumumab vedotin in advanced glycoprotein NMB-expressing breast cancer. J Clin Oncol. 2015;33:1609–19.
6. Chen C, Okita Y, Watanabe Y, Abe F, Fikry MA, Ichikawa Y, et al. Glycoprotein nmb is exposed on the surface of dormant breast cancer cells and induces stem cell-like properties. Cancer Res. 2018;78:6424–35.
7. Rose AAN, Biondini M, Curiel R, Siegel PM. Targeting GPNMB with glembatumumab vedotin: current developments and future opportunities for the treatment of cancer. Pharmacol Ther. 2017;179:127–41.
8. Tse KF, Jeffers M, Pollack VA, McCabe DA, Shadish ML, Khramtsov NV, et al. CR011, a fully human monoclonal antibody-auristatin E conjugate, for the treatment of melanoma. Clin Cancer Res. 2006;12:1373–82.
9. Bendell J, Saleh M, Rose AA, Siegel PM, Hart L, Sirpal S, et al. Phase I/II study of the antibody-drug conjugate glembatumumab vedotin in patients with locally advanced or metastatic breast cancer. J Clin Oncol. 2014;32:3619–25.
10. Vahdat LTF-TA, Schmid P, Blackwell K, Telli ML, Melisko M, Holgado E, et al. METRIC: A randomized international phase 2b study of the antibody-drug conjugate (ADC) glembatumumab vedotin (GV) in gpNMB-overexpressing, metastatic, triple-negative breast cancer (mTNBC) (Abstract P6-20-01.). Proceedings of the 2018 San Antonio Breast Cancer Symposium; 2018; San Antonio, TX Philadelphia (PA): AACR; Cancer Res 2019;79 4 Suppl.
11. Ott PA, Pavlick AC, Johnson DB, Hart LL, Infante JR, Luke JJ, et al. A phase 2 study of glembatumumab vedotin, an antibody-drug conjugate targeting glycoprotein NMB, in patients with advanced melanoma. Cancer. 2019;125:1113–23.
12. Qian X, Mills E, Torgov M, LaRochelle WJ, Jeffers M. Pharmacologically enhanced expression of GPNMB increases the sensitivity of melanoma cells to the CR011-vcMMAE antibody-drug conjugate. Mol Oncol. 2008;2:81–93.
13. Rose AA, Annis MG, Frederick DT, Biondini M, Dong Z, Kwong L, et al. MAPK pathway inhibitors sensitize BRAF-mutant melanoma to an antibody-drug conjugate targeting GPNMB. Clin Cancer Res. 2016;22:6088–98.
14. Neve RM, Chin K, Fridlyand J, Yeh J, Baehner FL, Fevr T, et al. A collection of breast cancer cell lines for the study of functionally distinct cancer subtypes. Cancer Cell. 2006;10:515–27.
15. Bergin ART, Loi S. Triple-negative breast cancer: recent treatment advances. F1000Res. 2019;8:1342.
16. Cheng Y, Tian H. Current development status of MEK inhibitors. Molecules. 2017;22:1551.
17. Pratilas CA, Taylor BS, Ye Q, Viale A, Sander C, Solit DB, et al. (V600E)BRAF is associated with disabled feedback inhibition of RAF-MEK signaling and elevated transcriptional output of the pathway. Proc Natl Acad Sci USA. 2009;106:4519–24.
18. Parker JS, Mullins M, Cheang MC, Leung S, Voduc D, Vickery T, et al. Supervised risk predictor of breast cancer based on intrinsic subtypes. J Clin Oncol. 2009;27:1160–7.
19. Liu H, Murphy CJ, Karreth FA, Emdal KB, White FM, Elemento O, et al. Identifying and targeting sporadic oncogenic genetic aberrations in mouse models of triple-negative breast cancer. Cancer Discov. 2018;8:354–69.
20. Jing J, Greshock J, Holbrook JD, Gilmartin A, Zhang X, McNeil E, et al. Comprehensive predictive biomarker analysis for MEK inhibitor GSK1120212. Mol Cancer Ther. 2012;11:720–9.
21. Slade L, Pulinilkunnil T. The MiTF/TFE family of transcription factors: master regulators of organelle signaling, metabolism, and stress adaptation. Mol Cancer Res. 2017;15:1637–43.
22. Raben N, Puertollano R. TFEB and TFE3: linking lysosomes to cellular adaptation to stress. Annu Rev Cell Dev Biol. 2016;32:255–78.
23. Martina JA, Puertollano R. Rag GTPases mediate amino acid-dependent recruitment of TFEB and MITF to lysosomes. J Cell Biol. 2013;200:475–91.
24. Martina JA, Diab HI, Lishu L, Jeong AL, Patange S, Raben N, et al. The nutrient-responsive transcription factor TFE3 promotes autophagy, lysosomal biogenesis, and clearance of cellular debris. Sci Signal. 2014;7:ra9.
25. Martina JA, Chen Y, Gucek M, Puertollano R. MTORC1 functions as a transcriptional regulator of autophagy by preventing nuclear transport of TFEB. Autophagy. 2012;8:903–14.
26. Roczniak-Ferguson A, Petit CS, Froehlich F, Qian S, Ky J, Angarola B, et al. The transcription factor TFEB links mTORC1 signaling to transcriptional control of lysosome homeostasis. Sci Signal. 2012;5:ra42.
27. Settembre C, Zoncu R, Medina DL, Vetrini F, Erdin S, Erdin S, et al. A lysosome-to-nucleus signalling mechanism senses and regulates the lysosome via mTOR and TFEB. Embo J. 2012;31:1095–108.
28. Hong SB, Oh H, Valera VA, Baba M, Schmidt LS, Linehan WM. Inactivation of the FLCN tumor suppressor gene induces TFE3 transcriptional activity by increasing its nuclear localization. PLoS ONE. 2010;5:e15793.
29. Hemesath TJ, Steingrímsson E, McGill G, Hansen MJ, Vaught J, Hodgkinson CA, et al. microphthalmia, a critical factor in melanocyte development, defines a discrete transcription factor family. Genes Dev. 1994;8:2770–80.
30. Pogenberg V, Ogmundsdóttir MH, Bergsteinsdóttir K, Schepsky A, Phung B, Deineko V, et al. Restricted leucine zipper dimerization and specificity of DNA recognition of the melanocyte master regulator MITF. Genes Dev. 2012;26:2647–58.
31. DeRose YS, Wang G, Lin YC, Bernard PS, Buys SS, Ebbert MT, et al. Tumor grafts derived from women with breast cancer authentically reflect tumor pathology, growth, metastasis and disease outcomes. Nat Med. 2011;17:1514–20.
32. Le Borgne R, Planque N, Martin P, Dewitte F, Saule S, Hoflack B. The AP-3-dependent targeting of the melanosomal glycoprotein QNR-71 requires a di-leucine-based sorting signal. J Cell Sci. 2001;114:2831–41.
33. Starling GP, Yip YY, Sanger A, Morton PE, Eden ER, Dodding MP. Folliculin directs the formation of a Rab34-RILP complex to control the nutrient-dependent dynamic distribution of lysosomes. EMBO Rep. 2016;17:823–41.
34. Schmidt LS, Linehan WM. FLCN: the causative gene for Birt-Hogg-Dubé syndrome. Gene. 2018;640:28–42.
35. Kong T, Ahn R, Yang K, Zhu X, Fu Z, Morin G, et al. CD44 promotes PD-L1 expression and its tumor-intrinsic function in breast and lung cancers. Cancer Res. 2020;80:444–57.
36. Xue Y, Meehan B, Macdonald E, Venneti S, Wang XQD, Witkowski L, et al. CDK4/6 inhibitors target SMARCA4-determined cyclin D1 deficiency in hypercalcemic small cell carcinoma of the ovary. Nat Commun. 2019;10:558.
37. Li W, Xu H, Xiao T, Cong L, Love MI, Zhang F, et al. MAGeCK enables robust identification of essential genes from genome-scale CRISPR/Cas9 knockout screens. Genome Biol. 2014;15:554.
38. Jolly C, Morimoto RI. Role of the heat shock response and molecular chaperones in oncogenesis and cell death. J Natl Cancer Inst. 2000;92:1564–72.
39. Giulino-Roth L, van Besien HJ, Dalton T, Totonchy JE, Rodina A, Taldone T, et al. Inhibition of Hsp90 Suppresses PI3K/AKT/mTOR Signaling and Has Antitumor Activity in Burkitt Lymphoma. Mol Cancer Ther. 2017;16:1779–90.
40. Agarraberes FA, Dice JF. A molecular chaperone complex at the lysosomal membrane is required for protein translocation. J Cell Sci. 2001;114:2491–9.
41. Bandyopadhyay U, Kaushik S, Varticovski L, Cuervo AM. The chaperone-mediated autophagy receptor organizes in dynamic protein complexes at the lysosomal membrane. Mol Cell Biol. 2008;28:5747–63.
42. Jongsma ML, Berlin I, Wijdeven RH, Janssen L, Janssen GM, Garstka MA, et al. An ER-associated pathway defines endosomal architecture for controlled cargo transport. Cell. 2016;166:152–66.
43. Woodford MR, Dunn DM, Blanden AR, Capriotti D, Loiselle D, Prodromou C, et al. The FNIP co-chaperones decelerate the Hsp90 chaperone cycle and enhance drug binding. Nat Commun. 2016;7:12037.
44. Pick E, Kluger Y, Giltnane JM, Moeder C, Camp RL, Rimm DL, et al. High HSP90 expression is associated with decreased survival in breast cancer. Cancer Res. 2007;67:2932–7.
45. Boshuizen J, Peeper DS. Rational cancer treatment combinations: an urgent clinical need. Mol Cell. 2020;78:1002–18.
46. van der Lienden MJC, Gaspar P, Boot R, Aerts J, van Eijk M. Glycoprotein non-metastatic protein B: an emerging biomarker for lysosomal dysfunction in macrophages. Int J Mol Sci. 2018;20:1.
47. Noda Y, Tsuruma K, Takata M, Ishisaka M, Tanaka H, Nakano Y, et al. GPNMB induces BiP expression by enhancing splicing of BiP Pre-mRNA during the endoplasmic reticulum stress response. Sci Rep. 2017;7:12160.
48. Martina JA, Puertollano R. TFEB and TFE3: The art of multi-tasking under stress conditions. Transcription. 2017;8:48–54.
49. Tanaka M, Homme M, Yamazaki Y, Shimizu R, Takazawa Y, Nakamura T. Modeling alveolar soft part sarcoma unveils novel mechanisms of metastasis. Cancer Res. 2017;77:897–907.
50. Zhitomirsky B, Assaraf YG. Lysosomal sequestration of hydrophobic weak base chemotherapeutics triggers lysosomal biogenesis and lysosome-dependent cancer multidrug resistance. Oncotarget. 2015;6:1143–56.
51. Li B, Castano AP, Hudson TE, Nowlin BT, Lin SL, Bonventre JV, et al. The melanoma-associated transmembrane glycoprotein Gpnmb controls trafficking of cellular debris for degradation and is essential for tissue repair. Faseb J. 2010;24:4767–81.
52. Sui X, Chen R, Wang Z, Huang Z, Kong N, Zhang M, et al. Autophagy and chemotherapy resistance: a promising therapeutic target for cancer treatment. Cell Death Dis. 2013;4:e838.
53. Settembre C, Di Malta C, Polito VA, Garcia Arencibia M, Vetrini F, Erdin S, et al. TFEB links autophagy to lysosomal biogenesis. Science. 2011;332:1429–33.
54. Vega-Rubin-de-Celis S, Peña-Llopis S, Konda M, Brugarolas J. Multistep regulation of TFEB by MTORC1. Autophagy. 2017;13:464–72.
55. Puertollano R, Ferguson SM, Brugarolas J, Ballabio A. The complex relationship between TFEB transcription factor phosphorylation and subcellular localization. Embo J. 2018;37:e98804.
56. Martina JA, Diab HI, Brady OA, Puertollano R. TFEB and TFE3 are novel components of the integrated stress response. Embo J. 2016;35:479–95.

57. Wada S, Neinast M, Jang C, Ibrahim YH, Lee G, Babu A, et al. The tumor suppressor FLCN mediates an alternate mTOR pathway to regulate browning of adipose tissue. Genes Dev. 2016;30:2551–64.
58. Hoffmann RM, Coumbe BGT, Josephs DH, Mele S, Ilieva KM, Cheung A, et al. Antibody structure and engineering considerations for the design and function of Antibody Drug Conjugates (ADCs). Oncoimmunology. 2018;7:e1395127.
59. Wang H, Lu M, Yao M, Zhu W. Effects of treatment with an Hsp90 inhibitor in tumors based on 15 phase II clinical trials. Mol Clin Oncol. 2016;5:326–34.
60. Jansson KH, Tucker JB, Stahl LE, Simmons JK, Fuller C, Beshiri ML, et al. High-throughput screens identify HSP90 inhibitors as potent therapeutics that target inter-related growth and survival pathways in advanced prostate cancer. Sci Rep. 2018;8:17239.
61. Bekki H, Kohashi K, Maekawa A, Yamada Y, Yamamoto H, Harimaya K, et al. Elevated expression of HSP90 and the antitumor effect of an HSP90 inhibitor via inactivation of the Akt/mTOR pathway in undifferentiated pleomorphic sarcoma. BMC Cancer. 2015;15:804.
62. Butler LM, Ferraldeschi R, Armstrong HK, Centenera MM, Workman P. Maximizing the therapeutic potential of HSP90 inhibitors. Mol Cancer Res. 2015;13:1445–51.
63. Dai C. The heat-shock, or HSF1-mediated proteotoxic stress, response in cancer: from proteomic stability to oncogenesis. Philos Trans R Soc Lond B Biol Sci. 2018;373:20160525.
64. Wang Y, McAlpine SR. N-terminal and C-terminal modulation of Hsp90 produce dissimilar phenotypes. Chem Commun. 2015;51:1410–3.
65. Pu J, Guardia CM, Keren-Kaplan T, Bonifacino JS. Mechanisms and functions of lysosome positioning. J Cell Sci. 2016;129:4329–39.
66. Kallunki T, Olsen OD, Jäättelä M. Cancer-associated lysosomal changes: friends or foes? Oncogene. 2013;32:1995–2004.
67. Petit CS, Roczniak-Ferguson A, Ferguson SM. Recruitment of folliculin to lysosomes supports the amino acid-dependent activation of Rag GTPases. J Cell Biol. 2013;202:1107–22.
68. El-Houjeiri L, Possik E, Vijayaraghavan T, Paquette M, Martina JA, Kazan JM, et al. The transcription factors TFEB and TFE3 link the FLCN-AMPK signaling axis to innate immune response and pathogen resistance. Cell Rep. 2019;26:3613–28.e6.
69. Lauwers E, Wang YC, Gallardo R, Van der Kant R, Michiels E, Swerts J, et al. Hsp90 mediates membrane deformation and exosome release. Mol Cell. 2018;71:689–702.e9.
70. Park S, Park JA, Jeon JH, Lee Y. Traditional and novel mechanisms of heat shock protein 90 (HSP90) inhibition in cancer chemotherapy including HSP90 cleavage. Biomol Ther. 2019;27:423–34.
71. Kopp LM, Malempati S, Krailo M, Gao Y, Buxton A, Weigel BJ, et al. Phase II trial of the glycoprotein non-metastatic B-targeted antibody-drug conjugate, glembatumumab vedotin (CDX-011), in recurrent osteosarcoma AOST1521: a report from the Children's Oncology Group. Eur J Cancer. 2019;121:177–83.
72. Nytko KJ, Thumser-Henner P, Russo G, Weyland MS, Rohrer Bley C. Role of HSP70 in response to (thermo)radiotherapy: analysis of gene expression in canine osteosarcoma cells by RNA-seq. Sci Rep. 2020;10:12779.
73. El-Houjeiri L, Biondini M, Paquette M, Kuasne H, Pacis A, Park M, et al. Folliculin impairs breast tumor growth by repressing TFE3-dependent induction of the Warburg effect and angiogenesis. J Clin Investig. 2021;131:e144871.
74. McGuirk S, Audet-Delage Y, Annis MG, Xue Y, Vernier M, Zhao K, et al. Resistance to different anthracycline chemotherapeutics elicits distinct and actionable primary metabolic dependencies in breast cancer. Elife. 2021;10:e65150.
75. Sirois I, Aguilar-Mahecha A, Lafleur J, Fowler E, Vu V, Scriver M, et al. A unique morphological phenotype in chemoresistant triple-negative breast cancer reveals metabolic reprogramming and PLIN4 expression as a molecular vulnerability. Mol Cancer Res. 2019;17:2492–507.
76. Sun C, Wang L, Huang S, Heynen GJ, Prahallad A, Robert C, et al. Reversible and adaptive resistance to BRAF(V600E) inhibition in melanoma. Nature. 2014;508:118–22.

ACKNOWLEDGEMENTS

We acknowledge technical assistance from the McGill GCRC Histology core facility for routine histological services. We acknowledge McGill Life Science Complex Advanced BioImaging Facility (ABIF) for technical assistance in acquisition/analysis of images. We acknowledge McGill Platform for Cellular Perturbation (MPCP) for providing the shRNAs libraries and technical assistance with screnning process and analysis. We acknowledge McGill Life Science Complex Cell Vision Core for technical assistance in acquisition/analysis of flow cytometry data. We acknowledge Génome Quebec and McGill University for support of the Q-CROC-03 trial. We acknowledge Dr. Alana Welm for providing us with HCI-010 PDX tumor model. We thank members of the Siegel laboratory, all collaborators and Dr. Ursini-Siegel for thoughtful discussions and critical reading of the paper. MB was the recipient of a Fonds de recherche du Québec—Santé (FRQS) post-doctoral fellowship. PMS is a William Dawson Scholar of McGill University. This work was supported by an operating grant from the Canadian Institutes of Health Research to PMS (PJT-153327).

AUTHOR CONTRIBUTIONS

MB and PMS designed the research. MB, AK, MGA, BEH, JAM, GM, and LE performed experiments. AANR, AAM, TG, RMJ, GM, and EB, performed computational analysis, statistical analysis, biostatistics. IS, AAM, SM, JSP, UMT, MB, RP, OS, SH, TK, and AP, provided reagents and expertise. MB and PMS wrote the paper.

COMPETING INTERESTS

The authors declare no competing interests.

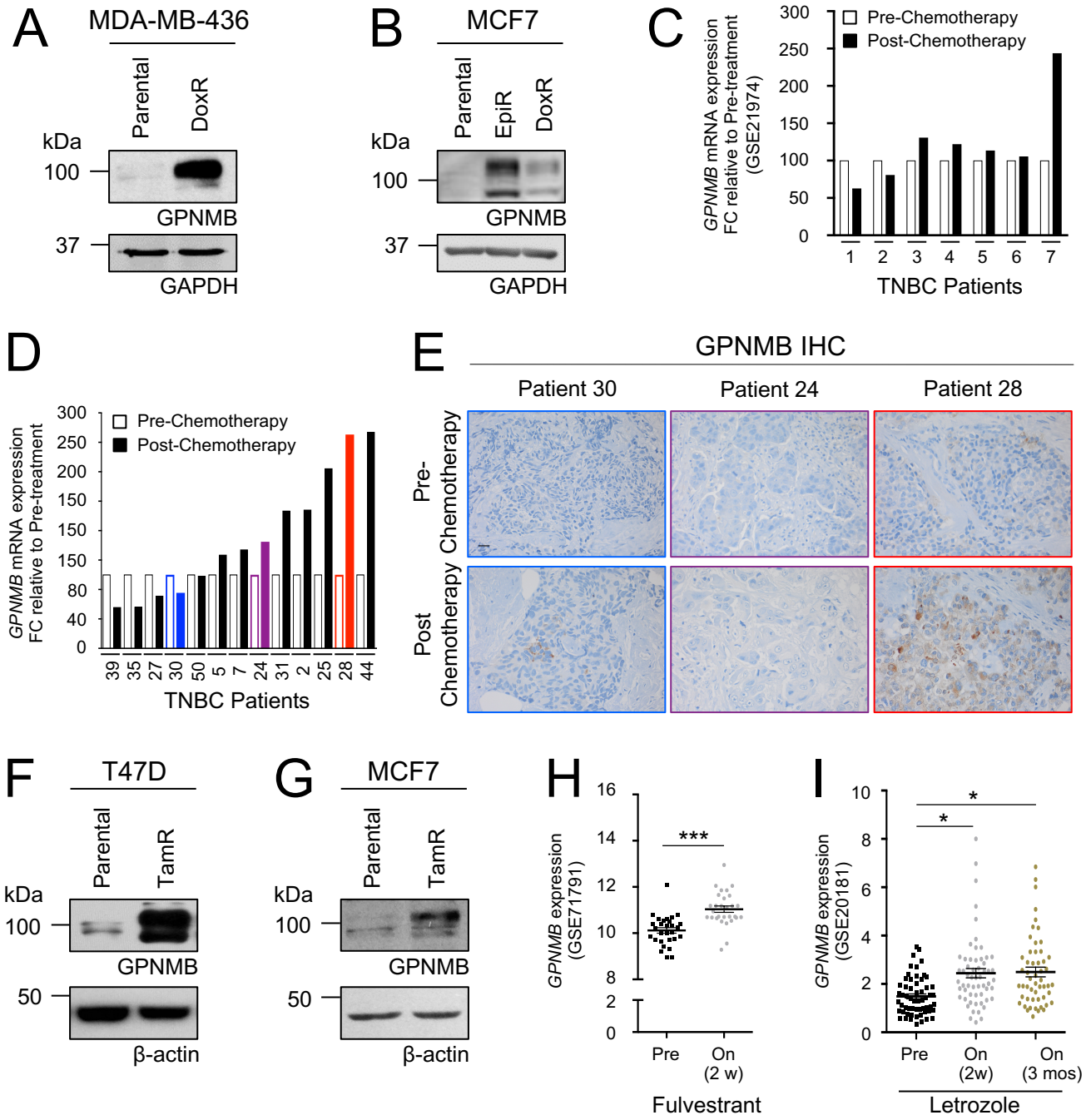
ADDITIONAL INFORMATION

Supplementary information The online version contains supplementary material available at https://doi.org/10.1038/s41388-022-02206-z.

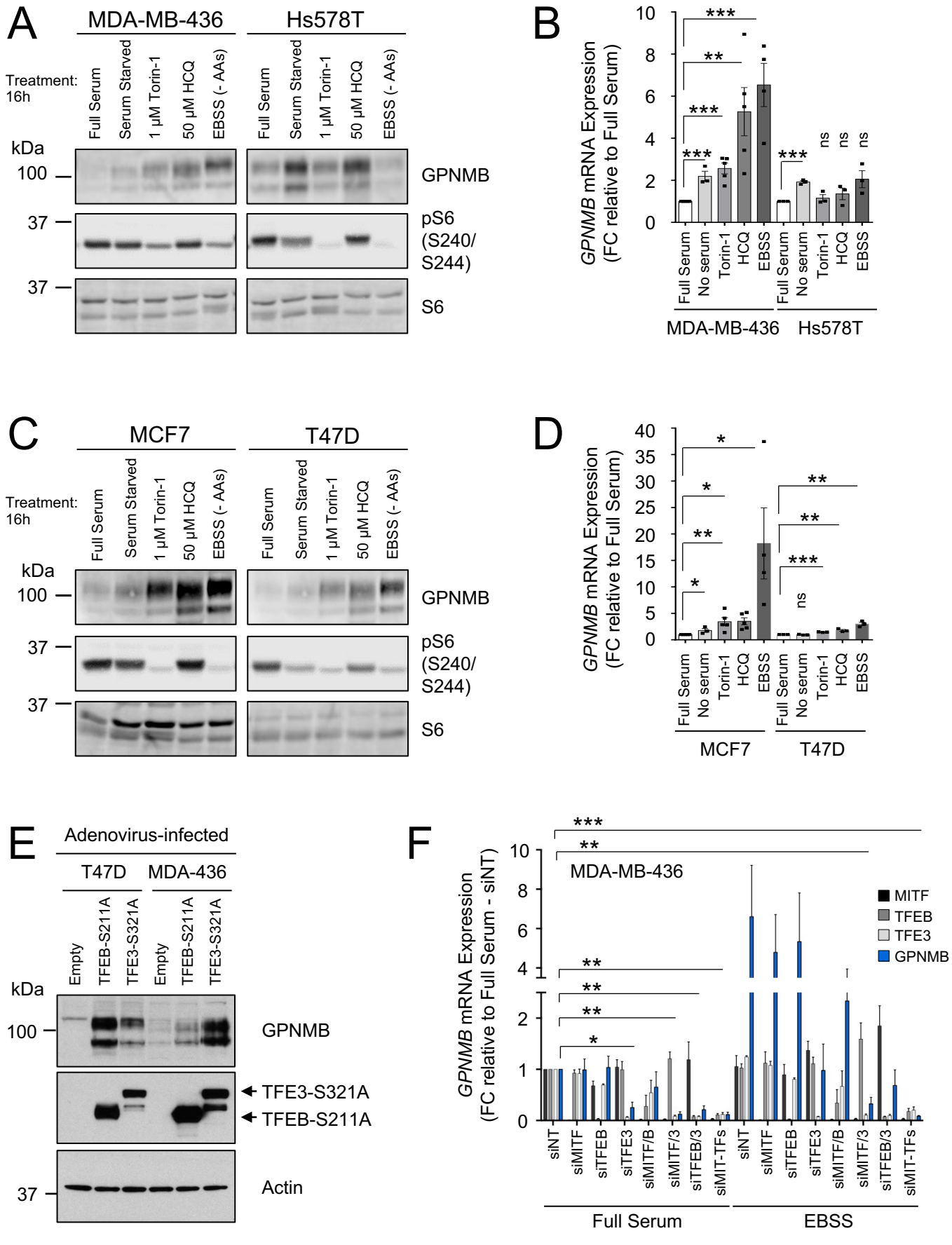
Correspondence and requests for materials should be addressed to Peter M. Siegel.

Reprints and permission information is available at http://www.nature.com/reprints

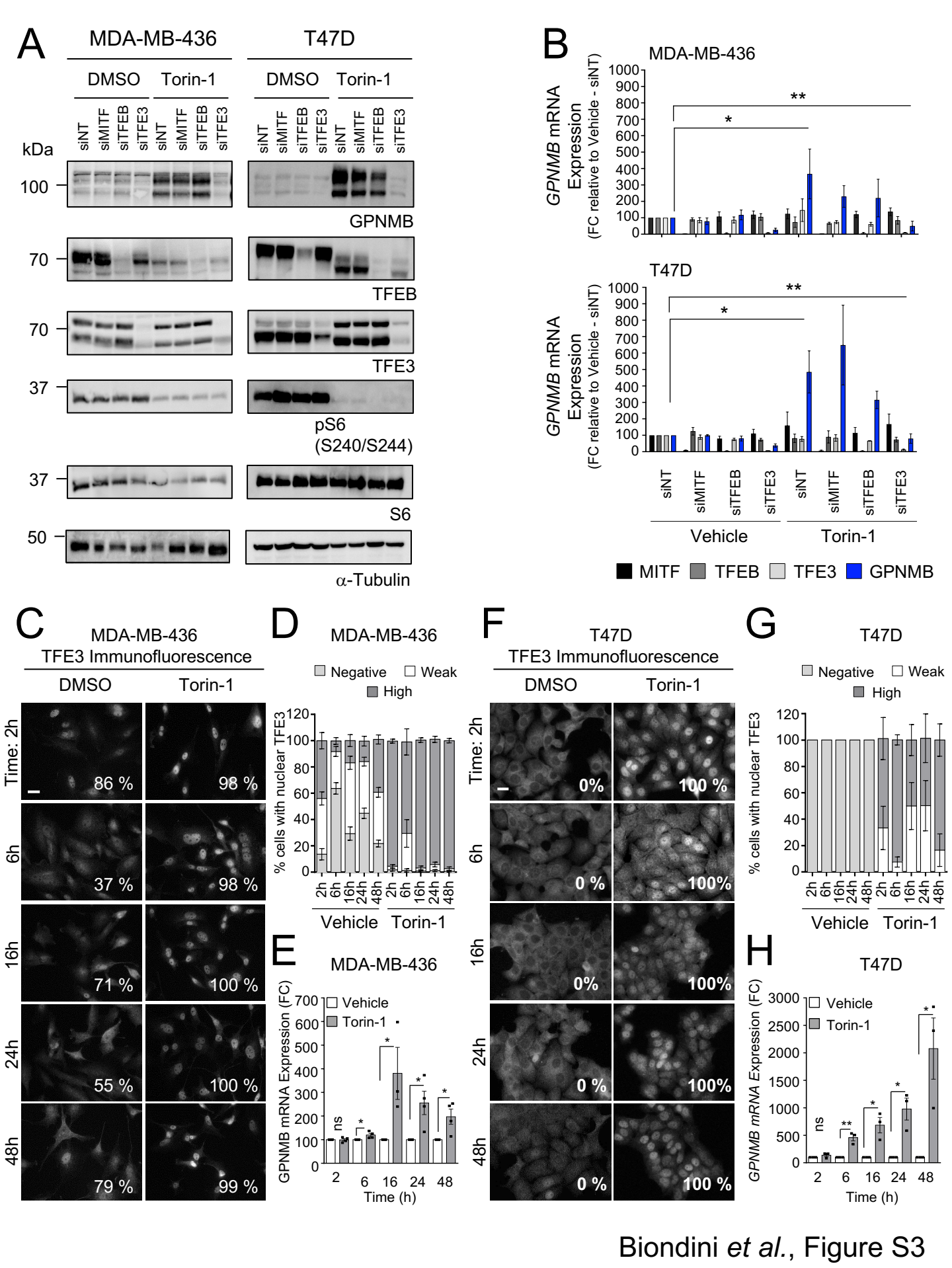
Publisher's note Springer Nature remains neutral with regard to jurisdictional claims in published maps and institutional affiliations.



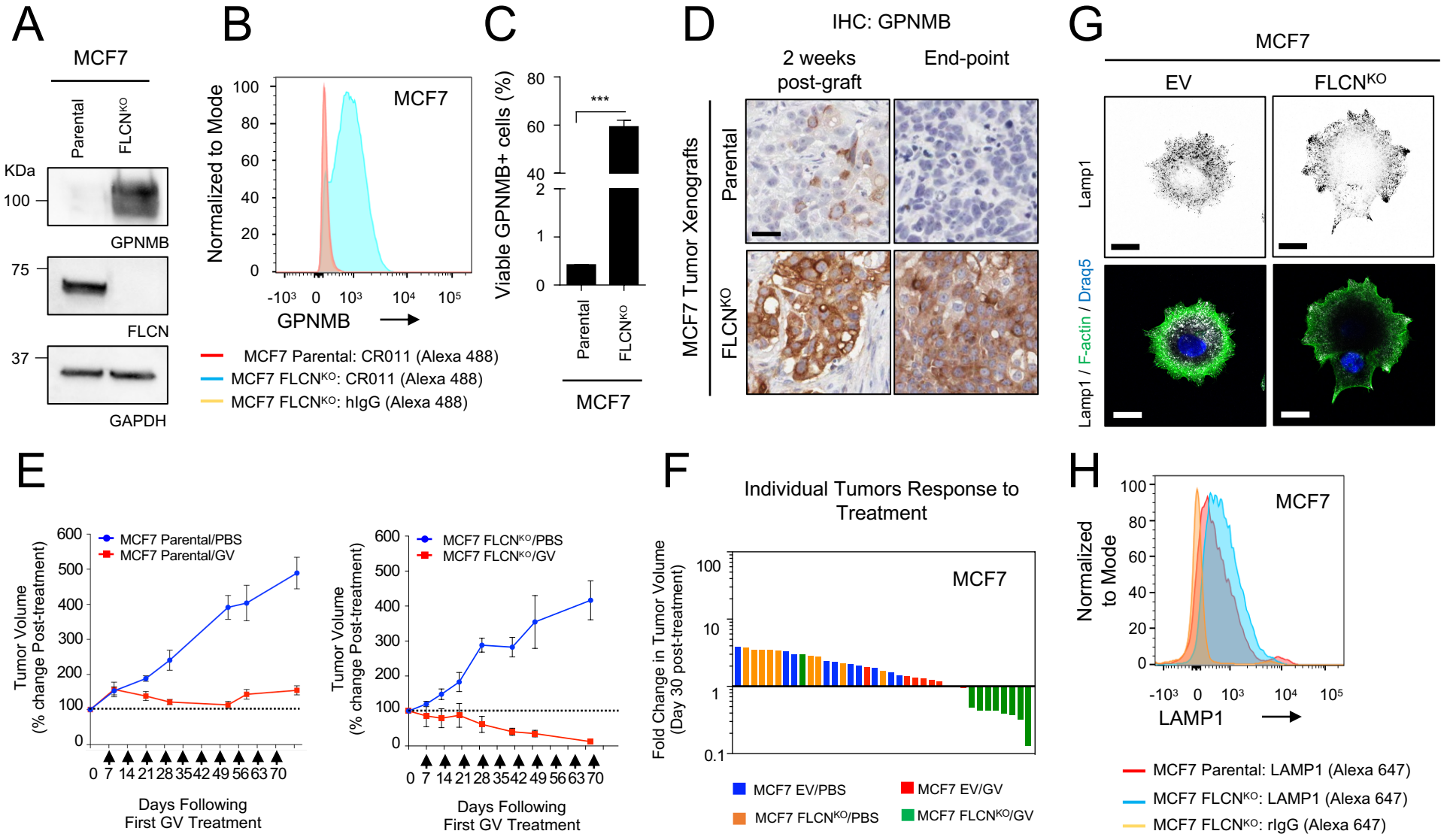
Biondini *et al.*, Figure S1



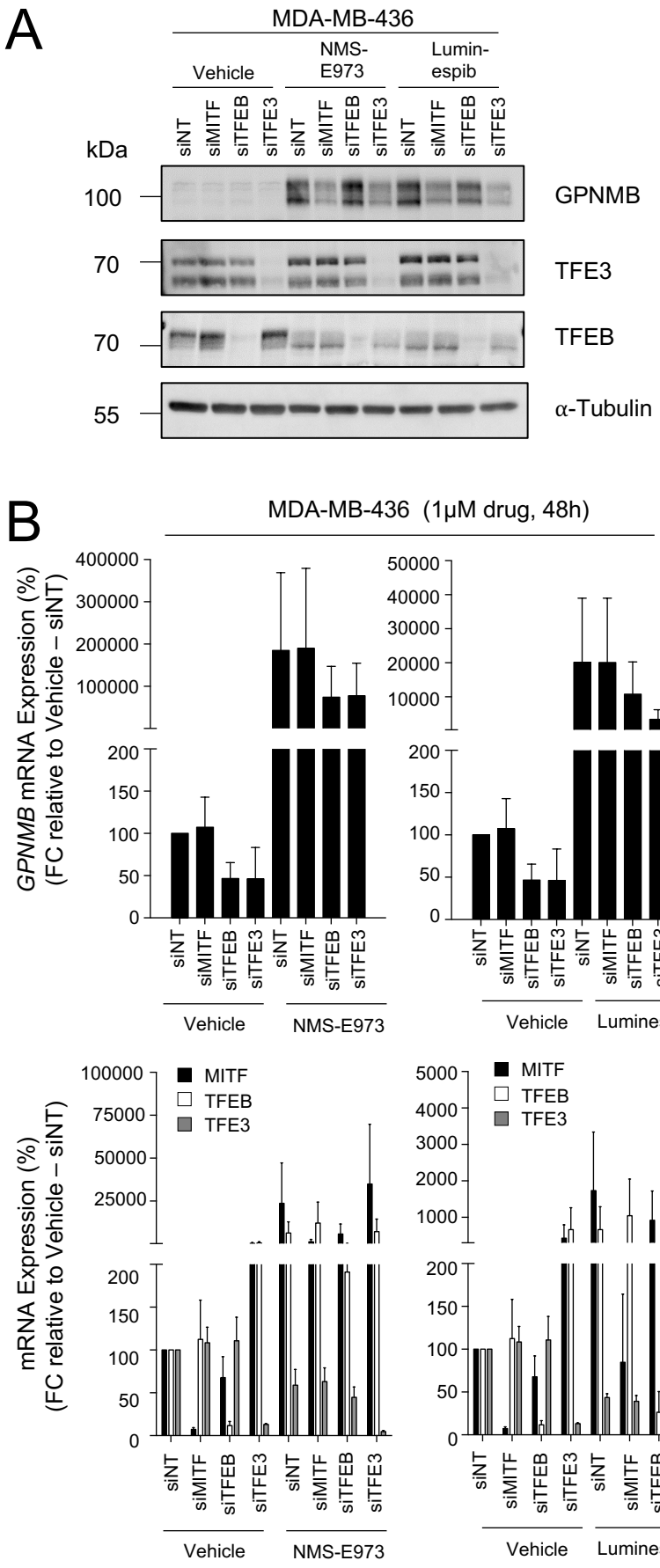
Biondini *et al.*, Figure S2



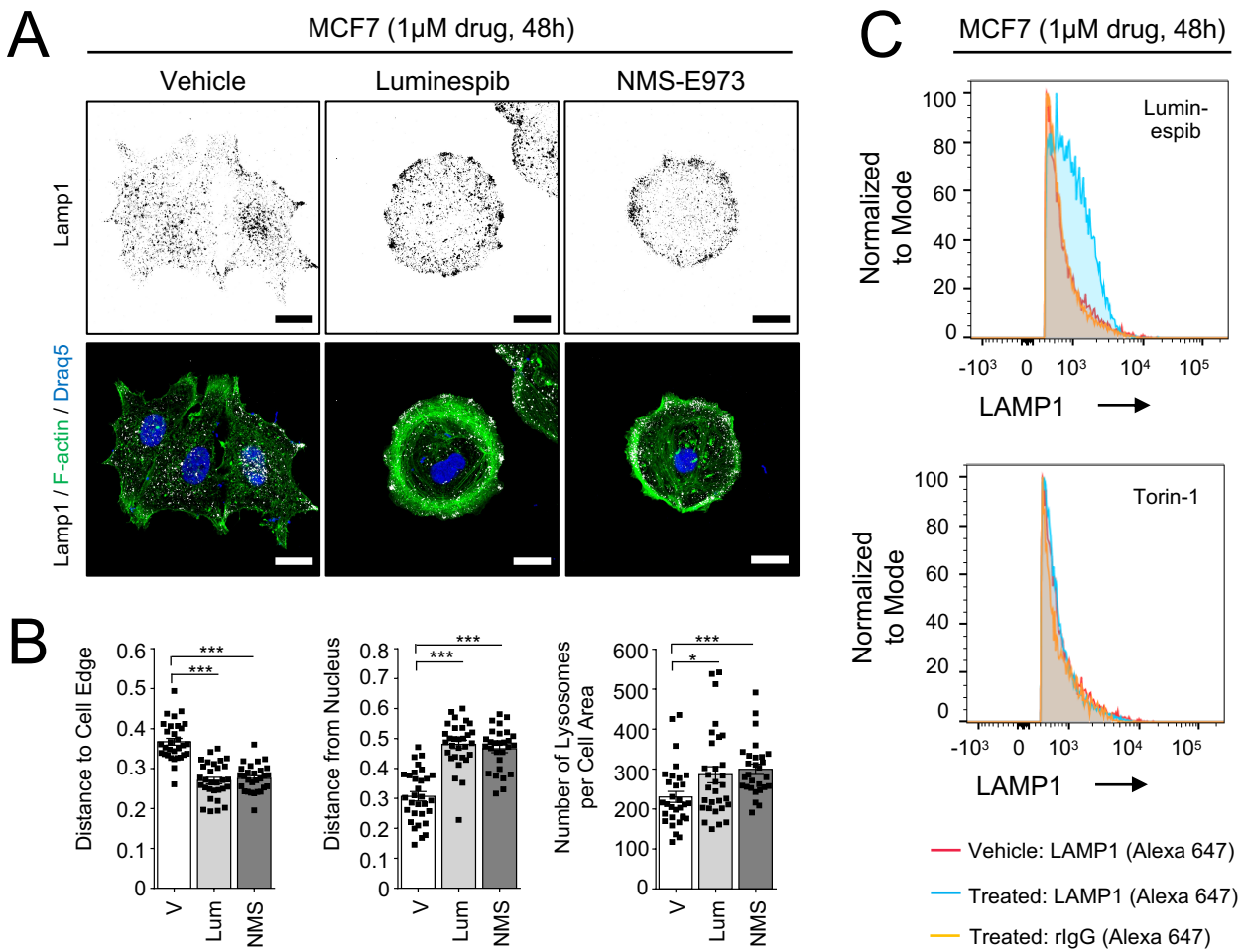
Biondini *et al.*, Figure S3



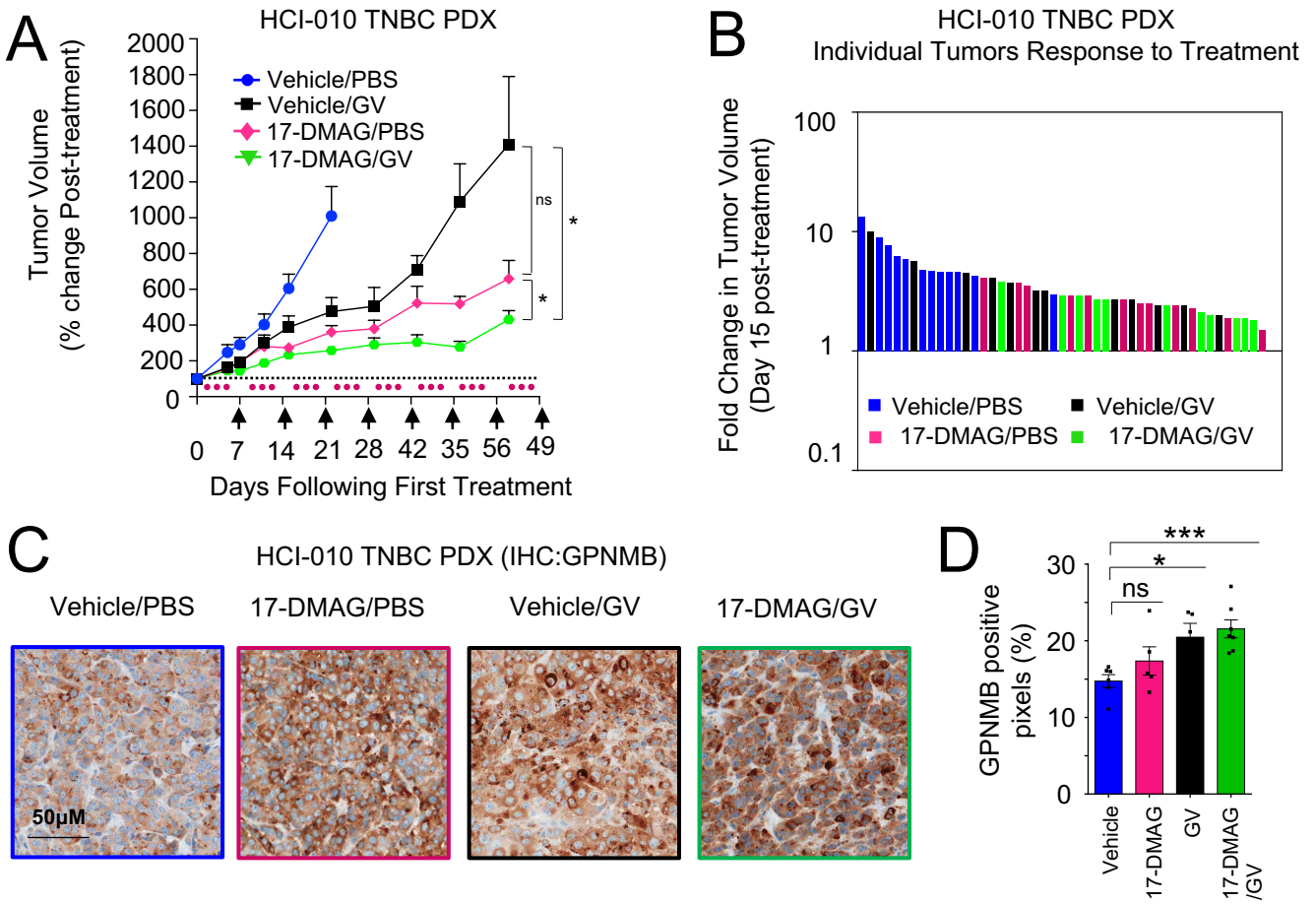
Biondini *et al.*, Figure S4



Biondini *et al.*, Figure S5



Biondini *et al.*, Figure S6



Biondini *et al.*, Figure S7

SUPPLEMENTARY FIGURE LEGENDS

Figure S1. GPNMB expression is enhanced in therapy-resistant breast cancer cells. **A** Immunoblot analysis of GPNMB expression in MCF7 cells with acquired resistance to epirubicin (EpiR) or doxorubicin (DoxR) compared to drug-sensitive parental MCF7 cells. GAPDH served as a loading control. **B** Immunoblot analysis of GPNMB expression in MCF7 that have become resistant to epirubicin and doxorubicin. GAPDH served as a loading control. **C** GPNMB mRNA expression in a dataset (GSE21974) comprising gene expression data from 32 women with primary invasive breast cancer who underwent biopsy before and after 4 cycles of epirubicin/cyclophosphamide followed by 4 cycles of docetaxel 100 mg/m2. Among these 32 patients, we restricted our analysis to 7 patients who were confirmed to be affected by TNBC. **D** GPNMB mRNA expression in a dataset containing gene expression data from 13 TNBC patients who underwent biopsy before and after receiving a taxane-based chemotherapy regimen (Q-CROC-03 project, NCT01276899). Colors were used for matching samples with the IHC images shown in E. **E** GPNMB expression as assessed by immunohistochemistry (IHC) from the biopsy material described in D. **F and G** Immunoblot analysis of GPNMB expression in T47D (F) and MCF7 (G) cells that have become resistant to tamoxifen. b-actin served as a loading control. **H** GPNMB mRNA levels in a dataset (GSE71791) containing gene expression profiles from sequential biopsies of the same ER+ breast tumors before (n=29) and after (n=29) two weeks of treatment with fulvestrant. Error bars indicate the SEM. ***P < 0.001, by unpaired Student's t test. **I** GPNMB mRNA levels in a dataset (GSE20181) consisting of gene expression profiles from sequential biopsies of the same ER+ breast tumors before (n=54) and after 2 weeks (n=54) or 3 months (n=54) of treatment with letrozole (2.5 mg/day, oral). Error bars indicate the SEM. *P < 0.05, by unpaired Student's t test. **J** Immunoblot analysis of GPNMB expression in MCF7, T47D (ER+) and SkBr3, BT474 (HER2+) cells treated with increasing doses of trametinib. Phosphorylation of ERK1/2 (T202/204) was assessed as a measure of MEK inhibition. Total ERK1/2 served as a loading control. **K** GPNMB mRNA levels in a dataset (GSE87418) containing gene expression data obtained from 6 TNBC patients who underwent sequential biopsies before and 24h after receiving trametinib for 7 days. Based on gene expression, tumors from patients 1 to 5 were classified as basal-like while the tumor in patient 6 was classified as claudin-low (NCT01467310).

Figure S2. Cellular stress induces GPNMB expression in breast cancer cells. **A** Immunoblot analysis of GPNMB expression in MDA-MB-436 and Hs578T cells exposed to serum deprivation, 1μM torin-1, 50μM hydroxychloroquine or amino acid deprivation (EBSS) for 16h. Phosphorylation of S6 (S240/S244) was assessed to confirm mTOR inhibition. S6 served as a loading control. **B** RT-qPCR analysis of GPNMB mRNA levels in cells treated as in (A). Graph depicts the mean ± SEM of the RNA fold change for GPNMB mRNA normalized to b2M mRNA from three or more independent experiments. **P ≤ 0.01, ***P ≤ 0.0001, by unpaired Student's t test. **C** Immunoblot analysis of GPNMB expression in MCF7 and T47D cells treated as described in A. Phosphorylation of S6 on S240/S244 was assessed to confirm mTOR inhibition. S6 served as a loading control. **D** RT-qPCR analysis of GPNMB mRNA levels in cells treated as in A. Graph depicts the mean ± SEM of the RNA fold change for GPNMB mRNA normalized to b2M mRNA from three or more independent experiments. *P ≤ 0.05 and **P ≤ 0.01, ***P ≤ 0.0001, by unpaired Student's t test. **E** MDA-MB-436 and T47D cells were infected with either empty adenovirus or adenovirus expressing constitutively nuclear TFEB-S211A or TFE3-S321A mutants. 48 h post-infection, total proteins extracted by cell lysis. Immunoblot analysis shows GPNMB, TFE3-Myc and TFEB-Flag expression. ß-actin served as a loading control. **F** Analysis of GPNMB mRNA levels in MDA-MB-436 cells transiently depleted of MITF, TFEB or TFE3. Graph depicts the mean ± SEM of the RNA fold change for GPNMB, MITF, TFEB and TFE3 mRNA normalized to b2M mRNA from three independent experiments. *P ≤ 0.05 and **P ≤ 0.01, ***P ≤ 0.0001, by unpaired Student's t test.

Figure S3. TFE3 is required for elevated GPNMB expression in response to torin-1 treatment. **A** Immunoblot analysis of GPNMB protein levels in MDA-MB-436 and T47D cells transiently depleted of MITF, TFEB or TFE3 and treated for 48h with 1μM torin-1. Immunoblots for TFEB or TFE3 confirmed the efficacy of the transient knockdowns for each transcription factor. The efficacy of torin-1 was assessed by immunoblotting for pS6 and S6. α-Tubulin served as a loading control. **B** RT-qPCR analysis of GPNMB mRNA levels in MDA-MB-436 and T47D cells treated as in A. MITF, TFEB and TFE3 mRNA levels were assessed to confirm the efficacy of transient knockdown of each family member. *P ≤ 0.05 and **P ≤ 0.01, by unpaired Student's t test. **C** Representative images of TFE3 localization in MDA-MB-436 cells treated for the indicated time

points with 1μM torin-1. The percentage of cells with TFE3 nucellar localization is indicated in each image. Scale bar: 10 μm, applies to all images. **D** Quantification of the experiment in C. Cells positive for nuclear TFE3 were divided into the percentage of cells with high, weak or negative staining, based on their mean nuclear fluorescence intensity. Error bars indicate the SEM. **E** RT-qPCR analysis of GPNMB mRNA levels in MDA-MB-436 treated with torin-1 over the indicated time points. Data represent the mean values derived from three independent experiments. Error bars indicate the SEM. *P ≤ 0.05, by unpaired Student's t test. **F** Representative images of TFE3 localization in T47D cells treated for the indicated time points with 1μM torin-1. The percentage of cells with TFE3 nucellar localization is indicated in each image. Scale bar: 10 μm, applies to all images. **G** Quantification of the experiment in F. Cells positive for nuclear TFE3 were divided into the percentage of cells with high, weak or negative staining, based on their mean nuclear fluorescence intensity. Error bars indicate the SEM. **H** RT-qPCR analysis of GPNMB mRNA levels in T47D cells treated with torin-1 over the indicated time points. Data represent the mean values derived from three independent experiments. Error bars indicate the SEM. *P ≤ 0.05 and **P ≤ 0.01, by unpaired Student's t test.

Figure S4. Loss of FLCN elevate GPNMB at cell surface and sensitize cancer cells to Glembatumumab Vedotin. **A** Immunoblot analysis of GPNMB and folliculin (FLCN) expression in parental and MCF7 $FLCN^{KO}$ breast cancer cells. α-Tubulin served as a loading control. **B** FACS-based analysis of cell-surface GPNMB localization in MCF7 $FLCN^{KO}$ cells. FACS plots reveal the shift in GPNMB cell surface localization following staining with the CR011 antibody, in MCF7 $FLCN^{KO}$ cells (in blue) relative to parental cells (in red). Yellow traces indicate cells treated with the indicated inhibitors and stained with hIgG antibody (isotype control). **C** FACS-based analysis of cell-surface GPNMB localization in MCF7 $FLCN^{KO}$ cells. Data represents the percentage of live cells positive for cell surface GPNMB localization in MCF7 FLCN KO relative to parental cells. Error bars indicate the SEM. ***P ≤ 0.001, by unpaired Student's t test. **D** Immunohistochemistry (IHC) analysis of GPNMB expression in samples from MCF7 $FLCN^{KO}$ and parental tumors xenografts. Samples were collected two weeks post mammary fat pad injection and at experimental endpoint (78 days for MCF7 tumors and 69 days for MCF7 $FLCN^{KO}$). ***P ≤ 0.0001, by unpaired Student's t test. **E** Growth curves of parental (left panel) or MCF7 $FLCN^{KO}$ (right panel) tumor xenografts following treatment with vehicle (blue line) or

5mg/Kg Glembatumumab Vedotin alone (red line). **F** Waterfall plot demonstrating responses of individual parental and MCF7 $FLCN^{KO}$ tumor xenografts to Glembatumumab Vedotin. Mice were treated as indicated in E. **G** Representative images of LAMP1 localization in parental and MCF7 $FLCN^{KO}$ cells. LAMP1 images are shown with an inverted lookup table to enhance visualization. Nucleus is in blue and F-actin in green. Scale bar: 20 μm. **H** FACS-based analysis of cell surface LAMP1 expression. FACS plots reveal a shift in LAMP1 cell surface localization in MCF7 $FLCN^{KO}$ cells (in blue) relative to parental cells (in red). Yellow traces indicate cells treated with the indicated inhibitors and stained with rIgG antibody (isotype control).

Figure S5. MiTF/TFE regulate GPNMB expression in response to HSP90 inhibition. **A** Immunoblot analysis of GPNMB in MDA-MB-436 cells transiently depleted of MITF, TFEB or TFE3 and stimulated for 48h with Luminespib (1 μM). TFEB and TFE3 levels were assessed by immunoblotting to confirm efficacy of each knockdown. α-Tubulin served as a loading control. **B** MDA-MB-436 cells were incubated for 48h with Luminespib (1 μM) and GPNMB mRNA levels were assessed by RT-qPCR. The efficiency of each MiTF/TFE family member knockdown was assessed by RT-qPCR analyses of MITF, TFEB and TFE3 levels. The graph depicts the mean ± SEM of the RNA fold change for the indicated mRNAs normalized to b2M mRNA from three or more independent experiments.

Figure S6. HSP90 inhibitors induce lysosomal scattering and fusion with the plasma membrane in MCF7 cells. **A** Representative images of LAMP1 localization in MCF7 cells treated with vehicle, luminespib or NMS-E973 for 48h. LAMP1 images are shown with an inverted lookup table to enhance visualization. Nucleus is in blue and F-actin in green. Scale bar: 20 μm. **B** Quantification of the images in A. Black squares indicate the average for each cell analyzed (n=31 for vehicle, n=30 for luminespib, n=28 for NMS-E973). Error bars indicate the SEM. *$P < 0.05$ and ***$P < 0.001$, by Mann-Whitney U test. **C** FACS-based analysis of cell surface LAMP1 localization in MCF7 cells incubated with vehicle, luminespib, NMS-E973 or torin-1 for 48h. FACS plots reveal the shift in LAMP1 cell surface expression in cells treated with the inhibitors (in blue) relative to vehicle treated cells (in red). Yellow traces indicate cells treated with the indicated inhibitors and stained with rIgG antibody (isotype control). **D** Immunoblot analysis of FLCN expression in MCF7 and MDA-MB-436 cells treated for 48h with HSP90 inhibitors or

torin. pS6/S6 and pAKT levels revealed the efficacy of mTOR inhibition with the indicated inhibitors. α-Tubulin served as a loading control.

Figure S7. A combination of HSP90 inhibition and Glembatumumab dramatically impairs the growth of TNBC cells in vivo. **A** Growth curves of HCI-010 tumors upon treatment with vehicle (blue line), 25mg/Kg 17- DMAG (fuchsia line), 5mg/Kg Glembatumumab Vedotin alone (black line) and 17-DMAG administered in combination with Glembatumumab Vedotin (green line). *P ≤ 0.01, by unpaired Student's t test. **B** Waterfall plot demonstrating responses of individual HCI-010 tumors to the indicated treatments. Mice were treated as indicated in A. **C** Immunohistochemistry (IHC) analysis of GPNMB expression in samples from HCI-010 TNBC PDX tumors treated with vehicle (blue), 25mg/Kg 17-DMAG (fuchsia), 5mg/Kg Glembatumumab Vedotin alone and 17-DMAG administered in combination with Glembatumumab Vedotin (green). **D** Quantification of GPNMB IHC expression in C. Error bars indicate the SEM. *P ≤ 0.05 and *** P ≤ 0.001, by unpaired Student's t test.

SUPPLEMENTARY METHODS

Cell lines

MDA-MB-436, Hs578T, MDA-MB-468 and MCF7 cells were cultivated at 37°C in a humidified incubator with 5% CO2 in DMEM (Cat. #: 319-005-CL, Wisent) containing 10% fetal bovine serum (Cat. #: 12483-020, GIBCO) and 100U/mL penicillin (Cat. #: 450-201-EL, Wisent). For Hs578T, the culture media was supplemented with 0.01 mg/ml human recombinant insulin (Cat. #: 511-016-CM, Wisent). T47D and BT474 cells were grown in RPMI 1640 (Cat. #: 350-000-CL, Wisent) supplemented with fetal bovine serum and antibiotics as indicated above. MCF7 and MCF7 FLCNKO were grown in DMEM supplemented with 10% fetal bovine serum and 100U/mL penicillin. MCF7 DoxR and EpiR cells were cultivated in DMEM containing 10% FBS in presence

of 98.1nM Doxorubicin or 852 nM Epirubicin, respectively. MDA-MB-436 DoxR cells culture conditions were described before (75).

Treatment

Hydroxychloroquine sulfate (Selleckchem, Cat. #: S4430); Doxorubicin Hydrochloride Salt (Selleckchem, Cat. #: S1208); Cisplatin (Selleckchem, Cat. #: S1166); Paclitaxel (Selleckchem, Cat. #: S1150); Fulvestrant (Selleckchem, Cat. #: S1191); Tamoxifen (Selleckchem, Cat. #: S1238); Trametinib (LC lab, Cat. #: T8123); Cobimetinib (UHN Shanghai, Cat. #: GDC-0973); Torin-1 (Selleckchem, Cat. #: S2827); Everolimus (LC lab, Cat. #: E-4040); AZD2014 (Selleckchem, Cat. #: S2783); INK-128 (Selleckchem, Cat. #: S2811); Rapamycin Hydrochloride Salt (LC lab, Cat. #: R-5000); Luminespib (MedChemExpress; Cat. #: HY-10215); Onalespib (Selleckchem Cat. #: S1163); NMS-E973 (Cayman Chem, Cat. #: 22352); 17-DMAG (Cayman Chem, Cat. #: 11036); ML345 (Sigma, Cat. #: SML1117); Acetazolamide (Selleckchem, Cat. #: S4506); Cyclosporin (Selleckchem, Cat. #: S2286); Penitrem A (Tocris, Cat. #: 4617), EBSS (HyClone, Cat. #: SH30029.02); Glembatumumab Vedotin was a gift from Dr. Tibor Keler (Celldex Therapeutics). All drugs were resuspended according to manufacturer's instructions and vehicle treatments were performed using the dissolving agents employed to resuspend each compound. PBS was employed as a vehicle treatment for Glembatumumab Vedotin.

siRNA and DNA transfections

siRNAs used in this study are non-targeting pool siRNA (Horizon Discovery, Cat. #: D-001810-10-05); human MITF (4268) pool siRNA (Horizon Discovery, Cat. #: L-008674-00-0005); human

TFEB (7942) pool siRNA (Horizon Discovery, Cat. #: L-009798-00-0005); human TFE3 (7030) pool siRNA (Horizon Discovery, Cat. #: L-00933-00-0005).

Immunoblotting

Primary antibodies used in this study: anti-GPNMB (1:1,000 dilution) (Cell Signaling, Cat. #: 38313); Anti-MITF Ab-1 (C5) (1:1,000 dilution) (Thermos Scientific, Cat. #: MS-771-P0); anti-TFE3 (1:1,000 dilution) (Cell Signaling, Cat. #: 14779); anti- TFEB (1:1,000 dilution) (Bethyl, Cat. #: A303-673A); anti-ERα (D8H8) (1:1,000 dilution) (Cell Signaling, Cat. #: 8644); anti-S6 ribosomal protein (Ser240/244) (1:1,000 dilution) (Cell Signaling, Cat. #: 2215); anti-S6 ribosomal protein (54D2) (1:1,000 dilution) (Cell Signaling, Cat. #: 2317); Anti-phospho-AKT (Ser473) (1:1,000 dilution) (Cell Signaling, Cat. #: 4060); anti-AKT (40D4) (1:1,000 dilution) (Cell Signaling, Cat. #: 2920); anti-phospho-Erk1/2 (Thr202/Tyr204) (1:1,000 dilution) (Cell Signaling, Cat. #: 9101); anti-phospho Erk1/2 (L34F12) (1:1,000 dilution) (Cell Signaling, Cat. #: 4696); anti-phospho-4E-BP1 (Thr37/Tyr46) (1:1,000 dilution) (Cell Signaling, Cat. #: 2855); anti-4E-BP1 (53H11) (1:1,000 dilution) (Cell Signaling, Cat. #: 9644); anti-GAPDH (1:5,000 dilution) (Millipore, Cat. #: MAB374); anti- α-Adaptin (1:5,000 dilution) (BD, Cat. #: 610502); anti- α-Tubulin (B-5-1-2) (1:5,000 dilution) (Sigma Aldrich, Cat. #: T5168); Peroxidase-AffiniPure Donkey Anti-Mouse (Jackson Labs Cat. #: 715-035-150); Peroxidase-AffiniPure Donkey Anti-Rabbit (Jackson Labs, Cat. #: 711-035-152); IRDye 800CW Donkey anti-Rabbit IgG antibody (LI-COR Biosciences, Cat. #: 926-32213); IRDye 680RD Donkey anti-Mouse IgG antibody (LI-COR Biosciences, Cat. #: 926-68072).

Immunofluorescence

Antibodies used for immunofluorescence in this study are: anti-TFE3 (1:1,000 dilution) (Cell Signaling, Cat. #: 14779); anti- TFEB (1:1,000 dilution) (Bethyl, Cat. #: A303-673A); anti-LAMP-1 (1:1,000 dilution) (D2D11) (Cell Signaling, Cat. #: 9091S); anti-Mouse Alexa Fluor 555 (Thermo Fisher, Cat. #: A-21422); anti-Rabbit Alexa Fluor 555 (Thermo Fisher, Cat. #: A-21430). Percentage of cells with nuclear MITF, TFEB and TFE3 and staining intensity was quantified with a home-made plug-in in Image J (https://imagej.nih.gov/ij/download.html).

Real-Time PCR

Primers used in this study are: Human *B2M* 5'-TATCCAGCGTACTCCAAAGA-3'and 3'-ACAAGTCTGAATGCTCCAC-5'; human *GPNMB* 5'-CTTCTGCTTACATGAGGGAGC-3' and 3'-GGCTGGTGAGTCACTGGTC-5'; human *MITF* 5'-CCAACAGCCCTATGGCTATGC-3'and 3'-CTGGGCACTCACTCTCTGC-5'; human *TFEB* 5'-ACCTGTCCGAGACCTATGGG-3' and 3'-CGTCCAGACGCATAATGTTTGTC-5'; human TFE3 5'-CCGTGTTCGTGCTGTTGGA-3'and 3'-CTCGTAGAAGCTGTCAGGAT-5'.

Flow cytometry

For surface staining of GPNMB, breast cancer cells were seeded in 6-well plates and left adhere overnight. Cells were treated for 48h with the indicated drugs and processed for flow cytometry. Briefly, cells were detached using cell dissociation buffer, enzyme-free, PBS and surface staining of GPNMB was performed in FACS buffer (2% FBS in PBS) for 30 min on ice. GPNMB cell surface staining was performed using anti-human GPNMC CR011 antibody (1: 500, gift from Celldex Therapeutics). Dead cells were identified by staining with LIVE/DEAD Fixable Aqua Dead Cell Stain Kit (Thermo Fisher, Cat. #: L34957) according to manufacturer's instruction. Data were acquired on Canto II cytometer (BD Biosciences) and analyses were performed using

FlowJo software (Tree Star). We excluded debris, doublets and dead cells from all analysis. Analyses were performed using FlowJo 10 (Tree Star, https://flowjo.com).

Immunofluorescence for lysosome positioning

Cells were seeded onto 18 mm glass coverslips coated with 5 μg cm^{-2} human fibronectin (Cat. #: F-0895, Sigma-Aldrich) diluted in 1X PBS. Cells were treated with specific drugs for the indicated times before fixation and stained with the immunofluorescence protocol described above. Cells were stained using an antibody against LAMP-1 (Cat. #: 9091, Cell Signaling) and Alexa Fluor 488 phalloidin (Cat. #: P5282, Sigma-Aldrich, 1:2000) to visualize F-actin. Cells were imaged on a Zeiss LSM 710 confocal microscope with a Plan-Apochromat 63x/1.4 NA oil immersion DIC objective lens. The following imaging parameters were common to all channels: 1 Airy unit, 1 digital gain, 1.58 μs pixel dwell time and 4-line averaging. An Ar ion laser tuned to 488 nm (1% power; 488 nm beam splitter; 493-572 nm detection) and master gain of 700 were used to capture F-actin. A 561 nm DPSS laser (2.5% power; 458/561 nm beam splitter; 561-659 nm detection) and master gain of 520 were used to capture LAMP1. A 633nm HeNe Red laser (5% power; 488/561/633 nm beam splitter; 638-755 nm detection) and master gain of 900 were used to capture Draq5.

Images were saved as 12-bit with 1024x1024 pixels resulting in an x,y pixel resolution of 0.132 μm. Cells were analyzed in Imaris (version 9.2.0; Bitplane AG, Zurich, Switzerland). The Spots tool was used to identify lysosomes stained by LAMP1. Estimated XY diameter was set to 0.5 μm with background subtraction enabled. A quality filter was applied to select all positive signals. A contour was then manually drawn around the cell based on F-actin staining. The number of lysosomes identified by LAMP1 staining was divided by the total surface area in contact with

241 the coverglass to obtain a normalized value. A distance transformation function was then used to
242 determine lysosome distance from the cell (contour) edges. The average distance of lysosomes
243 within each cell was divided by the maximum distance from the cell edge to obtain a normalized
244 value. Finally, a contour was manually drawn around the nucleus based on Draq5 staining to
245 determine lysosome distance from the nucleus. Values were normalized by dividing the average
246 distance of lysosomes within each cell by the furthest possible distance away from the nucleus.
247
248 **Lysosomal and GPNMB live dynamics**
249 MDA-MB-436 were seeded onto μ-dish 35-mm high glass bottom dishes (Cat. #: 81158, Ibidi)
250 coated with fibronectin. Cells were then treated with the indicated drugs and stained with 200 nM
251 LysoTracker Green DND-26 (Cat. #: L7526, Thermo Fisher Scientific) prior to live-cell imaging.
252 Although LysoTracker may label other organelles with low intracellular pH, it primarily localizes
253 to lysosomes and late endosomes. Images were acquired on a Leica DMI6000B inverted
254 microscope equipped with a Quorum WaveFx-X1 spinning disk confocal system (Quorum
255 Technologies, Guelph, ON), HCX PL APO 63x/1.40 NA oil immersion DIC objective lens and
256 two Prime BSI sCMOS cameras (Photometrics, Tuscon, AZ). A CU-501 stage-top incubator
257 system (Live Cell Instrument, Seoul, South Korea) was used to maintain cells in a 37°C
258 environment with 5% CO_2. For single-color imaging of LysoTracker, a 491 nm diode laser was
259 used to continuously illuminate cells for ~32.6 s. Emission signal was captured by a single camera
260 with exposure time set to 200 ms using stream acquisition. For two-color imaging of LysoTracker
261 and RFP-GPNMB, cells were seeded on fibronectin-coated dishes and allowed to adhere for 24h.
262 Cells were transfected with RFP-GPNMB using Lipofectamine 3000. Three hours post-
263 transfection culture media was changed, and cells were incubated overnight before drugs were

added. After 48h cells were imaged. Each cell was continuously illuminated with 491 and 561 nm diode lasers for ~32.6 s to capture LysoTracker Green and RFP-GPNMB, respectively. A dichroic mirror set to reflect light below, and pass light above, 565 nm, combined with a 565 nm long pass filter (Chroma Technologies, Bellows Falls, VT) was used to send the emission signals to the two separate cameras, thereby capturing both signals simultaneously. Stream acquisition was used with camera exposure times set to 200 ms. Spatially binning (2x2) was used to enhance the signal-to-noise ratio, resulting in an x,y pixel resolution of 0.1172 μm.

Cells were analyzed in Imaris as described for LAMP1 immunofluorescence. LysoTracker and GPNMB images were analyzed separately to generate independent spots. The quality filter was manually refined within a narrow range (4.5 – 8) to ensure all positive signals were identified. Object-based co-localization was then used to determine the percentage of LysoTracker spots that overlapped with GPNMB and vice-versa. The center-to-center distance threshold for co-localized objects was set to 0.4 μm to allow for slight misalignment between the two cameras. Pseudo-colored images of lysosome (LysoTracker) position relative to the cell edge were generated in MATLAB (version 9.8.0, Rel. R2020a) using X,Y and distance data obtained from Imaris. The Spots tool was also used to track LysoTracker spots over time. X,Y position data was exported into MATLAB to determine the total distance travelled by each lysosome within ~6.5 s. The speed of each lysosome within a cell was then averaged.

Immunology Letters 239 (2021) 32–41

Contents lists available at ScienceDirect

Immunology Letters

journal homepage: www.elsevier.com/locate/immlet

TLR ligand loaded exosome mediated immunotherapy of established mammary Tumor in mice

Muzaffer Yildirim [a,1], Tugce Canavar Yildirim [a,1], Nilsu Turay [a], Tugce Bildik [a], Bilgehan Ibibik [a], Irem Evcili [a], Pelin Gulizar Ersan [a,b], Unal M. Tokat [a,b], Ozgur Sahin [b], Ihsan Gursel [a,*]

[a] Thorlab, Department of Molecular Biology and Genetics, Bilkent University, Bilkent, 06800, Ankara, Turkey
[b] Drug Discovery & Biomedical Sciences (DDBS), College of Pharmacy, University of South Carolina, Columbia, SC 29208,Columbia

ARTICLE INFO

Keywords:
Cancer vaccine
TLR
Immune response
Breast tumor
Immunotherapy

ABSTRACT

Tumor-derived exosomes (TEXs) could be harnessed as an immunotherapeutic cancer vaccine. These nanovesicles are inherently possesses rich tumor antigen reservoirs. Due to their undesirable features such as poor or limited immunogenicity as well as facilitation of cancer development via mediating communication between tumor cells TEXs could be transformed into an effective immune adjuvant delivery system that initiates a strong humoral and cell-mediated tumor-specific immune response. Engineering TEXs to harbor immunostimulatory molecules still remains a challenge. Previously, we demonstrated that nucleic acid ligand encapsulated liposomes could trigger synergistic strong humoral, and cell mediated immune responses and provokes tumor regression to that of their standalone counterparts. In this study, we evaluated to immunogenicity of 4T1/Her2 cell-derived exosomes upon loading them with two potent immuno adjuvant, a TLR9 ligand, K-type CpG ODN and a TLR3 ligand, p(I:C). Engineered TEXs co-encapsulating both ligands displayed boosted immunostimulatory properties by activating antigen-specific primary and memory T cell responses. Furthermore, our exosome-based vaccine candidate elicited robust Th1-biased immunity as evidenced by elevated secretion of IgG2a and IFNγ. In a therapeutic cancer model, administration of4T1 tumor derived exosomes loaded with CpG ODN and p(I:C) to animals regress tumor growth in 4T1 tumor-bearing mice. Taken together this work implicated that an exosome-based therapeutic vaccine promoted strong cellular and humoral anti-tumor immunity that is sufficient to reverse established tumors. This approach offers a personalized tumor therapy strategy that could be implemented in the clinic.

1. Introduction

Immunotherapy has become a powerful clinical strategy to boost the activation of host immune system against tumors that evade immune surveillance and induce tolerance. These cancer therapies enhance antitumor immune responses with fewer off-target effects than traditional treatments, such as chemotherapy and radiation that lack tumor selectivity and have severe side effects [1]. Tumor antigen-based cancer immunotherapy has gained significant attention to elicit antigen-specific strong T and B cell responses, however, the purification of particular tumor antigens is challenging [2,3]. Therefore, identification of tumor-specific nanostructures that naturally harbors endogenous tumor antigens and further engineering these structures to co-deliver immune stimulating adjuvants yielding potent anti-tumor immunity is of great benefit during the management of established tumors. A depot system that permits simultaneous presentation of tumor antigen as well as initiating tumor-specific immune activation could offer effective tumor targeting while reducing undesirable toxicity could pave the way for patient specific anti-cancer immunotherapy [4,5].

Exosomes with a size between 30 and 150 nm are small extracellular vesicles secreted (any small sized EVs irrespective of their biogenesis) by all type of mammalian cells [6]. Hereafter, the term “exosomes” refers to small EVs in this work. They mediate a novel mode of intercellular communication through their bioactive cargos such as lipids, nucleic acids, metabolites, and proteins, which can be delivered to the target cells [7]. Using their natural delivery capabilities, exosomes have been successfully served as immunotherapeutic nanocarriers in cancer treatment [8]. Furthermore, they are attractive as a delivery system because

* Corresponding author.
E-mail address: ihsangursel@bilkent.edu.tr (I. Gursel).
[1] Equal Contribution

https://doi.org/10.1016/j.imlet.2021.08.004
Received 14 March 2021; Received in revised form 26 July 2021; Accepted 12 August 2021
Available online 18 August 2021
0165-2478/© 2021 European Federation of Immunological Societies. Published by Elsevier B.V. All rights reserved.

of their stability in circulation, biocompatibility, and low toxicity [9,10, 11].

Tumor derived exosomes (TEXs) are appropriate tumor specific antigen sources to induce immunity against tumor cells since they are capable of even presenting endogenous tumor-specific neoantigens [12]. They can transfer a wide spectrum of immunogenic tumor antigens expressed in parental tumor cells to DCs and elicit tumor-specific cytotoxic T lymphocytes [13, 14]. As well as their modification by different methods to enrich tumor antigens, immunostimulatory molecules and microRNAs, TEXs can be loaded with therapeutic cargo [15,16]. These engineered TEXs can increase their uptake by antigen presenting cells, upregulate the expression of cancer-specific antigenic epitopes, repress immunosuppressive targets in the tumor microenvironment, improve DC maturation and enhance tumor cell elimination [17,18,19]. Moreover, Moreover, the feasibility to isolate TEXs from patients' sera enables their use in personalized immunotherapy [20]. Taken together, TEXs as a modified carrier for immunostimulatory agents along with tumor antigens can be a novel candidate for tumor vaccine.

Among immunostimulatory agents, nucleic acid-based adjuvants are safe and effective inducer of innate immune effector functions [21,22]. CpG oligonucleotides (CpG ODNs) recognized by Toll-like receptor 9 (TLR9) is one of the most extensively used adjuvants in the clinic to stimulate immune response characterized by the production of Th1 and pro-inflammatory cytokines [23,24] K type CpG ODN activates B cells and trigger plasmacytoid dendritic cells (pDCs) to secrete tumor necrosis factor–α (TNF-α) [25]. Polyinosinic-polycytidylic acid (p(I:C)), a TLR3 agonist, is another potent adjuvant that has been widely studied as an anti-tumor drug in cancer patients [26]. p(I:C) is shown to induce type I and II interferons (IFN) and the activation of CD4+ and CD8+ *T* cell responses overcoming immunosuppressive function of regulatory T cells in the tumor microenvironment [27, 28, 29, 30].

The simultaneous delivery of tumor cell-derived exosomes and adjuvants to the same immune cells could effectively induce a potent anti-tumor immune response. Herein, we co-encapsulated CpG ODN and p(I:C) into 4T1/Her2 cell-derived exosomes. These 4T1 breast cancer cells were modified to overexpress Her2 tumor antigen that are present within TEXs. Our results revealed that dual adjuvant encapsulating exosome vaccine induced a strong Th1-biased Her2-specific immune response and increased the production of type II IFNs. We also demonstrated that dual adjuvant co-encapsulating exosome vaccine generated Her2-specific CD4+ memory T cell. Moreover, when used as a therapeutic vaccine, CpG ODN and p(I:C) loaded exosomes significantly regressed 4T1 tumor growth in mice. Taken together, we present an exosome-based therapeutic vaccine candidate that could promote strong cellular and humoral anti-tumor immune responses that offers an effective personalized tumor therapy strategy in the clinic.

2. Materials and methods

2.1. Materials

TLR9 ligand, CpG-ODN GACGTTGACGTTGACGTTGG was purchased from Alpha DNA (Canada). TLR3 ligand, p(I:C) was from Amersham (Piscataway, NJ, USA). Her2/E75 peptide was purchased from Immunostep (Spain). All cell culture media components were from Gibco (NY, USA) and Lonza (Walkersville, MD, USA). Cytokine ELISA reagents: recombinant cytokine, monoclonal unlabeled and biotinylated antibody against m-IFNγ were purchased from Mabtech (Cincinnati, OH, USA). P-nitrophenyl phosphate disodium salt substrate (PNPP) was purchased from Thermo Scientific (USA).

Immunoglobulin ELISA reagents: goat anti-mouse total IgG, IgG1, IgG2a monoclonal antibodies conjugated with alkaline phosphatase (AP) were from Southern Biotech (Birmingham, AL, USA). FACS antibodies conjugated to fluorescent chromophores were obtained from Biolegend. Rabbit monoclonal antibody against TSG101 and rabbit monoclonal antibody against Her2/ErbB2 were from Abcam (Cambridge, UK) and Cell Signaling (Massachusetts, USA) respectively. Cytofix/Cytoperm and Perm/wash buffer were purchased from BD (New Jersey, USA).

2.2. Mice and cell lines

Adult Balb/c mice (female, 6–8 weeks old) were kept in the Bilkent University animal housing facility of the Department of Molecular Biology and Genetics. Mice were housed under controlled conditions at 22 °C with 12 h light and 12 h dark cycles and provided with unlimited access of food and water. All experimental procedures were approved by the animal ethical committee of Bilkent University.

4T1-luc and 4T1/Her2 cell lines were cultured in Dulbecco's Modified Eagle Medium, (DMEM) with 10% fetal bovine serum (FBS). GFP tagged HER2 expressing mouse breast cancer cell line (4T1-HER2) was kindly provided by Prof. Michael Kershaw (Cancer Immunology Program, Peter MacCallum Cancer Center, Victoria, Australia) [41,42]. 4T1-luc cell line is originally developed by G Gary Sahagian [43].

2.3. Isolation of tumor derived exosomes from cell culture supernatant

Exosomes were isolated from 4T1/Her2 and 4T1-luc cell lines via differential ultracentrifugation method. Following supernatant collection from cultured cells, they were centrifuged at 1500 x g for 10 min at RT to discard the cell debris. Supernatants were transferred to ultracentrifugation tubes (Beckmann Coulter) and centrifuged at 10,000 x g for 10 min at +4 °C to remove any large particles, followed by a second centrifugation at 30,000 x g for 30 min. This generated a pellet consisting of medium sized EVs and an upper aqueous phase containing the exosomes. The supernatant was collected and passed through a 0.2 μm filter to ensure removal of larger particles. To sediment exosomes, filtered supernatant was centrifuged at 100,000 x g for 90 min at +4 °C. The pellet was washed once with PBS at 100,000 x g for another 90 min at +4 °C. Following washing, supernatants were aspirated, and the exosome pellet was resuspended in an appropriate volume of Ca^{2+}/Mg^{2+} free 1x PBS and used in further studies.

2.4. Exosome characterization

Forty μL of carboxyl modified latex beads (Life Technologies) were incubated with 40 μg of LEAF purified anti-mouse CD81 antibody (Biolegend) at RT for 30 min. Then, the volume was adjusted to 500 μL with 1x PBS and bead-antibody mix was incubated overnight at RT by continuous rotation. Following incubation, beads were blocked with 5% BSA containing 1x PBS for 4 h at RT by rotation. To analyze the specific molecules on exosomes, two μg of exosomes were mixed with anti-mouse CD81 conjugated beads and incubated at RT overnight. Following washing by centrifugation at 13,200 x g, bead-associated exosomes were incubated separately with 2 μg/mL anti-CD9-FITC, anti-CD81-PE antibodies in sodium azide containing FACS buffer or with their corresponding isotype controls for 30 min at RT. The exosome-bead complexes were washed and analyzed with Novocyte D3000 (Agilent, California, USA).

Total cellular and exosomal proteins were extracted using a RIPA lysis buffer and samples were vortexed and sonicated, respectively. Protein concentration was determined by BCA Protein Assay Reagent Kit (Thermo Scientific). Twenty five μg of cell lysate, medium sized EVs lysate or exosome lysate were separated on 10% SDS-polyacrylamide gel for 90 min at 120 V following 10 min run on 5% SDS-polyacrylamide resolving gel and then were transferred to PVDF membranes (Thermo Scientific) by applying 100 V for 90 min. Membranes were blocked with 5% non-fat dry milk containing 1x PBS-T for 2 h at RT. Then, blocked membranes were incubated with primary antibodies against TSG101 (Abcam) or Her2 (Cell Signaling) prepared in 5% non-fat dry milk containing 1x PBS-T at a 1:1000 dilution at +4 °C overnight. Following primary antibody incubation, membranes were washed and incubated

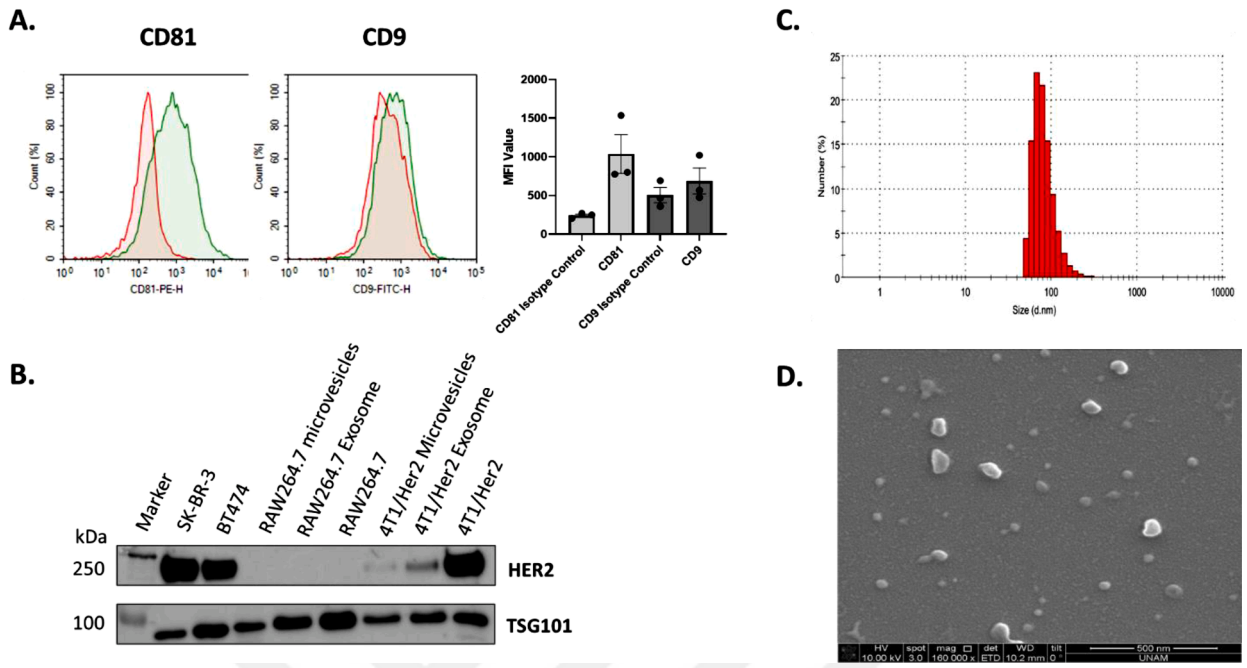


Fig. 1. Characterization of exosomes isolated from 4T1/Her2 cell line. A) Exosomes coupled to anti-CD81 conjugated beads were phenotyped using flow cytometry analysis. Bar graphs represent the average MFI values of specific antibodies to isotype control staining of 3 separate exosome batches. **B)** Western blot analysis of exosomal marker TSG101, and Her2 expression in total cell extracts and cell-derived exosomes. (SK-BR-3 and BT474 cell lines were used as positive controls and RAW264.7 cell line was used as a negative control) **C)** Dynamic Light Scattering (DLS) analysis showing average size distribution of 4T1/Her2 cell-derived exosomes (n = 3 independent batches) **D)** A representative scanning electron microscopy (SEM) image of 4T1/Her2 cell-derived exosomes. Scale bar represents 500 nm.

with 1:5000 diluted secondary antibodies, HRP conjugated horse anti-mouse IgG (Cell Signaling) for Tsg101 and Her2 in 5% non-fat dry milk supplemented 1x PBS-T at RT for 1 h Membranes were developed using the chemiluminescent detection kit, ECL+ from Amersham according to the manufacturer's protocols and visualized by Amersham Chemiluminescence Imager 600 (GE, Amersham).

To analyze the size of exosomes by dynamic light scattering (DLS) using Zetasizer Nano ZS (Malvern, UK), exosomes were diluted in PBS and triplicate readings of samples were recorded.

Purified exosomes were verified by scanning electron microscopy (SEM). Ten μL of the exosome solution were deposited on silica surfaces. After evaporation, samples were sputter-coated with 8 nm of Au/Pd alloy using a precision coating system (Gatan Inc, USA).

2.5. Loading of exosomes with CpG ODN and p(I:C)

Thirty μg of exosome were mixed with 30 μg CpG ODN and 30 μg pI:C. The mixture was snap-frozen in liquid nitrogen and lyophilized overnight in VirTis Bench Top K Freeze Dryer (SP Industries, PA, USA). The exosome-ligand powder mixture was rehydrated in a controlled fashion by addition of nuclease free ddH_2O. Then, this rehydrated mixture was vortexed for 15 s every 2 min for a period of 20 min. Next, 1 x Ca2 + /Mg2 + free PBS was added, and the mixture was incubated at RT for another 10 min. Then, the mixture was vortexed for 15 s and the controlled rehydration process was completed with the addition of 1x Ca2+/Mg2+ free PBS to adjust the desired concentration of ligand encapsulated exosome solution. As such prepared exosome formulations were maintained at +4 °C until further use.

The encapsulation efficiency was performed from three independent batches of each exosome preparations. To detect CpG ODN loading, 30 μg Cy5-labeled CpG ODN and 30 μg unlabeled pI:C were mixed with 30 μg of exosome. Following reconstitution as described above, the Cy5-signal was followed both from the exosome pellet and from the unencapsulated fraction of supernatant using fluorometer. Next, 30 μg unlabeled CpG ODN and 30 μg FITC-labelled pI:C were mixed with 30 μg of exosome, and same procedure was performed to identify the pIC loading. For each ligand the encapsulation efficiencies were found to be 88.8 ± 9.2% for the CpG ODN and 94.1 ± 7.3% for pIC.

2.6. Immunization of balb/c mice and splenocyte isolation

6–8 weeks-old female Balb/c mice (4 per group) were vaccinated 2 times in 2-week intervals intraperitoneally (I.P) with PBS, only 30 μg exosome, free form of 30 μg exosome+30 μg CpG ODN and 30 μg p(I:C) or exosome loaded with CpG ODN+p(I:C). Two weeks after the last booster dose, all mice were sacrificed and their splenocytes and blood serum were collected aseptically for the detection of cellular immune responses.

2.7. In vitro stimulation

Splenocytes (2×10^6 cell/mL in 250 μl) were stimulated with 10 μg/mL 4T1/Her2 cell-derived exosome for 72 h at 37 °C in a 5% CO_2 incubator. After stimulation, the supernatants were collected and used for IFNγ cytokine ELISA.

2.8. Enzyme-linked immunosorbent (ELISA) assay

Immulon 2 HB microtiter plates (Thermo Scientific, San Jose, CA, USA) were coated with Her2 E75 peptide (40 μg/mL), 4T1/Her2 cell lysate (10 μg/mL), 4T1/Her2 exosome lysate (10 μg/mL) and anti-mouse IFNγ (2 μg/mL) respectively, and then blocked with PBS-BSA. Serially diluted standards and culture supernatants or serially diluted mouse sera were added to plates for overnight at 4 °C. Cytokine was detected using biotinylated anti-mouse IFNγ (1 μg/mL) antibody followed by phosphatase-streptavidin whereas bound IgG subclasses were detected using alkaline phosphatase streptavidin conjugated anti-mouse IgG (1:1000), anti- mouse IgG1 (1:1000) and anti-mouse IgG2a

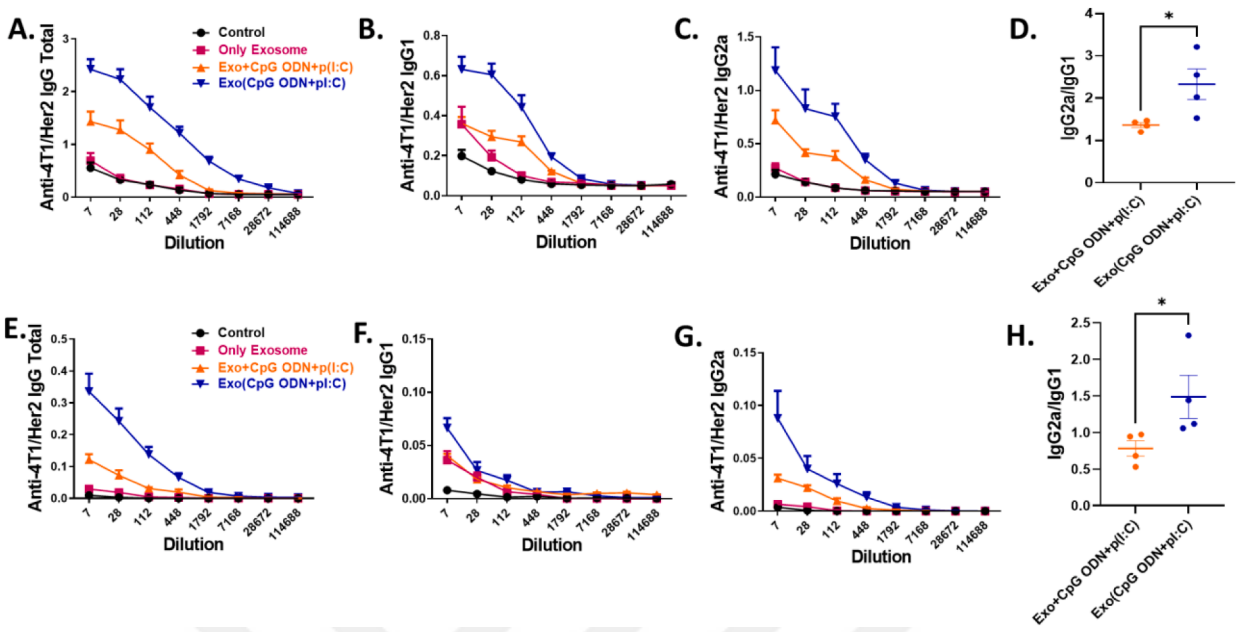


Fig. 2. 4T1/Her2 cell-derived exosomes loaded with CpG ODN and p(I:C) immunization generates sustained and magnified anti-4T1/Her2 immune responses. Mice ($n = 4$ mice/group) were injected i.p. with PBS, only 30 μg exosomes, free form of 30 μg exosomes+30 μg CpG ODN and 30 μg p(I:C) or exo(CpG ODN+p(I:C)) on days 0 and 14. Mice were sacrificed on day 28. **A-C)** Sera of immunized mice were investigated for systemic anti-4T1/Her2 antibody production against 4T1/Her2 cell lysate. End-point average titers of anti-4T1/Her2 total IgG, IgG1 and IgG2a responses of mice were shown. **D)** IgG2a/IgG1 ratio of individual mouse either immunized with free or immunized with exosomal formulation at 2 weeks after booster injection (at 1:120 dilution against 4T1/Her2 cell Lysate). Mann-Whitney test was used for statistical analysis. **E-G)** Sera of immunized mice were investigated for systemic anti-4T1/Her2 antibody production against protein extracts of 4T1/Her2 cell-derived exosomes. End-point average titers of anti-4T1/Her2 total IgG, IgG1 and IgG2a responses were shown. **H)** IgG2a/IgG1 ratio of individual mouse either immunized with free or immunized with exosomal formulation at 2 weeks after booster injection (at 1:15 dilution against protein extracts of 4T1/Her2 cell-derived exosomes). Mann-Whitney test was used for statistical analysis. The data indicate the mean ± SEM ($n = 4$). Statistically significant differences designated as follows: ns: $p > 0.05$, *:$p < 0.05$. Exo: exosome.

(1:1000) antibodies and developed by the addition of PNPP substrate.

2.9. Intracellular cytokine assay via flow cytometry

10^6 cells/mL of splenocytes in medium containing Brefeldin A (5 μg/mL, was included in the last 6 h) was stimulated with 4T1/Her2 derived exosomes (10 μg/mL) for 24 h at 37 °C. After stimulation, cells washed two times with stain buffer (2% FCS in PBS). Cells were stained with 1 μg/mL anti CD45-PE/Cy7, anti CD3-Pacific Blue, anti CD4-FITC, anti CD8-PE, anti CD44-APC/Cy7, anti CD62L-BV605 for 30 min at 4 °C. The cells were washed with stain buffer and fixed with Cytofix/Cytoperm solution. Fixed cells were washed two times with Perm/Wash buffer and then stained with 1 μg/mL anti IFNγ-FITC antibody for 30 min at 4 °C. The cells were washed with Perm/Wash buffer and suspended in 300 μL stain buffer for flow cytometric analysis with Novocyte D3000 (Agilent, California, USA).

2.10. The therapeutic model of 4T1-luc tumor mice model

6–8 week-old female Balb/c mice were injected with 2×10^5 4T1-luc tumor cells into right mammary fat pads orthotopically with 5–6 mice per group. Tumor-bearing mice were then intraperitoneally injected with a PBS and 30 μg exosome loaded with 30 μg CpG ODN and 30 μg p(I:C) at day =, 1, 4, 7, 10, 17, 24 and 31 after tumor inoculation. Tumor growth was monitored by measuring the tumor volume with a caliper after tumors become palpable. Tumor volumes were calculated as length × width^2/2.

For IVIS spectrum, Caliper Lifesciences Lumina III series was used to visualize tumor growth and each mouse received 150 mg Luciferin/kg according to the datasheet suggestion.

2.11. Statistical analysis

One-way ANOVA with Kruskal Wallis and Mann–Whitney tests were employed to assess the significance of differences among the groups. Survival analysis was performed using log-rank test (GraphPad Prism version 9, San Diego, California). $P < 0.05$ was statistically significant.

3. Results

3.1. Characterization of exosomes

Exosomes were isolated from the 4T1/Her2 cell culture supernatants using differential ultracentrifugation method as described in Material and Methods. Isolated exosomes were subjected to analysis of i) surface marker expression by flow cytometry, ii) exosome-specific protein and Her2 expression by immunoblotting, iii) size distribution by DLS and iv) morphological analysis by SEM. Exosomes were verified by detecting the expression of positive protein markers CD81, CD9 (Fig. 1A) and TSG101 (Fig. 1B). Tumor cell-derived exosomes are a good source of cellular components that stimulate the immune response, such as tumor-associated antigens. To check whether the isolated exosome pools carry antigen, we confirmed that purified exosomes of 4T1/Her2 cells also express Her2 whereas isolated exosomes of RAW264.7 as a negative control does not (Fig. 1B). The size of exosomes abundantly ranged from 40 to 190 nm (Ave. Mean Size:70 ± 20 nm, Fig. 1C). Under scanning electron microscopy (SEM), the purified exosomes exhibited a typical round-shaped structures (Fig. 1D). Collectively, these findings support that extracellular nanovesicles derived from 4T1/Her2 cell line displays convincing exosome features.

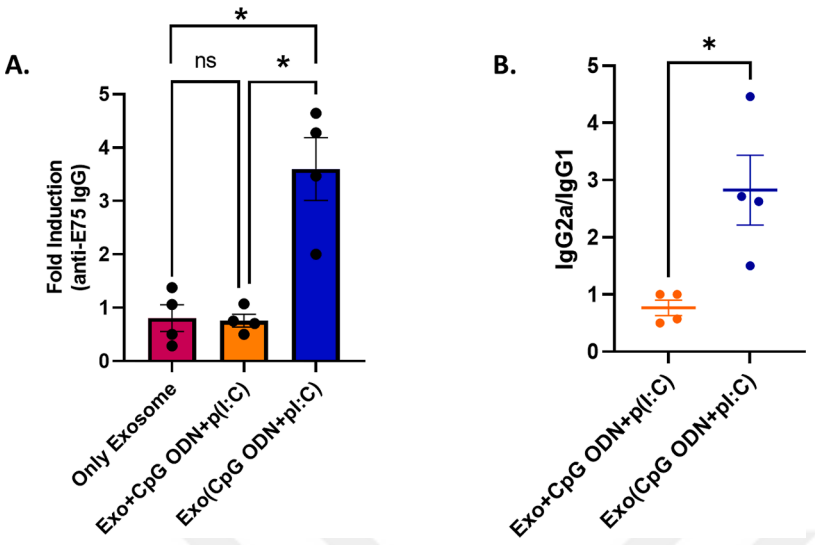


Fig. 3. 4T1/Her2 cell-derived exosome loaded with CpG ODN and p(I:C) immunization magnified anti-E75 immune responses. Mice (n = 4 mice/group) were injected i.p. with PBS, only 30 μg exosome, free form of 30 μg exosome+30 μg CpG ODN and 30 μg p(I:C) or exo(CpG ODN+p(I:C)) on days 0 and 14. Mice were sacrificed on 14 day after the booster injection **A)** Bar graphs showing fold induction over control group of sera of immunized mice for systemic antibody production against Her2/E75 peptide. **B)** IgG2a/IgG1 ratio of individual mouse either immunized with free or immunized with EV formulation at 2 weeks after booster injection (at 1:30 dilution against Her2/E75 peptide). Mann-Whitney test was used for statistical analysis. The data indicate the mean ± SEM (n = 4). Statistically significant differences designated as follows: ns: $p > 0.05$, *: $p < 0.05$. Exo: exosome.

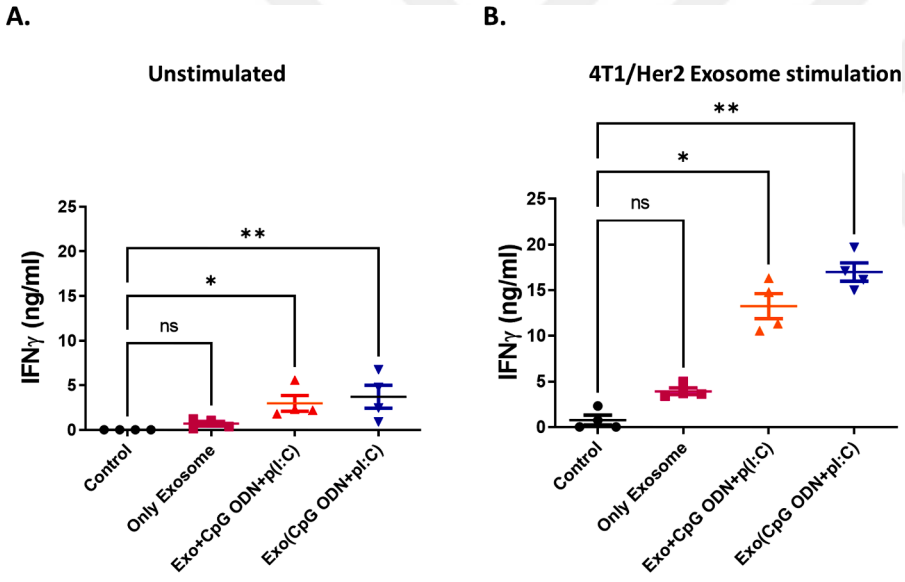


Fig. 4. IFNγ assay on ex vivo expanded splenocytes of mice immunized two times with PBS, unencapsulated 30 μg exosome, mixture of 30 μg Exosome + 30 μg CpG ODN and 30 μg p(I:C) or exosome co-loaded with (CpG ODN+p(I:C)) A) Fourteen days after the booster, the spleens of mice from each group were harvested and immune responses were evaluated using an IFNγ ELISA assay. **B)** Fourteen days after the booster, spleens of mice (n = 4) were harvested and incubated with 4T1/Her2 exosome in culture for 72 hrs and the secreted IFNγ levels were then evaluated using IFNγ ELISA kit. The data indicate the mean±SEM (n = 4). Statistical significance was analyzed by Kruskal Wallis test. Statistically significant differences designated as follows: ns: $p > 0.05$, *: $p < 0.05$, **: $p < 0.01$. Exo:exosome.

3.2. Humoral immune responses

We intended to develop an exosomal carrier system co-encapsulating two nucleic acid-based TLR ligands as immunoadjuvants naturally expressing tumor-associated antigen Her2 and analyzed its potency as a prophylactic and therapeutic vaccine. Previous studies have shown that tumor derived exosomes have a dual effect on the immune system, immunosuppressive or immunostimulatory effects. To combine and enhance the synergistic immunostimulatory activity of TLR3 (p(I:C)) and TLR9 (CpG ODN) ligands, we co-encapsulated them within 4T1/Her2 cell-derived exosomes thereby aimed to achieve simultaneous antigen and adjuvant delivery to relevant antigen presenting cell. Next, we assessed the humoral responses from sera of mice collected at day 28 following twice (@Day = 0 and 14) i.p. injection to Balb/c mice. 4T1/Her2-specific total IgG, IgG1 and IgG2a titers against 4T1/Her2 total cellular protein extract or 4T1/Her2 total exosome extract were analyzed by ELISA. As expected, there was no 4T1/Her2-specific antibody production in the control group and only exosome injected animals raised strong antibody titers. Besides, the level of 4T1/Her2 specific total IgG, IgG1 and IgG2a in sera of mice immunized with dual ligand-loaded exosomal group was significantly higher than those animals that was immunized with free combination of antigen containing exosome and TLR ligands (Fig. 2A–C and Fig 2E–G). We also detected significantly elevated IgG2a/IgG1 ratio after immunization with exosomes co-encapsulating p(I:C) and CpG ODN indicating the development of antigen specific Th1-biased immunity ($p = 0.0286$ for both antigens) (Fig. 2D and Fig 2H).

Furthermore, we analyzed whether exosome loaded with CpG ODN and p(I:C) produce Her2 specific antibodies. To assess this, we used Her2 specific E75 peptide. As shown in Fig. 3A, mice immunized with dual ligand loaded exosomes produced significantly higher Her2/E75 specific total IgG antibody compared to mice immunized with only exosome and free form of exosomal combination ($p = 0.0286$). We detected significantly elevated IgG2a/IgG1 ratio after immunization with CpG ODN plus p(I:C) loaded exosomes ($p = 0.0286$ for both antigens, Fig. 3B). Collectively these results pointed out that CpG ODN and p(I:C) loaded exosomes elicited anti-4T1/Her2 and Her2/E75 specific Th1-biased immunity.

3.3. Induction of specific IFNγ from splenocytes

To evaluate the type of immune response generated, splenocytes

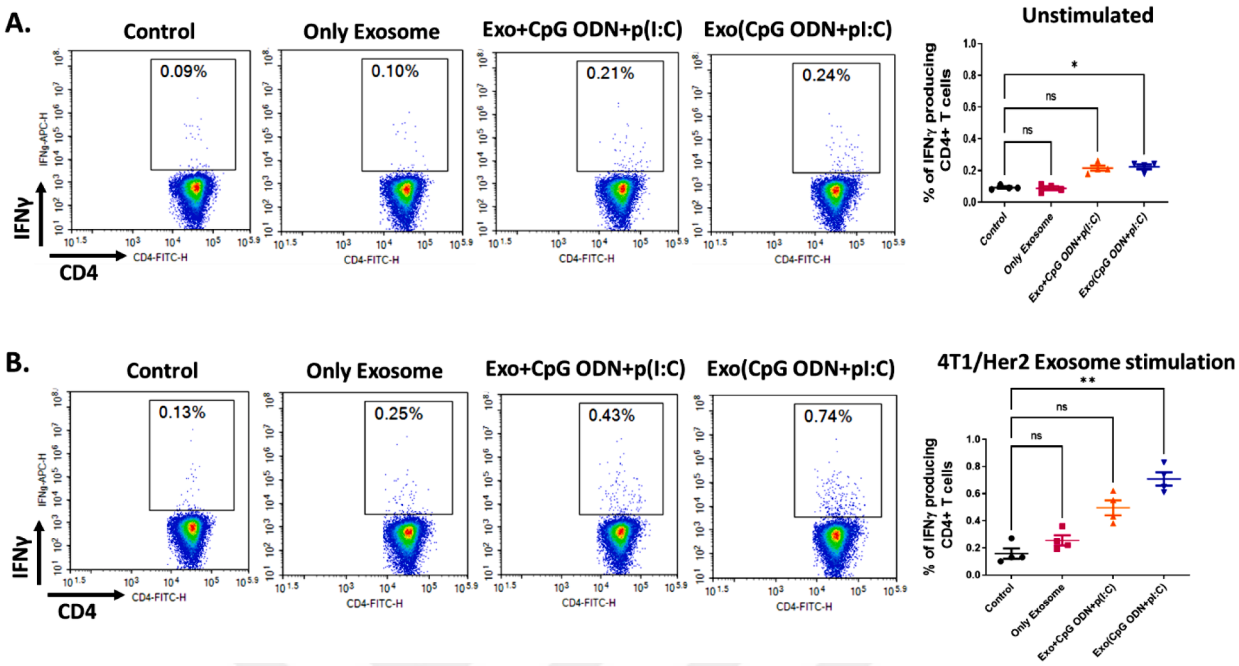


Fig. 5. Intracellular cytokine production from splenocytes of mice immunized two times with PBS, unencapsulated 30 μg exosome, mixture of 30 μg exosome plus 30 μg CpG ODN and 30 μg p(I:C) or exosome co-loaded with (CpG ODN+*p*(I:C)). A) Fourteen days after the booster, isolated splenocytes of different groups of vaccinated mice (4 mice from each group) were stained with CD45-PE/Cy7, CD3-Pacific Blue, CD4-FITC surface markers and then with anti-IFNγ-APC antibodies. **B)** Fourteen days later the booster, isolated splenocytes of different groups of vaccinated mice were stimulated with 4T1/Her2 exosome for 24 hrs in culture and stained with CD45-PE/Cy7, CD3-Pacific Blue, CD4-FITC surface markers and then with anti-IFNγ-APC antibodies. The frequency of IFN-γ producing cells within CD4+ population were determined by Novocyte 3000 Cell analyzer. The data indicate the mean±SEM ($n = 4$). Statistical significance was analyzed by Kruskal Wallis test. Statistically significant differences designated as follows: ns: $p > 0.05$, *:$p < 0.05$, **: $p < 0.01$. Exo:exosome.

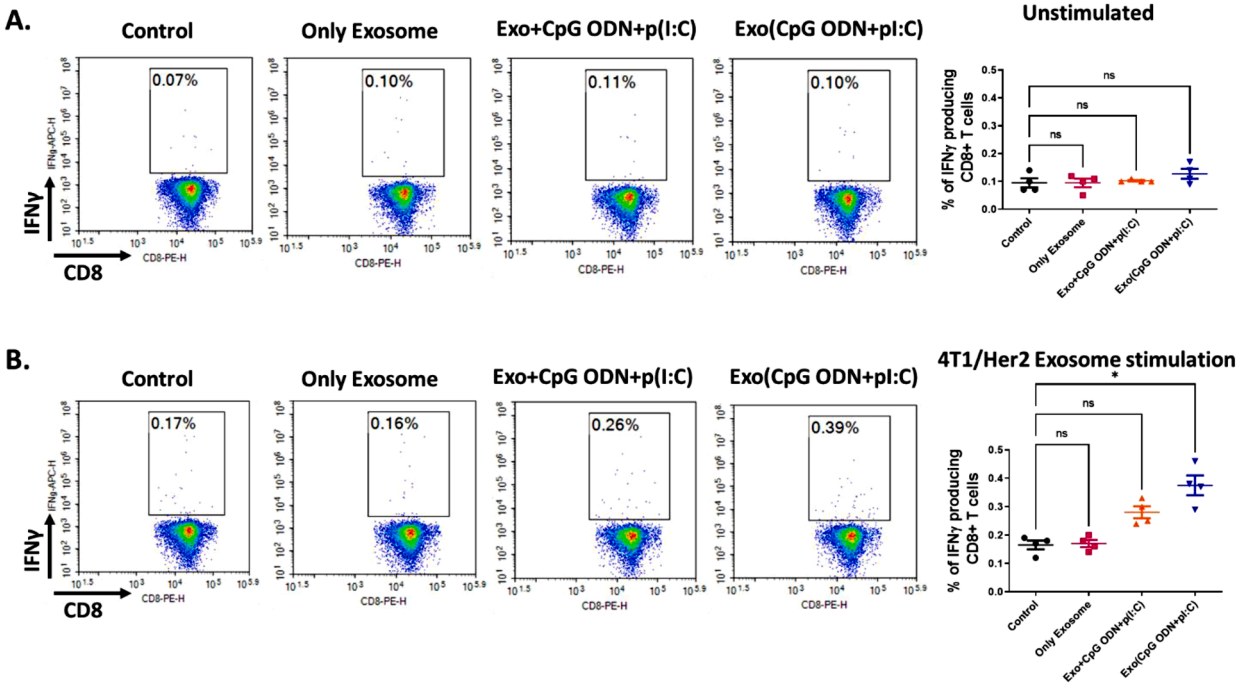


Fig. 6. Intracellular cytokine production assay on splenocytes of mice immunized two times with PBS, unencapsulated 30 μg exosome, mixture of 30 μg exosome + 30 μg CpG ODN and 30 μg p(I:C) or exosome co-loaded with (CpG ODN+p(I:C)). A) Fourteen days later after the booster, isolated splenocytes of different groups of vaccinated mice (4 mice from each group) were stained with CD45-PE/Cy7, CD3-Pacific Blue, CD8-PE surface markers and then with anti-IFNγ-APC antibodies. **B)** Fourteen days later after the booster, isolated splenocytes of different groups of vaccinated mice were incubated with 4T1/Her2 exosome for 24 hrs and stained with CD45-PE/Cy7, CD3-Pacific Blue, CD8-PE surface markers and then with anti-IFNγ-APC antibodies. The frequency of IFN-γ producing cells within CD8+ population were determined by Novocyte 3000 Cell analyzer. The data indicate the mean ± SEM ($n = 4$). Statistical significance was analyzed by Kruskal Wallis test. Statistically significant differences designated as follows: ns: $p > 0.05$, *:$p < 0.05$. Exo:exosome.

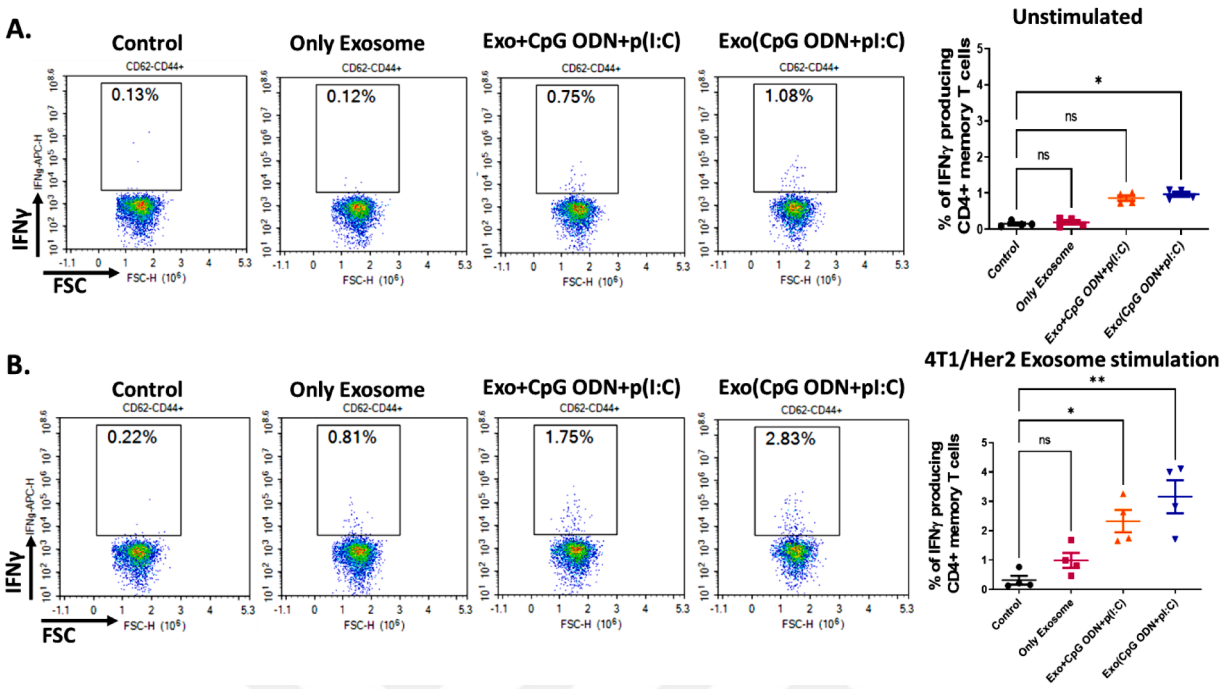


Fig. 7. IFN-γ producing CD4+ memory T cell assay on splenocytes of mice immunized two times with PBS, unencapsulated 30 μg exosome, mixture of 30 μg exosome+30 μg CpG ODN and 30 μg p(I:C) or co-loaded with (CpG ODN+*p*(I:C)). A) Fourteen days later after the booster, isolated splenocytes of different groups of vaccinated mice (4 mice from each group) were stained with CD45-PE/Cy7, CD3-Pacific Blue, CD4-FITC, CD44-APC/Cy7, CD62L-BV605 surface markers and then with anti-IFNγ-APC antibodies. **B)** Fourteen days later after the booster, isolated splenocytes of different groups of vaccinated mice were stimulated with 4T1/Her2 exosome in culture for 24 h and stained with CD45-PE/Cy7, CD3-Pacific Blue, CD4-FITC, CD44-APC/Cy7, CD62L-BV605 surface markers and then with anti-IFNγ-APC antibodies. CD4+ memory T cell was identified as CD45+CD3+CD4+CD8-CD44^{high}CD62L^{low}. The frequency of IFN-γ producing memory T cells within CD4+ population were determined by Novocyte 3000 Cell analyzer. The data indicate the mean ± SEM (n = 4). Statistical significance was analyzed by Kruskal Wallis test. Statistically significant differences designated as follows: ns: $p > 0.05$, *:$p < 0.05$, **: $p < 0.01$. Exo:exosome.

were isolated two weeks after the last booster injection and IFNγ production was analyzed by ELISA assay. As shown in Fig. 4A, we detected that both non-encapsulated combination and dual ligand co-encapsulated exosome group generated more IFNγ compared to control group ($p = 0.0143$, $p = 0.0089$, respectively). Furthermore, Fig. 4B shows that when the splenocytes of immunized mice were activated with 4T1/Her2 exosomes, specific IFNγ productions of non-encapsulated combination and co-encapsulated exosome group were boosted significantly compared to control groups ($p = 0.0347$, $p = 0.0019$, respectively).

3.4. CD4+ and CD8+ T cell responses

To further differentiate the contribution of TLR ligand co-encapsulation within exosomes on cellular immunity that was raised against 4T1 tumors, we performed IFNγ specific intracellular cytokine staining on splenocytes. To this end, the IFNγ + *T*-cell subsets following staining of CD4 and CD8 positive T cells were analyzed by flow cytometry. The data showed that before and after 4T1/Her2 exosome stimulation in culture the induction of IFNγ producing +CD4 *T* cells were significantly higher in mice immunized with exosomes loaded with TLR ligands compared to the control groups. ($P = 0.046$, $P = 0.0032$ respectively) (Fig. 5A, B).

As seen in Fig 6, similarly intracellular cytokine staining assay revealed that when splenocytes were stimulated overnight with 4T1/Her2 exosome in culture, only Exo(CpG ODN+p(I:C)) group had significantly augmented IFNγ production from CD8+ *T*-cells compared to the control group ($P = 0.0127$).

4T1/Her2 specific memory T-cell is one of the major contributing cell populations to eliminate Her2 expressing tumor cells, therefore, we analyzed the immunized mice splenocytes to assess the antigen-specific CD4+ memory T cell percentage. We determined that mice immunized with Exo(CpG ODN+p(I:C)) generated significantly higher IFNγ producing CD4+ memory T cell compared to the control group ($p = 0.016$) (Fig. 7A). When immunized mice cells were incubated with 4T1/Her2 expressing exosome, IFNγ producing CD4+ memory T cells expanded significantly in Exo(CpG ODN+ *p*(I:C)) treated group compared to the control group ($p = 0.0042$) (Fig. 7B).

3.5. Therapeutic effects of exosome vaccination in 4T1-luc bearing BALB/c mice

Considering the strong cellular and humoral immune responses in vaccinated mice (Figs. 2–7), it was expected that the immune responses would lead to antitumor activity in an established 4T1-luc tumor model. To evaluate if the cellular and humoral immune responses induced by the Exo(CpG ODN+p(I:C)) vaccination were potent enough to induce an in vivo antitumor effect, the mice were injected with 4T1-luc tumor cells orthotopically into the right mammary fat pads. Following after tumor inoculation, animals were intraperitoneally injected with Exo(CpG ODN+*p*(I:C)) and were observed for tumor regression during 36 days post tumor formation. As shown in Fig. 8A, during the days 10–36, the group of mice that received Exo(CpG ODN+p(I:C)) regressed tumor development significantly in comparison with untreated control group ($P = 0.0045$ for day 32 and $P = 0.0024$ for day 36). Also, the survival time was significantly prolonged in Exo(CpG ODN+p(I:C)) treated groups in comparison with the control group receiving PBS ($P = 0.0229$). All mice belonging to control group were dead by day 49 whereas 3 out of 5 mice treated with Exo(CpG ODN+p(I:C)) were alive by day 60. Furthermore, We analyzed the IFNγ secretion, helper T cell and cytotoxic T cell population from splenocytes of animals that treated with the PBS and CpG ODN+p(I:C) loaded exosomes at day= 1, 4, 7, 10, 17, 24 and 31 after tumor inoculation. As shown in Fig. 8B, Splenocytes from animals that treated with TLR ligands loaded formulation secretes

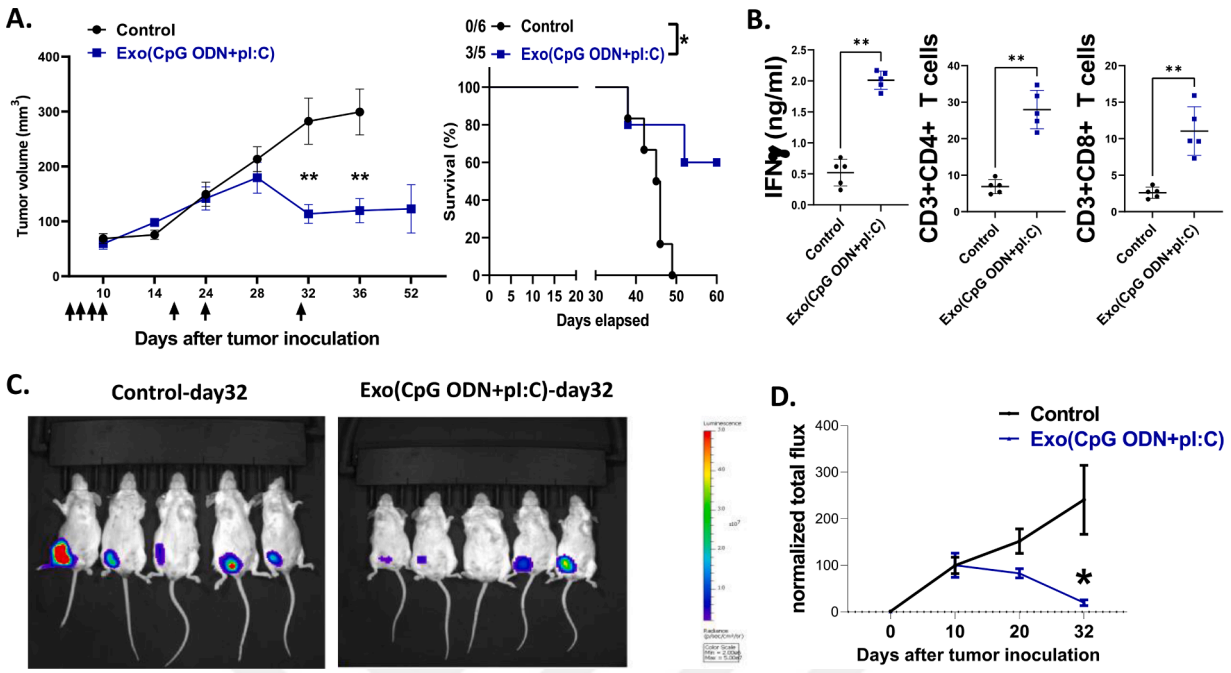


Fig. 8. Therapeutic effect of vaccination with PBS and exo(CpG ODN+*p*(I:C)) in BALB/c mice against a 4T1-luc in vivo established tumor mice model A) 4T1-luc tumor development is suppressed by immunization with exosome co-loaded with CpG ODN+*p*(I:C) (30ug each, arrows indicates i.p. injections of exosome vaccine formulation) and the effect of vaccination on the survival time of mice (6 for control group and 5 for vaccinated group) was observed during a 60-day period post tumor inoculation. **B)** IFNγ assay, Helper T cell and Cytotoxic T cell staining on ex vivo expanded splenocytes of mice treated with PBS, and exosome loaded formulation **C)** In vivo luciferase images of 4T1-luc tumors in control and vaccinated group at day 32. (IVIS Spectrum). **D)** Luciferin signal activity normalized to the signal obtained at day 1 following ortholog tumor injection. Tumor volume plot is collected from 2 independent experiments ($n = 5$ in each group). Mann-Whitney test was used for statistical analysis. Statistical significance for tumor volume and survival time was analyzed by Šídák's multiple comparisons test and Log-rank (Mantel-Cox) test, respectively. Normalized total flux was analyzed by Bonferroni's multiple comparisons test. Statistically significant differences designated as follows: ns: $p > 0.05$, *:$p < 0.05$, **: $p <$ 0.01.Exo:exosome.

significantly higher level of IFNγ. Also, we found that the percentage of CD4+ and CD8+ T cells in splenocytes are significantly higher than mice treated with TLR ligands loaded exosomes compared to control group($P = 0.0079$).The anti-tumor effect of Exo(CpG ODN+*p*(I:C)) group was evaluated by measurement using an IVIS imaging system. We measured bioluminescence activity every 10 days (day 0, day 10, day 20 and day 32 after tumor inoculation).As shown in the bioluminescence imaging results at day32, 1 out of 5 mice treated with Exo(CpG ODN+p(I:C)) had no luciferase signal (Fig. 8C) and exosome treated group had significantly lower luciferin activity over time (Fig. 8D)

Collectively, our findings implied that a combination of p(I:C) and CpG ODN ligands within exosomal formulations induced stronger and persistent humoral and cellular anti-4T1/Her2 specific immune response sufficient to regress tumor growth.

4. Discussion

Tumor-derived exosomes (TEXs) are promising candidates as the next generation immuno-therapeutic vaccines against cancers. Besides being a good reservoir of various tumor antigens, TEXs take an active role in the communication of tumor cells in all steps of cancer development and regulate immune responses through both immunosuppressive and immunostimulatory functions [31]. It is of great significance to consider the safety profile of ligand loaded exosomes as less detrimental cancer antigen carriers as they initiate inflammatory responses due to its immunostimulatory nature of its cargo. We anticipate that the safety concerns could be alleviated due to its inflammatory character when harnessed as a therapeutic vaccine carrier. Due to this differential role of TEXs, and their limited immunogenicity, their modifications into an effective immuno-adjuvant delivery system that can stimulate a strong humoral and cell-mediated immune responses remains a challenge. In this study, we modified 4T1/Her2-cell-derived exosomes by loading with two potent adjuvants, CpG ODN and p(I:C). Modified exosomes co-encapsulating both CpG ODN and p(I:C) have shown immunostimulatory properties by activating antigen-specific primary and memory T cell responses. Furthermore, our exosome-based adjuvant vaccine stimulated robust Th1 type immune responses via the elevated secretion of IgG2a antibody and IFNγ, resulting in tumor regression in 4T1 tumor-bearing mice.

Combination of TLR adjuvants like CpG ODN and p(I:C) triggers synergistic immune response more apparently than their standalone counterparts when given within a carrier system [32]. Therefore, we evaluated to immunogenicity of modified TEXs co-encapsulated with the combination of both adjuvants. As expected, administration of only tumor derived exosomes to the mice did not generate statistically significant responses while exosomes loaded with CpG ODN and p(I:C) significantly increased CD4+ and CD8+ *T* cell responses and the production of antigen-specific antibodies (Fig. 2-7). It is important to note that while mixing exosomes with CpG ODN and p(I:C) improves CD4+ and CD8+ *T* cell specific IFNγ this response is neither significant from untreated control nor exosome alone treated animals. In this respect, only encapsulation of ligands within exosomes triggered significantly higher IFNγ from the these animals, although comparison of mixture treated group vs ligand loaded exosome group animals did not yield significantly different responses. Since co-encapsulating CpG ODN and p(I:C) was the most active than other treatment groups, we investigated its potential therapeutic effect against the established 4T1 tumor model in mice. Our exosome-based adjuvant formulation significantly regressed tumor growth (Fig. 8). Furthermore, the simple co-administration of adjuvant with TEXs in clinical trials resulted in insufficient anti-tumor immunity due to inefficient simultaneous delivery of tumor antigen and adjuvant to the same antigen presenting cells (APCs) [33]. In the present study, we successfully encapsulated two adjuvants into TEXs carrying endogenous antigens and have shown that

compared to co-administration mixture of (Exo+CpGODN+p(I:C)), co-encapsulation Exo(CpG ODN+p(I:C)) strategy yielded i) stronger antigen-specific Th1-biased humoral immunity, ii) higher levels of IFNγ secretion and iii) more IFNγ producing CD4+ and CD8+ T cells (Fig. 2-6).

Induction of tumor antigen-specific cytotoxic T lymphocytes and humoral immune responses generated by efficient delivery of tumor antigens to APCs are essential requirements for effective cancer immunotherapy [34]. For this reason, vaccines against cancers focus on the identification of immunogenic antigen epitopes that selectively stimulates the induction of robust T helper cells, B cells and cytotoxic T cells [35]. However, only a few tumor-associated antigens have been identified for many cancer types and they can be poorly immunogenic or may not be found in a significant percentage of patients [36]. Moreover, the identification and purification of new epitopes that can be able to activate T and B cells are incredibly challenging. Using experimental approaches to screen immunodominant epitopes is quite expensive and its complexity is required the support of bioinformatic based predictions. Therefore, we proposed to harness tumor-derived exosomes isolated from the tumor biopsy or a tumor cell that are capable of expressing all biologically relevant antigens (including the neoantigens) as an efficient cancer vaccine carrier, thereby excludes the need to identify these epitopes. Her2 is considered as an ideal target for cancer vaccine development regarding its 100-fold higher overexpression in patients with breast cancer and correlates with poor clinical outcomes [37]. E75 is a 9-amino acid human leukocyte antigen– (HLA-) restricted peptide located in the Her2 extracellular domain, which is currently under clinical trials [38]. Studies have shown that E75 peptide vaccine improve CTL and CD4+ Th1 responses [39,40], however, this vaccine can be used in limited patient population due to HLA class I restriction. Using TEXs from HER2-overexpressing cell lines as an adjuvant delivery system overcomes this restriction and activate more broad immune responses, since these exosomes express a full length Her2 molecule (Fig. 1) as well as the whole panel of tumor related antigens. Therefore, TEXs are potent delivery systems that can stimulate a breadth of T cell clones by presenting multiple antigenic epitopes. Besides stimulating strong Th1 type immune responses via the elevated production of IgG2a antibody against 4T1/Her2-derived exosomes (Fig. 2), our 4T1/Her2--derived exosome-adjuvant formulation efficiently activated humoral immune responses against E75 peptide as well (Fig.3). Based on these findings, using tumor-derived exosomes as a delivery system for cancer immunotherapy is more convenient and suitable approach, as it is applicable to all cancer types, where biopsies are available from the patient.

In conclusion, we demonstrated that modified TEXs with CpG ODN and p(I:C) co-encapsulation generated humoral and cell-mediated immune responses and regress tumor growth in 4T1 tumor-bearing mice. as a well as extended survival (Fig. 8). The combination of adjuvants with tumor antigens inherently expressed by tumor-derived exosomes (without inserting additional antigen epitope) exerted stronger anti-tumor immune responses. These findings propose a useful TEX-based adjuvant delivery system as a promising cell-free vaccine and are of great interest for future vaccine design experiments in the clinical practice.

5. Funding

This work was supported by Ministry of Development (Grant name: UMRAM-ASI, Project #: 2015BSV302 to I.G.).

Declaration of competing interest

The authors confirm that there are no known conflicts of interest associated with this publication.

Acknowledgments

We thank Dr. Gamze Aykut for breeding and daily caring of our animals. We extend our appreciation to Prof. Dr. Mayda Gursel and Dr. Tamer Kahraman for their insightful comments and critical reading of the manuscript.

References

[1] A.D. Waldman, J.M. Fritz, M.J. Lenardo, A guide to cancer immunotherapy: from T cell basic science to clinical practice, Nat. Rev. Immunol. (2020) 20, https://doi.org/10.1038/s41577-020-0306-5.
[2] S. Stevanovic, Identification of tumour-associated T-cell epitopes for vaccine development, Nat. Rev. Cancer. 2 (2002), https://doi.org/10.1038/nrc841.
[3] T. Cancer, G. Atlas, Integrated genomic analyses of ovarian carcinoma the cancer genome atlas research network, Nature (2011) 474, https://doi.org/10.1038/nature10166.Integrated.
[4] R.S. Riley, C.H. June, R. Langer, M.J. Mitchell, Delivery technologies for cancer immunotherapy, Nat. Rev. Drug Discov. 18 (2019), https://doi.org/10.1038/s41573-018-0006-z.
[5] L. Zhou, P. Zhang, H. Wang, D. Wang, Y. Li, Smart nanosized drug delivery systems inducing immunogenic cell death for combination with cancer immunotherapy, Acc. Chem. Res. (2020) 53, https://doi.org/10.1021/acs.accounts.0c00254.
[6] M. Tkach, C. Théry, Communication by Extracellular Vesicles: where we are and where we need to go, Cell 164 (2016), https://doi.org/10.1186/s12951-020-00711-5, 10.1016/j.cell.2016.01.043.
[7] M. Colombo, G. Raposo, C. Théry, Biogenesis, secretion, and intercellular interactions of exosomes and other extracellular vesicles, Annu. Rev. Cell Dev. Biol. (2014) 30, https://doi.org/10.1146/annurev-cellbio-101512-122326.
[8] D. Ha, N. Yang, V. Nadithe, Exosomes as therapeutic drug carriers and delivery vehicles across biological membranes: current perspectives and future challenges, Acta Pharm. Sin. B. (2016) 6, https://doi.org/10.1016/j.apsb.2016.02.001.
[9] E.V. B.atrakova, M.S. Kim, Using exosomes, naturally-equipped nanocarriers, for drug delivery, J. Control. Release. (2015) 219, https://doi.org/10.1016/j.jconrel.2015.07.030.
[10] J.G. Van den Boorn, J. Daßler, C. Coch, M. Schlee, G. Hartmann, Exosomes as nucleic acid nanocarriers, Adv. Drug Deliv. Rev. (2013) 65, https://doi.org/10.1016/j.addr.2012.06.011.
[11] P. Vader, E.A. Mol, G. Pasterkamp, R.M. Schiffelers, Extracellular vesicles for drug delivery, Adv. Drug Deliv. Rev. (2016) 106, https://doi.org/10.1016/j.addr.2016.02.006.
[12] Y. Huang, K. Liu, Q. Li, Y. Yao, Y. Wang, Exosomes function in tumor immune microenvironment, Adv. Exp. Med. Biol. (2018), https://doi.org/10.1007/978-3-319-74470-4_7.
[13] J. Wolfers, A. Lozier, G. Raposo, A. Regnault, C. Théry, C. Masurier, C. Flament, S. Pouzieux, F. Faure, T. Tursz, E. Angevin, S. Amigorena, L. Zitvogel, Tumor-derived exosomes are a source of shared tumor rejection antigens for CTL cross-priming, Nat. Med. 7 (2001), https://doi.org/10.1038/85438.
[14] M. Jiang, W. Zhang, R. Zhang, P. Liu, Y. Ye, W. Yu, X. Guo, J. Yu, Cancer exosome-derived miR-9 and miR-181a promote the development of early-stage MDSCs via interfering with SOCS3 and PIAS3 respectively in breast cancer, Oncogene (2020) 39, https://doi.org/10.1038/s41388-020-1322-4.
[15] L. Alvarez-Erviti, Y. Seow, H. Yin, C. Betts, S. Lakhal, M.J.A. Wood, Delivery of siRNA to the mouse brain by systemic injection of targeted exosomes, Nat. Biotechnol. (2011) 29, https://doi.org/10.1038/nbt.1807.
[16] J.M. Cooper, P.B.O. Wiklander, J.Z. Nordin, R. Al-Shawi, M.J. Wood, M. Vithlani, A.H.V. Schapira, J.P. Simons, S. El-Andaloussi, L. Alvarez-Erviti, Systemic exosomal siRNA delivery reduced alpha-synuclein aggregates in brains of transgenic mice, Mov. Disord. (2014) 29, https://doi.org/10.1002/mds.25978.
[17] S.I. Ohno, M. Takanashi, K. Sudo, S. Ueda, A. Ishikawa, N. Matsuyama, K. Fujita, T. Mizutani, T. Ohgi, T. Ochiya, N. Gotoh, M. Kuroda, Systemically injected exosomes targeted to EGFR deliver antitumor microrna to breast cancer cells, Mol. Ther. (2013) 21, https://doi.org/10.1038/mt.2012.180.
[18] A. Taghikhani, Z.M. Hassan, M. Ebrahimi, S.M. Moazzeni, microRNA modified tumor-derived exosomes as novel tools for maturation of dendritic cells, J. Cell. Physiol. (2019) 234, https://doi.org/10.1002/jcp.27626.
[19] L. Wang, X. Zhou, W. Zou, Y. Wu, J. Zhao, X. Chen, G.G. Zhou, Exosomes containing miRNAs targeting HER2 synthesis and engineered to adhere to HER2 on tumor cells surface exhibit enhanced antitumor activity, J. Nanobiotechnology. 18 (2020).
[20] Z. Xu, S. Zeng, Z. Gong, Y. Yan, Exosome-based immunotherapy: a promising approach for cancer treatment, Mol. Cancer. 19 (2020), https://doi.org/10.1186/s12943-020-01278-3.
[21] C.J. Desmet, K.J. Ishii, Nucleic acid sensing at the interface between innate and adaptive immunity in vaccination, Nat. Rev. Immunol. (2012) 12, https://doi.org/10.1038/nri3247.
[22] S. Pandey, T. Kawai, S. Akira, Microbial sensing by toll-like receptors and intracellular nucleic acid sensors, Cold Spring Harb. Perspect. Biol. 7 (2015), https://doi.org/10.1101/cshperspect.a016246.
[23] D.M. Klinman, Immunotherapeutic uses of CpG oligodeoxynucleotides, Nat. Rev. Immunol. (2004) 4, https://doi.org/10.1038/nri1329.
[24] A.M. Krieg, CpG still rocks! Update on an accidental drug, Nucleic Acid Ther (2012) 22, https://doi.org/10.1089/nat.2012.0340.

[25] D.M. Klinman, D. Currie, I. Gursel, D. Verthelyi, Use of CpG oligodeoxynucleotides as immune adjuvants, Immunol. Rev. (2004) 199, https://doi.org/10.1111/j.0105-2896.2004.00148.x.
[26] C.H. Ewel, W.J. Urba, W.C. Kopp, J.W. Smith, R.G. Steis, J.L. Rossio, D.L. Longo, M. Jane Jones, W. Gregory Alvord, C.M. Pinsky, J.M. Beveridge, K.L. McNitt, S. P. Creekmore, Polyinosinic-Polycytidylic Acid Complexed with Poly-L-lysine and Carboxymethylcellulose in Combination with Interleukin 2 in Patients with Cancer: clinical and Immunological Effects, Cancer Res 52 (1992).
[27] J.L. Lepe-Zuniga, J. Rotbein, J.U. Gutterman, Production of interferon-α induced by dsRNA in human peripheral blood mononuclear cell cultures: role of priming by dsRNA-induced interferons-γ and -β, J. Interferon Res. 9 (1989) https://doi.org/10.1089/jir.1989.9.445.
[28] A.E. Gelman, J. Zhang, Y. Choi, L.A. Turka, Toll-like receptor ligands directly promote activated CD4 + T cell survival, J. Immunol. (2004) 172, https://doi.org/10.4049/jimmunol.172.10.6065.
[29] M.L. Salem, A.N. Kadima, D.J. Cole, W.E. Gillanders, Defining the antigen-specific T-cell response to vaccination and poly(I:C)/TLR3 signaling: evidence of enhanced primary and memory CD8 T-cell responses and antitumor immunity, J. Immunother. 28 (2005), https://doi.org/10.1097/01.cji.0000156828.75196.0d.
[30] R. Perret, S.R. Sierro, N.K. Botelho, S. Corgnac, A. Donda, P. Romero, Adjuvants that improve the ratio of antigen-specific effector to regulatory T cells enhance tumor immunity, Cancer Res 73 (2013), https://doi.org/10.1158/0008-5472.CAN-13-0875.
[31] W. Olejarz, A. Dominiak, A. Zołnierzak, G. Kubiak-Tomaszewska, T. Lorenc, Tumor-derived exosomes in immunosuppression and immunotherapy, J. Immunol. Res. (2020), https://doi.org/10.1155/2020/6272498.
[32] M. Krummen, S. Balkow, L. Shen, S. Heinz, C. Loquai, H.-.C. Probst, S. Grabbe, Release of IL-12 by dendritic cells activated by TLR ligation is dependent on MyD88 signaling, whereas TRIF signaling is indispensable for TLR synergy, J. Leukoc. Biol. (2010) 88, https://doi.org/10.1189/jlb.0408228.
[33] Y. Sun, J. Liu, Potential of cancer cell-derived exosomes in clinical application: a review of recent research advances, Clin. Ther. (2014) 36, https://doi.org/10.1016/j.clinthera.2014.04.018.
[34] A.W. P., J. M., J. R., More than one reason to rethink the use of peptides in vaccine design, Nat. Rev. Drug Discov. 6 (2007).
[35] J.S. Testa, R. Philip, Role of T-cell epitope-based vaccine in prophylactic and therapeutic applications, Future Virol 7 (2012), https://doi.org/10.2217/fvl.12.108.
[36] A. Arora, S.A. Ahmad, C.E. Binkley, W.M. Burke, A.E. Chang, V.M. Cimmino, K. M. Diehl, G.M. Doherty, D.A. DuBay, E.M. Gartner, P.G. Gauger, J.D. Geiger, S. D. Gitlin, K. Graziano, P.J. Hodul, E.H. Huang, M.D. Iannettoni, K.M. Woods Ignatoski, C. Johnston, J. Kim, J. Lin, Q.P. Ly, E.A. Newman, J.M. Pow-Sang, M. E. Ray, A. Rodriguez, D.E. Rollison, M.S. Sabel, E.A. Shaughnessy, D.M. Simeone, V.K. Sondak, S.L. Sugg, J.J. Sussman, S. Tsai, C.Y. Williams-Covington, K. Wilson, M.J. Wolfe, D.T. Woodrum, Contributors, Essentials Surg. Oncol. (2007), https://doi.org/10.1016/b978-0-8151-4385-7.50004-7.
[37] Y. Yarden, Biology of HER2 and its importance in breast cancer, Oncology (2001), https://doi.org/10.1159/000055396.
[38] R.L.B. Costa, B.J. Czerniecki, Clinical development of immunotherapies for HER2+ breast cancer: a review of HER2-directed monoclonal antibodies and beyond, Npj Breast Cancer 6 (2020), https://doi.org/10.1038/s41523-020-0153-3.
[39] E.A. Mittendorf, J.P. Holmes, S. Ponniah, G.E. Peoples, The E75 HER2/neu peptide vaccine, Cancer Immunol. Immunother (2008), https://doi.org/10.1007/s00262-008-0540-3.
[40] M.T. Hueman, A. Stojadinovic, C.E. Storrer, Z.A. Dehqanzada, J.M. Gurney, C. D. Shriver, S. Ponniah, G.E. Peoples, Analysis of naive and memory CD4 and CD8 T cell populations in breast cancer patients receiving a HER2/neu peptide (E75) and GM-CSF vaccine, Cancer Immunol. Immunother. (2007) 56, https://doi.org/10.1007/s00262-006-0188-9.
[41] M.H. Kershaw, J.T. Jackson, N.M. Haynes, et al., Gene-engineered T cells as a superior adjuvant therapy for metastatic cancer, J. Immunol. 173 (3) (2004) 2143–2150.
[42] C.S. Özverel, Y. Uyanikgil, İ. Karaboz, A. Nalbantsoy, Investigation of the combination of anti-PDL1 mAb with HER2/neu-loaded dendritic cells and QS-21 saponin adjuvant: effect against HER2 positive breast cancer in mice, Immunopharmacol Immunotoxicol 42 (4) (2020) 346–357, https://doi.org/10.1080/08923973.2020.1775644.
[43] M.Fang K.Tao, G.G.Sahagian J.Alroy, Imagable 4T1 model for the study of late stage breast cancer, BMC Cancer 8 (2008) 228, https://doi.org/10.1186/1471-2407-8-228.

nature COMMUNICATIONS

ARTICLE

https://doi.org/10.1038/s41467-020-16199-4 OPEN

Targeting lysyl oxidase (LOX) overcomes chemotherapy resistance in triple negative breast cancer

Ozge Saatci[1], Aysegul Kaymak[1], Umar Raza[2], Pelin G. Ersan[2], Ozge Akbulut[2], Carolyn E. Banister[1], Vitali Sikirzhytski[1], Unal Metin Tokat[2], Gamze Aykut[2], Suhail A. Ansari[2], Hayriye Tatli Dogan[3], Mehmet Dogan[4], Pouria Jandaghi[5,6], Aynur Isik[7], Fatma Gundogdu[8], Kemal Kosemehmetoglu[8], Omer Dizdar[9], Sercan Aksoy[9], Aytekin Akyol[7,8], Aysegul Uner[8,10], Phillip J. Buckhaults[1], Yasser Riazalhosseini[5,6] & Ozgur Sahin[1,2]✉

Chemoresistance is a major obstacle in triple negative breast cancer (TNBC), the most aggressive breast cancer subtype. Here we identify hypoxia-induced ECM re-modeler, lysyl oxidase (LOX) as a key inducer of chemoresistance by developing chemoresistant TNBC tumors in vivo and characterizing their transcriptomes by RNA-sequencing. Inhibiting LOX reduces collagen cross-linking and fibronectin assembly, increases drug penetration, and downregulates ITGA5/FN1 expression, resulting in inhibition of FAK/Src signaling, induction of apoptosis and re-sensitization to chemotherapy. Similarly, inhibiting FAK/Src results in chemosensitization. These effects are observed in 3D-cultured cell lines, tumor organoids, chemoresistant xenografts, syngeneic tumors and PDX models. Re-expressing the hypoxia-repressed miR-142-3p, which targets *HIF1A*, *LOX* and *ITGA5*, causes further suppression of the HIF-1α/LOX/ITGA5/FN1 axis. Notably, higher LOX, ITGA5, or FN1, or lower miR-142-3p levels are associated with shorter survival in chemotherapy-treated TNBC patients. These results provide strong pre-clinical rationale for developing and testing LOX inhibitors to overcome chemoresistance in TNBC patients.

[1] Department of Drug Discovery and Biomedical Sciences, University of South Carolina, Columbia, SC 29208, USA. [2] Faculty of Science, Department of Molecular Biology and Genetics, Bilkent University, 06800 Ankara, Turkey. [3] Department of Medical Pathology, Ankara Yildirim Beyazit University, 06800 Ankara, Turkey. [4] Department of Medical Pathology, Ankara Oncology Education and Research Hospital, 06200 Ankara, Turkey. [5] Department of Human Genetics, McGill University, Montreal, QC H3A 1B1, Canada. [6] McGill University and Genome Quebec Innovation Centre, Montreal, QC H3A 0G1, Canada. [7] Hacettepe University Transgenic Animal Technologies Research and Application Center, 06100 Ankara, Turkey. [8] Faculty of Medicine, Department of Pathology, Hacettepe University, 06100 Ankara, Turkey. [9] Department of Medical Oncology, Hacettepe University Cancer Institute, 06100 Ankara, Turkey. [10] Hacettepe University Molecular Pathology Research and Application Center, 06100 Ankara, Turkey. ✉email: sahinozgur@gmail.com

Triple negative breast cancer (TNBC) is the most aggressive subtype of breast cancer. It accounts for 10–20% of all patients, yet is responsible for 30% of all breast cancer deaths[1]. At the molecular level, TNBC is characterized by the lack of estrogen receptor alpha (ERα), progesterone receptor (PR) and epidermal growth factor receptor 2 (HER2/ErbB2)[2,3] expression. TNBC patients mostly rely on chemotherapy unlike other subtypes that can be treated with targeted therapies. Anthracyclines and taxane-based chemotherapy agents are among the most commonly used chemotherapeutics in both neo-adjuvant and adjuvant settings[4]. As compared to other subtypes, TNBC patients show low risk of recurrence if pathological complete response (pCR) is achieved[5]. However, while only 30–40% of TNBC patients show pCR towards treatment, the majority have <60% 5-year survival due to aggressive relapse[6]. Recently, the first immunotherapy for breast cancer was approved by the Food and Drug Administration (FDA) to treat locally advanced or metastatic TNBC patients. However, immunotherapy combined with chemotherapy produced only a 3 month improvement in progression-free survival, and improvement in overall survival was observed only in patients with PD-L1 positive tumors[7]. Therefore, there is still a dire need to identify novel molecular targets to improve the therapeutic benefit of chemotherapy given in first-line settings, as well as in patients with advanced, chemotherapy resistant TNBC. This will have immediate translational impact on improving the pCR rate to standard chemotherapy and will improve patient outcome for the most-aggressive breast cancer subtype.

Deregulation of distinct cell intrinsic processes, such as apoptosis[8], growth factor signaling[9], DNA repair[10] as well as alterations in the levels of drug transporter proteins[11] have previously been associated with chemoresistance. In addition, accumulating evidence suggest that the tumor extracellular matrix (ECM) may also confer resistance to therapy, either by providing a protective barrier that hinders access of anti-cancer drugs to tumors[12–14] or by activating survival signaling or blocking apoptosis upon interacting with the integrin type transmembrane receptors[15,16]. Integrins are heterodimeric cell surface receptors that control cell adhesion, cytoskeletal organization, signal transduction and cell migration via establishing focal adhesion complexes that serve as mechanical links that convey signals between ECM and the intracellular compartment of the interacting cell[17,18]. Activation of integrin signaling may lead to resistance to therapy[15,19,20] and acquisition of metastatic traits[21]. Notably, increased expression of several integrin subunits have previously been associated with poor patient outcome[19,22,23].

The ECM is a highly dynamic structure that is constantly remodeled by cells through altered synthesis, degradation, reassembly and chemical modifications[24]. While normal epithelial cells produce small amounts of ECM, fibroblasts and tumors cells produce large quantities of ECM molecules, such as collagen and fibronectin[25,26]. In addition, overexpression of ECM remodeling enzymes such as matrix metalloproteases (ECM degraders) and lysyl oxidases (ECM stiffeners) have previously been associated with tumor aggressiveness[24]. The lysyl oxidase (LOX) family proteins mediate the conversion of lysine residues in collagen and elastin precursors into highly reactive aldehydes thereby triggering cross-linking and stabilization of ECM proteins, specifically the type I collagen and elastin, and regulate cell adhesion, motility and invasion[27]. In preclinical breast cancer models, LOX secretion from breast cancer cells was shown to induce the pre-metastatic niche formation[28], and LOX inhibition suppressed lung metastasis[29]. LOX inhibition was also shown to sensitize pancreatic cancer to chemotherapy[30,31]. Furthermore, novel intracellular functions of the LOX family proteins have been reported, such as the stabilization of transcription factors and maintenance of chromosome stability[32]. Despite the relatively well-established roles of LOX in stimulating cancer metastasis, its contribution to chemoresistance in TNBCs has not yet been reported.

In this study, we combine in vivo-developed chemoresistant xenograft models with an unbiased, genome-wide transcriptomic approach, 3D cell culture systems, primary breast cancer organoids, syngeneic and patient-derived xenograft (PDX) models and patient data/tissue analyses to identify mechanisms of chemotherapy resistance in TNBCs. We show that chemoresistance is driven by the HIF-1α/miR-142-3p/LOX/ITGA5/FN1 axis and targeting either LOX or its downstream FAK/Src signaling pathway, or overexpressing miR-142-3p can overcome chemoresistance in TNBC.

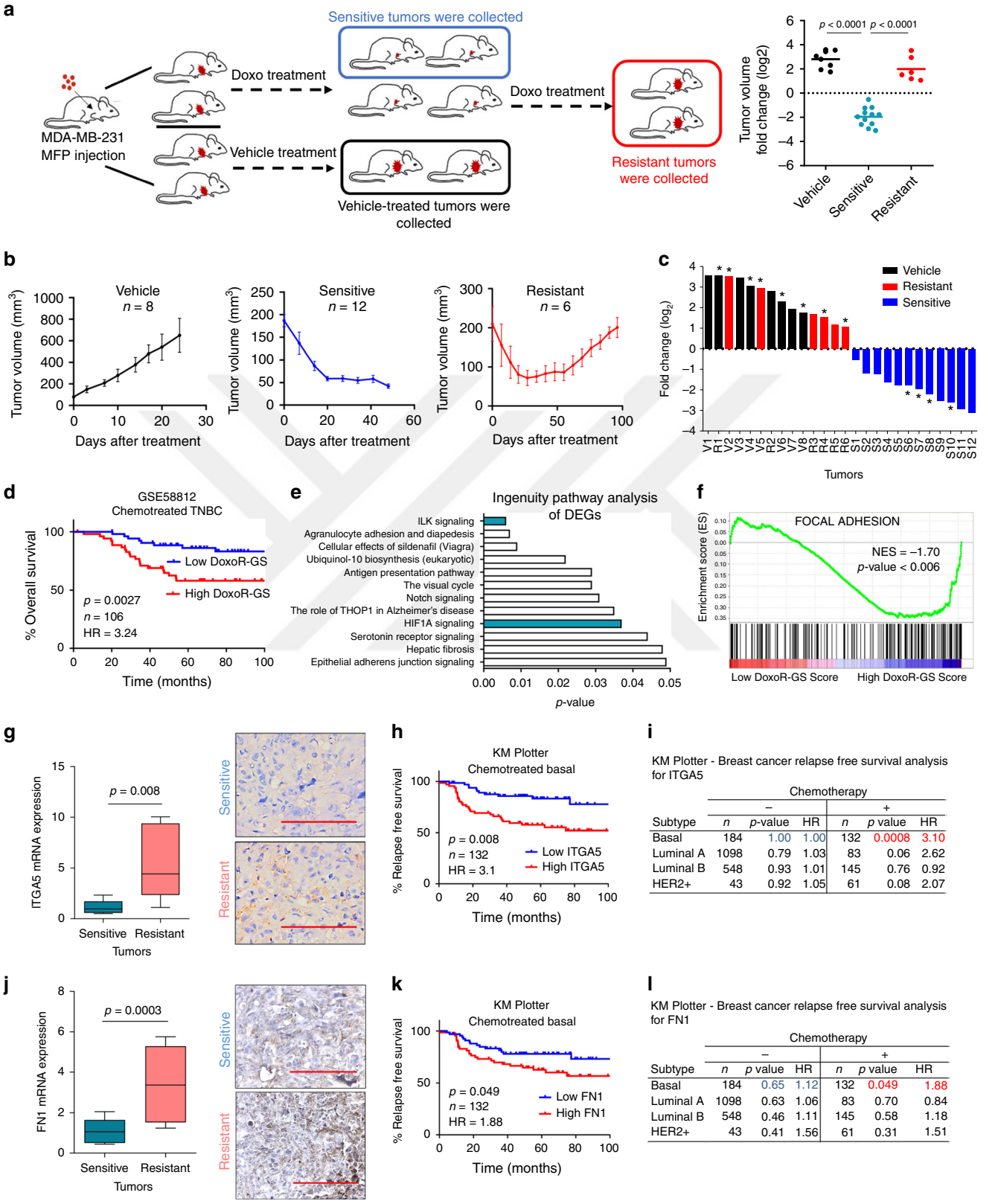
Results

Integrin signaling is a key mediator of chemoresistance in TNBCs. To elucidate the underlying mechanisms of chemoresistance in TNBCs, we modelled the clinical acquired resistance by using xenografts of the well-established TNBC cell line, MDA-MB-231[33,34]. Tumor-bearing mice were continuously treated with either vehicle or doxorubicin, and the fast-growing vehicle-treated mice were sacrificed, and tumors were denoted as vehicle. When tumors from the doxorubicin-treated group exhibited initial response to therapy and shrunk, tumors from some of the mice were collected and denoted as sensitive. The rest of the mice were kept under doxorubicin treatment until their tumors exhibited re-growth at rates comparable to vehicle-treated tumors, and those tumors were classified as resistant (Fig. 1a). The average growth curves and the Waterfall plot showing tumor volume fold change over time for vehicle-treated, doxorubicin-sensitive and -resistant tumors are depicted in Fig. 1b, c, respectively.

We performed RNA-sequencing (RNA-seq) on bulk tumors (four tumors from each group) to identify transcripts differentially expressed between doxorubicin-sensitive and -resistant tumors. We used the 441 most differentially expressed genes (fold change (FC) cut-off = 1.75, p-value < 0.05, Supplementary Data 1) to create a doxorubicin resistance gene signature (DoxoR-GS). We then tested its clinical relevance using gene expression profiling datasets of chemotherapy-treated TNBC patients (for details, see "Methods" section)[35]. Chemotherapy-treated TNBC patients from GSE58812[36] that have high DoxoR-GS scores exhibit poor overall survival (OS) as compared to those with low DoxoR-GS scores (Fig. 1d). These results were further confirmed using METABRIC dataset[37] (Supplementary Fig. 1a) and in another dataset (GSE31519) where we showed that expression of DoxoR-GS is significantly higher in patients who exhibit an event, described as either relapse- or distant metastasis (Supplementary Fig. 1b).

Having validated the clinical relevance of our in vivo-derived DoxoR-GS, we sought to identify the pathways that were most significantly represented among the differentially expressed genes. Ingenuity Pathway Analysis (IPA) revealed that integrin-linked kinase (ILK) signaling was the top deregulated pathway (Fig. 1e). Gene set enrichment analysis (GSEA) in chemotherapy-treated TNBC patients demonstrated that genes involved in focal adhesion signaling were significantly enriched in high DoxoR-GS scorers (Fig. 1f), underlining the importance of integrins and downstream focal adhesion in doxorubicin resistance.

Based on the RNA-seq analysis of our doxorubicin-resistant models, three integrin genes, *ITGA5*, *ITGA10* and *ITGB5* were significantly (FC cut-off = 1.5, p-value < 0.05) upregulated in resistant tumors (Fig. 1g and Supplementary Fig. 1c). We found that higher expression of only the integrin alpha 5 (ITGA5), but



not that of ITGA10 or ITGB5, is associated with shorter relapse-free survival (RFS) in chemotherapy-treated basal patients (Fig. 1h, i and Supplementary Fig. 1d, e). No such relationship was observed in patients with basal subtype of breast cancer who were not treated with chemotherapy or in patients with other subtypes (Fig. 1i). As around 70% of TNBCs are basal subtype, and 76% of basal subtype are TNBCs[38], we classified patients also as TNBC using ERα, PR, and HER2 expression and again observed a strong association between ITGA5 expression and RFS in chemotherapy-treated TNBC patients (Supplementary Fig. 2a). Importantly, we also detected a significant upregulation of fibronectin (FN1), the main ligand for ITGA5, in doxorubicin-

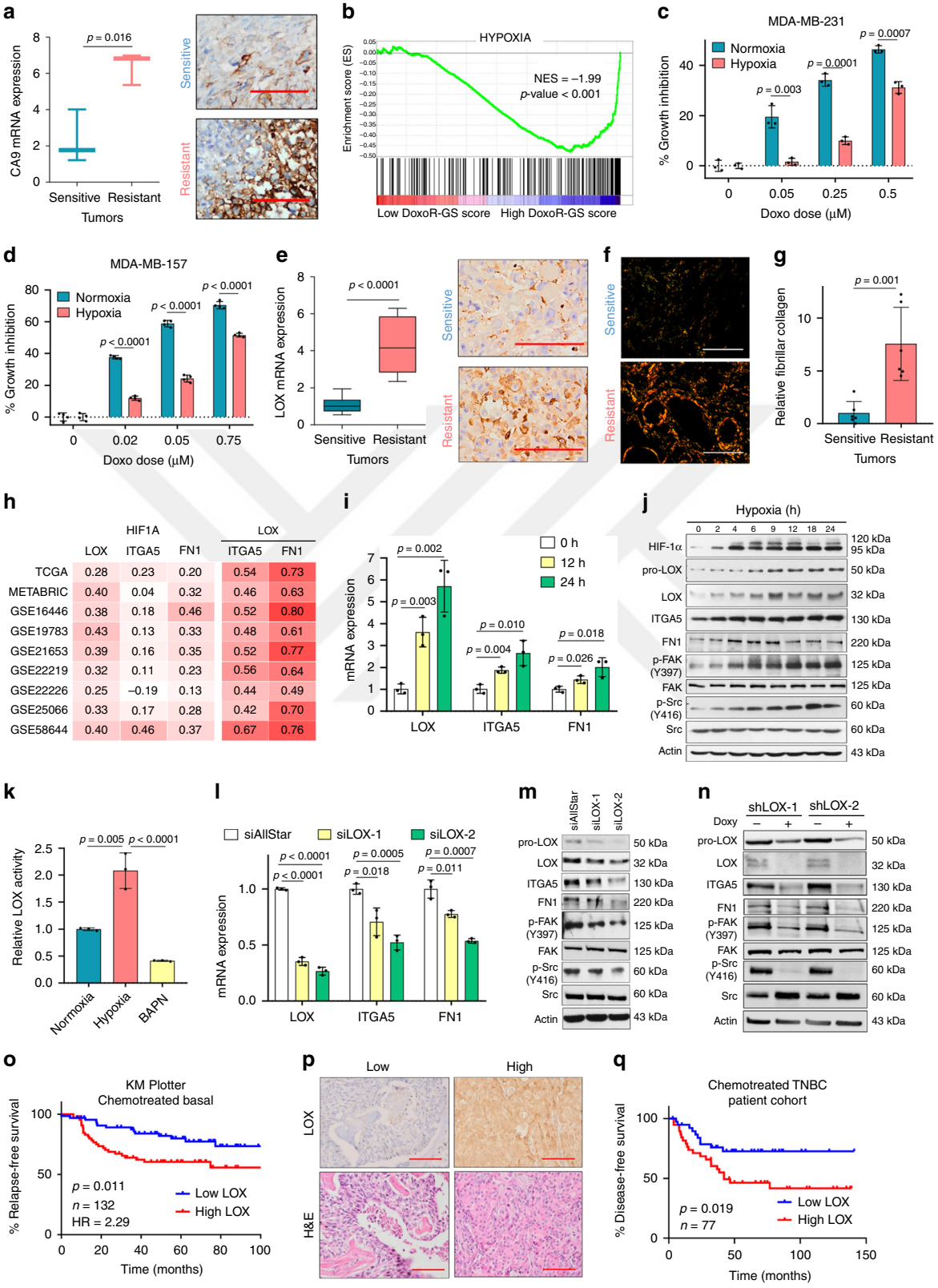
Fig. 1 Integrin signaling is a key mediator of chemoresistance in TNBCs. a Schematic representation of developing doxorubicin resistance in mice using the TNBC cell line, MDA-MB-231 (left panel). Tumor volume fold change (log2) of vehicle-treated, doxorubicin-sensitive and -resistant tumors (right panel). Clipart reprinted with permission from Springer Nature, *Nature Protocols*, FACS isolation of endothelial cells and pericytes from mouse brain microregions, Elizabeth E Crouch and Fiona Doetsch, Copyright 2018. **b** Tumor volumes of vehicle ($n = 8$), sensitive ($n = 12$) and -resistant ($n = 6$) tumors. **c** Waterfall plot of tumor volume fold change over time. Asterisk indicates tumors profiled by RNA-Seq. V vehicle; S sensitive; and R resistant. **d** Kaplan–Meier survival curve representing the percentage overall survival (OS) in chemotherapy-treated TNBC patients ($n = 106$) based on low vs. high (median) DoxoR-GS score. **e** Summary of IPA analysis showing top deregulated pathways in doxorubicin-resistant xenografts. **f** Genes associated with focal adhesion signaling are enriched in tumors of high DoxoR-GS scorers from GSE58812. **g** Expression of integrin alpha 5 (ITGA5) in doxorubicin-sensitive ($n = 8$) vs. -resistant ($n = 6$) xenografts at mRNA (left) and protein (right) levels, demonstrating membranous and cytoplasmic staining. **h** Kaplan–Meier survival curve representing the percentage relapse-free survival (RFS) in chemotherapy-treated basal patients ($n = 132$) based on low vs. high ITGA5 (median) expression. **i** Table summarizing association of ITGA5 with survival in patients of different subtypes that received or did not receive chemotherapy. **j** Expression of fibronectin (FN1) in doxorubicin-sensitive ($n = 12$) vs. resistant ($n = 12$) tumors at mRNA (left) and protein (right) levels, demonstrating mild to moderate cytoplasmic staining. **k** Kaplan–Meier survival curve representing the percentage RFS in chemotherapy-treated basal breast cancer patients ($n = 132$) based on low vs. high FN1 (median) expression. **l** Table summarizing association of FN1 with survival in patients of different subtypes that received or did not receive chemotherapy. Data on **b** represent mean ± SEM and all others represent mean ± SD. In Box plots, the box depicts median, 25th to 75th percentiles, and the whisker depicts min to max for this figure and all others. Two-sided Student's *t*-test was used to calculate statistical difference between two groups. Significance for survival analyses was calculated by log-rank (Mantel-Cox) test. NES Normalized enrichment score, HR hazard ratio. Scale bar = 100 μm for **g**, **j**. Source data are provided as a Source data file.

resistant tumors (Fig. 1j) and a significant association between high FN1 expression and poorer RFS in chemotherapy-treated basal patients (Fig. 1k, l). These results were further validated with another TNBC patient dataset (GSE58812) in which higher expression of either ITGA5 or FN1 is significantly associated with worse overall survival for the chemotherapy-treated TNBC patients (Supplementary Fig. 2b). Notably, when the patients are stratified based on ITGA5 and FN1 expressions in combination, a stronger separation of overall survival was achieved (Supplementary Fig. 2c, $p = 0.0008$; HR = 5.28). Altogether, these data suggest that deregulation of FN1-ITGA5 signaling could be a major driver of chemoresistance in TNBC.

Hypoxia-induced LOX hyperactivates ITGA5/FN1/FAK/Src axis. Hypoxia inducible factor-1 alpha (HIF-1α), encoded by the *HIF1A* gene, activates the transcription of several ECM-remodeling enzymes, including collagen prolyl and lysyl hydroxylases and lysyl oxidases thereby modulating ECM stiffness[39,40]. Importantly, our IPA analysis revealed a significant enrichment of HIF1A signaling in the doxorubicin-resistant tumors (Fig. 1e). Given the involvement of hypoxia in ECM remodeling[41,42], we hypothesized that HIF-1α could activate integrin and focal adhesion signaling. We first validated activation of the hypoxic response in chemoresistant tumors by demonstrating upregulation of the CA9 gene, which is a direct HIF-1α target gene and a well-established hypoxia marker[43]. CA9 mRNA and protein levels were significantly higher in resistant tumors (Fig. 2a). The induction of hypoxia signaling in the resistant tumors was not simply a result of an increase in tumor size, as there was no enrichment of hypoxia signaling in vehicle-treated tumors that are the largest in size vs. sensitive tumors (Supplementary Table 1). Furthermore, patients having high DoxoR-GS score also express high levels of hypoxia-related genes (Fig. 2b).

To experimentally demonstrate the acquisition of doxorubicin resistance under hypoxic conditions, we cultured MDA-MB-231 and MDA-MB-157 cells in normoxic vs. hypoxic conditions in the presence of increasing concentrations of doxorubicin. As shown in Fig. 2c, d, cells became less sensitive to growth inhibition induced by doxorubicin when grown under hypoxic conditions. Next, we performed Upstream Regulator analysis in IPA and found that 28 of 39 HIF-1α target genes had an expression direction consistent with the activation of HIF-1α (Supplementary Table 2). Among the actively transcribed genes upon HIF-1α activation during chemoresistance, we identified LOX, which is known to modulate ECM stiffness via collagen cross-linking and promote metastasis[44]. Upregulation of LOX in doxorubicin-resistant xenografts was validated by qRT-PCR and immunohistochemistry (Fig. 2e). While LOX, ITGA5, and FN1 mRNAs were upregulated between sensitive and resistant tumors under doxorubicin treatment, the fast-growing vehicle-treated tumors showed no upregulation of these genes, suggesting that their upregulation is specific to chemotherapy resistance (Supplementary Fig. 3a). Importantly, we demonstrated increased fibrillar collagen in resistant tumors compared to sensitive counterparts by picrosirius red staining (Fig. 2f, g). We then examined gene expression from 9 different breast cancer datasets and found correlation between *HIF1A* and *LOX*, *ITGA5*, and *FN1* mRNAs (Fig. 2h), supporting the upstream regulatory role of HIF1A in their transcription. Strikingly, the correlation of *LOX* with *ITGA5* and *FN1* mRNAs was the strongest among all pairs, even stronger than the correlation of these three genes with *HIF1A*. This suggested that hypoxia-induced LOX might specifically be regulating *ITGA5* and *FN1* expression, and the subsequent activation of intracellular downstream signaling could be contributing to doxorubicin resistance. Consistent with this, we detected a significant enrichment of hypoxia and focal adhesion signaling gene sets in tumors with high LOX expression (GSE58812[36], Supplementary Fig. 4a, b).

To test whether hypoxia can induce both LOX expression and integrin signaling, we cultured MDA-MB-231 cells under hypoxia for different time points and observed a prominent increase in HIF-1α protein stability that was followed by a coordinated upregulation of LOX, ITGA5 and FN1 mRNAs and protein levels (Fig. 2i, j). Hypoxia also resulted in activation of integrin signaling as shown by incases in p-FAK (Y397) and p-Src (Y416) (Fig. 2j). Moreover, LOX enzymatic activity was higher under hypoxia as compared to normoxia, potentially due to increased LOX expression (Fig. 2k). Here, BAPN, a LOX family inhibitor, was used as a negative control. The induction of LOX/ITGA5/FN1 and downstream signaling under hypoxic conditions has also been validated in another TNBC cell line, MDA-MB-157 (Supplementary Fig. 4c). Silencing LOX expression using two different siRNA sequences caused a LOX expression-dependent decrease in both ITGA5 and FN1 mRNA (Fig. 2l) and protein levels (Fig. 2m) together with attenuated downstream signaling (Fig. 2m). Moreover, stable and inducible knockdown of LOX with shRNAs also validated the inhibition of downstream signaling (Fig. 2n). These data strongly support a model in which LOX-mediated upregulation of ITGA5 and its ligand, FN1 play a role in hypoxia-mediated hyperactivation of integrin signaling.



To determine the clinical relevance of LOX expression in chemotherapy-treated TNBCs, we performed survival analyses and observed that higher *LOX* mRNA expression predicts poor RFS only in chemotherapy-treated basal breast cancer patients, but not in other breast cancer subtypes or in untreated cases (Fig. 2o and Supplementary Fig. 2d). Furthermore, in the GSE31519 dataset we observed that more than half of the patients that exhibit event, described as either a relapse or distant metastasis, express higher LOX levels (p-value = 0.012) (Supplementary Fig. 5a). Similarly, in another dataset (GSE25066), we observed that a significantly higher proportion of chemotherapy-treated TNBC patients with residual disease (RD) express higher levels of LOX (p-value = 0.011) (Supplementary Fig. 5b). Furthermore, TNBC patients with RD express significantly higher levels

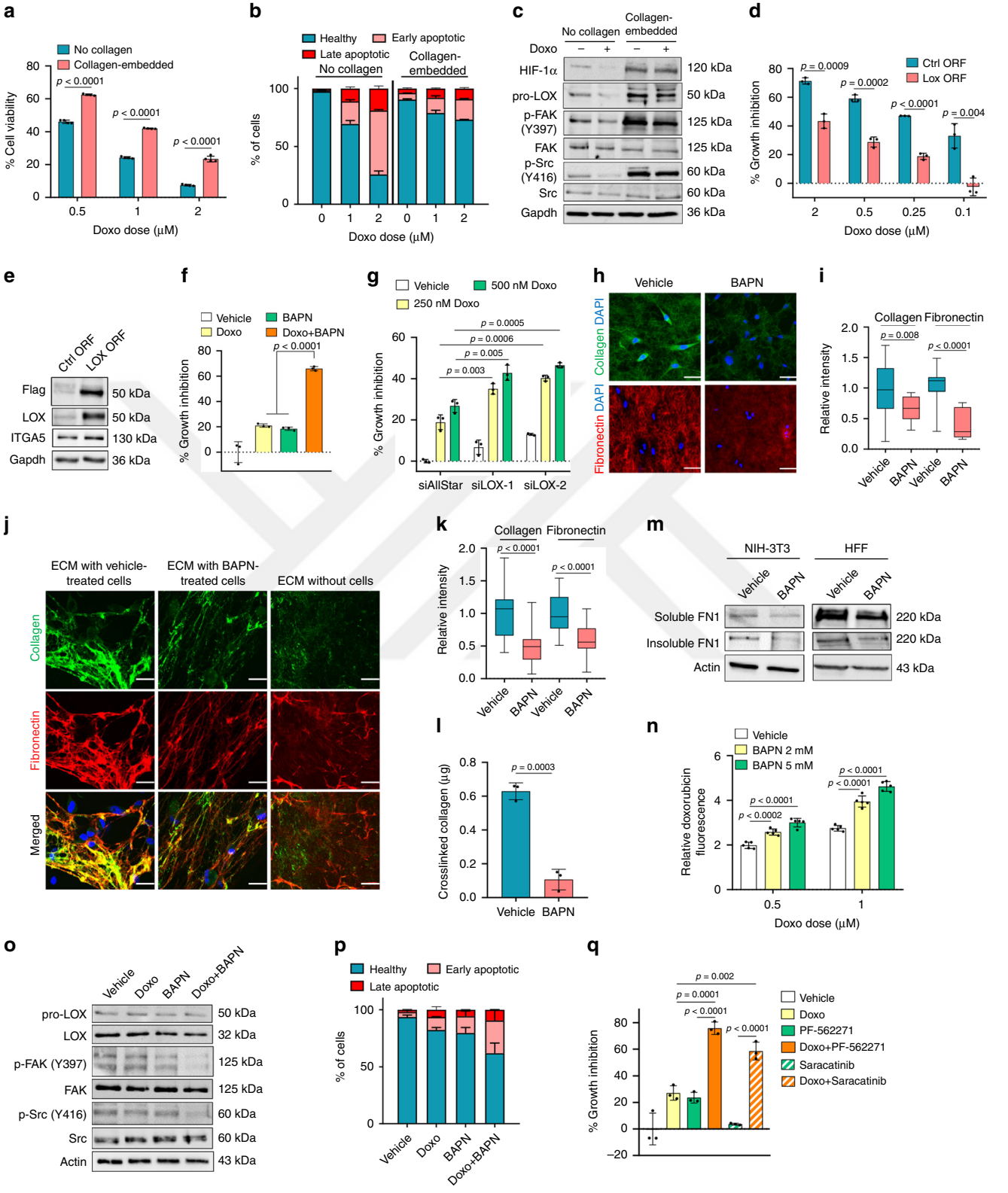
Fig. 2 Hypoxia-induced LOX hyperactivates ITGA5/FN1/FAK/Src axis in TNBCs. a Expression of a HIF-1α direct target gene, carbonic anhydrase 9 (CA9) in sensitive ($n = 3$) vs. resistant ($n = 3$) tumors at mRNA (left) and protein (right) levels, demonstrating predominantly membranous and mild cytoplasmic staining. **b** Genes upregulated upon hypoxia are enriched in patients with high DoxoR-GS score from GSE58812 ($n = 106$). **c**, **d**. % growth inhibition upon doxorubicin treatment of MDA-MB-231 (**c**) ($n = 3$) and MDA-MB-157 (**d**) ($n = 4$) cells grown under normoxic vs. hypoxic conditions. **e** Expression of LOX in sensitive ($n = 12$) vs. resistant ($n = 9$) tumors at mRNA (left) and protein (right) levels, demonstrating strong cytoplasmic and weak nuclear staining. **f**, **g** Representative images of Picrosirius red staining (**f**) and its quantification (**g**) ($n = 6$). **h** Heatmap summarizing the Pearson's correlation coefficients between *HIF1A* and *LOX*, *ITGA5* or *FN1* and between *LOX* and *ITGA5* or *FN1* in breast cancer patients. An intense red color shows a stronger positive correlation. **i** qRT-PCR analysis of *LOX*, *ITGA5*, and *FN1* under hypoxia ($n = 3$). **j** Western blot analyses of HIF-1α, LOX and integrin signaling members under hypoxia. **k** Relative LOX activity in MDA-MB-231 cells under hypoxia. BAPN was used as a negative control ($n = 3$). **l** qRT-PCR analysis of *LOX*, *ITGA5*, and *FN1* after transfection with siAllStar or siLOX ($n = 3$). **m**, **n** Western blot analyses in MDA-MB-231 cells transfected with siAllStar or siLOX (**m**) and after shLOX induction with doxycycline (**n**). **o** Kaplan–Meier survival curve representing the percentage RFS in chemotherapy-treated basal breast cancer patients ($n = 132$) separated based on low vs. high (median) LOX mRNA. **p** IHC images of TNBC patient tissues with low and high LOX protein expression. **q** Kaplan–Meier survival curve representing DFS in chemotherapy-treated TNBC patients ($n = 77$) separated from median based on LOX protein expression. Data represents mean ± SD. Two-sided Student's *t*-test was used to calculate statistical difference between two groups. Significance for survival analyses was calculated by log-rank (Mantel-Cox) test. NES Normalized enrichment score, HR hazard ratio. Scale bar = 100 μm for **a**, **e**, and **p**, and 400 μm for **f**. Source data are provided as a Source data file.

of LOX, ITGA5 and FN1 (Supplementary Fig. 5c–e). Importantly, we stained for LOX protein expression in tissues (Fig. 2p, Supplementary Table 3). In 77 TNBC patients treated with chemotherapy, we showed that higher LOX protein levels were significantly associated with worse disease-free survival (DFS) (p-value = 0.019, Fig. 2q). Although other LOX family members (LOXL1-4) have also been reported to be regulated by HIF-1α[45], none of them were significantly altered in doxorubicin-resistant xenografts (Supplementary Fig. 3b). Altogether, these data are consistent with a model in which hypoxia-induced LOX activates integrin signaling by upregulating ITGA5 and FN1, leading to poor survival and chemoresistance in TNBC patients.

LOX inhibition remodels ECM to confer chemosensitization. To test the potential role of LOX in mediating chemoresistance in TNBCs and elucidating the underlying mechanisms, we first embedded TNBC cells into a matrix of type I collagen, the major substrate of LOX, and demonstrated acquisition of resistance to doxorubicin in two different cell lines (Fig. 3a and Supplementary Fig. 4d) which was accompanied by protection against apoptosis (Fig. 3b and Supplementary Fig. 6a–c) and sustained levels of p-FAK and p-Src (Fig. 3c). Western blot analysis also demonstrated a decrease in HIF-1α expression and subsequently LOX levels upon doxorubicin treatment but only in cells cultured in the absence of collagen (Fig. 3c). Overexpressing LOX in MDA-MB-231 cells that were embedded in type I collagen conferred resistance to doxorubicin (Fig. 3d). Overexpression of LOX also caused a modest increase in ITGA5 protein levels (Fig. 3e). Analysis of LOX expression in a panel of breast cancer cell lines demonstrated that TNBC cells express relatively higher levels of LOX (Supplementary Fig. 7a). Importantly, inhibiting LOX using a LOX family inhibitor, BAPN in combination with doxorubicin in three different collagen I-embedded TNBC cell lines re-sensitized them to doxorubicin (Fig. 3f, Supplementary Fig. 7b). As BAPN is known to inhibit other LOX family members as well, we further confirmed the doxorubicin sensitization with LOX inhibition using two different siRNA sequences against LOX (Fig. 3g). Importantly, doxorubicin sensitization by LOX inhibition was specific to TNBC models. ERα+ cells express relatively low levels of LOX, and LOX inhibition did not lead to chemosensitization (Supplementary Fig. 7a, c). Finally, LOX inhibition sensitizes cells to two other DNA-damaging chemotherapy agents, epirubicin and paclitaxel (Supplementary Fig. 7d), which are common therapeutic options for TNBC patients[46].

To elucidate the mechanistic details of how LOX inhibition sensitizes TNBC cells to doxorubicin, we first examined the changes in ECM remodeling upon LOX inhibition. It has been reported that there is a molecular co-dependence between collagen cross-linking and fibronectin fibril assembly that causes reciprocal activation of both processes to ultimately increase ECM stiffness[47,48]. In addition, cell-mediated processes, such as binding of cell surface integrins to fibronectin dimers and subsequent recruitment of FAK to focal adhesion sites can trigger fibronectin fibrillogenesis[49–51]. We observed that both ITGA5 and FN1 expression, and subsequent FAK phosphorylation were dependent on LOX expression (Fig. 2). We therefore hypothesized that both collagen cross-linking (by LOX) and fibronectin deposition and assembly would be hindered by LOX inhibition. To test this hypothesis, we performed immunofluorescence staining of collagen and fibronectin in type I collagen-embedded MDA-MB-231 cells with and without LOX inhibition, and observed that TNBC cells are able to deposit large amounts of fibronectin into an ECM that is rich in collagen type I (Fig. 3h), and that LOX inhibition with BAPN decreased the extracellular deposition and assembly of fibronectin fibrils (Fig. 3h) and decreased overall extracellular fibrillar collagen content (Fig. 3i). This was validated using a cell-derived ECM system produced by human foreskin fibroblast (HFF) cells, better recapitulating the dynamics of ECM formation and stabilization. Growing cancer cells on fibroblast-derived ECM induced the formation of thick, cross-linked collagen fibers, as opposed to non-fibrillar, immature collagen in the ECM deposited in the absence of cancer cells (Fig. 3j). When LOX was inhibited with BAPN, we detected a significant decrease in the immunofluorescence staining intensities of both collagen and fibronectin, suggesting that cancer cell-derived LOX is required for the cross-linking of extracellular collagen into thick fibers and the subsequent fibronectin assembly during ECM maturation (Fig. 3k). Co-localization analysis demonstrated that almost half of the collagen fibers were in contact with fibronectin (similar to previous reports[47,48]), but co-localization was decreased by LOX inhibition (Supplementary Fig. 8a). Analysis of 3D images of vehicle and BAPN-treated cells cultured on top of HFF-derived ECM further demonstrated that cells are still in contact with the ECM even though LOX inhibition decreased the extracellular collagen and fibronectin content (Supplementary Fig. 8b, c). The decrease in collagen cross-linking and fibronectin assembly upon LOX inhibition was also validated by biochemical measurement of extracellular hydroxyproline content (Fig. 3l) and deoxycholate (DOC) lysis (Fig. 3m), respectively, which are standard methods used to assess the amount of collagen cross-linking and fibronectin deposition and assembly[52].

It has been proposed that LOX may reduce drug penetration under hypoxic conditions and lessen the cytotoxicity of chemo-agents in 3D collagen cultured cells and tumor models[53].



We showed that doxorubicin decreased the activation of FAK/Src signaling in 2D-cultured cells, but not in 3D collagen culture (Fig. 3c). Therefore, we tested if targeting LOX could increase doxorubicin penetration and decrease FAK/Src signaling, leading to apoptosis. To assess drug penetration, we quantified doxorubicin autofluorescence (ex: 495 nm, em: 595 nm[54]) and observed a significant increase in intracellular doxorubicin in combination-treated cells (Fig. 3n). This was accompanied by a decrease in FAK/Src phosphorylation (Fig. 3o) and induction of apoptosis (Fig. 3p and Supplementary Fig. 6d–g). Finally, we treated collagen-embedded cells with doxorubicin with and without inhibitors specific for FAK (PF-562271) or Src (Saracatinib) and observed a synergistic increase in growth inhibition (Fig. 3q), decreased phosphorylation of FAK and Src (Supplementary Fig. 9a), and induced apoptotic cell death (Supplementary Fig. 9b, c).

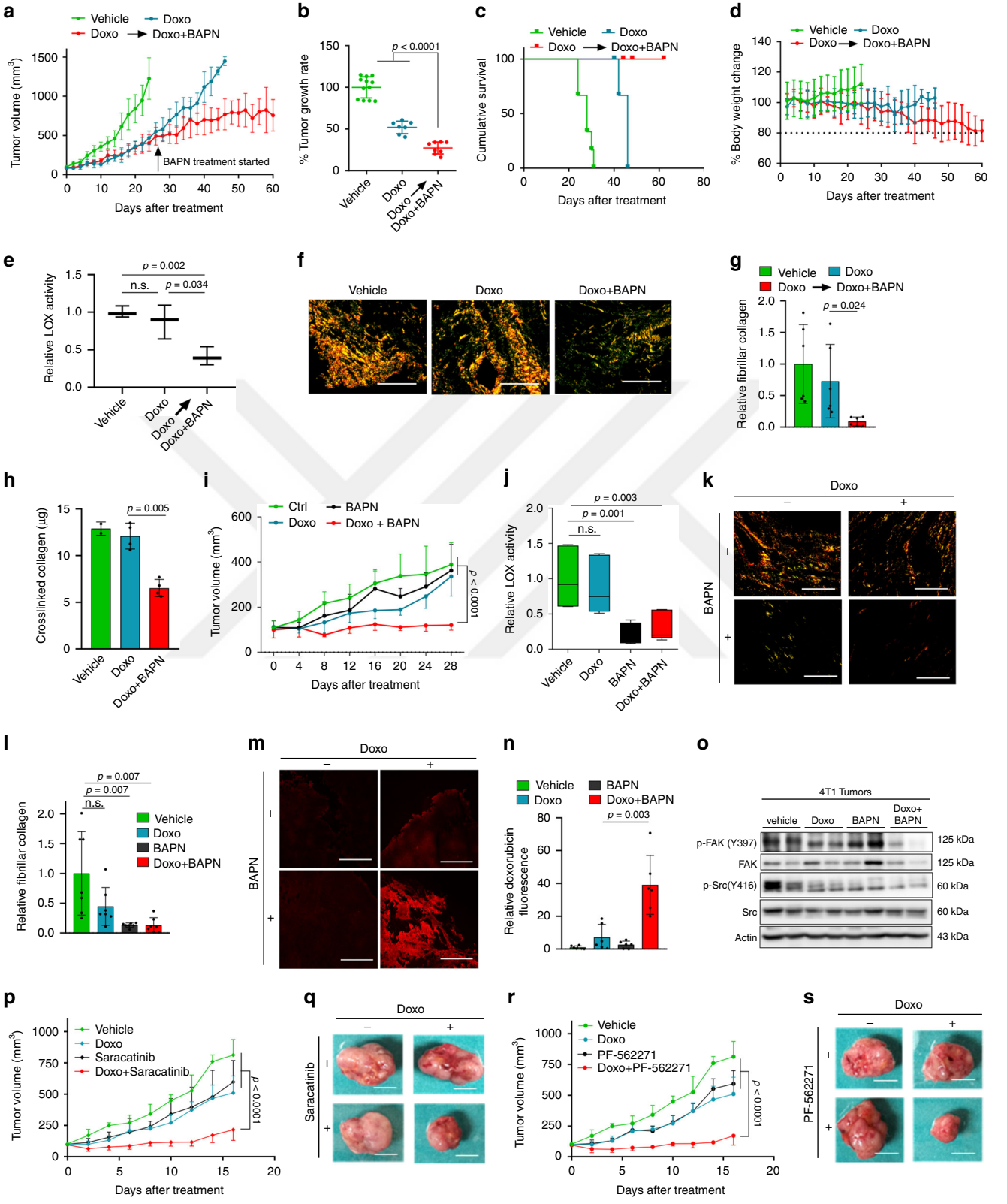
Fig. 3 LOX inhibition remodels ECM to confer chemosensitization in TNBCs. a Doxorubicin response of MDA-MB-231 cells cultured with or without type I collagen for 72 h ($n = 4$). **b** Apoptosis assay by Annexin V/DAPI staining from a ($n = 2$). **c** Western blot analysis in doxorubicin-treated cells grown with or without type I collagen. **d** Percentage growth inhibition in LOX-overexpressing cells embedded in collagen upon doxorubicin treatment ($n = 3$). **e** Western blot analyses upon LOX overexpression in MDA-MB-231 cells. **f**, **g** Percentage growth inhibition of collagen-embedded MDA-MB-231 cells treated with BAPN (**f**) or transfected with siLOX (**g**) in combination with doxorubicin ($n = 3$). **h**, **i** Immunofluorescence staining (**h**) and quantifications of the intensities (**i**) of extracellular type I collagen and fibronectin upon treatment of collagen-embedded cells with BAPN ($n = 18$ (vehicle), $n = 15$ (BAPN) for collagen, and $n = 18$ (vehicle), $n = 12$ (BAPN) for fibronectin). **j**, **k** Immunofluorescence staining (**j**) and quantifications of the intensities (**k**) of HFF-derived type I collagen and fibronectin incubated with vehicle or BAPN-treated MDA-MB-231 cells. ECM without cells represents the staining in the absence of MDA-MB-231 cells ($n = 29$ (vehicle), $n = 25$ (BAPN)). **l** Amount of cross-linked collagen in HFF-derived ECM incubated with vehicle- vs. BAPN-treated MDA-MB-231 cells ($n = 3$ different wells). **m** Western blot of soluble and insoluble FN1 obtained by deoxycholate lysis of NIH3T3- and HFF-derived ECM in contact with vehicle- vs. BAPN-treated MDA-MB-231 cells. **n** Changes in relative doxorubicin fluorescence upon BAPN-treatment in MDA-MB-231 cells embedded in type I collagen ($n = 5$). **o** Western blot analysis of LOX and FAK/Src signaling in collagen type I-embedded MDA-MB-231 cells upon doxorubicin and BAPN treatment for 24 h. **p** Annexin V/DAPI staining upon combination treatment for 72 h ($n = 2$). **q** Percentage growth inhibition induced by the combination of doxorubicin with FAK (PF-562271) or Src (Saracatinib) inhibitors in MDA-MB-231 cells embedded in type I collagen ($n = 3$). Data represents mean ± SD. Two-sided Student's *t*-test was used to calculate statistical difference between two groups. One-way ANOVA with Dunnett's test was performed to compare mean of combination-treated group with single agent treatments in **f**, **q**. Scale bar = 50 μm for **h**, **j**. Source data are provided as a Source data file.

Targeting LOX or FAK/Src overcomes chemoresistance in vivo. To test if inhibiting LOX could overcome doxorubicin resistance and enhance drug response in advanced, chemotherapy-refractory TNBCs, we re-derived doxorubicin resistance in vivo, using a protocol similar to our initial acquired resistance model (though with lower doxorubicin dose), by treating MDA-MB-231 xenografts with doxorubicin until an accelerated tumor growth was achieved despite the given therapy. At this point, some of the doxorubicin-resistant tumors were treated with the combination of doxorubicin and BAPN while the rest continued to receive doxorubicin alone. Strikingly, addition of LOX inhibitor to doxorubicin in these aggressive, fast-growing doxorubicin-resistant tumors led to a significant decrease in tumor growth rate (Fig. 4a, b) and improved survival (Fig. 4c) until experiment termination when the tumor volume cut-off was reached or due to almost a 20% decrease in body weight in BAPN-added treatment arm (Fig. 4d). We confirmed the reduction of LOX activity (Fig. 4e) and fibrillar collagen (Fig. 4f, g) upon addition of BAPN to doxorubicin. These results were further validated by performing biochemical collagen assay (Fig. 4h), suggesting that chemosensitization with LOX inhibition involves reduction in collagen cross-linking.

We also evaluated the effects of LOX inhibition on doxorubicin response in vivo in an immunocompetent setting using a syngeneic TNBC model. The 4T1 mouse mammary tumor cell line is a highly aggressive model that represents the TNBC subtype[55] and exhibits relatively low response to doxorubicin. We examined the expression of LOX in 4T1 cells grown in vitro as well as in tumors and found that they express LOX at a level similar to the high LOX-expressing MDA-MB-231 model (Supplementary Fig. 10a, b). We observed a strong inhibitory effect of the combination therapy on tumor growth in this immunocompetent tumor model (Fig. 4i and Supplementary Fig. 10c, d). The LOX activity assay and picrosirius red staining confirmed the suppression of LOX activity and collagen cross-linking, respectively in all BAPN-treated tumors (Fig. 4j–l). This was accompanied by increased penetration of doxorubicin (Fig. 4m, n) and inhibition of FAK/Src signaling in the combination-treated tumors (Fig. 4o). To test the effect of FAK or Src inhibition on doxorubicin response in vivo, we combined specific inhibitors of FAK (PF-562271) or Src (Saracatinib) with doxorubicin and observed a significant decrease in tumor growth (Fig. 4p–s) and tumor weight (Supplementary Fig. 10e, f) in combination-treated tumors, validating the key roles of FAK and Src in doxorubicin resistance.

Next, we tested combination of LOX inhibition with doxorubicin in a highly aggressive TNBC PDX model. We first analyzed the gene expression profiling and drug response data of 15 well-characterized TNBC PDX models (Jackson Lab) and observed a significant positive correlation between LOX expression and hypoxia and focal adhesion scores (Fig. 5a). Based on these analyses, we selected a TNBC PDX model (TM01278) that is resistant to doxorubicin (and several other chemotherapy agents) and expresses high levels of LOX, hypoxia and focal adhesion scores (Fig. 5a). Then, we generated organoid cultures of this doxorubicin-resistant PDX tumor and demonstrated that combination of LOX inhibitor with doxorubicin significantly decreased organoid size compared to single agent treatments after 9 days of treatment (Fig. 5b, c). In vivo testing also showed a significant decrease in tumor growth upon combination therapy in this chemoresistant PDX model expressing LOX (Fig. 5d–f). These results complement our in vitro and in vivo findings with established cell lines and increase the clinical relevance of LOX inhibition to overcome chemotherapy resistance in TNBC. Importantly, we demonstrated reduced LOX activity (Fig. 5g) and fibrillar collagen content upon LOX inhibition with BAPN (Fig. 5h, i), which was accompanied by enhanced drug penetration into tumors (Fig. 5j, k) and more effective down-regulation of downstream FAK/Src signaling in combination-treated tumors (Fig. 5l). Overall, we demonstrated that targeting LOX or its downstream FAK/Src overcomes chemotherapy resistance in highly aggressive, chemoresistant TNBC models.

Targeting LOX at the first-line potentiates chemoresponse. Having identified LOX as a determinant of chemoresistance in TNBC, we tested whether LOX is also a target in potentiating chemotherapy response in first-line settings in treatment-naïve models using our inducible shLOX expressing MDA-MB-231 derivatives (referred to 231.shLOX) (Supplementary Fig. 11a, b). Inhibiting LOX in combination with doxorubicin as a first-line therapy led to a stronger delay in tumor growth as compared to individual treatments (Fig. 6a–e). We confirmed LOX knockdown at mRNA (Fig. 6f) and protein levels (Fig. 6g, h) and the decrease in LOX activity (Supplementary Fig. 11c) together with down-regulation of its downstream ITGA5 (Supplementary Fig. 11d) after tumors were collected. We also demonstrated that other LOX family members did not decrease upon LOX knockdown (Supplementary Fig. 11e, f), further supporting our hypothesis that LOX inhibition is specifically involved in mediating chemoresponse in TNBCs. In consistent with the reduction in tumor growth, there was also a significant reduction in the proliferation marker, Ki-67 (Fig. 6i, j) and an increase in the expression of an apoptosis marker, Cleaved Caspase-3 (Fig. 6k, l) in combination-



treated group as compared to LOX inhibition or doxorubicin treatment alone. Furthermore, ITGA5 levels, phosphorylation of Src (p-Y416) and FAK (p-Y397) were reduced upon LOX knockdown in combination with doxorubicin (Fig. 6m–q).

Next, we examined the effect of combination therapy on the growth of a primary organoid model developed from a treatment-naïve TNBC patient. Combination treatment with doxorubicin and BAPN led to a significant reduction in organoid size as compared to individual treatment groups after 9 days of treatment (Fig. 6r, s). Altogether, these data demonstrate that inhibition of LOX could be a potential therapeutic strategy in combination with first-line chemotherapy in TNBCs.

Fig. 4 Targeting LOX or downstream FAK/Src overcomes TNBC chemoresistance in vivo. a Tumor growth in MDA-MB-231 xenografts treated with doxorubicin until resistance develops followed by treatment with the combination of doxorubicin (2.5 mg/kg) and the LOX inhibitor, BAPN (100 mg/kg) ($n = 12$, 7, and 8 tumors for vehicle, Doxo and Doxo+BAPN, respectively). **b** Tumor growth rates relative to vehicle from **a**. **c** Cumulative survival of mice from a. Mice were sacrificed when the tumor size cut-off was reached or when the body weight dropped to 80% of the initial body weight ($n = 6$, 4, and 4 mice for vehicle, Doxo and Doxo + BAPN, respectively). **d** Percentage change in the body weight of the mice from **c**. **e** Relative LOX activity in tumors from a ($n = 3$). **f** Representative images of Picrosirius red staining (f) and its quantification (**g**), in tumors from a ($n = 6$). **h** In vivo collagen assay in tumors from a ($n = 2$ (vehicle), $n = 4$ (Doxo, Doxo+BAPN)). **i** Tumor growth in 4T1 syngeneic model upon treatment with doxorubicin and BAPN, alone or in combination ($n = 4$ mice). **j** LOX activity in tumors from **i** ($n = 6$). **k**, **l** Representative images of Picrosirius red staining (k) and its quantification (l) in mice from i ($n = 7$). **m**, **n** Intratumoral doxorubicin levels upon treatment with the combination of doxorubicin and BAPN ($n = 6$). **o** Western blot analysis of FAK/Src signaling in combination-treated tumors from **i**. **p**, **q** Change in tumor growth (**p**) and representative images of tumors (**q**) in 4T1 model upon treatment with doxorubicin and Saracatinib, alone or in combination ($n = 4$). **r**, **s** Change in tumor growth (**r**) and representative images of tumors (**s**) in 4T1 model upon treatment with doxorubicin and PF-562271, alone or in combination ($n = 4$). Data represents mean ± SD. Two-sided Student's *t*-test was used to calculate statistical difference between two groups. Two-way ANOVA test was performed for comparing tumor growth over time among different treatment groups in **i**, **p**, and **r**. n.s. not significant. Scale bar = 400 μm for **f**, **k**; 200 μm for **m**, and 1 cm for **q**, **s**. Source data are provided as a Source data file.

miR-142-3p is a chemosensitizer regulating HIF1A/LOX/ITGA5. To elucidate the underlying molecular mechanisms of the coordinated activation of the HIF1A/LOX/ITGA5 axis under hypoxia, we sought for a common modulator. As miRNAs tend to function in a pathway-centric manner by targeting multiple genes in the same cascade[56], we searched for a potential miRNA modulator of HIF1A/LOX/ITGA5-mediated chemotherapy resistance. We examined all conserved miRNAs targeting *HIF1A*, *LOX*, and *ITGA5* and found eight common miRNAs having binding sites in the 3′-UTRs of these three genes (Fig. 7a). Out of these eight miRNAs, only two miRNAs, miR-142-3p, and miR-128-3p, showed an inverse correlation with HIF1A signature, and LOX and ITGA5 expression in basal subtype (Fig. 7b and Supplementary Fig. 12a–c). One of these two miRNAs, miR-142-3p, showed a significant association with OS specifically in chemotherapy-treated TNBC patients (Fig. 7c, d and Supplementary Fig. 12d). Furthermore, miR-142-3p was significantly downregulated in doxorubicin-resistant xenografts that we developed in vivo as compared to sensitive ones (Fig. 7e). Importantly, induction of hypoxia inhibited the expression of miR-142-3p (Fig. 7f), while silencing HIF1A upregulated miR-142-3p expression (Fig. 7g), suggesting that hypoxia-mediated downregulation of miR-142-3p potentially involves HIF1A.

We next tested to see if miR-142-3p could inhibit the expression of *HIF1A*, *LOX* or *ITGA5*. We overexpressed miR-142-3p in MDA-MB-231 cells and observed a significant downregulation of all three genes both at mRNA and protein levels, and a reduction in phosphorylation of downstream FAK/Src kinases (Fig. 7h, i). Importantly, downregulation of HIF1A, LOX and ITGA5 protein levels as well as decreased phosphorylation of FAK and Src was also seen in MDA-MB-231 xenografts stably expressing miR-142-3p (Fig. 7j and Supplementary Fig. 12e). The direct binding of miR-142-3p to the predicted binding sites in the 3′-UTRs of *HIF1A*, *LOX*, and *ITGA5* (Fig. 7k) was validated by a dual luciferase assay (Fig. 7l). Finally, ectopic expression of miR-142-3p in TNBC cells grown in type I collagen sensitized to doxorubicin-induced growth inhibition and apoptotic cell death (Fig. 7m–p). We interpret these results to indicate that HIF1A and miR-142-3p are involved in a double-negative feedback loop that further increases HIF1A, LOX and ITGA5 levels under hypoxic conditions, leading to chemoresistant tumors, and that overexpression of miR-142-3p overcomes chemoresistance by inhibiting HIF1A/LOX/ITGA5 axis.

Discussion

TNBC is the most aggressive subtype of breast cancer and is responsible for 30% of all breast cancer deaths. Chemotherapy is the mainstay treatment for TNBCs; however, resistance is common, significantly decreasing long-term survival[6]. Therefore, novel strategies are urgently needed to enhance the clinical benefit from chemotherapy. Here, we identified a mechanism of chemotherapy resistance that involves activation of the HIF1A/miR-142-3p/LOX/ITGA5/FN1 axis in TNBCs. We showed that inhibiting LOX reduces the expression of ITGA5 and FN1, decreases extracellular collagen cross-linking, fibronectin deposition/assembly and enhances drug penetration that ultimately result in inhibition of FAK/Src signaling, resulting in apoptosis and reversal of chemotherapy resistance in TNBC cells cultured in contact with ECM (Fig. 3). These results were validated in acquired resistant TNBC xenografts and de novo resistant 4T1 syngeneic TNBC model (Fig. 4) as well as in well-characterized chemoresistant TNBC PDXs (Fig. 5). We also showed that targeting LOX potentiates chemotherapy in first-line settings (Fig. 6). Importantly, targeting the signaling molecules downstream of LOX, FAK or Src, strongly sensitized cancer cells to chemotherapy when grown in collagen-embedded cultures or in vivo, showing the key role of these pro-survival signals in driving resistance (Fig. 4). Finally, we showed a double-negative feedback loop between HIF1A and miR-142-3p regulating HIF1A/LOX/ITGA5/FAK/Src axis and chemoresistance in TNBC (Fig. 7).

The ECM re-modeler, LOX is a well-known modulator of cancer metastasis[29,44]. LOX secretion from hypoxic tumors leads to collagen cross-linking at the pre-metastatic site and increases lung metastasis in TNBC models[28]. Moreover, higher LOX expression was observed in metastatic brain tumors of breast cancer patients[57]. Furthermore, Baker et al. demonstrated that LOX increases cell proliferation and invasion in colorectal cancer via Src activation[58] and enhances matrix stiffness, activates FAK, leading to invasion in vitro and metastasis in vivo in colorectal cancer[59]. In terms of the potential effects of LOX on drug response, a few studies have reported an involvement of LOX in drug resistance that primarily focused on altered distribution/penetration of chemotherapeutics, including paclitaxel and gemcitabine in tumors as a consequence of LOX-mediated ECM stiffness under hypoxic conditions[30,53]. In addition to forming a physical barrier, LOX-mediated ECM stiffness can also confer resistance via activating integrin receptors and the downstream effectors, FAK and Src kinases, leading to increased cellular survival[60]. For instance, Miller et al. demonstrated that combination of a LOX antibody with gemcitabine improved survival of a pancreatic ductal adenocarcinoma (PDAC) model via inhibiting key microenvironment-mediated pro-survival signals without any evidence of increased penetrance of gemcitabine into tumors upon LOX inhibition[31] in contrast to the studies described above[30,53]. Furthermore, it was recently shown that LOX might also be involved in transcriptional regulation of certain genes[61]. In our study, we showed that LOX

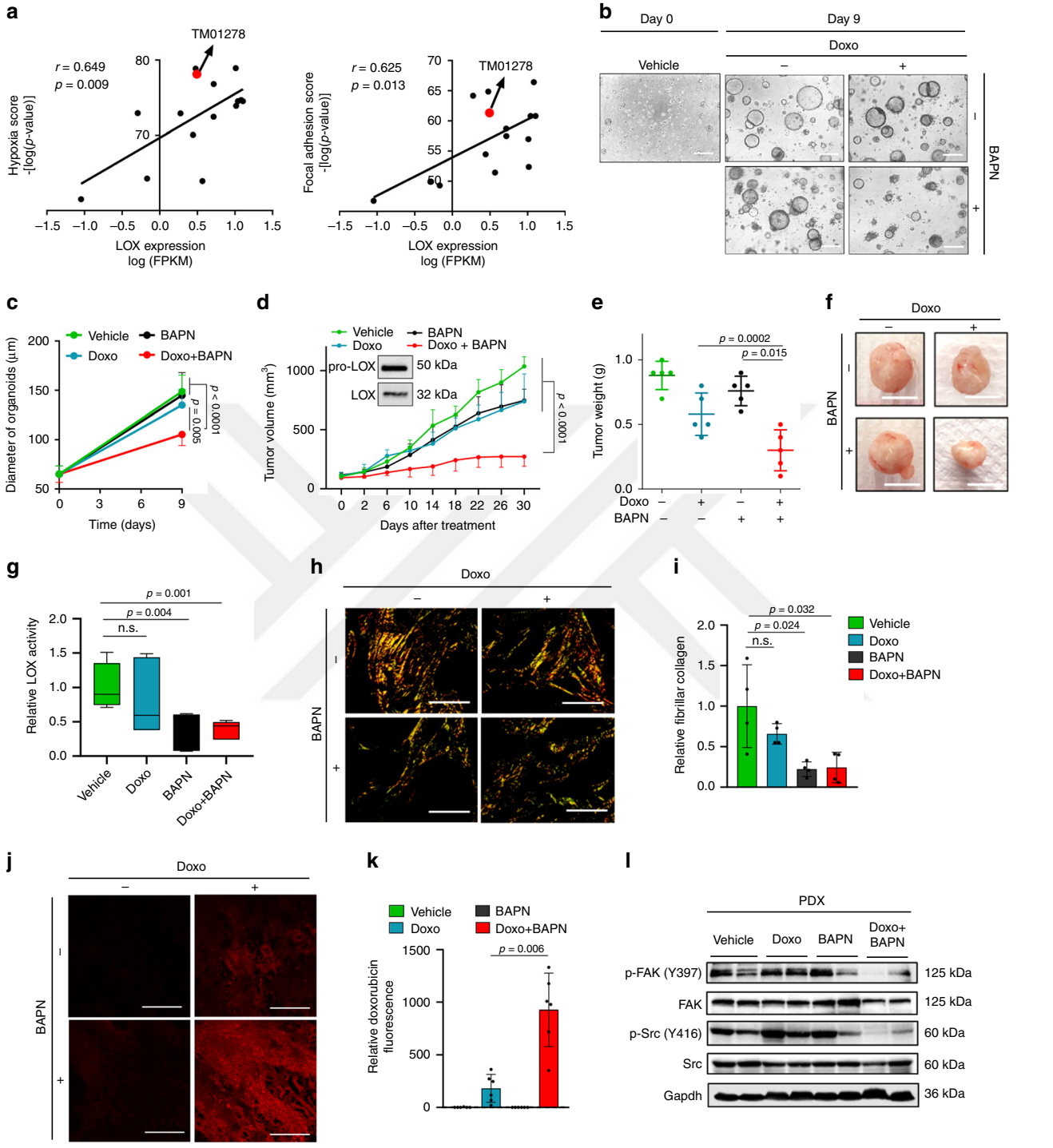
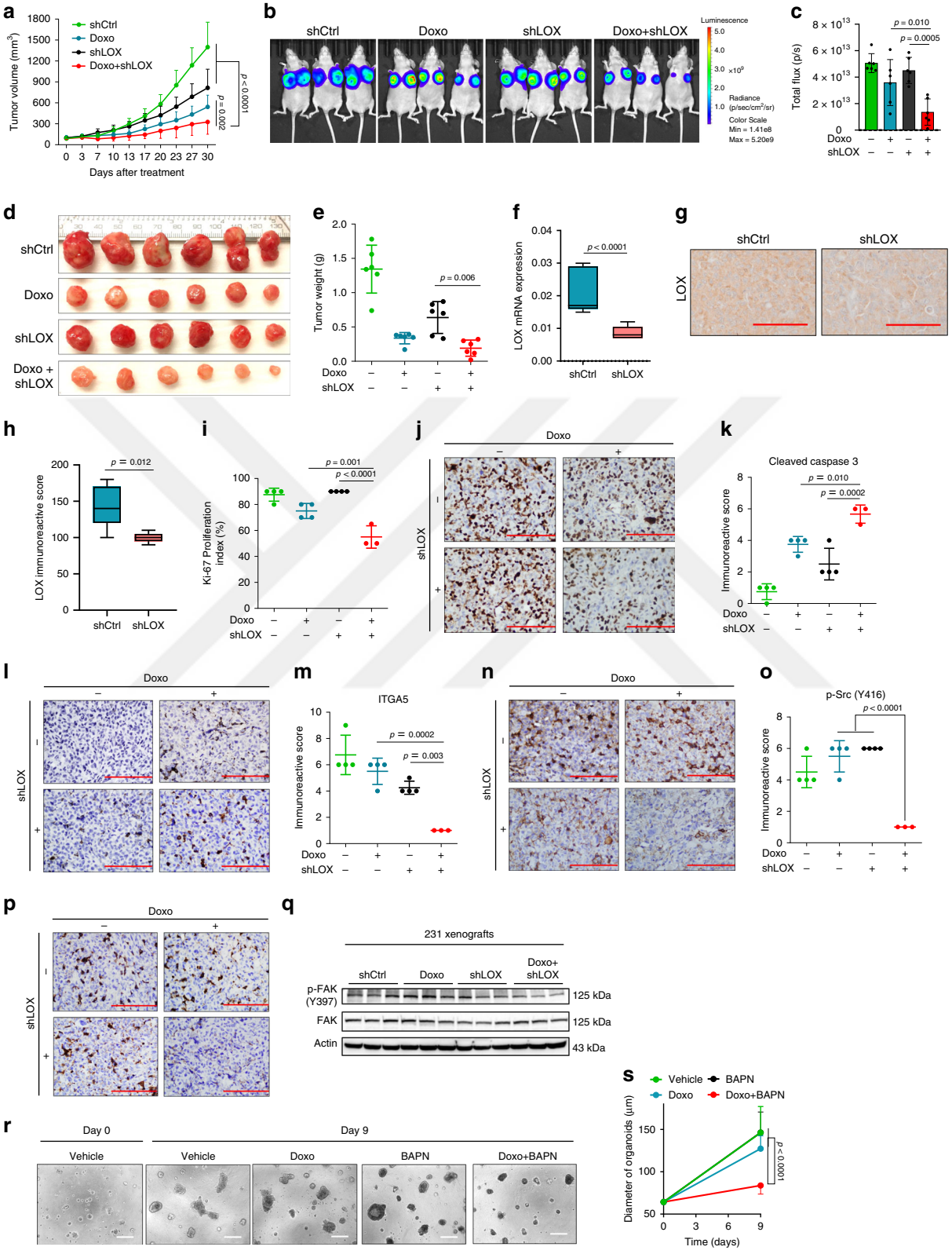


Fig. 5 Targeting LOX overcomes chemoresistance in highly aggressive TNBC PDXs. a Correlation analysis of *LOX* mRNA expression with hypoxia and focal adhesion scores in 15 different TNBC PDX models. Red dot shows the position of TM01278 PDX model selected. **b** Representative images of TM01278 PDX organoids at day 0 and day 9 after treatment with doxorubicin and BAPN treatment, alone or in combination. **c** Quantification of organoid diameter upon combination therapy for 9 days ($n = 12$ (vehicle, Doxo, BAPN), $n = 11$ (Doxo+BAPN)). **d**, **e** Tumor growth (**d**) and tumor weight (**e**) in TM01278 PDX upon treatment with doxorubicin and BAPN, alone or in combination ($n = 5$). Inset shows LOX expression in PDX tumors. **f** Representative images of tumors from **d**. **g** Relative LOX activity in tumors from **d** ($n = 8$ (vehicle), $n = 6$ (Doxo, BAPN, Doxo+BAPN)). **h**, **i** Representative images of Picrosirius red staining (**h**) and its quantification (i) in combination- and single agent-treated PDX tumors from d ($n = 4$). **j**, **k** Representative images of doxorubicin fluorescence in tumors from **d** (**j**), and its quantification (**k**) ($n = 6$). **l** Western blot analysis of FAK/Src signaling in PDXs treated with doxorubicin and BAPN, alone or in combination. Data represents mean ± SD. Two-sided Student's *t*-test was used to calculate statistical difference between two groups. One-way ANOVA with Dunnett's test was performed to compare mean of combination-treated group with single agent treatments in **e**. Two-way ANOVA test was performed for comparing tumor growth over time among different treatment groups in **d**. Scale bar = 100 µm for **b**, 1 cm for **f**, and 400 µm for **h** and 200 µm for **j**. n.s. not significant. Source data are provided as a Source data file.



overexpression upon acquisition of doxorubicin resistance, on one hand, leads to protection against doxorubicin-induced FAK/Src inhibition by increasing collagen cross-linking, fibronectin assembly and decreasing drug penetration, and on the other hand, increases ITGA5 and FN1 expression, ultimately leading to increased FAK/Src signaling and chemoresistance. Considering the known potential of inhibiting FAK/Src kinases to enhance response to different chemotherapy agents[62] and our data on the effect of LOX inhibition on FAK/Src signaling in chemosensitization, we propose that LOX inhibition reduces both the ECM stiffness to enhance drug penetration and the ITGA5/FN1 expression, thus culminating in inhibition of FAK/Src signaling, induction of apoptosis and chemosensitization. Overall, these findings suggest that LOX,

Fig. 6 Targeting LOX at the first-line settings potentiates chemoresponse in TNBCs. a Tumor volume in MDA-MB-231 xenografts upon shLOX induction in the presence or absence of doxorubicin treatment ($n = 6$). **b** IVIS images of mice from **a**. **c** Quantifications of luciferase intensity in tumors from **b** ($n = 6$). **d** Images showing isolated tumors from **a**. **e** Tumor weights in mice from **a** ($n = 6$). **f** qRT-PCR analysis of LOX in Ctrl ($n = 9$) vs. shLOX ($n = 9$) xenografts. **g**, **h** IHC staining of LOX and its quantification in Ctrl ($n = 5$) vs. shLOX ($n = 5$) tumors. **i**, **j** Ki-67 proliferation index of tumors from a ($n = 4$ (vehicle, Doxo, BAPN), $n = 3$ (Doxo+BAPN)). **k**–**p** Immunoreactive scores of Cleaved Caspase-3 (**k**, l), ITGA5 (**m**, **n**) and p-Src (Y416) (**o**, **p**) in tumors from a ($n = 4$ (vehicle, Doxo, BAPN), $n = 3$ (Doxo + BAPN)). **q** Western blot analysis of p-FAK and FAK in shLOX tumors in combination with doxorubicin. **r** Representative images of TNBC patient organoid, F149T at day 0 and day 9 after treatment with doxorubicin and BAPN, alone or in combination. **s** Quantification of organoid diameter upon combination therapy for 9 days ($n = 12$ (Day 0), $n = 9$ (vehicle, Day 9), $n = 11$ (Doxo, BAPN, Doxo+BAPN, Day 9)). Data represents mean ± SD. Two-sided Student's *t*-test was used to calculate statistical difference between two groups. One-way ANOVA with Dunnett's test was performed to compare mean of combination-treated group with single agent treatments in **c**, **e**, **i**, **k**, **m**, **o**, and **s**. Two-way ANOVA test was performed for comparing tumor growth over time among different treatment groups in **a**. Scale bar = 100 μm for **g**, **j**, **l**, **n**, **p**, **r**. Source data are provided as a Source data file.

which has primarily been studied in the context of metastasis, may also confer resistance to chemotherapy, making it a highly attractive therapeutic target.

Given the functional contribution of ECM modulation on different aspects of tumorigenesis, several inhibitors against multiple ECM modulators, such as matrix metalloproteinases, or the ECM-sensing integrin receptors have so far been developed. However, none of them achieved clinical success due to context-dependent efficacy, low specificity or severe toxicity[63]. Furthermore, inhibitors targeting the HIF pathway have so far been unable to enter clinics due to the complexity of the HIF pathway and the difficulty in targeting protein-protein interactions[64]. Therefore, identification of the well-defined modulators of ECM that are specifically overexpressed in aggressive, chemoresistant tumors, such as LOX that stands out as an attractive target with strong translational profile will be beneficial towards achieving a superior clinical outcome[44,65]. In this line, we demonstrated that more than half of the chemoresistant TNBC patients express high levels of LOX mRNA (Supplementary Fig. 5a, b) and are therefore expected to respond to LOX targeting therapies in combination with chemotherapy. In addition, we showed that high expression of LOX protein is significantly associated with survival in a cohort of chemotherapy-treated TNBC patients. Moreover, we also demonstrated a superior anti-tumorigenic effect of doxorubicin in vivo and in a TNBC organoid when combined with BAPN in the first-line settings (Fig. 6) that altogether supports the translational potential of targeting LOX with a potentially large target population in the clinic. Although BAPN is the most commonly used LOX inhibitor, it inhibits all LOX family members. In this line, there have been several recent efforts to identify novel and selective small molecule inhibitors against different family members, including LOX[66] and LOXL2[67] that can hopefully be tested in clinics to improve patient outcome in aggressive cancers, including the chemoresistant TNBCs. Moreover, our in vitro and in vivo data showing strong chemosensitization upon inhibiting FAK or Src kinases suggest that FAK/Src axis is critical for tumor cell survival in the presence of chemotherapy and targeting these proteins could also be an effective strategy to overcome chemoresistance in TNBCs in the future. Indeed, inhibitors of FAK and Src kinases are currently being tested in clinical trials and demonstrate promising results when combined with targeted therapies or chemotherapy (e.g. NCT03875820 and NCT02389309, respectively).

Signaling pathways need to be tightly regulated and are repressed in the absence of a stimulus. This ensures that target genes are activated only in the presence of a signal. miRNAs have been shown to be key regulators of this repression by inhibiting the expression of several transcripts[68]. Furthermore, others and us have previously shown that expression of genes functioning in the same cascade can be co-regulated by the same miRNA to ensure its robustness[56,68]. Therefore, we asked if miRNAs can inhibit the HIF1A/LOX/ITGA5 axis and confer chemosensitivity. We identified miR-142-3p to be significantly downregulated in chemoresistant tumors by HIF1A, and its overexpression inhibits HIF1A, LOX and ITGA5 in a robust double-negative feedback loop, thus sensitizes cells to chemotherapy. Although we have shown that miR-142-3p is significantly associated with survival specifically in chemotherapy-treated TNBC patients, future studies including miRNA profiling or in situ hybridization in large chemotherapy-treated patient cohorts are warranted to fully uncover the potential of this miRNA as a biomarker and a therapy sensitizer in TNBCs.

In summary, we uncovered a molecular mechanism of chemotherapy resistance in TNBC involving hypoxia-driven LOX expression, which on one hand, leads to increased collagen cross-linking, fibronectin assembly and decreased drug penetration, and on the other hand, increases ITGA5 and FN1 expression, collectively leading to increased FAK/Src signaling, decreased apoptosis and chemoresistance. Furthermore, hypoxia-driven repression of miR-142-3p increases HIF1A, LOX, and ITGA5 expression, leading to further activation of FAK/Src signaling (Fig. 8). Based on these results, we propose that targeting LOX or its downstream FAK or Src or restoring the hypoxia-inhibited miR-142-3p can overcome chemoresistance by effectively blocking FAK/Src signaling (Fig. 8). Overall, our results provide valuable insights into how chemoresistance can be modulated at multiple levels and a pre-clinical support for inhibiting a key ECM-remodeler, LOX in TNBCs to potentiate chemotherapy response.

Methods

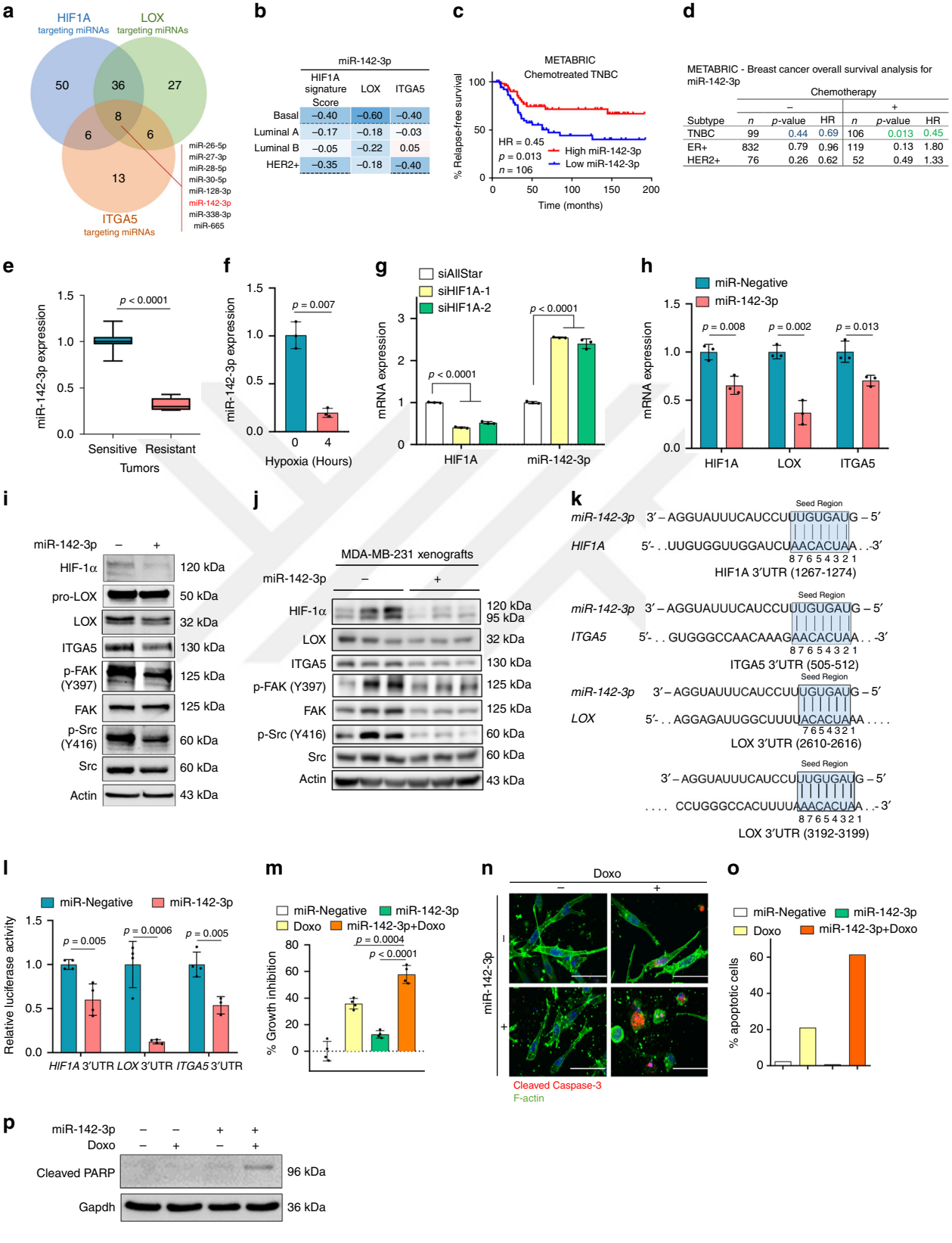
In vivo experiments. To develop doxorubicin-resistant xenografts, 6–8-weeks-old female athymic nu/nu mice were injected with 2×10^6 MDA-MB-231 cells into mammary fat pads (MFP). Mice were randomly allocated into two groups, and vehicle or doxorubicin treatments (5 mg/kg, weekly, i.v.) were started when tumors became palpable. Vehicle-treated tumors were collected and designated as vehicle. Half of the doxorubicin-treated mice were sacrificed when they were responsive to treatment, and tumors were collected and designated as sensitive. The remaining mice continued to receive doxorubicin until their tumors started regrowth. Then, these mice were also sacrificed, and tumors were collected and designated as resistant.

To test the role of LOX or FAK or Src inhibition to overcome chemotherapy resistance in immunocompetent setting, 2×10^5 4T1 cells were injected into the MFPs of 6–8 weeks-old Balb/c mice. Mice were treated with vehicle, doxorubicin (2.5 mg/kg, once a week, i.v.), BAPN (100 mg/kg, daily, ip.), PF-562271 (15 mg/kg, daily, oral), Saracatinib (25 mg/kg, daily, oral), or their combinations with doxorubicin. Once the vehicle group reached at 800 mm^3, all mice were sacrificed, and tumor weight was measured.

For shLOX induction experiments using the luciferase overexpressing MDA-MB-231.Luc2GFP cells, doxycycline was given to induce shLOX expression at 100 ug/ml in drinking water when the tumors reach at 100 mm^3. All mice were sacrificed; tumors were collected and weighed once the vehicle-treated tumors reached at 1500 mm^3. For bioluminescence imaging, mice were intraperitoneally injected with 150 mg/kg D-luciferin (Perkin Elmer, MA, USA), and images were acquired with Lumina III In Vivo Imaging System (Perkin Elmer, MA, USA). Analysis was performed with Living image software by measuring photon flux.

For PDX experiments, 2–3 mm^3 pieces of frozen PDX tumors were placed into the flank region of NSG mice. When tumors become palpable, mice were distributed into treatment groups. Doxorubicin (2 mg/kg, once a week, i.v.) and BAPN (100 mg/kg, daily, i.p.) was given individually or in combination for 30 days after which mice were sacrificed and tumors were collected for downstream analysis.

Primary tumor growth was monitored by measuring the tumor volume at least twice a week with a caliper after tumors became palpable. Tumor volumes were calculated as length × $width^2/2$. All mice used were of the same age and similar body weight. All animal experiments have been approved by the Animal Ethics Committee of Bilkent University or the Institutional Animal Care and Use



Committee of University of South Carolina. All mice were maintained under a temperature-controlled environment with a 12-h light/dark cycle and received a standard diet and water ad libitum.

Patient tumor-derived and PDX-derived organoids. For the generation of patient organoids, breast cancer surgical patients were consented under an IRB approved protocol for the USC-Palmetto Health Biorepository. TNBC organoids were established from a fresh surgical tissue by cutting the tumor into small pieces and incubating in collagenase A solution with ROCK inhibitor on a shaker at 37 °C for 30 min. The collagenase activity was inhibited by adding FBS, and pipetting was done to ensure the formation of almost a single cell solution. After several washes with PBS, the cell pellet was dissolved in matrigel. Breast organoid media containing ROCK and GSK inhibitors was added after the matrigel solidified[69]. For the PDX organoid, a small, 2–3 mm^3 piece of the PDX tumor that was freshly excised from an NSG mouse was minced and separated into single cell suspension as previously described[70]. For drug testing studies, organoids were disrupted to single

Fig. 7 miR-142-3p regulates HIF1A/LOX/ITGA5 axis to confer chemosensitization in TNBC. a Venn diagram of combinatorial target prediction analysis. Number of miRNAs targeting *HIF1A* (blue), *LOX* (green) and *ITGA5* (orange) is shown. Eight miRNAs predicted to target all three genes are shown. **b** Heatmap showing Pearson's correlation coefficients between miR-142-3p and *HIF1A* gene signature score, *LOX* and *ITGA5* mRNA expressions in patients from GSE19783. An intense blue color shows a stronger negative correlation. **c** Kaplan–Meier survival curve in chemotherapy-treated TNBC patients ($n = 106$) based on low vs. high (median) miR-142-3p expression. **d** Table summarizing the association of miR-142-3p expression with survival in different breast cancer subtypes with or without chemotherapy. **e**, **f** qRT-PCR analyses of miR-142-3p expression in doxorubicin-sensitive ($n = 11$) vs. doxorubicin-resistant ($n = 12$) xenografts (**e**) and in MDA-MB-231 cells under hypoxia for 4 h ($n = 3$) (**f**). **g**. qRT-PCR of miR-142-3p upon transfection with two different siRNAs targeting HIF1A for 48 h ($n = 3$). **h**, **i** qRT-PCR ($n = 3$) (**h**) and western blot (**i**) analyses of HIF/LOX/ITGA5 axis upon miR-142-3p transfection. **j**. Western blot analyses of the HIF1A/LOX/ITGA5 axis in MDA-MB-231 xenografts stably expressing miR-142-3p. **k** Graphical representation of miR-142-3p binding sites within the 3′-UTRs of *HIF1A*, *LOX* and *ITGA5*. **l**. Luciferase reporter assay with 3′-UTRs of *HIF1A*, *LOX* or *ITGA5* in MDA-MB-231 cells transfected with miR-Negative or miR-142-3p ($n = 4$ (*HIF1A* and *LOX*), $n = 3$–4 for (*ITGA5*)). **m** Percentage growth inhibition in collagen-embedded MDA-MB-231 cells after transfection with miR-142-3p in the presence or absence of doxorubicin ($n = 4$). **n** Immunofluorescence staining of Cleaved Caspase-3 (red) and F-actin (green) in miR-Negative or miR-142-3p transfected MDA-MB-231 cells in the presence or absence of doxorubicin. **o**. Quantification of Cleaved Caspase-3 positive cells from **n**. **p**. Western blot of cleaved PARP upon miR-142-3p transfection with or without doxorubicin treatment for 72 h. Data represents mean ± SD. Two-sided Student's *t*-test was used to calculate statistical difference between two groups. One-way ANOVA with Dunnett's test was performed to compare mean of combination-treated group with single agent treatments in **m**. Significance for survival analyses was calculated by log-rank (Mantel-Cox) test. HR hazard ratio. Scale bar = 50 μm for **n**. Source data are provided as a Source data file.

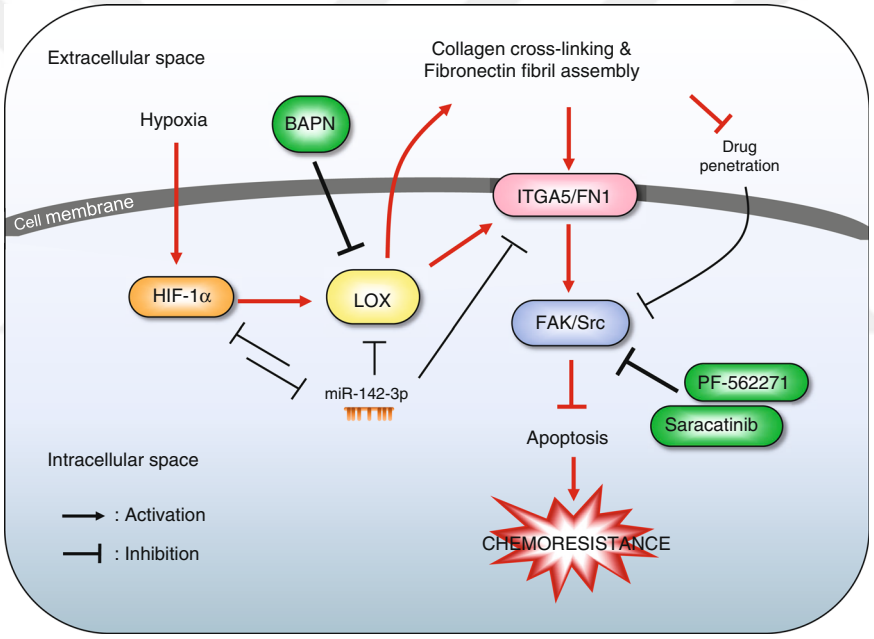


Fig. 8 Mechanistic summary and targeting approaches for overcoming chemoresistance. In the hypoxic, chemoresistant TNBC tumor microenvironment, hypoxia induces HIF-1α which then increases the transcription of LOX. LOX, on one hand, increases the expressions of ITGA5 and its ligand, fibronectin in tumor cells and on the other hand, it induces collagen cross-linking and fibronectin fibril assembly leading to reduced drug penetration into tumor cells. In meantime, hypoxia-mediated downregulation of miR-142-3p, which directly targets HIF1A, LOX and ITGA5, leads to further activation of the HIF1A/LOX/ITGA5/FN1 axis. Overall, this culminates in the activation of FAK/Src signaling, blockage of drug-induced apoptosis and chemoresistance in TNBCs. Therefore, using inhibitors targeting LOX (e.g. BAPN) or its downstream FAK (e.g. PF-562271) or Src (Saracatinib) could overcome chemoresistance in TNBCs.

cells by digesting at 37 °C for 30 min with TrypLE (A1217701, Gibco, NY, USA) in the presence of 10uM Rock inhibitor (s1049, Selleckchem, TX, USA). Organoids were plated into wells of 96-well plate (20,000 cells/well) on a collagen-coated surface with media containing 2% matrigel (356252, Corning, NY, USA). Drugs were added 72 h after plating (final concentration of doxorubicin at 40 nM and BAPN at 25 mM). Cells were grown in the presence of drug(s) or vehicle for 9 days, and the diameter of organoids were measured.

Whole-transcriptome sequencing (RNA-seq) and data analyses. rRNA-depleted stranded libraries for each condition (four biological replicates for each of vehicle, doxorubicin-sensitive tumors and doxorubicin-resistant tumors) were generated and multiplexed. Paired-end 100 bp sequencing was performed using the Illumina HiSeq 2000 platform at McGill University and Genome Quebec Innovation Centre. In all, 60–70 million sequencing reads were obtained for each sample. Raw sequence reads were aligned to the UCSC human reference genome (hg19) using TopHat. with default parameters. To count the mapped reads, HTSeq was used with the reference genome annotation (USCS, hg19). In order to determine differentially expressed genes between doxorubicin-sensitive and doxorubicin-resistant groups, Bioconductor package, edgeR, was utilized.

Patient data analyses. To analyze the effects of LOX expression on the survival of chemotherapy-treated TNBCs, we performed IHC staining of LOX in primary tumor samples from 77 TNBC patients that were diagnosed with breast cancer between 2006 and 2015 at Hacettepe University School of Medicine, Ankara, Turkey and treated with chemotherapy (35% adjuvant anthracycline-based therapy, 43% anthracyclines in combination with taxanes and 22% other chemotherapy agents). The study was approved by the Non-Interventional Clinical Research Ethics Committee of Hacettepe University (approval no: 2020/02-40). To generate DoxoR-GS scores in patients from METABRIC, GSE31519 and GSE58812, we used the top 441 differentially (up or down-regulated) expressed mRNAs between doxorubicin-sensitive vs. -resistant xenografts with a fold change cut-off of 1.75 and *p*-value cut-off of 0.05 (Supplementary Data 1). First, expression of these 441 genes in patients were converted into *z*-scores. Then, the sum of *z*-scores of the downregulated genes in the DoxoR-GS was subtracted from the sum of *z*-scores of

the upregulated genes for each patient[35] using the SPSS Statistics software. Chemotherapy-treated patient subgroup from the KM Plotter database (release version 2017) were created by selecting the adjuvant chemotherapy-treated patients and excluding the endocrine-treated ones. In GSE19783 dataset, patients are stratified based on the PAM50 subtyping (basal patients were selected) and ERα, PR and HER2 expression.

Statistics and reproducibility. The results are represented as mean ± standard deviation (SD) or mean ± standard error of the mean (SEM), as indicated in the figure legends. All statistical analyses were performed in GraphPad Prism Software using two-sided Student's t-test for comparisons between two groups, one-way ANOVA followed by Dunnett multiple comparison test for comparing combination treatment group with single agent-treated groups, and two-way ANOVA for comparing tumor volume change over time among different treatment groups. Survival curves were generated based on median separation using Kaplan–Meier method, and significance between groups was calculated by Log-rank test. For correlation analysis, Pearson correlation coefficients were calculated. Experiments were repeated two to three times independently with similar results.

Methods for cell culturing, cell-based assays, transient and stable transfections, qRT-PCR and Western blot analysis, immunofluorescence, immunohistochemical and Picrosirius red staining, Annexin V/DAPI staining, hypoxia, cloning, dual luciferase, LOX activity, collagen and deoxycholate lysis assays, other animal experiments, measuring doxorubicin penetration in vitro and in vivo, and patient data and pathway analyses were provided in Supplementary Methods. The list of primers for qRT-PCR, antibodies for Western blotting, IF and IHC as well as the primer sequences for 3′-UTR cloning are provided in Supplementary Table 4.

Reporting summary. Further information on research design is available in the Nature Research Reporting Summary linked to this article.

Data availability

The RNA-Seq data has been uploaded to the Sequence Read Archive (SRA) of NCBI with the submission ID: SUB6918779 (https://www.ncbi.nlm.nih.gov/bioproject/PRJNA607780). Data presented on Figs. 1d, f, 2b and Supplementary Figs. 2b, c, 4a, b were generated by analyzing the data available under the accession number GSE58812 from GEO depository (https://www.ncbi.nlm.nih.gov/geo/). Data presented on Figs. 1h, i, k, l, 2o and Supplementary Figs. 1d, e, 2a, d were generated by analyzing the KM Plotter database (http://kmplot.com/analysis/). Data presented on Fig. 7c, d and Supplementary Figs. 1a, 12d were generated by analyzing the METABRIC data from EMBL European Genome–Phenome Archive (http://www.ebi.ac.uk/ega/) with an accession number EGAS00000000122. GSEA gene sets were downloaded from the GSEA MSigDB Collections website: https://www.gsea-msigdb.org/gsea/msigdb/collections.jsp. Data presented on Fig. 7b and Supplementary Fig. 12a, b, c were generated by analyzing the data available under the accession number GSE19783 from NCBI. Data presented on Supplementary Figs. 1b, 5a were generated by analyzing the data available under the accession number GSE31519 from NCBI. Data presented on Supplementary Fig. 5b–e were generated by analyzing the data available under the accession number GSE25066 from NCBI. Data presented on Fig. 2h was generated by analyzing the data available under the accession numbers GSE16446, GSE19783, GSE21653, GSE22219, GSE22226, GSE25066, GSE58644 from NCBI and under METABRIC datasets and The Cancer Genome Atlas (TCGA) data. The source data underlying Figs. 1a–h, j, k; 2a–e, g–o, q; 3a–g, i, k–q; 4a–e, g–j, l, n–p, r; 5a, c–e, g, i, k–l; 6a, c, e–f, h, i, k, m, o, q, s; 7b, c, e–j, l, m, p and Supplementary Figs. 1a–c; 2a–c; 3a–b; 4c, d; 5c–e; 6b, f; 7a–d; 8a, c; 9a, c; 10a–c, e, f; 11b–f; 12e are provided as a Source Data file. All the other data supporting the findings of this study are available within the article and its Supplementary Information files and from the corresponding author upon reasonable request. A reporting summary for this article is available as a Supplementary Information file.

Received: 19 August 2019; Accepted: 20 April 2020;
Published online: 15 May 2020

References

1. Saraiva, D. P., Guadalupe Cabral, M., Jacinto, A. & Braga, S. How many diseases is triple negative breast cancer: the protagonism of the immune microenvironment. *ESMO Open* **2**, e000208 (2017).
2. Yadav, B. S., Chanana, P. & Jhamb, S. Biomarkers in triple negative breast cancer: a review. *World J. Clin. Oncol.* **6**, 252–263 (2015).
3. Foulkes, W. D., Smith, I. E. & Reis-Filho, J. S. Triple-negative breast cancer. *N. Engl. J. Med.* **363**, 1938–1948 (2010).
4. Mayer, E. L. & Burstein, H. J. Chemotherapy for triple-negative breast cancer: is more better? *J. Clin. Oncol.* **34**, 3369–3371 (2016).
5. Prowell, T. M. & Pazdur, R. Pathological complete response and accelerated drug approval in early breast cancer. *N. Engl. J. Med.* **366**, 2438–2441 (2012).
6. Liedtke, C. et al. Response to neoadjuvant therapy and long-term survival in patients with triple-negative breast cancer. *J. Clin. Oncol.* **26**, 1275–1281 (2008).
7. Schmid, P. et al. Atezolizumab and Nab-Paclitaxel in advanced triple-negative breast cancer. *N. Engl. J. Med.* **379**, 2108–2121 (2018).
8. Grassilli, E., Ballabeni, A., Maellaro, E., Del Bello, B. & Helin, K. Loss of MYC confers resistance to doxorubicin-induced apoptosis by preventing the activation of multiple serine protease- and caspase-mediated pathways. *J. Biol. Chem.* **279**, 21318–21326 (2004).
9. Dai, Z., Huang, Y. & Sadee, W. Growth factor signaling and resistance to cancer chemotherapy. *Curr. Top. Med. Chem.* **4**, 1347–1356 (2004).
10. Deffie, A. M. et al. Multifactorial resistance to adriamycin: relationship of DNA repair, glutathione transferase activity, drug efflux, and P-glycoprotein in cloned cell lines of adriamycin-sensitive and -resistant P388 leukemia. *Cancer Res.* **48**, 3595–3602 (1988).
11. Calcagno, A. M. et al. Single-step doxorubicin-selected cancer cells overexpress the ABCG2 drug transporter through epigenetic changes. *Br. J. Cancer* **98**, 1515–1524 (2008).
12. Netti, P. A., Berk, D. A., Swartz, M. A., Grodzinsky, A. J. & Jain, R. K. Role of extracellular matrix assembly in interstitial transport in solid tumors. *Cancer Res.* **60**, 2497–2503 (2000).
13. Senthebane, D. A., et al. The role of tumor microenvironment in chemoresistance: to survive, keep your enemies closer. *Int. J. Mol. Sci.* **18**, e1586 (2017).
14. Zhou, H. et al. Hyaluronidase embedded in nanocarrier PEG shell for enhanced tumor penetration and highly efficient antitumor efficacy. *Nano Lett.* **16**, 3268–3277 (2016).
15. Meads, M. B., Gatenby, R. A. & Dalton, W. S. Environment-mediated drug resistance: a major contributor to minimal residual disease. *Nat. Rev. Cancer* **9**, 665–674 (2009).
16. Sethi, T. et al. Extracellular matrix proteins protect small cell lung cancer cells against apoptosis: a mechanism for small cell lung cancer growth and drug resistance in vivo. *Nat. Med.* **5**, 662–668 (1999).
17. Humphries, J. D., Byron, A. & Humphries, M. J. Integrin ligands at a glance. *J. cell Sci.* **119**, 3901–3903 (2006).
18. Kechagia, J. Z., Ivaska, J. & Roca-Cusachs, P. Integrins as biomechanical sensors of the microenvironment. *Nat. Rev. Mol. cell Biol.* **20**, 457–473 (2019).
19. Aoudjit, F. & Vuori, K. Integrin signaling in cancer cell survival and chemoresistance. *Chemother. Res. Pract.* **2012**, 283181 (2012).
20. Seguin, L., Desgrosellier, J. S., Weis, S. M. & Cheresh, D. A. Integrins and cancer: regulators of cancer stemness, metastasis, and drug resistance. *Trends cell Biol.* **25**, 234–240 (2015).
21. Longmate, W. & DiPersio, C. M. Beyond adhesion: emerging roles for integrins in control of the tumor microenvironment. *F1000Res.* **6**, 1612 (2017).
22. Schaffner, F., Ray, A. M. & Dontenwill, M. Integrin alpha5beta1, the fibronectin receptor, as a pertinent therapeutic target in solid tumors. *Cancers* **5**, 27–47 (2013).
23. Yao, E. S. et al. Increased beta1 integrin is associated with decreased survival in invasive breast cancer. *Cancer Res.* **67**, 659–664 (2007).
24. Bonnans, C., Chou, J. & Werb, Z. Remodelling the extracellular matrix in development and disease. *Nat. Rev. Mol. Cell Biol.* **15**, 786–801 (2014).
25. Naba, A., et al. The matrisome: in silico definition and in vivo characterization by proteomics of normal and tumor extracellular matrices. *Mol. Cell. Proteomics.* **11**, M111.014647 (2012).
26. Xiong, G. X. & Xu, R. Function of cancer cell-derived extracellular matrix in tumor progression. *J. Cancer Metastasis Treat.* **2**, 357–364 (2016).
27. Kagan, H. M. & Li, W. Lysyl oxidase: properties, specificity, and biological roles inside and outside of the cell. *J. Cell. Biochem.* **88**, 660–672 (2003).
28. Erler, J. T. et al. Hypoxia-induced lysyl oxidase is a critical mediator of bone marrow cell recruitment to form the premetastatic niche. *Cancer cell* **15**, 35–44 (2009).
29. Rachman-Tzemah, C. et al. Blocking surgically induced lysyl oxidase activity reduces the risk of lung metastases. *Cell Rep.* **19**, 774–784 (2017).
30. Le Calve, B. et al. Lysyl oxidase family activity promotes resistance of pancreatic ductal adenocarcinoma to chemotherapy by limiting the intratumoral anticancer drug distribution. *Oncotarget* **7**, 32100–32112 (2016).
31. Miller, B. W. et al. Targeting the LOX/hypoxia axis reverses many of the features that make pancreatic cancer deadly: inhibition of LOX abrogates metastasis and enhances drug efficacy. *EMBO Mol. Med.* **7**, 1063–1076 (2015).
32. Barker, H. E., Cox, T. R. & Erler, J. T. The rationale for targeting the LOX family in cancer. *Nat. Rev. Cancer* **12**, 540–552 (2012).
33. Chavez, K. J., Garimella, S. V. & Lipkowitz, S. Triple negative breast cancer cell lines: one tool in the search for better treatment of triple negative breast cancer. *Breast Dis.* **32**, 35–48 (2010).
34. Holliday, D. L. & Speirs, V. Choosing the right cell line for breast cancer research. *Breast Cancer Res.* **13**, 215 (2011).
35. Dancik, G. M. & Theodorescu, D. Robust prognostic gene expression signatures in bladder cancer and lung adenocarcinoma depend on cell cycle related genes. *PloS ONE* **9**, e85249 (2014).
36. Jezequel, P. et al. Gene-expression molecular subtyping of triple-negative breast cancer tumours: importance of immune response. *Breast Cancer Res.* **17**, 43 (2015).
37. Curtis, C. et al. The genomic and transcriptomic architecture of 2,000 breast tumours reveals novel subgroups. *Nature* **486**, 346–352 (2012).

38. Bertucci, F. et al. How basal are triple-negative breast cancers? *Int. J. Cancer* **123**, 236–240 (2008).
39. Gilkes, D. M., Bajpai, S., Chaturvedi, P., Wirtz, D. & Semenza, G. L. Hypoxia-inducible factor 1 (HIF-1) promotes extracellular matrix remodeling under hypoxic conditions by inducing P4HA1, P4HA2, and PLOD2 expression in fibroblasts. *J. Biol. Chem.* **288**, 10819–10829 (2013).
40. Pez, F. et al. The HIF-1-inducible lysyl oxidase activates HIF-1 via the Akt pathway in a positive regulation loop and synergizes with HIF-1 in promoting tumor cell growth. *Cancer Res.* **71**, 1647–1657 (2011).
41. Rana, M. K., Srivastava, J., Yang, M., Chen, C. S. & Barber, D. L. Hypoxia increases the abundance but not the assembly of extracellular fibronectin during epithelial cell transdifferentiation. *J. Cell Sci.* **128**, 1083–1089 (2015).
42. Ju, J. A. et al. Hypoxia selectively enhances integrin alpha5beta1 receptor expression in breast cancer to promote metastasis. *Mol. Cancer* **15**, 723–734 (2017).
43. Olive, P. L. et al. Carbonic anhydrase 9 as an endogenous marker for hypoxic cells in cervical cancer. *Cancer Res.* **61**, 8924–8929 (2001).
44. Cox, T. R., Gartland, A. & Erler, J. T. Lysyl oxidase, a targetable secreted molecule involved in cancer metastasis. *Cancer Res.* **76**, 188–192 (2016).
45. Wong, C. C. et al. Hypoxia-inducible factor 1 is a master regulator of breast cancer metastatic niche formation. *Proc. Natl Acad. Sci. USA* **108**, 16369–16374 (2011).
46. Senkus, E. et al. Primary breast cancer: ESMO clinical practice guidelines for diagnosis, treatment and follow-up. *Ann. Oncol.* **26**(Suppl. 5), v8–v30 (2015).
47. Kubow, K. E. et al. Mechanical forces regulate the interactions of fibronectin and collagen I in extracellular matrix. *Nat. Commun.* **6**, 8026 (2015).
48. Sottile, J. & Hocking, D. C. Fibronectin polymerization regulates the composition and stability of extracellular matrix fibrils and cell-matrix adhesions. *Mol. Biol. Cell* **13**, 3546–3559 (2002).
49. Ilic, D. et al. FAK promotes organization of fibronectin matrix and fibrillar adhesions. *J. Cell Sci.* **117**, 177–187 (2004).
50. Wierzbicka-Patynowski, I. & Schwarzbauer, J. E. The ins and outs of fibronectin matrix assembly. *J. Cell Sci.* **116**, 3269–3276 (2003).
51. Wu, C., Keivens, V. M., O'Toole, T. E., McDonald, J. A. & Ginsberg, M. H. Integrin activation and cytoskeletal interaction are essential for the assembly of a fibronectin matrix. *Cell* **83**, 715–724 (1995).
52. Varadaraj, A., Magdaleno, C. & Mythreye, K. Deoxycholate fractionation of fibronectin (FN) and biotinylation assay to measure recycled FN fibrils in epithelial cells. *Bio Protoc.* **8**, e2972 (2018).
53. Schutze, F. et al. Inhibition of lysyl oxidases improves drug diffusion and increases efficacy of cytotoxic treatment in 3D tumor models. *Sci. Rep.* **5**, 17576 (2015).
54. Liang, P. C. et al. Doxorubicin-modified magnetic nanoparticles as a drug delivery system for magnetic resonance imaging-monitoring magnet-enhancing tumor chemotherapy. *Int J. Nanomed.* **11**, 2021–2037 (2016).
55. Bouchard, G. et al. Stimulation of triple negative breast cancer cell migration and metastases formation is prevented by chloroquine in a pre-irradiated mouse model. *BMC Cancer* **16**, 361 (2016).
56. Uhlmann, S. et al. Global microRNA level regulation of EGFR-driven cell-cycle protein network in breast cancer. *Mol. Syst. Biol.* **8**, 570 (2012).
57. Cha, Y. J., Jung, W. H. & Koo, J. S. Site-specific expression of amine oxidases in breast cancer metastases. *Tumour Biol.* **40**, 1010428318776822 (2018).
58. Baker, A. M. et al. The role of lysyl oxidase in SRC-dependent proliferation and metastasis of colorectal cancer. *J. Natl Cancer Inst.* **103**, 407–424 (2011).
59. Baker, A. M., Bird, D., Lang, G., Cox, T. R. & Erler, J. T. Lysyl oxidase enzymatic function increases stiffness to drive colorectal cancer progression through FAK. *Oncogene* **32**, 1863–1868 (2013).
60. Cooper, J. & Giancotti, F. G. Integrin signaling in cancer: mechanotransduction, stemness, epithelial plasticity, and therapeutic resistance. *Cancer cell* **35**, 347–367 (2019).
61. Boufraqech, M. et al. Lysyl Oxidase (LOX) transcriptionally regulates SNAI2 expression and TIMP4 secretion in human cancers. *Clin. Cancer Res.* **22**, 4491–4504 (2016).
62. Bolos, V., Gasent, J. M., Lopez-Tarruella, S. & Grande, E. The dual kinase complex FAK-Src as a promising therapeutic target in cancer. *Onco Targets Ther.* **3**, 83–97 (2010).
63. Lampi, M. C. & Reinhart-King, C. A. Targeting extracellular matrix stiffness to attenuate disease: from molecular mechanisms to clinical trials. *Sci. Transl. Med.* **10**, eaao0475 (2018).
64. Burroughs, S. K. et al. Hypoxia inducible factor pathway inhibitors as anticancer therapeutics. *Future Med. Chem.* **5**, 553–572 (2013).
65. Rodriguez, C., Rodriguez-Sinovas, A. & Martinez-Gonzalez, J. Lysyl oxidase as a potential therapeutic target. *Drug New Perspect.* **21**, 218–224 (2008).
66. Leung, L. et al. Anti-metastatic Inhibitors of Lysyl Oxidase (LOX): design and structure-activity relationships. *J. Med. Chem.* **62**, 5863–5884 (2019).
67. Hutchinson, J. H. et al. Small molecule Lysyl oxidase-like 2 (LOXL2) inhibitors: the identification of an inhibitor selective for LOXL2 over LOX. *ACS Med. Chem. Lett.* **8**, 423–427 (2017).
68. Inui, M., Martello, G. & Piccolo, S. MicroRNA control of signal transduction. *Nat. Rev. Mol. Cell Biol.* **11**, 252–263 (2010).
69. Sachs, N. et al. A living biobank of breast cancer organoids captures disease heterogeneity. *Cell* **172**, 373–386 e310 (2018).
70. Liu, C. et al. PRDM1 silences stem cell-related genes and inhibits proliferation of human colon tumor organoids. *Proc. Natl Acad. Sci. USA* **115**, E5066–E5075 (2018).

Acknowledgements

We thank Madeleine Arseneault and Ozlem Sener Sahin for technical and organizational support, and Jitao David Zhang for his help with the initial analysis of RNA-Seq data. We also thank the Center for Targeted Therapeutics (CTT) Microscopy and Flow Cytometry Core (Dr. Chang-uk Lim) of the University of South Carolina, for assistance with flow cytometry. This work was supported by National Institutes of Health Grant 2P20GM109091-06 (O.S.), and in part by European Commission FP7 Marie Curie Career Integration Grant PCIG14-GA-2013-631149 (O.S.), European Molecular Biology Organization (EMBO) Installation Grant 2791 (O.S.), the American Cancer Society Institutional Research Grant IRG-17-179-04 (O.S.), the American Cancer Society Research Scholar Grant RSG-19-194-01-CSM (O.S.), Susan G. Komen Interdisciplinary Graduate Training to Eliminate Cancer Disparities (IGniTE-CD) GTDR17500160 (Ozge S.), the scholarship from Higher Education Commission of Pakistan (U.R.), and research scholarship of the Fonds de recherche du Québec—Santé (FRQS) (Y.R.).

Author contributions

Ozge S., A.K., and U.R. designed and performed experiments, acquired and analyzed data, interpreted data, and prepared the paper; P.G.E. and O.A. contributed to in vivo experiments, IHC staining and data collection; C.E.B. generated TNBC patient organoids; V.S. contributed to confocal microscopy experiments and data analyses; S.A.A. performed cloning and luciferase reporter experiments; U.M.T. contributed to RNA-seq analyses; G.A. contributed to in vivo experiments; H.T.D., M.D., performed the IHC staining of xenografts and contributed to data interpretation; P.J. performed RNA-sequencing; A.I., F.G., K.K., A.A., and A.U. performed the IHC staining of TNBC patient tissues and contributed to data interpretation; O.D. and S.A. provided clinical information of TNBC patients and contributed to data analyses; P.J.B. contributed to TNBC tumor organoid experiments and critically read and edited the manuscript; Y.R. performed RNA-sequencing, and critically read and edited the manuscript; O.S. designed the study, oversaw experiments and data analyses, and prepared the paper. All authors reviewed and commented on the paper.

Competing interests

The authors declare no competing interests.

Additional information

Supplementary information is available for this paper at https://doi.org/10.1038/s41467-020-16199-4.

Correspondence and requests for materials should be addressed to O.S.

Peer review information *Nature Communications* thanks Matthew Ellis and the other, anonymous, reviewer(s) for their contribution to the peer review of this work. Peer reviewer reports are available.

Reprints and permission information is available at http://www.nature.com/reprints

Publisher's note Springer Nature remains neutral with regard to jurisdictional claims in published maps and institutional affiliations.

Open Access This article is licensed under a Creative Commons Attribution 4.0 International License, which permits use, sharing, adaptation, distribution and reproduction in any medium or format, as long as you give appropriate credit to the original author(s) and the source, provide a link to the Creative Commons license, and indicate if changes were made. The images or other third party material in this article are included in the article's Creative Commons license, unless indicated otherwise in a credit line to the material. If material is not included in the article's Creative Commons license and your intended use is not permitted by statutory regulation or exceeds the permitted use, you will need to obtain permission directly from the copyright holder. To view a copy of this license, visit http://creativecommons.org/licenses/by/4.0/.

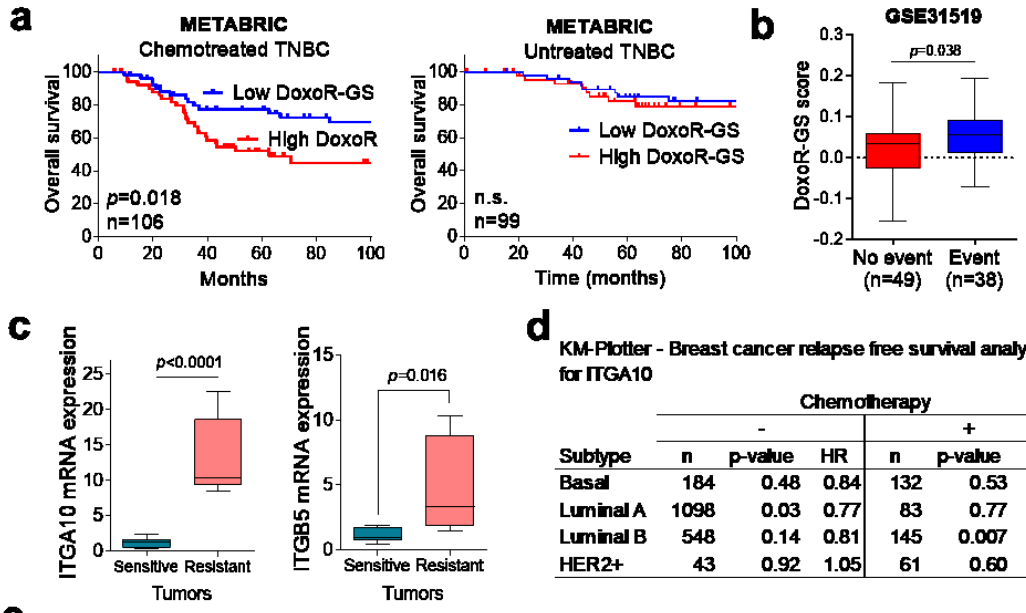
© The Author(s) 2020

SUPPLEMENTARY INFORMATION

Targeting lysyl oxidase (LOX) overcomes chemotherapy resistance in triple negative breast cancer

Saatci et al.

Supplementary Figures



d

KM-Plotter - Breast cancer relapse free survival analysis for ITGA10

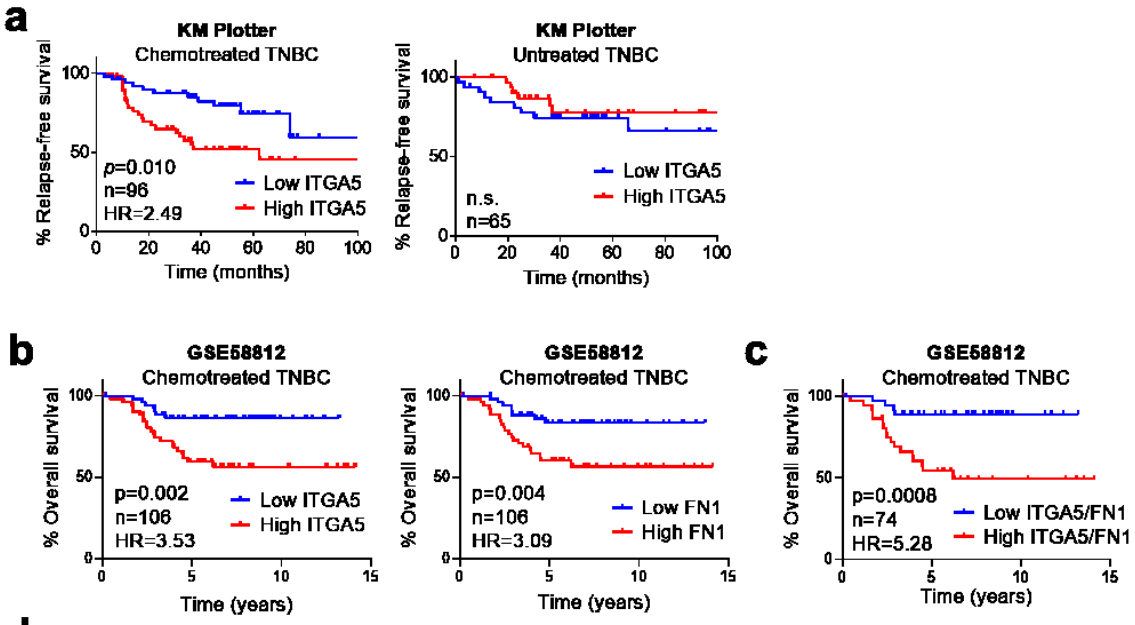
	Chemotherapy					
	-			+		
Subtype	n	p-value	HR	n	p-value	HR
Basal	184	0.48	0.84	132	0.53	0.82
Luminal A	1098	0.03	0.77	83	0.77	1.15
Luminal B	548	0.14	0.81	145	0.007	0.45
HER2+	43	0.92	1.05	61	0.60	0.81

e

KM-Plotter - Breast cancer relapse free survival analysis for ITGB5

	Chemotherapy					
	-			+		
Subtype	n	p-value	HR	n	p-value	HR
Basal	184	0.92	0.98	132	0.13	1.63
Luminal A	1098	0.14	0.84	83	0.94	1.04
Luminal B	548	0.09	0.79	145	0.87	1.05
HER2+	43	0.18	2.09	61	0.02	2.63

Supplementary Figure 1. Association of DoxoR-GS and integrins with chemoresistance in TNBCs. a. Kaplan-Meier survival curves representing percentage overall survival (OS) in chemotherapy-treated (n=106) and untreated (n=99) TNBC patients from METABRIC based on low vs. high (median) DoxoR-GS score. **(b)** Expression levels of DoxoR-GS score in patients from GSE31519 that has no event (n=49) vs. event (n=38), described as either relapse- or distant metastasis. **c.** qRT-PCR analysis showing the expression of *ITGA10* and *ITGB5* in doxorubicin sensitive (n=8) vs. resistant (n=6) tumors. **d, e.** Tables summarizing the results of Kaplan-Meier relapse-free survival (RFS) analysis based on ITGA10 (d) and ITGB5 (e) expression (median) in patients representing different breast cancer subtypes that received or did not receive chemotherapy. Data represents mean ± SD. In Box plots, the box depicts median, 25th to 75th percentiles, and the whisker depicts min to max. Two-sided Student's t-test was used to calculate statistical difference between two groups. Significance for survival analyses was calculated by log-rank (Mantel-Cox) test. n.s., not significant, HR: hazard ratio. Source data are provided as a Source Data file.

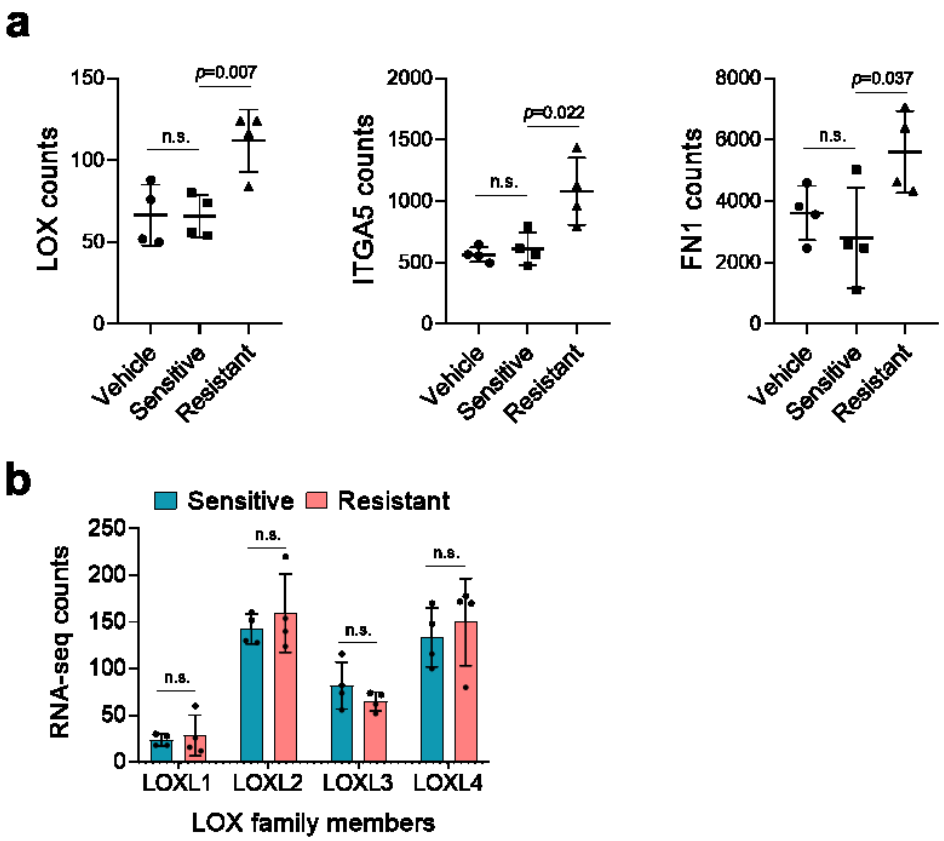


d

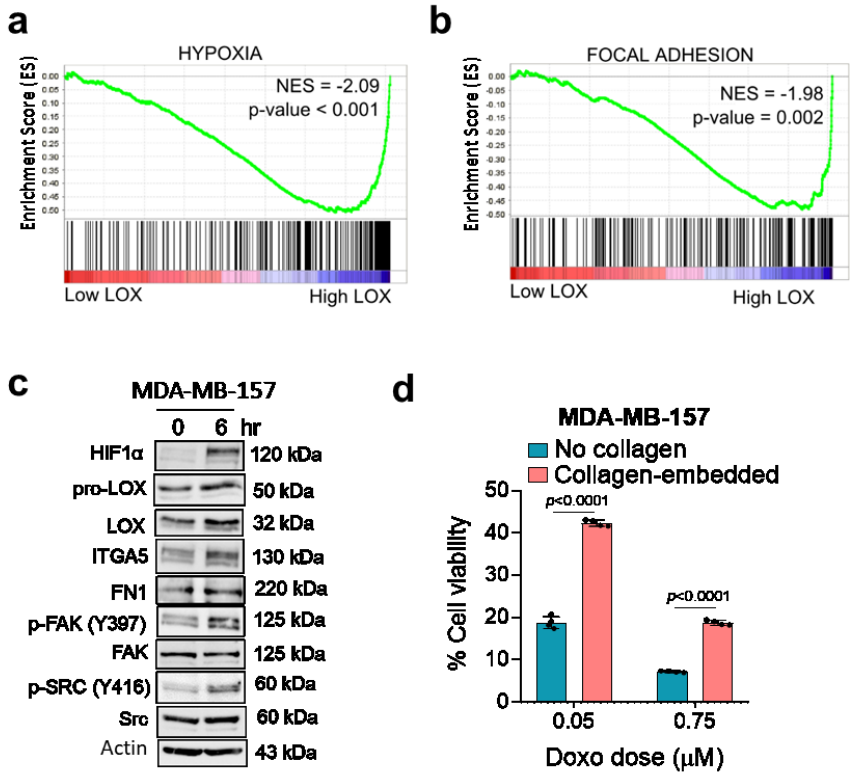
KM-Plotter - Breast cancer relapse free survival analysis for LOX

	Chemotherapy					
	-			+		
Subtype	n	p-value	HR	n	p-value	HR
Basal	184	0.72	1.09	132	0.01	2.29
Luminal A	1098	0.84	1.03	83	0.81	0.90
Luminal B	548	0.58	1.08	145	0.63	1.15
HER2+	43	0.85	1.11	61	0.28	1.56

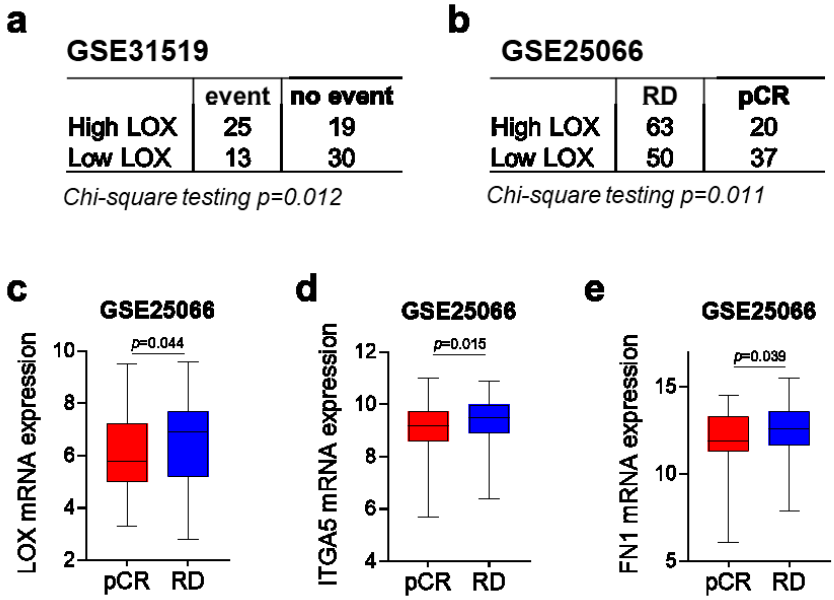
Supplementary Figure 2. Association of ITGA5/FN1/LOX with prognosis in breast cancer. a. Kaplan-Meier survival curves representing the percentage RFS in chemotherapy-treated (n=96) and untreated TNBC (n=65) patients based on low vs. high (median) ITGA5 expression. **b.** Kaplan-Meier survival curves representing the percentage OS in chemotherapy-treated TNBC patients from GSE58812 that were separated based on ITGA5 and FN1 levels from median (n=106). **c.** Kaplan-Meier survival curves representing the percentage OS in chemotherapy-treated TNBC patients from GSE58812 that were separated based on combined ITGA5 and FN1 levels from median (n=74). **d.** Table summarizing LOX expression-based Kaplan-Meier RFS analysis of patients representing different breast cancer subtypes that received or did not receive chemotherapy. Significance for survival analyses was calculated by log-rank (Mantel-Cox) test. n.s., not significant, HR: hazard ratio. Source data are provided as a Source Data file.



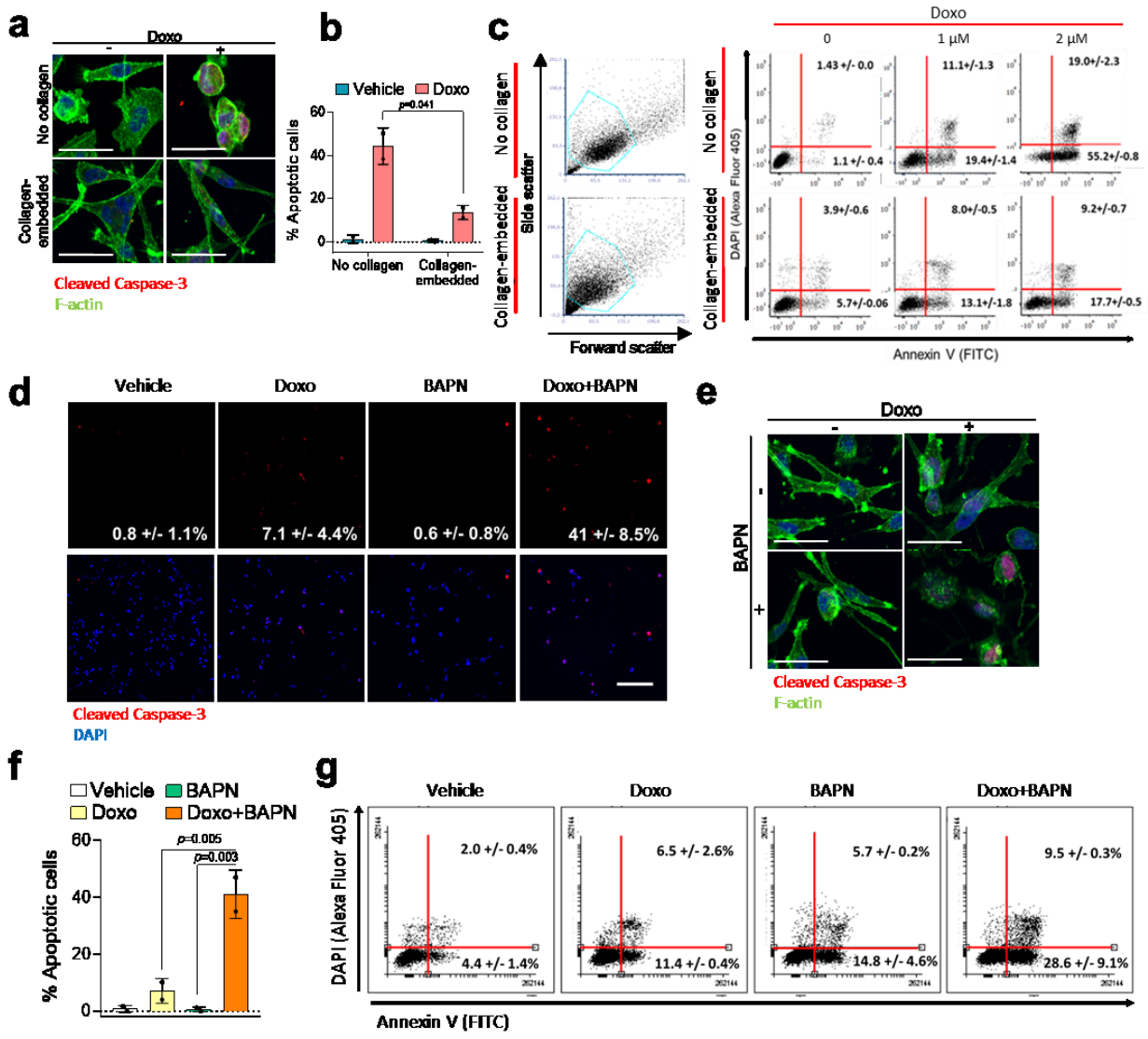
Supplementary Figure 3. Association of LOX family/ITGA5/FN1 expression with chemoresistance. **a.** RNA-Seq read counts of LOX, ITGA5 and FN1 in vehicle-treated, doxorubicin-sensitive and -resistant MDA-MB-231 tumors (n=4). **b.** Bar-graphs showing the expression of LOX family members from the RNA-Seq data of doxorubicin-sensitive (n=4) vs. doxorubicin-resistant (n=4) tumor xenografts. Data represents mean ± SD. Two-sided Student's t-test was used to calculate statistical difference between two groups. n.s., not significant. Source data are provided as a Source Data file.



Supplementary Figure 4. Association of LOX with hypoxia and FA and hypoxic regulation of LOX/ITGA5/FN1 in MDA-MB-157. a, b. Enrichment plots for genes involved in hypoxia (a) and focal adhesion (b) in chemotherapy-treated TNBC patients from GSE58812 (n=106) with low vs. high (median) LOX expression. **c.** Western blot analysis of LOX, ITGA5, and FN1 and the downstream markers in MDA-MB-157 cells cultured in hypoxic conditions. **d.** Doxorubicin response of MDA-MB-157 cells cultured with or without type I collagen for 72 hours (n=4). Data represents mean ± SD. Two-sided Student's t-test was used to calculate statistical difference between two groups. NES: normalized enrichment score. Source data are provided as a Source Data file.

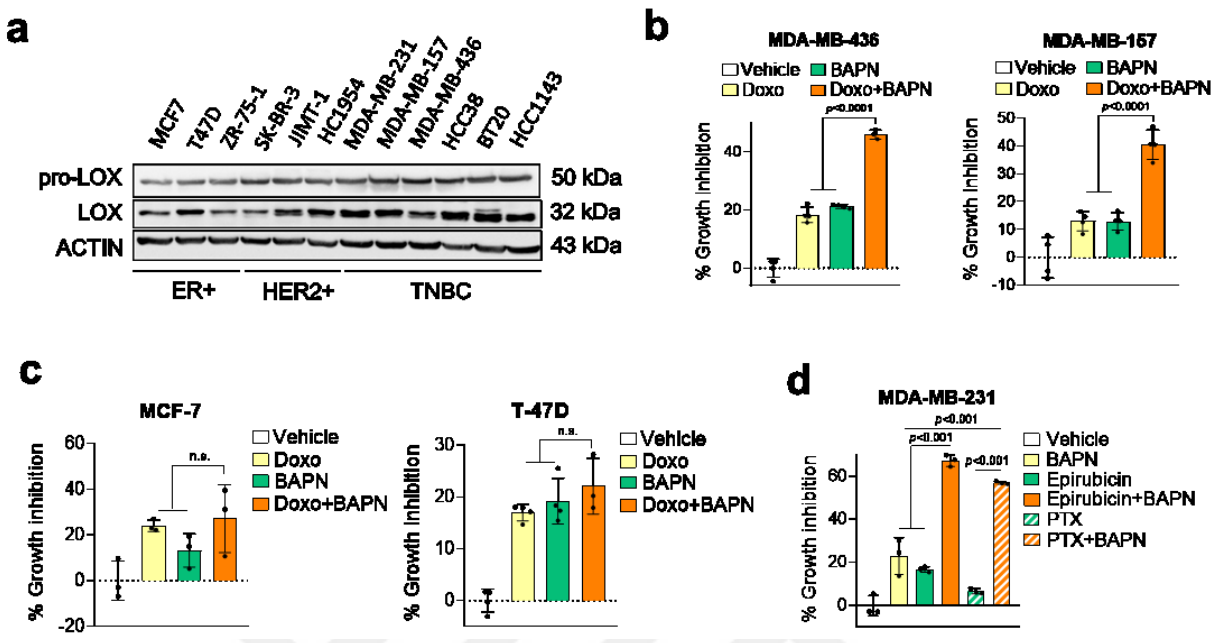


Supplementary Figure 5. Association of LOX with disease progression in chemotreated-TNBC patients. a, b. The association of LOX expression with disease progression and therapy response using GEO databases, GSE31519 (a) and GSE25066 (b). Number of patients in each group is provided, and the statistical testing was performed by chi-square testing. **c-e.** Levels of LOX, ITGA5 and FN1 in patients with pathologic complete response (pCR, n=57) vs. residual disease (RD, n=113) from GSE25066. Data represents mean ± SD. In Box plots, the box depicts median, 25th to 75th percentiles, and the whisker depicts min to max. Two-sided Student's t-test was used to calculate statistical difference between two groups. Source data are provided as a Source Data file.

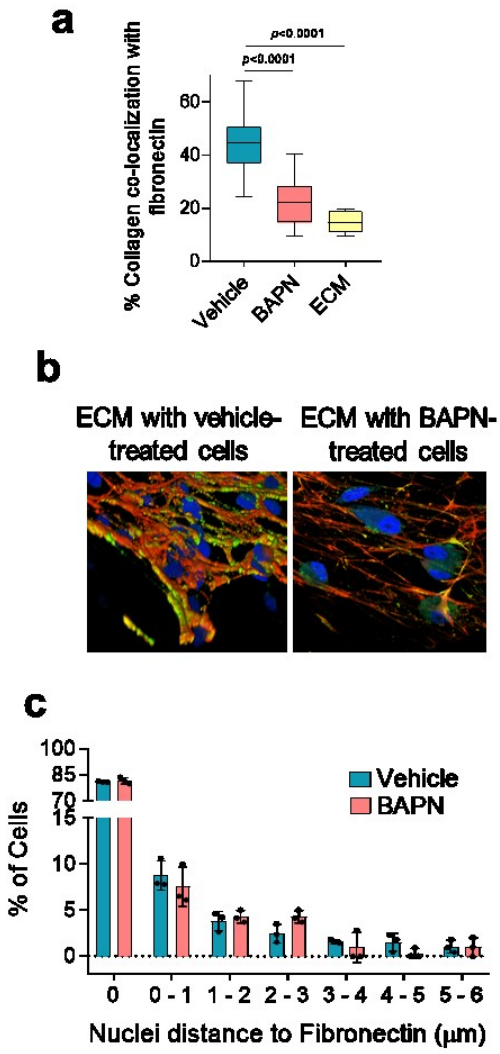


Supplementary Figure 6. Apoptosis assessment upon collagen-embedding. a, b. Cleaved Caspase-3 (red) and phalloidin (green) staining (a) and the percentage of Cleaved Caspase-3 positive cells (b) under doxorubicin treatment in the absence or presence of collagen type I (n=2). **c.** Dot plots showing the percentage of single or double positive cells for Annexin V and DAPI (right panel) (n=2). Gating strategy was provided on the left panel. **d.** Cleaved Caspase-3 (red) and DAPI (blue) staining of single agent- vs. combination-treated cells. Numbers on the right corner show the % apoptotic cells, n=2. **e, f.** Cleaved Caspase-3 (red) and phalloidin (green) staining (e) and the percentage of Cleaved Caspase-3 positive cells (f) under combination treatment in the presence of type I collagen (n=2). **g.** Dot plots showing the percentage of single or double positive cells for Annexin V and DAPI under doxorubicin and BAPN treatment, alone or in combination (n=2). Data represents mean ± SD. Two-sided Student's t-test was used

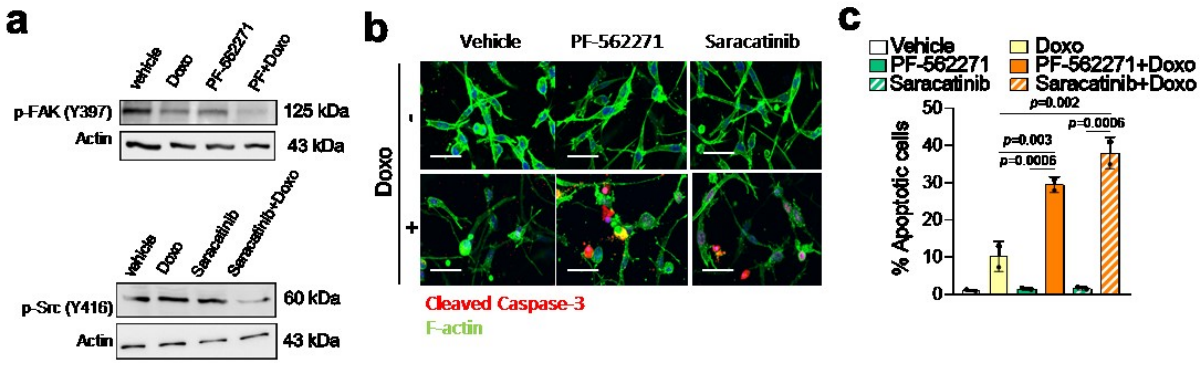
to calculate statistical difference between two groups. One-way ANOVA with Dunnett's test was performed to compare mean of combination-treated group with single agent treatments in **f**. Scale bar=50 μm for **a**, **d** and **e**. Source data are provided as a Source Data file.



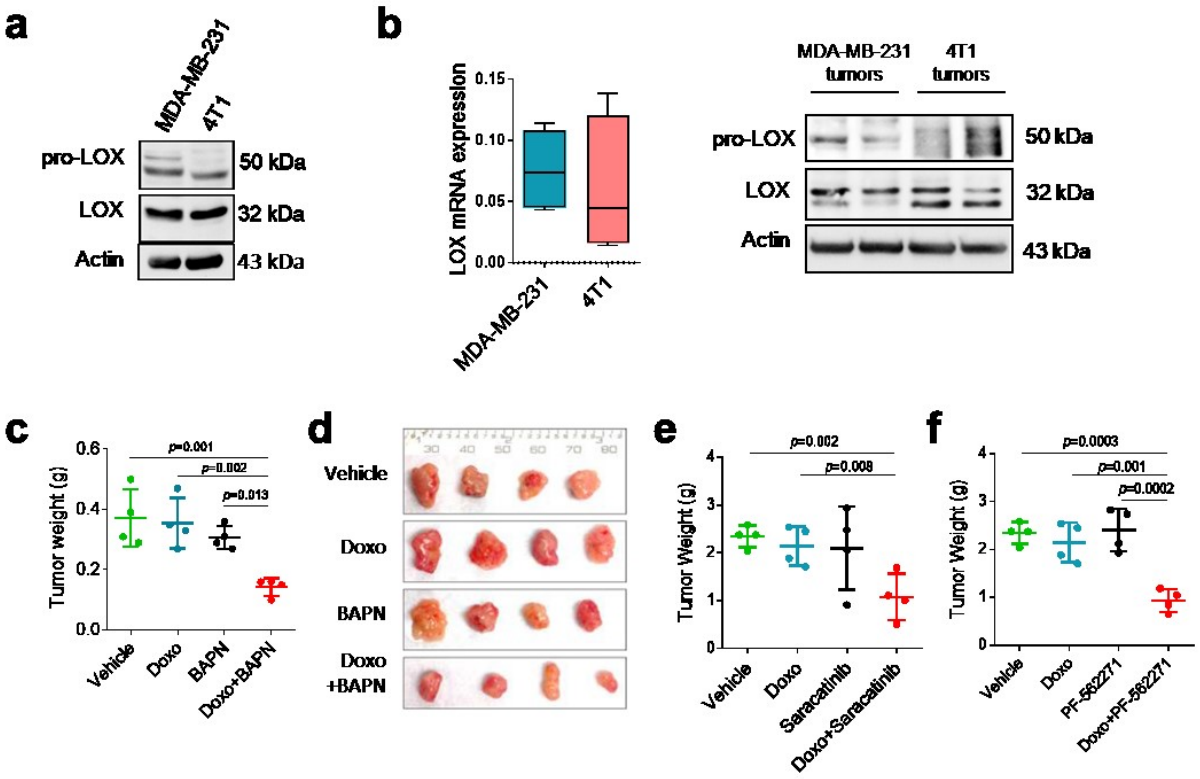
Supplementary Figure 7. Association of LOX with chemoresponse in breast cancer subtypes. a. Western blot analysis of LOX and pro-LOX in a panel of breast cancer cell lines. **b.** % growth inhibition upon Doxo+BAPN treatment of collagen I-embedded MDA-MB-436 (left panel) and MDA-MB-157 cells (right panel) (n=3-4). **c.** % growth inhibition upon Doxo+BAPN treatment of type I collagen-embedded ER+ models (n=3-4). **d.** % growth inhibition upon paclitaxel (PTX) or epirubicin treatment in combination with BAPN in collagen I-embedded MDA-MB-231 cells (n=3). Data represents mean ± SD. One-way ANOVA with Dunnett's test was performed to compare mean of combination-treated group with single agent treatments in **b-d**. Source data are provided as a Source Data file.



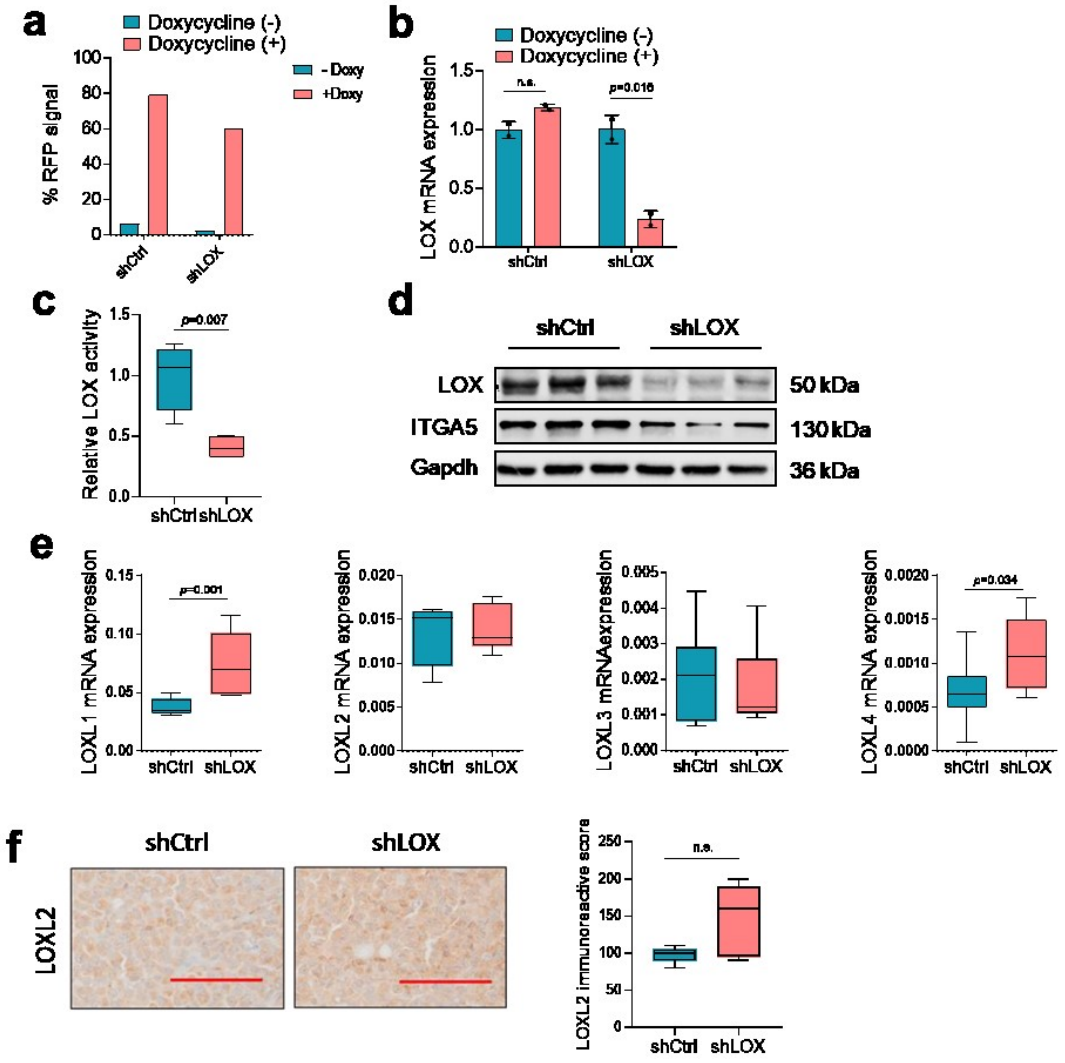
Supplementary Figure 8. Collagen/fibronectin co-localization and cell contact upon LOX inhibition. **a.** Co-localization of collagen fibers with fibronectin in HFF-derived ECM from vehicle (n=30) vs. BAPN-treated (n=25) MDA-MB-231 cells. Only ECM (n=9) group represents the staining of type I collagen and fibronectin in the absence of MDA-MB-231 cancer cells. **b.** 3D images of HFF-derived ECM showing the contact of cancer cells with the surrounding ECM. **c.** The percentage of cells having a range of predefined distances of cell nuclei to the surrounding ECM fibers. A distance of '0' indicates direct contact (n=3). Data represents mean ± SD. In Box plots, the box depicts median, 25th to 75th percentiles, and the whisker depicts min to max. Two-sided Student's t-test was used to calculate statistical difference between two groups. Source data are provided as a Source Data file.



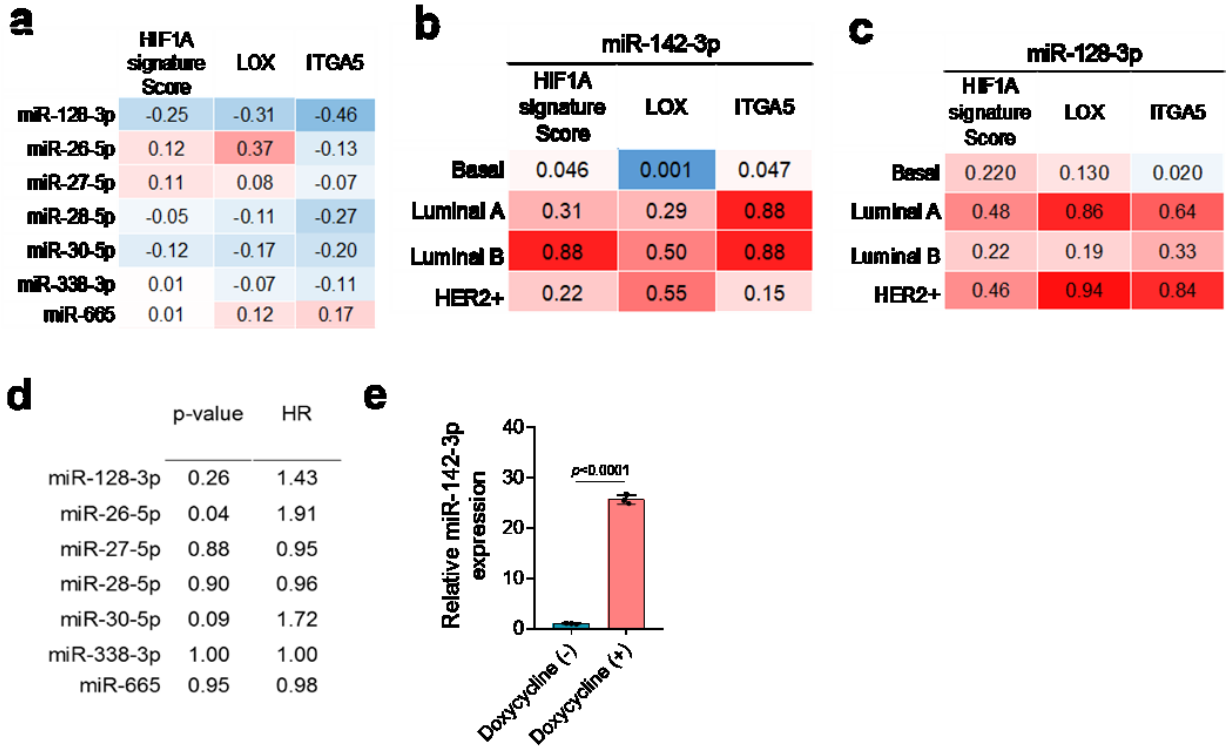
Supplementary Figure 9. Change in FAK/Src signaling and apoptosis upon Doxo+FAK/Src inhibition. a. Western blot analysis of p-FAK and p-Src levels upon treatment of collagen I-embedded MDA-MB-231 cells with doxorubicin in combination with PF-562271 or Saracatinib. **b, c**. Cleaved Caspase-3 (red) and F-actin (green) staining (b) and the quantification of apoptotic fraction (c) in collagen I-embedded MDA-MB-231 cells treated with PF-532271 or Saracatinib in combination with doxorubicin for 48 hours (n=2). Data represents mean ± SD. One-way ANOVA with Dunnett's test was performed to compare mean of combination-treated group with single agent treatments in **c**. Scale bar= 50 μm. Source data are provided as a Source Data file.



Supplementary Figure 10. LOX expression in 4T1 model and tumor weights upon doxorubicin sensitization. a. Western blot analysis of LOX in MDA-MB-231 and 4T1 cells. **b.** qRT-PCR (n=9) and western blot analysis of LOX in MDA-MB-231 and 4T1 tumors. **c.** Change in tumor weight in 4T1 tumors in Balb/c mice upon treatment with doxorubicin and BAPN (n=4). **d.** Images of tumors isolated from the mice in c. **e, f.** Change in tumor weight in 4T1 tumors in Balb/c mice upon treatment with doxorubicin and Saracatinib (e) or PF562271(f) (n=4). Data represents mean ± SD. In the Box plot, the box depicts median, 25th to 75th percentiles, and the whisker depicts min to max. One-way ANOVA with Dunnett's test was performed to compare mean of combination-treated group with single agent treatments in **c**, **e** and **f**. Source data are provided as a Source Data file.



Supplementary Figure 11. Expression of LOX family members upon LOX knockdown *in vivo*. a. Validation of the induction of the red fluorescent protein (RFP)-labelled shRNA expression by measuring RFP signal upon doxycycline treatment. **b.** qRT-PCR analysis of LOX in MDA-MB-231 cells after induction of shRNA upon doxycycline treatment (n=2). **c**. Relative LOX activity in tumors that were collected at the end of the experiment (n=4). **d.** Western blot analysis of LOX and ITGA5 in shCtrl vs. shLOX tumors. **e.** Expression of other LOX family members in shCtrl vs. shLOX tumors (n=9). **f.** IHC staining and quantification of LOXL2 in shCtrl vs. shLOX tumors (n=5). Data represents mean ± SD. In Box plots, the box depicts median, 25th to 75th percentiles, and the whisker depicts min to max. Two-sided Student's t-test was used to calculate statistical difference between two groups. Scale bar=100 µm. Source data are provided as a Source Data file.



Supplementary Figure 12. Patient data analyses of miRNAs predicted to target HIF1A/LOX/ITGA5. **a**. Summary table of the Pearson correlation coefficients between miRNAs and HIF1A gene signature, LOX and ITGA5 expression in patients from GSE19783. An intense blue color shows a stronger negative correlation. **b, c.** Summary of the p-values for the Pearson correlation analysis between miR-142-3p (b) and miR-128-3p (c) expression and HIF1A gene signature score, LOX and ITGA5 expressions. An intense blue color shows a stronger negative correlation. **d.** Summary table of the p-values and hazard ratios (HRs) for Kaplan-Meier overall survival analysis based on the expression of miRNAs in chemotherapy-treated TNBC patients (n=106) separated from median. Data were retrieved from METABRIC. **e.** qRT-PCR of miR-142-3p upon doxycycline induction in MDA-MB-231 xenografts inducibly expressing miR-142-3p (n=3). Data represents mean ± SD. Two-sided Student's t-test was used to calculate statistical difference between two groups. Significance for survival analyses was calculated by log-rank (Mantel-Cox) test. Source data are provided as a Source Data file.

Supplementary Tables

Supplementary Table 1. Gene Set Enrichment Analysis (GSEA) of RNA-Seq data of TNBC xenografts in patient datasets for hypoxia

signaling.

	Sensitive vs. Vehicle		Sensitive vs. Resistant	
Name of the gene set	**NES**	**p-value**	**NES**	**p-value**
HALLMARK_HYPOXIA	0.63	0.99	-2.25	< 0.001
HARRIS_HYPOXIA	0.89	0.70	-2.25	< 0.001
MANALO_HYPOXIA_UP	0.86	0.85	-1.85	< 0.001
PID_HIF1_TFPATHWAY	1.1	0.31	-1.9	< 0.001
WINTER_HYPOXIA_METAGENE	0.83	0.91	-1.9	< 0.001

Supplementary Table 2. IPA-based Upstream Regulator Analysis using RNA-seq data of chemoresistant TNBC xenografts.

Gene ID	Log2 FC	Prediction (based on expression direction)	Literature findings
ADM	1.68	Activated	HIF1A upregulates
ANGPTL4	1.22	Activated	HIF1A upregulates
BHLHE40	0.74	Activated	HIF1A upregulates
BNIP3	0.73	Activated	HIF1A upregulates
BNIP3L	1.12	Activated	HIF1A upregulates
C9orf9	1.29	Activated	HIF1A upregulates
CXorf40B	1.02	Activated	HIF1A upregulates
EGLN3	1.62	Activated	HIF1A upregulates
EREG	1.05	Activated	HIF1A upregulates
ERO1L	0.63	Activated	HIF1A upregulates
FN1	1.09	Activated	HIF1A upregulates
HILPDA	0.97	Activated	HIF1A upregulates
HK2	0.86	Activated	HIF1A upregulates
ITGA5	0.84	Activated	HIF1A upregulates
L1CAM	0.70	Activated	HIF1A upregulates
LOX	0.80	Activated	HIF1A upregulates
MMP1	0.88	Activated	HIF1A upregulates
NDRG1	1.23	Activated	HIF1A upregulates
NEK8	0.71	Activated	HIF1A upregulates
PFKFB3	1.26	Activated	HIF1A upregulates
PFKFB4	0.80	Activated	HIF1A upregulates
PGF	0.79	Activated	HIF1A upregulates
PGK1	0.84	Activated	HIF1A upregulates
PLAC8	0.69	Activated	HIF1A upregulates
PPFIA4	0.95	Activated	HIF1A upregulates
PTGS2	1.57	Activated	HIF1A upregulates
SLC2A1	0.91	Activated	HIF1A upregulates
SLC2A3	1.26	Activated	HIF1A upregulates
AKAP12	1.15	Affected	HIF1A regulates
ANKRD37	0.74	Affected	HIF1A regulates
ANKZF1	0.63	Affected	HIF1A regulates
BRCA1	-1.43	Affected	HIF1A regulates
CITED2	0.86	Affected	HIF1A regulates
DNASE1	-1.03	Affected	HIF1A regulates
FAM13A	0.78	Affected	HIF1A regulates
IL17RA	0.65	Affected	HIF1A regulates
MMP9	-1.73	Affected	HIF1A regulates
TAF9B	0.62	Affected	HIF1A regulates
SSBP1	0.66	Inhibited	HIF1A downregulates

Supplementary Table 3. Clinical features of 77 TNBC cases treated with chemotherapy.

ID	Age	ER	PR	HER2	Grade	Morphology	ID	Age	ER	PR	HER2	Grade	Morphology
1	35	0	0	0	3	invasive ductal carcinoma	39	48	0	0	0	3	invasive ductal carcinomaa
2	51	0	0	0	3	NA	40	44	0	0	0	2	invasive ductal carcinoma
3	52	0	0	0	3	invasive ductal carcinoma	41	64	0	0	0	3	metaplastic carcinoma
4	58	0	0	0	NA	invasive ductal carcinomaa	42	59	0	0	0	3	invasive pleomorphic lobular carcinoma
5	77	0	0	0	3	invasive ductal carcinoma	43	73	0	0	0	NA	invasive ductal carcinomaa
6	66	0	0	0	NA	invasive carcinoma	44	56	0	0	0	3	invasive ductal carcinoma
7	41	0	0	0	3	invasive ductal carcinoma	45	42	0	0	NA	3	invasive ductal carcinoma
8	55	0	0	0	NA	invasive carcinoma	46	83	0	0	0	2	invasive ductal carcinoma
9	46	0	0	0	2	invasive ductal carcinomaa	47	34	0	0	0	3	invasive ductal carcinoma
10	49	0	0	0	NA	invasive ductal carcinomaa	48	37	0	0	0	3	invasive ductal carcinoma
11	43	0	0	0	3	invasive ductal carcinoma	49	40	0	0	0	3	metaplastic carcinoma
12	73	0	0	0	2	invasive ductal carcinoma	50	57	0	0	0	3	medullary carcinoma
13	56	0	0	0	3	malignant neoplasm	51	42	0	0	0	NA	invasive ductal carcinomaa
14	53	0	0	0	3	NA	52	72	0	0	0	3	invasive ductal carcinoma
15	37	0	0	0	3	invasive ductal carcinoma	53	28	0	0	0	3	NA
16	32	0	0	0	3	metaplastic carcinoma	54	32	0	0	0	3	invasive ductal carcinoma
17	34	0	0	0	NA	invasive ductal carcinomaa	55	33	0	0	0	NA	metastatic carcinoma
18	53	0	0	0	2	mixed invasive carcinoma	56	56	0	0	0	3	ductal carcinoma in situ
19	46	0	0	0	3	medullary invasive ductal carcinoma	57	54	0	0	0	3	invasive ductal carcinoma
20	33	0	0	0	3	invasive ductal carcinoma	58	50	0	0	0	3	invasive ductal carcinoma
21	44	0	0	0	3	invasive ductal carcinoma	59	60	0	0	0	3	invasive ductal carcinoma
22	52	0	0	0	2	ductal carcinoma in situ	60	68	0	0	0	2	invasive ductal carcinoma
23	68	0	0	0	3	invasive ductal carcinoma	61	74	0	0	0	3	invasive ductal carcinoma
24	38	0	0	0	NA	invasive ductal carcinomaa	62	40	0	0	0	3	invasive ductal carcinoma
25	40	0	0	0	3	invasive ductal carcinoma	63	54	0	0	0	3	invasive ductal carcinomaa
26	70	0	0	0	NA	invasive ductal carcinomaa	64	51	0	0	0	NA	metastatic
27	52	0	0	0	NA	metaplastic carcinoma	65	55	0	0	0	3	invasive ductal carcinoma
28	55	0	0	0	3	metastatic carcinoma	66	66	0	0	0	NA	NA
29	51	0	0	0	NA	invasive ductal carcinomaa	67	62	0	0	0	3	invasive ductal carcinoma
30	58	0	0	0	3	invasive carcinoma	68	42	0	0	0	2	NA
31	66	0	0	0	NA	invasive ductal carcinomaa	69	45	0	0	0	3	NA
32	46	0	0	0	3	invasive ductal carcinoma	70	60	0	0	0	3	invasive ductal carcinoma
33	50	0	0	0	3	invasive ductal carcinoma	71	41	0	0	0	3	invasive ductal carcinoma
34	53	0	0	0	3	metaplastic carcinoma	72	62	0	0	0	NA	invasive ductal carcinomaa
35	61	0	0	0	NA	invasive carcinoma	73	82	0	0	0	2	invasive ductal carcinoma
36	26	0	0	0	NA	pleomorphic carcinoma	74	45	0	0	0	3	invasive ductal carcinoma
37	56	0	0	0	2	invasive ductal carcinoma	75	56	0	0	0	3	NA
38	37	0	0	0	3	NA	76	42	0	0	0	NA	invasive ductal carcinomaa
							77	47	0	0	0	3	invasive ductal carcinoma

Supplementary Table 4. Sequences of primers used for 3'-UTR cloning and in qRT-PCR analysis, and list of antibodies used in Western blot or immunohistochemistry or immunofluorescence.

S4A. Sequences of forward and reverse primers used in qRT-PCR analysis.

Gene Symbol	Gene ID	Forward Primer (5' → 3')	Reverse Primer (5' → 3')
ACTB	60	CCAACCGCGAGAAGATGA	CCAGAGGCGTACAGGGATAG
GAPDH	2597	GCCCAATACGACCAAATCC	AGCCACATCGCTCAGACAC
HIF1A	3091	CCACAGGACAGTACAGGATG	TCAAGTCGTGCTGAATAATACC
LOX	4015	GGATACGGCACTGGCTACTT	GACGCCTGGATGTAGTAGGG
ITGA5	3678	GTCGGGGGCTTCAACTTAGAC	CCTGGCTGGCTGGTATTAGC
ITGA10	8515	GTGTGGATGCTTCATTCCAG	GCCATCCAAGACAATGACAA
ITGB5	3693	GGGAGTTTGCAAAGTTTCAGAG	TGTGCGTGGAGATAGGCTTT
FN1	2335	CTGGCCGAAAATACATTGTAAA	CCACAGTCGGGTCAGGAG

S4B. List of antibodies used in Western blot (WB), immunofluorescence (IF) and immunohistochemistry (IHC) analysis.

Antibody	Provider	Catalog number	WB dilution	IF dilution	IHC dilution
Alexa Fluor® 488 anti-mouse	Life Technologies	A-11001	-	1:200	-
Alexa Fluor® 488 anti-rabbit	Life Technologies	A-11034	-	1:200	-
Alexa Fluor® 647 anti-mouse	Life Technologies	A-31571	-	1:200	-
Alexa Fluor® 647 anti-rabbit	Life Technologies	A-31573	-	1:200	-
Alexa Fluor™ 488 Phalloidin	Life Technologies	A12379	-	1:400	-
Beta-actin	MP Biomedicals	691001	1:10000	-	-
CA9	Novus Biologicals	NB100-417	-	-	1:100
Cleaved Caspase -3	Cell Signaling Technology	9664	1:1000	1:200	1:400
Cleaved PARP	Cell Signaling Technology	5625	1:1000	-	-
Collagen I	Abcam	ab34710	-	1:200	-
FAK	Cell Signaling Technology	3285	1:1000	-	-
Flag	Sigma	F1804	1:1000	-	-
FN1	Santa Cruz	sc-81767	1:1000	1:200	-
GAPDH	Santa Cruz	sc-47724	1:10000	-	-
HIF1A	Abcam	51608	1:1000	-	1:300
HRP-coupled anti-mouse IgG	Cell Signaling Technology	7076S	1:10000	-	-
HRP-coupled anti-rabbit IgG	Cell Signaling Technology	7074S	1:10000	-	-
ITGA5	Sigma	HPA002642	1:1000	-	1:1000
Ki-67	ThermoFisher Scientific	MA5-14520	-	-	1:100
LOX	Abcam	174316	1:2000	-	1:400
LOX	Novus	NB100-2530	1:2000	-	1:400
LOXL2	Novus	NBP1-32954	-	-	1:200
phospho-FAK (Y397)	Abcam	39967	1:1000	-	-
phospho-Src (Y416)	Cell Signaling Technology	2101	1:1000	-	1:300
Src	Cell Signaling Technology	2108	1:1000	-	-

S4C. Sequences of forward and reverse primers used for 3'-UTR cloning.

Gene Symbol	Gene ID	Forward Primer (5' → 3')	Reverse Primer (5' → 3')
HIF1A	3091	CCGCTCGAGCATGTAGACTGCTGGGGC	ATTTGCGGCCGCCCACAGAAGATGTTTATTTGATGTAAC

LOX	4015	CCGCTCGAGTTCAATCCCTGAAATGTCTGC	ATTTGCGGCCGCCATAAAGCCAATGTCTGAGCA
ITGA5	3678	CCGCTCGAGCCCAATTTCAGACTCCCATTCCTG	ATTTGCGGCCGCGTTCTGGTCAGTGGGGGCAC

Supplementary Methods

Cell culture and reagents

Human TNBC cell lines, MDA-MB-231, MDA-MB-157, MDA-MB-436, HCC38, BT20 and HCC1143; ER+ cell lines, MCF-7, T47D and ZR-75-1; and HER2+ cell lines, SK-BR-3, JIMT-1, HCC1954; the human embryonic kidney cells, HEK293FT; mouse mammary cancer cell line, 4T1; and mouse embryonic fibroblast, NIH-3T3 were obtained from ATCC (Manassas, VA, USA). MDA-MB-231 cell line expressing luciferase and GFP (MDA-MB-231.Luc2GFP) that was used in the *in vivo* shLOX experiment was a kind gift from Dr. Dihua Yu (MD Anderson Cancer Center). Human foreskin fibroblast (HFF) cell line was a kind gift from Dr. Mythreye Karthikeyan (University of South Carolina). The original source of these modified cells is ATCC. All the cells were cultured in Dulbecco Modified Eagle Medium (Lonza, NJ, USA) supplemented with 50 U/ml penicillin/streptomycin, 1% non-essential amino acids and 10% fetal bovine serum (Lonza, NJ, USA). The media for ER+ cell lines were further supplemented with insulin (0.1 µg/ml). The cell lines were authenticated and tested for mycoplasma contamination regularly using MycoAlert mycoplasma detection kit (Lonza, NJ, USA). The cumulative culture length of cells between thawing and use in this study was less than 20 passages.

Transient transfection with miRNA mimics, siRNAs and reporters

Transfections were carried out by seeding cells in media containing no antibiotics, and changing media with growth factor reduced Optimem (Gibco, MA, USA) prior to transfection with Lipofectamine 2000 (Invitrogen, CA, USA) in 6-well or 96-well format[1,2]. miR-142-3p mimic and siLOX transfections were done at 40 nM concentrations, and RNA or protein was isolated after 48 hours of transfection. Reporter constructs carrying the 3'-UTRs of human *HIF1A* (NM_001530), *LOX* (NM_002317) and *ITGA5* (NM_002205) were used at a dose of 50 ng (for 96-well experiments) per well for the luciferase reporter assay experiments.

Cell viability assays

To assess the effects of LOX inhibition on doxorubicin response, cells were embedded in 0.5 mg/ml type I collagen in 96 well plates and were treated with BAPN (SantaCruz, TX, USA) or FAK inhibitor, PF-562271 (Selleckchem, TX, USA) or Src inhibitor, Saracatinib (Selleckchem, TX, USA) alone or in combination with doxorubicin for 36 hours. Cell viability was measured with 3D Cell Titer Glo Luminescent Cell Viability (Promega, WI, USA) assay according to the manufacturer's protocol using SoftMax Pro Software (Molecular Devices, CA, USA). To compare doxorubicin response between cells grown in the absence or presence of type I collagen, doxorubicin treatment was done for 72 hours. For the assessment of cell viability upon combination of doxorubicin with miR-142-3p overexpression, cells were transfected with 40 nM miR-142-3p mimic for 36 hours, and then embedded in 0.5 mg/ml type I collagen and treated with 500 nM doxorubicin for 48 hours.

Quantitative RT-PCR analysis

Total RNA was extracted from cultured cells and mice xenograft tumors using TRIsure (Bioline, Luckenwalde, Germany). For the latter, tumors were sliced into small pieces, a part of which was homogenized for complete lysis. Then, cDNA synthesis was performed using RevertAid RT Reverse Transcription Kit (Life Technologies, MA, USA) following manufacturer's protocol. Quantitative real-time PCR assay was carried out using Light Cycler 480 SYBR Green I Master kit in triplicates and data were collected with CFX Manager Software (Biorad, CA, USA). *GAPDH* and *HPRT* were used as housekeeping genes. The sequences of the qRT-PCR primers are provided in Supplementary Table 4a. For miRNA qRT-PCR experiments, *RNU44* and *RNU48* were used as housekeeping genes, and qRT-PCR was performed by TaqMan Real-Time PCR Assays (Thermo Fisher Scientific, MA, USA). For data analysis, $\Delta\Delta C_T$ method was utilized using Excel (Microsoft, WA, USA).

Western blotting

Protein isolation and Western blotting were done as previously described[1,2]. Briefly, proteins were extracted using RIPA lysis buffer with the addition of protease and phosphatase inhibitor cocktails, and protein concentrations were measured using the BCA Protein Assay Reagent Kit (Thermo Fisher Scientific, MA, USA). For extracting proteins from collagen-embedded cells, cells were treated with 1.5 mg/ml of collagenase solution containing phosphatase inhibitor cocktail for 10 minutes at 37 °C. Equal amounts of protein were separated using 8-10% SDS-PAGE gel. Separated proteins were transferred to PVDF membranes (Bio-Rad, CA, USA) using a Trans-Blot turbo transfer system (Bio-Rad, CA, USA) and incubated with primary antibodies (Supplementary Table 4b). Horseradish peroxidase-conjugated anti-mouse or anti-rabbit antibodies (Cell signaling Technology, MA, USA) were used as secondary antibodies, and signals were detected by enhanced chemiluminescence (Thermo Fisher Scientific, MA, USA). Images were acquired using Image Lab Software (Biorad, CA, USA).

Cell embedding in type I collagen matrix

Collagen solution was prepared at a concentration of 0.5-1 mg/ml from the rat tail collagen I (Corning, USA) with a neutralization step including the addition of 1N NaOH solution. Cell pellets were resuspended in neutralized collagen mix in PBS. While $8x10^3$ cells in 60 µl or in 30 µl were seeded into 96-well or µ-Slide 8-well glass bottom chambers, respectively; $3x10^5$ cells in 1 ml were seeded into 6 well plates. After 1 hour of incubation at room temperature, media was added on top of the solidified collagen, and the cells embedded in collagen were incubated at 37 °C for the desired amount of time. Drug treatments were done 12 hours after cell seeding.

Fibroblast-derived ECM

Generation of human foreskin fibroblasts (HFFs) derived ECM was performed by seeding HFFs onto coverslips with a cell density of $2x10^5$ cells per well and incubating at 37 °C for 6 days. Fibroblast cells were then removed using an extraction buffer containing 25 mM ammonium hydroxide and 0.5% Triton X-100. 20 ug/ml *DNAse I* treatment was done for 30 min to get rid of the remaining cell debris[3]. $2x10^5$

MDA-MB-231 cells treated with 10 mM BAPN or transfected with 40 nM miR-142-3p were seeded onto the extracted ECM and incubated for 72 hours at 37 °C followed by immunofluorescence staining of type I collagen and fibronectin.

Analysis of fibronectin fibril assembly by DOC lysis

DOC lysis assay was done by seeding MDA-MB-231 cells pretreated with vehicle or BAPN onto ECM, derived from HFF or NIH3T3 cells. After an additional 2 days of BAPN treatment, the matrix was solubilized by scraping in DOC lysis buffer that contains 2% Sodium Deoxycholate, 0.02 M Tris-HCl pH 8.8, 2 mM PMSF, 2 mM EDTA, 2 mM Iodoacetic Acid and 2 mM N-ethylmalemide. The solution was passed through 23G needle for 5 times. After shaking on ice for 30 min, samples were centrifuged at 21,130g for 30 min at +4. The supernatant was collected as the soluble fraction, mixed with 4X loading dye and boiled at 95 ºC for 5 min. The insoluble pellet was resuspended in 20 uL SDS lysis buffer, and then mixed with 4X loading dye followed by boiling at 95 ºC for 5 min. Samples were analyzed by Western blotting[4].

Immunofluorescence staining

Immunofluorescence staining of cells or type I collagen and/or fibronectin was done in µ-Slide 8-well glass bottom chambers (Ibidi, Germany). Cells were fixed with 4% paraformaldehyde for 20 min, permeabilized with 0.5% Triton X-100 for 10 min and blocked in 5% BSA-PBS. For staining of type I collagen and fibronectin, no permeabilization was done. Samples were incubated with primary and secondary Alexa Fluor 647 or 488-labeled antibodies for 1.5 hours at room temperature. Cells were also counterstained with DAPI for 5 min. Images were acquired using ZEN 2012 SP5 (Black) LSM 700 (Carl Zeiss, DE). Images were analyzed using the ImageJ software[5]. To quantify the cleaved Caspase-3 positive cells, the intensity from the red channel (the color for cleaved caspase 3) was adjusted to almost zero and the same intensity was applied to all other images (Supplementary Fig. 6d). Then, red signals that overlap with DAPI were quantified. A minimum of 200 cells were counted. As doxorubicin has intrinsic fluorescence with a

maximum excitation and emission wavelengths of 495 and 595 nM[6], respectively, we also acquired images from unstained, doxorubicin-treated cells, but detected no background fluorescence in green or red channels at the laser power and gain used for F-actin (green) or cleaved Caspase-3 visualizations.

For the analysis of ECM structures, images from 5-9 different areas in each biological replicate were acquired. For 3D collagen embedded samples, total collagen intensity of collagen was calculated as remaining "total green area" after the subtraction of the green intensity derived from intracellular collagen. Since fibronectin did not give any cell-derived signal in our system, fibronectin intensity was calculated as "total red area" of each sample. For co-localization quantification, a color threshold was applied to measure the spatial overlap between channels in identical pixel positions. To analyze the minimal distances of each nuclei (DAPI) to fibronectin, a 3D distance map was created. Calculated distances were clustered into 6 groups where "0" value represents the percentage of cells in contact with fibronectin.

Annexin V/DAPI staining

Cells were embedded in collagen I and treated with different drug combinations for 72 hours. After 72 hours, cells were washed once with PBS and the collagen matrix was degraded by applying 1.5 mg/ml collagenase for 5 minutes at 37 ºC. Cells were recovered from collagen matrix by pipetting several times, and the collagenase activity was inhibited by adding equal amount of media with 10% FBS. Cells were counted and 100,000 cells per group were collected, centrifuged and washed once with PBS. Cell pellet was dissolved in 100 µL Annexin V binding buffer and 1.5 µL of FITC-conjugated Annexin V was added. Cells were incubated at room temperature for 15 min in the dark followed by incubation with DAPI for an additional 5 minutes. Finally, cell solution was diluted in Annexin V binding buffer followed by data collection with BD FACSDiva software (BD, NJ, USA) and analysis with De Novo FCS Express software.

Hypoxia assay

Cells were seeded into 6-well plates and incubated overnight at 37 ºC in normoxic conditions. 24 hours later, plates were placed in Hypoxia Incubator Chamber (StemCell, MA, USA) in 1% Oxygen at 37 °C for

0-24 hours. After each time point, cells were collected by trypsinization and preserved for RNA and protein isolations.

Cloning the 3'-UTRs of the target genes

The construction of plasmids carrying the 3′-UTR sequences of human *HIF1A*, *LOX* and *ITGA5* genes was done by amplifying the 3′-UTR regions of *HIF1A*, *LOX* and *ITGA5* by PCR using genomic DNA of the MDA-MB-231 cell line and cloning downstream of the *Renilla* luciferase open reading frame in the psiCHECK-2 vector (Promega, WI, USA) using *XhoI* and *NotI* restriction sites[7]. The 3′-UTRs of *HIF1A*, *LOX* and *ITGA5* containing binding sites for miR-142-3p were amplified using primers listed in Supplementary Table 4c. These amplicons were ligated separately into psiCHECK-2 vector backbone.

Dual luciferase reporter assay

Dual-luciferase reporter assay was performed by seeding cells into 96-well plates and co-transfecting with miR-142-3p mimic and the 3'UTRs cloned into psiCHECK-2 vector. 24 hours after transfection, cells were lyzed, transferred to a white plate and the Dual Luciferase Reporter Assay (Promega, WI, USA) was performed according to manufacturer's instructions[7]. Luciferase activity was measured in Synergy HT microplate reader (BioTek, Vermont, USA), and the values were normalized to *firefly* luciferase activity.

LOX activity assay

LOX activity within cells or within tumors was measured using fluorometric LOX Activity Assay Kit (Abcam, MA, USA) according to manufacturer's instructions. Briefly, serially diluted replicates of tumor lysates or cell supernatants were incubated with reagent mix, and subsequently measured in fluorescence microplate reader at Ex/Em = 540/590 nm wavelength. Tumor lysates were prepared by sonicating tissue samples in extraction buffer (6 M urea, 10 mM Tris pH 7.4 and protease inhibitors) followed by centrifugation.

Collagen Assay

Collagen Assay from Abcam (ab222942) was performed following manufacturer's instructions. Briefly, fibroblast-derived ECM that was pre-incubated with BAPN or vehicle-treated cancer cells was solubilized in acid/pepsin mixture (0.5 M acetic acid and 0.1 mg/ml of pepsin) overnight at +4 ºC. The mixture is neutralized with 10 N NaOH and vortexed. Cell debris was removed by brief centrifugation, and the supernatant was collected as the soluble fraction. For HFF-derived ECM experiments, cell culture media was also collected as the soluble fraction. Then, the insoluble pellet was dissolved in 10 N NaOH at 120 ºC for 1 hour, followed by neutralization with 10 N HCl. For tumors samples a minimum of 10 mg tumor pieces were sonicated and hydrolyzed in 10 N NaOH for 1 hour at 120 ºC.

Lentiviral vector constructs and infections

TRIPZ inducible lentiviral non-silencing shRNA Control (RHS4743) and LOX shRNA vectors were obtained from Dharmacon. To produce viral particles, 6 μg of each of these vectors and 4.3 μl of trans-lentiviral packaging mix (Dharmacon, CO, USA) were used to co-transfect HEK293FT cells in 6-wells plate with $CaCl_2$ reagent (Dharmacon, CO, USA). 48 hours post-transfection, viral particles were harvested, and used to transduce MDA-MB-231 cells. 96 hours post-transduction, stably transfected cells were selected with 1 μg/ml of puromycin for 3-4 days.

Immunohistochemistry

Immunohistochemistry was performed on 3 μm cut sections using automated bond-max system (Leica microsystems GmbH, Wetzlar, Germany). Briefly, paraffin-embedded specimens were deparaffinized in Dewax solution and subjected to heat-mediated antigen-retrieval for 30 minutes at 90°C using Epitope Retrieval Solution 2 (EDTA-buffer pH 8.8) followed by peroxidase blocking for 5 minutes. Tissues were then incubated with the primary antibody (Supplementary Table 4b) for 15 minutes and with Post Primary Reagent for 8 minutes followed by washing with Bond Wash solution for another 6 minutes. Subsequently, tissues were incubated with Bond Polymer for 8 minutes and developed with DAB-Chromogen for 8

minutes followed by hematoxylin/eosin (H&E) counterstaining. Images were acquired using Olympus BX50 microscope. Immunoreactive scores were calculated as described previously[8].

For staining patient tumor samples, TMAs were constructed from formalin- fixed paraffin-embedded (FFPE) tissues of TNBC patients by the Advanced Tissue Arrayer (ATA100; Chemicon, Temecula, CA, USA) with the approval from the Non- Interventional Clinical Research Ethics Committee of Hacettepe University (approval no: 2020/02-40). Four- micrometer- thick sections were stained with H&E for histologic assessment of the samples in the TMAs. For histological analysis of each protein, the unstained slides were de-paraffinized and rehydrated gradually in decreasing concentrations of ethanol. Endogenous peroxidase activity was blocked with 3% H_2O_2 in methanol. Antigen retrieval was done by microwaving for 10 minutes in citrate buffer (pH 6.0) solution or 30 minutes in 10 mM EDTA buffer (pH 8.0). Slides were incubated with the primary antibodies for 1 hour at room temperature. The UltraVision Polyvalent (Rabbit-Mouse) HRP Kit (TP-125-HL, Thermo Scientific/LabVision), and the avidin-biotin peroxidase method was then used. The signals were developed using the chromogen, 3,3′-diaminobenzidine (DAB, TA-125-HD, Thermo Scientific/LabVision). Finally, samples were briefly counterstained with hematoxylin. The slides were dehydrated and prepared for microscopic examination.

Picrosirius Red staining

Tumor tissues obtained from mice were cut and fixed in a solution of 10% neutral buffered formalin and then embedded in paraffin. Slides were first deparaffinized by incubation at 60 °C for 10 min followed by two washes with xylene for 5 min each. Samples were hydrated by decreasing concentrations of ethyl alcohol (100%, 95%, 80% and 70%, respectively) and rinsed in distilled water. Hydrated sections were stained with Picrosirius Red Stain Kit (Polysciences, Inc.) according to manufacturer protocol and then, dehydrated with 100% ethanol. Sections were mounted after they were cleared in xylene for 5 minutes. Samples were analyzed using a bright field/polarized light microscope (Axiovert 200, Carl Zeiss, DE) with the Axiovision software (Carl Zeiss, DE). Images were converted to RGB, and the intensity of the red channel, representing collagen type I[9-11] was quantified using ImageJ software.

Measuring doxorubicin penetration *in vitro* and *in vivo*

As doxorubicin has intrinsic fluorescence with a maximum excitation and emission wavelengths of 495 and 595 nM, respectively[6], we quantified relative doxorubicin levels in cells embedded in collagen I *in vitro* by measuring the fluorescence intensity coming from doxorubicin or doxorubicin+BAPN treated cells at an excitation and emission wavelengths of 495 and 595 nM, respectively using a microplate reader. For measuring intratumoral doxorubicin levels, we embedded freshly excised tumors in optimum cutting temperature (OCT) compound, froze on dry ice, and stored at –80 °C. Cryostat sections were cut from each tumor, mounted on glass slides, and allowed to air-dry. Doxorubicin autofluorescence was detected using Zeiss LSM700 Confocal Microscopy with the 488 laser.

***In vivo* experiments**

In order to recapitulate *in vivo* resistant model for testing doxorubicin+BAPN combination once tumors develop doxorubicin resistance, MDA-MB-231 xenografts were developed and treated with doxorubicin (2.5 mg/kg) until tumors exhibit accelerated growth despite given therapy as described above. When the tumor volume reached 500 mm^3, they were randomly separated into two groups. One group continued to receive doxorubicin, while the other was treated with doxorubicin and BAPN (100 mg/kg, every other day, i.p.) combination. Survival was calculated using a predefined tumor volume cut-off of 1500 mm^3 or extensive toxicity as determined by a more than 20% decrease in body weight.

To test the role of miR-142-3p on hypoxia/LOX/integrin axis *in vivo*, inducible miR-142-3p overexpressing MDA-MB-231-Luc2-GFP cells were injected into nude mice. Doxycycline was given to induce miR-142-3p expression at 1 mg/ml in drinking water when the tumors reach 70-80 mm^3 for 6 days. Then, mice were sacrificed, and tumors were collected to examine protein expression *via* Western Blotting and miR-142-3q levels *via* qRT-PCR.

Patient data and pathway analyses

Patient data were retrieved from the NCBI GEO database (GSE16446[12], GSE19783[13], GSE21653[14], GSE22219[15], GSE22226[16], GSE25066[17], GSE58644[18], GSE31519 and GSE58812[19]) and from online survival analysis tool, KM-plotter[20], the Molecular Taxonomy of Breast Cancer International Consortium[21] project data from EMBL European Genome–Phenome Archive (http://www.ebi.ac.uk/ega/) with an accession number EGAS00000000122 and The Cancer Genome Atlas (TCGA) data from Chipbase V2 (rna.sysu.edu.cn/chipbase/). For pathway enrichment, the core analysis was performed at IPA platform using top differentially expressed (up- or down-regulated) mRNAs with an adjusted p-value cut-off of 0.05, from doxorubicin sensitive and resistant xenografts. GSEA was performed using gene sets related to hypoxia and integrin signaling downloaded from the GSEA website: http://software.broadinstitute.org/gsea/index.jsp.

Supplementary References

1. Saatci, O., *et al.* Targeting PLK1 overcomes T-DM1 resistance via CDK1-dependent phosphorylation and inactivation of Bcl-2/xL in HER2-positive breast cancer. *Oncogene* **37**, 2251-2269 (2018).
2. Mishra, R.R., *et al.* Reactivation of cAMP Pathway by PDE4D Inhibition Represents a Novel Druggable Axis for Overcoming Tamoxifen Resistance in ER-positive Breast Cancer. *Clinical cancer research : an official journal of the American Association for Cancer Research* **24**, 1987-2001 (2018).
3. Kaukonen, R., Jacquemet, G., Hamidi, H. & Ivaska, J. Cell-derived matrices for studying cell proliferation and directional migration in a complex 3D microenvironment. *Nature protocols* **12**, 2376-2390 (2017).
4. Varadaraj, A., Magdaleno, C. & Mythreye, K. Deoxycholate Fractionation of Fibronectin (FN) and Biotinylation Assay to Measure Recycled FN Fibrils in Epithelial Cells. *Bio Protoc* **8**(2018).
5. Schindelin, J., *et al.* Fiji: an open-source platform for biological-image analysis. *Nat Methods* **9**, 676-682 (2012).
6. Liang, J.Y., *et al.* Simple and rapid monitoring of doxorubicin using streptavidin-modified microparticle-based time-resolved fluorescence immunoassay. *Rsc Adv* **8**, 15621-15631 (2018).
7. Raza, U., *et al.* The miR-644a/CTBP1/p53 axis suppresses drug resistance by simultaneous inhibition of cell survival and epithelial-mesenchymal transition in breast cancer. *Oncotarget* **7**, 49859-49877 (2016).
8. Fedchenko, N. & Reifenrath, J. Different approaches for interpretation and reporting of immunohistochemistry analysis results in the bone tissue - a review. *Diagnostic pathology* **9**, 221 (2014).
9. Cox, T.R., *et al.* LOX-mediated collagen crosslinking is responsible for fibrosis-enhanced metastasis. *Cancer research* **73**, 1721-1732 (2013).
10. Junqueira, L.C., Cossermelli, W. & Brentani, R. Differential staining of collagens type I, II and III by Sirius Red and polarization microscopy. *Arch Histol Jpn* **41**, 267-274 (1978).
11. Raj, Y., *et al.* Evaluation of the Nature of Collagen Fibers in KCOT, Dentigerous Cyst and Ameloblastoma using Picrosirius Red Stain - A Comparative Study. *J Clin Diagn Res* **9**, ZC01-04 (2015).
12. Desmedt, C., *et al.* Multifactorial approach to predicting resistance to anthracyclines. *Journal of clinical oncology : official journal of the American Society of Clinical Oncology* **29**, 1578-1586 (2011).
13. Enerly, E., *et al.* miRNA-mRNA integrated analysis reveals roles for miRNAs in primary breast tumors. *PloS one* **6**, e16915 (2011).
14. Sabatier, R., *et al.* A gene expression signature identifies two prognostic subgroups of basal breast cancer. *Breast cancer research and treatment* **126**, 407-420 (2011).
15. Buffa, F.M., *et al.* microRNA-associated progression pathways and potential therapeutic targets identified by integrated mRNA and microRNA expression profiling in breast cancer. *Cancer research* **71**, 5635-5645 (2011).
16. Esserman, L.J., *et al.* Chemotherapy response and recurrence-free survival in neoadjuvant breast cancer depends on biomarker profiles: results from the I-SPY 1 TRIAL (CALGB 150007/150012; ACRIN 6657). *Breast cancer research and treatment* **132**, 1049-1062 (2012).
17. Hatzis, C., *et al.* A genomic predictor of response and survival following taxane-anthracycline chemotherapy for invasive breast cancer. *Jama* **305**, 1873-1881 (2011).
18. Tofigh, A., *et al.* The prognostic ease and difficulty of invasive breast carcinoma. *Cell reports* **9**, 129-142 (2014).
19. Jezequel, P., *et al.* Gene-expression molecular subtyping of triple-negative breast cancer tumours: importance of immune response. *Breast cancer research : BCR* **17**, 43 (2015).

20. Gyorffy, B.*, et al.* An online survival analysis tool to rapidly assess the effect of 22,277 genes on breast cancer prognosis using microarray data of 1,809 patients. *Breast cancer research and treatment* **123**, 725-731 (2010).
21. Curtis, C.*, et al.* The genomic and transcriptomic architecture of 2,000 breast tumours reveals novel subgroups. *Nature* **486**, 346-352 (2012).

Clinical Cancer Research

Reactivation of cAMP Pathway by PDE4D Inhibition Represents a Novel Druggable Axis for Overcoming Tamoxifen Resistance in ER-positive Breast Cancer

Rasmi R. Mishra[1], Nevin Belder[1], Suhail A. Ansari[1], Merve Kayhan[1], Hilal Bal[1], Umar Raza[1], Pelin G. Ersan[1], Ünal M. Tokat[1], Erol Eyüpoğlu[1], Özge Saatci[1], Pouria Jandaghi[2,3], Stefan Wiemann[4], Ayşegül Üner[5], Caglar Cekic[1], Yasser Riazalhosseini[2,3], and Özgür Şahin[1,6]

Downloaded from http://aacrjournals.org/clincancerres/article-pdf/24/8/1987/2050104/1987.pdf by Bilkent University user on 31 August 2022

Abstract

Purpose: Tamoxifen remains an important hormonal therapy for ER-positive breast cancer; however, development of resistance is a major obstacle in clinics. Here, we aimed to identify novel mechanisms of tamoxifen resistance and provide actionable drug targets overcoming resistance.

Experimental Design: Whole-transcriptome sequencing, downstream pathway analysis, and drug repositioning approaches were used to identify novel modulators [here: phosphodiesterase 4D (PDE4D)] of tamoxifen resistance. Clinical data involving tamoxifen-treated patients with ER-positive breast cancer were used to assess the impact of PDE4D in tamoxifen resistance. Tamoxifen sensitization role of PDE4D was tested *in vitro* and *in vivo*. Cytobiology, biochemistry, and functional genomics tools were used to elucidate the mechanisms of PDE4D-mediated tamoxifen resistance.

Results: PDE4D, which hydrolyzes cyclic AMP (cAMP), was significantly overexpressed in both MCF-7 and T47D tamoxifen-resistant (TamR) cells. Higher PDE4D expression predicted worse survival in tamoxifen-treated patients with breast cancer ($n = 469$, $P = 0.0036$ for DMFS; $n = 561$, $P = 0.0229$ for RFS) and remained an independent prognostic factor for RFS in multivariate analysis ($n = 132$, $P = 0.049$). Inhibition of PDE4D by either siRNAs or pharmacologic inhibitors (dipyridamole and Gebr-7b) restored tamoxifen sensitivity. Sensitization to tamoxifen is achieved via cAMP-mediated induction of unfolded protein response/ER stress pathway leading to activation of p38/JNK signaling and apoptosis. Remarkably, acetylsalicylic acid (aspirin) was predicted to be a tamoxifen sensitizer using a drug repositioning approach and was shown to reverse resistance by targeting PDE4D/cAMP/ER stress axis. Finally, combining PDE4D inhibitors and tamoxifen suppressed tumor growth better than individual groups *in vivo*.

Conclusions: PDE4D plays a pivotal role in acquired tamoxifen resistance via blocking cAMP/ER stress/p38-JNK signaling and apoptosis. *Clin Cancer Res; 24(8); 1987–2001. ©2018 AACR.*

Introduction

More than 70% of breast tumors express estrogen receptor alpha (ERα) and consequently receive various endocrine therapies modulating ERα (1, 2). ER-targeted therapies include (i) selective ER modulators (SERMs) like tamoxifen and raloxifene, (ii) aromatase inhibitors (AI) such as letrozole, anastrozole, and exemestane, and (iii) selective ER downregulators (SERDs) like fulvestrant. Tamoxifen is widely used as the standard first-line adjuvant therapy since its discovery in 1970 for treatment of patients with ER-positive breast cancer, particularly in premenopausal women (3, 4). Several clinical trials have showed that treatment with adjuvant tamoxifen for at least 5 years reduces the breast cancer recurrence and mortality rates by around half and one-third, respectively, throughout the first 15 years (3–5). However, approximately 20%–30% cases of high risk, advanced ER-positive breast cancer develop *de novo* or acquired resistance to tamoxifen, despite its clinical success (6).

The mechanism of tamoxifen resistance is partially understood and involves multiple factors. Most common mechanisms include the activation of several receptor tyrosine kinases (RTKs), for example, EGFR, HER2, fibroblast growth factor receptor 1 (FGFR1), and insulin-like growth factor-1 receptor (IGF-1R). This leads to enhanced activity of kinases downstream of these receptors such as extracellular-regulated kinase (ERK) 1/2, AKT, and p21-activated kinase-1 (PAK1), and promotes tumor growth and metastasis (7, 8). Furthermore, altered expressions of cell survival molecules such as c-Myc, Bad, and Bcl-2 are correlated with poor

[1]Department of Molecular Biology and Genetics, Faculty of Science, Bilkent University, Ankara, Turkey. [2]Department of Human Genetics, McGill University, Montreal, Quebec, Canada. [3]McGill University and Genome Quebec Innovation Centre, Montreal, Quebec, Canada. [4]Division of Molecular Genome Analysis, German Cancer Research Center (DKFZ), Heidelberg, Germany. [5]Department of Pathology, Faculty of Medicine, Hacettepe University, Ankara, Turkey. [6]National Nanotechnology Research Center (UNAM), Bilkent University, Ankara, Turkey.

Note: Supplementary data for this article are available at Clinical Cancer Research Online (http://clincancerres.aacrjournals.org/).

Corresponding Author: Özgür Şahin, Bilkent University, Department of Molecular Biology and Genetics, Faculty of Science, B Building SB-247, Ankara 06800, Turkey. Phone: 90-312-290-2402; Fax: 90-312-266-5097; E-mail: sahinozgur@gmail.com

doi: 10.1158/1078-0432.CCR-17-2776

©2018 American Association for Cancer Research.

Translational Relevance

Tamoxifen remains an important hormonal therapy for patients with ER-positive breast cancer; however, development of resistance is a major obstacle for therapeutic success. Therefore, there is an urgent need for identification of novel druggable targets overcoming resistance. In this study, we identified phosphodiesterase 4D (PDE4D)/cAMP/ER stress axis as a novel tamoxifen resistance mediator in ER-positive breast cancer. Tamoxifen-treated patients with breast cancer with higher PDE4D expression showed poorer distant metastasis and relapse-free survival, and higher PDE4D expression remained an independent prognostic factor in multivariate analysis. Moreover, inhibition of PDE4D by either siRNAs or pharmacologic inhibitors restored tamoxifen sensitivity both *in vitro* and *in vivo*. Overall, our study uncovered a cAMP pathway, specifically PDE4D, as a critical modulator of tamoxifen resistance, and thus paves the way for testing cAMP inducers, some of which are already FDA approved such as dipyridamole and the over-the-counter drug acetylsalicylic acid (aspirin), in tamoxifen-refractory patients with ER-positive breast cancer.

survival of patients under endocrine therapy (9, 10). In addition, involvement of noncoding RNAs, such as microRNAs (miRNAs) and long noncoding RNAs (lncRNA), in tamoxifen resistance has been described. For example, several oncogenic miRNAs, for example, miR-519 and miR-221/222 confer tamoxifen resistance (11, 12), while reexpression of miR-375, let-7, or miR-342 induce tamoxifen sensitivity via their respective mRNA target genes (11, 12). Recently, upregulation of a few lncRNAs, for example, HOTAIR and BCAR4, has also been shown to confer tamoxifen resistance (11).

With nearly 1.2 million new ER-positive breast cancer cases diagnosed in 2012 worldwide (http://www.wcrf.org/) and significant number of cases developing inevitable drug resistance, there is an immediate need for identification of novel druggable targets to overcome tamoxifen resistance. Here, we aim to identify novel mechanisms of tamoxifen resistance and thus pave the way for testing new combinations to improve survival in tamoxifen refractory, ER-positive breast cancer.

Materials and Methods

Cell culture

Human breast cancer cell lines MCF-7 and T47D were purchased from ATCC and cultured in phenol red–free DMEM (Gibco) with 10% FBS, 0.1% insulin, 50 U/mL penicillin/streptomycin, 1% nonessential amino acids (Gibco). Tamoxifen-resistant MCF-7 cells (MCF-7 TamR) were generated as described previously (12). In brief, MCF-7 and T47D TamR cells were grown in the presence of 5 μmol/L of 4-hydroxytamoxifen (Sigma-Aldrich) for 1 year. In parallel, parental MCF-7 and T47D cells were maintained under identical conditions without tamoxifen. Cells were routinely tested for mycoplasma contamination using MycoAlert detection kit (Lonza), and were authenticated by STR sequencing (Promega) at German Cancer Research Center (DKFZ). The cumulative culture length of the cells between thawing and use in the study was less than 20 passages.

Reagents and chemicals

Reagents and other chemicals including their catalog numbers are as following: tamoxifen (Sigma, T176), acetylsalicylic acid (Sigma, A5376), dipyridamole (Tocris, 691), Gebr-7b (Millipore/Calbiochem, 524748), 6-Bnz-cAMP sodium salt (Tocris, 5255), 8-pCPT-2-O-Me-cAMP-AM (Tocris, 4853), cAMPS-Sp triethylammonium salt (Tocris, 1333) and thapsigargin (Sigma, T9033), and SQ22536 (Sigma, AB120642).

Whole-transcriptome sequencing (RNA-Seq) and data analysis

Ribosomal RNA (rRNA)-depleted libraries were generated for each sample, and these sequences were multiplexed. RNA sequencing was performed for each condition (MCF-7 parental and MCF-7 TamR) in triplicates using the Illumina HiSeq 2000 platform at McGill University and Genome Quebec Innovation Centre. Details are provided in Supplementary Data.

Generation of TamR gene signature and bioinformatics analysis

Tamoxifen resistance gene signature (TamR-GS) was generated comprising of the top 417 differentially expressed mRNAs ($\log_2$ FC $\pm$ 2 and $P \leq 0.05$) between MCF-7 TamR cells and their parental counterparts. For the calculation of the TamR-GS score, the sum of z-scores of the downregulated genes in the TamR-GS was subtracted from the sum of z-scores of the upregulated genes for each patient. This method of calculating a gene signature score by using the mRNA expression data has been reported previously (13). In survival analysis and GSEA, patients were separated either from the median or from 25th percentile, as low and high PDE4D or TamR-GS scorers based on their PDE4D expression or the TamR-GS score, respectively. Details of the bioinformatic analysis are provided in Supplementary Data.

qRT-PCR analysis

Total RNA was extracted from cultured cells using TRIsure (Bioline), and cDNAs were generated using RevertAid RT Reverse Transcription Kit (Life Technologies). qRT-PCR analysis was performed with gene-specific primers using LightCycler 480 SYBR Green I Master kit (Roche). *HPRT1*, *GAPDH*, and *ACTB* were used as housekeeping genes. The average C_t value was calculated from triplicates of each sample, and the relative mRNA expression was determined. Sequences of the qRT-PCR primers are listed in Supplementary Table S1.

Transient transfection with siRNAs and overexpression vectors

PDE4D-specific siRNAs were purchased from Dharmacon (Supplementary Table S2). Transfections were done with 20 nmol/L siRNA using Lipofectamine 2000 (Invitrogen) according to manufacturer's instructions. PDE4D cDNA (NM_006203.4) present in pcDNA3.1+/C-(K) DYK mammalian expression vector (GenScript) was used for overexpression experiments. Briefly, 50 ng (for 96-well plate) or 500 ng (for 6-well plate) of PDE4D plasmid DNA was transiently transfected using Effectene transfection reagent (Qiagen).

Inhibitor treatments, cell proliferation and apoptosis assays

Details of the inhibitor treatments, cell proliferation, and apoptosis assays are provided in Supplementary Materials and Methods section in Supplementary Data.

Downloaded from http://aacrjournals.org/clincancerres/article-pdf/24/8/1987/2050104/1987.pdf by Bilkent University user on 31 August 2022

Western blotting

Total protein was extracted using RIPA buffer (150 mmol/L NaCl, 50 mmol/L Tris base pH 8.0, 1 mmol/L EDTA, 0.5% sodium deoxycholate, 1% NP40, 0.1% SDS, 1 mmol/L DTT, and 1 mmol/L Na_3VO_4) supplemented with Complete Protease Inhibitor (Roche). Protein concentrations were measured using BCA Protein Assay (Thermo Scientific). Equal amounts of protein lysates (15–20 μg) were separated on a 10% SDS-PAGE, transferred onto polyvinylidene difluoride membrane (Bio-Rad) and incubated with primary antibodies (Supplementary Table S3). The blots were developed using enhanced chemiluminescence (ECL) detection kit (Amersham Biosciences) after incubation with horseradish peroxidase–conjugated secondary antibody. β-Actin was used as a loading control.

Intracellular cAMP measurements

To measure intracellular cAMP levels, 10,000 cells were seeded per well in 96-well plates. Following day, cells were treated with PDE4D inhibitors (dipyridamole or Gebr-7b or aspirin) alone or vehicle-only or in combination with tamoxifen (5.0 μmol/L) for 20 minutes. After treatment, cells were washed with PBS and incubated with 100-μL ice-cold 0.6 mol/L perchloric acid followed by 15 μL 2.5 mol/L potassium carbonate for neutralization. Cells were incubated on ice for 30 minutes and then centrifuged at 13,000 rpm to collect the clear lysate. Twenty microliters of the clear lysate was used for measurement of cAMP concentration with the LANCE Ultra cAMP detection reagents (PerkinElmer) according to the manufacturer's protocol.

Mouse xenograft studies

All animal work was approved by the Institutional Animal Care and Use Committee of Bilkent University. In xenograft studies, female athymic nude mice were used. All mice were maintained under a temperature-controlled environment with a 12-hour light/dark cycle and received a standard diet and water *ad libitum*. Primary tumors with MCF-7 TamR cells were developed in 6- to 8-week-old mice. Slow release estradiol pellets (0.36 mg, 60 days; Innovative Research of America) were implanted subcutaneously (s.c) at the nape of the neck one day before injection. A total of 1×10^7 MCF-7 TamR cells were injected subcutaneously into both left and right sides of mammary fat pads. Tumor growth was regularly monitored, and size measurements were performed two times per week. Tumor volume was calculated using the formula (length $\times$ width^2)/2. After tumor size reached 100 mm^3, mice were randomly divided into 8 groups, with 5 tumors per group. Animals were treated with vehicle, tamoxifen (2 mg/kg in corn oil, by oral gavage), dipyridamole (15 mg/kg in PBS: PEG 400 (1: 1), daily intraperitoneally), Gebr-7b (3 μg/kg in 0.5 % methyl 2-hydroxyethyl cellulose+0.005% DMSO, daily via intraperitoneally), aspirin [100 mg/kg in PBS: PEG 400 (1: 1), daily intraperitoneally) or combinations. The body weight and tumor size of each mouse were recorded twice a week. Mice were sacrificed 28 days after initiation of the treatment, and the tumors were collected and stored for subsequent analysis.

IHC

Tumor samples isolated from the MCF-7 TamR xenografts were fixed in 10% formalin and processed into paraffin blocks. Histologic sections were taken with 5-μm thickness and deparaffinized. All sections were prepared for Haematoxylin & Eosin, Ki-67 (Dako, catalog no: 7240) and ApopTag Fluorescein *In Situ* Apoptosis Detection Kit (Millipore SiGMa), staining according to the standard procedures.

Statistical analysis

All statistical analyses were performed using either Student *t* test or one-way ANOVA (multiple comparisons) in GraphPad Prism 6 (GraphPad Software, Inc). All results were represented as mean $\pm$ standard deviation (SD) and obtained from three independent experiments. The Kaplan–Meier survival plot, HR, and log-rank *P* values were calculated and plotted using GraphPad Prism. The differences were considered statistically significant if $P < 0.05$ and indicated by, *, $P < 0.05$; **, $P < 0.01$.

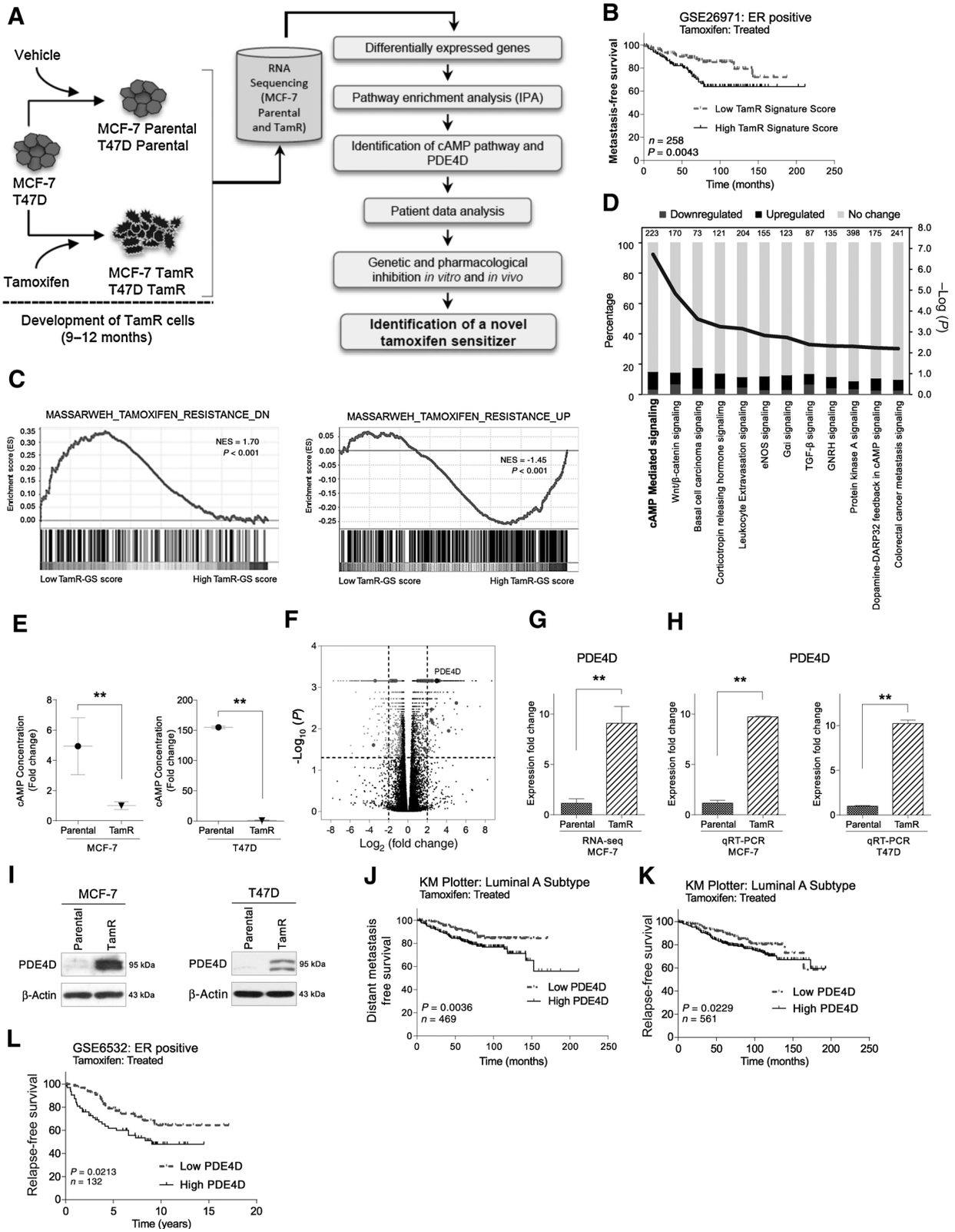
Results

Whole-transcriptome sequencing combined with pathway enrichment and patient data analyses identify PDE4D as a potential mediator of tamoxifen resistance.

We had previously developed, characterized, and reported an acquired tamoxifen-resistant model of MCF-7 cell line (MCF-7 TamR cells and their sensitive counterpart MCF-7 parental) to identify miRNA regulators of tamoxifen resistance (12, 14). To further understand the molecular underpinnings of tamoxifen resistance, and to identify novel druggable targets in ER-positive breast cancer, we performed whole-transcriptome sequencing in these cells, and derived a tamoxifen resistance gene signature (TamR-GS) comprising the most differentially expressed mRNAs ($\log_2$FC ± 2 and $P \leq 0.05$; 417 genes; Supplementary Table S4) between sensitive and resistant cells (Fig. 1A). To examine the clinical relevance of our tamoxifen-resistant cell line and the TamR-GS, we applied this signature to a gene expression profiling data of tumors obtained from patients treated with tamoxifen (GEO dataset GSE26971), and assigned each patient a TamR-GS score by subtracting the sum of *z*-scores of the downregulated genes in the TamR-GS from the sum of *z*-scores of the upregulated genes (see Materials and Methods for details). We observed that the patients with high TamR-GS scores showed poor metastasis-free survival (MFS) as compared with their counterparts with low TamR-GS score (Fig. 1B), confirming the clinical relevance of our cell line. Furthermore, we performed gene-set enrichment analysis (GSEA) after separating tamoxifen-treated, ER-positive patients from GSE22220 as low or high TamR-GS scorers and found that genes downregulated in tamoxifen-resistant xenografts were significantly enriched in patients having low TamR-GS scores while genes upregulated in the same xenografts were significantly enriched in patients having high TamR-GS scores, further supporting the validity of our tamoxifen-resistant cells (Fig. 1C). Ingenuity Pathway Analysis (IPA) indicated that the most significantly enriched canonical pathway in MCF-7 TamR cells compared with their parental cells was cAMP-mediated signaling ($P < 8.77 \times 10^{-8}$; Fig. 1D). Therefore, we measured the cellular cAMP levels in sensitive and resistant derivatives of MCF-7 and of an additional cell line, T47D, which has recently been developed and characterized in our laboratory (Supplementary Fig. S1A–S1D). We observed that the TamR derivatives of both cell lines have markedly lower cellular cAMP levels compared with their sensitive counterparts (Fig. 1E). These observations confirmed our pathway analysis results, and suggest a possible involvement of cAMP pathway in acquired tamoxifen resistance.

Investigating the mechanisms responsible for the observed deregulation of cAMP pathway, we examined the expression of genes associated with this pathway and observed that majority of

Downloaded from http://aacrjournals.org/clincancerres/article-pdf/24/8/1987/2050104/1987.pdf by Bilkent University user on 31 August 2022



Downloaded from http://aacrjournals.org/clincancerres/article-pdf/24/8/1987/2050104/1987.pdf by Bilkent University user on 31 August 2022

these genes (25 of 33 with differential expression) are upregulated in TamR cells (big gray circles in Fig. 1F and PDE4D as black circle), and three of them were validated by qRT-PCR (Supplementary Fig. S2A). Two phosphodiesterases; PDE10A (32.4-fold; $P < 0.002$) and PDE4D (9.1-fold; $P < 0.0007$) were among the most significantly upregulated genes in MCF-7 TamR cells (Supplementary Fig. S2A; Fig. 1G), which are amenable for therapeutic intervention. PDE10A can hydrolyze both cAMP and cGMP, whereas PDE4D is a cAMP-specific phosphodiesterase and thus both are important regulators of cAMP signaling (15). However, siRNA-mediated silencing of PDE10A in MCF-7 TamR did not restore tamoxifen sensitivity (Supplementary Fig. S2B). On the other hand, qRT-PCR and Western blotting (WB) validated the substantial upregulation of PDE4D in both MCF-7 TamR and T47D TamR cells compared with their sensitive counterparts (Fig. 1H and I), and siRNA-mediated knockdown resulted in tamoxifen sensitization as described below. Therefore, we focused on the role of PDE4D, but not that of PDE10A, in tamoxifen resistance.

To determine whether expression of PDE4D is associated with tamoxifen resistance in breast cancer, we first examined PDE4D expression in tamoxifen-treated luminal A breast cancer patients ($n = 469$) using KM plotter tool (16). We found a significant association between higher PDE4D expression and poorer distant metastasis-free survival (DMFS; $P = 0.0036$; $n = 469$) in tamoxifen-treated patients with luminal A breast cancer (Fig. 1J). We also found a significant association between higher PDE4D expression and poorer relapse-free survival (RFS; $P = 0.029$; $n = 561$) in tamoxifen-treated patients (Fig. 1K and L). Particularly, prognostic effect of PDE4D expression was specific to tamoxifen treatment, as high or low PDE4D expression alone could not significantly predict survival in systemically untreated (no treatment received) luminal A patients (Supplementary Fig. S3A and S3B) or patients who did not receive endocrine therapy, but may have received chemotherapy (Supplementary Fig. S3C and D). Notably, PDE4D expression remained an independent prognostic factor in the multivariate analysis by using an expression profiling dataset of tamoxifen-treated patients with breast cancer, GSE6532 (Supplementary Table S5). Overall, our results demonstrate that there is an inverse correlation between cellular cAMP and PDE4D levels, and PDE4D expression has an independent prognostic role in tamoxifen-treated patients with luminal A breast cancer. These results suggested that PDE4D might regulate tamoxifen resistance in breast cancer.

Genetic or pharmacologic inhibition of PDE4D resensitizes tamoxifen-resistant breast cancer cells *in vitro*

To test whether modulating PDE4D expression can overcome tamoxifen resistance, siRNA-mediated knockdown of PDE4D was carried out in both MCF-7 TamR and T47D TamR cells using two different siRNA sequences, and cell proliferation was assessed. The efficiency of PDE4D knockdown was validated by qRT-PCR and Western blot analysis (Supplementary Fig. S4A and S4B). Silencing of endogenous PDE4D restored sensitivity to tamoxifen in both TamR cells (Fig. 2A and B). To further test whether PDE4D could drive tamoxifen resistance *in vitro*, a PDE4D overexpression construct was transiently transfected into MCF-7 and T47D parental cells (Fig. 2C), and these cells were subjected to a cell proliferation assay, which showed significantly increased cell proliferation in PDE4D-transfected cells as compared with control cells (empty vector) in the presence of tamoxifen (Fig. 2D). Next, we sought to examine the effects of pharmacologic inhibition of PDE4D via PDE4D inhibitors (PDE4Is) on tamoxifen sensitization by using Gebr-7b, a highly potent and specific PDE4D inhibitor (17), and dipyridamole (Dipy), a nonselective PDE inhibitor predicted to be a PDE4D inhibitor in our Ingenuity Pathway Analysis (IPA). To examine the effects of pharmacologic inhibition of PDE4D on tamoxifen sensitization, MCF-7 TamR, and T47D TamR cells were treated with dipyridamole or Gebr-7b in the absence and presence of tamoxifen. Combinatorial treatment (tamoxifen with either of the examined PDE4Is) inhibited cell growth in a dose-dependent manner for both dipyridamole (Fig. 2E and F) and Gebr-7b (Fig. 2G and H) in both TamR cell lines. Notably, among the two PDE4Is, Gebr-7b was more potent and showed stronger proliferation inhibitory effect together with tamoxifen at doses as low as 10 ng/mL, which is in agreement with the selective inhibitory effect of Gebr-7b on PDE4D. Altogether, our results demonstrate that inhibition of PDE4D activity acts as a tamoxifen sensitizer in tamoxifen-resistant breast cancer cells.

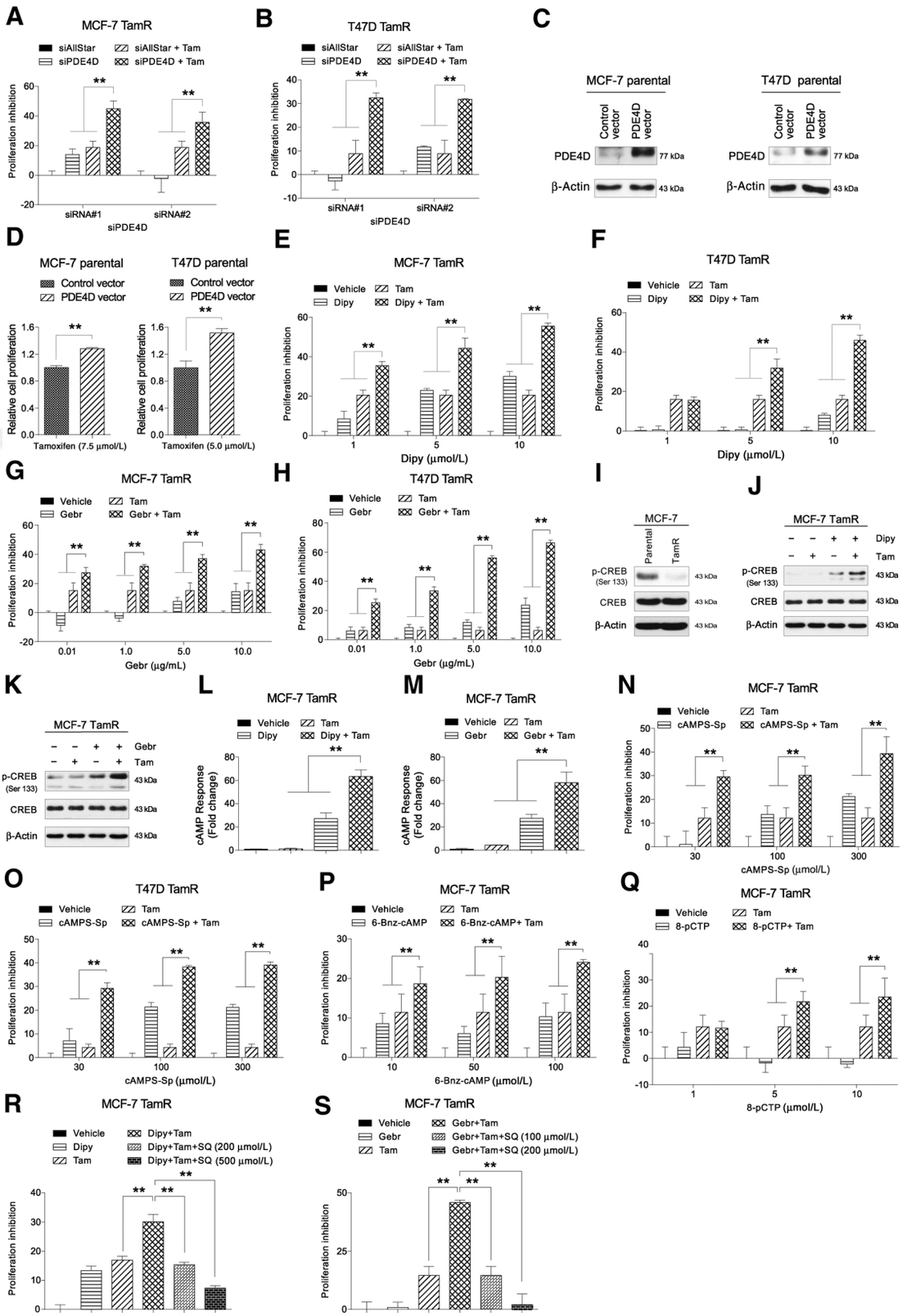
Elevation of cAMP levels overcomes tamoxifen resistance and is necessary for PDE4D inhibition–mediated tamoxifen sensitization

cAMP binds to and activates cAMP-dependent protein kinase A (PKA) and Rap guanine nucleotide-exchange factor 3 (RAPGEF3), more commonly known as EPAC (exchange protein directly activated by cAMP; refs. 18, 19). Furthermore, cAMP induction and thus activated PKA and EPAC induce phosphorylation of the transcription factor cAMP response element-binding protein (CREB) at Ser133 (20). In line with these reports, we observed significantly higher levels of phosphorylated CREB (p-CREB) in parental cells compared with TamR cells (Fig. 2I) corresponding to higher cAMP levels (Fig. 1E). As PDE4D is a cAMP-specific phosphodiesterase, we tested whether pharmacologic inhibition of PDE4D increases cellular cAMP levels and increases the phosphorylation of CREB. We observed an increase

Figure 1.

Whole-transcriptome sequencing combined with pathway enrichment and patient data analyses identify PDE4D as a potential mediator of tamoxifen resistance. **A,** Workflow of the identification and validation of PDE4D as a novel modulator of tamoxifen resistance. Whole-transcriptome analysis followed by pathway enrichment, *in vitro*, and *in vivo* assays and analyses of clinical data identify cAMP pathway and its component PDE4D as novel regulator of tamoxifen resistant in MCF-7 cells. **B,** Association of high and low TamR signature score with metastasis-free survival (MFS) in patients with breast cancer treated with tamoxifen validating the clinical relevance of our TamR cell line. **C,** Enrichment plots of tamoxifen-treated ER-positive patient tumors from GSE22226 with low and high TamR-GS scores. **D,** Ingenuity Pathway Analysis (IPA) of significantly enriched pathways (z-score $>\pm1$) in MCF-7 TamR cells compared with the parental MCF-7 cells. **E,** Intracellular levels of cAMP in parental MCF-7 and T47D cells compared with MCF-7 TamR and T47D TamR cells, respectively. **F,** Volcano plot showing significantly differentially expressed genes in MCF-7 TamR cells compared with parental ones. The genes belonging to cAMP signaling are shown as big gray circles and PDE4D is highlighted with a big black circle. **G,** PDE4D expression in MCF-7 TamR cells compared with parental MCF-7 cells in RNA-Seq data. FPKM values were used to calculate expression fold change in RNA-Seq data. **H,** qRT-PCR validations of PDE4D upregulation in TamR cells. **I,** Western blot analysis of PDE4D expression in parental and TamR MCF-7 and T47D cells. β-Actin was used as a loading control. **J–L,** DMFS (**J**), and RFS (**K**), and RFS (**L**; univariate analysis) of patients with luminal A breast cancer who underwent tamoxifen therapy with respect to the PDE4D expression.

Downloaded from http://aacrjournals.org/clincancerres/article-pdf/24/8/1987/2050104/1987.pdf by Bilkent University user on 31 August 2022



Downloaded from http://aacrjournals.org/clincancerres/article-pdf/24/8/1987/2050104/1987.pdf by Bilkent University user on 31 August 2022

in the phosphorylated CREB (Fig. 2J and K) and intracellular cAMP levels (Fig. 2L and M; Supplementary Fig. S5A and S5B) in both MCF-7 and T47D TamR cells when treated with dipyridamole or Gebr-7b. Interestingly addition of tamoxifen along with dipyridamole or Gebr-7b led to further increase in p-CREB and cAMP levels (Fig. 2J–M).

Next, we tested whether elevated cAMP levels by PDE4D inhibition will sensitize resistant cells to tamoxifen by using stable cell–permeable cAMP analogues (21). Treatment with general cAMP analogue, cAMPS-Sp, triethylammonium salt (cAMPS-Sp) resulted in sensitization of both MCF-7 TamR and T47D TamR cells to tamoxifen in a dose-dependent manner (Fig. 2N and O). Treatment with PKA-specific analogue (6-Bnz-cAMP sodium salt) or EPAC- specific analogue (8-pCPT-2-O-Me-cAMP-AM) also sensitized cells to tamoxifen in a dose-dependent manner (Fig. 2P and Q). To further prove that the sensitizer role of PDE4D in tamoxifen resistance is due to its ability to increase cAMP levels, MCF-7 TamR cells were pretreated with SQ22536, a specific adenylyl cyclase inhibitor, to prevent cAMP accumulation even in the presence of PDE4D inhibitors and tamoxifen. SQ22536 completely reversed the sensitization of resistant cells by both dipyridamole (Fig. 2R) and Gebr-7b (Fig. 2S) in a dose-dependent manner. Overall, these results suggest that PDE4D reduces intracellular cAMP to cause tamoxifen resistance.

Activation of stress-related kinases downstream of cAMP leads to apoptosis and tamoxifen sensitization

Elevated cAMP levels are known to activate the stress-related kinases (p38 and JNK) and subsequently lead to phosphorylation and activation of CREB (18, 22). Importantly, PI3K pathway crosstalks with cAMP signaling (23), and activated AKT was shown to play a critical role in endocrine resistance (14). Therefore, we initially examined the basal expression and phosphorylation levels of JNK, p38/SAPK and AKT in parental and tamoxifen-resistant cells. Western blot analysis showed that phosphorylation levels of JNK and p38 were significantly reduced while those of AKT were upregulated in TamR cells compared with the parental ones in both MCF-7 and T47D cells (Fig. 3A; Supplementary Fig. S6A). To test the effects of elevated cAMP on the phosphorylation status of JNK and p38 proteins, MCF-7 TamR cells were treated with PDE4D siRNA or cAMP analogue (cAMPS-Sp). Elevated levels of cAMP resulted in activation of JNK and p38 proteins. Interestingly, p-JNK and p-p38 signals were further enhanced in the treatment groups combined with tamoxifen (Fig. 3B and C). Inhibition of PDE4D via treatment with dipyridamole or Gebr-7b also resulted in similar increase in p-JNK and p-p38 as in case of cAMP-Sp or PDE4D siRNA (Fig. 3D and E). Significant decrease in phosphorylated AKT (both Thr-308 and Ser-473) levels was observed upon treatment with PDE4D siRNA, cAMPS-Sp, dipyridamole, and Gebr-7b, especially when combined with tamoxifen (Fig. 3B–E). These results suggest that elevated cAMP levels upon PDE4D inhibition activates JNK and p38 signaling and inhibits AKT activation.

As AKT pathway is a major regulator of cell survival, and PDE4D is a potential oncogenic protein regulating cancer cell proliferation and apoptosis (24), apoptosis levels were evaluated where MCF-7 TamR cells were treated with dipyridamole or Gebr-7b alone or in combination with tamoxifen for 72 hours. Pharmacologic inhibition of PDE4D in combination with tamoxifen activated cleavage of caspase-7 and PARP proteins and induced apoptosis (Fig. 3F–I). Finally, treatment with JNK inhibitor SP600125 or p38 inhibitor SB203580 completely reversed the measurable effects of PDE4Is on proliferation inhibition and sensitization to tamoxifen, confirming the mediatory roles of JNK or p38 pathways in this context (Fig. 3J and K).

PDE4D inhibition–mediated cAMP induction leads to ER stress conferring tamoxifen sensitivity

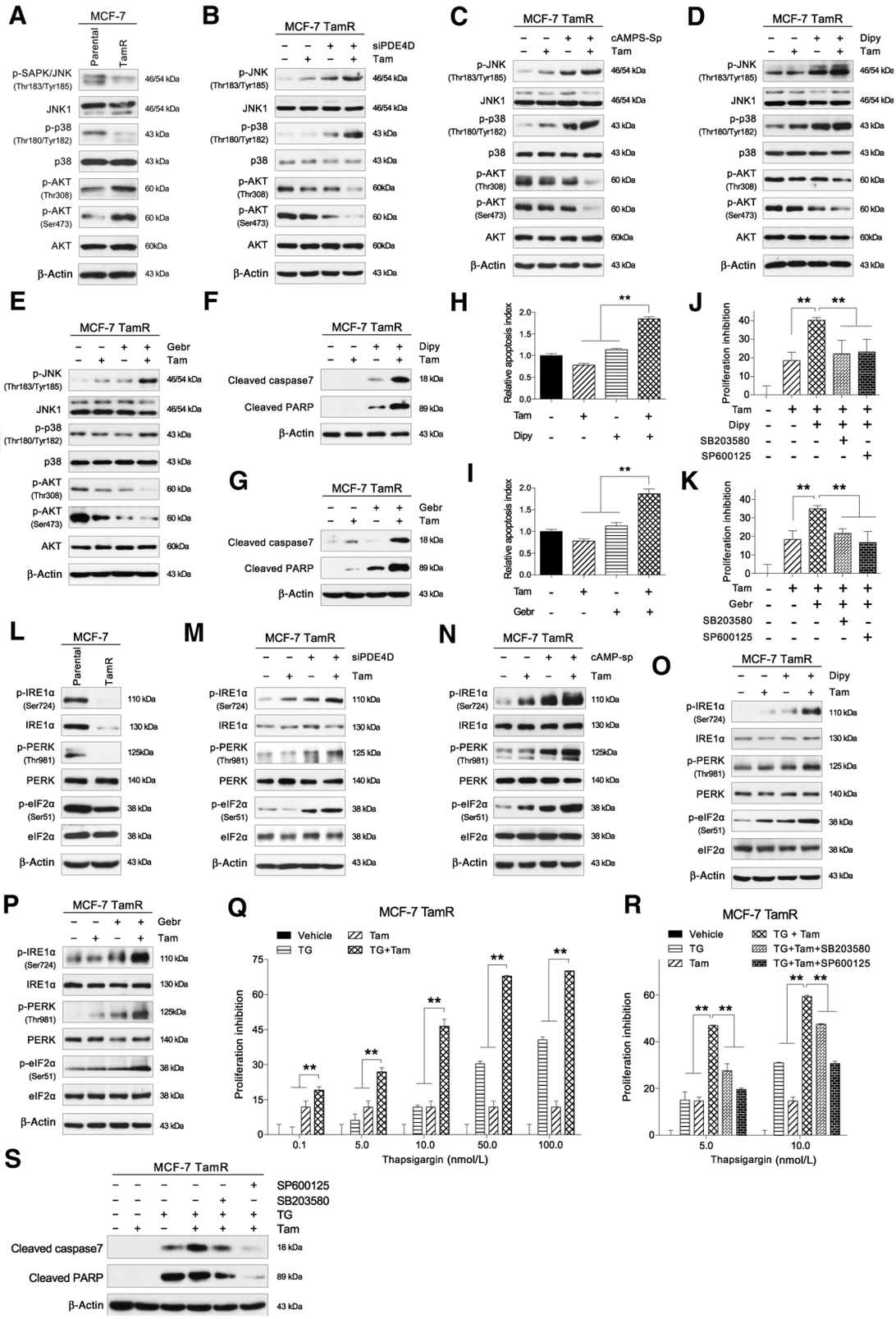
One of the well-known mediators of p38/JNK–induced apoptosis is activation of unfolded protein response (UPR)/ER stress pathway (25). Therefore, we examined whether elevated PDE4D activity regulates ER stress response to cause tamoxifen resistance. We observed that activated inositol-requiring enzyme 1α (IRE1α), protein kinase RNA-like ER kinase (PERK), and eukaryotic translation initiator factor 2α (eIF2α) levels were significantly reduced in both MCF-7 TamR and T47D TamR cells compared with their parental counterparts (Fig. 3L; Supplementary Fig. S6B). We then examined possible consequences of PDE4D inhibition on ER stress pathway. Notably, treatment with PDE4D siRNAs or with a cell-permeable cAMP analogue (cAMPS-Sp) resulted in activation of IRE1α, PERK and eIF2α proteins, especially when combined with tamoxifen (Fig. 3M and N). Similar results were obtained with pharmacologic inhibition of PDE4D with dipyridamole or Gebr-7b (Fig. 3O and P).

To further prove that induction of ER stress is directly involved in tamoxifen sensitization, we investigated the effects of a well-known ER stress inducer thapsigargin (TG) (26) on tamoxifen sensitization in MCF-7 TamR cells. While a certain level of proliferation inhibition was observed with thapsigargin alone, combination of thapsigargin with tamoxifen further inhibited cell proliferation (Fig. 3Q). Importantly, the blockade of JNK or p38 pathways by SB203580 or SP600125 reversed the combinatorial

Figure 2.

Inhibition of PDE4D overcomes tamoxifen resistance and increasing cAMP levels is necessary for PDE4D inhibition–mediated tamoxifen sensitization. **A** and **B,** Cell proliferation of tamoxifen-resistant cells MCF-7 TamR (**A**) and T47D TamR (**B**) transfected with two different siRNA sequences against PDE4D in the absence and presence of tamoxifen. The concentrations of tamoxifen used were 7.5 μmol/L and 5.0 μmol/L for MCF-7 TamR and T47D TamR cells, respectively. **C,** PDE4D overexpression was detected using DYKDDDDK tagged antibody in parental MCF-7 and T47D cells. Predicted molecular weight of overexpressed protein is 77 KDa (**D**) Cell proliferation after ectopic expression of PDE4D in parental MCF-7 and T47D cells. **E–H,** Tamoxifen sensitization with pharmacologic PDE4D inhibition with different doses of PDE inhibitor (dipyridamole) and PDE4D-specific inhibitor (Gebr-7b) in MCF-7 TamR (**E** and **G**) and T-47D TamR (**F** and **H**) cells. **I,** Western blot analysis showing reduced p-CREB in MCF-7 TamR cells relative to parental cells. β-Actin was used as a loading control. **J** and **K,** Western blot analysis of p-CREB in MCF-7-TamR cells treated with tamoxifen (5.0 μmol/L) in combination with PDE inhibitor (dipyridamole; **J**) and PDE4D inhibitor (Gebr-7b; **K**), respectively. **L–M,** Intracellular cAMP levels in MCF-7 TamR cells upon treatment with tamoxifen (5.0 μmol/L) in combination with PDE inhibitor (dipyridamole) (**L**) and PDE4D inhibitor (Gebr-7b; **M**), respectively. **N–Q,** Tamoxifen sensitization with different doses of general cAMP analogue (cAMP-Sp; **N** and **O**), PKA-specific analogue (6-Benz-cAMP; **P**) and EPAC-specific analogue (8-pCPT-2-O-Me-cAMP; **Q**) in the presence of 7.5 μmol/L tamoxifen. **R** and **S,** Cell proliferation of the resistant MCF-7 cells pretreated with SQ22536, a specific cAMP inhibitor, in combination with tamoxifen and PDE inhibitor (dipyridamole; **R**) and PDE4D inhibitor (Gebr-7b; **S**). Dipy: dipyridamole, Gebr: Gebr-7b, 8-pCPT: 8-pCPT-2-O-Me-cAMP.

Downloaded from http://aacrjournals.org/clincancerres/article-pdf/24/8/1987/2050104/1987.pdf by Bilkent University user on 31 August 2022



Downloaded from http://aacrjournals.org/clincancerres/article-pdf/24/8/1987/2050104/1987.pdf by Bilkent University user on 31 August 2022

effect of thapsigargin and tamoxifen on the proliferation inhibition (Fig. 3R) and apoptosis (Fig. 3S), establishing JNK/p38 signaling as the mediator of ER stress-induced tamoxifen sensitization. Taken together, our results demonstrate that pharmacologic blockade of PDE4D elevates cAMP levels, which results in cAMP-dependent activation of ER stress downstream kinases, leading to apoptosis in tamoxifen-resistant cells.

Pharmacologic blockade of PDE4D by dipyridamole or Gebr-7b overcomes tamoxifen resistance *in vivo*

To examine whether targeting PDE4D overcomes tamoxifen resistance *in vivo*, xenografts using tamoxifen resistant MCF-7 TamR cells were generated. The dipyridamole or Gebr-7b combination with tamoxifen inhibited the growth of the MCF-7 TamR tumors in nude mice compared to the vehicle or single-agent treatments (Fig. 4A and B). Tumor weights were also significantly less in combination-treated groups as compared with vehicle or individual treatments (Fig. 4C). While the expression level of Ki-67, a marker of cell proliferation, was markedly reduced, fluorescence-based TUNEL assay showed an increased apoptosis in combination treatments with tamoxifen and PDE4Is (Fig. 4D and E). These results demonstrate that pharmacologic inhibition of PDE4D results in tamoxifen sensitization in resistant tumors *in vivo*.

Aspirin overcomes tamoxifen resistance via increasing cAMP levels and activation of ER stress–mediated p38/JNK signaling leading to apoptosis

Although there are several resistance mechanisms put forward for tamoxifen resistance, one of the major challenges is to identify druggable targets which may help rapid translation into clinic. Our IPA results predicted that acetylsalicylic acid (ASA), commonly known as aspirin, could be a potential PDE4D inhibitor. Analysis of disease-associated and drug-induced phenotypes in terms of their differential gene expression profiles can predict the cytotoxic effect of a drug on the model system being used. Therefore, we analyzed our TamR-GS based on its correlation with the aspirin-responsive genes (provided in Connectivity map analysis; ref. 27). As shown in Fig. 5A, the genes upregulated in our TamR-GS are significantly downregulated and vice versa by aspirin treatment in MCF-7 cells ($P = 0.0004$; details are given in Methods). This suggests that resistance phenotype can be reversed by aspirin treatment, that is, aspirin might be repositioned to treat tamoxifen resistance. Importantly, such a negative correlation was not observed with other COX inhibitors and lapatinib, an EGFR/HER2 inhibitor, ($P = 0.053$, $P = 0.655$, $P = 0.12$ for piroxicam, diclofenac, and lapatinib, respectively), suggesting that the therapeutic effect of aspirin on tamoxifen resistance might not rely on its inhibitory action on COX pathway. Rather, it could be due to COX-independent activities, one of which could be PDE4D inhibition as predicted by IPA. We further tested potential clinical effects of aspirin treatment by evaluating the correlation between TamR-GS and the expression of aspirin-responsive genes generated from GSE76583 (28) in patients treated with tamoxifen. We observed a significant negative correlation between the expression of TamR-GS and aspirin-responsive genes in tamoxifen-treated patients ($r = -0.21$, $P = 0.0004$; Fig. 5B). Our analysis suggests that tamoxifen-resistant patients could potentially be responsive to aspirin treatment by restoring aspirin-responsive genes which are expressed at low levels. All these results prompted us to test whether aspirin can act as tamoxifen sensitizer, as seen with PDE4D inhibition. Therefore, we treated both MCF-7 TamR and T47D TamR cells with increasing concentration of aspirin alone or in combination with tamoxifen for 72 hours. Aspirin significantly resensitized both MCF-7 TamR and T47D TamR cells to tamoxifen (Fig. 5C and D). We also observed that cellular cAMP (Fig. 5E; Supplementary Fig. S7) and p-CREB levels (Fig. 5F) were increased substantially upon treatment with aspirin in combination with tamoxifen in both MCF-7 and T47D TamR cells. Remarkably, treatment with SQ22536 completely abrogated the sensitizer effects of aspirin (Fig. 5G), confirming that tamoxifen sensitization effects of aspirin is mediated by cAMP pathway.

To test whether increased cAMP upon tamoxifen and aspirin combination induces the activation of stress-related kinases, we treated the MCF-7 TamR cells with aspirin alone or in combination with tamoxifen. While aspirin treatment alone significantly increased p-JNK and p-p38 levels, phosphorylation of AKT (Thr-308) was decreased. Importantly, the combination of aspirin and tamoxifen had a stronger effect on the phosphorylation status of all the proteins tested (Fig. 5H), phenocopying the effects of dipyridamole and Gebr-7b in combination with tamoxifen. Specific inhibition of JNK by SP600125 or p38 by SB203580 completely reversed the effects of aspirin and tamoxifen combination on the proliferation inhibition and sensitization in MCF-7 TamR cells (Fig. 5I). Treatment with aspirin also increased the levels of p-IRE1α, p-PERK, and p-eIF2α, and they were further

Figure 3.

Induction of cAMP activates stress-related kinases downstream of ER stress pathway and resensitizes tamoxifen-resistant breast cancer cells. **A,** Western blot analysis of stress-related kinases (JNK and p38) and AKT pathway in parental and tamoxifen-resistant MCF-7 cells. β-Actin was used as a loading control. **B–E,** Western blot analysis of stress-related kinases and AKT pathway in MCF-7 TamR cells upon knockdown of PDE4D with PDE4D specific siRNA (**B**), treatment with cAMP analogue (cAMPS-Sp; **C**), treatment with PDE inhibitor (dipyridamole; **D**), and treatment with PDE4D-specific inhibitor (Gebr-7b; **E**) in combination with tamoxifen (5.0 μmol/L). **F** and **G,** Western blot analysis for apoptosis markers in MCF-7 TamR cells after treatment with dipyridamole (**F**) and Gebr-7b (**G**) in combination with tamoxifen (5.0 μmol/L). **H** and **I,** Luminescence-based caspase-3/7 assay in MCF-7 TamR cells upon treatment with PDE inhibitor (dipyridamole; **H**) and PDE4D-specific inhibitor (Gebr-7b; **I**) in combination with tamoxifen (7.5 μmol/L). **J** and **K,** Cell proliferation of the resistant MCF-7 cells treated with PDE inhibitor (dipyridamole; **J**) and PDE4D-specific inhibitor (Gebr-7b; **K**) together with p38 inhbitor (SB203580) or JNK inhibitor (SP600125) in presence of tamoxifen (7.5 μmol/L). **L,** Western blot analysis of ER stress–related proteins in parental and tamoxifen-resistant MCF-7cells. β-Actin was used as a loading control. **M–P,** Western blot analysis of ER stress–related proteins in MCF-7 TamR cells upon knockdown of PDE4D (**M**), treatment with cAMP analogue (cAMPS-Sp; **N**), treatment with PDE inhibitor (dipyridamole; **O**), and treatment with PDE4D-specific inhibitor (Gebr-7b; **P**) in combination with tamoxifen (5.0 μmol/L). **Q,** Cell proliferation of the resistant MCF-7 cells treated with ER stress inducer (thapsigargin) in the absence and presence of tamoxifen (7.5 μmol/L). **R,** Cell proliferation of the resistant MCF-7 cells treated with thapsigargin in the absence and presence of tamoxifen (7.5 μmol/L) or together with p38 inhibitor (SB203580) or JNK inhibitor (SP600125) in presence of tamoxifen. **S,** Western blot analysis for apoptosis markers for combination therapies in MCF-7 TamR cells after treatment with thapsigargin alone or in combination with tamoxifen (5.0 μmol/L) or together with p38-inhbitor (SB203580) or JNK inhibitor (SP600125) in presence of tamoxifen (5.0 μmol/L). TG, thapsigargin.

Downloaded from http://aacrjournals.org/clincancerres/article-pdf/24/8/1987/2050104/1987.pdf by Bilkent University user on 31 August 2022

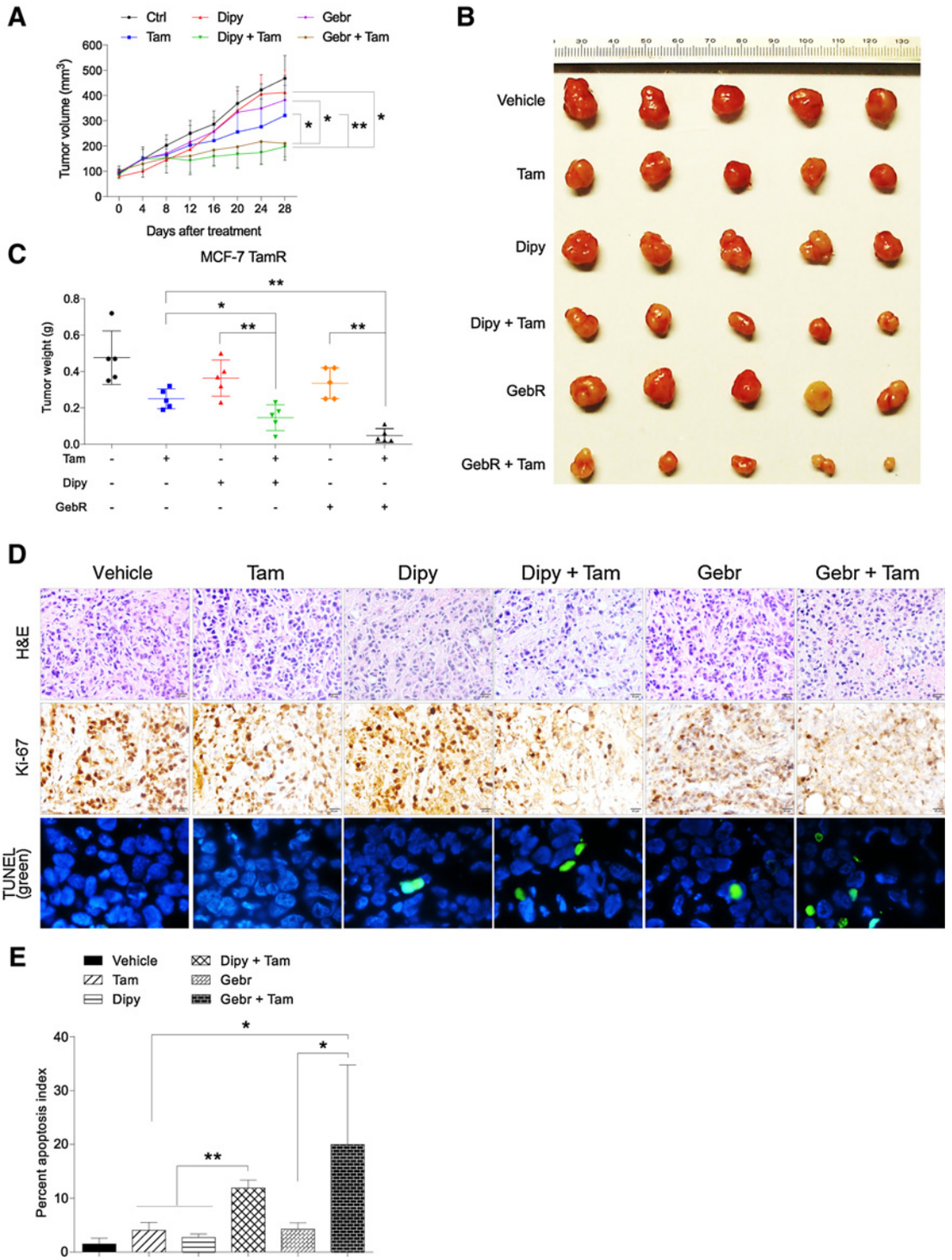


Figure 4.

Dipyridamole or Gebr-7b overcomes tamoxifen resistance *in vivo*. **A,** Tumor growth in MCF-7 TamR xenografts treated with tamoxifen and dipyridamole or Gebr-7b, individually or in combination. Treatments were started when tumor volumes reached around 100 mm^3. Mice were treated daily with tamoxifen (2 mg/kg), dipyridamole (15 mg/kg), Gebr-7b (3 μg/kg), or combinations for 28 days. **B,** Pictures of the tumors from mice treated with vehicle, tamoxifen, dipyridamole, Gebr-7b or the combination from the treatment groups. **C,** Tumor weights of the treatment groups. Statistical significance was determined with an unpaired, two-tailed Student *t* test. **D,** H&E, Ki-67, and fluorescence-based TUNEL stainings of the tumors. Pictures of H&E and Ki-67 stainings were taken at 40× while TUNEL was taken at 100× magnification. **E,** Quantification of the apoptotic cells from TUNEL staining.

Downloaded from http://aacrjournals.org/clincancerres/article-pdf/24/8/1987/2050104/1987.pdf by Bilkent University user on 31 August 2022

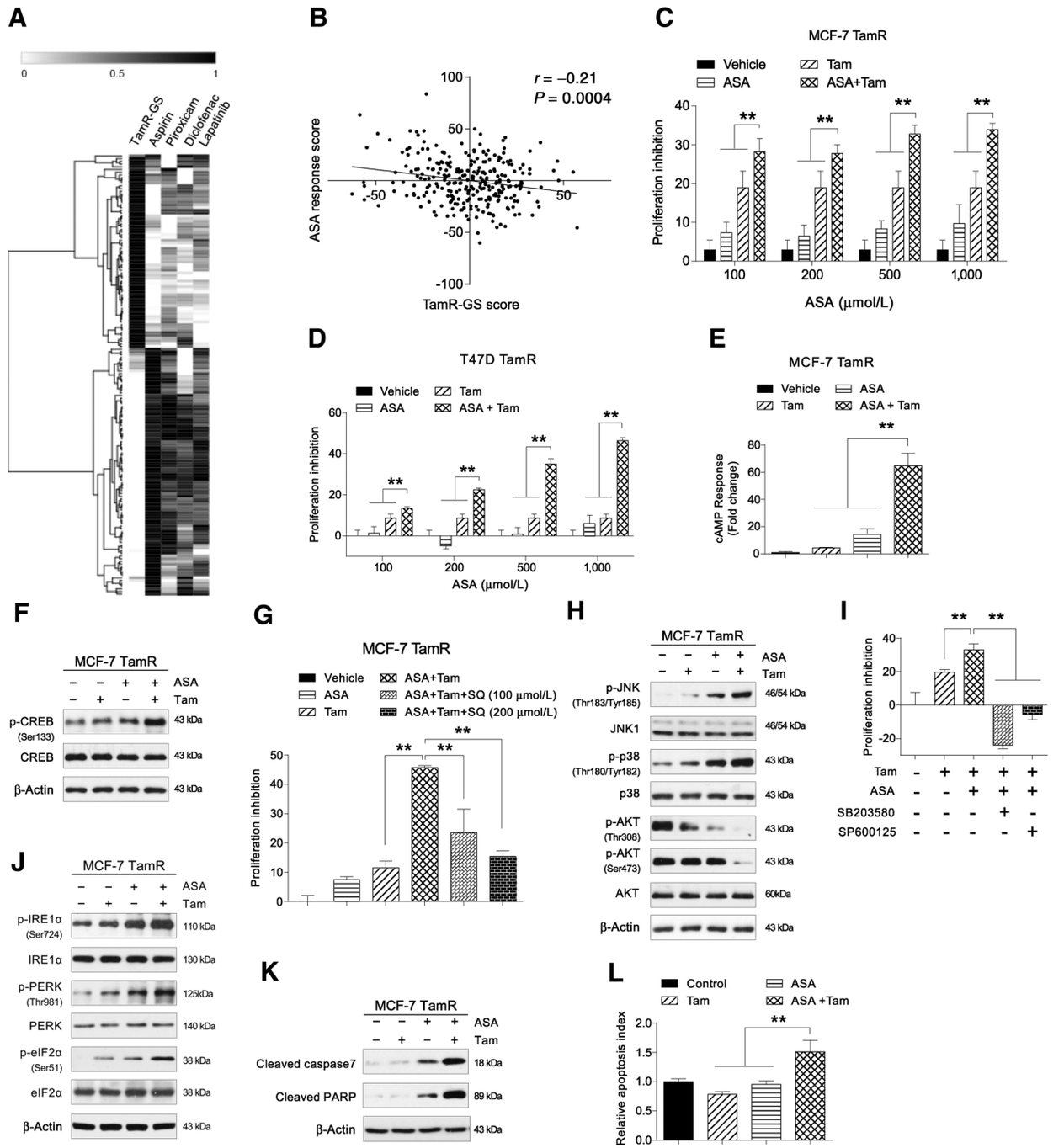


Figure 5.

Aspirin overcomes tamoxifen resistance via modulating cAMP levels and activation of ER stress–mediated p38/JNK signaling leading to apoptosis. **A,** The heatmap showing the genes in TamR-GS that are reversed by aspirin treatment, but not with other COX inhibitors (piroxicam, diclofenac) and lapatinib, a EGFR/Her2 inhibitor. The positions are normalized, and black shows the upregulated genes while white shows the downregulated genes. **B,** The correlation between TamR-GS and aspirin response score in patients from GSE26971. **C** and **D,** Tamoxifen sensitization with aspirin at different doses in MCF-7 TamR (**C**) and T-47D TamR (**D**) cells. The concentrations of tamoxifen used were 7.5 μmol/L and 5.0 μmol/L for MCF-7 TamR and T-47D TamR cells, respectively. **E,** Intracellular cAMP levels in MCF-7 TamR cells upon treatment with aspirin in combination with tamoxifen (5.0 μmol/L). **F,** Western blot analysis of p-CREB in MCF-7 TamR cells treated with aspirin in combination with tamoxifen (5.0 μmol/L). β-Actin was used as a loading control. **G,** Cell proliferation of the MCF-7 TamR cells pretreated with SQ22536, a specific cAMP inhibitor, in combination with aspirin and tamoxifen (7.5 μmol/L). **H,** Western blot analysis of stress-related kinases and AKT pathway in MCF-7 TamR treated with aspirin in the absence and presence of tamoxifen (5.0 μmol/L). **I,** Cell proliferation of the MCF-7 TamR cells treated with aspirin together with p38 inhibitor (SB203580) or JNK inhibitor (SP600125) in the presence of tamoxifen (7.5 μmol/L). **J,** Western blot analysis of ER stress–related proteins in MCF-7 TamR cells upon treatment with aspirin in combination with tamoxifen (5.0 μmol/L). **K,** Western blot analysis for apoptosis markers for combination therapies in MCF-7 TamR cells. **L,** Luminescence-based caspase-3/7 assay in MCF-7 TamR upon treatment with aspirin in combination with tamoxifen (7.5 μmol/L).

Downloaded from http://aacrjournals.org/clincancerres/article-pdf/24/8/1987/2050104/1987.pdf by Bilkent University user on 31 August 2022

increased in aspirin and tamoxifen combination (Fig. 5J). These effects were further reflected in apoptosis where aspirin in combination with tamoxifen resulted in apoptosis as evidenced by the cleavage of caspase-7 and PARP and increase in relative apoptosis index (Fig. 5K and L).

To examine whether aspirin overcomes tamoxifen resistance *in vivo*, we generated xenografts using tamoxifen resistant MCF-7 TamR cells. The aspirin and tamoxifen combination inhibited the growth of the MCF-7 TamR tumors in nude mice as compared with the vehicle or single agents (Fig. 6A and B). Tumor weights were also significantly lower in the combination-treated group as compared with vehicle or individual treatment (Fig. 6C). We observed a reduced cell proliferation shown by Ki-67 staining and an enhanced apoptosis shown by fluorescence-based TUNEL assay in combination therapy (Fig. 6D and E). Overall, our results indicate a novel mechanism where aspirin overcomes tamoxifen resistance by modulating the PDE4D activity and increasing cAMP levels both *in vitro* and *in vivo*.

Discussion

Endocrine therapy is the most effective way to treat patients with early-stage, hormone-positive breast cancer, and tamoxifen is the preferred therapy, especially for premenopausal women. Despite its favorable efficacy, 20%–30% of patients acquire resistance during endocrine therapy, including tamoxifen (6). Multiple factors are responsible for resistance to tamoxifen, and various targeted therapies in combination with tamoxifen can be employed, depending on the pretreatment menopausal status or the change in menopausal status during the course of therapy, as well as on the risk of developing metastatic disease (29, 30). Major strategies to overcome tamoxifen resistance in breast cancer include use of an EGFR inhibitor (gefitinib), a HER2 inhibitor (trastuzumab), a dual kinase inhibitor (lapatinib), or an mTOR inhibitor (everolimus), depending upon the causal factor (31, 32). Recently, FDA has approved CDK4/6 inhibitor (palbociclib) to be used in combination with SERDs (fulvestrant) or AI (letrozole) for advanced ER-positive cancers, including those who progressed on tamoxifen (33, 34). Furthermore, fulvestrant has demonstrated clinical efficacy for patients with a second relapse after responding to tamoxifen and AIs (35). Another randomized trail demonstrated an improved median progression-free survival (PFS) in ER-positive, premenopausal metastatic patients when treated with tamoxifen plus ovarian function suppresser (36). Although early-stage disease is manageable owing to use of more potent endocrine agents, resistance inevitably develops in advance, metastatic disease (37). Therefore, identification of new targeted therapies for improving patient outcome is desirable. Here, we employed a systematic functional genomics approach to decipher the molecular mechanisms of tamoxifen resistance through combining whole-transcriptome sequencing, pathway enrichments, *in vitro* and *in vivo* assays and clinical data. This led us to identify PDE4D as a novel druggable target for overcoming tamoxifen resistance in breast cancer. PDE4D inhibition via specific siRNAs or pharmacologic inhibitors (dipyridamole and Gebr-7b) resulted in an increase in cAMP levels, induction of ER stress and increased JNK/p38 phosphorylation followed by apoptosis, overcoming resistance. Strikingly, we identified a novel mechanism by which aspirin through modulation of PDE4D and intracellular cAMP levels (similar to the effects of both PDE4D-specific inhibitor and PDE general inhibitor) overcomes tamoxifen resistance both *in vitro* and *in vivo*, highlighting the possibility of drug repositioning to expedite clinical application of our findings (Fig. 6F and G).

In the last few years, the potential role of PDEs as a target for treating inflammatory diseases, including asthma, depression, chronic obstructive pulmonary disorder (COPD) etc., has been studied. For example, roflumilast, a nonselective PDE4 inhibitor has been approved by FDA for treatment of erectile dysfunction and COPD (38). Importantly, recent studies have shown PDE4D as proliferation promoting factor in lung cancer cells (24). Inhibition of PDE4 by rolipram was shown to have antitumor effect in medulloblastoma, glioblastoma and in several hematologic malignancies making PDEs attractive targets for cancer therapy (39, 40). However, the role of PDE4D as a mediator of drug resistance has not been reported yet. We observed that blockade of PDE4D by siRNAs or specific inhibitors, for example, dipyridamole and Gebr-7b, has an antiproliferative effect on the tamoxifen-resistant breast cancer cells. Recent studies demonstrated that PDE4 inhibitors (e.g., rolipram) induce augmentation of intracellular cAMP levels leading to release of cytochrome c, reduction of antiapoptotic proteins, for example, Bcl-2 and Bcl-xL levels and activation of proapoptotic proteins, e.g., BAD, resulting in apoptosis (39). It has also been demonstrated that induction of cAMP by activation of PKA signaling induces apoptosis by activating PP2A, which dephosphorylate BAD and allowing apoptosis to commence through mitochondrial pathway. PP2A is an abundant phosphatase, which negatively regulates various signaling pathways through dephosphorylation of AKT (41). Our result also demonstrate that dephosphorylation of AKT is achieved through sustained activation of cAMP levels through cAMP analogs (cAMP-Sp) or by knockdown of PDE4D or by PDE4Is (dipyridamole and Gebr-7b) in combination with tamoxifen. Our results not only further support these findings with respect to increased apoptosis upon cAMP induction (here: upon combination of PDE4D inhibitors with tamoxifen), but also suggest that one of the mechanisms of cAMP-induced apoptosis is via inducing ER stress/p38/JNK pathways.

Under chronic ER stress, cells become incompetent to take care of unfolded protein load, and apoptosis is therefore triggered. There are three classes of ER stress–induced cell death sensors in mammals: IRE1α, PERK, and ATF6 (42). Activated IRE1α cleaves XBP1 mRNA and activates ASK1. Similarly, activated PERK phosphorylates eIF2α, which leads to the inhibition of protein synthesis and induction of ATF4, which in turn regulates genes involved in apoptosis, growth arrest, and DNA damage response (25, 26). UPR is an adaptive cellular response that evolves to regulate protein folding homeostasis, and if the UPR fails to resolve the misfolding condition, then cells undergo apoptosis (43). Hence, UPR is becoming an attractive target for cancer therapy. In response to various extracellular stimuli, G-protein coupled receptors (GPCR) are responsible for cAMP accumulation in cells. Conversion of cAMP from ATP is mediated by adenylate cyclases (AC) which, in turn, are activated via GPCRs. In response to cellular stress, both JNK and p38 MAPKs are activated by GPCRs. It has been known that cAMP and cAMP-elevating agents activate JNK and p38 MAP kinases (19, 20, 44). As evident from the literature, there is a connection between cAMP, p38/JNK signaling and apoptosis. However, it has not been known that cAMP-induced activation of p38 MAPK and JNK signaling is preceded by induction of ER stress. Our study shows that elevated levels of cAMP can potentially lead to the activation

Downloaded from http://aacrjournals.org/clincancerres/article-pdf/24/8/1987/2050104/1987.pdf by Bilkent University user on 31 August 2022

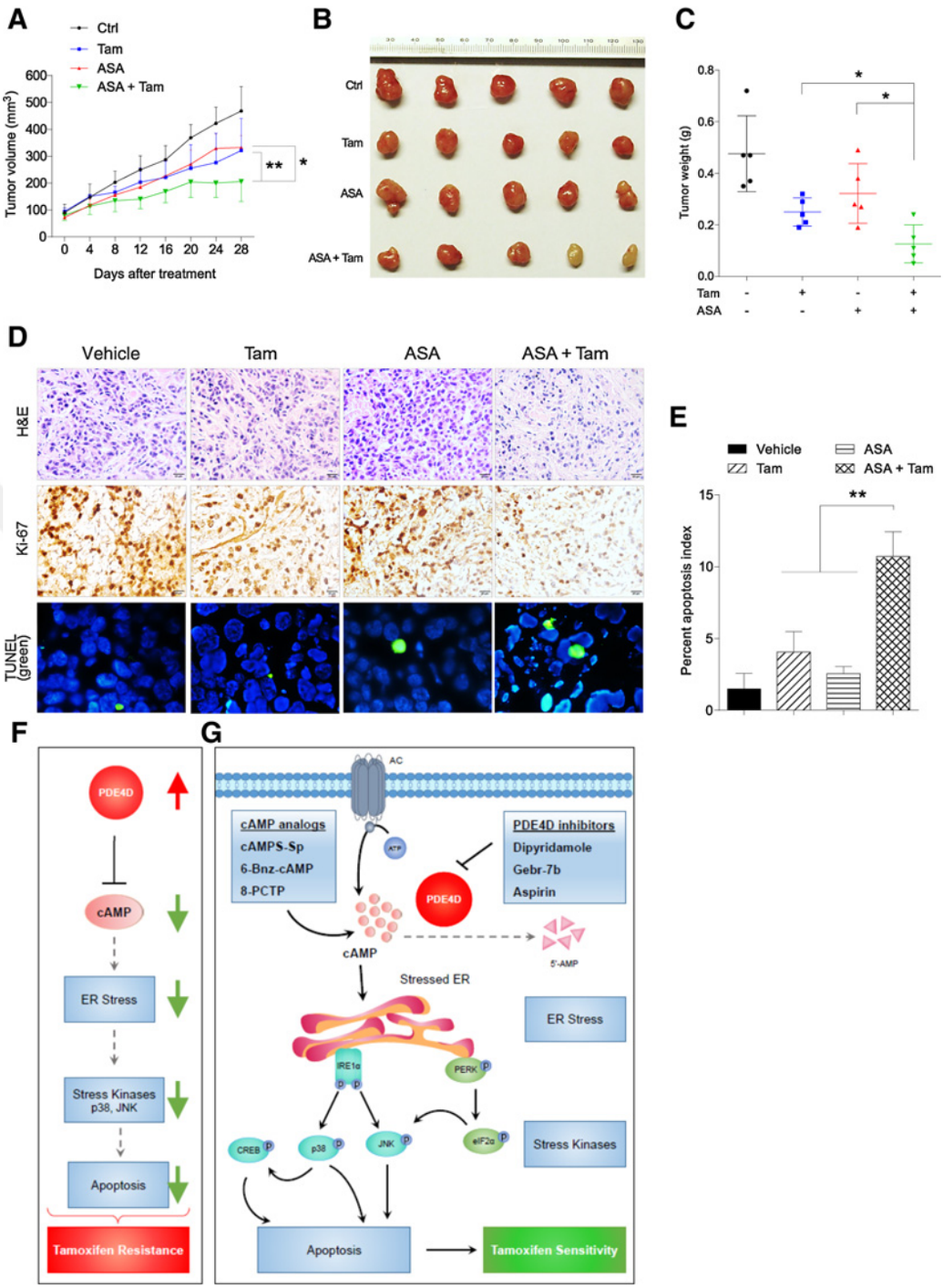


Figure 6.

Aspirin overcomes tamoxifen resistance *in vivo* and schematic summary of findings. **A,** Tumor growth in MCF-7 TamR xenografts treated with tamoxifen and aspirin individually or in combination. Treatments were started when tumor volumes reached around 100 mm^3. Mice were treated daily with tamoxifen (2 mg/kg), aspirin (100 mg/kg) or their combination for 28 days. Note that the vehicle control and Tam groups are the same as in Fig. 4. ASA; aspirin. **B,** Pictures of the tumors from mice treated with vehicle, tamoxifen, aspirin, or the combination from the treatment groups. **C,** Tumor weights of the treatment groups. Statistical significance was determined with an unpaired, two-tailed Student *t* test. **D,** H&E, Ki-67, and fluorescence-based TUNEL stainings of the tumors. Pictures of H&E and Ki-67 stainings were taken at 40× while TUNEL was taken at 100× magnification. **E,** Quantification of the apoptotic cells from TUNEL staining. **F,** Elevated PDE4D levels in TamR cells leads to a decreased cAMP level, subsequently giving rise to a decrease in ER stress, activation of stress kinases and apoptosis conferring tamoxifen resistance. **G,** Inhibition of PDE4D (with dipyridamole, Gebr-7b or aspirin) or inducing cAMP directly (with cAMPS-Sp, 6-Bnz-cAMP, or 8-PCTP) together with tamoxifen leads to elevated cAMP levels, induction of ER stress and increased JNK/p38 phosphorylation leading to activation and phosphorylation of CREB followed by apoptosis and tamoxifen sensitization.

Downloaded from http://aacrjournals.org/clincancerres/article-pdf/24/8/1987/2050104/1987.pdf by Bilkent University user on 31 August 2022

of ER stress pathway that necessitates stress-related kinases to induce apoptosis. In the context of tamoxifen resistance, we showed, for the first time, that modulation of cAMP levels through cAMP analogues (cAMPS-Sp) or by knockdown of PDE4D or by PDE4Is (dipyridamole and Gebr-7b) in combination with tamoxifen results in stepwise induction of cAMP, activation of ER stress, elevated phosphorylation of JNK and p38 MAPK and apoptosis to overcome tamoxifen resistance in breast cancer. Thus, targeting PDE4D, or induction of cAMP in general, can be used as a sensitizer for overcoming tamoxifen resistance in breast cancer cells.

Aspirin, a more than a century old drug, has been termed as a "wonder drug" by many clinicians (45). Aspirin belongs to the group of nonsteroidal anti-inflammatory drugs (NSAID), and is one of the most widely used drugs over a century. In several meta-analyses, regular use of aspirin was associated with a reduced cancer incidence, decreased distant metastases, and improvement of overall and disease-free survival (DFS) in patients with breast cancer who had acquired chemoresistance (46, 47). However, mechanisms underlying these protective effects are still poorly known. Aspirin has been known to exert anticancer effects, most of which are attributed to its COX-2 inhibitory function (46, 47). However, here we showed, for the first time, that aspirin can be repositioned to treat tamoxifen resistance by utilizing a different mechanism other than COX-2 inhibition to cause antitumoral effects *in vitro* and *in vivo* by targeting PDE4D and elevating cAMP. While dipyridamole has been used as an anticoagulant over a half-decade, and aspirin is in use as an anti-inflammatory drug over a decade, Gebr-7b is a newly developed cell-permeable and the most specific PDE4D inhibitor of all PDE4Is available. Emesis associated with PDE4Is is an apparent translational concern; however, Gebr-7b has been shown to be 100–3,000 times less emetic than other PDE4D inhibitors in three different species (*Suncus murinus*, beagle dog, and cynomolgus monkey; ref. 48); thus showing its promising potential for clinics. Although Gebr-7b has not been tested in a clinical trial yet, dipyridamole and aspirin could be used in combination with tamoxifen for overcoming tamoxifen resistance in future.

In summary, we have uncovered a novel molecular mechanism of tamoxifen resistance by an in-depth characterization of two different tamoxifen resistant cells and identified PDE4D as a novel drug target in tamoxifen-refractory ERα-positive breast cancer. We believe that our results are the first, to the best of our knowledge, in providing cAMP induction as a novel concept for tamoxifen sensitization. As all three drugs which we showed to induce cAMP levels are readily available, and some of them are FDA approved (e.g., aspirin or dipyridamole), these drugs in combination with tamoxifen may offer new ways to overcome resistance in patients with ER-positive breast cancer.

Disclosure of Potential Conflicts of Interest

R. R. Mishra and Ö. Şahin have a pending patent (patent number: 14790/4) with Turkish Patent and Trademark Office on the use of cAMP inducers for the treatment of tamoxifen resistant breast cancer. No potential conflicts of interest were disclosed by the other authors.

Authors' Contributions

Conception and design: C. Cekic, Ö. Şahin
Development of methodology: R.R. Mishra, H. Bal, P. Jandaghi, C. Cekic
Acquisition of data (provided animals, acquired and managed patients, provided facilities, etc.): R.R. Mishra, N. Belder, S.A. Ansari, M. Kayhan, U. Raza, P.G. Ersan, S. Wiemann, Y. Riazalhosseini, Ö. Şahin
Analysis and interpretation of data (e.g., statistical analysis, biostatistics, computational analysis): R.R. Mishra, Ü.M. Tokat, Ö. Saatci, S. Wiemann, A. Üner, C. Cekic, Y. Riazalhosseini, Ö. Şahin, E. Eyüpoğlu
Writing, review, and/or revision of the manuscript: R.R. Mishra, A. Üner, C. Cekic, Ö. Şahin
Administrative, technical, or material support (i.e., reporting or organizing data, constructing databases): S. Wiemann, A. Üner, Ö. Şahin
Study supervision: Ö. Şahin

Acknowledgments

This project was supported by EMBO Installation Grant 2791 (to Ö. Şahin). Ü.M. Tokat is a scholar of TÜBİTAK BİDEB 2211/A Scholarship Program. We thank Gamze Aykut for helping us with mouse xenografts studies.

The costs of publication of this article were defrayed in part by the payment of page charges. This article must therefore be hereby marked *advertisement* in accordance with 18 U.S.C. Section 1734 solely to indicate this fact.

Received September 24, 2017; revised December 6, 2017; accepted January 25, 2018; published OnlineFirst January 31, 2018.

References

1. Davies C, Pan H, Godwin J, Gray R, Arriagada R, Raina V, et al. Long-term effects of continuing adjuvant tamoxifen to 10 years versus stopping at 5 years after diagnosis of oestrogen receptor-positive breast cancer: ATLAS, a randomised trial. Lancet 2013;381:805–16.
2. Viedma-Rodriguez R, Baiza-Gutman L, Salamanca-Gomez F, Diaz-Zaragoza M, Martinez-Hernandez G, Ruiz Esparza-Garrido R, et al. Mechanisms associated with resistance to tamoxifen in estrogen receptor-positive breast cancer (review). Oncol Rep 2014;32:3–15.
3. Fisher B, Costantino JP, Wickerham DL, Redmond CK, Kavanah M, Cronin WM, et al. Tamoxifen for prevention of breast cancer: report of the national surgical adjuvant breast and bowel project P-1 study. J Natl Cancer Inst 1998;90:1371–88.
4. Vogel VG, Costantino JP, Wickerham DL, Cronin WM, Cecchini RS, Atkins JN, et al. Update of the national surgical adjuvant breast and bowel project study of tamoxifen and raloxifene (STAR) P-2 trial: preventing breast cancer. Cancer Prev Res 2010;3:696–706.
5. Early Breast Cancer Trialists' Collaborative G, Davies C, Godwin J, Gray R, Clarke M, Cutter D, et al. Relevance of breast cancer hormone receptors and other factors to the efficacy of adjuvant tamoxifen: patient-level meta-analysis of randomised trials. Lancet 2011;378:771–84.
6. Nass N, Kalinski T. Tamoxifen resistance: from cell culture experiments towards novel biomarkers. Pathol Res Pract 2015;211:189–97.
7. Gutierrez MC, Detre S, Johnston S, Mohsin SK, Shou J, Allred DC, et al. Molecular changes in tamoxifen-resistant breast cancer: relationship between estrogen receptor, HER-2, and p38 mitogen-activated protein kinase. J Clin Oncol 2005;23:2469–76.
8. Holm C, Rayala S, Jirstrom K, Stal O, Kumar R, Landberg G. Association between Pak1 expression and subcellular localization and tamoxifen resistance in breast cancer patients. J Natl Cancer Inst 2006;98:671–80.
9. Cannings E, Kirkegaard T, Tovey SM, Dunne B, Cooke TG, Bartlett JM. Bad expression predicts outcome in patients treated with tamoxifen. Breast Cancer Res Treat 2007;102:173–9.
10. Planas-Silva MD, Bruggeman RD, Grenko RT, Smith JS. Overexpression of c-Myc and Bcl-2 during progression and distant metastasis of hormone-treated breast cancer. Exp Mol Pathol 2007;82:85–90.

Downloaded from http://aacrjournals.org/clincancerres/article-pdf/24/8/1987/2050104/1987.pdf by Bilkent University user on 31 August 2022

11. Rondon-Lagos M, Villegas VE, Rangel N, Sanchez MC, Zaphiropoulos PG. Tamoxifen resistance: emerging molecular targets. Int J Mol Sci 2016;17: pii: E1357.
12. Ward A, Shukla K, Balwierz A, Soons Z, Konig R, Sahin O, et al. MicroRNA-519a is a novel oncomir conferring tamoxifen resistance by targeting a network of tumour-suppressor genes in ER+ breast cancer. J Pathol 2014;233:368–79.
13. Dancik GM, Owens CR, Iczkowski KA, Theodorescu D. A cell of origin gene signature indicates human bladder cancer has distinct cellular progenitors. Stem Cells 2014;32:974–82.
14. Ward A, Balwierz A, Zhang JD, Kublbeck M, Pawitan Y, Hielscher T, et al. Re-expression of microRNA-375 reverses both tamoxifen resistance and accompanying EMT-like properties in breast cancer. Oncogene 2013; 32:1173–82.
15. Azevedo MF, Faucz FR, Bimpaki E, Horvath A, Levy I, de Alexandre RB, et al. Clinical and molecular genetics of the phosphodiesterases (PDEs). Endocr Rev 2014;35:195–233.
16. Gyorffy B, Lanczky A, Eklund AC, Denkert C, Budczies J, Li Q, et al. An online survival analysis tool to rapidly assess the effect of 22,277 genes on breast cancer prognosis using microarray data of 1,809 patients. Breast Cancer Res Treat 2010;123:725–31.
17. Bruno O, Romussi A, Spallarossa A, Brullo C, Schenone S, Bondavalli F, et al. New selective phosphodiesterase 4D inhibitors differently acting on long, short, and supershort isoforms. J Med Chem 2009;52:6546–57.
18. Delghandi MP, Johannessen M, Moens U. The cAMP signalling pathway activates CREB through PKA, p38 and MSK1 in NIH 3T3 cells. Cell Signal 2005;17:1343–51.
19. He J, Wang C, Sun Y, Lu B, Cui J, Dong N, et al. Exendin-4 protects bone marrow-derived mesenchymal stem cells against oxygen/glucose and serum deprivation-induced apoptosis through the activation of the cAMP/PKA signaling pathway and the attenuation of ER stress. Int J Mol Med 2016;37:889–900.
20. Cuadrado A, Nebreda AR. Mechanisms and functions of p38 MAPK signalling. Biochem J 2010;429:403–17.
21. Dostmann WR, Taylor SS, Genieser HG, Jastorff B, Doskeland SO, Ogreid D. Probing the cyclic nucleotide binding sites of cAMP-dependent protein kinases I and II with analogs of adenosine 3',5'-cyclic phosphorothioates. J Biol Chem 1990;265:10484–91.
22. Hochbaum D, Tanos T, Ribeiro-Neto F, Altschuler D, Coso OA. Activation of JNK by Epac is independent of its activity as a Rap guanine nucleotide exchanger. J Biol Chem 2003;278:33738–46.
23. Rovida E, Stecca B. Mitogen-activated protein kinases and Hedgehog-GLI signaling in cancer: a crosstalk providing therapeutic opportunities? Semin Cancer Biol 2015;35:154–67.
24. Pullamsetti SS, Banat GA, Schmall A, Szibor M, Pomagruk D, Hanze J, et al. Phosphodiesterase-4 promotes proliferation and angiogenesis of lung cancer by crosstalk with HIF. Oncogene 2013;32:1121–34.
25. Darling NJ, Cook SJ. The role of MAPK signalling pathways in the response to endoplasmic reticulum stress. Biochim Biophys Acta 2014;1843:2150–63.
26. Lytton J, Westlin M, Hanley MR. Thapsigargin inhibits the sarcoplasmic or endoplasmic reticulum Ca-ATPase family of calcium pumps. J Biol Chem 1991;266:17067–71.
27. Lamb J, Crawford ED, Peck D, Modell JW, Blat IC, Wrobel MJ, et al. The Connectivity Map: using gene-expression signatures to connect small molecules, genes, and disease. Science 2006;313:1929–35.
28. Guo H, Liu J, Ben Q, Qu Y, Li M, Wang Y, et al. The aspirin-induced long non-coding RNA OLA1P2 blocks phosphorylated STAT3 homodimer formation. Genome Biol 2016;17:24.
29. Klijn JG, Beex LV, Mauriac L, van Zijl JA, Veyret C, Wildiers J, et al. Combined treatment with buserelin and tamoxifen in premenopausal metastatic breast cancer: a randomized study. J Natl Cancer Inst 2000;92: 903–11.
30. Tevaarwerk AJ, Wisinski KB, O'Regan RM. Endocrine therapy in premenopausal hormone receptor-positive breast cancer. J Oncol Pract 2016;12: 1148–56.
31. Huober J, Fasching PA, Barsoum M, Petruzelka L, Wallwiener D, Thomssen C, et al. Higher efficacy of letrozole in combination with trastuzumab compared to letrozole monotherapy as first-line treatment in patients with HER2-positive, hormone-receptor-positive metastatic breast cancer - results of the eLEcTRA trial. Breast 2012;21:27–33.
32. Osborne CK, Neven P, Dirix LY, Mackey JR, Robert J, Underhill C, et al. Gefitinib or placebo in combination with tamoxifen in patients with hormone receptor-positive metastatic breast cancer: a randomized phase II study. Clin Cancer Res 2011;17:1147–59.
33. Cristofanilli M, Turner NC, Bondarenko I, Ro J, Im SA, Masuda N, et al. Fulvestrant plus palbociclib versus fulvestrant plus placebo for treatment of hormone-receptor-positive, HER2-negative metastatic breast cancer that progressed on previous endocrine therapy (PALOMA-3): final analysis of the multicentre, double-blind, phase 3 randomised controlled trial. Lancet Oncol 2016;17:425–39.
34. Finn RS, Crown JP, Ettl J, Schmidt M, Bondarenko IM, Lang I, et al. Efficacy and safety of palbociclib in combination with letrozole as first-line treatment of ER-positive, HER2-negative, advanced breast cancer: expanded analyses of subgroups from the randomized pivotal trial PALOMA-1/ TRIO-18. Breast Cancer Res 2016;18:67.
35. Robertson JF, Osborne CK, Howell A, Jones SE, Mauriac L, Ellis M, et al. Fulvestrant versus anastrozole for the treatment of advanced breast carcinoma in postmenopausal women: a prospective combined analysis of two multicenter trials. Cancer 2003;98:229–38.
36. Kim HA, Ahn SH, Nam SJ, Park S, Ro J, Im SA, et al. The role of the addition of ovarian suppression to tamoxifen in young women with hormone-sensitive breast cancer who remain premenopausal or regain menstruation after chemotherapy (ASTRRA): study protocol for a randomized controlled trial and progress. BMC Cancer 2016;16:319.
37. Garcia-Becerra R, Santos N, Diaz L, Camacho J. Mechanisms of resistance to endocrine therapy in breast cancer: focus on signaling pathways, miRNAs and genetically based resistance. Int J Mol Sci 2012;14:108–45.
38. Rabe KF. Update on roflumilast, a phosphodiesterase 4 inhibitor for the treatment of chronic obstructive pulmonary disease. Br J Pharmacol 2011; 163:53–67.
39. Lerner A, Epstein PM. Cyclic nucleotide phosphodiesterases as targets for treatment of haematological malignancies. Biochem J 2006;393: 21–41.
40. Goldhoff P, Warrington NM, Limbrick DD Jr., Hope A, Woerner BM, Jackson E, et al. Targeted inhibition of cyclic AMP phosphodiesterase-4 promotes brain tumor regression. Clin Cancer Res 2008;14:7717–25.
41. Moon EY, Lerner A. PDE4 inhibitors activate a mitochondrial apoptotic pathway in chronic lymphocytic leukemia cells that is regulated by protein phosphatase 2A. Blood 2003;101:4122–30.
42. Maly DJ, Papa FR. Druggable sensors of the unfolded protein response. Nat Chem Biol 2014;10:892–901.
43. Han J, Back SH, Hur J, Lin YH, Gildersleeve R, Shan J, et al. ER-stress-induced transcriptional regulation increases protein synthesis leading to cell death. Nat Cell Biol 2013;15:481–90.
44. Li J, Dou X, Li S, Zhang X, Zeng Y, Song Z. Nicotinamide ameliorates palmitate-induced ER stress in hepatocytes via cAMP/PKA/CREB pathway-dependent Sirt1 upregulation. Biochim Biophys Acta 2015;1853: 2929–36.
45. Desborough MJ, Keeling DM. The aspirin story - from willow to wonder drug. Br J Haematol 2017;177:674–83.
46. Algra AM, Rothwell PM. Effects of regular aspirin on long-term cancer incidence and metastasis: a systematic comparison of evidence from observational studies versus randomised trials. Lancet Oncol 2012;13: 518–27.
47. Saha S, Mukherjee S, Khan P, Kajal K, Mazumdar M, Manna A, et al. Aspirin suppresses the acquisition of chemoresistance in breast cancer by disrupting an NFkappaB-IL6 signaling axis responsible for the generation of cancer stem cells. Cancer Res 2016;76:2000–12.
48. Bruno O, Fedele E, Prickaerts J, Parker LA, Canepa E, Brullo C, et al. GEBR-7b, a novel PDE4D selective inhibitor that improves memory in rodents at non-emetic doses. Br J Pharmacol 2011;164:2054–63.

Downloaded from http://aacrjournals.org/clincancerres/article-pdf/24/8/1987/2050104/1987.pdf by Bilkent University user on 31 August 2022

SUPPLEMENTAL DATA

Re-activation of cAMP pathway by PDE4D inhibition represents a novel druggable axis for overcoming tamoxifen resistance in ER-positive breast cancer cells

Rasmi R. Mishra[1], Nevin Belder[1], Suhail A. Ansari[1], Merve Kayhan[1], Hilal Bal[1], Umar Raza[1], Pelin G. Ersan[1], Ünal M. Tokat[1], Erol Eyüpoğlu[1], Özge Saatci[1], Pouria Jandaghi[2,3], Stefan Wiemann[4], Ayşegül Üner[5], Caglar Cekic[1], Yasser Riazalhosseini[2,3] and Özgür Şahin[1,6*]

[1]Department of Molecular Biology and Genetics, Faculty of Science, Bilkent University, 06800 Ankara, Turkey

[2]Department of Human Genetics, McGill University, Montreal, QC, H3A 1B1, Canada

[3]McGill University and Genome Quebec Innovation Centre, Montreal, QC, H3A 0G1, Canada

[4]Division of Molecular Genome Analysis, German Cancer Research Center (DKFZ), INF580, 69120, Heidelberg, Germany.

[5]Department of Pathology, Faculty of Medicine, Hacettepe University, Ankara, Turkey

[6] National Nanotechnology Research Center (UNAM), Bilkent University, 06800 Ankara, Turkey

Supplementary Materials and Methods

Whole transcriptome sequencing (RNA-Seq) and data analysis

RNA sequencing was performed for each condition (MCF-7 parental and MCF-7 TamR) in triplicates using the Illumina HiSeq 2000 platform at McGill University and Genome Quebec Innovation Centre. Around 65 million paired-end 2×100bp reads were generated for each replicate. FASTQC tool was used to check the quality of the sequencing data. Raw FASTQ sequences were aligned to the UCSC human reference genome (hg19) using TopHat v2.1.0 with default parameters. *Cufflinks* was used to assemble and quantify transcripts from the mapped sequences. By utilizing reference genome annotation (UCSC hg19), *Cuffmerge* produced a single merged reference transcripts for differential expression analysis. For the identification of the differentially expressed genes, *Cuffdiff* was used with the default parameters (1).

Generation of TamR gene signature and bioinformatics analysis

In order to test the clinical relevance of TamR-GS in predicting survival in tamoxifen-treated ER-positive BC patients, we have utilized a publicly available mRNA expression profiling dataset, GSE26971, stored in Gene Expression Omnibus (GEO) database (2). This dataset contains mRNA expression profiles of 277 early stage, tamoxifen treated ER-positive BC patients, who were treated with adjuvant tamoxifen monotherapy. We have downloaded the mRNA expression data for the genes in our TamR-GS, together with the clinicopathological properties. Gene set enrichment analysis (GSEA) was performed using gene sets related to tamoxifen resistance available at the Broad Institute website (http://software.broadinstitute.org/gsea/index.jsp). For multivariate survival analysis, Cox regression was performed in SPSS software, by using the GEO dataset with accession number, GSE6532, which contains mRNA expression profiles of 414 ER-positive BC patients, among whom 277 received tamoxifen therapy. Analysis of the effects of aspirin treatment on TamR-GS was done by utilizing the Connectivity Map data which is a collection of differential gene expression profiles in cancer cells treated with different compounds (3). The data matrix of the gene ranks in different instances where MCF-7 cells were

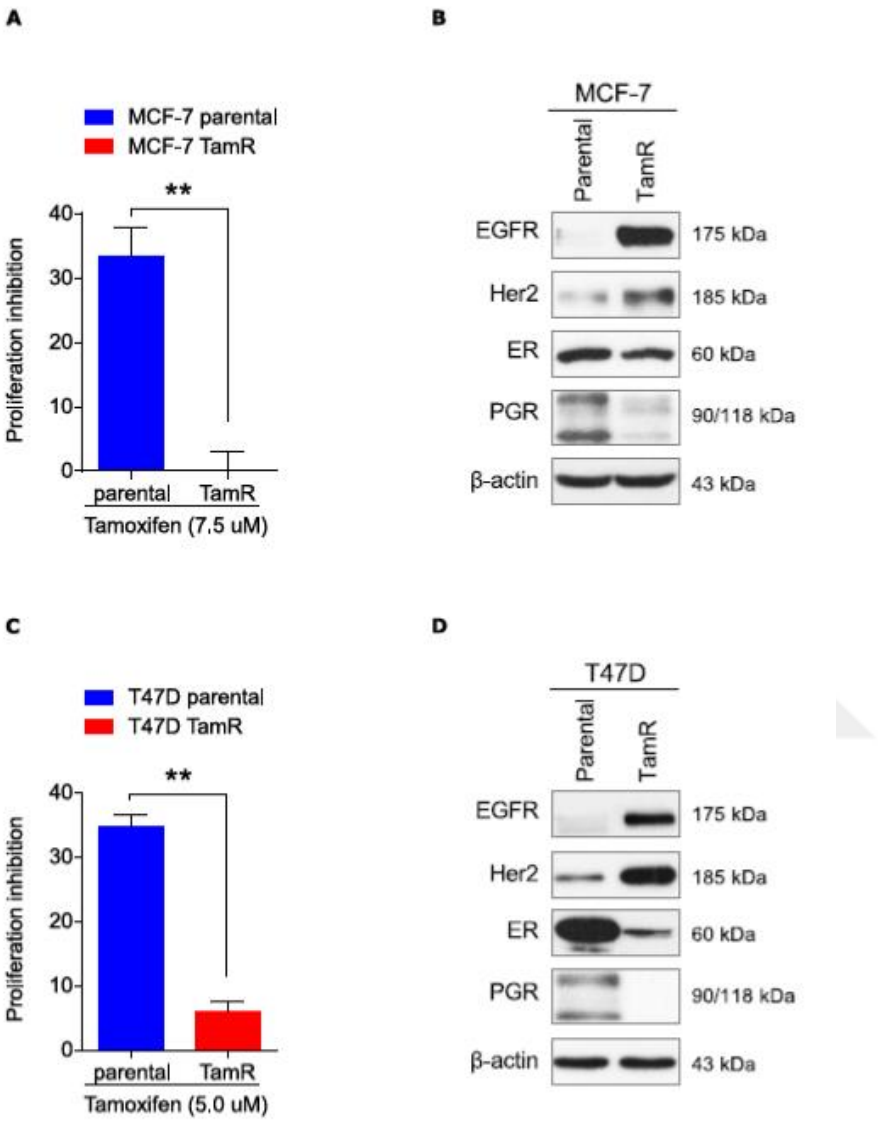
treated with aspirin, celecoxib, piroxicam and nimesulide were downloaded, and the average of gene ranks in two different instances was taken for each drug. Here, the genes are ranked in descending order based on the expression in treatment group relative to control group. Differential expression of genes upon aspirin treatment was determined based on a method as described (4). A relative gene rank was calculated as the relative ranking of a gene in aspirin treated MCF-7 cells versus the ranking in PC3 cells which are shown to be less responsive to aspirin than MCF-7 cells (5, 6). If a gene in our TamR-GS was ranked lower in MCF-7 cells than in the non-responsive PC3 cells upon aspirin treatment, then this gene was said to be upregulated by aspirin, and the relative ranking was calculated by taking the ratio of the ranking in PC3 to the ranking in MCF-7 cells. If a downregulated gene in our TamR-GS was found to be upregulated with aspirin, then it was taken as a reversed gene and vice versa. For those genes that showed opposite regulation between tamoxifen resistance and aspirin treatment, a similar analysis was also done for the other COX inhibitors (piroxicam and diclofenac) for generating heat map. Lapatinib responsive genes were taken from Hedge P.S. et al (7), where T47D cells were treated with a high dose of lapatinib and gene expression profiling was performed. The significance between TamR-GS and drug response signatures was calculated by Wilcoxon signed rank test. The aspirin responsive genes used to separate patients in GSE26971 was generated from a dataset of primary cultured colorectal cancer (CRC) cells which are treated with aspirin. 205 genes regulated by aspirin treatment of CRC cells (p-value<0.0001 and FC cut-off of 4) were common to our list of differentially expressed genes in tamoxifen resistance and used to generate the aspirin response score in patients from GSE26971 with the same method as described above.

Inhibitor treatments, cell proliferation and apoptosis assays

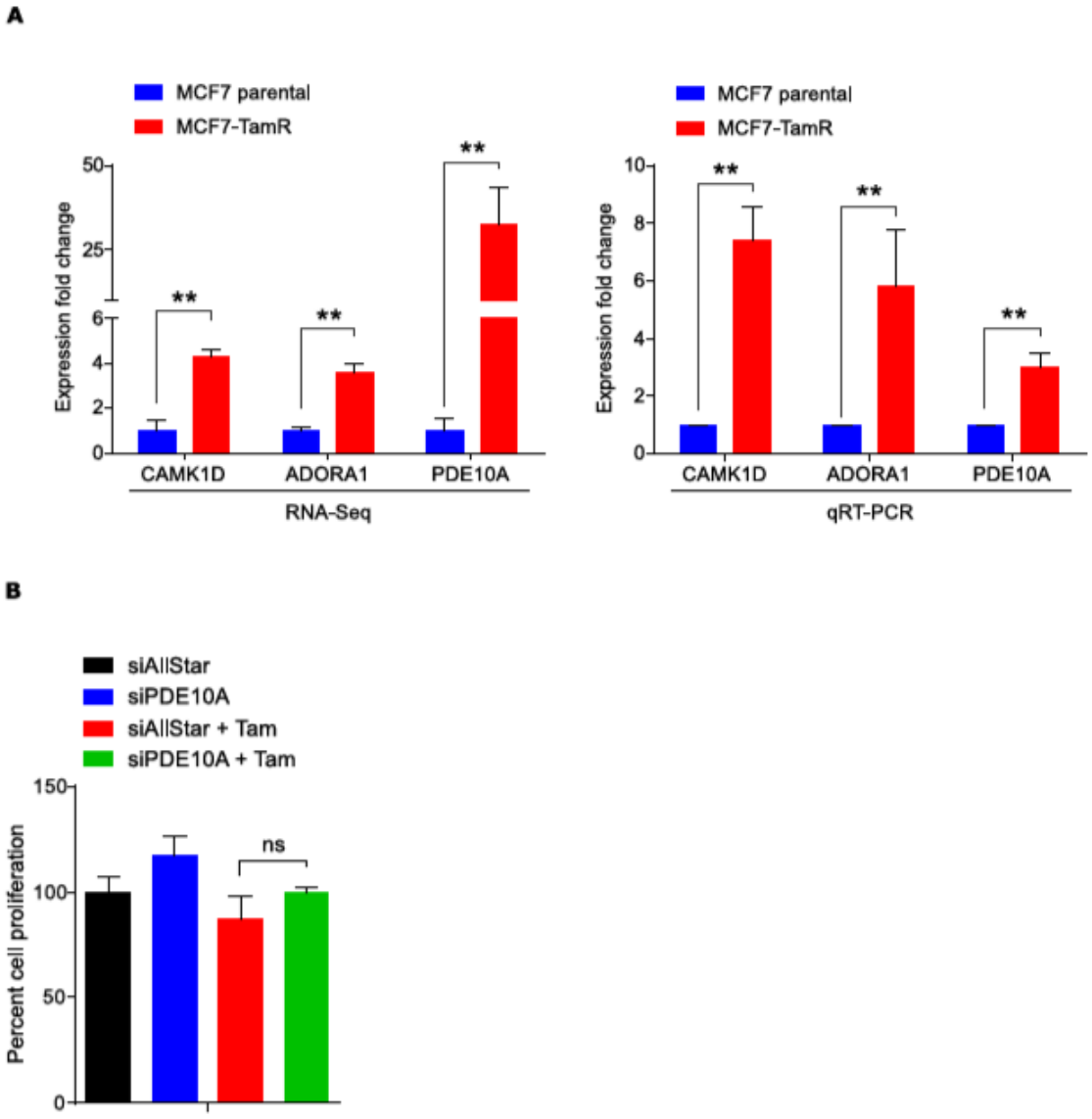
MCF-7 TamR and T47D TamR cells were seeded at a density of 6,000 and 5,000 cells/well in 96-well plates, respectively. Cells were treated with general or selective PDE4D inhibitors e.g., dipyridamole (1, 5 and 10 μM), or Gebr-7b (0.1, 1, 5 and 10 μg/ml) or aspirin (100, 200, 500 and 1000 μM) or with general cAMP analog cAMPS-Sp, triethylammonium salt (30, 100, and 300 μM) or PKA specific 6-Bnz-cAMP

sodium salt (10, 50, and 100 μM) or EPAC specific 8-pCPT-2-O-Me-cAMP-AM analog (1, 5, and 10 μM) alone or in combination with tamoxifen (7.5 μM and 5.0 μM for MCF-7 TamR and T47D TamR respectively). Following 72 h post-treatment, relative cell numbers were quantified using Cell Titer-Glo Luminescent Cell Viability Assay (Promega, USA), and apoptosis was assessed by Caspase-Glo 3/7 assay (Promega, WI, USA) according to the manufacturer's instructions. The relative apoptosis index was calculated by taking the ratio of the luminescence signal generated from the treated to untreated groups. This normalized luminescence value was defined as the relative apoptosis index, which was set to 1 for un-treated group. In other words, the relative index demonstrates the fold change of apoptosis in treated samples as compared to control.

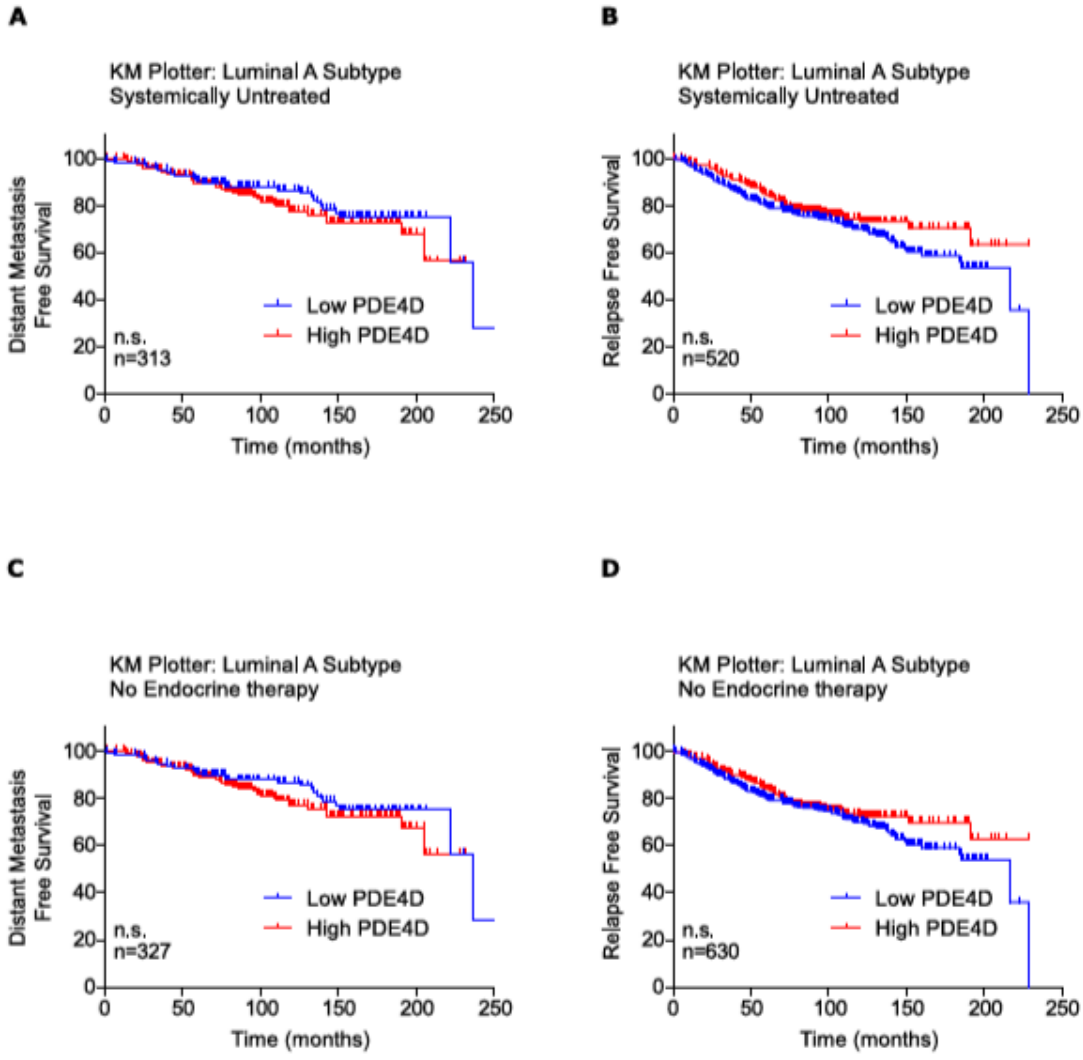
Supplementary Figures



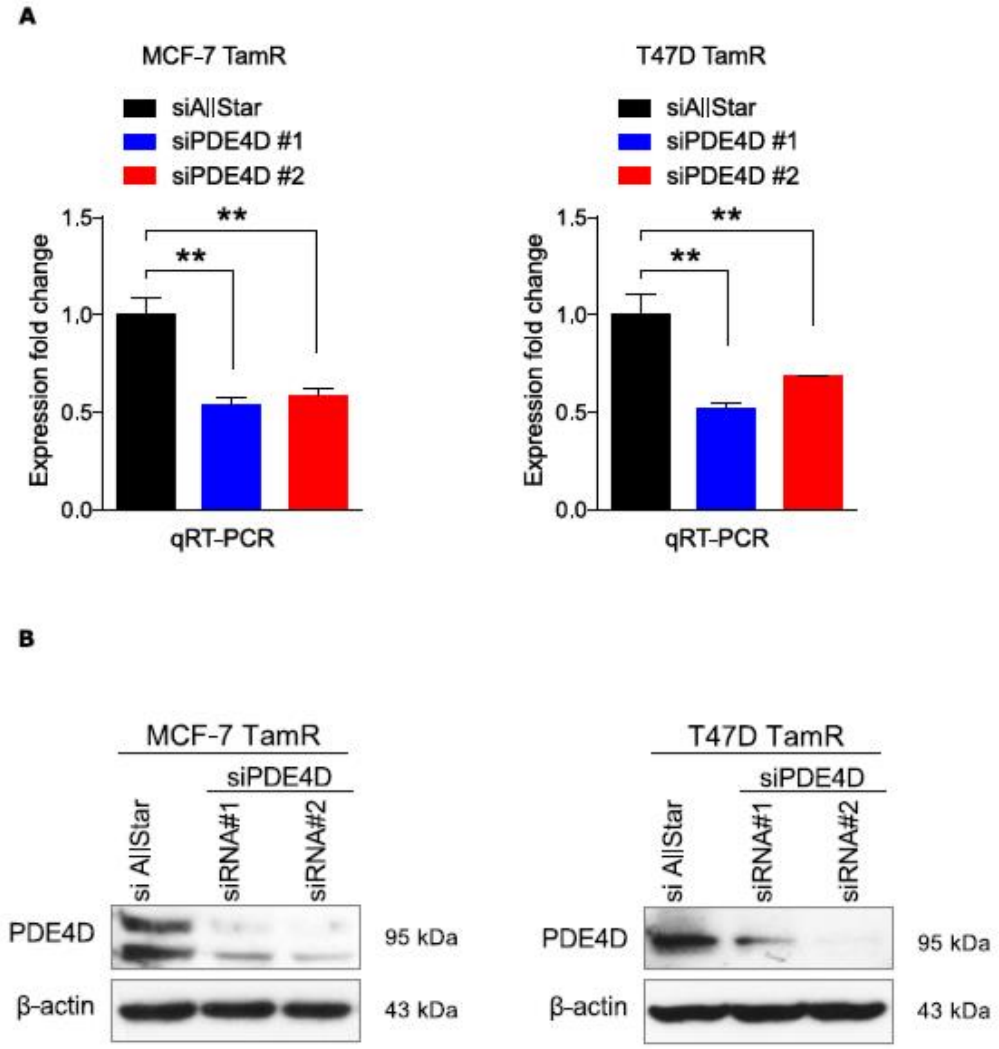
Supplementary Figure 1. Characterization of tamoxifen resistant MCF-7 and T47D cells. (A) Proliferation inhibition of parental and MCF-7 TamR cells in the presence of 7.5 uM tamoxifen. **(B)** Western blot analysis of molecular markers of tamoxifen resistance e.g. EGFR, HER2, ER and PR in parental and MCF-7 TamR cells. **(C)** Proliferation inhibition of parental and T47D TamR cells in the presence of 5 uM tamoxifen. **(D)** Western blot analysis of molecular markers of tamoxifen resistance e.g. EGFR, HER2, ER and PR in parental T47D and TamR cells. β-actin was used as a loading control.



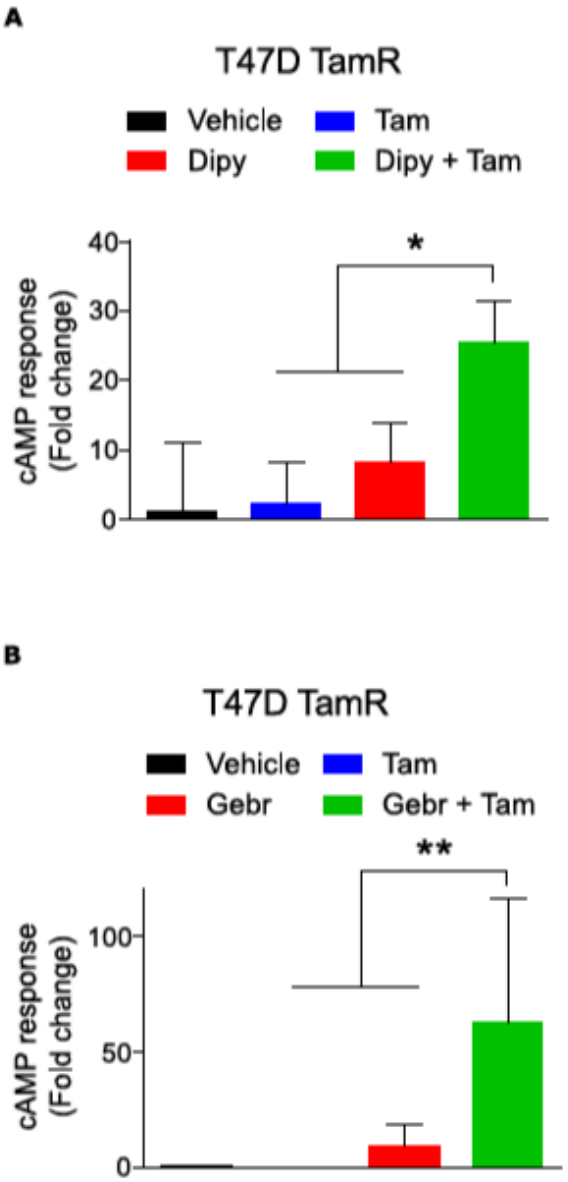
Supplementary Figure 2. Validation of RNA-Seq results by qRT-PCR and testing tamoxifen sensitization by siRNA knockdown of PDE10A in MCF-7 TamR cells. (A) Expression of three cAMP pathway genes in MCF-7 TamR cells compared with parental MCF-7 cells in RNA-Seq data (left panel) and the qRT-PCR validation (right panel). FPKM values were used to calculate expression fold change in the RNA-Seq data. **(B)** Cell proliferation of MCF-7 TamR cells transfected with siRNA sequences against PDE10A in the absence and presence of tamoxifen. The concentration of tamoxifen used was 7.5 µM.



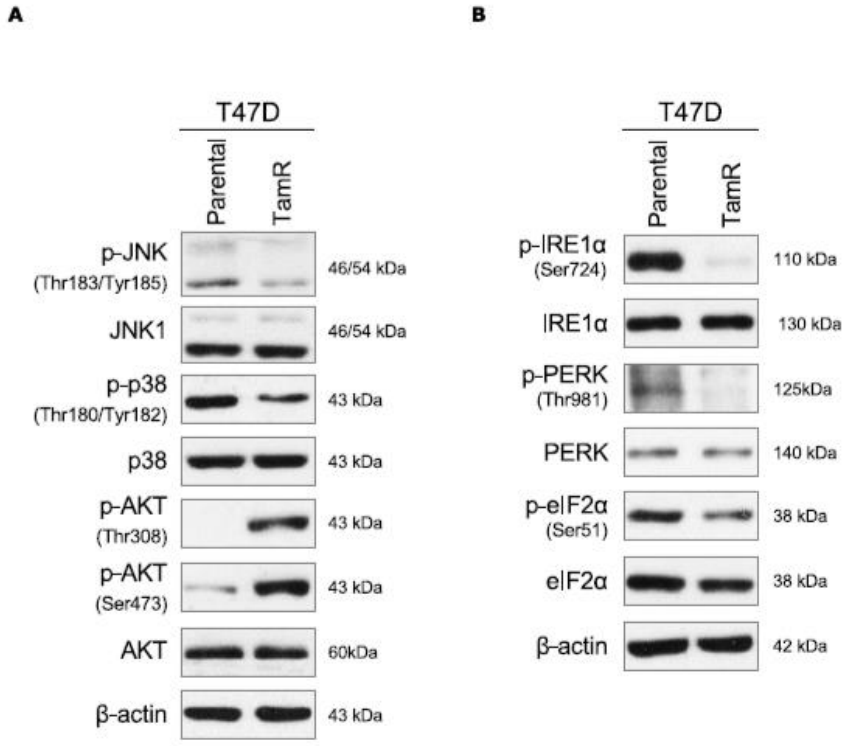
Supplementary Figure 3. Survival analyses in high and low PDE4D-expressing Luminal A breast cancer. Distant-metastasis-free- (left panel) and relapse-free-survival (right panel) of luminal A breast cancer patients who did not receive any type of therapy (systemically untreated) **(A)** or of patients who received therapies other than endocrine therapy **(B)** with respect to PDE4D expression.



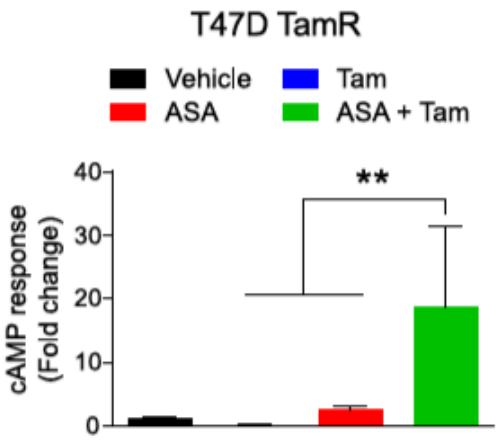
Supplementary Figure 4. Validation of PDE4D knockdown in MCF-7 TamR and T47D TamR cells. **(A)** qRT-PCR validation of PDE4D knockdown in MCF-7 TamR and T47D TamR cells. **(B)** Western blot analysis of PDE4D in MCF-7 TamR and T47D TamR cells treated with two different siRNAs. β-actin was used as a loading control.



Supplementary Figure 5. Intracellular cAMP levels upon PDE or PDE4D inhibitors in combination with tamoxifen in T47D TamR cells. Intracellular cAMP levels in T47D TamR cells upon treatment with tamoxifen in combination with **(A)** PDE inhibitor (dipyridamole) or **(B)** PDE4D inhibitor (Gebr-7b).



Supplementary Figure 6. Western blot analysis of stress-related kinases and ER stress markers in T47D WT and TamR cells. (A) Western blot analysis of stress-related kinases (JNK and p38) and Akt pathway in T47D WT and TamR cells. **(B)** Western blot analysis of ER stress-related proteins in T47D WT and T47D TamR cells. β-actin was used as a loading control.



Supplementary Figure 7. Intracellular cAMP levels upon aspirin in combination with tamoxifen in T47D TamR cells.

Supplementary Tables

Table S1. List of primers used for qRT-PCR.

Gene	**Primer Sequence**
PDE4D	Foward: 5'- CCACGATAGCTGCTCAAACAA -'3
	Reverse: 5'- GTGCCATTGTCCACATCAAAA -'3
ACTB	Foward: 5'- CCAACCGCGAGAAGATGA -'3
	Reverse: 5'- CCAGAGGCGTACAGGGATAG -'3
HPRT	Foward: 5'- TGACCTTGATTTATTTTGCATACC -'3
	Reverse: 5'- CGAGCAAGACGTTCAGTCCT -'3
GAPDH	Foward: 5'- GCCCAATACGACCAAATCC -'3
	Reverse: 5'- AGCCACATCGCTCAGACAC -'3

Table S2. List of siRNAs with their catalog numbers

siRNA	**Cat. No.**	**Company**
PDE4D #1	D-004757-01	Dharmacon
PDE4D #2	D-004757-02	Dharmacon

Table S3. List of antibodies used for western blot (WB)

Primary Antibodies	Species	WB	Supplier / Cat. No.
PDE4D	Rabbit	1:1250	Santa Cruz/ sc-25814
EGFR	Rabbit	1:1000	Cell signaling / 2646
Her2	Mouse	1:1000	Thermo Fisher/ MA5-13105
ER	Mouse	1:1000	Santa Cruz/ sc-8002
PGR	Rabbit	1:1000	Santa Cruz/ sc-7208
p-ERK (Thr202/Tyr204)	Rabbit	1:1000	Cell signaling/ 4376
ERK	Rabbit	1:1000	Cell signaling/ 4695
p-JNK (Thr183/Tyr185)	Rabbit	1:2000	Cell signaling/ 4668
JNK1	Mouse	1:1000	Cell signaling/ 3708
p-p38 (Thr180/Tyr182)	Rabbi	1:2000	Cell signaling/ 4511
p38	Rabbi	1:2000	Cell signaling/ 9212
p-AKT (Thr308)	Rabbit	1:1000	Cell signaling/ 4056
p-AKT (Ser473)	Rabbit	1:1000	Cell signaling/ 4058
AKT	Rabbit	1:1000	Cell signaling/ 9272
p-CREB (S133)	Rabbit	1:3000	Cell signaling/ 9198
CREB	Rabbit	1:2000	Cell signaling/ 4820
p-IRE1α (S724)	Rabbit	1:3000	Abcam/ ab124945
IRE1α	Rabbit	1:1000	Cell signaling/ 3294
p-PERK (Thr981)	Rabbit	1:1000	Santa Cruz/ sc32577
PERK	Rabbit	1:2000	Cell signaling/ 5683
p-eIF2α (Ser51)	Rabbit	1:1000	Cell signaling/ 3597
eIF2α	Rabbit	1: 2000	Santa Cruz/ sc11386
Cleaved Caspase 7 (Asp198)	Rabbit	1:1000	Cell signaling/ 8438
Cleaved PARP (Asp214))	Rabbit	1:1000	Cell signaling/ 5625
DYKDDDDK-Tag Antibody	Mouse	1:1000	GenScript/ A00187
β-actin	Mouse	1:20000	MP Biomedicals / 691001

Table S4. Significantly differentially expressed genes between parental and resistant MCF-7 cells in TamR-GS

Gene name	log2 (fold_change)	q_value	Gene name	log2 (fold_change)	q_value
CDH12	-7.24	0.000697	TRPC6	-4.16	0.000697
ATP6V0D2	-7.23	0.000697	KLK7	-4.13	0.010069
CALCR	-6.98	0.000697	ME3	-4.11	0.000697
KLK11	-6.71	0.000697	AMER2	-4.08	0.000697
FXYD4	-6.35	0.000697	CDH26	-4.05	0.000697
MAOB	-6.04	0.000697	FBXO2	-4.01	0.000697
CA2	-5.83	0.000697	FYB	-4.00	0.000697
GALNT5	-5.79	0.039244	C3orf70	-3.99	0.000697
TMEM26	-5.73	0.000697	GALNT13	-3.97	0.000697
LDHB	-5.59	0.000697	COL12A1	-3.96	0.000697
KRT13	-5.53	0.000697	INHBA	-3.96	0.005769
KLHL4	-5.48	0.000697	SCEL	-3.94	0.001884
HS3ST3A1	-5.48	0.000697	SERPINA1	-3.94	0.000697
CDH18	-5.40	0.000697	ERBB4	-3.88	0.000697
SLC38A11	-5.40	0.001315	RBP7	-3.88	0.000697
NPR1	-5.27	0.000697	HLA-DRB1	-3.87	0.000697
RGS22	-5.13	0.000697	FUT3	-3.86	0.000697
AGR3	-5.08	0.000697	SRSF10	-3.85	0.000697
SLC9A4	-4.87	0.000697	KLK8	-3.81	0.000697
PZP	-4.82	0.000697	KLK9	-3.81	0.000697
PKHD1L1	-4.80	0.000697	GJA1	-3.80	0.000697
STAT6	-4.77	0.000697	SIGLEC15	-3.80	0.000697
BMPER	-4.73	0.000697	SLITRK4	-3.78	0.000697
TNFSF10	-4.71	0.000697	PSAPL1	-3.77	0.015134
KIAA0226L(RUBCNL-010)	-4.67	0.000697	KLK12	-3.71	0.000697
ZCCHC11	-4.66	0.000697	FBLN2	-3.70	0.000697
LOXL1	-4.63	0.000697	ARHGAP36	-3.70	0.000697
RFX8	-4.55	0.000697	KCNV1	-3.69	0.003402
PGR	-4.52	0.000697	C3orf30	-3.69	0.000697
TMTC1	-4.42	0.000697	RP11-484M3.5	-3.69	0.000697
GRIK2	-4.37	0.000697	UPK1B	-3.69	0.000697
EPHA7	-4.29	0.000697	UGT2B15	-3.66	0.003402
MUC5AC	-4.28	0.000697	AKR1C2	-3.65	0.000697
MYO3B	-4.26	0.000697	RIN1	-3.63	0.000697
TNFSF12	-4.17	0.01286	HLA-DRB5	-3.57	0.000697
TNFSF13	-4.17	0.01286	GPER1	-3.57	0.024799

Gene name	log2 (fold_change)	q_value	Gene name	log2 (fold_change)	q_value
GLRA3	-3.54	0.000697	TENM3	-3.00	0.000697
RAMP3	-3.53	0.000697	SERPINA3	-2.99	0.000697
CCDC85A	-3.52	0.000697	SERPINA4	-2.99	0.000697
SGK1	-3.51	0.000697	SERPINA5	-2.99	0.000697
SH3RF2	-3.50	0.000697	CAPN12	-2.97	0.001315
EVPLL	-3.49	0.001884	NMNAT2	-2.95	0.000697
SYBU	-3.48	0.000697	C6orf141	-2.94	0.000697
MITF	-3.47	0.010069	EXOC3L4	-2.92	0.001315
VILL	-3.47	0.000697	ASCL1	-2.90	0.000697
SCGB3A2	-3.46	0.000697	IPCEF1	-2.90	0.000697
NPY1R	-3.41	0.000697	MCOLN2	-2.89	0.000697
NIM1K	-3.39	0.000697	PTPRH	-2.89	0.000697
TNFAIP2	-3.36	0.000697	SORCS2	-2.88	0.000697
ARMCX4	-3.34	0.000697	SPRR3	-2.88	0.000697
NECAB1	-3.32	0.019054	WLS	-2.87	0.000697
RYR1	-3.27	0.000697	SNAI2	-2.87	0.000697
TLR2	-3.27	0.001315	TSPAN2	-2.86	0.000697
IFNLR1	-3.21	0.000697	BPIFB1	-2.86	0.000697
PTHLH	-3.21	0.000697	STAT5A	-2.84	0.000697
CITED4	-3.20	0.000697	CACNA1C	-2.83	0.000697
ACOT11	-3.17	0.000697	ITGAL	-2.82	0.000697
CAPS2	-3.17	0.000697	TMEM64	-2.80	0.000697
SRPX2	-3.15	0.008821	HS3ST5	-2.80	0.033841
CREG2	-3.13	0.000697	PIK3R5	-2.79	0.000697
KLK13	-3.13	0.000697	COL21A1	-2.77	0.000697
ANKRD35	-3.11	0.000697	ST6GALNAC1	-2.77	0.000697
KCNK2	-3.10	0.000697	LUZP2	-2.77	0.001884
FCGR2A	-3.10	0.004394	EHD2	-2.76	0.002911
FCGR2B	-3.10	0.000697	AKR1C1	-2.74	0.000697
SYTL4	-3.09	0.000697	AKR1C3	-2.74	0.000697
STC1	-3.09	0.000697	DIRAS2	-2.69	0.000697
PDZRN3	-3.06	0.000697	PRTFDC1	-2.68	0.000697
ADAM2	-3.05	0.000697	NPTX1	-2.68	0.000697
CPA6	-3.05	0.000697	ZNF488	-2.68	0.000697
ELOVL2	-3.04	0.000697	VWA3B	-2.67	0.000697
GALM	-3.03	0.045613	GSTA1	-2.66	0.000697
SCARA5	-3.03	0.000697	GSTA2	-2.66	0.000697
RNF183	-3.02	0.01286	CILP2	-2.64	0.000697
CCDC153	-3.01	0.000697	APOD	-2.63	0.000697

Gene name	log2 (fold_change)	q_value	Gene name	log2 (fold_change)	q_value
BCAN	-2.62	0.012071	PLLP	-2.28	0.000697
TMEM255B	-2.60	0.000697	SLPI	-2.26	0.000697
MICALCL	-2.58	0.002405	ADAMTS9	-2.25	0.000697
RAB31	-2.58	0.000697	IGSF1	-2.25	0.000697
GP1BB	-2.56	0.000697	TIMP2	-2.23	0.000697
SEPT5	-2.56	0.000697	ARL11	-2.23	0.000697
C10orf107	-2.56	0.030038	SARDH	-2.23	0.000697
PTGES	-2.54	0.000697	HCK	-2.22	0.000697
RBM24	-2.54	0.000697	INPP1	-2.21	0.003402
TMEM106A	-2.53	0.029405	CTSS	-2.20	0.02281
SLC52A1	-2.53	0.000697	MAPK13	-2.19	0.037803
GLA	-2.52	0.000697	SUGCT	-2.19	0.006685
FAM198B	-2.50	0.000697	BMP5	-2.18	0.000697
ARHGAP26	-2.50	0.000697	CYP4F8	-2.18	0.026113
SCUBE2	-2.46	0.000697	DOCK10	-2.18	0.000697
LAMC2	-2.45	0.000697	PMAIP1	-2.15	0.000697
RGCC	-2.45	0.024494	NXPH3	-2.15	0.000697
FHL1	-2.41	0.000697	KLK5	-2.15	0.000697
SDK2	-2.41	0.000697	KLK6	-2.15	0.000697
CAPN9	-2.38	0.000697	TTLL10	-2.15	0.02969
LRRIQ3	-2.38	0.004394	PCDH7	-2.14	0.000697
ATRNL1	-2.38	0.000697	COL4A5	-2.12	0.000697
KIAA1377 (CEP126)	-2.37	0.000697	GULP1	-2.12	0.000697
HEY2	-2.37	0.000697	TGFBR2	-2.12	0.000697
ADAMTSL3	-2.37	0.000697	DCLK1	-2.12	0.000697
MAP2K6	-2.37	0.000697	COL6A3	-2.11	0.000697
HLA-DQB1	-2.35	0.000697	AGR2	-2.11	0.000697
TRIB2	-2.35	0.000697	GCNT4	-2.11	0.000697
C3	-2.34	0.019054	AGT	-2.10	0.000697
ITGAM	-2.34	0.045056	FAHD2B	-2.06	0.000697
PCP4L1	-2.33	0.000697	NXNL2	-2.04	0.000697
DPYD	-2.32	0.000697	NCCRP1	-2.04	0.000697
OSBPL3	-2.31	0.008411	FBN1	-2.04	0.000697
STX11	-2.31	0.001884			
NEK9	-2.30	0.016623			
SULF1	-2.29	0.000697			
CDKN1C	-2.28	0.000697			
C1orf106	-2.28	0.000697			
WDR90	-2.28	0.000697			

Gene name	log2 (fold_change)	q_value	Gene name	log2 (fold_change)	q_value
DMRTA1	2.00	0.008411	AREG	2.22	0.000697
ARHGEF6	2.01	0.000697	IGF2BP2	2.22	0.006685
GALNT12	2.01	0.000697	SEMA5B	2.23	0.000697
ELF5	2.03	0.000697	EBF4	2.23	0.000697
QDPR	2.03	0.000697	RGS16	2.23	0.000697
FAM231D	2.03	0.038412	AOX1	2.23	0.000697
CLCN4	2.04	0.000697	SNTG2	2.25	0.001315
SORL1	2.04	0.000697	GPNMB	2.26	0.000697
MYLK3	2.04	0.013989	RNF144A	2.27	0.000697
PAQR5	2.05	0.045613	JDP2	2.27	0.000697
APBB1IP	2.06	0.00756	ANXA6	2.27	0.000697
MSRB3	2.06	0.024799	SLC6A17	2.30	0.003402
FBXO42	2.06	0.010069	FER1L6	2.31	0.000697
ALDH3B2	2.07	0.000697	PARP9	2.31	0.000697
PNCK	2.08	0.000697	LAMB1	2.32	0.001884
FOXI1	2.08	0.000697	CLCA2	2.32	0.000697
PPFIBP2	2.09	0.000697	KCNK3	2.34	0.000697
CAMK1D	2.10	0.000697	ASS1	2.34	0.000697
NMU	2.11	0.000697	BCAT1	2.34	0.000697
TXNIP	2.11	0.000697	PGM5	2.35	0.000697
CD82	2.11	0.000697	IFIH1	2.36	0.000697
BATF2	2.11	0.001884	CTRB1	2.37	0.000697
FLT3	2.12	0.000697	IRX3	2.38	0.000697
ERG	2.12	0.000697	SCUBE3	2.39	0.000697
LAMP3	2.12	0.003402	GTF2A1L	2.39	0.000697
NLRP1	2.13	0.023172	STON1	2.39	0.000697
UPK3A	2.13	0.000697	KIF12	2.40	0.000697
CDKL2	2.13	0.001315	MX2	2.40	0.003402
PRKD1	2.14	0.000697	ANKH	2.41	0.000697
ACOX2	2.14	0.000697	PTGER4	2.43	0.000697
SPRY1	2.15	0.000697	UBE2L6	2.43	0.000697
FAXC	2.15	0.000697	KCNMA1	2.43	0.001315
MT1X	2.16	0.000697	PHGDH	2.44	0.000697
MT2A	2.16	0.000697	GNAI1	2.45	0.006222
ADAMTS15	2.19	0.000697	CHRM1	2.45	0.003402
ADCY7	2.19	0.000697	NCR3LG1	2.47	0.000697
WNT5B	2.19	0.027773	AKAP6	2.47	0.000697
ZNF827	2.19	0.001884	GHR	2.47	0.001884
EGFR	2.21	0.000697	SERHL2	2.49	0.000697

Gene name	log2 (fold_change)	q_value	Gene name	log2 (fold_change)	q_value
SYT12	2.49	0.000697	C2orf54	2.94	0.000697
SLC7A5	2.49	0.000697	ATP6V0A4	2.94	0.000697
CRAT	2.50	0.000697	AMBP	2.95	0.000697
TSPEAR	2.52	0.000697	CHST11	2.95	0.000697
ADAMTS20	2.52	0.000697	CPVL	2.98	0.001884
FGFR4	2.52	0.000697	HOPX	2.98	0.000697
C15orf59	2.54	0.000697	PDE4D	2.98	0.000697
PTGER3	2.55	0.007125	ABCA4	2.99	0.000697
NPR3	2.55	0.000697	IL34	2.99	0.002405
ADM2	2.57	0.000697	PRKAA2	3.00	0.000697
FGFBP2	2.58	0.000697	VSTM2L	3.00	0.000697
PROM1	2.58	0.000697	CDH5	3.00	0.000697
LDLRAD4	2.59	0.000697	KCNB1	3.06	0.00756
EYA4	2.60	0.000697	ABCC11	3.10	0.001315
PPP1R9A	2.60	0.000697	GPR65	3.11	0.000697
SLC18B1	2.60	0.000697	FGD5	3.12	0.009249
BANK1	2.60	0.000697	TGFB3	3.12	0.000697
TM4SF4	2.61	0.026467	NFIA	3.13	0.000697
FXYD2	2.61	0.000697	LIMCH1	3.15	0.000697
FXYD6	2.61	0.000697	UBE2QL1	3.15	0.000697
RND1	2.62	0.000697	CTRB2	3.21	0.000697
SERTAD2	2.62	0.000697	IRF8	3.22	0.000697
MCTP1	2.62	0.000697	GABRP	3.23	0.000697
FSTL5	2.65	0.000697	CNGB1	3.23	0.000697
FFAR2	2.68	0.000697	TM4SF18	3.27	0.000697
CXADR	2.69	0.000697	SLC25A27	3.28	0.000697
CAMP	2.71	0.036551	RCN1	3.30	0.000697
OSBPL6	2.72	0.000697	BTC	3.30	0.000697
MME	2.73	0.000697	RCAN1	3.32	0.000697
NCBP2L	2.73	0.000697	DSC2	3.36	0.000697
NOTUM	2.73	0.001315	GJA3	3.36	0.000697
ABCG2	2.77	0.000697	VWDE	3.37	0.000697
WDFY4	2.80	0.000697	FAM84A	3.45	0.000697
SLC28A2	2.80	0.014378	AUTS2	3.50	0.000697
ALDH1L2	2.82	0.001884	OAS2	3.51	0.012451
CCR1	2.85	0.002911	RSAD2	3.60	0.004849
C1QL4	2.87	0.000697	ATP8A2	3.69	0.000697
ZNF347	2.89	0.008411	GRAMD2	3.71	0.005769
PLCB2	2.89	0.000697	TNFSF15	3.73	0.000697

Gene name	log2 (fold_change)	q_value	Gene name	log2 (fold_change)	q_value
SLC6A19	3.76	0.000697	UMODL1	4.46	0.000697
CMPK2	3.80	0.000697	RFTN1	4.57	0.000697
INHA	3.84	0.000697	CLDN1	4.67	0.000697
GALNT14	3.84	0.000697	GLYATL2	4.67	0.000697
SYNPO	3.86	0.000697	KCNMB1	4.72	0.001315
MUM1L1	3.89	0.000697	PRRT4	4.76	0.000697
TTYH1	3.94	0.000697	SLC25A48	4.77	0.000697
ANO2	3.94	0.000697	LEMD1	4.88	0.000697
DLX2	3.95	0.000697	WNT11	4.95	0.000697
TM4SF1	4.00	0.000697	STXBP6	4.98	0.000697
SGCE	4.01	0.000697	PDE10A	5.02	0.002405
GUCY1A2	4.02	0.000697	ZNF175	5.07	0.004394
JAKMIP2	4.04	0.000697	EHF	5.10	0.000697
SPINK1	4.05	0.000697	LRFN5	5.14	0.000697
SYT13	4.09	0.000697	EPGN	5.24	0.000697
NUPR1	4.12	0.000697	PLS3	5.28	0.000697
BFSP2	4.12	0.001315	KRT81	5.47	0.000697
FPR1	4.22	0.01126	PEG10	6.66	0.000697
EIF4E1B	4.31	0.000697	ARHGAP6	7.00	0.000697
DDX60	4.33	0.000697			

Table S5. Multivariate analysis performed in GSE6532 by selecting PDE4D, age, tumor grade and size as covariates

Parameter	Univariate analysis (p-value)	Multivariate analysis (p-value)
PDE4D	0.024	0.049
AGE	0.240	0.055
Tumor Grade	0.110	0.243
Tumor Size	0.053	0.320

Supplementary References

1. Trapnell C, Roberts A, Goff L, Pertea G, Kim D, Kelley DR, et al. Differential gene and transcript expression analysis of RNA-seq experiments with TopHat and Cufflinks. Nat Protoc. 2012;7(3):562-78.

2. Filipits M, Rudas M, Jakesz R, Dubsky P, Fitzal F, Singer CF, et al. A new molecular predictor of distant recurrence in ER-positive, HER2-negative breast cancer adds independent information to conventional clinical risk factors. Clin Cancer Res. 2011;17(18):6012-20.
3. Lamb J, Crawford ED, Peck D, Modell JW, Blat IC, Wrobel MJ, et al. The Connectivity Map: using gene-expression signatures to connect small molecules, genes, and disease. Science. 2006;313(5795):1929-35.
4. Chen B, Ma L, Paik H, Sirota M, Wei W, Chua MS, et al. Reversal of cancer gene expression correlates with drug efficacy and reveals therapeutic targets. Nat Commun. 2017;8:16022.
5. Olivan M, Rigau M, Colas E, Garcia M, Montes M, Sequeiros T, et al. Simultaneous treatment with statins and aspirin reduces the risk of prostate cancer detection and tumorigenic properties in prostate cancer cell lines. Biomed Res Int. 2015;2015:762178.
6. Sali P, Jewell AP. IL-1 does not reverse the anti-proliferative effect of aspirin in breast cancer cells. Int Semin Surg Oncol. 2006;3:24.
7. Hegde PS, Rusnak D, Bertiaux M, Alligood K, Strum J, Gagnon R, et al. Delineation of molecular mechanisms of sensitivity to lapatinib in breast cancer cell lines using global gene expression profiles. Mol Cancer Ther. 2007;6(5):1629-40.